MACROMOLECULES CONTAINING METAL and METAL-LIKE ELEMENTS

VOLUME 10

Photophysics and Photochemistry of Metal-Containing Polymers

Edited by

ALAA S. ABD-EL-AZIZ

CHARLES E. CARRAHER, Jr.

PIERRE D. HARVEY

CHARLES U. PITTMAN, Jr.

MARTEL ZELDIN

Macromolecules Containing Metal and Metal-Like Elements

Volume 10

Macromolecules Containing Metal and Metal-Like Elements

Volume 10

Photophysics and Photochemistry of Metal-Containing Polymers

Edited by

Alaa S. Abd-El Aziz
University of British Columbia Okanagan, Kelowna, British Columbia, Canada

Charles E. Carraher, Jr.
Department of Chemistry and Biochemistry, Florida Atlantic University, Boca Raton, Florida, and Florida Center for Environmental Studies, Palm Beach Gardens, Florida

Pierre D. Harvey
Department of Chemistry, University of Sherbrooke, Sherbrooke, Québec, Canada

Charles U. Pittman, Jr.
Department of Chemistry, Mississippi State University, Mississippi State, Mississippi

Martel Zeldin
Department of Chemistry, University of Richmond, Richmond, Virginia

A JOHN WILEY & SONS, INC., PUBLICATION

Published by John Wiley & Sons, Inc., Hoboken, New Jersey
Published simultaneously in Canada

Library of Congress Cataloging-in-Publication Data:

ISBN 978-0-470-59774-3
ISSN 1545-438X

Printed in the United States of America

10 9 8 7 6 5 4 3 2 1

Contributors

Cetin Aktik, Bishop's University, Sherbrooke, Québec, Canada

Shawkat M. Aly, University of Sherbrooke, Sherbrooke, Québec, Canada

Yong Cao, South China University of Technology, Guangzhou, China

Charles E. Carraher, Jr. Florida Atlantic University, Boca Raton, Florida

Wai Kin Chan, The University of Hong Kong, Hong Kong, China

Chi-Ming Che, The University of Hong Kong, Hong Kong, China

Junwu Chen, South China University of Technology, Guangzhou, China

Sébastien Clément, University of Sherbrooke, Sherbrooke, Québec, Canada

Bevin Daglen, University of Oregon, Eugene, Oregon

Starr Dostie, Bishop's University, Sherbrooke, Québec, Canada

Fabrice Guyon, Université Franche-Comté, Besançon, France

Pierre D. Harvey, University of Sherbrooke, Sherbrooke, Québec, Canada

Jérôme Husson, Université de Franche-Comté, Besançon, France

Michael Knorr, Université de Franche-Comté, Besançon, France

Chi-Chung Kwok, The University of Hong Kong, Hong Kong, China

Antonio Laguna, University of Zaragoza, Zaragoza, Spain

José M. López-de-Luzuriaga, University of La Rioja, Logroño, Spain

Chris S. K. Mak, The University of Hong Kong, Hong Kong, China

Mariko Miyachi, The University of Tokyo, Tokyo, Japan

Hiroshi Nishihara, The University of Tokyo, Tokyo, Japan

Mihai Scarlete, Bishop's University, Sherbrooke, Québec, Canada

Ginger V. Shultz, University of Oregon, Eugene, Oregon

Ben Zhong Tang, The Hong Kong University of Science & Technology, Hong Kong, China

David R. Tyler, University of Oregon, Eugene, Oregon

Wai-Yeung Wong, Hong Kong Baptist University, Hong Kong, China

Contents

Preface

This volume of the series focuses on the photochemistry and photophysics of metal-containing polymers. Metals imbedded within macromolecular protein matrices form the basis for the photosynthesis of plants. Metal–polymer complexes form the basis for many revolutionary advances occurring now. The contributors to many of these advances are authors of chapters in this volume. Application areas covered in this volume include nonlinear optical materials, solar cells, light-emitting diodes, photovoltaic cells, field-effect transistors, chemosensing devices, and biosensing devices. At the heart of each of these applications are metal atoms that allow the assembly to function as required. The use of boron-containing polymers in various electronic applications was described in Volume 8 of this series.

This volume begins with an introduction to some basic photophysics and photochemistry concepts. Chapter 2 deals with luminescent properties of isocyanides bridges chelating various metals forming conjugated structures. Chapter 3 deals with copper polymers assembled by thioether ligands and the properties induced by various geometrical assemblies. Chapter 4 covers metal-containing polymers in forming organic solar cells. These materials include dye-sensitized solar cells and organic thin-film solar cells derived from ruthenium complexes, polyferrocenylsilanes, platinum acetylides, hyperbranched materials, and other metal-containing polymers. The use of functional silolane-containing polymers in light production, photovoltaic cells, field-effect transistors, and chemosensors is described in Chapter 5. The use of polysilane thin films for electronic and optical device applications is reviewed in Chapter 6. While chemists have spent much effort to understand and prevent degradation of materials, recent efforts to generate materials that purposely degrade have accelerated as part of green materials research. Chapter 7 describes studies to promote desired degradation behavior in materials through the use of metal-containing polymers. Platinum-containing poly(aryleneethynylene)s offer useful optical and photophysical properties, allowing their use in phosphorescence color tuning, optoelectronic and photonic devices, optical power limiters, light-emitting devices, and in the construction of photovoltaic cells. These platinum-containing polymers are described in Chapter 8. The synthesis of a wide range of polymetalic gold derivatives is described in Chapter 9. Gold offers some distinct advantages over other metals in having the lowest electrochemical

potential, being the most electronegative, possibility having a mononegative oxidation state, and in forming diatomic molecules in the vapor state whose dissociation energy is higher than other diatomic molecules. These characteristics are employed to make potentially useful luminescent materials. The formation of various functional self-assembled zinc coordination polymers is described in Chapter 10. Such materials have potential application in polymer light-emitting devices. The construction of biophotosensors and biophotoelectrodes from metal complex oligomers and polymers is described in Chapter 11.

Overall, this volume describes what is possible with metal-containing polymers when the metal is an essential ingredient in obtaining desired optical and electronic properties.

Series Preface

Most traditional macromolecules are composed of less than 10 elements (mainly C, H, N, O, S, P, C1, F), whereas metal and semi-metal-containing polymers allow properties that can be gained through the inclusion of nearly 100 additional elements. Macromolecules containing metal and metal-like elements are widespread in nature with metalloenzymes supplying a number of essential physiological functions including respiration, photosynthesis, energy transfer, and metal ion storage.

Polysiloxanes (silicones) are one of the most studied classes of polymers. They exhibit a variety of useful properties not common to non-metal-containing macromolecules. They are characterized by combinations of chemical, mechanical, electrical, and other properties that, when taken together, are not found in any other commercially available class of materials. The initial footprints on the moon were made by polysiloxanes. Polysiloxanes are currently sold as high-performance caulks, lubricants, antifoaming agents, window gaskets, O-rings, contact lens, and numerous and variable human biological implants and prosthetics, to mention just a few of their applications.

The variety of macromolecules containing metal and metal-like elements is extremely large, not only because of the large number of metallic and metalloid elements, but also because of the diversity of available oxidation states, the use of combinations of different metals, the ability to include a plethora of organic moieties, and so on. The appearance of new macromolecules containing metal and metal-like elements has been enormous since the early 1950s, with the number increasing explosively since the early 1990s. These new macromolecules represent marriages among many disciplines, including chemistry, biochemistry, materials science, engineering, biomedical science, and physics. These materials also form bridges between ceramics, organic, inorganic, natural and synthetic, alloys, and metallic materials. As a result, new materials with specially designated properties have been made as composites, single- and multiple-site catalysts, biologically active/inert materials, smart materials, nanomaterials, and materials with superior conducting, nonlinear optical, tensile strength, flame retardant, chemical inertness, superior solvent resistance, thermal stability, solvent resistant, and other properties.

There also exist a variety of syntheses, stabilities, and characteristics, which are unique to each particular material. Further, macromolecules containing metal and metal-like elements can be produced in a variety of geometries, including linear, two-dimensional, three-dimensional, dendritic, and star arrays.

In this book series, macromolecules containing metal and metal-like elements will be defined as large structures where the metal and metalloid atoms are (largely) covalently bonded into the macromolecular network within or pendant to the polymer backbone. This includes various coordination polymers where combinations of ionic, sigma-, and pi-bonding interactions are present. Organometallic macromolecules are materials that contain both organic and metal components. For the purposes of this series, we will define metal-like elements to include both the metalloids as well as materials that are metal-like in at least one important physical characteristic such as electrical conductance. Thus the term includes macromolecules containing boron, silicon, germanium, arsenic, and antimony as well as materials such as poly(sulfur nitride), conducting carbon nanotubes, polyphosphazenes, and polyacetylenes.

The metal and metalloid-containing macromolecules that are covered in this series will be essential materials for the twenty-first century. The first volume is an overview of the discovery and development of these substances. Succeeding volumes will focus on thematic reviews of areas included within the scope of metallic and metalloid-containing macromolecules.

Alaa S. Abd-El-Aziz
Charles E. Carraher Jr.
Pierre D. Harvey
Charles U. Pittman Jr.
Martel Zeldin

CHAPTER 1

Introduction to Photophysics and Photochemistry

Shawkat M. Aly,[1] Charles E. Carraher Jr.,[2] and Pierre D. Harvey[1]

[1]*Département de Chimie, Université de Sherbrooke, Sherbrooke, PQ, Canada J1K 2R1*

[2]*Department of Chemistry and Biochemistry, Florida Atlantic University, Boca Raton, FL 33431*

CONTENTS

Macromolecules Containing Metal and Metal-like Elements,
Volume 10: Photophysics and Photochemistry of Metal-Containing Polymers,
Edited by Alaa S. Abd-El Aziz, Charles E. Carraher Jr., Pierre D. Harvey, Charles U. Pittman Jr., Martel Zeldin.

I. GENERAL

Photophysics and photochemistry both deal with the impact of energy in the form of photons on materials. Photochemistry focuses on the chemistry involved as a material is impacted by photons, whereas photophysics deals with physical changes that result from the impact of photons. This chapter will focus on some of the basic principles related to photophysics and photochemistry followed by general examples. Finally, these principles will be related to photosynthesis. In many ways, there is a great similarity between a material's behavior when struck by photons, whether the material is small or macromolecular. Differences are related to size and the ability of polymers to transfer the effects of radiation from one site to another within the chain or macromolecular complex.

The importance of the interaction with photons in the natural world can hardly be overstated. It forms the basis for photosynthesis converting carbon dioxide and water into more complex plant-associated structures. This is effectively accomplished employing chlorophyll as the catalytic site (this topic will be dealt with more fully later in the chapter). Chlorophyll contains a metal atom within a polymeric matrix, so it illustrates the importance of such metal–polymer combinations. Today, with the rebirth of green materials and green chemistry use of clean fuel—namely, sunlight—is increasing in both interest and understanding.

Polymer photochemistry and physics have been recently reviewed, and readers are encouraged to investigate this further in the suggested readings given at the end of the chapter. Here, we introduce some of the basic concepts of photophysics and photochemistry. We also illustrate the use of photochemistry and photophysics in the important area of solar energy conversion.

II. PHOTOPHYSICS AND PHOTOCHEMISTRY

Photophysics involves the absorption, transfer, movement, and emission of electromagnetic, light, energy without chemical reactions. By comparison, photochemistry involves the interaction of electromagnetic energy that results in chemical reactions. Let us briefly review the two major types of spectroscopy with respect to light. In absorption, the detector is placed along the direction of the incoming light and the transmitted light is measured. In emission studies, the detector is placed at some angle, generally 90°, away from the incoming light.

When absorption of light occurs, the resulting polymer, P^*, contains excess energy and is said to be excited.

$$P + h\nu \rightarrow P^* \tag{1}$$

The light can be simply reemitted.

$$P^* \rightarrow h\nu + P \tag{2}$$

Of much greater interest is light migration, either along the polymer backbone or to another chain. This migration allows the energy to move to a site of interest. Thus, for plants, the site of interest is chlorophyll. These 'light-gathering' sites are referred to as *antennas*. Natural antennas include chlorophyll, carotenoids, and special pigment-containing proteins. These antenna sites harvest the light by absorbing the light photon and storing it in the form of an electron, which is promoted to an excited singlet energy state (or other energy state) by the absorbed light.

Bimolecular occurrences can occur, leading to an electronic relaxation called *quenching*. In this approach P^* finds another molecule or part of the same chain, A, transferring the energy to A.

$$P^* + A \rightarrow P + A^* \tag{3}$$

Generally, the quenching molecule or site is initially in its ground state.

Eliminating chemical rearrangements, quenching most likely ends with electronic energy transfer, complex formation, or increased nonradioactive decay. Electronic energy transfer involves an exothermic process, in which part of the energy is absorbed as heat and part is emitted as fluorescence or phosphorescence radiation. Polarized light is taken on in fluorescence depolarization, also known as *luminescence anisotropy*. Thus if the chain segments are moving at about the same rate as the reemission, part of the light is depolarized. The extent of depolarization is then a measure of the segmental chain motions.

Complex formation is important in photophysics. Two terms need to be described here. First, an *exciplex* is an excited state complex formed between

two different kinds of molecules, one that is excited and one that is in its ground state. The second term, *excimer*, is similar, except the complex is formed between like molecules. Here we will focus on excimer complexes that form between two like polymer chains or within the same polymer chain. Such complexes can be formed between two aromatic structures. Resonance interactions between aromatic structures, such as two phenyl rings in polystyrene, give a weak intermolecular force formed from attractions between the π-electrons of the two aromatic entities. Excimers involving such aromatic structures give strong fluorescence.

Excimer formation can be described as follows where $[PP]^*$ is the excimer.

$$P^* + P \rightarrow [PP]^* \tag{4}$$

The excimer decays, giving two ground state aromatic sites and emission of fluorescence.

$$[PP]^* \rightarrow h\nu + 2P \tag{5}$$

As always, the energy of the light emitted is less than that originally taken on. Through studying the amount and energy of the fluorescence, radiation decay rates, depolarization effects, excimer stability, and structure can be determined.

III. LIGHT ABSORPTION

Light is composed of particles known as photons, each of which has the energy of Planck's quantum, hc/λ; where h is Plank's constant, c is velocity of light, and λ is the wavelength of the radiation. Light has dualistic properties of both waves and particles; ejection of electrons from an atom as a result of light bombardment is due to the particle behavior, whereas the observed light diffraction at gratings is attributed to the wave properties. The different processes related to light interactions with molecules can be represented as in Figure 1.

The absorption of light by materials produces physical and chemical changes. On the negative side, such absorption can lead to discoloration generally as a response to unwanted changes in the material's structure. Absorption also can lead to a loss in physical properties, such as strength. In the biological world, it is responsible for a multitude of problems, including skin cancer. It is one of the chief modes of weathering by materials. Our focus here is on the positive changes effected by the absorption of light. Absorption of light has intentionally resulted in polymer cross-linking and associated insolubilization. This forms the basis for coatings and negative-lithographic resists. Light-induced chain breakage is the basis for positive-lithographic resists.

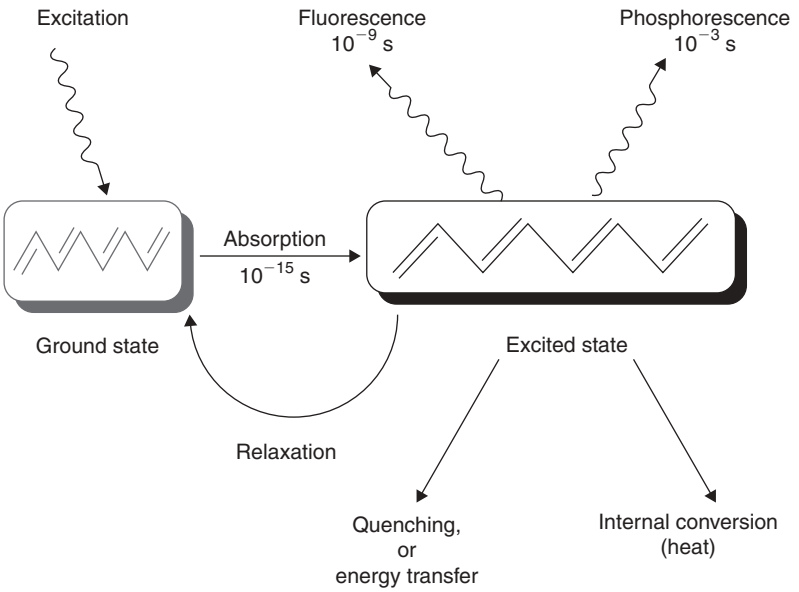

FIGURE 1. Different processes associated with light interaction with a molecule.

Photoconductivity forms the basis for photocopying, and photovoltaic effects form the basis for solar cells being developed to harvest light energy.

It is important to remember that the basic laws governing small and large molecules are the same.

The Grotthus-Draper law states that photophysical/photochemical reactions occur only when a photon of light is absorbed. This forms the basis for the First Law of Photochemistry—that is, only light that is absorbed can have a photophysical/photochemical effect.

We can write this as follows.

$$M + \text{light} \rightarrow M^* \tag{6}$$

where M^* is M after it has taken on some light energy acquired during a photochemical reaction. The asterisk is used to show that M is now in an excited state.

Optical transmittance, T, is a measure of how much light that enters a sample is absorbed.

$$T = I/I_o \tag{7}$$

If no light is absorbed then $I = I_o$. Low transmittance values indicate that lots of the light has been absorbed.

Most spectrophotometers give their results in optical absorbency, A, or optical density, which is defined as

$$A = \log(I/I_o) \tag{8}$$

so that

$$A = \log(1/T) = -\log T \tag{9}$$

Beer's law states that A, the absorbance of chromophores, increases in proportion to the concentration of the chromophores, where k is a constant.

$$A = kc \tag{10}$$

Beer's law predicts a straight-line relationship between absorbance and concentration and is often used to determine the concentration of an unknown after construction of the known absorbance verses concentration line.

The optical path, l, is the distance the light travels through the sample. This is seen in looking at the color in a swimming pool, where the water is deeper colored at the deep end because the optical path is greater. This is expressed by Lambert's law, where k' is another empirical constant.

$$A = k'l \tag{11}$$

To the eye some colors appear similar but may differ in intensity, when c and l are the same. These solutions have a larger molar absorption coefficient, ε, meaning they adsorb more. The larger the adsorption coefficient the more the material adsorbs.

The Beer-Lambert law combines the two laws, giving

$$A = \varepsilon lc \tag{12}$$

The proportionality constant in the Lambert's law is ε.

The extinction coefficients of chromophores vary widely from <100 1/Mcm, for a so-called forbidden transition, to greater than 10^5 1/Mcm for fully allowed transitions.

We can redefine the elements of the Beer-Lambert law, where l is the sample thickness and c is the molar concentration of chromophores. This can be rearranged to determine the penetration depth of light into a polymer material. Here l is defined as the path length, where 90% of the light of a particular wavelength is absorbed so A approaches 1, giving

$$l(\text{in } \mu\text{m}) = 10^4 \varepsilon c \tag{13}$$

This relationship holds when the polymer chromophore (or any chromophore) is uniformly distributed in a solution or bulk. In polymers with a high chromophore concentration, l is small and the photochemical/photophysical phenomenon occurs largely in a thin surface area.

Let us briefly examine the color of a red wine. The wine contains color sites, or chromophores. The photons that are not captured pass through and give us the red coloration. We see color because a chromophore interacts with light.

Molecules that absorb photons of energy corresponding to wavelengths in the range 190 nm to $\sim$1000 nm absorb in the UV-VIS region of the spectrum. The molecule that absorbs a photon of light becomes excited. The energy that is absorbed can be translated into rotational, vibrational, or electronic modes. The quantized internal energy E_{int} of a molecule in its electronic ground or excited state can be approximated, with sufficient accuracy for analytical purposes, by

$$E_{\text{int}} = E_{\text{el}} + E_{\text{vib}} + E_{\text{rot}} \tag{14}$$

where E_{el}, E_{vib}, and E_{rot} are the electronic, vibrational, and rotational energies, respectively. According to the Born-Oppenheimer approximation, electronic transitions are much faster than atomic motion. Upon excitation, electronic transitions occur in about 10^{-15} s, which is very fast compared to the characteristic time scale for molecular vibrations (10^{-10} to 10^{-12} s).[1] Hence the influence of vibrational and rotational motions on electronic states should be almost negligible. Franck-Condon stated that electronic transition is most likely to occur without changes in the position of the nuclei in the molecular entity and its environment. It is then possible to describe the molecular energy by a potential energy diagram in which the vibrational energies are superimposed upon the electronic curves (Fig. 2).

For most molecules, only one or two lower energy electronic transitions are normally postulated. Thus one would expect that the UV-VIS spectrum would be relatively simple. This is often not the case. The question is, Why are many bands often exhibiting additional features? The answer lies in the Franck-Condon principle, by which vibronic couplings are possible for polyatomic molecules. Indeed, both vibronic and electronic transitions will be observed in the spectrum, generating vibrationally structured bands, and sometimes even leading to broad unresolved bands.[2] Each resolved absorption peak corresponds to a vibronic transition, which is a particular electronic transition coupled with a vibrational mode belonging to the chromophore. For solids (when possible) and liquids, the rotational lines are broad and overlapping, so that no rotational structure is distinguishable.

To apply this concept for a simple diatomic molecule, let's consider the example given in Figure 3. At room temperature, according to the Boltzman distribution, most of the molecules are in the lowest vibrational level (ν) of the ground state (i.e., $\nu = 0$). The absorption spectrum presented in Figure 3b exhibits, in addition to the pure electronic transition (the so-called 0-0

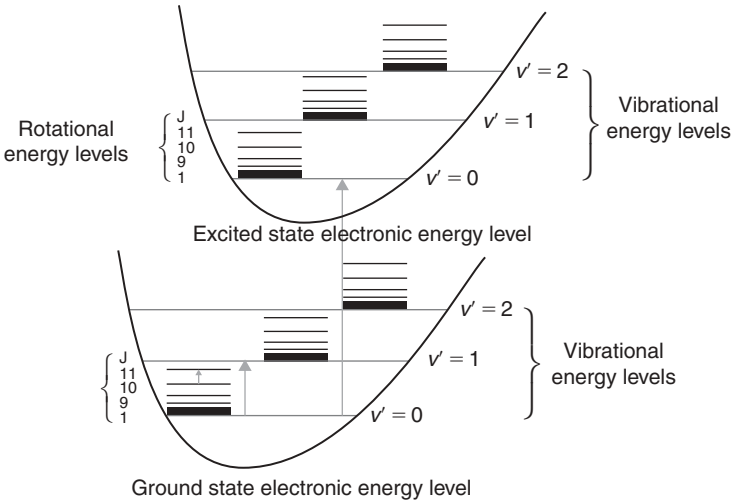

FIGURE 2. The relative ordering of electronic, vibrational, and rotational energy levels. (Modified from Ref. 1.)

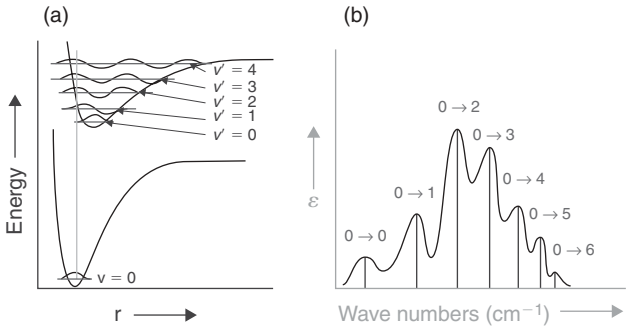

FIGURE 3. (a) Potential energy diagram for a diatomic molecule, illustrating the Franck-Condon excitation. (b) Intensity distribution among vibronic bands as determined by the Franck-Condon principle. (Modified from Ref. 2.)

transition), several vibronic peaks whose intensities depend on the relative position and shape of the potential curve.

The transition from the ground to the excited state, where the excitation goes from $\nu = 0$ (in the ground state) to $\nu = 2$ (in the excited state), is the most probable for vertical transitions because it falls on the highest point in the vibrational probability curve in the excited state. Yet many additional transitions occur, so that the fine structure of the vibronic broad band is a result of the probabilities for the different transitions between the vibronic levels.

Note that, there are two kinds of spectra—namely, excitation and absorption. The absorption and excitation spectra are distinct but usually overlap,

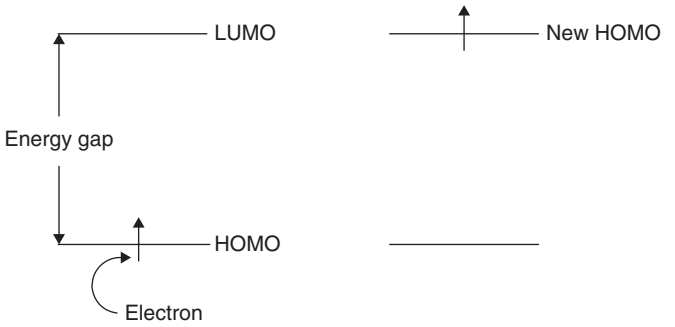

FIGURE 4. A photon being absorbed by a single molecule of chromophore.

sometimes to the extent that they are nearly indistinguishable. The excitation spectrum is the spectrum of light emitted by the material as a function of the excitation wavelength. The absorption spectrum is the spectrum of light absorbed by the material as a function of wavelength. The origin of the occasional discrepancies between the excitation and absorption spectra are due to the differences in structures between the ground and the excited states or the presence of photo reactions or the presence of nonradiative processes that relax the molecule to the ground state without passing through the luminescent states (i.e., S_1 and T_1).

Visible color is normally a result of changes in the electron states. Molecules that reside in the lowest energy level are said to be in the ground state or unexcited state. We will restrict our attention to the electrons that are in the highest occupied molecular orbital (HOMO) and the lowest unoccupied molecular orbital (LUMO). These orbitals are often referred to as the frontier orbitals.

Excitation of photons results in the movement of electrons from the HOMO to the LUMO (Fig. 4).

Photon energies can vary. Only one photon can be accepted at a time by an obtital. This is stated in the Stark-Einstein law also known as the Second Law of Photochemistry—if a species absorbs radiation, then one particle (molecule, ion, atom, etc.) is excited for each quantum of radiation (photon) that is absorbed.

Remember that a powerful lamp will have a greater photon flux than a weaker lamp. Further, photons enter a system one photon at a time. Thus every photon absorbed does not result in bond breakage or other possible measurable effect. The quantum yield, ϕ, is a measure of the effectiveness for effecting the desired outcome, possibly bond breakage and formation of free radicals.

$$\phi = \text{number of molecules of reactant consumed}/\text{number of photons consumed} \tag{15}$$

Quantum yields can provide information about the electronic excited state relaxation processes, such as the rates of radiative and nonradiative

processes. Moreover, they can also find applications in the determination of chemical structures and sample purity.[3] The emission quantum yield can be defined as the fraction of molecules that emits a photon after direct excitation by a light source.[4] So emission quantum yield is also a measure of the relative probability for radiative relaxation of the electronically excited molecules.

Quantum yields vary greatly; the photons range from very ineffective (10^{-6}) to very effective (10^{6}). Values >1 indicate that some chain reaction, such as in a polymerization, occurred.

We often differentiate between the primary quantum yield, which focuses on only the first event (here the quantum yield cannot be >1), and secondary quantum yield, which focuses on the total number of molecules formed via secondary reactions (here the quantum yield can be high). The common emission quantum yield measurement involves the comparison of a very dilute solution of the studied sample with a solution of approximately equal optical density of a compound of known quantum yield (standard reference). The quantum yield of an unknown sample is related to that of a standard by equation 16.[5]

$$\Phi_u = \left[\frac{(A_s F_u n^2)}{(A_u F_s n_0^2)}\right] \Phi_s \tag{16}$$

where, the subscript u refers to 'unknown', and s to the comparative standard; Φ is the quantum yield, A is the absorbance at a given excitation wavelength, F is the integrated emission area across the band, and n and n_0 are the refractive indices of the solvent containing the unknown and the standard, respectively.

For the most accurate measurements, both the sample and standard solutions should have low absorptions (≤ 0.05) and have the similar absorptions at the same excitation wavelength.[5]

IV. LUMINESCENCE

Luminescence is a form of cold body radiation. Older TV screens operated on the principle of luminescence, by which the emission of light occurs when they are relatively cool. Luminescence includes phosphorescence and fluorescence. In a TV, electrons are accelerated by a large electron gun sitting behind the screen. In the black-and-white sets, the electrons slam into the screen surface, which is coated with a phosphor that emits light when hit with an electron. Only the phosphor that is hit with these electrons gives off light. The same principle operates in the old-generation color TVs, except the inside of the screen is coated with thousands of groups of dots, each group consisting of three dots (red, green, and blue). The kinetic energy of the electrons is absorbed by the phosphor and reemitted as visible light to be seen by us.

Fluorescence involves the molecular absorption of a photon that triggers the emission of a photon of longer wavelength (less energy; Fig. 2). The energy difference ends up as rotational, vibrational, or heat energy loses.

Here excitation is described as

$$S_o + h\nu_{ex} \rightarrow S_1 \tag{17}$$

and emission as

$$S_1 \rightarrow h\nu_{em} + S_o \tag{18}$$

where S_o is the ground state and S_1 is the first excited state.

The excited state molecule can relax by a number of different, generally competing pathways. One of these pathways is conversion to a triplet state that can subsequently relax through phosphorescence or some secondary nonradiative step. Relaxation of the excited state can also occur through fluorescence quenching. Molecular oxygen is a particularly efficient quenching molecule because of its unusual triplet ground state.

Watch hands that can be seen in the dark allow us to read the time without turning on a light. These watch hands typically are painted with phosphorescent paint. Like fluorescence, phosphorescence is the emission of light by a material previously hit by electromagnetic radiation. Unlike fluorescence, phosphorescence emission persists as an afterglow for some time after the radiation has stopped. The shorter end of the duration for continued light emission is 10^{-3} s but the process can persist for hours or days.

An energy level diagram representing the different states and transitions is called a Jablonski diagram or a state diagram. The Jablonski diagram was first introduced in 1935; a slightly modified version is presented in Figure 5.[2,6] The different energy levels are given in this figure, where S_0 represents the electronic ground state and S_1 and S_2 represent the first and second singlet excited states, respectively. The first and second triplet states are denoted T_1 and T_2, respectively.

In the singlet states, all electron spins are paired and the multiplicity of this state is 1. The subscript indicates the relative energetic position (electronic level) compared to other states of the same multiplicity. On the other hand, in the triplet states, two electrons are no longer antiparallel and the multiplicity is 3. The triplet state is more stable than the singlet counterpart (S) and the source for this energy difference is created by the difference in the Coulomb repulsion energies between the two electrons in the singlet versus triplet states and the increase in degree of freedom of the magnetic spins. Because the electrons in the singlet excited state are confined within the same orbital, the Coulomb repulsive energy between them is higher than in the triplet excited state where these electrons are now in separate orbitals. The splitting between these two states (S-T) also depends on the nature of the orbital.

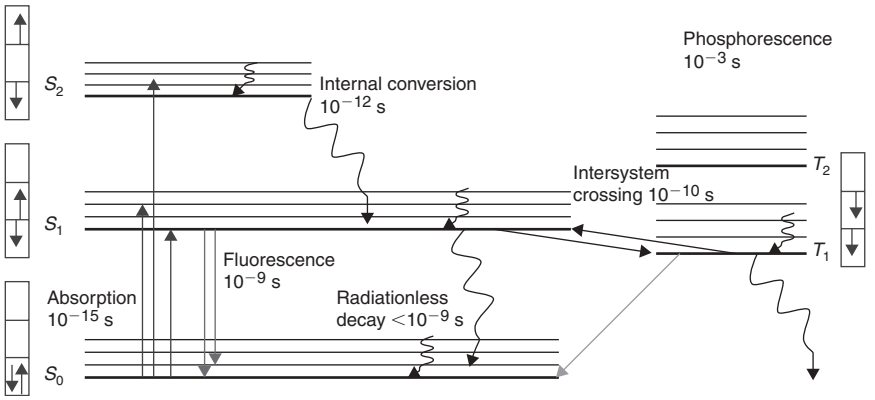

FIGURE 5. Jablonski diagram showing the various processes associated with light absorption and their time scale. *Arrows in boxes*, the relative spin states of the paired electrons. (Modified from Ref. 2.)

Let's consider a case where the two orbitals involved in a transition are similar (i.e., two *p*-orbitals of an atom, or two π-orbitals of an aromatic hydrocarbon). For this situation the overlap between them may be high, and the two electrons will be forced to be close to each other resulting in the *S*-*T* splitting being large. The other situation is the case where the two orbitals are different (i.e., $n \rightarrow \pi^*$ or $d \rightarrow \pi$ transitions), resulting in a small overlap. Because the overlap is small, the two electrons will have their own region of space in which to spread, resulting in a minimization of the repulsive interactions between them, and hence the *S*-*T* splitting will be small.

Absorption occurs on a time scale of about 10^{-15} s.[2] When inducing the promotion of an electron from the HOMO to the LUMO, the molecule passes from an electronic ground singlet state S_0 (for diamagnetic molecules) to a vibrational level of an upper singlet or triplet excited state S_n or T_n, respectively. The energy of the absorbed photon determines which excited state is accessible. After a while, the excited molecule relaxes to the ground state via either radiative (with emission of light) or nonradiative (without emission of light) processes. The radiative processes (for diamagnetic molecules) include either the spin-allowed fluorescence or spin-forbidden phosphorescence. Nonradiative processes include intersystem crossings (ISCs), a process allowing a molecule to relax from the S_n to the T_n manifolds, and internal conversions (IC and IP), a stepwise (vibrational) energy loss process relaxing molecules from upper excited states to any other state without or with a change in state multiplicity, respectively.[2]

An internal conversion (IC) is observed when a molecule lying in the excited state relaxes to a lower excited state. This is a radiationless transition between two different electronic states of the same multiplicity and is possible when there is a good overlap of the vibrational wave functions (or probabilities) that are involved between the two states (beginning and final).

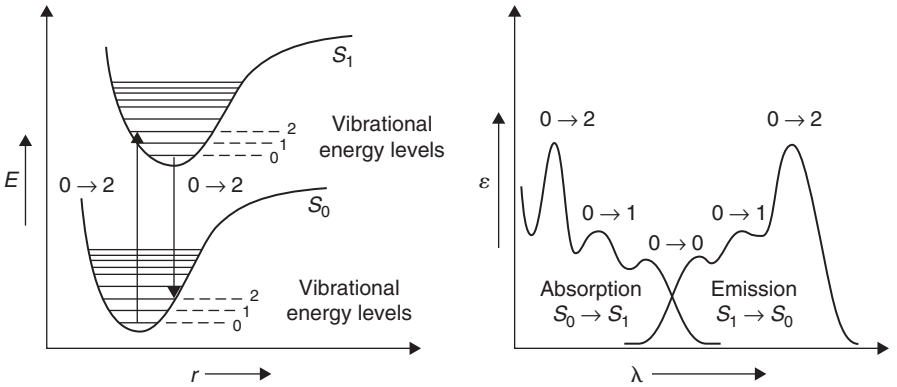

FIGURE 6. Potential energy curves and vibronic structure in fluorescence spectra. (Modified from Ref. 2.)

Internal conversion occurs on a time scale of 10^{-12} s, which is a time scale associated with molecular vibrations. A similar process occurs for an internal conversion, (IP) when it is accompanied by a change in multiplicity (such as triplet T_1 down to S_0). Upon nonradiative relaxation, heat is released. This heat is transferred to the media by collision with neighboring molecules.

Fluorescence (Fig. 6) is a radiative process in a diamagnetic molecule involving two states (excited and ground states) of the same multiplicity (e.g., $S_1 \rightarrow S_0$ and $S_2 \rightarrow S_0$). Fluorescence spectra show the intensity of the emitted light versus the wavelength. A fluorescence spectrum is obtained by initial irradiation of the sample, normally at a single wavelength, where the molecule absorbs light. The lifetime of fluorescence is typically on the order of 10^{-8}–10^{-9} s (i.e., an ns time scale) for organic molecules and faster for metal-containing compounds (10^{-10} s or shorter).

In general, the fluorescence band, typically $S_1 \rightarrow S_0$, is a mirror image of the absorption band ($S_0 \rightarrow S_1$), as illustrated in Figures 6 and 7. This is particularly true for rigid molecules, such as aromatics. Once again, the Franck-Condon principle is applicable, and hence the presence of vibronic bands is expected in the fluorescence band. However there are numerous exceptions to this rule, particularly when the molecule changes geometry in its excited state. Another observation is that the emission is usually red shifted in comparison with absorption. This is because the vibronic energy levels involved are lower for fluorescence and higher for absorption, as illustrated in Figure 6. The difference in wavelength between the 0-0 absorption and the emission band is usually known as the *Stokes shift*. The magnitude of the Stokes shift gives an indication of the extent of geometry difference between the ground and excited states of a molecule as well as the solvent–solute reorganization.[2]

Another nonradiative process that can take place is known as *intersystem crossing* from a singlet to a triplet or triplet to a singlet state. This process is very rapid for metal-containing compounds. This process can take place on a

time scale of $\sim 10^{-6}$–10^{-8} s for an organic molecule, while for organometallics it is $\sim 10^{-11}$ s. This rate enhancement is due to spin-orbit coupling present in the metal-containing systems—that is, an interaction between the spin angular momentum and the orbital angular momentum, which allows mixing of the spin angular momentum with the orbital angular momentum of S_n and T_n states. Thus these singlet and triplet states are no longer "pure" singlets and triplets, and the transition from one state to the other is less forbidden by multiplicity rules. A rate increase in intersystem crossing can also be achieved by the heavy atom effect,[7] arising from an increased mixing of spin and orbital quantum number with increased atomic number. This is accomplished either through the introduction of heavy atoms into the molecule via chemical bonding (internal heavy atom effect) or with the solvent (external heavy atom effect). The spin-orbit interaction energy of atoms grows with the fourth power of the atomic number Z.

In addition to the increase in the intersystem crossing rate, heavy atoms exert more effects, which can be summarized as follows. Their presence acts (1) to decrease the phosphorescence lifetime due to an increase in the non-radiative rates, (2) to decrease the fluorescence lifetime, and (3) to increase the phosphorescence quantum yield. The presence of a heavy atom affects not only the rate for intersystem crossing but also the energy gap between the singlet and the triplet states, where the rate for the intersystem crossing increases as the energy gap between S_1 and T_1 decreases. Moreover, the nature of the excited state exerts an important effect on the intersystem crossing. For example the $S_1(n,\pi^*) \rightarrow T_2(\pi,\pi^*)$ (e.g., as in benzophenone) transition occurs almost three orders of magnitude faster than the $S_1(\pi,\pi^*) \rightarrow T_2(\pi,\pi^*)$ transition (e.g., as in anthracene)[6].

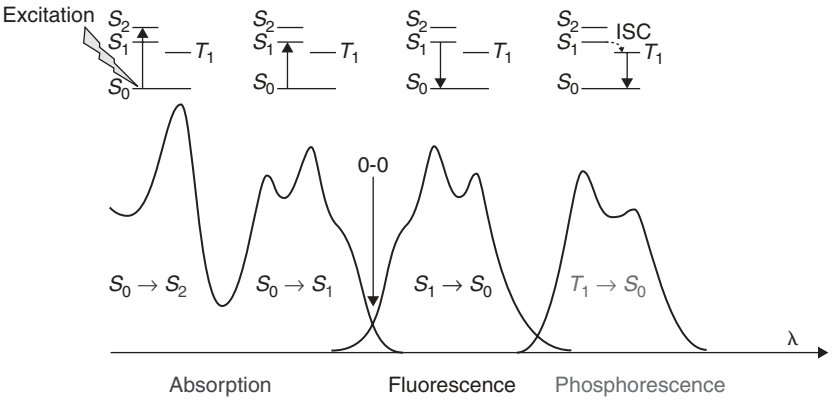

FIGURE 7. Relative positions of absorption, fluorescence, and phosphorescence The 0-0 peak is common to both absorption and fluorescence spectra (see Fig. 6). *ISC*, Intersystem crossing. (Modified from Ref. 2.)

Relaxation of triplet state molecules to the ground state can be achieved by either internal conversion (nonradiative IP) or phosphorescence (radiative). Emissions from triplet states (i.e., phosphorescence) exhibit longer lifetimes than fluorescence. These long-lived emissions occur on time scale of 10^{-3} s for organic samples and 10^{-5}–10^{-7} s for metal-containing species. This difference between the fluorescence and the phosphorescence is associated with the fact that it involves a spin-forbidden electronic transition. Moreover, as already noted, the phosphorescence bands are always red shifted in comparison with their fluorescence counterpart because of the relative stability of the triplet state compared to the singlet manifold (Fig. 7).[2] Nonradiative processes in the triplet states increase exponentially with a decrease in triplet energies (energy gap law). Hence phosphorescence is more difficult to observe when the triplet states are present in very low energy levels. It is also often easier to observe phosphorescence at lower temperatures, at which the thermal decay is further inhibited.[8]

V. EMISSION LIFETIME

The luminescence lifetime is the average time the molecule remains in its excited state before the photon is emitted. From a kinetic viewpoint, the lifetime can be defined by the rate of depopulation of the excited (singlet or triplet) states following an optical excitation from the ground state.[9] Luminescence generally follows first-order kinetics and can be described as follows.

$$[S_1] = [S_1]_o e^{-\Gamma t} \tag{19}$$

where $[S_1]$ is the concentration of the excited state molecules at time t, $[S_1]_o$ is the initial concentration and Γ is the decay rate or inverse of the luminescence lifetime.

Various radative and nonradiative processes can decrease the excited state population. Here, the overall or total decay rate is the sum of these rates:

$$\Gamma_{\text{total}} = \Gamma_{\text{radiative}} + \Gamma_{\text{nonradiative}} \tag{20}$$

For a complete photophysical study, it is essential to study not only the emission spectrum but also the time domain because it can reveal a great deal of information about the rates and hence the kinetics of intramolecular and intermolecular processes. The fundamental techniques used to characterize emission lifetimes of the fluorescence and the phosphorescence are briefly described next.

When a molecule is excited (eq. 21), it is promoted from the ground to the excited state. This excited molecule can then relax to the ground state after

loosing its extra energy gained from the exciting source via a radiative (eq. 22) and nonradiative (eq. 23) processes:

$$A_0 + h\nu \rightarrow A^* \tag{21}$$

$$A^* \rightarrow A_0 + h\nu' \quad (\text{radiative processes}, k_r) \tag{22}$$

$$A^* \rightarrow A_0 + \text{heat} \quad (\text{nonradiative processes}, k_n) \tag{23}$$

Therefore, we can write

$$-\frac{d[A^*]}{dt} = (k_r + k_n)[A^*]t = -\frac{t}{\tau} \tag{24}$$

where $[A^*]$ is the concentration of the species A in its excited state at a given time t and k_r and k_n are the rate constants for the radiative and nonradiative processes, respectively.

The relative concentration of A^* is given by

$$\ln \frac{[A^*]_t}{[A^*]_{t=0}} = -(k_r + k_n)t = -\frac{t}{\tau} \tag{25}$$

Hence the mean lifetime (τ) of $[A^*]$ is

$$\tau = 1/(k_r + k_n) \tag{26}$$

where k_r and k_n are the rate constants for the radiative and nonradiative processes, respectively, represented by equations 22 and 23.

Thus the measured unimolecular radiative lifetime is the reciprocal of the sum of the unimolecular rate constants for all the deactivation processes. The general form of the equation is given by

$$\tau = \frac{1}{\sum_i k_i} \tag{27}$$

where τ is observed radiative lifetime and the rate constant k_i represents the unimolecular or pseudo-unimolecular processes that deactivate A^*.[10]

The lifetime can be measured from a time-resolved experiment in which a very short pulse excitation is made, followed by measurement of the time-dependent intensity, as illustrated in Figure 8.

The intensity decays are often measured through a polarizer oriented at some angle such as about 55° from the vertical z-axis to avoid the effects of

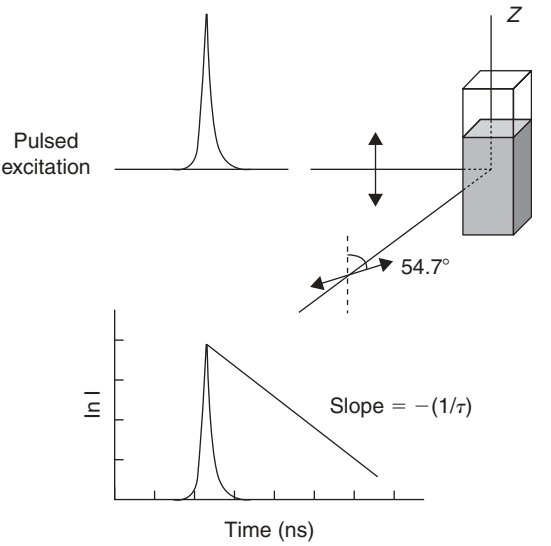

FIGURE 8. Time-domain lifetime measurement. (Modified from Ref. 11.)

anisotropy on the intensity decay.[11] Then the log of the recorded intensity is plotted against time to obtain a straight line predictable from the integration of the equation 24. The slope of this line is the negative reciprocal of the lifetime. When more than one lifetime is present in the decay traces, then there is more than one radiative pathway to relaxation. This often signifies that more than one species is emitting light at the excitation wavelength. The analysis of such multicomponent decays involves the deconvolution of an equation of the same form of equation 24 where a weighing factor for each component is added to each component.

One possible explanation for the polyexponential curves can be an exciton process. The exciton phenomenon is a delocalization of excitation energy through a material. A description of this is given in Figure 9. It shows a one-dimentional coordination or organometallic polymer denoted by $-|M_n|\text{-}|M_n|\text{-}|M_n|\text{-}|M_n|\text{-}$, where M_n represent a mononuclear ($n = 1$) or polynuclear center ($n > 1$). The incident irradiation is absorbed by a single chromophore, $|M_n|$, along the backbone, and then this stored energy is reversibly transmitted via an energy transfer process to the neighboring chromophore (with no thermodynamic gain or loss; i.e., $\Delta G^0 = 0$). This newly created chromophore can reemit, or not, the light ($h\nu_2$, $h\nu_3$, $h\nu_4$,...) at a given moment.

The interactions between the different units in the excited states are called *excimers*. These excimers can be excited dimers, trimers, tetramers, etc. These excited oligomers have different wavelengths and emission lifetimes. The extent of the interactions in the excited state (dimers, trimers, tetramers) is hard to predict because it depends on the amplitude of the interactions

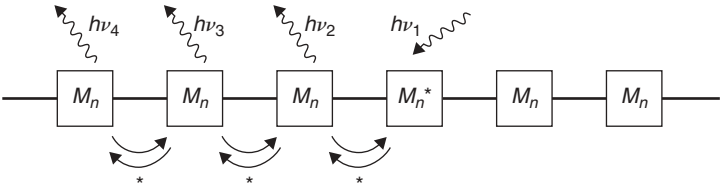

FIGURE 9. The excitation process.

and the relaxation rates. Hence the lifetime decay curve will have a poly-exponential nature.

VI. GROUND AND EXCITED STATE MOLECULAR INTERACTIONS

Ground state intermolecular interactions are present in some systems and require measurements of the binding constants. These interactions are manifested by the spectral changes experienced in the absorption spectra. Therefore, these changes can be monitored as a function of the concentration of the substrates leading to the extraction of the binding constants. On the other hand, intermolecular and intramolecular excited state interactions refer to the energy and electron transfer operating in the excited states of different dyad or polyad systems. These can also be excimers, dimers, or oligomers that are formed only in the excited states. Studies of photo-induced energy and electron transfers involve the measurement of their corresponding rates. The theory and methods used to characterize the different types of interactions are described next. Binding constant considerations are described elsewhere.[13]

A. Energy and Electron Transfer (Excited State Interactions and Reactions)

The possible deactivation pathways of the excited state are summarized in Figure 10. We discuss here the fluorescence and phosphorescence relaxation pathways and the thermal deactivation processes.

A transfer of the excitation energy from the donor to the acceptor will occur when an energy acceptor molecule is placed at the proximity of an excited energy donor molecule. After energy transfer, the donor relaxes to its ground state and the acceptor is promoted to one of its excited states. A photo-induced electron transfer can be initiated after photoexcitation when an excited single electron in the LUMO of the electron donor is transferred to a vacant molecular orbital (LUMO) of the acceptor.

The mechanisms for the energy and electron transfers are outlined below.

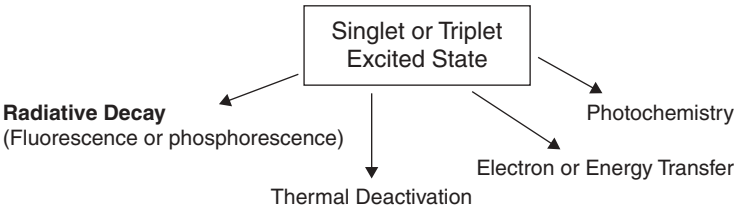

FIGURE 10. Different pathways for the deactivation of the excited state.

B. Energy Transfer

In presence of a molecule of a lower energy excited state (acceptor), the excited donor (D^*) can be deactivated by a process known as energy transfer which can be represented by the following sequence of equations.

$$D + h\nu \rightarrow D^* \tag{28}$$

$$D^* + A \rightarrow D + A^* \tag{29}$$

For energy transfer to occur, the energy level of the excited state of D^* has to be higher than that for A^* and the time scale of the energy transfer process must be faster than the lifetime of D^*. Two possible types of energy transfers are known—namely, radiative and nonradiative (radiationless) energy transfer.

Radiative transfer occurs when the extra energy of D^* is emitted in form of luminescence and this radiation is absorbed by the acceptor (A).

$$D^* \rightarrow h\nu + D \tag{30}$$

$$h\nu + A \rightarrow A^* \tag{31}$$

For this to be effective, the wavelengths where the D^* emits need to overlap with those where A absorbs. This type of interaction operates even when the distance between the donor and acceptor is large (100 Å). However this radiative process is inefficient because luminescence is a three-dimensional process in which only a small fraction of the emitted light can be captured by the acceptor.

The second type, radiationless energy transfer, is more efficient. There are two different mechanisms used to describe this type of energy transfer: the Förster and Dexter mechanisms.

i. Förster Mechanism

The Förster mechanism is also known as the coulombic mechanism or dipole-induced dipole interaction. It was first observed by Förster.[14,15] Here the emission band of one molecule (donor) overlaps with the absorption band of another molecule (acceptor). In this case, a rapid energy transfer may occur without a photon emission. This mechanism involves the migration of energy by the resonant coupling of electrical dipoles from an excited molecule (donor) to an acceptor molecule. Based on the nature of interactions present between the donor and the acceptor, this process can occur over a long distances (30−100 Å). The mechanism of the energy transfer by this mechanism is illustrated in Figure 11.

In Figure 11, an electron of the excited donor placed in the LUMO relaxes to the HOMO, and the released energy is transferred to the acceptor via coulombic interactions. As a result, an electron initially in the HOMO of the acceptor is promoted to the LUMO. This mechanism operates only in singlet states of the donor and the acceptor. This can be explained on the basis of the nature of the interactions (dipole-induced dipole) because only multiplicity-conserving transitions possess large dipole moments. This can be understood considering the nature of the excited state in both the singlet and the triplet states. The triplet state has a diradical structure, so it is less polar, making it difficult to interact over long distances (i.e., Förster mechanism).

The rate of energy transfer (k_{ET}) according to this mechanism can be evaluated by the equation 32:[1]

$$k_{ET} = k_D R_F^6 \left(\frac{1}{R}\right)^6 \tag{32}$$

where k_D is the emission rate constant for the donor, R is the inter-chromophore separation, and R_F is the Förster radius, which can be defined as the distance between the donor and the acceptor at which 50% of the excited state decays by energy transfer—that is, the distance at which the energy transfer has the same rate constant as the excited state decay by the radiative and nonradiative channels ($k_{ET} = k_r + k_{nr}$). R_F is calculated by the overlap of the emission spectrum of the donor excited state (D^*) and the absorption spectrum of the acceptor (A).[1]

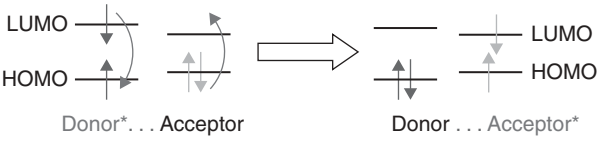

FIGURE 11. Mechanism of energy transfer action according to Förster.

ii. Dexter Mechanism

The Dexter mechanism is a nonradiative energy transfer process that involves a double electron exchange between the donor and the acceptor (Fig. 12).[16] Although the double electron exchange is involved in this mechanism, no charge separated-state is formed.

The Dexter mechanism can be thought of as electron tunneling, by which one electron from the donor's LUMO moves to the acceptor's LUMO at the same time as an electron from the acceptor's HOMO moves to the donor's HOMO. In this mechanism, both singlet-singlet and triplet-triplet energy transfers are possible. This contrasts with the Förster mechanism, which operates in only singlet states.

For this double electron exchange process to operate, there should be a molecular orbital overlap between the excited donor and the acceptor molecular orbital. For a bimolecular process, intermolecular collisions are required as well. This mechanism involves short-range interactions ($\sim$6–20 Å and shorter). Because it relies on tunneling, it is attenuated exponentially with the intermolecular distance between the donor and the acceptor.[17] The rate constant can be expressed by the following equation.

$$k_{ET} = \frac{2\pi}{h} V_0^2 J_D \qquad \exp\left(-\frac{2R_{DA}}{L}\right) \tag{33}$$

where R_{DA} is distance between the donor and the acceptor, J_D is the integral spectral overlap between the donor and the acceptor, L is the effective Bohr radius of the orbitals between which the electron is transferred, h is Plank's constant, and V_0 is the electronic coupling matrix element between the donor and acceptor at the contact distance.

Comparing the two energy transfer mechanisms, the Förster mechanism involves only dipole–dipole interactions, and the Dexter mechanism operates through electron tunneling. Another difference is their range of interactions. The Förster mechanism involves longer range interactions (up to $\sim$30–100 Å), but the Dexter mechanism focuses on shorter range interactions ($\sim$6 up to 20 Å) because orbital overlap is necessary. Furthermore, the Förster mechanism is used to describe interactions between singlet states, but the Dexter mechanism can be used for both singlet-singlet and triplet-triplet interactions. Hence for the singlet-

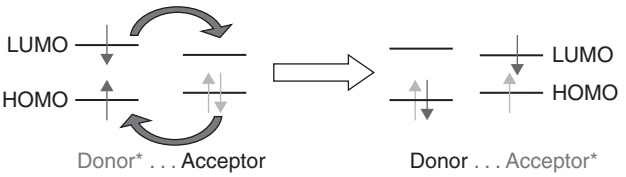

FIGURE 12. Mechanism of energy transfer action according to the Dexter mechanism.

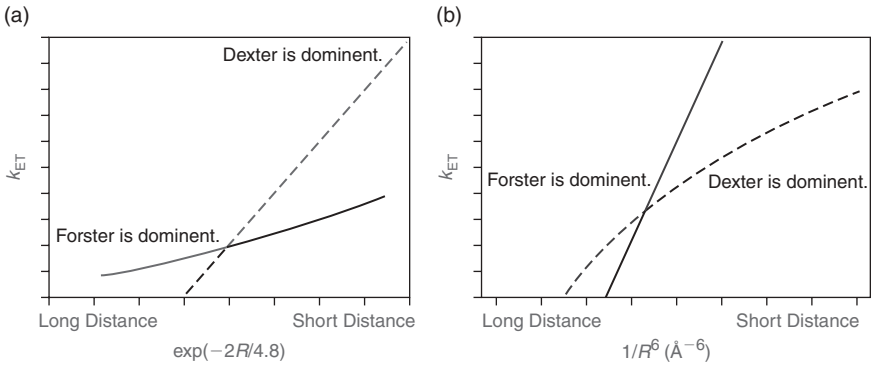

FIGURE 13. Qualitative theoretical plots for (a) and (b) k_{ET} versus $1/R^6$ (Förster). k_{ET} versus $\exp(-2R/4.8)$ (Dexter) (Modified from Ref. 18.)

singlet energy transfer, both mechanisms are possible. Simulated graphs using reasonable values for the parameters for the two mechanisms have been constructed for the purpose of distinguishing between the zones where Förster and Dexter mechanisms are dominant.[18] The experimental values of the energy transfer rates in cofacial bisporphyrin systems were found to agree with the theoretically constructed graphs (Fig. 13).[18]

In these graphs a Bohr radius value (L) of 4.8 Å (the value for porphyrin) is used in the Dexter equation 33.[18] Also, the solid lines correspond to hypothetical situations in which only the Förster mechanism operates; the dotted lines are hypothetical situations for when the Dexter mechanism is the only process.[18] The curved lines are simulated lines obtained with equation 32 (Förster) or 33 (Dexter) but transposed onto the other graph (i.e., Förster equation plotted against Dexter formulation and vice versa).

These plots clearly suggest the presence of a crossing point between the two mechanisms. There is a zone in which one mechanism is dominant and vice versa. All in all, the relaxation of an excited molecule via energy transfer processes will use all the pathways available to it so the total rate for energy transfer can be better described as k_{ET} (total) = k_{ET} (Förster)+k_{ET} (Dexter). According to Figure 13, the distance at which there is a change in dominant mechanism is $\sim$5 Å.

C. Electron Transfer

Photo-induced electron transfer (PET) involves an electron transfer within an electron donor-acceptor pair. The situation is represented in Figure 14.

Photo-induced electron transfer represents one of the most basic photochemical reactions and at the same time it is the most attractive way to convert light energy or to store it for further applications. In Figure 14, one can see a

process taking place between a donor and acceptor after excitation, resulting in the formation of a charge separated state, which relaxes to the ground state via an electron-hole recombination (back electron transfer).

A theory used to study and interpret the photo-induced electron transfer in solution was described by Marcus.[19–25] In this theory, the electron transfer reaction can be treated by transition state theory where the reactant state is the excited donor and acceptor and the product state is the charge-separated state of the donor and acceptor (D^+-A^-), shown in Figure 15.

According to the Franck-Condon principle, the photoexcitation triggers a vertical transition to the excited state, which is followed by a rapid nuclear equilibration. Without donor excitation, the electron transfer process would be highly endothermic. However, after exciting the donor, electron transfer occurs at the crossing of the equilibrated excited state surface and the product state.

The change in Gibbs free energy associated with the electron transfer event is given by the following relation.[19]

$$\Delta G^{\#} = \frac{(\lambda + \Delta G^0)^2}{4\lambda} \tag{34}$$

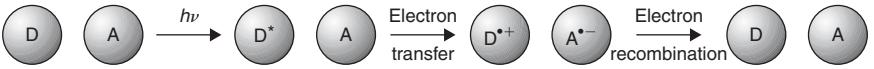

FIGURE 14. Photo-induced electron transfer process.

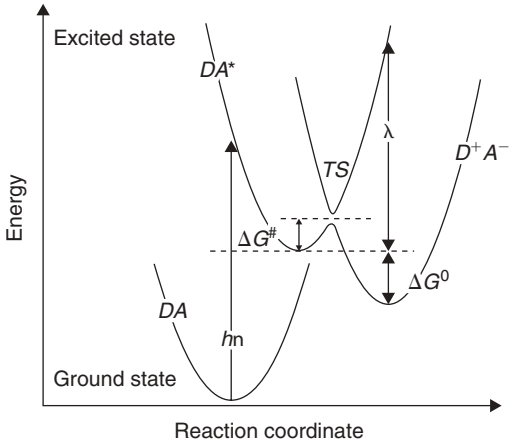

FIGURE 15. Potential energy surfaces for the ground state (*DA*), the excited state (*DA**, reactant state), and the charge-separated state (D^+-A^-, product state), proposed by Marcus's theory. λ, total reorganization energy; *TS*, transition state. (Modified from Ref. 19.)

The total reorganization energy (λ), which is required to distort the reactant structure to the product structure without electron transfer, is composed of solvent (λ_S) and internal (λ_i) components ($\lambda = \lambda_i + \lambda_S$). The reaction free energy (ΔG^0), is the difference in free energy between the equilibrium configuration of the reactant (DA^*) and of the product states (D^+A^-). The internal reorganization energy represents the energy change that occurs in bond length and bond angle distortions during the electron transfer step and is usually represented by a sum of harmonic potential energies. In the classical Marcus theory, the electron transfer rate is given by equation 35.[22,22]

$$k_{ET} = \kappa_{ET}\nu_n \exp\left(\frac{-\Delta G^{\#}}{k_B T}\right) \tag{35}$$

where ν_n is the effective frequency of motion along the reaction coordinate and κ_{ET} is the electronic transmission factor.

The transmission factor is related to the transition probability (P_0) at the intersection of two potential energy surfaces, as given by the Landau-Zener theory.[24]

$$\kappa_{ET} = \frac{2P_0}{1 + P_0} \tag{36}$$

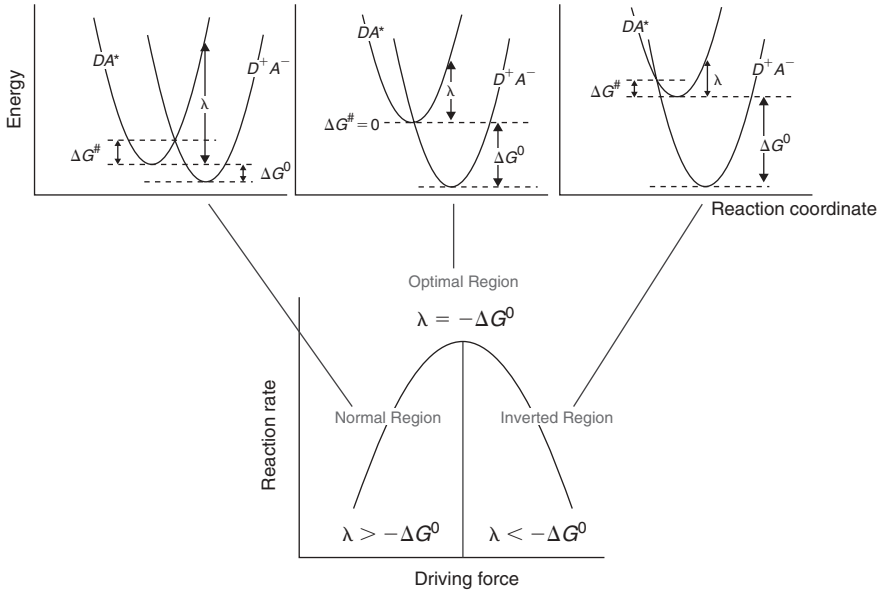

FIGURE 16. The free energy regimes for electron transfer (top) and the corresponding reaction rate dependence on the free energy (bottom; driving force is ΔG^0-λ). (Modified from Ref. 19.)

A graph showing the change of the driving force for the electron transfer rate, calculated from Marcus theory, versus the rate constant is given in Figure 16 (bottom).

Using equation 35 to estimate the electron transfer rate, we can assign the Marcus normal region as that where the free reaction energy (ΔG^0) is decreased, leading to an increase of the electron transfer rate (k_{ET}). The second region that can be identified in Figure 16 is the optimal or activationless region, where the driving force for electron transfer equals the reorganization energy—that is, $-\Delta G^0 = \lambda$. If ΔG^0 becomes even more negative, the activation barrier $\Delta G^{\#}$ reappears, resulting in a decrease in the values of k_{ET}. This last situation is observed over the region known as the inverted Marcus region and was first experimentally demonstrated by Closs and Miller.[25] The potential energy illustrating the different Marcus regimes can be seen in Figure 16 (top).

VII. NONLINEAR OPTICAL BEHAVIOR

Nonlinear optics (NLO) involves the interaction of light with materials resulting in a change in the frequency, phase, or other characteristics of the light. There are a variety of frequency-mixing processes. Second-order NLO behavior includes second harmonic generation of light that involves the frequency doubling of the incident light. Frequency mixing where the frequency of two light beams are either added or subtracted. Electrooptic effects can occur where both frequency and amplitude changes and where rotation of polarization occurs. NOL behavior has been found in inorganic and organic compounds and in polymers. The structural requirement is the absence of an inversion center requiring the presence of asymmetric centers and/or poling. Poling is the application of a high voltage field to a material that orients some or all of the molecule dipoles generally in the direction of the field. The most effective poling in polymers is found when they are poled above the T_g (which allows a better movement of chain segments) and then cooled to lock in the poled structure. Similar results are found for polymers that contain side chains that are easily poled. Again, cooling helps lock in the poled structure. At times, cross-linking is also employed to help lock in the poled structure.

Third-order NLO behavior generally involves three photons, resulting in effects similar to those obtained for second-order NLO behavior. Third-order NLO behavior does not require the presence of asymmetric structures.

Polymers that have been already been found to offer NLO behavior include polydiacetylenes and a number of polymers with liquid crystal side chains. Polymers are also employed as carriers of materials that themselves are NLO materials. Applications include communication devices, routing components, and optical switches.

VIII. PHOTOCONDUCTIVE AND PHOTONIC POLYMERS

Some polymeric materials become electrically conductive when illuminated with light. For instance, poly(*N*-vinylcarbazole) is an insulator in the dark, but when exposed to UV radiation it becomes conductive. The addition of electron acceptors and sensitizing dyes allows the photoconductive response to be extended into the visible and NIR regions. In general, such photoconductivity depends on the materials ability to create free-charge carriers, electron holes, through absorption of light, and to move these carriers when a current is applied.

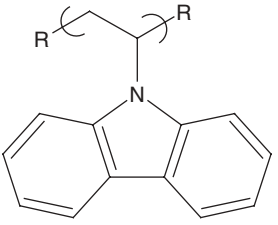

Poly(*N*-vinylcarbazole).

Related to this are materials whose response to applied light varies according to the intensity of the applied light. This is nonlinear behavior. In general, polymers with whole-chain delocalization or large-area delocalization in which electrons are optically excited may exhibit such nonlinear optical behavior.

A photoresponsive sunglass whose color or tint varies with the intensity of the sunlight is an example of nonliner optical material. Some of the so-called smart windows are also composed of polymeric materials whose tint varies according to the incident light. Currently, information is stored using electronic means but optical storage is becoming common place with the use of CD-ROM and WORM devices. Such storage has the advantages of rapid retrieval and increased knowledge density (i.e., more information stored in a smaller space).

Since the discovery of doped polyacetylene, a range of polymeric semiconductor devices has been studied, including normal transistors, field-effect transistors (FETs) photodiodes, and light-emitting diodes (LEDs). Like conductive polymers, these materials obtain their properties from their electronic nature, specifically the presence of conjugated π-bonding systems.

In electrochemical light-emitting cells, the semiconductive polymer can be surrounded asymmetrically with a hole-injecting material on one side and a low work function electron injecting metal (such as magnesium, calcium, or aluminum) on the other side. The emission of light may occur when a charge carrier recombines in the polymer as electrons from one side and holes from the other meet.

Poly(*p*-phenylene vinylene) (PPV) was the first reported (1990) polymer to exhibit electroluminescence.[26] PPV is employed as a semiconductor layer. The layer was sandwiched between a hole-injecting electrode and electron-injecting metal on the other. PPV has an energy gap of about 2.5 eV and thus produces a yellow-green luminescence when the holes and electron recombine. Today, many other materials are available that give a variety of colors.

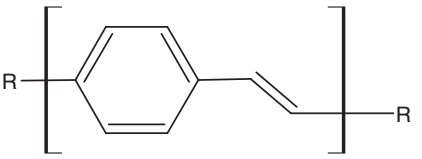

Poly(*p*-phenylene vinylene).

A number of poly(arylene vinylene) (PAV) derivatives have been prepared. Attachment of electron-donating substituents, such as two methoxy groups (**3**), act to stabilize the doped cationic form and thus lower the ionization potential.[26] These polymers exhibit both solvatochromism (color change as solvent is changed) and thermochromism (color is temperature dependent).

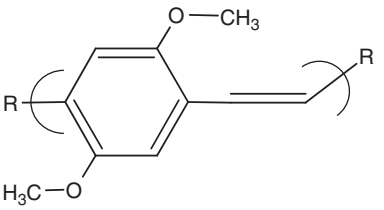

Poly(2,5-dimethoxy-*p*-phenylene vinylene).

The introduction of metals into polymers that can exhibit entire chain electron delocalization is at the basis of much that is presented in this volume. These metal-containing sites are referred to as *chromophores*, and the combination of metal chromophores exhibiting metal to ligand charge transfer (MLCT) excited states opens new possibilities for variation of electronic and optical properties needed for the continual advancement in electronics and electronic applications. Application areas include light-emitting polymeric diodes, solar energy conversion, and nonlinear optical materials and materials exhibiting photorefraction, electrochromism, and electrocatalysis.

One of the major reasons for interest in this area is the ease with which the new hybrid materials' properties can be varied by changing the metal, metal oxidation state, metal matrix, and polymer. Multiple metal sites are readily available. This allows the metal-containing system to have a high degree of tunability. This is due to the often strong electronic interaction between the metal

and the delocalized electron systems. The already noted variety of available metal sites is further leveraged by the increasingly capability of modern synthetic methodologies to achieve the desired structures. But the presence of metal atoms is at the heart of this.

IX. PHOTOSYNTHESIS

The recent environmental issues related to the greenhouse effect and atmospheric contamination heighten the importance of obtaining energy from clean sources, such as photosynthesis. Photosynthesis also acts as a model for the creation of synthetic light-harvesting systems that might mimic chlorophyll in its ability to convert sunlight into usable energy. The basis of natural photosynthesis was discovered by Melvin Calvin. Using carbon-14 as a tracer, Calvin and his team found the pathway that carbon follows in a plant during photosynthesis. They showed that sunlight supplies the energy through the chlorophyll site, allowing the synthesis of carbon-containing units, mainly saccharides or carbohydrates. Chlorophyll is a metal embedded in a protein polymer matrix and illustrates the importance of metals in the field of photochemistry and photophysics. A brief description of the activity of chlorophyll in creating energy from the sun follows.

The maximum solar power density reaching Earth is approximately 1350 W/m^2. When this energy enters the Earth's atmosphere, the magnitude reaching the surface drops approximately to 1000 W/m^2 owing to atmospheric absorption.[27,28] The amount that is used by plants in photosynthesis is about seven times the total energy used by all humans at any given time, thus it is a huge energy source.

Solar energy is clean and economical energy, but it must be converted into useful forms of energy. For example, solar energy can be used as a source of excitation to induce a variety of chemical reactions.

Natural examples for conversion of light energy are plants, algae, and photosynthetic bacteria that used light to synthesize organic sugar-type compounds through photosynthesis.

In photosynthesis, green plants and some bacteria harvest the light coming from the sun by means of their photosynthetic antenna systems. The light harvesting starts with light gathering by antenna systems, which consist of pigment molecules, including chlorophylls, carotenoids, and their derivatives. The absorbed photons are used to generate excitons, which travel via Förster energy transfers toward the reaction centers (RCs). This overall series of processes is represented in Figure 17.

In reaction centers, this energy drives an electron transfer reaction, which in turn initiates a series of slower chemical reactions. Energy is saved as redox energy,[29,30] inducing a charge separation in a chlorophyll dimer called the special

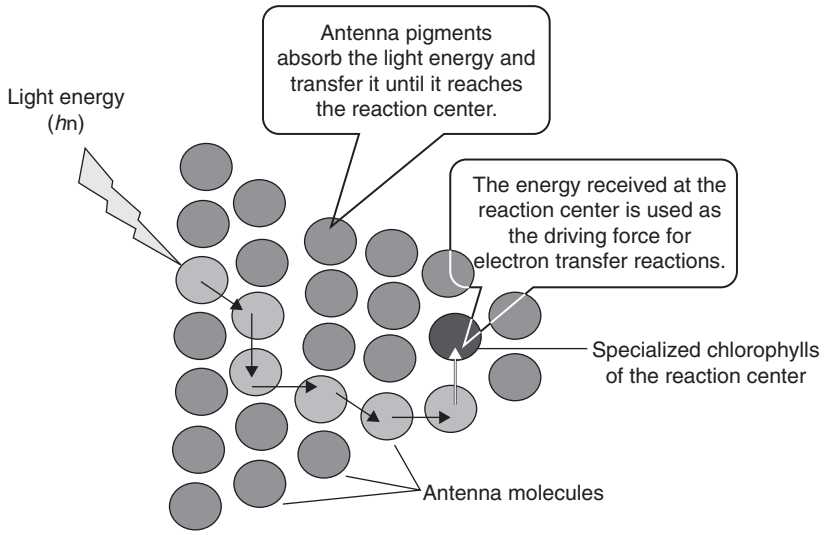

FIGURE 17. Light is absorbed by the antenna, and the energy is transferred to the reaction center, where charge separation takes place to generate chemical energy.

pair $(\text{chlorophyll})_2$. Charge separation, which forms the basis for photosynthetic energy transfer, is achieved inside these reaction centers (eq. 37).

$$(\text{Chlorophyll})_2 + \text{Energy} \rightarrow (\text{Chlorophyll})_2^+ + e^- \tag{37}$$

Specialized reaction center proteins are the final destination for the transfered energy. Here, it is converted into chemical energy through electron-transfer reactions. These proteins consist of a mixture of polypeptides, chlorophylls (plus the special pair), and other redox-active cofactors. In the RCs, a series of downhill electron transfers occur, resulting in the formation of a charge separated state. Based on the nature of the electron acceptors, two types of reaction centers can be described. The first type (photosystem I) contains iron-sulfur clusters (Fe_4S_4) as their electron acceptors and relays, whereas the second type (photosystem II) features quinones as their electron acceptors. Both types of RCs are present in plants, algae, and cyanobacteria, whereas the purple photosynthetic bacteria contain only photosystem II and the green sulfur bacteria contain a photosystem I.[31,32] To gain a better understanding of these two types of RCs each will be further discussed.

A. Purple Photosynthetic Bacteria

In the mid-1980s, Deisenhofer reported his model for the structure of photosystem II for two species of purple photosynthetic bacteria (*Rhodopseudomonas viridis* and *Rhodobacter*) based on X-ray crystallography of

the light-harvesting device II (LH II).[33] Photosynthetic centers in purple bacteria are similar but not identical models for green plants. Because they are simpler and better understood, they will be described here. The photosynthetic membrane of purple photosynthetic bacteria is composed of many phospholipid-filled ring systems (LH II) and several larger dissymmetric rings (LH I) stacked almost like a honeycomb. Inside the LH I is a protein called the reaction center as illustrated in Figure 18.[34,35]

The LH II complex antenna is composed of two bacteriochlorophyll a (BCHl) molecules, which can be classified into two categories. The first one is a set of 18 molecules arranged in a slipped face-to-face arrangement and is located close to the membrane surface perpendicularly to these molecules. The second ring is composed of 9 BCHl in the middle of the bilayer. The first 18 BCHl have an absorption maximum at 850 nm and are collectively called B850, while the second (9 BCHl) have an absorption maximum at 800 nm and are called B800. These structures are contained within the walls of protein cylinders with radii of 1.8 and 3.4 nm. Once the LH II complex antenna absorbs light, a series of very complex nonradiative photophysical processes are triggered. First the excitation energy migrates via energy transfers involving the hopping of excitation energy within almost isoenergetic subunits of a single complex. This is followed by a fast energy transfer to a lower energy complex with minimal losses (Fig. 19). These ultrafast events occur in the singlet state (S_1) of the BCHl pigments and are believed to occur by a Förster mechanism.[34]

The energy collected by the LH II antenna is transferred to another antenna complex known as LH I, which surrounds the RC. The photosynthetic reaction centers of bacteria consist mainly of a protein that is embedded in and spans a lipid bilayer membrane. In the reaction center, a series of electron transfer reactions are driven by the captured solar energy. These electron transfer reactions convert the captured solar energy to chemical energy in the

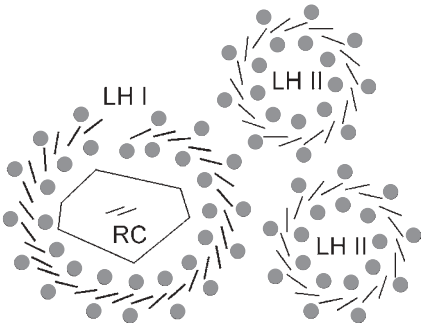

FIGURE 18. Two light-harvesting II (LH II) units next to one light-harvesting I (LH I) unit. *Gray circles*, polypeptides, *bars*, rings of interacting bacteriochlorophylls a (called B850). In the middle of LH I, there is the reaction center (RC), where the primary photo-induced electron transfer takes place from the special pair of bacteriochlorophylls b.[34]

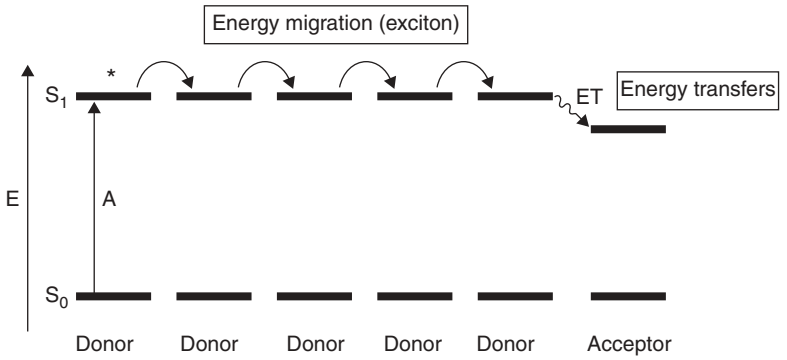

FIGURE 19. The exciton and energy transfer processes. (Modified from Ref. 8.)

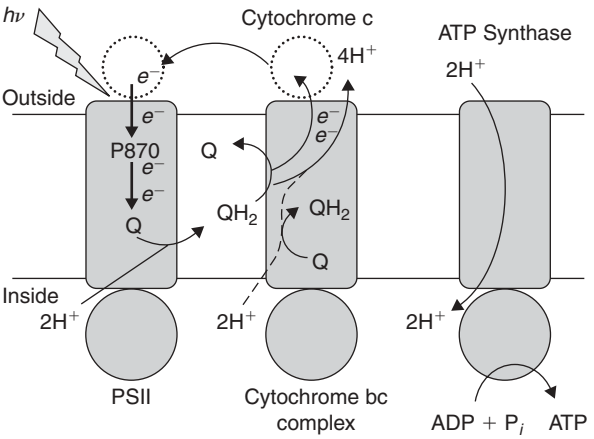

FIGURE 20. A cross-section of the photosynthetic membrane in the purple photosynthetic bactemria. PS II, photosystem II; *P870*, special pair; *Q*, plastoquinone; QH_2, dihydroplastoquinone; *ADP*, adenosine diphosphate; *ATP*, adenosine triphosphate.

form of a charge separation process across the bilayer.[36–38] The mechanism of this process is illustrated in Figure 20.

A special BCHl (P870) pair is excited either by the absorption of a photon or by acquiring this excitation energy from an energy transfer from the peripheral antenna BCHl (not shown in the figure for simplicity), triggering a photoinduced electron transfer inside the RC.[36] Two photoinduced electrons are transferred to a plastoquinone located inside the photosynthesis membrane. This plastoquinone acts as an electron acceptor and is consequently reduced to a semiquinone and finally to a hydroquinone. This reduction involves the uptake of two protons from water on the internal cytoplasmic side of the membrane. This hydroquinone then diffuses to the next component of the apparatus, a proton pump called the cytochrome bc1 complex (Fig. 20).

The next step involves the oxidation of the hydroquinone back to a quinone and the energy released is used for the translocation of the protons across the membrane. This establishes a proton concentration and charge imbalance (proton motive force; pmf). Thus the oxidation process takes place via a series of redox reactions triggered by the oxidized special pair BCHl (P870), which at the end is reduced to its initial state. The oxidation process is ultimately driven, via various cytochrome redox relays, by the oxidized P870. Oxidized P870 becomes reduced to its initial state in this sequence. Finally, the enzyme ATP synthase allows protons to flow back down across the membrane driven by the thermodynamic gradient, leading to the release of ATP formed from adenosine diphosphate and inorganic phosphate (P_i). The ATP fills the majority of the energy needs of the bacterium.[37]

B. Green Sulfur Bacteria

The observation of a photosynthetic reaction center in green sulfur bacteria dates back to 1963.[39] Green sulfur bacteria RCs are of the type I or the Fe-S-type (photosystem I). Here the electron acceptor is not the quinine; instead, chlorophyll molecules (BChl 663, 8^1-OH-Chl a, or Chl a) serve as primary electron acceptors, and three Fe_4S_4 centers (ferredoxins) serve as secondary acceptors. A quinone molecule may or may not serve as an intermediate carrier between the primary electron acceptor (Chl) and the secondary acceptor (Fe-S centers).[40] The process sequence leading to the energy conversion in RC I is shown in Figure 21.

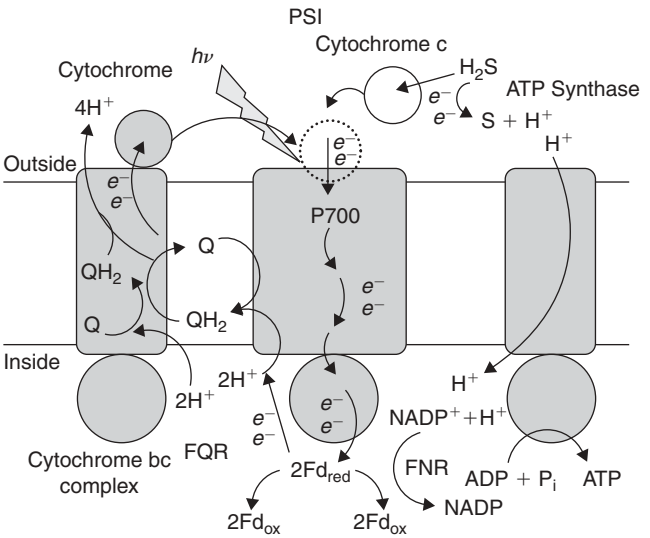

FIGURE 21. Photosystem I (PS I). P_{700}, special pair; Q, plastoquinone; QH_2, dihydroplastoquinone; *NADP*, nicotinamide adenine dinucleotide phosphate; *FQR*, ferredoxin-quinone reductase; *FNR*, ferredoxin-NADP reductase; *Fd*, ferredoxin; *ADP*, adenosine diphosphate; *ATP*, adenosine triphosphate.

A large number of chlorophyll antennas are used to harvest the solar energy, which in turn are used to excite the special pair P_{700}. The P_{700} donor will in turn transfer an electron to a primary acceptor (A_0, phyophytin) and in less than 100 ps to a secondary acceptor (A_1, a phylloquinone). The electron received by A_1 is in turn transferred to an iron-sulfur cluster and then to the terminal iron-sulfur acceptor.[41]

X. ORGANOMETALLIC POLYMERS AND SYNTHETIC PHOTOSYNTHESIS SYSTEMS

Organic and organometallic polymers exhibit potential applications in photonics. Organometallic polymers have received a lot of interest because they could combine the advantages of the high luminescence of the organic moiety with the high carrier density, mobility, steady chemical properties, and physical strength of inorganic materials. Research on such materials is expanding because of their potential use as electric components such as FETs, LEDs, and solar cells.

Much effort involving solar energy conversion is based on the natural chlorophyll system as a model. Here a metal atom is embedded within a polymer matrix that exhibits high electron mobility (delocalization). Ruthenium,[42–52] platinum,[53–59] and palladium[53–59] are the most employed metals. The use of materials containing the bis(2,2-bipyridine)ruthenium II moiety is common with ruthenium because this moiety absorbs energy in the UV region and emits it at energies approximating those needed to cleave water molecule bonds. The use of solar energy to create hydrogen that is harvested and later converted to useful energy has been a major objective.

Here we focus on a more direct conversion of solar energy into energy to charge batteries. For this purpose, metal-containing polymers can be classified into three types (types I, II, and III), as illustrated in Figure 22.[60,61] In type I, the metal centers are connected to the conjugated polymer backbone through saturated linkers, such as alkyl chains. Polymers of type I act as a conducting support. The electronic, optical, and chemical properties of the metal ions in

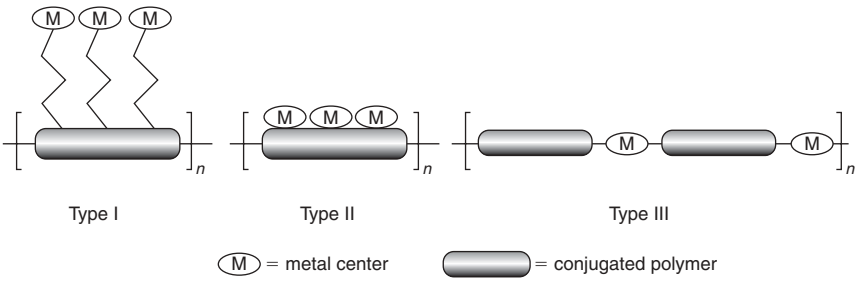

FIGURE 22. Types of metal-containing polymers. (Modified from Ref. 61a.)

this type of polymer remain the same as they would be if they were alone (i.e., unattached to the polymer backbone). In the second type, the metal centers are electronically coupled to the conjugated polymer backbone. This affects both the polymer and the metal group properties. The metal centers for type III are located directly within the conjugated backbone. In this last type, there are strong interactions between the metal center and the organic bridge. For this arrangement, the electronic interactions between the organic bridge and the metal group are possible, and new properties can be obtained because of the combination of the characteristics of the organic polymers with the common properties of the transition metals.[60,61]

Heavy metal atoms in the polymer backbone increases the intersystem crossing rate of the organic lumophores due to enhanced spin-orbit coupling. This populates more of the triplet states facilitating the study of interactions on both singlet and triplet states.[61] The study of energy transfer in organic and organometallic polymers is important. In fact, various types of organic and organometallic systems (oligomers and polymers) have been specifically designed for intramolecular energy transfer studies. Molecular architecture was found to play an important role in the efficiency of the energy transfer. The bridge between the donor and the acceptor chromophores exerts an important effect on the rates as well as the mechanism through which the energy transfer occurs.[62,63] A through-bond mechanism operates very efficiently for the cases of rigid saturated hydrocarbon bridges, while through-space mechanism are efficient for flexible bridges.[64,65]

Harvey et al. studied the photophysical properties of macromolecules built on M-P and M-CN (isocyanide) bonds, including the metal in the backbone. (This topic is reviewed in Chapter 2. The presence of the metal atom associated with the porphyrin moiety is examined here.

Photosynthesis is a source of inspiration for scientists interested in non-natural systems that convert light into chemical potential or electrical energy. Molecular wires, optoelectronic gates, switches, and rectifiers are typical examples of molecular electronic devices envisioned for use in energy or electron transfer processes.[66–69] A basic device structure, stimulating the natural systems, needs a scaffold on which the energy or charge transfer can be induced. Such a scaffold is represented in Figure 23.

The approach for this system is the mimicry of the highly efficient photosynthesis process in biological systems, by which an antenna device collects the light energy before a series of exciton, energy, and electron transfers, which lead to the synthesis of the plant's fuel.[70–73]

Porphyrins are an interesting class of compounds used for the study of energy- and electron-transfer functions of the natural photosynthetic machinery. The interest in porphyrins is motivated in part by their photocatalytic activity and electronic properties.[74] Porphyrins are also structurally related to chlorophyll.

Cofacial bisporphyrin systems use rigid spacers to provide a unique placement of two chromophores (donor and acceptor) at a given distance,

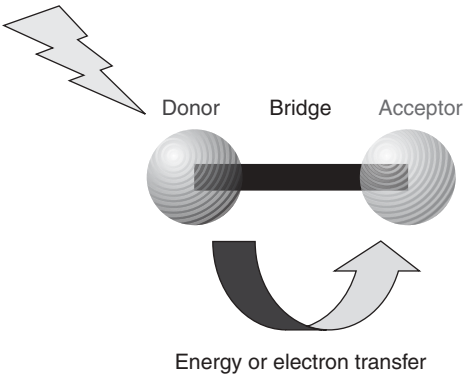

FIGURE 23. A scaffold for photo-induced intramolecular energy or electron transfer.

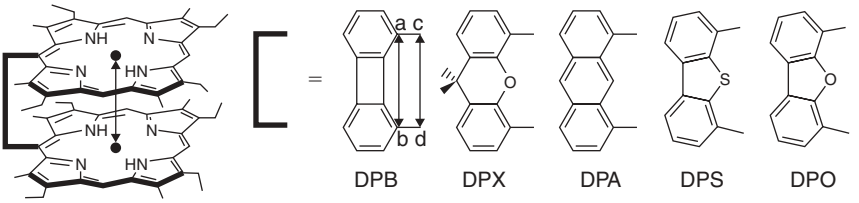

FIGURE 24. Examples of cofacial face-to-face porphyrin systems with different spacers. (Modified from Ref. 75.)

inducing a through-space energy transfer as the shortest pathway for intermolecular interactions and communications.[75]

Recently, the effect of the donor-acceptor separation has been studied.[76] Both the fluorescence lifetime and quantum yield were found to decrease as the distance between the two porphyrins—C_{meso}-C_{meso} (cd) and CC_{meso}-CC_{meso} (ab)—decreases (Fig. 24). As the two rings get closer to each other, they interact more strongly, and hence nonradiative deactivation becomes more pronounced.[75,76]

The rate dependence for the S_1 energy transfer (S_1 ET) for such systems exhibits a dependence of the energy transfer (k_{ET}) rate on the C_{meso}-C_{meso} distance. The rate increases as the distance decreases.[75] Face-to-face donor-acceptor separations are on the order of $\sim$3.5 Å verses the corresponding various donor-acceptor separations in the living supramolecular structures (found in plants, algae, and cyanobacteria) (Fig. 24 and 25) which are found to have separation distances to $\sim$20 Å. Despite this observation, the S_1 energy transfer data are strikingly slower (two orders of magnitude).[34] This leads to the question, What is missing?

Both through-space and through-bond energy transfer mechanisms are known, by which singlet-singlet energy transfer occurs through both

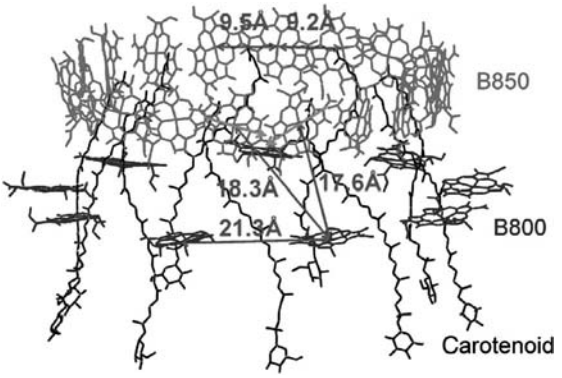

FIGURE 25. A LH II ring showing only the chlorophyll for the B850 network, the noninteracting B800 bacteriochlorophylls, and the rhodopin glucosides. Two of the B850 units are marked with *arrows*, representing the transition moments. (Modified from Ref. 34.)

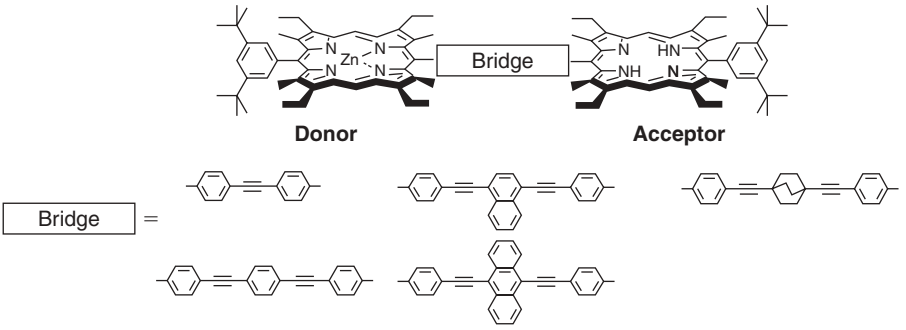

FIGURE 26. Some donor-bridge-acceptor systems by which energy transfer occurs through both Förster and Dexter mechanisms. (Modified from Ref. 78.)

Coulombic or dipole-dipole interaction (Förster) and double electron exchange (Dexter) mechanisms.

Different donor-bridge-acceptor based dyads based on metallated and free base porphyrins, by which singlet-singlet energy transfer occurs through both Förster and Dexter mechanisms are given in Figure 26.[77,78] The S_1 energy transfer in these systems occurs via a contribution from both coulombic and double electron exchange, which have almost the same magnitude and are not affected by the donor and acceptor distances. The electronic interactions depend on the donor-bridge energy gap and the bridge conformation (planar or nonplanar). Studies of the energy transfer rate as a function of the energy gap between the donor and the bridge have facilitated the separation of the two mechanisms. The rates observed for systems with the biggest energy gap were found to be almost equal to the Förster energy transfer rates.

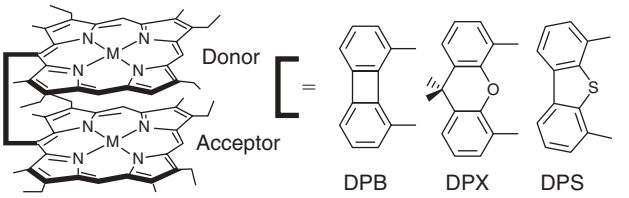

Spacer	DPB	DPB	DPB	DPX	DPX	DPX	DPX	DPS	DPS
M	Pt	2H	2H	Pt	2H	2H	Zn	2H	Zn
M'	Pt	Pt	Pd	Pt	Pt	Pd	Pd	Pd	Pd

FIGURE 27. Examples of cofacial bisporphyrin systems containing heavy atoms. (Modified from Ref. 75.)

Harvey's group studied energy transfers arising from the longer-lived triplet states as well as from the singlet states. These studies involved porphyrins containing a heavy metal (e.g., Pt and Pd), as shown in Figure 27.[79] Spin orbit coupling of the heavy atom increased the intersystem crossing rates, thus increasing the population of the triplet excited state. Triplet energy transfers can be analyzed only according to the Dexter mechanism because the Förster mechanism does not operate in the triplet excited states due to their diradical nature and the multiplicity change during the process. Energy transfer for the Dexter mechanism occurs via a double electron exchange—HOMO (acceptor)→HOMO(donor) and LUMO(donor)→LUMO (acceptor)—between triplet states of the donor and acceptor. In these systems (Fig. 27), the Pd- and Pt-metallated chromophores act as triplet donors, whereas the free base and Zn-containing complexes are the energy acceptors.

Analyses of energy transfer rates revealed that no sensitive transfer was detected for systems in which the spacer was DPS. In contrast, for dyads with the DPB and DPX spacers containing dyads, energy transfer occurred. This result was explained on the basis that singlet states energy transfer occurs via both Förster and Dexter mechanisms in the DPB- and DPX-containing dyads: C_{meso}-C_{meso} = 3.80 and 4.32 Å, respectively. The singlet energy transfer mechanism proceeded predominantly via a Dexter mechanism. Conversely, singlet energy transfer in the DPS-containing dyad, C_{meso}-C_{meso} = 6.33 Å, operated predominantly according to the Förster mechanism. This latter mechanism is inactive in the triplet states.[77] Thus, at such long distances, orbital overlap is poor and energy transfer is either weak or nil. This concept is of importance for designing molecular switches based on the distance separating the donor from the acceptor.

Through-bond energy transfer was also observed for porphyrin systems (regardless whether it occurs via a Förster or a Dexter mechanism). Through-bond energy transfer was reported for the rhodium meso-tetraphenylporphyrin-tin (2,3,7,13,17,18-hexamethyl-8,12-diethylcorrole), which exhibits a Rh-Sn bond

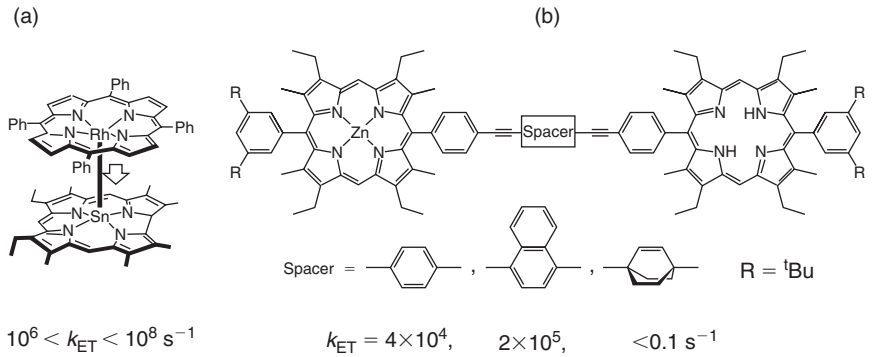

FIGURE 28. Porphyrin systems with through-bond energy transfer.

length of 2.5069 Å and a 3.4 Å separation between the average macrocycle planes, Figure 28.[75]

A photophysical study of these porphyrin systems showed the presence of significant intramolecular triplet energy transfer with an estimated k_{ET} ranging between 10^6 and $10^8\ s^{-1}$. Rates for the through-bond process were found to be three to five orders of magnitude larger than the through-space energy transfer. Other examples for through-bond energy transfer are shown in Figure 28.[80,81] The intramolecular energy transfer rates within these systems were found to be slower than those estimated for cofacial systems by two or three orders of magnitude.[34] These results can be helpful in predicting the rates for energy transfer (k_{ET}) for unknown systems.

A similar observation was made by Albinson, using Zn(II)porphyrin as the donor and free base porphyrin as the acceptor. The solvent viscosity and temperature were investigated as factors affecting the donor-acceptor interactions (Fig. 29).[32] In this example, and in agreement with Figure 28,[75] the rate increased with an increase of conjugation. Conversely, energy transfer is completely turned off when the conjugation is broken by the presence of the saturated system. This indicates that the through-bond energy transfer process occurs from the higher energy triplet state of Zn(II)porphyrin to the lower lying triplet state of the free base porphyrin.

The triplet energy transfer rates were measured over temperatures from 295 K to 280 K. The free energies of activation were found to be in the range of 1.0–1.7 kcal/mol (about 4–8 kJ/mol) in low-viscosity solvents, whereas in high-viscosity solvents, the temperature dependence is less pronounced. The triplet energy transfer was dependent on the solvent viscosity. Dramatically slower rates are observed in high-viscosity solvents due to smaller electronic coupling. The triplet-excited donor porphyrin was suggested to adopt conformation in less viscous solutions, which have a much larger electronic coupling than is possible in highly-viscous media. The porphyrins considered in the study are prone to conformational change in the triplet-manifold. This was

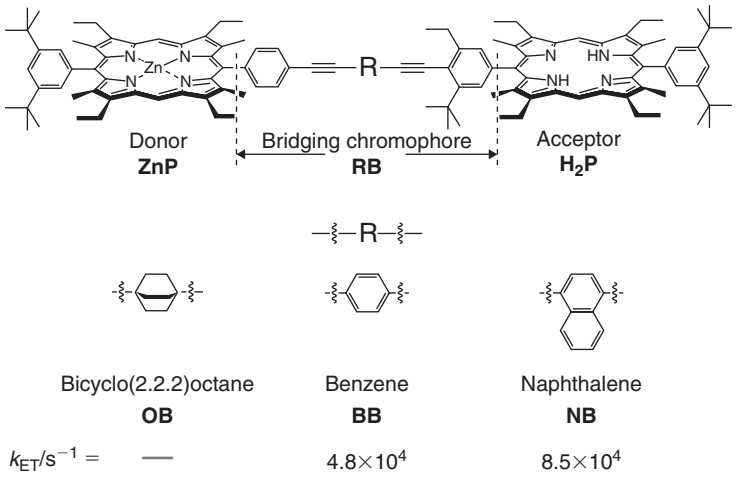

FIGURE 29. Porphyrin systems with through-bond energy transfer. (Modified from Ref. 82.)

explained on conformational grounds. In a donor-spacer-acceptor system (Fig. 29), with the ground state exhibiting a dihedral angle near 90°, the electronic coupling is changed in the triplet state to a situation in which the phenyl group should rotate toward the plane of the porphyrin macrocycle, leading to a considerable increase in the electronic coupling. This conformational freedom is lost when the solvent rigidifies, leading to a decrease in the coupling between the donor and the bridge. In solvents of low viscosity, another observation was made. Indeed, the change in temperature led to a triplet state distortion, inducing slower rates for triplet energy transfers.

All in all, the nature of the donor-acceptor linker is undoubtedly a controlling factor for the energy transfer, especially in the case of the triplet state interactions in which the mechanism of the interaction proceeds according to the Dexter mechanism (i.e., double electron exchange). This analysis illustrates the importance of studying different donor-acceptor spacers and their geometries during photo-induced energy transfer.

XI. SUMMARY

Interest in the electronic properties of π-conjugated oligomers and polymers and polymers containing metal atoms continues to increase greatly. The metal site can offer chromophores that exhibit metal to ligand charge transfer (MLCT) excited states in the π-conjugated polymers systems. This allows a variety of electronic and optical properties that are finding application in numerous areas, including solar energy conversion devices, nonlinear optical

materials (NLOs), and polymer light-emitting diodes (PLEDs), with applications in physical and chemical sensing, electrochromism, and a wide scope of electrocatalysis. The presence of the metal allows the synthesis of a wide variety of materials, with a variety of optical, electronic, chemical, and physical characteristics. The particular properties are changed and tuned by varying the metal, metal oxidation state, and metal environment. This volume describes some of these materials and applications for metal-containing sites embedded within polymer matrices and it suggests others.

XII. REFERENCES ADDITIONAL READINGS

N. S. Allen, *Photochemistry,* **36,** *232* (2007).

V. Balzani, S. Campagna, *Photochemistry and Photophysics of Coordination Compounds,* Springer Verlag, New York, 2007.

C. Carraher, *Polymer Chemistry,* 7th ed., Taylor & Francis, Boca Raton, FL, 2008.

R. Dessauer, *Photochemistry,* Elsevier, New York, 2006.

D. Neckers, *Advances in Photochemistry,* Wiley, Hoboken, NJ, 2007.

D. Phillips, *Polymer Photophysics,* 2nd ed., Springer, New York, 2007.

V. Ramamurthy, *Semiconductor Photochemistry and Photophysics,* CRC Press, Boca Raton, FL, 2003.

N. Turro, V. Ramamurthy, J. Scaiano, *Principles of Molecular Photochemistry,* University Science Books, New York, 2009.

XIII. REFERENCES

1. B. Valeur, *Molecular Fluorescence: Principles and Applications,* Wiley-VCH, Weinheim, Germany, 2002.
2. J. Michl, V. Bonacic-Koutechy, *Electronic Aspects of Organic Photochemistry,* Wiley Interscience, New York, 1990.
3. A. Khan, S. Muller, S. Hecht, *Chem. Commun., 584 (*2005).
4. J. N. Demas, G. A. Crosby, *J. Phys. Chem.,* **75,** *991* (1971).
5. D. F. Eaton, *Pure Appl. Chem.,* **60,** *1107* (1988).
6. C. Carraher, *Polymer Chemistry,* 7th ed., Taylor & Francis, New York, 2008.
7. E. U. Condon, G. H. Shortley, *The Theory of Atomic Spectra,* Cambridge University Press, Cambridge, UK, 1935.
8. R. Engleman, J. Jortner, *Mol. Phys.,* **18,** *145* (1970).
9. J. R. Lakowicz, *Topics in Fluorescence Spectroscopy,* vol. 1, *Techniques*, Kluwer Academic/Plenum Publishers, New York, 1999.
10. N. J. Turro, *Molecular Photochemistry,* Benjamin, New York, 1967.
11. J. R. Lakowicz, *Principles of Fluorescence Spectroscopy,* Springer, New York, 2006.
12. Nobel Lecture, 1967. http://nobelprize.org/nobel_prizes/chemistry/laureates/1967/porter-lecture.pdf.
13. K. A. Conors, *Binding Constants,* Wiley, New York, 1987.

14. T. H. Förster, *Ann. Phys.,* **2,** *55* (1948).
15. T. H. Förster, *Discuss. Faraday Soc.,* **27,** *7* (1959).
16. D. L. Dexter, *J. Chem. Phys.,* **21,** *836* (1953).
17. A. Mistra, P. Kumar, M. Kalalasanan, S. Chandra, *Semicond. Sci. Technol.,* **21,** *R35* (2006).
18. S. Faure, C. Stern, R. Guilard, P. D. Harvey, *J. Am. Chem. Soc.,* **126,** *1253* (2004).
19. R. A. Marcus, *Pure Appl. Chem.,* **69,** *13* (1997).
20. R. A. Marcus, *Annu. Rev. Phys. Chem.,* **15,** *155* (1964).
21. R. A. Marcus, *Angew. Chem.,* **105,** *1161* (1993).
22. R. A. Marcus, *J. Chem. Phys.,* **24,** *966* (1956).
23. R. A. Marcus, *J. Chem. Phys.,* **43,** *679* (1965).
24. L. D. Landau, *Phys. Z. SSR.,* **2,** *46* (1932).
25. J. R. Miller, J. Beitz, R. Huddleston, *J. Am. Chem. Soc.,* **106,** *5057* (1984).
26. C. Carraher, *Introduction to Polymer Chemistry,* Taylor & Francis, New York, 2007.
27. N. J. Ekins-Daukes, M. Guenette, *Boomerang Trans.,* **1,** *10* (2006).
28. (a) G. P. Smestad, *Optoelectronics of Solar Cells,* SPIE Press Washington, DC, 2002. (b) J. Rostalski, D. Meissner, *Sol. En. Mat. Sol. Cell.,* **61,** *87* (200).
29. R. van Grondelle, J. Dekker, T. Gillbro, V. Sundsrom, *Biochem. Biophys. Acta,* **1,** *1187* (1994).
30. R. E. Blankenship, *Molecular Mechanisms of Photosynthesis,* Blackwell Science, Oxford, 2002.
31. R. E. Blankenship, *Photosynth. Res.,* **33,** *91* (1992).
32. W. Hillier, G. Babcock, *Plant Physiol. J.,* **125,** *33* (2001).
33. P. Heathcote, M. R. Jones, P. Fyfe, *Phil. Trans. R. Soc. Lond. B,* **358,** *231* (2003).
34. P. D. Harvey, C. Stern, C. Gros, R. Guilard, *J. Inorg. Biochem.,* **102,** *395* (2008).
35. K. Iida, J. Inagaki, K. Shinohara, Y, Suemori, M. Ogawa, T. Dewa, M. Nango, *Langmuir,* **21,** *3069* (2005).
36. D. Gust, T. Moore, A. L. Moore, *Acc. Chem. Res.,* **34,** *40* (2001).
37. X. Hu, T. Ritz, A. Damjanovic, F. Auternieth, K. Schulten, *Q. Rev. Biophys.,* **35,** *1* (2002).
38. R. Horton, L. Moran, G. Schrimqeour, M. Perry, D. Rawn, *Principles of Biochemistry,* Pearson Prentice Hall, Upper Saddle River, NJ, 2006.
39. R. E. Blankenship, M. Madigan, C. E. Bauer, *Anoxygenic Photosynthetic Bacteria,* Kluwer Academic Publishers, Dordrecht, 2004.
40. J. M. Olson, *Photochem. Photobiol.,* **64,** *1* (1996).
41. M. Guergova-Kuras, B. Boudreus, A. Joliot, P. Joliot, K. Redding, *PNAS,* **98,** *4437* (2001).
42. K. Metera, H. Steiman, *Polym. Mater. Sci. Eng.,* **95,** *88* (2006).
43. A. Mozer, Y. Wada,, K. Jiang, N. Masaki, S. Yanagida, S. Mori, *Am. Inst. Physics.,* **89,** *435* (2006).
44. K. Man, H. Wong, W. Chan, B. Aleksandra, E. Beach, S. Rozeveld, *Langmui,* **22,** *3368* (2006).
45. F. Krebs, M. Biancardo, *Sol. Energy Sol. Cells.,* **90,** *142* (2006).
46. C. Carraher, *Macromolecules Containing Metal and Metal-like Elements,* vol. 7, Wiley, Hoboken, 2006, ch. 3.
47. C. Carraher, *Macromolecules Containing Metal and Metal-like Elements,* vol. 5. Wiley, Hoboken, 2005, ch. 13.

48. C. Carraher, A. Taylor-Murphy, *Polym. Mater. Sci. Eng.,* **76,** *409* (1997) and **86**, *291* (2002).
49. C. Carson, R. Gerhardt, R. Tannenbaum, *J. Phys. Chem.,* **111,** *14114* (2007).
50. C. Carraher, Q. Zhang, *Polym. Mater. Sci. Eng.,* **71,** *505* (1997) and **73**, *398* (1995).
51. C. Carraher, Q. Zhang, *Metal-Containing Polymeric Materials,* Plenum, NY, 1996.
52. F. Guo, Y. Kim, J. Reynolds, K. Schanze, *Chem. Commun., 1887 (*2006).
53. W. Wong, X. Wang, Z. He, A. Djurisic, B. Aleksandra, C. Yip, K. Cheung, H. Wang, H. Wang, C. Mak, W. Chan, *Nature Mater.,* **6,** *521* (2007).
54. P. D. Harvey, Z. Michel, *Z. Inorg. Chem.,* **32,** *4721* (1993).
55. J. Berube, K. Gagnon, D. Fortin, A. Decken, P. D. Harvey, *Inorg. Chem.,* **45,** *2812* (2006).
56. S. Clement, L. Guyard, M. Knorr, S. Dilsky, C. Strohmann, M. Arroyo, *J. Organomet. Chem.,* **692,** *839* (2007).
57. D. Evard, S. Clement, D. Lucas, B. Ganquet, M. Knorr, C. Strohmann, A. Decken, Y. Mugnier, P. D. Harvey, *Inorg. Chem.,* **45,** *1305* (2006).
58. I. Feinstein, *Rev. Inorg. Chem.,* **13,** *1* (1993).
59. I. Feinstein-Jaffe, A. Efrati, *J. Mol. Cat.,* **35,** 255 (1986) and **40**, *1* (1987).
60. W.-Y. Wong, S. Poon, *J. Inorg. Polym.,* **18,** *155* (2008), and references therein.
61. (a) M. O. Wolf, *Adv. Mater.,* **13,** *545* (2001). (b) W.-Y. Wong, *JIOPM,* **15,** *197* (2005).
62. A. Sen, V. Krishna, *Chem. Phys. Lett.,* **294,** *499* (1998).
63. N. Mataga, H. Yao, T. Okada, Y. Kanada, Y. A. Harriman, *Chem. Phys.,* **131,** *473* (1989).
64. D. Holten, D. Bocian, J. Lindsey, *Acc. Chem. Res.,* **35,** *57* (2002).
65. (a) S. L. James, *Coord. Rev.,* **276,** *32* (2003). (b) T. Tanase, *Bull. Chem. Soc. Jpn.,* **75,** *1407* (2002).
66. (a) J. M. Tour, *Acc. Chem. Res.,* **33,** *791* (2000). (b) R. W. Wagner, J. S. Lindsey, J. *Am. Chem. Soc.,* **116,** *9759* (1994).
67. (a) R. W. Wagner, J. S. Lindsey, J. Seth, V. Palaniappan, D. J. Bocia, *J. Am. Chem. Soc.,* **118,** *3996* (1996). (b) A. P. Silva, I. Dioxon, H. Gunaratne, T. Gunnlaughsson, P. Maxwell, T. E. Rice, *J. Am. Chem. Soc.,* **121,** *1393* (1999).
68. A. S. Martin, J. R. Sambles, *Physics Rev. Lett.,* **70,** *218* (1993).
69. D.H. Waldeck, D. N. Beratan, *Science,* **261,** *576* (1993).
70. P. D. Harvey in K. M. Kadish, K. M. Smith, R. Guildard, eds., *The Porphyrin Handbook,* vol. 18, Academic Press, San Diego, CA, 2003, and references therein.
71. X. Peng, N. Aratani, A. Takagi, T. Masumoto, T. Kawal, I. Hwang, T. Ahn, D. Kim, A. Osuka, *J. Am. Chem. Soc.,* **126,** *4468* (2004).
72. R. Takahashi, Y. Kobuke, *J. Am. Chem. Soc.,* **125,** *2372* (2003).
73. D. Kim, A. Osuka, *Acc. Chem. Res.,* **37,** *735* (2004).
74. J. Foekema, A. Schenning, D. Vriezema, F. Benneker, K. Norgaard, J. Kroon, T. Bjornholm, M. Feiters, A. Rowan, R. Nolte, *J. Phys. Org. Chem.,* **14,** *501* (2001), and references therein.
75. P.D. Harvey, C. Stern, C. Gros, R. Guilard, *Coord. Chem. Rev.,* **251,** *401* (2007).
76. F. Bolze, C. P. Gros, M. Drouin, E. Espinosa, P. D. Harvey, R. Guilard, *J. Organomet. Chem.,* **643–644,** *89* (2002).
77. S. Faure, C. Stern, E. Espinosa, J. Douville, R. Guilard, P. D. Harvey, *Chem. Eur. J.,* **11,** *3469* (2005).
78. (a) A. Kyrchenko, B. Albinsson, *Chem. Phys. Lett.,* **366,** *291* (2002). (b) K. Pettersson, A. Kyrchenki, E. Ronnow, T. Ljungdahl, J. Martensson, B. Albinsson, *J. Phys. Chem. A.,* **110,** *310* (2006).

79. J. Poulin, C. Stern, R. Guilard, P. D. Harvey, *Photochem. Photobiol.,* **82,** *171* (2006).
80. K. Kilsa, J. Kajanus, J. Martensso, B. Albinsson, *J. Phys. Chem. B.,* **103,** *7329* (1999).
81. J. Andreasson, J. Kajanus, J. Martensson, B. Albinsson, *J. Am. Chem. Soc.,* **122,** *9844* (2000).
82. J. Andreasson, A. Kyrychenki, J. Martensson, B. Albinsson, *Photochem. Photobiol. Sci.,* **1,** *111* (2002).

CHAPTER 2

Luminescent Organometallic Coordination Polymers Built on Isocyanide Bridging Ligands

Pierre D. Harvey,[1] Sébastien Clément,[1] Michael Knorr,[2] and Jérôme Husson[2]

[1]*Département de Chimie, Université de Sherbrooke, Sherbrooke, Québec, Canada*

[2]*Institut UTINAM UMR CNRS 6213, Université de Franche-Comté, Besançon, France*

CONTENTS

Macromolecules Containing Metal and Metal-like Elements,
Volume 10: Photophysics and Photochemistry of Metal-Containing Polymers,
Edited by Alaa S. Abd-El Aziz, Charles E. Carraher Jr., Pierre D. Harvey, Charles U. Pittman Jr., Martel Zeldin.

I. INTRODUCTION

Isocyanides, RN≡C, often alternatively named isonitriles, represent an interesting and well-established class of ligands in organometallic coordination chemistry.[1] Nowadays, these unsaturated compounds are also emerging more and more in the domain of material science. For example, the elaboration of self-assembled monolayers (SAMs) has been performed with these substrates.[2–5] Functional isocyanide metal complexes have recently been used as building blocks for the construction of supramolecular materials, which can be, for instance, employed as hydrogen-bonded liquid crystals.[6] The facile multiple insertion of aromatic isocyanides into the metal-carbon bond of heterodinuclear organometallic μ-acetylide complexes of the type $[Cl(PR_3)_2Pd\text{-}C{\equiv}C\text{-}Pt(PR_3)_2Cl]$ was also studied in detail, which led in the initial phase to the formation of organometallic oligomers. In the presence of an excess of CNR, these oligomeric species can be reactivated, and living polymerization finally affords polyisocyanide materials with narrow polydispersity. Moreover, the materials exhibit a helical arrangement of the organic chains, which are end capped with the organometallic $MCl(PR_3)_2$ moieties.[7,8] This chapter describes the preparation and the photophysical properties of polymeric isocyanide-based organometallic networks, in which the CNR ligand acts primarily as a linker between metal centers. However, for completeness, some recent examples of luminescent polynuclear systems bearing simple monodentate CNR ligands are also discussed.

In general, textbooks describe isocyanides as stronger σ-donor and weaker π-acceptor ligands than the isoelectronic carbon monoxide ligand. However, the modification of the R residue in CNR allows us to fine-tune the σ-donor/π-acceptor propensities of these ligands. Lentz and collaborators demonstrated that fluorinated isocyanides also behave as powerful π-acceptor ligands.[9] It is noteworthy that trifluoromethyl isocyanide is one of the strongest known π-acceptors, which may even exceed CO. Like CO, metal-coordinated CNRs may adopt a wide range of bonding modes, spanning from terminal to semi-bridging and to the symmetric μ_2-bridging coordination, as depicted in Figure 1.

The analogy with both surface-bound and cluster faces bridging μ_3-CO has its counterpart in the μ_3-CNR ligation. This triply bridging bonding mode was crystallographically evidenced in some homometallic and heterometallic

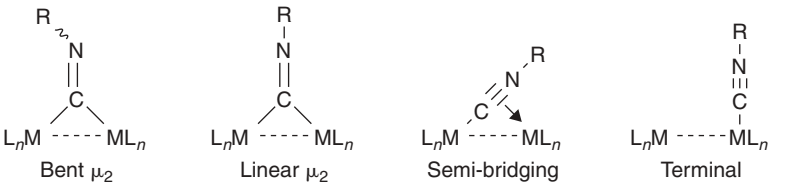

FIGURE 1. Different bonding modes of isocyanide ligands.

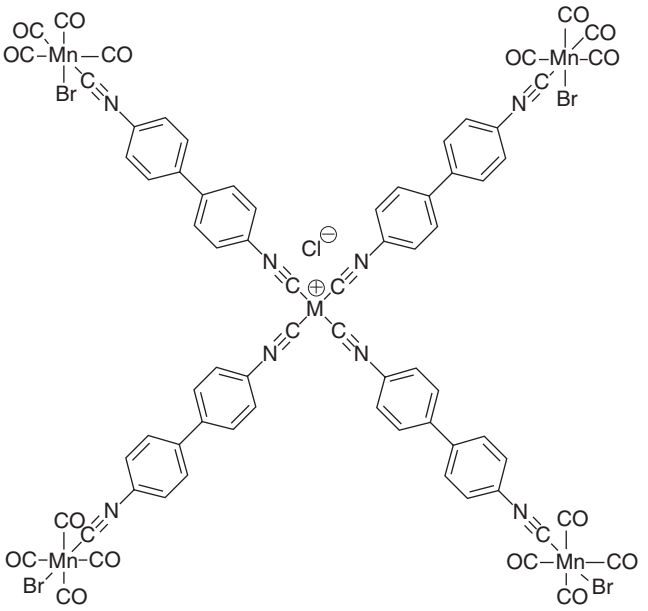

FIGURE 2. Example of a heteropentanuclear system (M = Rh, Ir) assembled by bridging 4,4′diisocyanobiphenyl linkers. (From Ref. 11.)

transition metal clusters. In addition, organic chemistry offers several strategies to synthesize functionalized compounds exhibiting two or more isocyanide groups, thus allowing the use of such compounds in the presence of low-valent "soft" metal ions as potential linkers (or connecting nodes) for the formation of oligonuclear and macromolecular systems.[4,5,10–13] It is therefore not surprising that these versatile propensities of isocyanides stimulated some research groups in the early 1980s to extend their uses as ligands in traditional molecular systems to the construction of polymetallic systems and coordination polymers.

One of the first reports on these materials deals with the reaction of $[Rh(CO)_2Cl]_2$ with aromatic diisocyanides to produce two-dimensional (2D) coordination polymers with stacked layer arrangements, as established from their X-ray powder diffraction patterns (Fig. 2).[14–16] Related 2D layered

network topologies was also investigated for Ir-containing polymers. Indeed, these materials are obtained by the reaction of the dinuclear $[Ir(1,5\text{-}COD)Cl]_2$ precursor with aromatic diisoyanides.[17] Novel organometallic aryldiisocyanide polymers of the Group 6 transition metals (Cr, Mo, W) were first prepared and characterized in 1988.[18] Their extreme sensitivity toward air oxidation also allowed the preparation of the oxidized 4,4′-diisocyanobiphenyl-tungsten(II) and -molybdenum(II) polymers and their corresponding mixed-valence materials. Ordered copper aryldiisocyanide polymers of type $\{[CuL_2]PF_6\}_n$ ($L = 1,4\text{-}(CN)_2C_6H_4$, $4\text{-}CNC_6H_4C_6H_4NC\text{-}4'$) were reported to form from Cu(I) precursors, such as $[Cu(MeCN)_4]PF_6$ in MeCN solution.[19] Original conjugated ruthenium-containing molecular rods with metal-vinyl linkages were isolated upon the reaction of the dinuclear vinyl complexes of type $[RuCl(CO)(PPh_3)_2]_2(\mu\text{-}CH{=}CH\text{-}R\text{-}CH{=}CH)]$ ($R = p\text{-}C_6H_4$, $p\text{-}C_6H_4\text{-}C_6H_4$) with 2,3,5,6-tetramethylphenyl diisocyanide.[20] The chemistry, characterization, and applications of the formed aryl diisocyanide organometallic coordination polymers containing various transition metals was reviewed by Feinstein-Jaffe in 1993.[21] These polymeric materials soon found applications in heterogeneous catalysis. The catalytic activity of palladium-, platinum- and rhodium-containing materials was probed for hydrogenation of alkenes and alkynes and the isomerization of 1-hexene under mild conditions.[22–24] The observation that three-dimensional (3D) coordination polymers of Ru(II) with 1,4-diisocyanobenzene ligands need 350 nm UV irradiation before exhibiting catalytic activity was rationalized by initial photochemical generation of electron-deficient active Ru-sites for olefin coordination.[25,26] In the area of molecular electronics, several papers focused the study of the electrical properties and conductivity of iron- and rhodium-diisocyanide coordination polymers.[27,28] Another area in which oligomeric and polymeric isocyanide-linked compounds are emerging concerns the design of luminescent and photonic materials. The scope of this contribution covers recent developments on the preparation of such compounds, including their structural features and their photophysics. For comparison purposes, related luminescent model compounds are also described in the two sections on polymetallic arrays and coordination polymers assembled through terminal and bridging disisocyanide and trisisocyanide ligands.

II. LUMINESCENT ORGANOMETALLIC POLYNUCLEAR SYSTEMS AND COORDINATION POLYMERS CONTAINING A TERMINAL ISOCYANIDE LIGAND

In this section, we describe the construction of metal-containing polymers and supramolecular assemblies, in which metallic centers are linked by a bridging diisocyanide ligand along with their photophysical properties (Fig. 3).

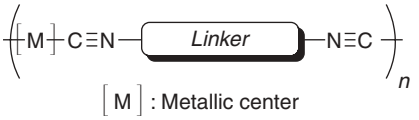

FIGURE 3. General structural motif of an organometallic polymer with a bridging diisocyanide linker.

Interesting examples of assemblies of star-shaped polymetallic systems with D_{3h} symmetry using 1,3,5-tris[(4-isocyano-3,5-diisopropyl-phenyl)ethynyl] benzene as the connecting node were provided by Kang and Ko.[12] The authors used the coordination ability of this functional trisisocyanide to attach a broad variety of transition metal fragments such as AuCl, AuSPh $Cr(CO)_5$, and $[(\eta^5\text{-Cp*})RhCl_2]$. The coordination of rhenium- and platinum-containing fragments, such as $[Re(bpy)(CO)_3(MeCN)]PF_6$ and [(CNN)PtCl] (CNN = *o*-6-phenyl-2,2′-bipyridine), yielded the two luminescent Re(I) and Pt(II) trisisocyanide complexes A and B (Fig. 4).

The photophysical properties of these two complexes are summarized by their UV-visible absorption, emission and excitation spectra (Fig. 5).

The absorption bands near 340 nm are assigned to metal to ligand charge transfer (MLCT). Similarly, the broad emission bands arises from the lowest energy of a MLCT excited state. In this case, the quantum yields were also measured, and a strong ligand field effect on the luminescence properties was quoted. All in all, the existence of these complexes confirms that the isocyanide ligands are versatile building blocks for the preparation of luminescent oligomers and polynuclear species.

Luminescent copper- and silver-containing coordination polymers were prepared by Harvey and collaborators using 1,8-diisocyano-*p*-menthane (dmb) as the coordinating unit.[29,30] This aliphatic diisonitrile ligand can adopt two conformations as depicted in Figure 6.

The polymer thus obtained, $\{[Ag(dmb)_2Y]\}_n$ (Y=counter-anion), is a one-dimensional (1D) material, in which each silver atom is coordinated in a tetrahedral fashion and doubly bridged by dmb ligands with the adjacent Ag neighbors.[31] The tetrahedral geometry about the Ag metals is found distorted where the C-Ag-C angles deviate from the ideal 109.42°. Different counteranions were investigated, and the structure proved to be variable. The solid-state arrangement was confirmed by X-ray analysis (Fig. 7). Despite their limited solubility, it was possible to demonstrate by ^{13}C NMR, T_1 (spin-lattice relaxation time) and by measuring nuclear Overhauser enhancement (NOE) constants that the polymers dissociate in oligomers of 7−9 units long in solution. Moreover, these polymers were investigated for their photophysical properties, because they exhibit a strong luminescence ($\lambda_{emi} \sim 500$ nm) upon UV light irradiation ($\lambda_{exc} = 250$ nm). Several investigations were then conducted on these materials to better understand their structures and properties.[30,32] Using dmb again as the bridging unit, Ag(I) and Cu(I) as the

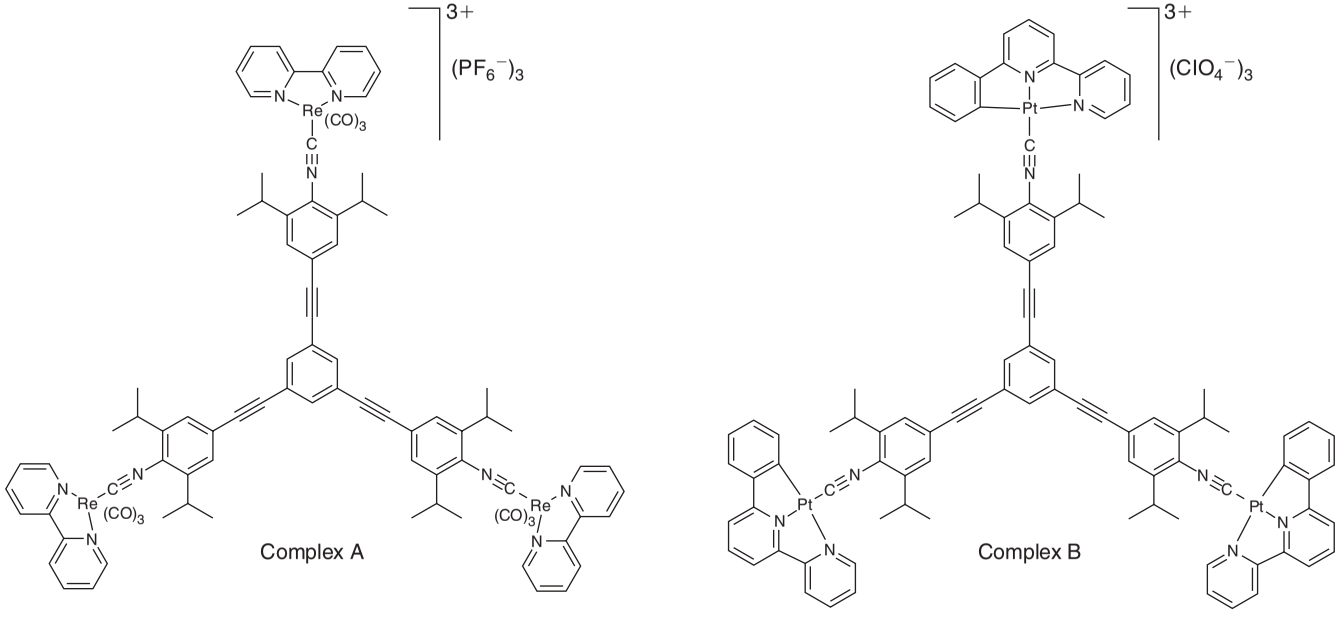

FIGURE 4. Luminescent trinuclear complexes bearing terminal isocyanides.

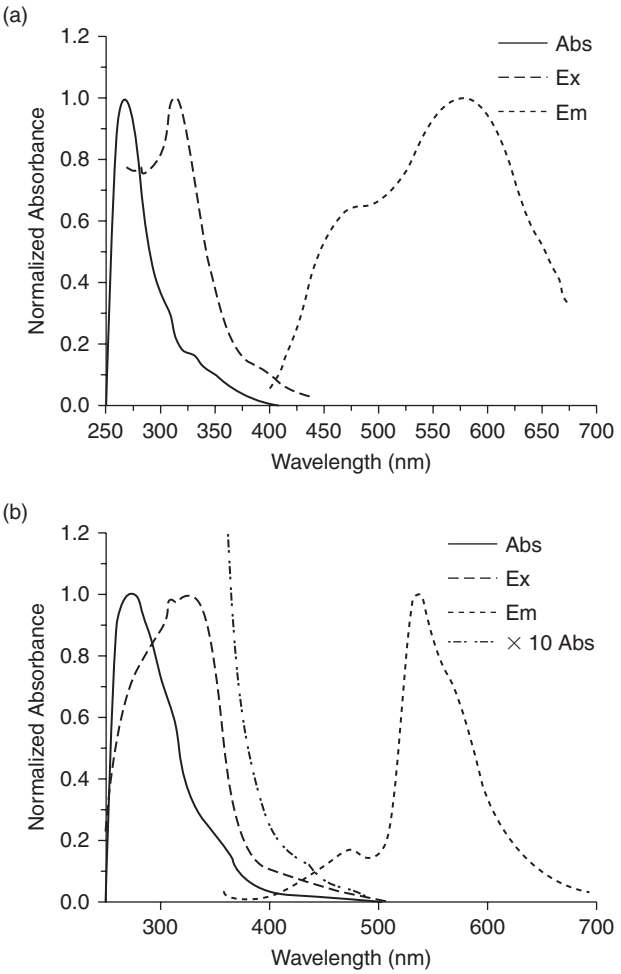

FIGURE 5. UV-visible (*Abs*), excitation (*Ex*), and emission (*Em*) spectra of complex A (a) and complex B (b) as 1.10^{-5} M solutions in CH_2Cl_2/DMF at 298 K. (Modified from Ref. 12.)

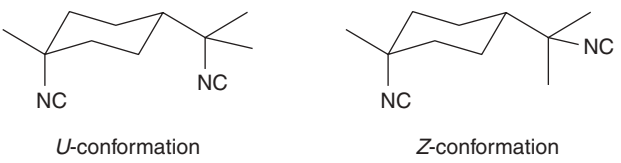

FIGURE 6. Both conformations of the 1,8-diisocyano-*p*-menthane (dmb) ligand.

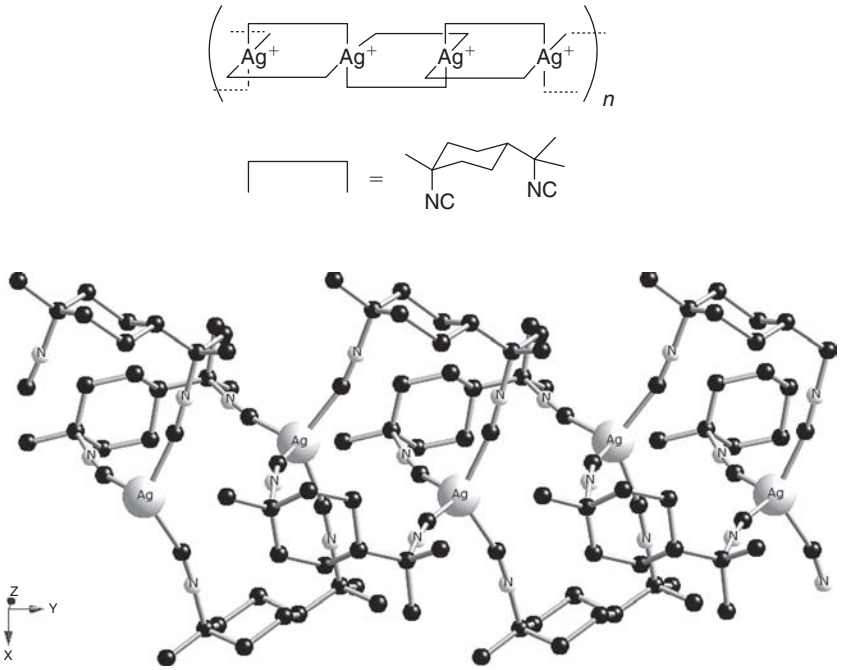

FIGURE 7. The $\{[Ag(dmb)_2^+]\}_n$ polymers (top) and the crystal structure of $\{[Ag(dmb)_2]BF_4\}_n$ (bottom). (Counteranions are omitted.)

metallic centers, and different counteranions (BF_4^-, PF_6^-, NO_3^-, ClO_4^-, CH_3COO^-), researchers were able to obtain a broad range of novel metallopolymers. The 1D structure of the polymers was again confirmed by X-ray analysis. It turned out that regardless of the metal ion (Ag or Cu), the same 1D arrangement was always observed. Calorimetric properties were also studied and the glass transition temperatures (T_g) were noted.

Thermogravimetric analysis (TGA) demonstrated that these polymers showed limited thermal stability for these materials, with decomposition occurring at temperatures >130°C. This stability is thought to be related to the M-CNR bond. The *Tg* data ranged from 37° to 96°C. The X-ray powder diffraction (XRD) pattern data provided complementary information concerning morphology of the polymers, as summarized in Table 1.

Different approaches were used to determine the molecular weight for the $\{[M(dmb)_2]Y\}_n$ polymers. First, the average molecular weights in weight (M_w) were measured using light-scattering techniques. But an innovative way to determine M_n (average molecular weight in number) was the use of NMR techniques, namely T_1 and NOE constant measurements.[33] From these experiments, it appeared that some polymers, especially those with Ag (I), are rather oligomeric in solution with the number of repetitive units ranging between 7 and 9 (Table 2).

TABLE 1. Calorimetric Properties and Morphologies of $\{[M(dmb)_2]Y\}_n$ Polymers

Polymers	T_g (°C)	T_{dec} (°C)	Morphology
$\{[Ag(dmb)_2]BF_4\}_n$ (**1**)	38–44	165–166	Highly crystalline
$\{[Ag(dmb)_2]PF_6\}_n$ (**2**)	None	170–171	Highly crystalline
$\{[Ag(dmb)_2]CH_3COO\}_n$ (**3**)	37	180	Highly crystalline
$\{[Ag(dmb)_2]NO_3\}_n$ (**4**)	58	133–134	Highly crystalline
$\{[Ag(dmb)_2]ClO_4\}_n$ (**5**)	40	168–170	Highly crystalline
$\{[Cu(dmb)_2]BF_4\}_n$ (**6**)	None	176	Highly crystalline
$\{[Cu(dmb)_2]BF_4\}_n$ (**7**)	57	178	Semicrystalline
$\{[Cu(dmb)_2]BF_4\}_n$ (**8**)	45	165	Amorphous
$\{[Cu(dmb)_2]NO_3\}_n$ (**9**)	79	148–150	Amorphous
$\{[Cu(dmb)_2]ClO_4\}_n$ (**10**)	96	140	Semicrystalline

TABLE 2. Molecular Weight Determination using Light Scattering and NMR

Polymers	M_w (light scattering)	M_w (NMR)	Number of Units
$\{[Ag(dmb)_2]BF_4\}_n$ (**1**)	≤10 000	4026	7
$\{[Ag(dmb)_2]NO_3\}_n$ (**4**)	—	4400	8
$\{[Ag(dmb)_2]ClO_4\}_n$ (**5**)	—	5291	9
$\{[Cu(dmb)_2]BF_4\}_n$ (**8**)	160 000	—	301
$\{[Cu(dmb)_2]ClO_4\}_n$ (**10**)	≤10 000	—	—

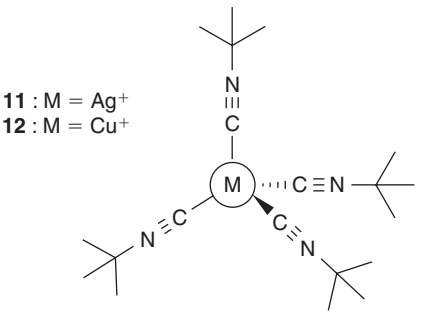

FIGURE 8. Structural motif of reference complex $[M(CN\text{-}t\text{Bu})_4]^+$.

The photophysical properties were also investigated in detail. To fully understand the photophysics of these polymers, these were compared with monomeric complexes, namely $[M(CN\text{-}t\text{Bu})_4]BF_4$, as model compounds (M = Cu (I), Ag(I)) (Fig. 8).

The absorption spectra of these polymers were very similar to that of the model compounds (Fig. 9). Calculations (DFT, B3LYP, 3-21G*) performed on the model compounds, $[M(CN\text{-}t\text{Bu})_4]^+$, predicted that the lowest energy

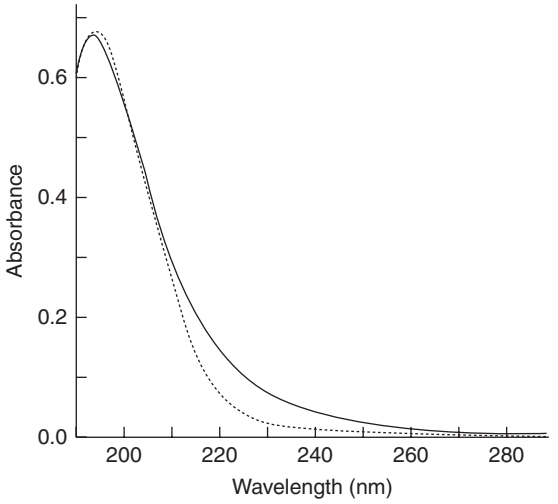

FIGURE 9. Absorption spectra of polymer **1** (solid line) and the model compound **11** (*dotted line*). (Modified from Ref. 30.)

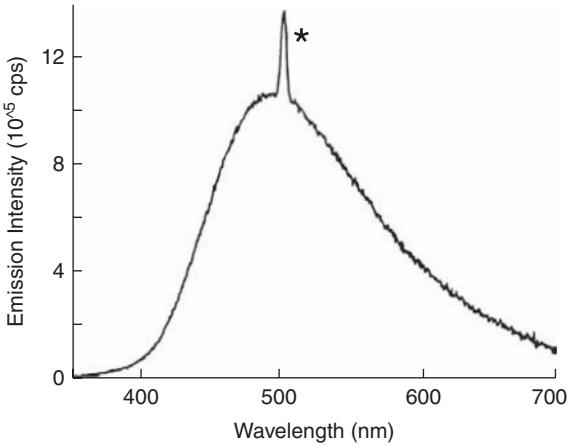

FIGURE 10. Emission spectrum of polymer **2** in KBr pellets at 77 K ($\lambda_{exc} = 250$ nm). The sharp peak (*) located at 500 nm is due to the first harmonic of the excitation line. (Modified from Ref. 30.)

electronic transition is a MLCT, consistent with the d^{10} electronic configuration of the metal and the presence of empty π^* orbitals on the CN fragments.

The materials are weakly luminescent at room temperature. However, intense blue emissions are observed at 77 K, both in the solid state and in solution. The emission bands are very broad, and generally centered around 500 nm (Fig. 10; Table 3).

TABLE 3. Emission Data of the Model Compounds and Polymeric Materials at 77 K

	λ_{emi} (nm)		
Compound	EtOH Solution	Solid State	KBr Pellets
$[Cu(CN\text{-}tBu)_4]BF_4$	510	490	514
$\{[Cu(dmb)_2]BF_4\}_n$	548	517	550
$[Ag(CN\text{-}tBu)_4]BF_4$	435	474	467
$\{[Ag(dmb)_2]BF_4\}_n$	502	486	510
$\{[Ag(dmb)_2]PF_6\}_n$	484	467	467
$\{[Ag(dmb)_2]NO_3\}_n$	435	489	499
$\{[Ag(dmb)_2]CH_3CO_2\}_n$	454	492	492

A large difference in λ_{max} emission between the monomeric and polymeric species is noted. This observation suggests that M···M interactions play a role in the stabilization of the emissive state. Emission lifetimes range from 7 to 600 μs. Such long lifetimes along with the large Stokes shift indicate the presence of a phosphorescence and allow one to assign the luminescence to a ^{3}MLCT state, the metal being in its d^{10} electronic configuration. The emission decays for the polymeric materials unexpectedly revealed a polyexponential kinetic. In addition, comparison of the decay curve in the solid state or in solution showed only settled differences, which were attributed to slightly different deactivation pathways. Time-resolved emission spectroscopy in the μs time scale demonstrated that the broad emission is composed of an infinite number of emission bands. In addition, it was demonstrated that the counteranions play a role in the deactivation mechanism because the emission lifetime decays were not the same from one counterion to another. A typical emission decay trace is presented in Figure 11 as an example.

The time-resolved emission spectra at early delay times exhibit emission bands that are blue shifted with respect to the steady-state spectrum. The comparison of both the approximated lifetimes and the emission maxima of the short-lined species closely resembles that observed for the mononuclear model complexes ML_4^+. On the other hand, the longer-lived species (i.e., longer decay times) exhibit red-shifted emission bands. These emission features are due to an exciton process consistent with an energy delocalization within the backbone similar to eximer emissions. This process is particularly useful for energy migration across a material. To corroborate the existence of this phenomenon, the polarization ratios of these emissions were also measured. The polarization ratio, N, turned out to be oscillating around $N = 1$ (in a scale that can vary between 0.5 and 3) all along the emission band, indicating that the emitted light was depolarized. The result is entirely consistent with the exciton process because the information about the transition moment is lost in the reversible energy migration across the polymer chain.

Other functional polymers were prepared for which the counteranions (BF_4^-, PF_6^-, ...) were replaced by the tetracyano-*p*-quinodimethane radical

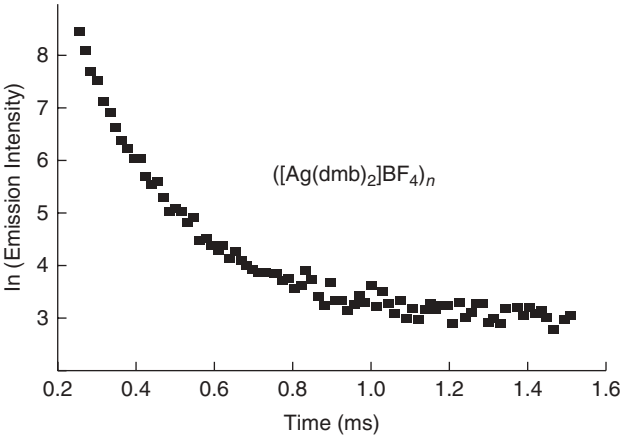

FIGURE 11. Typical emission decay trace for the polymer $\{[Ag(dmb)_2]BF_4\}_n$ in the solid state at 77 K. (Modified from Ref. 30.)

FIGURE 12. Structure $TCNQ^-$ (left) and TCNQ (right)

anion ($TCNQ^-$) (Fig. 12), thus providing materials of the type $\{[M(dmb)_2]TCNQ\}_n$ (M = Cu, Ag).[34] These new materials were readily prepared by counteranion metathesis with $TCNQ^-$. They are electrically insulating materials because of the coupling of the radicals and the lack of appropriate structure for the creation of a valence and conducting bands of the materials. However, conductive materials were obtained by doping the polymers with neutral TCNQ (Fig. 12) in acetonitrile solution and subsequent evaporation of the solvent. The isolated materials exhibited semiconducting properties based on the measurements of the resistivity as a function of the temperature (i.e., the graph of the conductivity as a function of the reverse of the temperature gave a negative slope).

X-ray analysis reveals a sandwich structure for these semi-conducting materials of formula $\{[M(dmb)_2]TCNQ\textit{n}TCNQ^\circ\}_n$ (N = 1, 1.5), the polymeric chains of $\{M(dmb)_2\}_n^{n+}$ are separated by layers of $TCNQ^-$ and neutral TCNQ (i.e., mixed-valence $TCNQ^-$ layers). The latter layer is responsible for the conductivity. Since TCNQ is an electron acceptor, electron transfer from the polymer to the mixed valence TCNQ layer is also possible from the Cu(I) center to the $TCNQ^-$ nTCNQ° layer. This photoinduced electron transfer from

the electron-rich d^{10} Cu(I) center in $\{Cu(dmb)_2^+\}_n$ to the TCNQ neutral species was indeed demonstrated. This process is indicated in equations 1 and 2:

$$\{Cu(dmb)_2\}_n^{n+} + h\nu \rightarrow \{Cu(dmb)_2\}_n^{n+*} \quad (1)$$

$$\{Cu(dmb)_2\}_n^{n+*} + TCNQ \rightarrow \{Cu(dmb)_2\}_n^{(n+1)+} + TCNQ^- \quad (2)$$

This photoprocess creates a hole defined by a d^9 Cu(II) center within the d^{10} Cu(I) chain, which can be stabilized by hole delocalization along the polymer backbone (exciton). The presence of π-stacked $TCNQ^{n-}$ in the lattice generates a valence and conducting band, which lead to photoconducting materials in these cases and photovoltaic cells.[35] Such devices were indeed constructed by spin-coating an acetonitrile solution of $\{[Cu(dmb)_2]TCNQ\}_n$ and neutral TCNQ onto a semitransparent and semiconducting SnO_2 glass. A counter electrode was then prepared by evaporating Al.[31] The typical setup for such a photovoltaic cell is presented in Figure 13.

Upon irradiation, a charge separation state is created, as indicated by equations 1 and 2, in which $TCNQ^{n-}$ is now $TCNQ^{(n+1)-}$ in the $\{[Cu(dmb)_2]TCNQ.nTCNQ^\circ\}_n$ materials. The reaction $\{Cu(dmb)_2\}_n^{(n+1)+} + 1\ e^- \rightarrow \{Cu(dmb)_2\}_n^{n+}$ occurs at the cathode surface, whereas the process $TCNQ^{(n+1)-} \rightarrow 1\ TCNQ^{n-} + 1\ e^-$, occurs at the anode, hence completing the circuit. Unfortunately, the resulting photocurrents were modest in comparison with other organic-based solar cells described in the literature.[35] However, no precautions were taken against impurities included in the air (dust) and solvent. Better photocurrent can still be obtained with more rigourous handling conditions.

Subsequently, structural variations on these polymers were made by replacing one dmb ligand with a diphosphine assembling ligand, diphenylphosphinomethane (dppm).[36] A scheme of such a 1D polymer is presented in Figure 14. This structure was elucidated upon X-ray analysis of a single crystal for M = Ag(I).

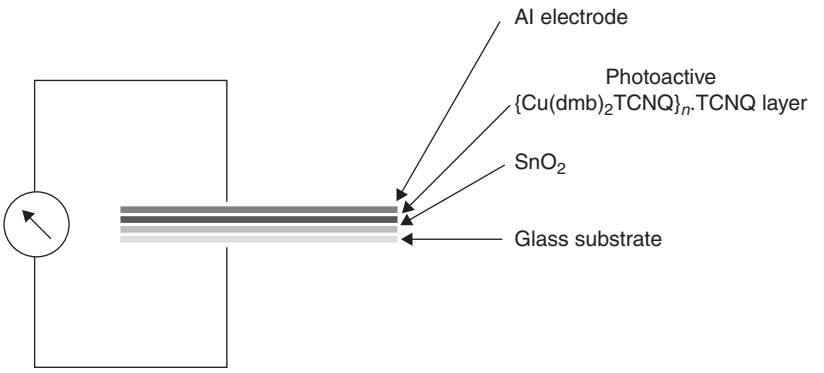

FIGURE 13. Structure of a solar cell designed with $\{[Cu(dmb)_2]TCNQ \cdot TCNQ^\circ\}_n$.

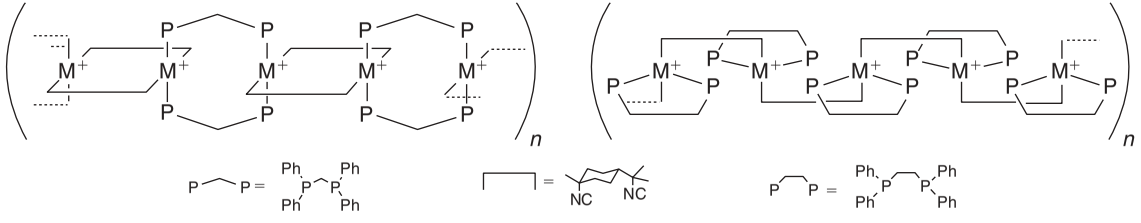

FIGURE 14. The mixed-ligand coordination polymers (M = Cu, Ag). The conteranion is BF_4^-.

It is interesting to note that in case of bisdiphenylphosphinoethane (compounds **15** and **16**), the diphos ligand is no longer bridging but chelating.

A better description of the photonic properties of the polymers was made by comparison with model compounds **17**–**20** (Fig. 15).

The electronic spectra for the new mixed-ligand 1D polymers exhibit an absorption band at ≈272 nm, assigned to a MLCT (rather than ππ* arising from the phenyl group). Solid-state emission spectra were recorded for both the model compounds and the polymers. The luminescence appears as broad bands located between 480 and 550 nm. Large Stokes shifts were observed, and the corresponding emission lifetimes (τ_e) ranged between 18 and 48 μs (Table 4). These experimental data indicate that these emissions are in fact phosphorescence.

Palladium(II)- and platinum(II)-containing polymers assembled by diisocyanide ligands are generally not luminescent.[37] Because photoinduced labilization of the ligand in M–C≡N–R systems is possible, absence of luminescence can occur when this photochemical process happens, and consequently the light energy is "wasted." As a result, luminescence is often not observed at room temperature in solution for such coordination polymers. Occasionally, only weak emissions at low temperature in the solid state can be detected.

Luminescence properties were reported for polymers that exhibit Pt(I) or Pd(I) in the main chain. A typical example is the ring-stressed complex $Pd_2(dmb)_2X_2$ (where X = Cl or Br).[38] The latter exists as a binuclear complex in solution but forms a polymer in the solid state (Fig. 16).

While the binuclear complexes are emissive in glass solutions at 77 K, only a weak luminescence was observed for the polymers in a solid state. A

17 M = Ag x = 1
18 M = Ag x = 2
19 M = Cu x = 1
20 M = Cu x = 2

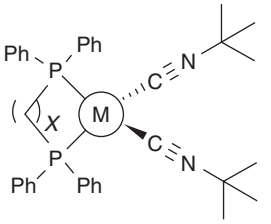

FIGURE 15. Structure of model compounds **17**–**20**. The environment about the metal is tetrahedral, based on X-ray structures.

TABLE 4. Emission Data for the Model Compounds and Corresponding Coordination Polymers in the Solid State at 298 K

Compounds	λ_{em} (nm)	Emission Lifetimes (τ_e in μs)
$\{[Ag(dppe)(dmb)](BF_4)\}_n$ (**15**)	548	27
$\{[Cu(dppe)(dmb)](BF_4)\}_n$ (**16**)	480	38
$[Ag(dppe)(CN\text{-}tBu)_2](BF_4)$ (**17**)	515	21
$[Cu(dppe)(CN\text{-}tBu)_2](BF_4)$ (**20**)	540	42

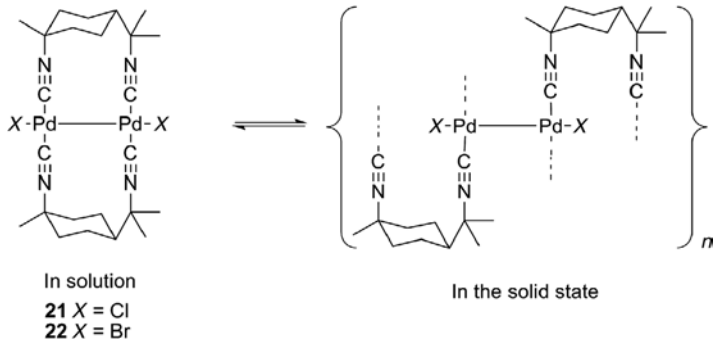

FIGURE 16. Equilibrium between the monomeric $Pd_2(dmb)_2X_2$ complex in solution and the polymeric $\{Pd_2(dmb)_2X_2\}_n$ in solid state.

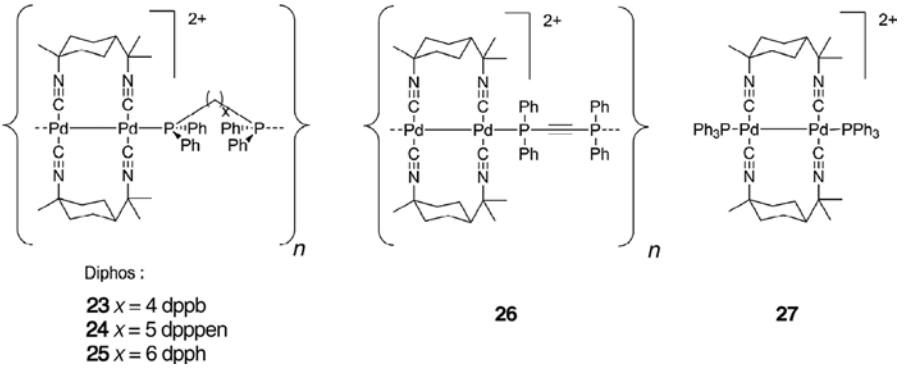

FIGURE 17. Structure of polymers **23**–**26** and model compound **27**.

possible explanation for this phenomenon is an efficient emission auto quenching occurring within the polymer (i.e., nonradiative energy transfer across the solid followed by thermal relaxation).[39]

Some other polymers of the same type with valence (I) were also prepared (Fig. 17). They exhibit almost the same structure, except that halides are replaced by diphosphine ligands (diphos) such as bis(diphenylphosphino) butane (dppb), bis(diphenylphosphino)pentane (dpppen), and bis(diphenylphosphino)hexane (dpph).[36,40] Again a model complex, compound **25**, was studied as reference (Fig. 17). The electronic spectra exhibit an absorption band near 480 nm. These coordination materials are not luminescent at room temperature but are luminescent in solution in butyronitrile at low temperature (i.e., 77 K). Density functional theory (DFT) calculations showed that luminescence arises from a $d\sigma$-$d\sigma^*$ triplet excited state. In these polymers, the nature of the phosphine ligand has a crucial effect on absorption and emission bands. Such behavior is explained by the increase in electronic density on the

TABLE 5. Photophysical Properties of Polymers **23**–**26** and model compound **27** in 2-MeTHF at 77 K

Compounds	λ_{abs} (nm)	λ_{em} (nm)	τ_e (ns)	φ_e
21	480	632	1.87	0.026
22	484	634	2.70	0.071
23	485	636	2.24	0.046
24	488	638	2.30	0.15
25	475	627	2.75	0.14

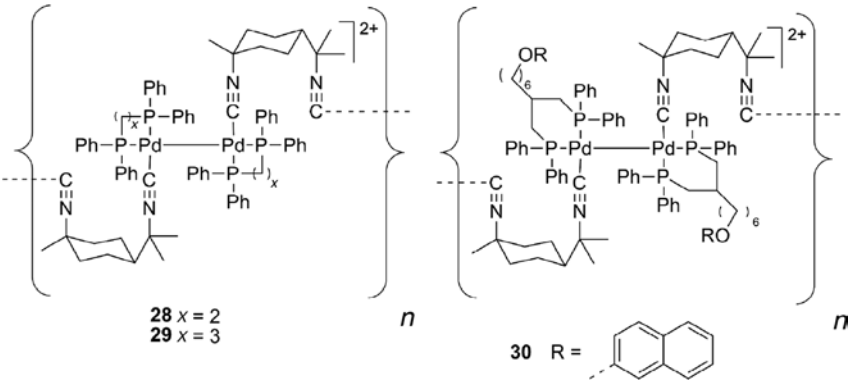

FIGURE 18. Polymers **28**–**30**.

P-atom due to an inductive effect, hence destabilizing the HOMO. The LUMO of the chromophore $Pd(CNR)_2(P)$ is stabilized, going from a saturated chain $P(CH_2)_nP$ to P–C≡C–P, via coupling of the empty *d* orbitals located onto P and the empty π-orbital located onto ethynyl fragment. The emission lifetimes in these polymers were surprisingly short (a few ns). Nevertheless, the quantum yields obtained are larger than expected for such short lifetimes (Table 5). This phenomenon remains unexplained.

Other examples of Pd-Pd bond-containing organometallic polymers were synthesized and described.[40] Their structures are different in that the diphosphine acts as a chelating ligand instead of a bridging M_2-support (Fig. 18).

In comparison with polymers **23**–**26**, absorption and emission bands of unsupported Pd-Pd bonded polymers **28**–**30** are blue shifted (Table 6), which is consistent with the structural change about the metals. The latter are composed of two phosphines and one isocyanide ligand, whereas the formers exhibit two isocyanides and one phosphine ligand around the Pd center.

Parallel to this series, Pd- and Pt-containing polymers **31** and **32** were also recently prepared (Fig. 19), together with model compounds **33** and **34**.[41] The

TABLE 6. Photophysical Properties of Polymers **28**–**29** in 2-MeTHF at 77 K

Compounds	λ_{abs} (nm)	λ_{em} (nm)	τ_e (ns)	ϕ_e
28	424	509	1.94	0.13
29	406	508	1.50	0.12
30	390	500	1.98	0.17

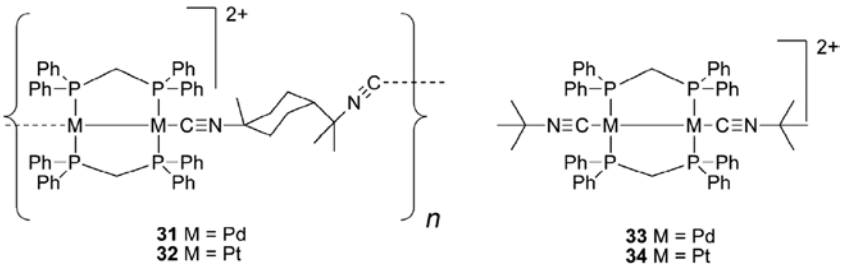

FIGURE 19. Structural motif of M_2-bond-containing polymers **31** and **32** and their model compounds **33** and **34**.

TABLE 7. Photophysical Properties of Polymers **31**–**32** and model compounds **33**–**34** in 2-MeTHF at 77 K

Compounds	λ_{abs} (nm)	λ_{em} (nm)	τ_e (μs)
31	328	675	3200
32	332	676	4100
33	366	730	—
34	366	750	6.2

main difference in their structures compared to the previous polymers is the fact that the diphos moiety spans both metallic centers, acting as bridges.

The photophysical properties of compounds **31**–**34** are presented in Table 7. Compared to the Pd-based materials, the Pt-based ones exhibit longer emission lifetimes. This is rationalized by the more stable Pt-Pt and Pt-L bonds compared to the more photolabile Pd-Pd and Pd-L ones. Therefore, the energy-wasting photo-induced cleavage (here bond cleavage process) does not occur or at least in a much less efficiency for the Pt-materials, thus reducing efficient nonradiative excited state deactivation.

The same phenomenon is observed[41] in conjugated 1D polymers **35** and **36** and their corresponding model compounds **37** and **38** (Fig. 20; Table 8). In these polymers, the bridging dmb ligand is replaced by a conjugated 1,4-diisocyanobenzene derivative. A large red shift is observed in the emission bands, which is readily attributed to electronic conjugation along the backbone of the polymers through aromatic units. The conjugation is also felt from the

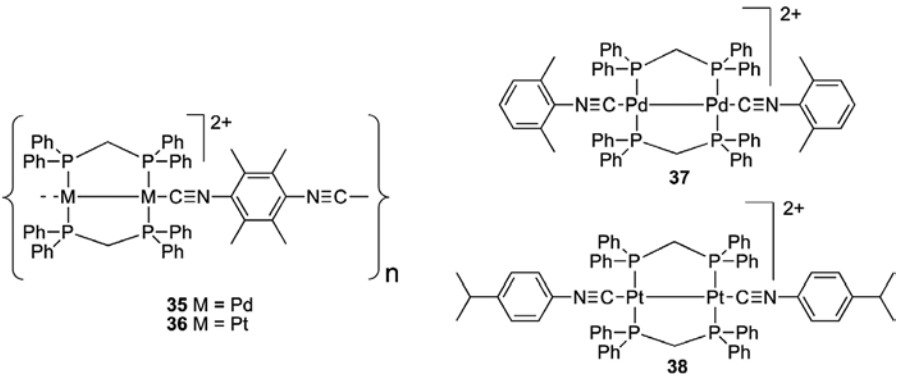

FIGURE 20. Structure of polymers **35**–**36** and model compounds **37**–**38**.

TABLE 8. Photophysical Properties of Polymers **35** and **36** and their corresponding model compounds **37** and **38** in 2-MeTHF at 77 K

Compounds	λ_{abs} (nm)	λ_{em} (nm)	τ_e
35	370	720	3.7 ns
36	344	715	3.1 μs
37	364	635	4.5 ns
38	340	673	3.1 μs

increase in thermal stability depicted in the TGA traces compared with those of the nonconjugated polymers **31** and **32**. The triplet state from which luminescence arises is now placed lower in energy (i.e., the emission bands are red shifted with respect to that of polymers **31** and **32**). This observation is clearly consistent with the presence of conjugation along the backbone of polymers **35** and **36**.

Finally, mixed-valence cluster-containing polymers were also synthesized.[40,42,43] Indeed Pd- or Pt-centers exhibiting a valence of +0.5 were used. Palladium-containing polymer **39** (Fig. 21) incorporates Pd_4 arrays, which are linked one to another by a dmb ligand, whereas the two Pd atoms inside the Pd_4 unit are coordinated by two dmb molecules each. The analogous Pt_4 polymers **40**–**42** were also prepared. The main difference is that the linking dmb unit is replaced by a diphos ligand (Fig. 21).

The photophysical data for these materials were studied as well (Table 9). The emission lifetimes are again very short, but those arising from the Pt materials are longer than those arising from Pd analogues. Low emission intensity is also noticed for these materials. Again, such behavior can be explained by the energy-wasting photo-induced cleavage of M-M or M-L bonds.

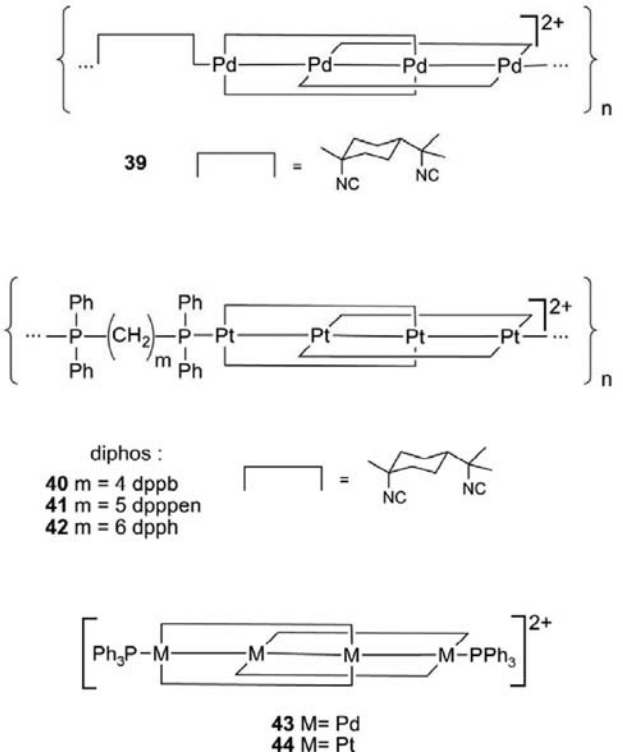

FIGURE 21. Structure of $\{Pd_4(dmb)_4(dmb)\}_n^{2+}$ **39**, $\{Pt_4(dmb)_4(diphos)\}_n^{2+}$ **40**–**42**, and model compounds **43**–**44**.

TABLE 9. Photophysical Properties of Polymers **39**–**42** and model compounds **43**–**44** in ethanol solution at 77 K

Compounds	λ_{abs} (nm)	λ_{em} (nm)	τ_e (ns)
39	488	720	1.14
40	394	736	4.78
41	394	750	5.15
42	394	755	5.17
43	534	635	0.67
44	412	750	2.71

III. LUMINESCENT POLYMERIC SYSTEMS CONTAINING AN ISOCYANIDE LIGAND ASSEMBLED VIA M···M INTERACTIONS

Diverse supramolecular structures have been prepared when using isocyanidegold(I) compounds owing to the presence of weak Au-Au interactions. Such aurophilic contacts are facilitated by the low steric bulk of the isocyanide

ligands, which allows the assembly of rod-like molecules.[44] These interactions are found attractive when the contact between adjacent Au···Au are less than the sum of Van der Waals radii of 3.6 Å.[45,46] Theoretical studies reveal that this weakly bonding interaction is the result of a combination of correlation and relativistic effects.[47–49] Experimental studies reveal that the strength of this attractive aurophilic interaction is comparable to hydrogen bonding, 7–11 kcal/mol.[50,51] Consequently, these interactions represent a significant factor in determining the solid-state organization of many isocyanidegold(I) complexes: The molecules associate to form dimers, larger linear or cyclic oligomers, 1D continuous or pleated extended chains, and 2D polymeric sheets.[45,52–55] Moreover, due to these aurophilic interactions, the photophysical properties of the polymeric structure in solution are different from those observed in the solid state.

Some gold-containing polymers incorporating isocyanide assembling ligand on one side and an alkynyl moiety on the other side were described by Puddephatt and collaborators.[56] Again these materials were compared to model compounds (Fig. 22).

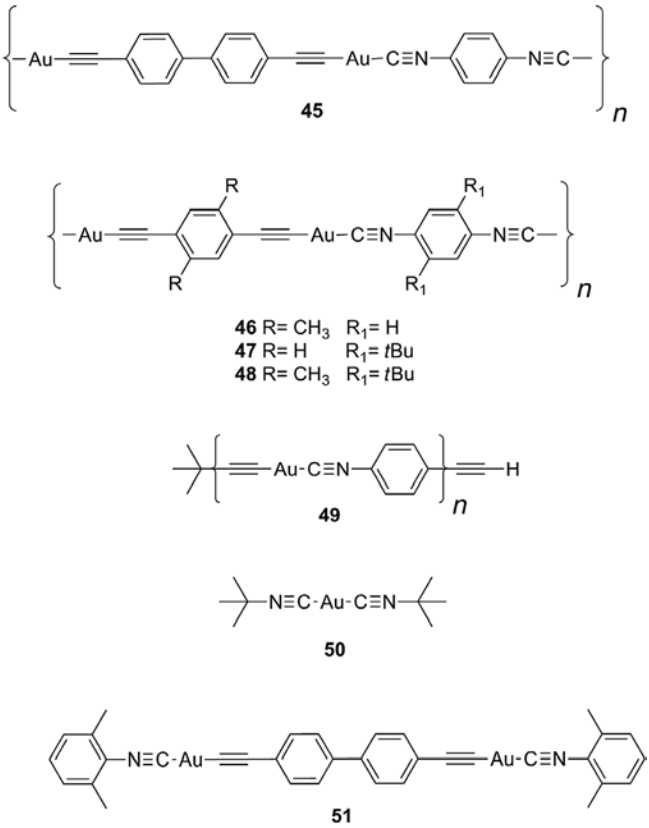

FIGURE 22. Structure of luminescent gold-containing polymers and of model compounds.

The luminescence spectra of these polymers were recorded both in solution (in dichloromethane, when solubility was sufficient) and in the solid state. The emission maxima recorded in the solid state are presented in Table 10.

The model compounds exhibit emissions of weak intensity in the range 420–550 nm. A red shift is observed in the solid state. The presence of aurophilic interactions in the solid state was demonstrated by X-ray crystallography ($d_{Au\text{-}Au} = 3.176$ Å). A red shift of the emission band is observed when going from the mononuclear model complexes **50** and **51** to polymer **48** (Fig. 23). This indicates that conjugation exist in these materials.

Harvey and collaborators reported also a 1D material in which Au(I) centers form a linear chain without halogen bridging units.[55] The complex Au_2(tmb)Cl_2 (tmb = 2,5-dimethyl-2,5-diisocyanohexane) obtained by the stoechiometric

TABLE 10. Emission Maxima for Polymers **45**–**49** and Model Compounds **50** and **51**, in the Solid State at 298 K

Compounds	λ_{em} (nm)
45	585[a]
46	585[a]
47	585[a]
48	585[a]
49	585[a]
50	470[a]
51	550[b]

[a] $\lambda_{exc} = 350$ nm.
[b] $\lambda_{exc} = 433$ nm.

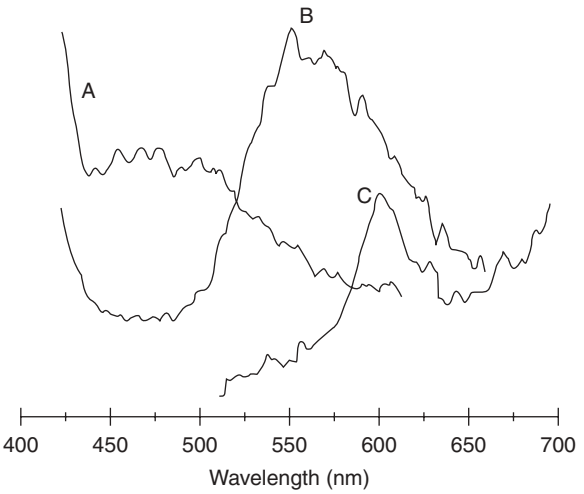

FIGURE 23. Emission spectra of model compounds **50** (*A*) and **51** (*B*) and polymer **48** (*C*), illustrating the red shift. (Modified from Ref. 56.)

reaction of $H[AuCl_4]$ with tmb exhibits weak intermolecular Au···Au interactions in the solid state (Fig. 24).

The presence of these aurophilic interactions was confirmed unambiguously by Raman spectroscopy ($\nu(Au\cdots Au) = 50\ cm^{-1}$) and by interatomic Au···Au distances (3.3063 (3) Å) obtained by single crystal X-ray data. This Au···Au separation is an intermediate value between the intermolecular Au···Au distances found in solid $K[Au(CN)_2]$ (3.64 Å)[57,58] and Au(MeNC)(CN) (3.52–3.72(4) Å),[59] the Van der Waals contacts (3.4 Å),[60] and the typical $r(Au_2)$ values (2.76–3.10 Å) for Au(I) dimers.[61,62] The solid-state UV-visible absorption spectra exhibit an absorption at 292 nm for $Au_2(tmb)Cl_2$ in KBr pellets (Fig. 25), whereas in solution, the latter is observed at $\lambda_{max} = 272$ nm.

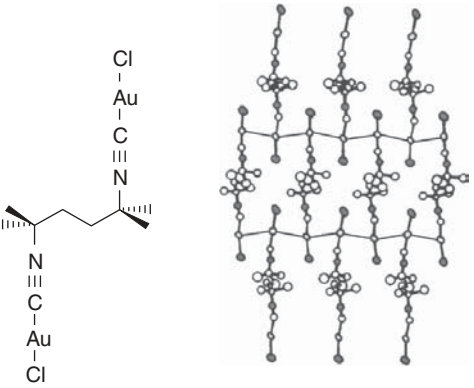

FIGURE 24. The molecular structure of $Au(tmb)_2Cl_2$ (*left*) and the X-ray structure of its polymeric form in the solid state (*right*). *Dotted line*, the Au···Au interactions. The H-atoms are omitted for clarity. (Modified from Ref. 55.)

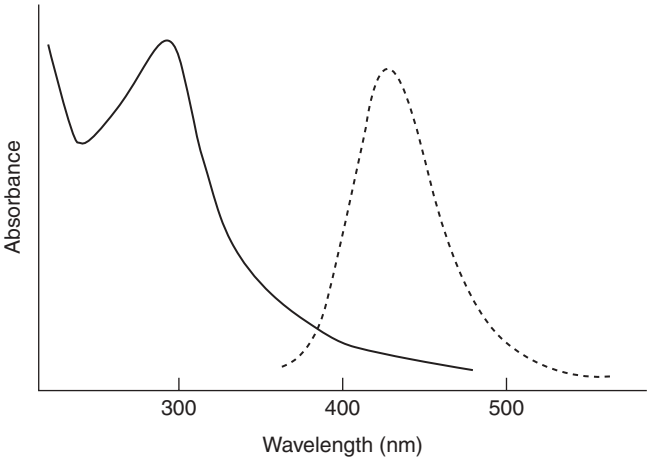

FIGURE 25. Solid-state UV-visible (—) and emission (···) spectra of $Au_2(tmb)Cl_2$ in KBr pellets. (Modified from Ref. 55.)

Therefore, this low-energy band is assigned to a metal-centered $d \rightarrow p$ transition instead of as arising from Au···Au interactions. The solid-state luminescence spectrum (Fig. 25) exhibits a phosphorescence emission band centered at 417 nm. This value compares favorably with those reported for solids $K[Au(CN)_2]$[58] and $Au_2(dmb)(CN)_2$.[63]

Two-coordinate Au (I) complexes are typically colorless but may display strong luminescence in the visible region, depending on the nature of the ligand.[63] For example, the luminescence from solutions of $K[Au(CN)_2]$ can be tuned to appear anywhere from 275 to 470 nm, depending on the concentration and solvent.[64] More recently, Balch and collaborators.[65] reported the distinct luminescence behavior of polymorphic yellow and colorless forms of $[(\text{cyclohexyl isocyanide})_2Au^I]PF_6$. The positions of the luminescence bands in these polymorph crystals are probably determined by crystal packing forces. In these two cases, the cations form infinite chains through aurophilic interactions. However, although bulky cyclohexyl groups are present, the longest Au···Au distance (2.9803(6) Å) in the yellow crystal is on the short end of the aurophilic attractions and is much shorter than the corresponding distances in the colorless polymorph (3.1822(3) Å). In Figure 26a, the absorption spectra for acetonitrile solutions of the two forms of $[(C_6H_{11}NC)_2Au^I](PF_6)$ are identical, with λ_{max} at 244 and 216 nm. The absorption is assigned to MLCT that involves an excitation from the filled d^{10} gold d_z^2 orbital to a π^* orbital of the ligand.[66] However, each of the two polymorphs displays a distinct luminescence spectrum (Fig. 26b and c). The emission spectrum of colorless solid at 298 K exhibits a maximum at 424 nm, whereas the yellow solid shows an emission at longer wavelength (480 nm). The excitation spectra of the colorless and yellow crystalline polymorphic complexes display maxima at 353 and 394 nm, respectively. However, the onset of the excitation spectra occurs at a longer wavelength than that seen in the absorption spectrum (Fig. 26a), indicating extended Au···Au interactions between cations in their solid-state supramolecular structures.

Structure and luminescence properties properties of $(R\text{-NC})Au^ICN$ (R = *n*Bu, *t*Bu, *i*Pr, Me, Cy) were also investigated by Balch and collaborators.[45] By varying R, negligible variation in the UV-visible spectra of $(CyNC)Au^ICN$, $(n\text{BuNC})Au^ICN$, and $(i\text{PrNC})Au^ICN$ in acetonitrile solutions were observed, and all ressemble that of the spectrum of $(MeCN)Au^ICN$ in solution described by Chastain and Mason.[66] The absorption bands in the ultraviolet region were assigned to MLCT from the d^{10} filled gold orbitals. The crystalline forms of all five complexes are luminescent at room temperature, but they are nonluminescent in solution. Two more examples: (CyNC)AuCN and (*t*BuNC) AuCN, form simple zigzag chains (Fig. 27). The emission bands show a dependence on the excitation wavelength.

Consequently, the luminescence is assigned unambiguously to the presence of aurophilic interactions. The photophysical data obtained for these alkylisocyanides gold(I) complexes are presented in Table 11.

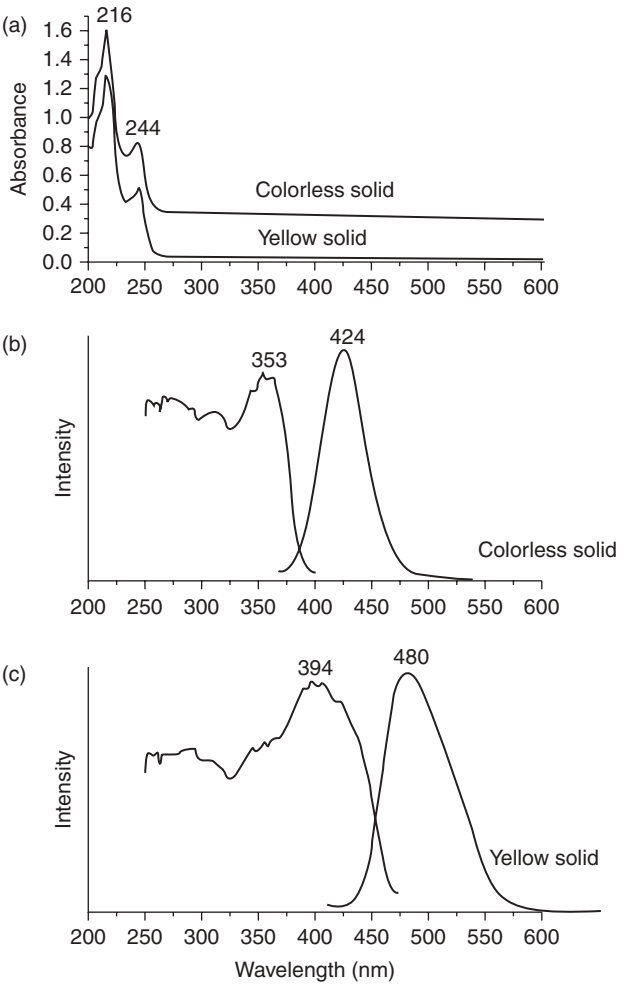

FIGURE 26. (a) The absorption spectra of acetonitrile solutions of the yellow andcolorless (offset by 0.4 absorbance units) polymorphs of $[(C_6H_{11}\text{-}NC)_2Au^I](PF_6)$. The emission (right side) and excitation (left side) spectra of the colorless (b) and the yellow (c) polymorphs of $[(C_6H_{11}\text{-}NC)_2Au^I](PF_6)$. (Modified from Ref. 65.)

Balch and collaborators also examined the effects of the different halide ligands on the self-organization and the luminescence of $(CyNC)Au^IX$ (X = Cl, Br, I).[46] These complexes display orange-red unstructured phosphorescence bands with extremely large Stokes shift ($(15-20) \times 10^3$ cm^{-1}). The spectroscopic data (Table 12) obtained for the series of isostructural complexes suggests that differences in supramolecular organization found in the crystals do not strongly influence the spectroscopy. However, these latter results contrast with the previous observations on complexes of type $(RNC)Au^ICN$

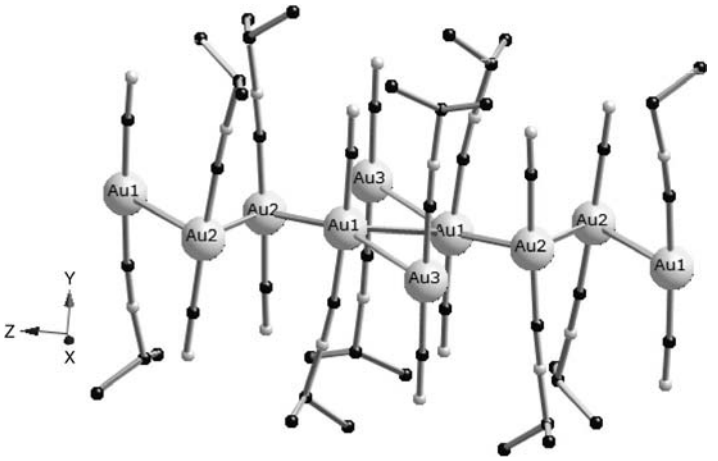

FIGURE 27. Crystal structure of (*i*PrNC)Au^{I}CN · 0.5 CH_2Cl_2. Hydrogens atoms are omitted.

TABLE 11. Photophysical Data for (RNC)Au^{I}NC Complexes in the Solid State at 298 K

Compounds	λ_{em} (nm)	τ_e
(*t*BuNC)Au^{I}CN	371	1.2 μs
(*n*BuNC)Au^{I}CN	389	0.70 μs
(MeNC)Au^{I}CN	393	140 ns
(CyNC)Au^{I}CN	403	0.70 μs
(*i*PrNC)Au^{I}CN	430	1.2 μs

TABLE 12. Photophysical Data for (RNC)Au^{I}NC Complexes in the Solid Sate Obtained at 298 K

Compounds	λ_{em} (nm)
(CyNC)Au^{I}Cl	610
(CyNC)Au^{I}Br	610
(CyNC)Au^{I}I	625

($\lambda_{em} = 371-430$ nm). Clearly, changing from a π-acceptor anionic ligand in (CyNC)Au^{I}CN to a π-donor anionic ligand in (CyNC)Au^{I}X alters the electronic properties of these complexes and, consequently, their luminescence behavior. Note that the luminescence and absorption characteristics of (CyNC)Au^{I}X are rather similar to those communicated for the related compound (CO)Au^{I}Cl.[67]

In all these examples, it is clearly established that there is a need to have intramolecular or intermolecular closed-shell Au···Au interactions in order to

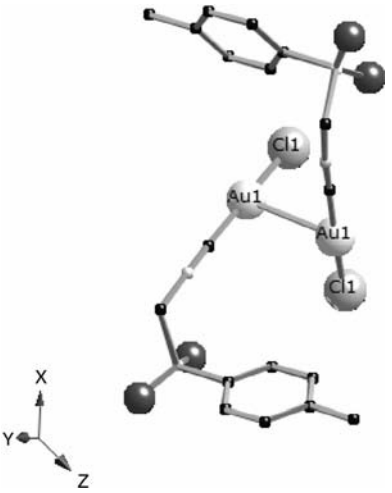

FIGURE 28. Crystal structure of the dimer [AuCl(*p*-tosyl)methylisonitrile]$_2$. Hydrogen atoms are omitted.

observe Au-centered luminescence in two-coordinate complexes. However, no direct relationship between the luminescence energy and the crystallographic ground-state distances has been established so far.[68] This observation contrasts with the situation encountered in the luminescent systems based on other metals. Elbjeirami and collaborators have recently described a crossed dimeric compound chloro((*p*-tosyl)methylisonitrile)gold(I) exhibiting a higher emission energy ($\lambda_{em} = 478$ nm), despite a very short intermolecular Au$\cdots$Au distance (3.0634(4) Å) compared to the extended-chain compounds such as CyNCAu^{I}X ($\lambda_{em} = 610-625$ nm) (Fig. 28).[69]

For CyNCAu^{I}X, the molecules stack in extended chains, not as dimers. Hence, the emission occurs at lower energy than the excited state with the shortening of Au$\cdots$Au distances and with a greater distorsion. In conclusion, the emission energies are more sensitive to the association modes than to the ground-state Au$\cdots$Au distances in (RNC)Au^{I}X complexes. Such conjugation in the excited state is a promising property of such materials for future applications in optoelectronics.

IV. LUMINESCENT ORGANOMETALLIC POLYMETALLIC SYSTEMS AND COORDINATION POLYMERS CONTAINING BRIDGING ISOCYANIDES

Despite the importance of isonitriles as assembling ligands and substrates in organometallic and coordination chemistry, reported studies concerning the structure and the reactivity of homobimetallics and heterobimetallics M(μ-CNR)

M possessing an isonitrile bridge between the metal centers are more scarce in comparison with the homodinuclear and heterodinuclear compounds bearing bridging carbonyls.[37,41]

Bent and linear μ-CNR bonding modes are the two forms in homobimetallic M(μ-CN-R)M systems. The first complexes, **52**–**57**, of the bent type in the Ni triad [XPd(μ-dppm)$_2$(μ-C=N-R)PdX] (R = C_6H_{11}, C_6H_5, CH_3, X = Br, Cl) were prepared by Balch and collaborators in 1977[70] and were investigated for their properties to form inclusion compounds.[71–74] The platinum (**58, 59**)[75] and nickel (**60**–**63**) analogues[76,77] were also investigated a few years later (Fig. 29). These homobimetallics complexes were obtained by insertion of one isocyanide into the M-M bond of [XM(μ-dppm)$_2$MX] (M = Pd, Pt) or by reaction of [Ni^I_2(CNMe)$_8$][PF_6]$_2$ with bis(diphenylphosphinomethane) (dppm).

The photophysical data for the binuclear system [Ni_2(μ-L)(CNMe)$_2$ (μ-dppm)$_2$] (L=C=N-R, C=N-(Me)(R)$^+$, NO^+) complexes were examined by Kubiak and collaborators.[78] The nature of the lowest energy electronic absorption band for these isocyanide complexes was assessed by varying the nature of the bridging ligand and the solvent. The electronic absorption spectra of these species exhibit an intense, broad band centered between 350 and 450 nm. Hypsochromic shifts of the emission band with the solvent polarity (a difference as large as 85 nm was noticed) and a bathochromic shift and increase of the maxima with the nature of the aryl group led the authors to assign the lowest excited states to a metal to μ-ligand charge transfer ($M_2 \rightarrow \mu$–LCT).

Before our work on the assembly of metallopolymers through bridging diisocyanides, there was just one precedent in the literature on metal-organic frameworks with bridging CNR ligand where one C atom bridges two metals.[79] Upon treatment of the molecular precursor [Pd(CNMe)$_4$](BF_4)$_2$ with 4,4-diisocyanobiphenyl, IR characterization of the precipitated organometallic polymer revealed strong IR absorptions in the 2180 cm^{-1} region, typical for terminal bound CNR groups, along with bands at 1700 and 1600 cm^{-1}. These

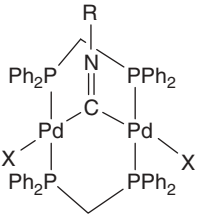

52 X = Br, R = Cy
53 X = Cl, R = Cy
54 X = Br, R = Ph
55 X = Cl, R = Ph
56 X = Br, R = Me
57 X = Cl, R = Me

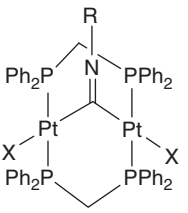

58 X = I, R = *p*-tolyl
59 X = Cl, R = *p*-tolyl

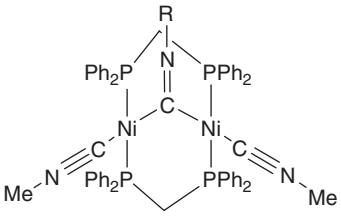

60 R = Ph
61 R = *p*-tolyl
62 R = *p*-Cl-Ph
63 R = Me

FIGURE 29. Some examples of homobimetallic complexes with μ-CNR ligands.

latter are readily attributed to a μ_2-bonding mode. Based on this spectroscopic information, the authors proposed a polymeric network (Fig. 30).

In the case of the heterobimetallic systems, the few examples known so far are [ClPt(μ-dppm)$_2$(μ-C=N-Me)Ni(CNMe)]Cl (**64**), reported by Kubiak and collaborators, which is obtained via a transmetallation of [(CNMe)]Ni (μ-dppm)$_2$(μ-C=N-Me)Ni(CNMe)] with [Pt(dppm)Cl$_2$].[80] The other examples are the mixed M-Pt systems **65**–**74** (M = W, Fe, Mo, Cr) containing a disphosphine backbone (dppm or dppa), as described by Knorr and collaborators[81–84] (Fig. 31). These complexes were obtained via substitution of the bridging carbonyl by an isocyanide ligand.

Uson and collaborators described an A-frame PdPt complex [C$_6$F$_5$Pd (μ-C=N-*p*-tolyl)(μ-dppa)$_2$PtC$_6$F$_5$] (**75**),[85] and more recently, [XPd(μ-dppm)$_2$ (μ-C=N-R)Pt(CN-R)]$^+$ (**76**–**78**) and [ClPd(μ-dppm)$_2$(μ-C=N-R)PtCl] (**79**–**81**) were reported by Knorr and collaborators[86–88] (Fig. 32). In the bis(isonitrile) heterobimetallics **76**–**78**, a site selectivity in the second CNR ligand coordination (Pd vs. Pt) was noticed. The additional isocyanide is systematically coordinated on the Pt site.[86,88] This distinct selectivity between Pd and Pt was explained by the greater lability of the Cl$^-$ ion on the Pt center as well as a better stabilization of the positive charge on the electron-rich Pt$^{\mathrm{I}}$ center.[88] The question arises as to why the addition of ligand isocyanide sometimes produces the A-frame compound whereas under similar conditions, a d^9-d^9 isocyanide

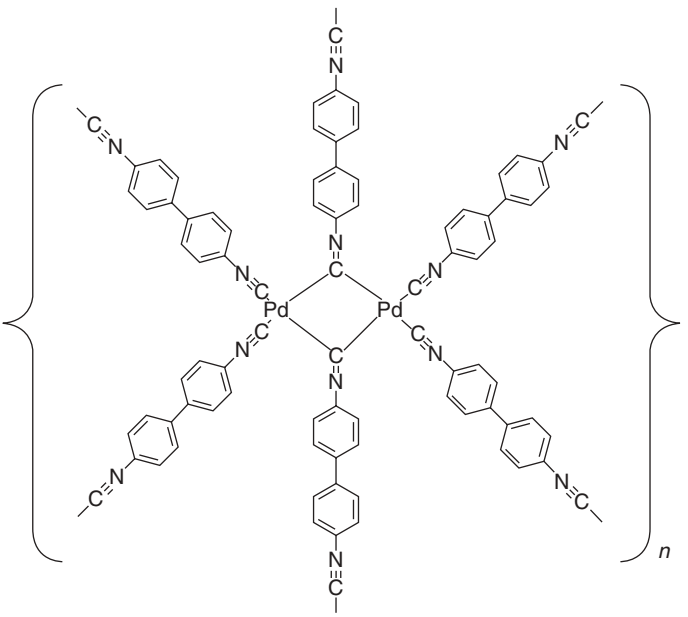

FIGURE 30. Proposed structure of the organometallic polymer prepared from Pd(II) and 4,4-diisocyanobiphenyl.

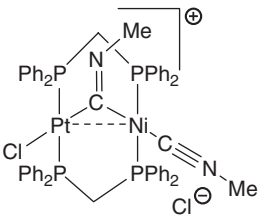

64

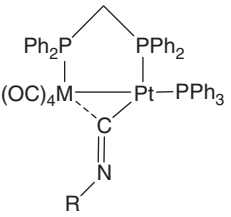

65 M = W, R = CF_3
66 M = W, R = CH_2SO_2tolyl
67 M = W, R = $CH_2PPh_3[PF_6]$
68 M = Cr, R = CH_2SO_2tolyl
69 M = Mo, R = CH_2SO_2tolyl

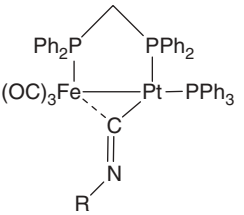

70 R = 2,6 xylyl
71 R = *o*- or *p*-anisyl
72 R = benzyl
73 R = tosylmethyl
74 R = *p*-$C_6H_4NH_2$

FIGURE 31. Heterobimetallic complexes with μ-CNR ligands.

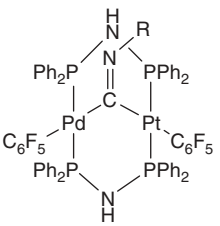

75 R = *p*-tolyl

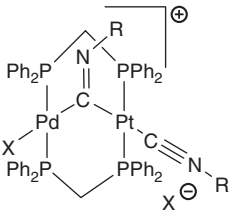

76 X = Cl, R = [2.2]paracyclophane
77 X = Cl, R = *o*-anisyl
78 X = I ,R = *o*-anisyl

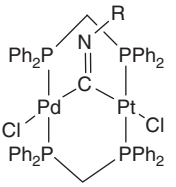

79 R = [2.2]paracyclophane
80 R = *o*-anisyl
81 R = CH_2PPh_3

FIGURE 32. Heterobimetallic PdPt complexes with μ-CNR ligands.

terminal salt could be obtained, as described above. Knorr and collaborators recently reported that the isocyanide bonding mode is related to various subtle parameters: (1) the π-acceptor propensity of isocyanide ligand, (2) the nature of the M-X bond, (3) the polarity of the solvent, and (4) the nature of the metal center.[89] Bimetallic complexes of the type $[ClM(\mu\text{-dppm})_2MCl]$ (M = Pd, Pt) contain two electron-donating bidentate dppm ligands. This donation in these low-valent, electron-rich systems could be, at least, partially compensated by back bonding in the μ-CNR ligand π*-orbitals. Based on the theoretical work of Howell and empirical observations on homodinuclear and heterodinuclear systems,[81,84,89,90] it seems that the π-acceptor propensity of the CNR ligand is decisive for the bonding mode and determinates the C=N-R angle. Based on calculations,[89] a C=N-R angle $<140°$ indicates a strong back bonding and, consequently, a strong π-acceptor ability for the isocyanide.

The photophysical properties of the heterobimetallics A-frame compounds **77**, **78**, and **80** were investigated. The absorption spectrum of these compounds exhibit low energy bands in the 350−450 nm range, which are better resolved at 77 K. These broad bands are characteristic of an A-frame

environment about the metal centers. The full width at half maximum (FWHM) was found to be relatively constant whatever the nature of the halide. The $\sim$350 nm band, which is encountered at the same position as that of d^9-d^9 homo- and hetero-M-M bonded complexes (M = Pd, Pt and M = Pd, Pt) may stem from the weak M$\cdots$M interactions.[91] With reference to previous studies on d^8-d^8 binuclear complexes[78,92] and molecular orbital analysis, the low energy band at $\sim$ 450 nm may be assigned to a charge transfer (CT) process from the metal to μ-ligand ($M_2 \rightarrow \mu-$LCT). The photophysical data for these compounds are presented in Table 13.

The emission spectra in frozen butyronitrile (Fig. 33) exhibit broad and unstructured bands at λ_{max} = 710 nm for **77** and at λ_{max} = 715 nm for **78**. These values compare favorably with other A-frame d^8-d^8 systems based on iridium and platinum metal centers.[91–93] The λ_{max} and the non-radiative deactivation values of dinuclear complexes **77** and **78** are in the order **77** < **78**, indicating that the nature of the excited states is influenced by the nature of the halide.[94]

TABLE 13. Emission Data for Polymers **77**–**78** and the Model Compound **80**, in Solid State at 298 K

Compound	λ_{abs} / nm	FWHM /cm^{-1}	λ_{emi} /nm	τ_e / μs	ϕ_e
77	384, 449	1650, 2100	710	3.06	0.0079
78	396, 456	1600, 2150	715	12.70	0.0043
80	390	3100	584, 677	0.52	0.0027

[a] λ_{exc} = 350 nm.
[b] λ_{exc} = 433 nm.

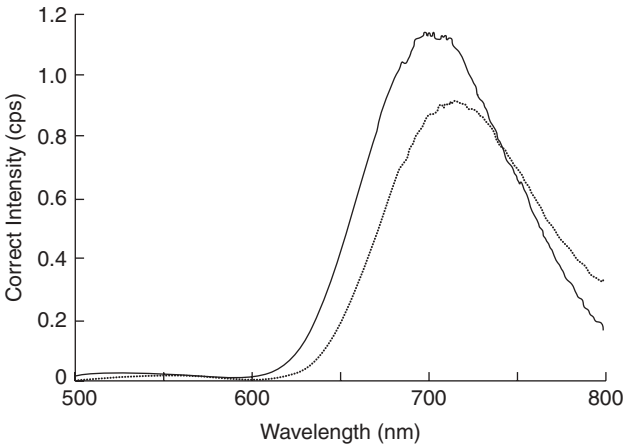

FIGURE 33. Emission spectrum of [XPd(μ-dppm)$_2$(μ-C = N-C_6H_4-2-OCH_3)Pt(CN-C_6H_4-2-OCH_3)]X (**77**. X = Cl, **78**. X = I). in butyronitrile at 77 K. λ_{exc} = 450 nm.

Several examples of oligomers built on bridging diisocyanide have been reported. A dimer of diiron diisocyanide (**79**) was described by Fehlhammer and collaborators[95] (Fig. 34). This compound was prepared by the reaction of dinuclear $[FeCp_2(CO)_3NCMe]_2$ prepared *in situ* with half an equivalent of 1,2-diisocyanobenzene. The μ_2-CNR bridge was evidenced by the presence of a very strong band at 1675 cm^{-1} in IR. The two bent CNC arrays were used for further functionalization. The two basic sp^2-N atoms were protonated with HBF_4, leading to the dicationic salt **80;** due to the conformation of the Fe-dimer, pentametal complexes **81** were obtained by chelating a binary metal(II) halide.

Other examples of oligomers are the dimers of a trinuclear cluster **82** and **83** (Fig. 35) supported by dppms and two triply-bridging I^- ligands.[96] The two

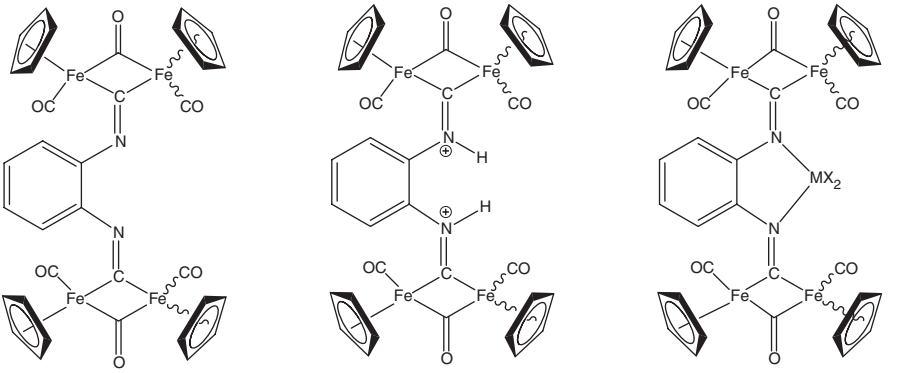

FIGURE 34. Compounds **79** to **81**.

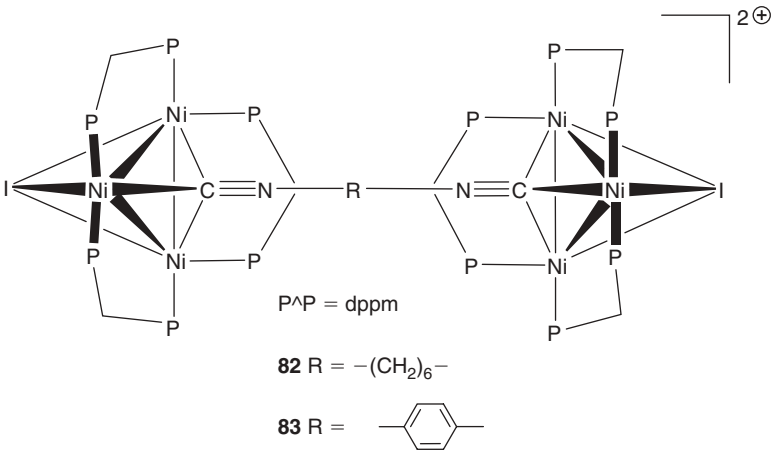

FIGURE 35. Structure of trinuclear Ni clusters linked by diNC ligands.

fragments are assembled together by flexible and rigide diisocyanides. The oligomers were unambiguously identified by plasma desorption (PD) and fast-atom bombardment mass spectrometry (FAB-MS). This material was obtained by the reaction of the cluster $[Ni_3(\mu_3\text{-}I)_2(dppm)_3]$ with 1,6-diisocyanohexane in benzene. The polymerization stopped at the dimer level because the iodide is a poor leaving group on Ni. Its extraction is very difficult under mild conditions and without a strong Lewis acid.[97]

Puddephatt and collaborators also reported a series of oligomers (**84**, **85**) and polymers of clusters **86**[98,99] (Fig. 36). The syntheses consist of reacting the known precursors $M_3(\mu\text{-}dppm)_3(CO)^{2+}$ (M = Pd, Pt) with the 1,4-diisocyanotetramethylbenzene in the appropriate ratios in CH_2Cl_2. Their reliable identification was performed by using model clusters containing monoisocyanides and spectroscopy. These polymers exhibit extensive dissociation in solution and fluxion motions of the isocyanide ligand. Unfortunately, no photophysical data were described for these clusters of the Ni triad.

Taking advantage of the recently discovered site selectivity in ligand binding on the Pt atom of the heterobimetallic $ClPd(\mu\text{-}dppm)_2PtCl$ and the better understanding of the isocyanide bonding mode described earlier,[86–89] Knorr, Harvey, and others recently designed the first A-frame-containing organometallic polymer using the bridging diisocyanide ligand 1,2-bis-(2-isocyanophenoxyethane (diNC). This diisocyanide was first prepared by Angelici and collaborators.[100,101] Due to the ideal position of the isocyanide groups, which can coordinate with donor groups at 90° angles to each other as this occurs in square-planar or octahedral complexes, diNC and *t*BudiNC were initially used as chelating linkers in Pt, Mo, Cr, or W complexes.[100] Such chelates are anticipated to exhibit a larger stability (i.e., binding constant) than

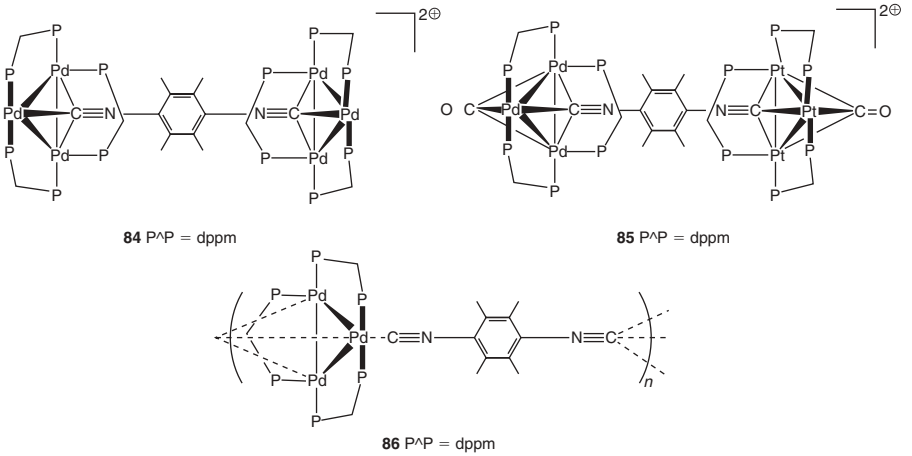

FIGURE 36. Structure of the dimers of clusters $M_3(dppm)_3^{2+}$, **84** and **85**, as model compounds and polymer **86** $(Pd_3(dppm)_3(diiso)^{2+})_n$ (diiso = 1,4-diisocyanotetramethylbenzene).

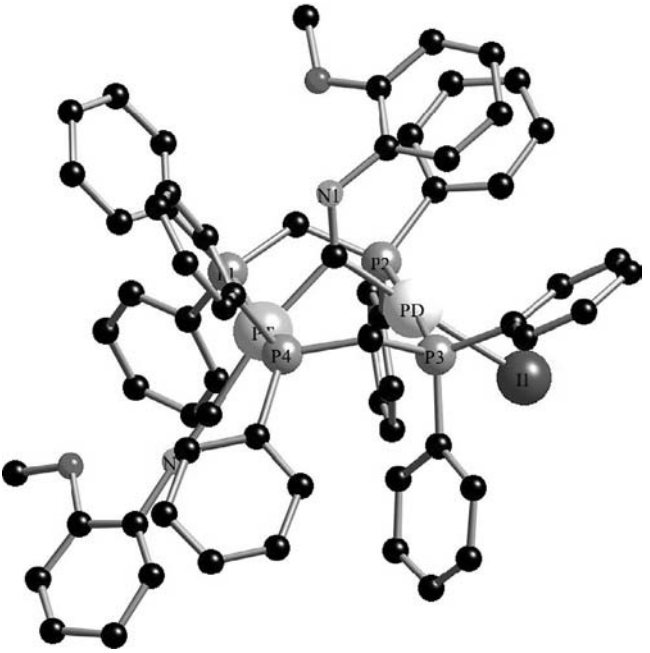

FIGURE 37. Molecular structure of the model compound[IPd(μ-dppm)$_2$(μ-C=N-C$_6$H$_4$-2-OCH$_3$)Pt(CN-C$_6$H$_4$-2-OCH$_3$)]$^+$.

the corresponding monodentate phenyl isocyanide and benzonitrile complexes. The electronic spectra for these chelates (i.e., free ligands) exhibit the two lowest energy bands, which are assigned as MLCT transitions of the type $d\pi \rightarrow \pi^*_{CN}$. The position of the $d\pi \rightarrow \pi^*_{CN}$ bands for the d^6 compounds varies in energy in the following order: Cr(0) < Mn(I) < Fe(II) ~Co(III).[102]

Based on the results obtained for the model ligand *o*-anisylisocyanide and on X-ray diffraction study (Fig. 37) where the first *o*-anisylisocyanide spanned the two metal centers and the second is coordinated at the Pt site, the A-frame heterobimetallic polymer **87** (Fig. 38) based on Pd(μ-dppm)$_2$Pt was prepared from the direct reaction between the heterobimetallic ClPd(μ-dppm)$_2$PtX and diNC.[87]

This novel class of materials containing a bridging and terminal isocyanide was investigated in more detail (influence of the counterion, and comparison with the homonuclear complexes ClM(μ-dppm)$_2$MCl (M = Pd, Pt) as starting material) to address the nature of the excited states.[103] These new orange species are weakly soluble and precipitated readily, thus hampering characterization in solution. The solid-state IR spectra confirm the A-frame geometry in which the two distinct absorptions for the bridging and terminal coordinated isocyanides are observed at the expected positions (~1620 and 2160 cm^{-1}, respectively). Estimation of the average molecular weight in number (*Mn*) values by the spin lattice relaxation time (T_1) and NOE ^{31}P NMR measurements indicates that these species can be only small oligomers (i.e., dimer), not anything larger in

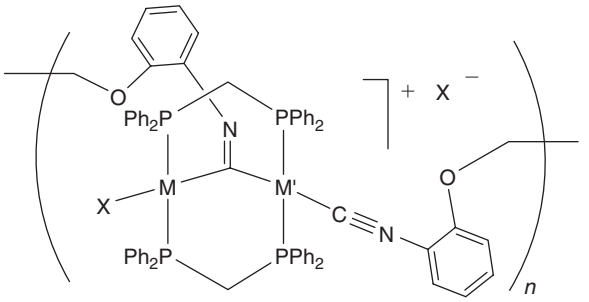

87 M = M' = Pd, X = Cl
88 M = M' = Pd, X = I
89 M = Pd, M' = Pt, X = Cl
90 M = Pd, M' = Pt, X = I
91 M = M' = Pt, X = Cl
92 M = M' = Pt, X = I

FIGURE 38. Structure of A-Frame bimetallic containing polymers **87**–**92**.

solution, which is completely consistent with the observed solubility. The TGA traces indicate a good thermal stability for these new materials where decomposition occurs at temperatures exceeding 210°C.

The absorption spectra of these polymers exhibit two low energy bands in the 350–450 nm range (Table 14). The spectral similarity with the model compounds **77** and **78** is striking and unambiguously address the A-frame environment about the metal atoms as being the same. Based on the comparison with model compounds **77** and **78**, the nature of the electronic transition and the excited states are certainly of the same as those described for the formers. The fact that these bands were not red shifted with respect to the corresponding model compound unsurprisingly indicates that the electronic coupling between the A-frame unit along the polymer is weak due to absence of conjugation.

These A-frame-containing organometallic polymers, **87**–**92**, are moderately luminescent at 77 K in butyronitrile but are not luminescent at room temperature, both in the solid state and in solution. This feature may be associated with an energy-wasting photo-induced M_2-(μ-isocyanide) bond scission or a ligand dissociation in the excited states. Moreover, this finding is not surprising because recent studies on the electronic communication of the isocyanide bridge through the A-frame structure indicates that the conjugated C=N linker exhibits moderate electronic communication properties.[104] For example, the [2.2]paracyclophane (PCP)-containing isocyanide **93**, which is itself luminescent, exhibits electronic communication via the bridging isocyanide group in the A-frame complex **94** (Fig. 39).

TABLE 14. Photophysical Parameters of **87**–**92** in Butyronitrile and in the Solid State at 77 K[a]

Polymer	λ_{abs} / nm	λ_{emi} / nm	τ_e / μs	ϕ_e	λ_{emi} (Solid) / nm
87	386, 450	680	0.20	0.0048	725
88	351, 428	705	0.19	0.0028	740
89	374, 440	660	0.18	0.0056	705
90	374, 430	730	0.78	0.0048	735
91	360, 444	615	1.78	0.003	635
92	364, 468	635	2.12	0.002	715

[a] From Ref. 89.

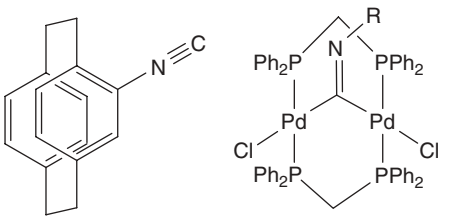

93 PCP-NC **94** R = PCP

FIGURE 39. Structure of the isocyanide functionalized [2.2]paracyclophane **93** and the A-Frame complex **94**.

At 77 K in butyronitrile, the PCP-NC ligand exhibits two broad (FWHM = 12000 and 45000 cm^{-1}, respectively) unstructured emission bands at λ_{max} around 370 and 480 nm (Fig. 40a). The emission bands do not shift with different solvents. The first emission maxima is assigned to fluorescence (fluorescence lifetime, $\tau_F \sim 1.85$ ns in PrCN). The second band is due to phosphorescence, as deduced from the long lifetime ($\tau_P \sim 3.37$ s in PrCN) and the large Stokes shift. After coordination of the isocyanide on the homo-bimetallic ClPd(μ-dppm)$_2$PdCl complex, the resulting product **94** exhibits a strong emission band (in 2-MeTHF) centered at 480 nm and a weak luminescence at ~360 nm (Fig. 40b). These two features are assigned to the phosphorescence and fluorescence of the PCP-NC unit, respectively. No emission is detected in the 550–850 nm region. According to Kasha's rule, the upper excited states should deactivate to the lowest excited state before one sees emission. However, the spectra exhibit clear evidence of luminescence arising from upper excited states (i.e., from the PCP fragment). These upper energy emissions are observable due to lack of efficient nonradiative relaxation (i.e., electronic communication) between the upper states localized in the PCP ligand (IL ππ*) and the lowest energy excited states located in the A-frame ClPd (μ-dppm)$_2$(μ-C=N-PCP)PdCl complex. This result is consistent with the fact that no coordination polymer containing an isocyanide linker has so far been reported as conducting (where conductivity proceeds across the CN group).

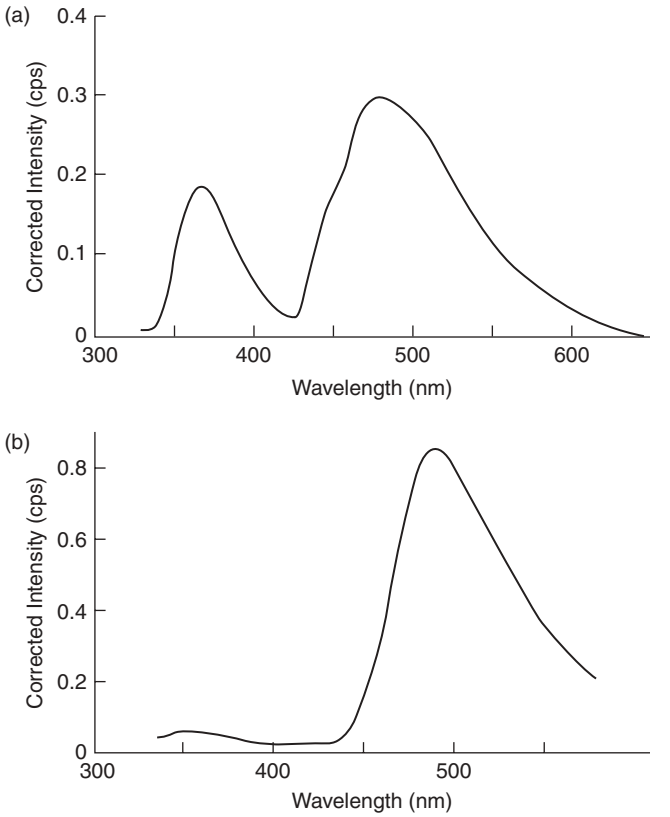

FIGURE 40. (a) Emission spectrum of PCP-NC **93** in butyronitrile at 77 K. (b) Emission spectrum of ClPd(μ-dppm)$_2$(μ-C=N-PCP)PdCl **94**. $\lambda_{exc} = 310$ nm. (Modified from Ref. 104.)

Unstructured emission bands are observed with maxima (λ_{emi}) in the 550−750 nm range for the A-frame organometallic polymers **87**−**92**. These later values are in good agreement with those obtained for the heterobimetallic complexes **77**−**78** containing a bridging isocyanide acting as model compounds. The band maxima for these dinuclear materials in solution or in the solid state follow the order Cl < I, indicating that the nature of the excited states is influenced by the nature of the halide.

The emission spectra of homobimetallic and heterobimetallic polymers **89** and **91** in PrCN at 77 K are shown in Figure 41 as examples. Details of the photophysical parameters are presented in Table 14.

Based on the model compounds **77** and **78** described earlier, the emission bands in these homobimetallics and heterobimetallic systems can be assigned to a charge transfer going from the fragment M(CN-C_6H_4-OCH_2) to M(μ-C=N-C_6H_4-OCH_2). These materials are also luminescent in the solid state at 77 K, providing an emission band in the 650−750 nm range. The emission spectrum for

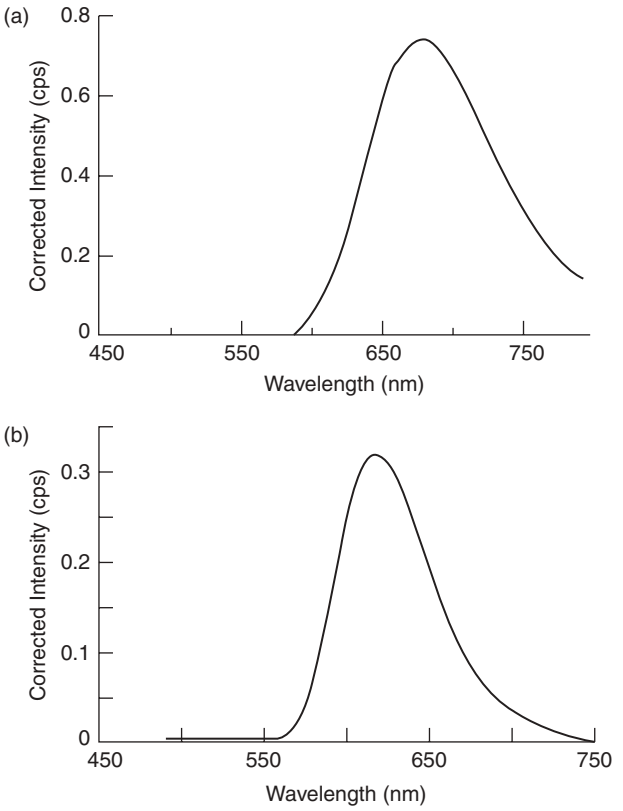

FIGURE 41. Emission spectra in butyronitrile of **89** (a) and **91(b)** at 77 K. $\lambda_{exc} = 450$ nm. (Modified from Ref. 104.)

([ClPt(μ-dppm)$_2$(μ-CN-C$_6$H$_4$-2-OCH$_2$CH$_2$O-2-C$_6$H$_4$-NC)Pt]Cl)$_n$ (**91**) in the solid state at 77 K, is shown in Figure 42 as an example. Red shifts of the emission band by about 20−50 nm were observed in the solid state compared to the solution one. To explain this observation, a polymer (solid)-oligomer (solution) equilibrium is proposed. Evidence for the oligomer is provided by T_1 and NOE constant measurements. This behavior was previously described by Harvey and collaborators for the Pd$_2$(dmb)$_2$Cl$_2$ binuclear complexes[40] and other d^8 Pd(diphos)(isocyanide)-containing polymers (diphos = Ph$_2$P-(CH$_2$)$_m$-PPh$_2$; m = 2-6).[37]

The emission lifetimes for these materials are found in the μs time scale, consistent with a phosphorescence process. The lifetime data for Pd-containing materials are significantly shorter than those of the Pt analogues (by about two orders of magnitude). Compared to the heterobimetallic model compounds [ClPd(μ-dppm)$_2$(μ-C=N-C$_6$H$_4$-2-OCH$_3$)Pt(CN-C$_6$H$_4$-2-OCH$_3$)]Cl (**77**) ($\tau_e = 3.06$ μs, $\Phi_e = 0.0079$) and [ClPd(μ-dppm)$_2$(μ-C=N-C$_6$H$_4$-2-OCH$_3$)Pt (CN-C$_6$H$_4$-2-OCH$_3$)]I (**78**) ($\tau_e = 12.7$ μs, $\Phi_e = 0.0043$), shorter values were obtained for the heterobimetallic-containing polymers **89** and **90**. The other

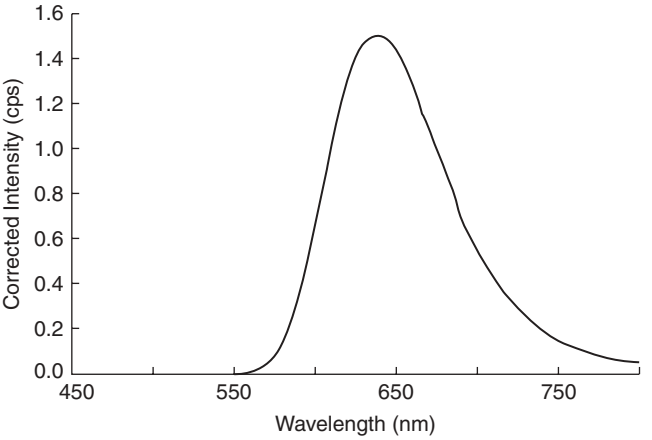

FIGURE 42. Emission spectrum of **91** in the solid state at 77 K. $\lambda_{exc} = 450$ nm. (Modified from Ref. 87.)

polymeric materials also have the same features: short lifetimes ($0.18 < \tau_e < 0.78$ μs) and low phosphorescence quantum yields ($0.002 < \varphi_e < 0.005$). This decrease photophysical data compared to the A-frame model compounds is consistent with an increase in nonradiative processes associated with supplementary vibrational modes present in the polymers but also deactivations promoted by intramolecular collisions.

V. CONCLUSION

The organometallic and coordination polymers built on monoisocyanides, diisocyanides and polyisocyanides are of growing interest, notably with the hope of designing new materials with optical and photonic properties. The $-N{\equiv}C-$ bridges are known to provide electronic communication, although in a somewhat lesser extent than that of the ethynyl group, $-C{\equiv}C-$, but still large enough to provide evidence of conjugation. For completely conjugated polymers, there is an opportunity to design photonic devices, notably solar cells. Because relatively little has been done on such a family of polymers so far, further progress in this area is anticipated.

VI. ACKNOWLEDGMENTS

PDH thanks the Natural Sciences and Engineering Research Council of Canada (NSERC) for funding and the CEMOPUS (Centre d'Excellence sur les Matériaux Optiques et Photoniques de l'Université de Sherbrooke). MK

thanks the French Ministère de la Recherche et Technologie for financial support and a PhD. grant for SC. SC acknowledges the Fonds Québécois de la Recherche en Science Naturelles et en Technologie (FQRNT) for a post-doctoral fellowship.

VII. REFERENCES

1. E. Singleton, H. E. Oosthuizen, *Adv. Organomet. Chem.,* **22,** *209* (1983).
2. J. I. Henderson, S. Feng, G. M. Ferrence, T. Bein, C. P. Kubiak, *Inorg. Chim. Acta.,* **242,** *115* (1996).
3. Y. Lee, G. M. Morales, L. Yu, *Angew. Chem. Int. Ed. Engl.,* **44,** *4228* (2005).
4. U. Siemeling, D. Rother, C. Bruhn, H. Fink, T. Weidner, F. Träger, A. Rothenberger, D. Fenske, A. Priebe, J. Maurer, R. Winter, *J. Am. Chem. Soc.,* **127,** *1102* (2005).
5. M. Toriyama, T. R. Maher, T. C. Holovics, K. Vanka, V. W. Day, C. Berrie, W. H. Thompson, M. V. Barybin, *Inorg. Chem.,* **47,** *3284* (2008).
6. S. Coco, E. Espinet, P. Espinet, I. Palape, *Dalton Trans., 3267* (2007).
7. K. Onitsuka, K. Yanai, F. Takei, T. Joh, S. Takahashi, *Organometallics,* **13,** *3862* (1994).
8. F. Takei, K. Yanai, K. Onitsuka, S. Takahashi, *Chem. Eur. J.,* **6,** *983* (2000).
9. D. Lentz, *Angew. Chem. Int. Ed. Engl.,* **33,** *1315* (1994).
10. A. Efraty, I. Feinstein, L. Wackerle, A. Goldman, *J. Org. Chem.,* **45,** *4059* (1980).
11. A. Efraty, I. Feinstein, *Inorg. Chim. Acta., L211* (1981).
12. J. H. Paek, K. H. Song, I. Jung, S. O. Kang, J. Ko, *Inorg. Chem.,* **46,** *2787* (2007).
13. F. E. Hahn, *Angew. Chem. Int. Ed. Engl.,* **32,** *650* (1993).
14. A. Efraty, I. Feinstein, F. Frolow, L. Wackerle, *J. Chem. Soc. Chem. Commun., 864* (1980).
15. A. Efraty, I. Feinstein, F. Frolow, L. Wackerle, *J. Am. Chem. Soc.,* **102,** *6341* (1980).
16. I. Feinstein-Jaffe, F. Frolow, L. Wackerle, A. Goldman, A. Efraty, *J. Chem. Soc. Dalton Trans., 469* (1988).
17. A. Efraty, I. Feinstein, F. Frolow, *Inorg. Chem.,* **21,** *485* (1982).
18. I. Feinstein-Jaffe, S. E. Maisuls, *J. Organomet. Chem.,* **350,** *57* (1988).
19. I. Feinstein-Jaffe, I. Biran, D Mahalu, S. Cohen, S. A. Lawrence, *Inorg. Chim. Acta.,* **154,** *129* (1988).
20. G. Jia, W. F. Wu, R. C. Y. Yeung, H. P. Xia, *J. Organomet. Chem.,* **539,** *53* (1997).
21. I. Feinstein, *Rev. Inorg. Chem.,* **13,** *1* (1993).
22. I. Feinstein-Jaffe, A. Efrati, *J. Mol. Cat.,* **35,** *255* (1986).
23. I. Feinstein-Jaffe, A. Efrati, *J. Mol. Cat.,* **40,** *1* (1987).
24. S. A. Lawrence, P. A. Sermon, I. Feinstein-Jaffe, *J. Mol. Cat.,* **51,** *117* (1989).
25. R. Tannenbaum, *Chem. Mater.,* **6,** *550* (1994).
26. R. Tannenbaum, *J. Mol. Cat. A.,* **107,** *207* (1996).
27. H. Ryu, Y.-G. Kang, S. Knecht, L. R. Subramanian, M. Hanack, *Synth. Met.,* **87,** *69* (1997).
28. C. G. Carson, R. A. Gerhardt, R. Tannenbaum, *J. Phys. Chem. B.,* **111,** *14114* (2007).
29. D. Perreault, M. Drouin, A. Michel, P. D. Harvey, *Inorg. Chem.,* **31,** *3688* (1992).

30. D. Fortin, M. Drouin, M. Turcotte, P. D. Harvey, *J. Am. Chem. Soc.,* **119,** *531* (1997).
31. P. D. Harvey, D. Fortin, *Coord. Chem. Rev.,* **171,** *351* (1998).
32. M. Turcotte, P. D. Harvey, *Inorg. Chem.,* **41,** *2971* (2002).
33. P. D. Harvey, *Macromol. Symp.,* **209,** *67* (2004).
34. D. Fortin, M. Drouin, P. D. Harvey, *Inorg. Chem.,* **39,** *2758* (2000).
35. H. Spanggaard, F. C. Krebs, *Solar Energy Mater. Solar Cells,* **83,** *125* (2004).
36. E. Fournier, S. Sicard, A. Decken, P. D. Harvey, *Inorg. Chem.,* **43,** *1491* (2004).
37. D. Samar, J.- F. Fortin, D. Fortin, A. Decken, P. D. Harvey, *J. Inorg. Organomet. Polym. Mater.,* **15,** *411* (2005).
38. D. Perreault, M. Drouin, A. Michel, P. D. Harvey, *Inorg. Chem.,* **31,** *2740* (1992).
39. P. D. Harvey, Z. Murtaza, *Inorg. Chem.,* **32,** *4721* (1993).
40. S. Sicard, J.- F. Bérubé, D. Samar, A. Messaoudi, D. Fortin, F. Lebrun, J.- F. Fortin, A. Decken, P. D. Harvey, *Inorg. Chem.,* **43,** *5321* (2004).
41. J. F. Bérubé, K. Gagnon, D. Fortin, A. Decken, P. D. Harvey, *Inorg. Chem.,* **45,** *2812* (2006).
42. T. Zhang, M. Drouin, P. D. Harvey, *Inorg. Chem.,* **38,** *957* (1999).
43. T. Zhang, M. Drouin, P. D. Harvey, *Inorg. Chem.,* **38,** *1305* (1999).
44. J. D. E. T. Wilton-Ely, H. Ehlich, A. Schier, H. Schmidbaur, *Helv. Chim. Acta.,* **84,** *3216* (2001).
45. R. L. White-Morris, M. Stender, D. S. Tinti, A. L. Balch, D. Rios, S. Attar, *Inorg. Chem.,* **42,** *3237* (2003).
46. R. L. White-Morris, M. M. Olmstead, A. L. Balch, O. Elbjeirami, M. A. Omary, *Inorg. Chem.,* **42,** *6741* (2003), and references therein.
47. P. Pykkö, J. Li, N. Runeberg, *Chem. Phys. Lett.,* **218,** *133* (1994).
48. P. Pykkö, F. Mendizabal, *Chem. – Eur. J.,* **3,** *1458* (1997).
49. P. Pykkö, N. Runeberg, F. Mendizabal, *Chem. – Eur. J.,* **3,** *1451* (1997).
50. H. Schmidaur, W. Graf, G. Müller, *Angew. Chem. Int. Ed.,* **27,** *417* (1988).
51. D. E. Harwell, M. D. Mortimer, C. B. Knobler, F. A. L. Anet, M. F. Hawthorme, *J. Am. Chem. Soc.,* **118,** *2679* (1996).
52. D. S. Engleton, D. F. Chodosh, R. L. Webb, L. L. Davis, *Acta Crystallogr., Sect. C,* **42,** *36* (1986).
53. D. Lentz, S. Willemson, *J. Organomet. Chem.,* **612,** *96* (2000).
54. T. J. Mathieson, A. G. Langdon, N. B. Milestone, B. K. Nicholson, *J. Chem. Soc., Dalton Trans., 201* (1999).
55. D. Perreault, M. Drouin, A. Michel, P. D. Harvey, *Inorg. Chem.,* **30,** *2* (1991).
56. M. J. Irwin, J. J. Vittal, R. J. Puddephatt, *Organometallics,* **16,** *3541* (1997).
57. A. Rosenweig, D. T. Cromer, *Acta Crystallogr.,* **12,** *709* (1959).
58. N. Nagasundaram, G. Roper, J. Biscoe, J. W. Chai, H. H. Patterson, N. Blom, A. Ludi, *Inorg. Chem.,* **25,** *2947* (1986).
59. S. Esperas, *Acta Chem. Scand. A,* **30,** *527* (1976).
60. A. Bondi, *J. Phys; Chem.,* **68,** *441* (1964).
61. M. N. I. Khan, J. P. Jr. Fackler, C. King, J. C. Wang, S. Wang, *Inorg. Chem.,* **27,** *1672* (1988).
62. J. D. Basil, H. H. Murray, J. P. Jr. Fackler, J. Tocher, A. M. Mazany, B. Trzcinska-Bancroft, H. Knachel, D. Dudis, T. J. Delord, D. O. Marler, *J. Am. Chem. Soc.,* **107,** *6908* (1985).
63. C.-M. Che, W.-T. Wong, T.-F. Lai, H. L. Kwong, *J. Chem. Soc., Chem. Commun., 243* (1989).
64. M. A. Rawashdesh-Omary, M. A. Omary, H. H. Patterson, J. P. Jr. Fackler, *J. Am. Chem. Soc.,* **123,** *11237* (2001).
65. R. L. White-Morris, M. M. Olmstead, A. L. Balch, *J. Am. Chem. Soc.,* **125,** *1033* (2003).

66. S. K. Chastain, W. R. Mason, *Inorg. Chem.,* **21,** *3717* (1982).
67. O. Elbejeirami, S. Yockel, C. F. Campana, A. K. Wilson, M. A. Omary, *Organometallics,* **26,** *2550* (2007).
68. J. M. Forward, J. P. Jr. Fackler, Z. Assefa, D. M. Roundhill and J. P. Fackler Jr., els. *Optoelectronic Properties of Inorganic Compounds,* Plenum, New York, ch. *6* (1999).
69. O. Elbjeirami, M. A. Omary, M. Stender, A. L. Balch, *Dalton Trans., 3173* (2004).
70. M. M. Olmstedd, H. Hope, L. S. Benner, A. L. Balch, *J. Am. Chem. Soc.,* **99,** *5502* (1977).
71. R. Markevich, R. J. Puddephatt, J. J. Vittal, *Zeit. Kristall,* **212,** *409* (1997).
72. R. Bishop, A. L. Fowler, D. C. Craig, M. L. Scudder, *J. Coord. Chem.,* **37,** *107* (1996).
73. L. S. Benner, A. L. Balch, *J. Am. Chem. Soc.,* **100,** *6099* (1978).
74. M. L. Kullberg, C. P. Kubiak, *Inorg. Chem.,* **25,** *26* (1986).
75. K.R. Grundy, K.N Robertson, *Organometallics,* **2,** *1736* (1983).
76. D. L. DeLaet, D. R. Powell, C. P. Kubiak, *Organometallics,* **4,** *954* (1985).
77. D. L. DeLaet, P. E. Fanwick, C. P. Kubiak, *Organometallics,* **5,** *1807* (1986).
78. K. S. Ratliff, D. L. DeLaet, J. Gao, P. E. Fanwick, C. P. Kubiak, *Inorg. Chem.,* **29,** *4022* (1990).
79. I. Feinstein, C. Barash, *Inorg. Chim. Acta.,* **185,** *3* (1991).
80. K. S. Ratliff, P. E. Fanwick, C. F. Kubiak, *Polyhedron,* **9,** *2651* (1990).
81. M. Knorr, I. Jourdain, D. Lentz, S. Willemsen, C. Strohmann, *J. Organomet. Chem.,* **684,** *216* (2003).
82. M. Knorr, I. Jourdain, G. Crini, K. Frank, H. Sachdev, C. Strohmann, *Eur. J. Inorg. Chem.,* **9,** *2419* (2002).
83. M. Knorr, C. Strohmann, *Eur. J. Inorg. Chem.,* **2,** *241* (2000).
84. M. Knorr, C. Strohmann, *Organometallics,* **18,** *248* (1999).
85. R. Uson, J. Fornies, F. Martinez, R. Navarro, M. Cuz Frias, *Inorg. Chim. Acta.,* **132,** *217* (1987).
86. S. Clément, L. Guyard, M. Knorr, S. Dilsky, C. Strohmann, M. Arroyo, *J. Organomet. Chem.,* **692,** *839* (2007).
87. S. Clément, S. Mohammed Aly, K. Gagnon, A. S. Abd-El-Aziz, M. Knorr, P. D. Harvey, *J. Inorg. Organomet. Polym.,* **18,** *104* (2008).
88. D. Evrard, S. Clément, D. Lucas, B. Hanquet, M. Knorr, C. Strohmann, A. Decken, Y. Mugnier, P. D. Harvey, *Inorg. Chem.,* **45,** *1305* (2006).
89. S. Clément, S. Mohammed Aly, D. Bellows, J.-F. Bérubé, D. Fortin, F. Brisach, C. Strohmann, M. Knorr, L. Guyard, P. D. Harvey, *Inorg. Chem.*, **48,** *4118* (2009).
90. J. A. Howell, J. Y. Saillard, A. L. Beuze, G. Jaouen, *J. Chem. Soc., Dalton Trans., 2533* (1982).
91. C. M. Che, V. W.-W. Yam, W.-T. Wong, T. F. Lai, *Inorg. Chem.,* **28,** *2908* (1989).
92. J. L. Marshall, M. D. Hopkins, V. M. Miskowski, H. B. Gray, *Inorg. Chem.,* **31,** *5034* (1992).
93. A. L. Balch, *J. Am. Chem. Soc.,* **98,** *8049* (1976).
94. H. A. Nieuwenhius, D. J. Stufkens, A. Vicek Jr, *Inorg. Chem.,* **34,** *3879* (1995).
95. W. P. Fehlhammer, S. Schrölkamp, W. Sperber, *Inorg. Chim. Acta.,* **212,** *207* (1993).
96. D. A. Morgenstern, C. C. Bonham, A. P. Rothwell, K. Y. Wood, C. P. Kubiak, *Polyhedron,* **14,** *1129* (1995).
97. F. Lemaître, D. Lucas, K. Groison, P. Richard, Y. Mugnier, P. D. Harvey, *J. Am. Chem. Soc.,* **125,** *5511* (2003).
98. M. Rashidi, E. Kristoff, J. J. Vittal, R. J. Puddephatt, *Inorg. Chem.,* **33,** *1497* (1994).

99. A. M. Bradford, E. Kristof, M. Rashidi, D.-S. Yang, N. C. Payne, R. J. Puddephatt, *Inorg. Chem.,* **33,** *2355* (1994).
100. R. J. Angelici, M. H. Quick, G. A. Kraus, D. T. Plummer, *Inorg. Chem., 2178* (1982).
101. R. J. Angelici, M. H. Quick, G. A. Kraus, *Inorg. Chim. Acta.,* **44,** *L137* (1980).
102. D. T. Plummer, R. J. Angelici, *Inorg. Chem.,* **22,** *4063* (1983).
103. S. Clément, S.M. Aly, J. Husson, D. Fortin, L. Guyard, A. S. Abd-El-Aziz, P. D. Harvey, *Eur. J. Inorg. Chem.*,**17,** *2536* (2009).
104. S. Clément, S.M. Aly, D. Fortin, L. Guyard, M. Knorr, A. S. Abd-El-Aziz, P. D. Harvey, *Inorg. Chem.,* **47,** *10816* (2008).

CHAPTER 3

Luminescent Oligomeric and Polymeric Copper Coordination Compounds Assembled by Thioether Ligands

Michael Knorr and Fabrice Guyon

Institut UTINAM UMR CNRS 6213, Université de Franche-Comté, Faculté des Sciences et des Techniques, 16, Route de Gray, 25030 Besançon, France

CONTENTS

Macromolecules Containing Metal and Metal-like Elements,
Volume 10: Photophysics and Photochemistry of Metal-Containing Polymers,
Edited by Alaa S. Abd-El Aziz, Charles E. Carraher Jr., Pierre D. Harvey, Charles U. Pittman Jr., Martel Zeldin.

I. INTRODUCTION

Although structurally characterized coordination polymers of copper(I) and copper(II) have been literature known for several decades,[1–4] an almost explosive increase of articles dealing with the construction, structural features and properties of copper-based coordination polymers has been noticed during the last decade. This plethora, which goes in line with the recent progress made in supramolecular chemistry and in the domain of crystal engineering, may be explained for several reasons: First of all, copper coordination polymers often posses beautiful and fascinating architecture. These networks resulting from self-assembly processes may adopt mono-dimensional (1D), bidimensional (2D), and three-dimensional (3D) topologies. Apart from this purely aesthetic argument and the structural diversity, the intrinsic propensities of soft (according the HSAB principle) diamagnetic d^{10} Cu(I) and harder paramagnetic d^9 Cu(II) ions, such as reversible redox processes and magnetism, combined with a wide range of possible coordination numbers around a copper center and the existence of so-called cuprophilic interaction, have stimulated numerous studies on the magnetic properties of metal-organic copper coordination polymers[5–14] and on the preparation of polymeric mixed-valence Cu(I)-Cu(II) species.[15–29] Without a doubt, the emergence of new synthetic procedures such as crystal engineering under hydrothermal or solvothermal conditions, have contributed to the development of novel copper-based materials.[30] In the domain of photonic materials, an increasing number of articles are dedicated to the use of polynuclear and polymeric copper compounds for nonlinear optics (NLO).[31–38]

Last, it is literature known that even simple molecular 0D copper complexes (which are for the most part dinuclear or tetranuclear) often exhibit rich luminescence properties and photophysics, which have been investigated both experimentally and theoretically in detail during the last three decades.[39–89] Several review articles have addressed the photophysics of copper compounds and other d^{10} metals.[90–93] This important feature has motivated many researchers in the quest of novel efficient luminescent materials to develop new supramolecular and polymeric architectures incorporating Cu(I) centers both as lumophores and as connecting nodes in self-assembling processes. Although the majority of these compounds are assembled by halides (including the pseudohalides CN^- and SCN^-) and organic ligands with one or several nitrogen donor sites, some luminescent organometallic representatives with isocyanide or olefinic π-coordination have been prepared and reviewed.[94–95] Since one of the research topics of the authors concerns the coordination chemistry of sulfur-rich organic ligands, the focus of this chapter is limited to luminescent Cu(I) coordination polymers assembled (or at least ligated) by organosulfur ligands. Included also are organosulfur ligands with additional nitrogen donor sites, regardless whether the principal metal-ligand interactions occur by Cu–S or Cu–N bonds (or a combination of both of them). This

chapter, which is not exhaustive, presents some selected examples of luminescent and crystallographically characterized thioether-based coordination polymers of our group and describes for comparison related macromolecular systems and recent research activities of other groups working in this domain. For completeness, some luminescent molecular model complexes are also included.

II. BACKGROUND INFORMATIONS

The interest devoted to copper(I) halides and pseudohalides as inorganic components for the construction of coordination polymers stems basically from the strong coordinating nature of the counteranions of these metal salts. Consequently, halides and pseudohalides are incorporated as essential inorganic elements in the resulting metal-organic framework and offer the possibility for assembling cluster units of various nuclearities with donors such as phosphines, anilines, pyridyl type ligands, and thioethers. Copper(I) iodide is without doubt the most employed building block. Combined with monodentate ligands (L), this salt produces complexes of general formula $Cu_nI_nL_m$ which display a fascinating diversity of stoichiometries and geometries as exemplified in Scheme 1.[101–104] When ligand and metal are reacted in a 1:1 molar ratio, the most common motif consists in the tetranuclear cubane-like Cu_4X_4 cluster, in which the halide centers act as triply bridging ligands. Using an excess of ligand favors generally the formation of iodide-bridged rhomboid dimers or the ring-opened form of this latter, named *zigzag* polymer. The cubane motif may also be destabilized for the benefit of a step-cubane tetramer or an open-cubane structure in the case of bulky ligands.

The very rare open-cubane tetramer is derived from the step-cubane motif by breaking one of the two Cu-X bonds associated with each of the terminal Cu centers and completing the tetrahedral coordination sphere of the terminal Cu centers by the ligation of a further donor. The bridging nature of the halide disappears only using sterically demanding bases such as 2,6- and 3,5-dimethylpyridine to give mononuclear compounds of type $CuXL_3$ and $CuXL_2$.[105,106]

With ditopic ligands, rhomboid dimers, zigzag, and staircase chains may be incorporated in 2D networks, whereas Cu_4X_4 clusters act as connecting units of coordination polymers of dimensionality varying from 1D to 3D. Another very scarce motif is the hexagon prism $Cu_6(\mu_3\text{-}X)_6$ unit, which has been encountered only in 2D networks assembled by rigid tripodal ligands of C_3 symmetry. There is no example of a molecular '0D' $Cu_6(\mu_3\text{-}X)_6$ compound ligated by monodentate ligands. It should also be noted that the use of polytopic ligands sometimes results in the formation of coordination polymers incorporating two different inorganic core motifs (see compounds **2** and **41**″).

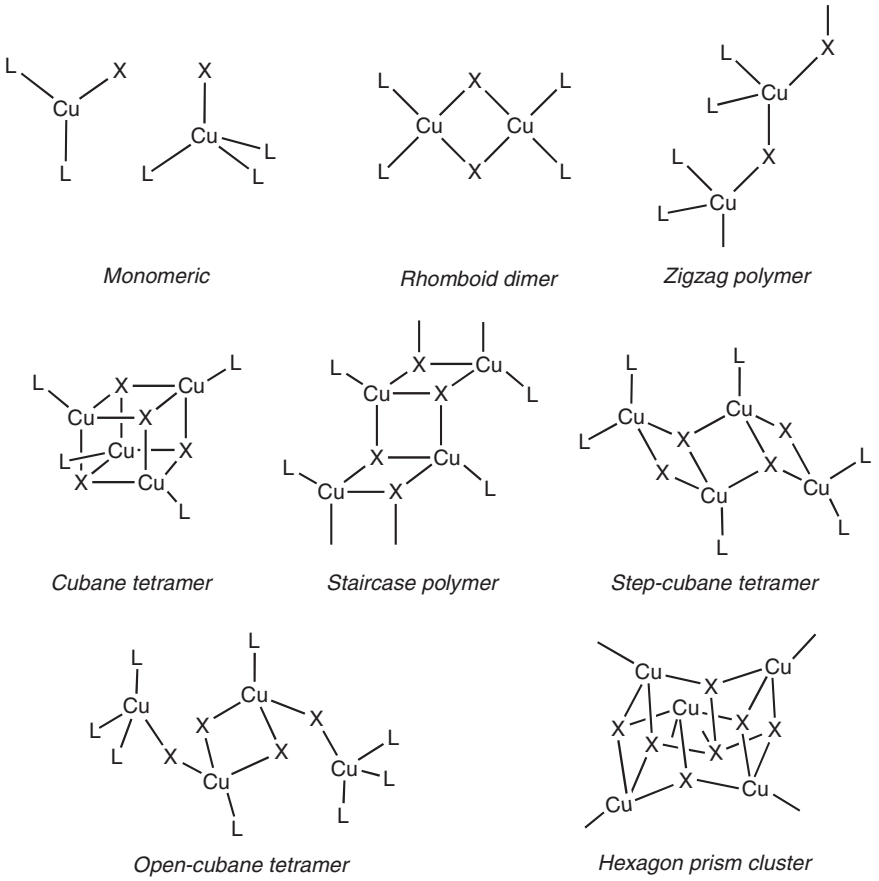

SCHEME 1

As mentioned in the introduction, the interest in copper coordination polymers, in particular those incorporating the Cu_4I_4 unit, stems from their remarkable photophysical properties. The peculiar luminescent properties of molecular and polymeric CuI • L adducts were first identified by Hardt and co-workers in the early 1970s. The first structural characterizations of these CuI • L adducts were conducted later in the mid-1970s by the groups of White and Holt.[45,107,108] Hardt observed that some copper halides complexes with cyclic nitrogen bases reversibly alter their fluorescence color in function of temperature and introduced the term '*luminescence thermochromism*' to describe this phenomenon.[109–112] The temperature dependence of the emission spectra was correlated with the presence of the cubane Cu_4I_4 motif by studying the luminescent properties of structurally characterized compounds and in particular the $[Cu_4I_4py_4]$ (py = pyridine and pyridine derivatives) cluster, which served as model compound for experimental and theoretical

studies.[41,44,107,113–117] This tetranuclear complex displays two distinct emissions: an intense low-energy band ($\sim$600 nm) dominates at room temperature, while the relative intensity of the high-energy transition ($\sim$450 nm) increases at low temperature. Following the progress of computational methods, extended Hückel, ab initio, DFT and recently TDDFT calculations have been performed to provide a theoretical understanding of the photophysical properties of the $[Cu_4I_4L_4]$ systems.[67,118–120] It is now established that the low-energy emission results from a triplet cluster excited state (^{3}CC), which presents a profound deformation of the cluster core geometry (increasing of the Cu-I distances associated with the shortening of the Cu-Cu distances) compared to the ground state. Concerning the high-energy transition, a ^{3}XLCT is involved. The others luminescent copper halides motifs have been much less studied on a theoretical level,[122] and the nature of the excited states responsible of the emissions are not always clearly understood.

III. LUMINESCENT COPPER POLYMERS ASSEMBLED BY THIOETHER LIGANDS

A. Copper Polymers Assembled by Monothioether Ligands RSR

Cuprous halides are known to form polymeric networks with a variety of simple aliphatic thioether RSR or heterocyclic compounds such as tetrahydrothiophene.[4,123] The first report on the rational construction of Cu(I) coordination polymers of this type stems from Potenza and co-workers who reacted CuX with neat Me_2S, Et_2S, and Bu_2S.[4] Whereas Me_2S reacts with CuX to give 1:1 complexes, similar reaction with Et_2S produced a homologous series of complexes with a ligand to Cu ratio of 3:4. The unusual stoichiometry of the Et_2S complexes was established by X-ray diffraction determination of the crystal structure of $[(Et_2S)_3\{Cu_4(\mu_3\text{-}I)_4\}]_n$ **1** and revealed a 1D coordination polymer consisting of infinite chains of sulfide-bridged Cu_4I_4 cores, each of which resembling a distorted cube with alternating vertices of Cu and I, as depicted in Figure 1. The individual Cu–S distances clearly reflect the presence of both bridging [Cu–S distances 2.331(8) and 2.337(6) Å] and terminal [Cu–S distances 2.297(10) and 2.298(9) Å] ligands. Each Cu atom exists in a distorted tetrahedral environment provided by three bridging I atoms and an Et_2S ligand. The intramolecular Cu–Cu distances range from 2.741(6) to 2.901(5) Å.

In anticipation of the intrinsic luminescence properties of these polymeric materials incorporating polymetallic CuX substructures, we resynthesized the CuI and CuBr adducts with Et_2S under similar reaction conditions to study the luminescence properties of these diethyl sulfide compounds. The presence of Cu_4I_4 cubane clusters in the polymer could be easily detected by the very strong

fluorescence noticed upon irradiation of a solid sample with UV-light at 366 nm using a laboratory UV lamp. This simple technique proved to be quite reliable for all compounds incorporating the Cu_4I_4 motif prepared by us (see below), regardless of the dimensionality of the network. Indeed, polymer **1** exhibits intense luminescence at $\sim$545 nm after excitation at 360 nm (Fig. 2). Undoubtedly, this emissive behavior is due to a metal cluster-centered MCC transition, since the mean Cu$\cdots$Cu separation of 2.81 Å is close to the sum of the Van der Waals radii (2.80 Å) of two Cu atoms.

Because the crystal structure of the CuBr • Et_2S adduct **2** has not yet been described, we have grown single crystals in form of large colorless blocks from heptane and determined the solid-state structure. It is surprising, that the architecture of the resulting 1D network differs much from that of $[(Et_2S)_3\{Cu_4(\mu_3\text{-}I)_4\}]_n$ **1** and consists of centrosymmetric rhomboid Cu dimers [Cu(1)−S distances 2.297 (10) and 2.298(9) Å, Cu(1)−Cu(1)# distance 3.0454(7) Å], which are linked to a

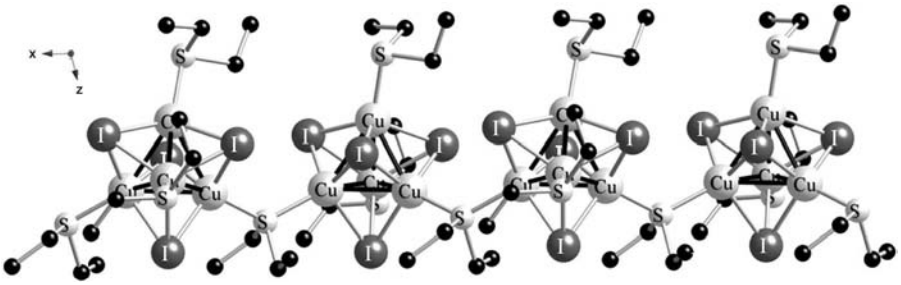

FIGURE 1. View of the Et_2S-bridged 1D ribbon of $[(Et_2S)_3\{Cu_4(\mu_3\text{-}I)_4\}]_n$ **1** along the *c*-axis.

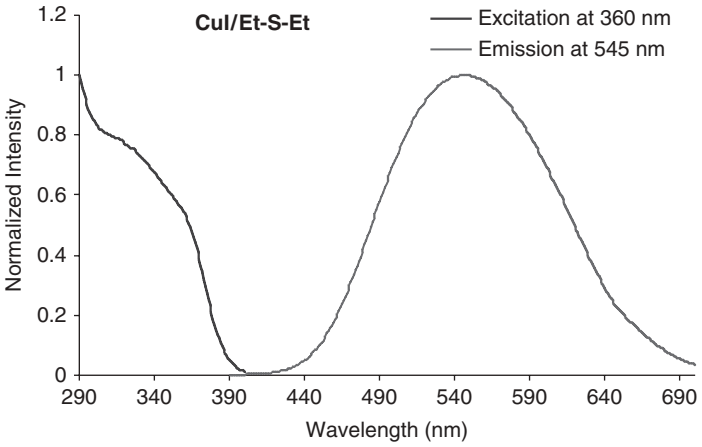

FIGURE 2. Excitation (left) and emission (right) spectra of $[(Et_2S)_3\{Cu_4(\mu_3\text{-}I)_4\}]_n$ **1** at 298 K.

distorted open-stepped cubane Cu_4Br_4 motif [Cu(1)−S(1) distance 2.3365(8) and Cu(1)−S(2) distance 2.3415(7) Å, Cu(2)−Cu(3) distance 2.7311(5) and Cu(1)−Cu(1)# distance 3.0125(8) Å] by two μ-Et_2S ligands in an alternating manner, thus giving rise to an infinite one-dimensional chain. Note that copper polymers incorporating two different inorganic core motifs are very rare. The parallel arrangement of these undulating chains is shown in Figure 3b.

This material is also emissive and exhibits in the solid state at ambient temperature after excitation at 360 nm a broad unstructured emission centered at 524 nm. The shoulder at about 412 nm shown in Figure 4 is always present, independently of the excitation wavelength.

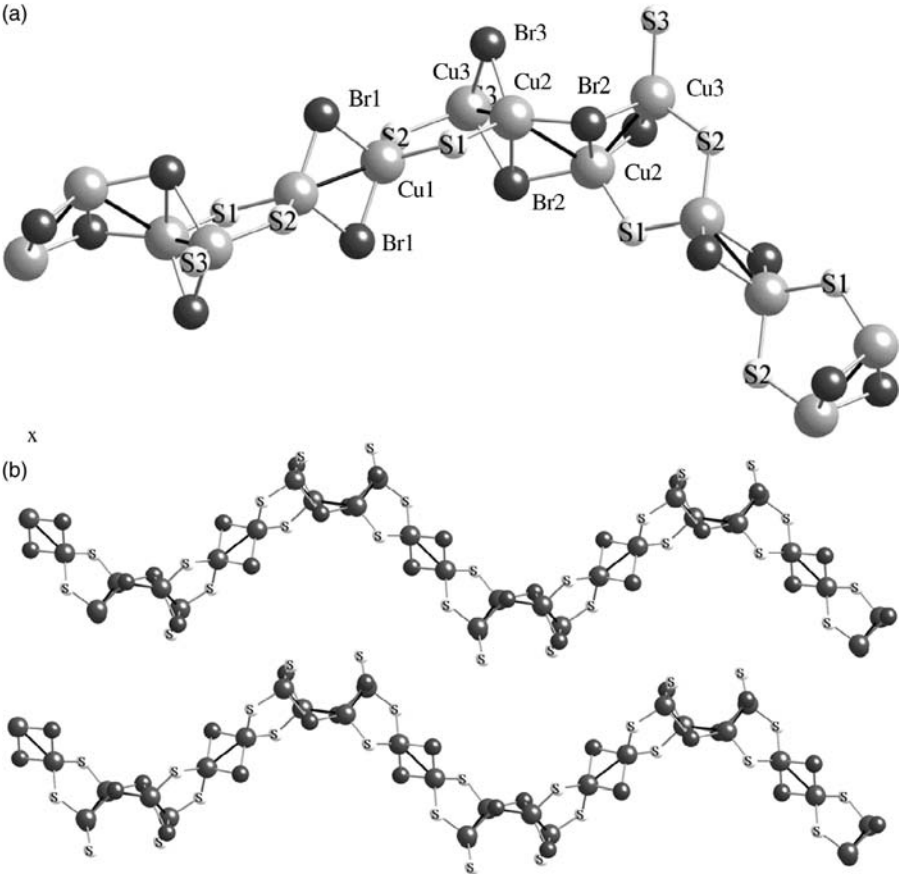

FIGURE 3. (a) View of the Et_2S-bridged 1D chain of **2**, incorporating dinuclear $Cu_2(\mu\text{-}Br)_2$ and tetranuclear $Cu_4(\mu\text{-}Br)_4$ motifs along the *c* axis. The ethyl groups are omitted for clarity. (b) View on the *b,c* plane of **2**, showing the undulating arrangement of the chains.

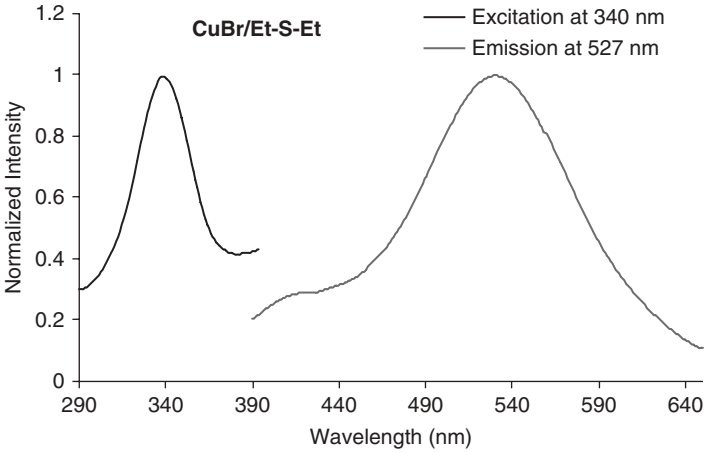

FIGURE 4. Excitation (left) and emission (right) spectra of solid 1D polymer **2** at 298 K.

According to Kopf et al., direct treatment of CuI with neat dimethyl sulfide (DMS) results in formation of the 1D metal-organic polymer **3** with a 2:3 CuI to DMS ratio, in which rhomboid $Cu(\mu\text{-}I)_2Cu$ motifs [Cu−Cu distance 2.684(1) Å] are ligated by two terminal and one bridging Me_2S ligand, as show in Scheme 2a and Figure 5.[123] Unfortunately, the photophysical properties of **3** have not been studied. The structural comparison between polymers **1** and **3** reveals that even an "innocent" variation of the thioether ligand (Et_2S vs. Me_2S) may have a dramatic impact on the topology of the resulting framework.

More recently, Dai et al. demonstrated that an unique 2D double-layered polymer with composition $[(Me_2S)_3\{Cu_4(\mu\text{-}I)_4\}]_n$ **4** containing helical chains can be constructed according Scheme 2c under solvothermal conditions.[124]

The formation of dimethyl sulfide is rationalized by P_2S_5-induced deoxygenation of dimethylsulfoxide. Performing the same reaction with CuBr or CuCl under identical conditions lead to formation of 2D polymers with composition $[(Me_2S)(CuX)]_n$ incorporating rhomboid $Cu(\mu\text{-}X)_2Cu$ (X = Br, Cl) motifs. A single-crystal X-ray analysis of **4** revealed that it is a 2D polymer, in which two μ-Me_2S ligands assemble distinct Cu_4I_4 cluster units. In contrast to the "closed" cubane-like $Cu_4(\mu_3\text{-}I)_4$ core encountered for **1** (Fig. 6), the Cu_4I_4 unit of **4** is named by the authors as "flower basket shaped", because it can be described as a partially opened structural variation of the widespread closed tetrahedral Cu_4I_4 motif, which is also found in many other thioether bearing Cu polymers. Figure 6 reveals that in the core motif of compound **4** three Cu atoms are presented in an isosceles trigonal arrangement, which is located in the waist position of the flower basket. The fourth Cu atom (Cu_1) lies at the handle position of flower basket bridges I_1 and I_1# atoms. Two adjacent Cu_4I_4 units are bridged by two μ-Me_2S ligands, forming a 2D network with a

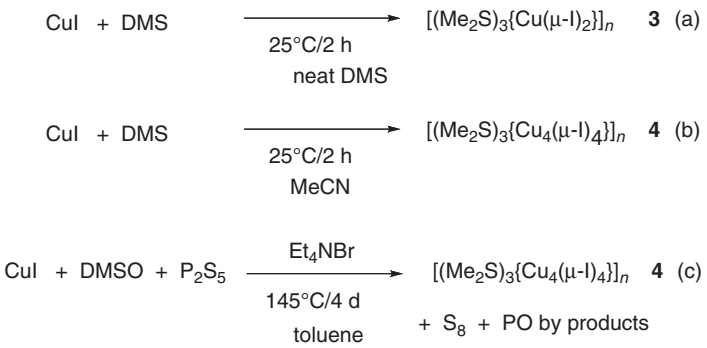

SCHEME 2

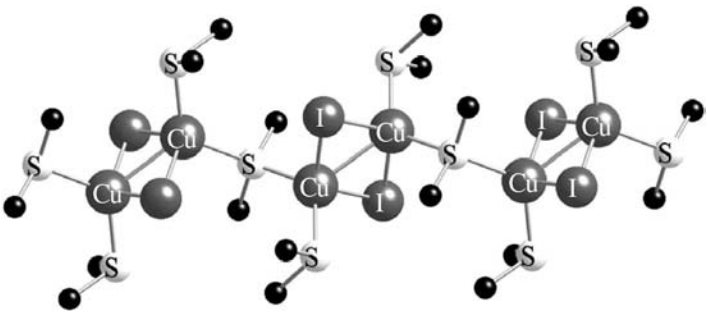

FIGURE 5. View of the 1D chain of coordination polymer **3** along the *z*-axis.

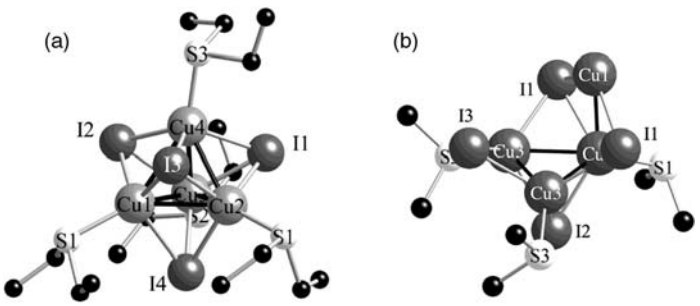

FIGURE 6. Comparison of the closed cubane-like core unit (a) of $[(Et_2S)_3\{Cu_4(\mu_3\text{-}I)_4\}]_n$ **1** with the flower-basket-shaped core unit (b) of $[(Me_2S)_3\{Cu_4(\mu\text{-}I)_4\}]_n$ **4**.

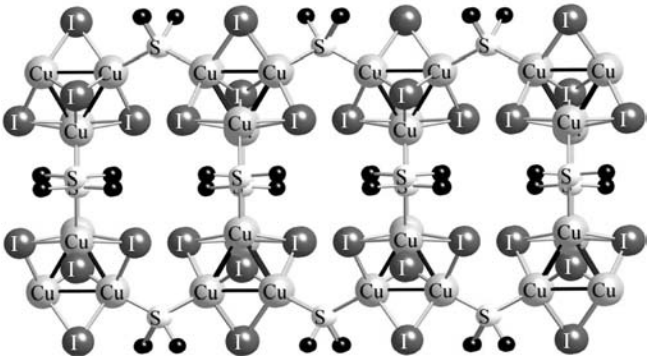

FIGURE 7. View along the *a,b* plane of 2D polymer $[(Me_2S)_3\{Cu_4(\mu\text{-}I)_4\}]_n$ **4**.

double-layered structure, containing 1D infinite helices as secondary motif (Fig. 7).

To evaluate the impact of the solvent on the composition of the material, we reacted a saturated solution of CuI in acetonitrile with a fourfold excess of DMS at ambient temperature, according Scheme 2b. After cooling, formation of colorless crystals was observed. It is surprising that a single-crystal X-ray analysis performed at 115 K revealed that, instead of the expected 1D polymer $[(Me_2S)_3\{Cu(\mu\text{-}I)_2\}]_n$ **3**, the 2D compound $[(Me_2S)_3\{Cu_4(\mu\text{-}I)_4\}]_n$ **4** has been formed.

This material is strongly luminescent upon irradiation at 366 nm using a laboratory UV lamp. According to Dai et al., upon excitation at 290 nm there is an intense emission of compound **4** in the solid state at 545 nm, originating from a triplet cluster-centered (CC) excited state and assigned to a combination of iodine-copper charge transfer (XMCT) and metal cluster-centered transition [MCC, $d_{Cu} \rightarrow (s,p)_{Cu}$] in orbital parentage (Fig. 8).[124] This interpretation is supported by the existence of short attractive Cu−Cu interactions in a range between 2.6689(1) and 2.7138(12) Å, bond distances significantly less than twice the van der Waals radius of Cu (see earlier for compound **1**). The photophysical data of our alternatively prepared polymer **4** are at $\lambda_{excit} = 290$ nm, in accordance with those of Dai's group; after excitation at 370 nm, a very strong emission at $\sim$551 nm is observed.

The angular ligand 4,4′-dipyridylsulfide (dps) shown in Scheme 3 has been reacted with a variety of metal salts such as $Zn(CH_3COO)_2$, $AgClO_4$ and CuI in a 1:1 ratio to afford luminescent coordination polymers of these d^{10} ions.[125] In the latter case, the resulting 2D polymer of composition $[\{Cu(\mu\text{-}I)_2Cu\}(dps)_2]_n$ **5** possessing a noninterpenetrating (4,4) network has been structurally analyzed.

The coordination of dps on the Cu(I) centers occurs exclusively through the two pyridyl nitrogens, no short contacts between the thioether sulfur and

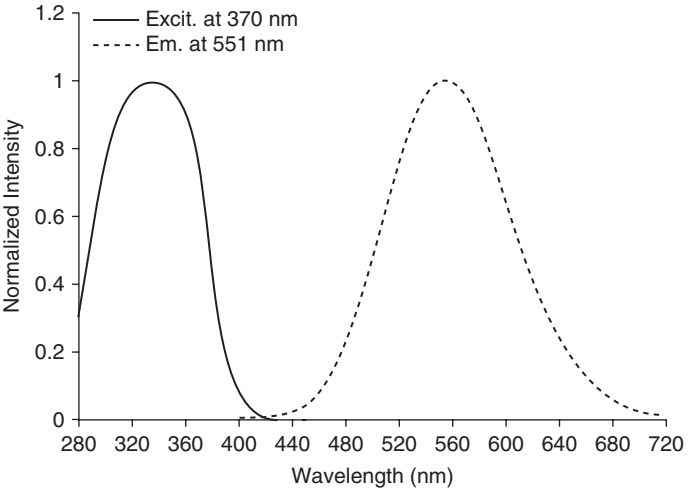

FIGURE 8. Excitation (left) and emission (right) spectra of $[(Me_2S)_3\{Cu_4(\mu_3\text{-}I)_4\}]_n$ **4** at 298 K.

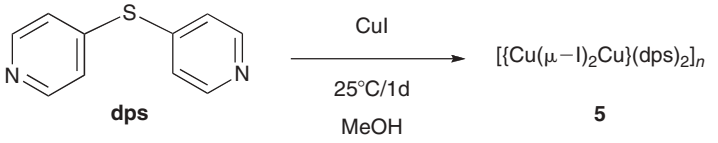

SCHEME 3

the Cu atoms are evidenced (Fig. 9a). All the Cu_2I_2 rhomboids are interconnected by four dps ligands in a crisscross fashion to generate a 2D framework.

Based on the close Cu···Cu interaction of only 2.647(1) Å, the observation of a very intense structureless solid-state emission at ~544 nm after excitation at 350 nm is attributed to a combination of MCC, a mixture of iodide to copper XMCT charge transfer and metal-centered *d* to *s* MC excited states (Fig. 9b). Additional contributions stemming from LMCT and MLCT are supposed.

This functionalized thioether dps ligand is also formed under solvothermal conditions at 120°C by in situ cleavage of both S−S and $S-C_{(sp2)}$ bonds of starting material 4,4′-dithiopyridin.[126] In the presence of CuI in a 1:2 ratio using MeCN as the reaction medium, polymeric $[\{Cu_4(\mu_3\text{-}I)_4\}(dps)_2]_n$ (**6**) was isolated in 85% yield according Scheme 4.

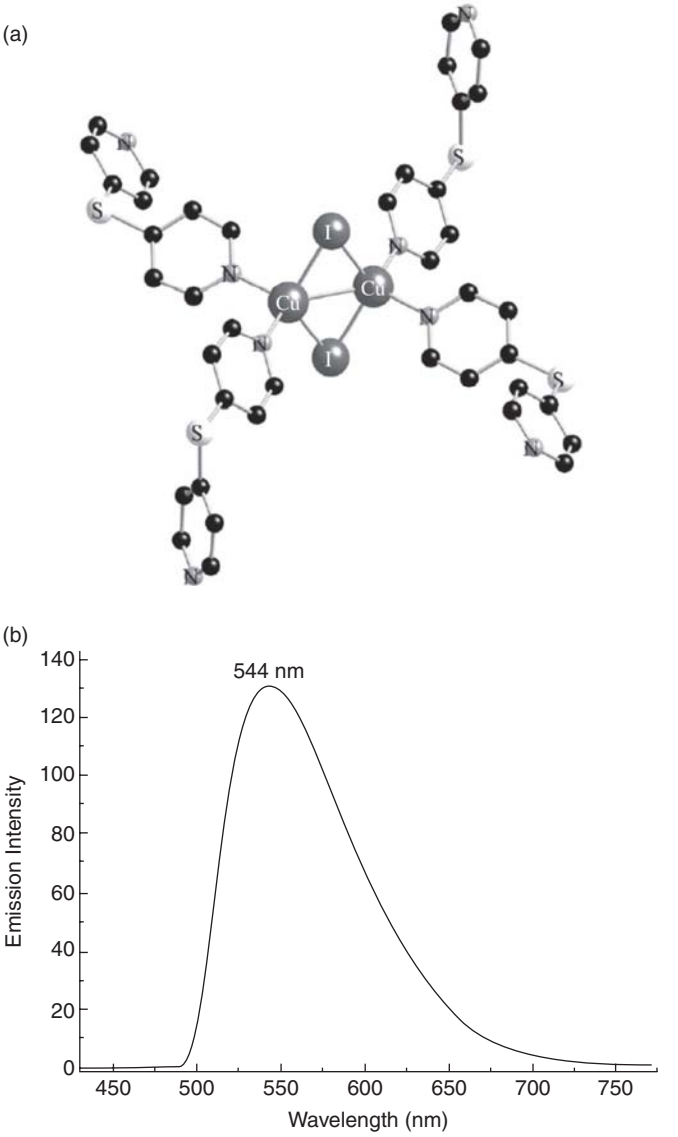

FIGURE 9. (a) View of the core unit of 2D polymer $[\{Cu(\mu\text{-}I)_2Cu\}(dps)_2]_n$ (**5**). (b) Solid-state emission spectrum of **5** recorded at ambient temperature. (Modified from Ref. 125.)

The structure of material **6** is a 2D coordination network of twofold interpenetration, in which cubane-like Cu_4I_4 clusters act as connecting nodes and the dps ligands as the spacer. The intramolecular Cu−Cu distances range from 2.563(1) to 2.734(2) Å. Like in the case of $[\{Cu(\mu\text{-}I)_2Cu\}(dps)_2]_n$ **5**, ligation

of dps occurs exclusively through the pyridyl nitrogen atoms. The resulting 2D undulating net of (4,4) topology has enough empty space to allow a twofold interpenetration of the sheets (Fig. 10).

The Uv-vis absorption spectrum of **6** recorded in reflectance mode at room temperature exhibits absorption bands at 242, 340, and 396 nm, attributed to the dps ligands and Cu_4I_4 units, respectively. Due to the quite short Cu···Cu interactions below the sum of the Van der Waals radii, this material displays an intense orange-red unstructured emission at $\sim$563 nm after excitation at 352 nm. The fluorescence lifetime τ of **6** has been determined to be 2.61 μs.

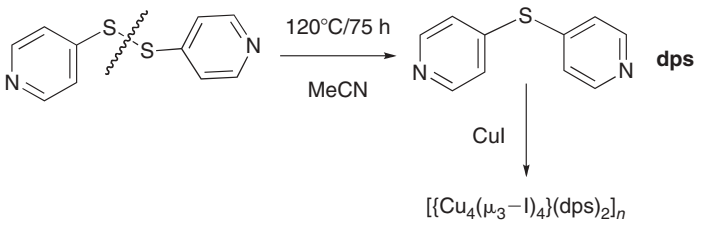

SCHEME 4

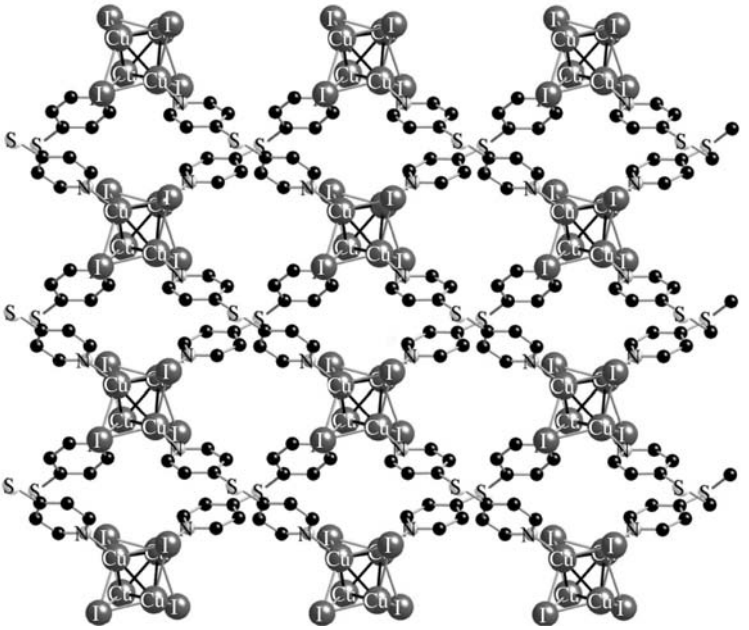

FIGURE 10. View on the *a,b* plane of 2D polymer $[\{Cu_4(\mu_3\text{-}I)_4\}(dps)_2]_n$ **6** showing the two-fold interpenetrating sheets.

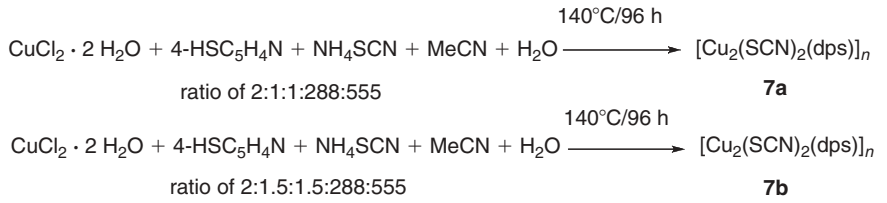

SCHEME 5

A further interesting example of in situ generation of the dps ligand via desulfation coupling of 4-pyridinethiol during the hydrothermal treatment of a mixture of $CuCl_2$, 4 pyridylthiol, and NH_4SCN in aqueous MeCN has been described.[127] Under identical reaction conditions (140°C, 96 h), but slightly varying 4-pyridylthiol and NH_4SCN ratios, the reaction led to two polymorphs of CuSCN coordination polymers with identical stoichiometry $[Cu_2(SCN)_2(dps)]_n$ **7a**,**b**, according Scheme 5.

Polymorph **7a** (space groupe *Pcca*) is a two-dimensional tubular sheet constructed by an unprecedented $[CuSCN]_n$ column and dps ligand. The $[CuSCN]_n$ column can be described as two zigzag chains arranged with approximate C_{2v} symmetry, one chain being connected to the other by Cu−S contacts. An alternative description of the $[CuSCN]_n$ column of **7a** is the stacking of $[CuSCN]_2$ dimers, alternately rotated by 90° and linked by Cu-N contacts. Polymorph **7b** (space group P_2/c) is a 2D planar sheet assembled by $[Cu(SCN)]_n$ staircase chains and dps ligands. The $[CuSCN]_n$ staircase can be viewed as an alternating fusion of four-membered Cu-S-Cu-S rings and eight-membered Cu-S-C-N-Cu-S-C-N rings. The two polymorphs represent very rare examples of coordination polymers that exhibit similar local coordination geometry of the metal and the same topology, but different CuSCN structural motifs.

The supramolecular isomers **7a,b** possess also quite different photoluminescent properties: Based to the similar energy of emission bands for free dps ligand (536 nm) and **7a** (538 nm), the structureless emission band in **7a** is tentatively assigned to an intraligand LC transition (Fig. 11). The emission of **7b** is found red shifted at 636 nm, with an intense and broad band shape ranging from 450 to 800 nm. Since LC transitions should be shifted by less than 1000 cm^{-1} compared to those of the free ligands, the authors conclude that the observed emission band in **7b** is too low in energy to originate from the dps ligands. For MLCT transitions, the antibonding π^* orbitals of the ligands must be positioned at comparable energies to the metal ion orbitals to ensure a sufficient overlap for efficient transitions. The antibonding π^* orbitals of dps in **7b** are expected to be at too high energy; therefore, the authors exclude also MLCT emission. By comparison with other CuSCN coordination polymers featuring similar luminescent properties, the origin of the transition in **7b** is supposed to stem from both MC and LMCT excited states.

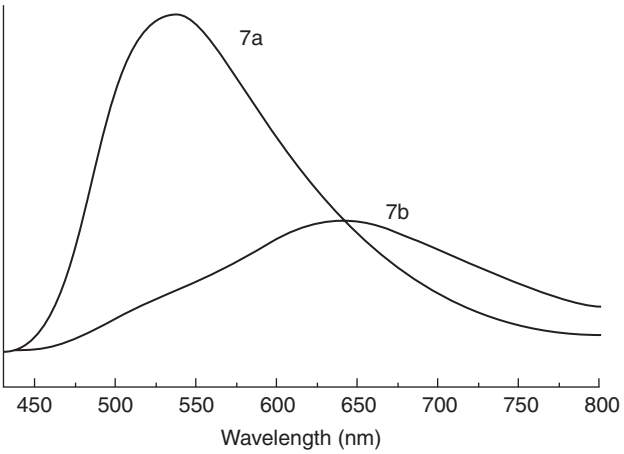

FIGURE 11. Solid-state emission spectra of supramolecular isomers **7a**,**b** recorded at ambient temperature with maxima at ~538 and 636 nm after excitation at 260 nm, respectively. (Modified from Ref. 127.)

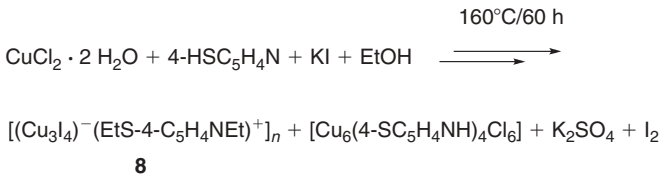

SCHEME 6

The potential of solvothermal syntheses for the construction of copper polymers combining unique structural features with rich photoluminescent properties is further demonstrated in the example of a simultaneous redox, alkylation, and self-assembly reaction. Despite the complicated processes shown in Scheme 6, the yellow ionic 1D polymer $[(Cu_3I_4)(EtS\text{-}4\text{-}C_5H_4NEt)^+]_n$ **8** is formed in large amount as major product upon heating a mixture of $CuCl_2 \bullet 2H_2O$, KI, 4-pyridinethiol, and EtOH in a molar ratio of 1:1:1:500 at 160°C for 60 h.[128] In addition, the nonluminescent hexanuclear μ_3-thion-bridged cluster $[Cu_6(4\text{-}SC_5H_4NH)_4Cl_6]$ has also been isolated as byproduct. The formation of metal-organic compound **8** is rationalized by in situ generation of the monothioether salt [EtS-4-C_5H_4NEt]I, stemming from alkylation of thiol 4-HSC_5H_4N with EtI. Ethyl iodide itself originates from the reaction of HI with ethanol.

Single-crystal X-ray analysis of compound **8** revealed that it was a novel 1D inorganic-organic hybrid coordination polymer (Fig. 12), possessing a linear chain composed by trinuclear Cu_3I_4 units. The three Cu atoms form a slightly distorted equilateral triangle. A noteworthy structural feature of **8** are

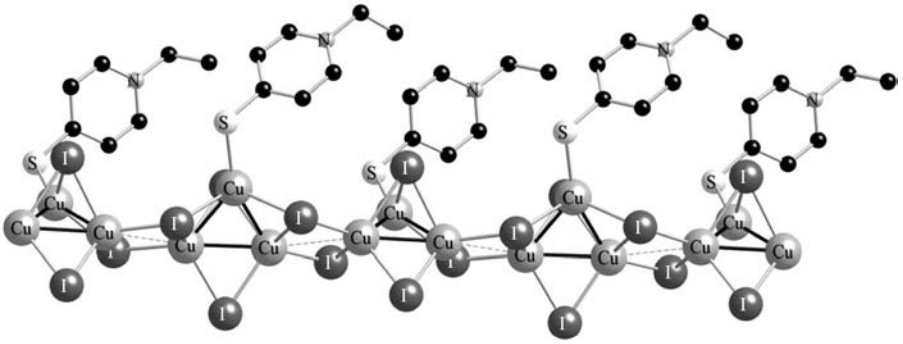

FIGURE 12. View of the 1D chain of coordination polymer **8** along the *c* axis. The ethyl groups of the $[EtS\text{-}4\text{-}C_5H_4NEt]^+$ thioether ligand are omitted for clarity.

the relatively short Cu−Cu distances in the range between 2.6736(18) and 2.7681(17) Å, implying strong Cu−Cu interactions. These cluster triangles are in contact with their neighbors through a further loose metal-metal interaction of 3.163 Å. The *N*-ethylated $[EtS\text{-}4\text{-}C_5H_4NEt]^+$ thioether ligand is bound to the inorganic ribbon through the S atom.

The emission spectrum of compound **8** exhibits in the solid state at room temperature an intense emission at 558 nm after excitation at 371 nm. According to the photoluminescent properties of Cu_4I_4 clusters, the emission band might be assigned to a combination of iodide-to-copper charge transfer (LMCT) and *d*-*s* transitions by Cu−Cu interaction within Cu_3 clusters.

The related ligands 2-(pyridin-2-ylmethylthio)pyridine and bis(6-methyl-2-pyrazylmethyl)sulfide depicted in Scheme 7 react with CuI in MeCN solution to afford supramolecular networks linked by additional weak S···S interactions and intermolecular π-π contacts, or self-complementary N···H-C hydrogen bonds, respectively.[129,130] Since no photophysical studies have been performed on these Cu_4I_4 or Cu_6I_6 containing supramolecular materials, a detailed structural description of these compounds is renounced. The ligand 8-(4-pyridylsulfanylmethyl)quinoline is reported to construct a 2D network of composition $[Cu_3I_3L(CH_3CN)]_n$ upon mixing with CuI in MeCN as reaction medium.[131] The inorganic part of this material consists of merlon-like 1D double-stranded (CuI)*n* chains with short Cu···Cu interactions of 2.652(2) Å between the chains. The resulting staircase ribbons are linked via the thioether and the pyridyl donor sites of the ligand to generate a 2D sheet.

To investigate the effect of methyl group substitution adjacent to a pyridyl *N*-donor, three bis(pyridylmethyl)sulfide ligands were synthesized (Scheme 7) and ligated with CuI in a 1:2 ratio.[132] The dimethylated ligand bis(6-methyl-2-pyridylmethyl)sulfide gives rise to a tetranuclear complex with two Cu_2I_2 bridges in which the Cu centers are four-coordinate. The asymmetric ligand 2-(6-methylpyridyl)methyl(2-pyridyl)methylsulfide gives a tetranuclear complex, which contains two parallel Cu_2I_2 bridges. In each Cu_2I_2 bridge, one Cu center is three and the other four coordinate. In contrast, the ligand bis(2-pyridylmethyl)

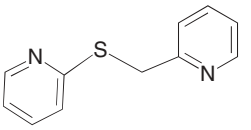

2-(Pyridin-2-ylmethylthio)pyridine

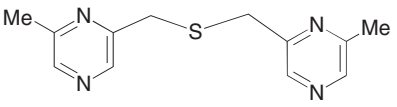

Bis(6-methyl-2-pyrazylmethyl)sulfide

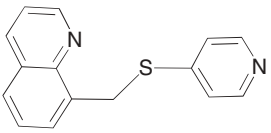

8-(4-Pyridylsulfanylmethyl)quinoline

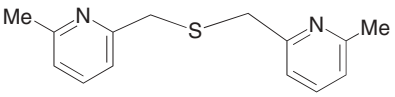

Bis(6-methyl-2-pyridylmethyl)sulfide

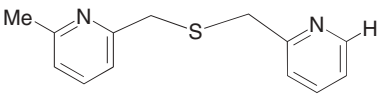

2-(6-Methylpyridyl)methyl(2-pyridyl)methylsulfide

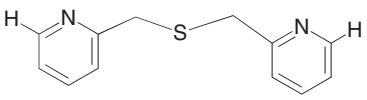

Bis(2-pyridylmethyl)sulfide

SCHEME 7

sulfide, with no Me substitution, gives rise to a 1D coordination polymer with CuI chains. In all three cases, the coordination of the ligands occurs both by the sulfide function and by the pyridyl nitrogens. It was concluded that the differences in the complexes were a result of both the electronic and steric effects arising from the Me substitution of the pyridine donors and that no one effect completely dominated.

B. Copper Polymers Assembled by Aromatic Dithioether Ligands

The coordination mode of aromatic dithioether ligands of the type ArS$(CH_2)_n$SAr which may be considered as the sulfur analogues of the ubiquitous diphosphanes $Ar_2P(CH_2)_nPAr_2$, depends in a sensible manner from the number of methylene units in the $(CH_2)_n$ spacer: In the case of Rh, Pd, and Pt for $n = 1$, a η^1-bonding mode is sometimes encountered, examples for this monodendate coordination mode are $[(\eta^5\text{-}C_5Me_5)IrCl_2(\eta^1\text{-}PhSCH_2SPh)\}]$, *trans*-$[PdCl_2(\eta^1\text{-}PhSCH_2SPh)_2]$, and *cis*-$[PtCl_2(\eta^1\text{-}PhSCH_2SPh)_2]$.[133,134] In addition, bis(phenylthio)methane is known to act as bridging ligand, thus assembling polynuclear compounds.[135]

Although 1,2-bis(phenylthio)ethane and 1,3-bis(phenylthio)propane may also adopt a bridging coordination mode in some coordination polymers, formation of stable six- or seven-membered chelate complexes is in general

preferred for $n = 2$ or 3. Some representative examples for that chelating coordination mode are *cis*-[$PtCl_2${$PhS(CH_2)_nSPh$}$_2$] ($n = 2,3$), tetrahedral [Cu{$PhS(CH_2)_nSPh$}$_2$][BF_4] ($n = 2,3$), octahedral [$SnCl_4${$PhS(CH_2)_3SPh$}$_2$], and [(η^5-C_5Me_5)Rh(H_2O){$PhS(CH_2)_2SPh$)}][triflate]$_2$.[136–139] However, a significant change is noticed when the number of methylene units reaches $n = 4$, 5, and 6. A relationship between ligand chain length and structure about a $PdCl_2$ fragment has been established by Sanger et al. Based on IR data, the formation of ligand-bridged palladium complexes of *trans*-geometry have been proposed for $n = 4-6$.[140] Recently, an X-ray diffraction study on [Pd{$PhS(CH_2)_5SPh$}Cl_2]$_n$ confirmed that 1,5-bis(phenylthio)pentane indeed spans the Pd-centers, generating a polymeric chain complex.[141] The crystal engineering with the ligand 1,4-bis(phenylthio)butane on Ag(I) salts under different conditions (varying the solvent, metal to ligand ratios, and counterions) gave rise to a number of 2D frameworks with fascinating structural motifs.[142] Very recently, luminescent gold polymers spanned by this flexible ligand have been synthesized by Brisse et al.[143] We have previously shown that the complexation of $PhS(CH_2)_4SPh$ on HgX_2 (X = Cl, Br) in a 1:2 ratio allows the assembly of 2D coordination polymers of the type [{$PhS(CH_2)_4SPh$}Hg_2X_4]$_n$ (X = Cl, Br).[144]

With the objective to elaborate low-cost luminescent CuX coordination polymers with easily accessible dithioether ligands of the type $ArS(CH_2)_nSAr$, our group embarked on a project to construct CuX metal-organic polymers assembled by such dithioether ligands with varying spacer lengths and -SAr aromatic groups to evaluate the impact of these systematic variations on the luminescence properties, dimensionality, and cluster nuclearity of the resulting hybrid organic-inorganic materials. Furthermore, the influence of the halide ion on the architecture was studied.

Reaction of CuI with bis(phenylthio)methane in acetonitrile in a 2:1 molar ratio gave air-stable colorless crystals of general formula [{$Cu_4(\mu_3$-I)$_4$}{μ-$PhSCH_2SPh$}$_2$]$_n$ **9** (Scheme 8). Modification of the molar ratio—for example, a 1:1 or 1:2 molar ratio—had no influence on the composition of the resulting material and only compound **9** was formed.[145] The crystal structure of **9** (Fig. 13) consists of cubane-like Cu_4I_4 clusters linked by bridging dithioether ligands to

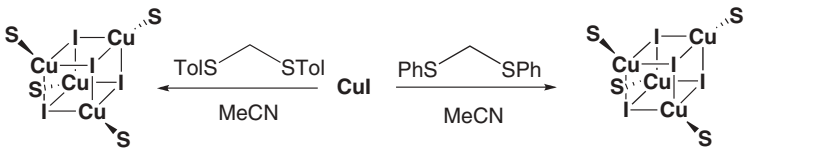

1D [Cu_4I_4{μ-$TolSCH_2STol$}$_2$]$_n$

10

1D [Cu_4I_4{μ-$PhSCH_2SPh$}$_2$]$_n$

9

SCHEME 8

form an infinite chain with Cu−S distances of 2.292(2) and 2.301(2) Å. The Cu−I bond lengths fall in the range of 2.6077(11)−2.7704(11) Å. The Cu−Cu distances [2.6173(18)−2.7864(14) Å] are somewhat below to the sum of the Van der Waals radii (2.8 Å) and lie clearly below those observed for $[(Et_2S)_3\{Cu_4(\mu_3\text{-}I)_4\}]_n$ **1**. In contrast to single-bridged **1**, two adjacent Cu_4I_4 cores are linked by two flexible dithioether ligands, thus leading to the formation of a 1D necklace structure. All phenyl substituents adopt a parallel orientation with a short C_{ipso}-C_{ipso} distance of 3.502 Å.

Despite the fact that the phenyl groups of neighboring ribbons are somewhat interpenetrated, there are no close interribbon interactions between the 1D chains of coordination polymer **9**, the separation between the midpoints of two adjacent Cu_4I_4 units being 11.64 Å (Fig. 14).

In order to evaluate the influence of additional methyl groups at the *para*-position of the −SAr groups, we also reacted CuI under analogous conditions with bis(*p*-tolylthio)methane in acetonitrile in a 2:1 molar ratio (Scheme 8). An X-ray diffraction study revealed that colorless polymer **10** of general formula $[\{Cu_4(\mu_3\text{-}I)_4\}\{\mu\text{-}p\text{-}TolSCH_2STol\}_2]_n$ is isostructural with **9**, crystallizing in the monoclinic space group C_2/c.

Figure 15 illustrates that again tetranuclear $Cu_4(\mu_3\text{-}I)_4$ units are doubly bridged by the dithioether ligand to form a 1D ribbon. Within the tetranuclear cluster, the Cu−Cu distances range between 2.652(3) and 2.829(2) Å, the mean separation of **10** being somewhat superior to that encountered in **9** (2.730 vs. 2.678 Å at 173 K). Also the Cu−S distances of 2.320(3) and 2.328(3) Å are slightly elongated compared to **9**, the Cu−I bond lengths fall in the range of 2.634(2)−2.756(2) Å.

As expected, both materials **9** and **10** exhibit interesting luminescence properties. The superposed solid-state emission spectra of **9** and **10** are depicted

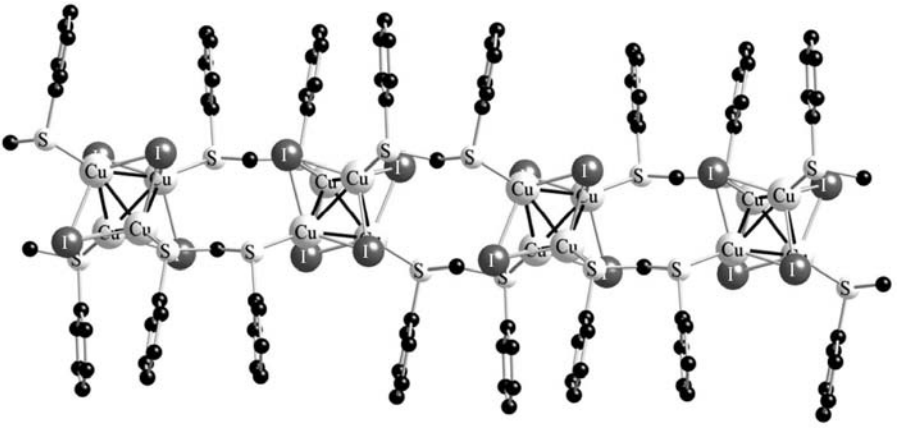

FIGURE 13. View on the 1D chain of polymer **9** along the *c* axis. H atoms are omitted for clarity.

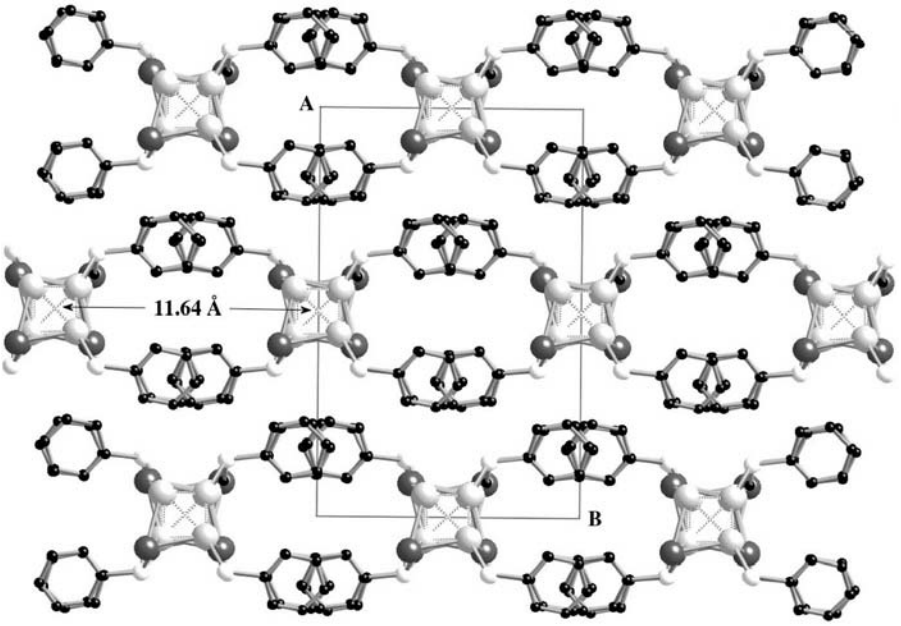

FIGURE 14. View of packing of $[Cu_4I_4\{\mu\text{-}PhSCH_2SPh\}_2]_n$ **9** on the *ab* plane.

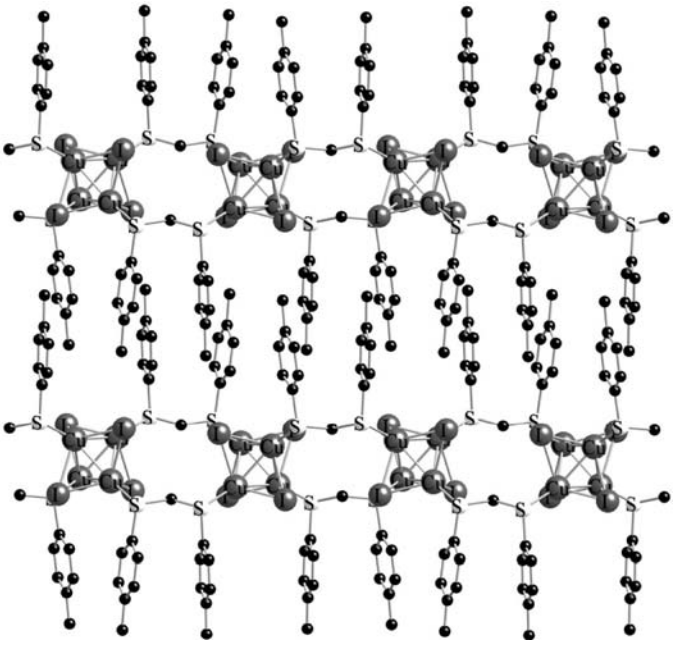

FIGURE 15. View of the parallel arrangement of the 1D chains of $[\{Cu_4(\mu_3\text{-}I)_4\}\{\mu\text{-}p\text{-}TolSCH_2STol\}_2]_n$ **10** along the *c* axis. H atoms are omitted for clarity.

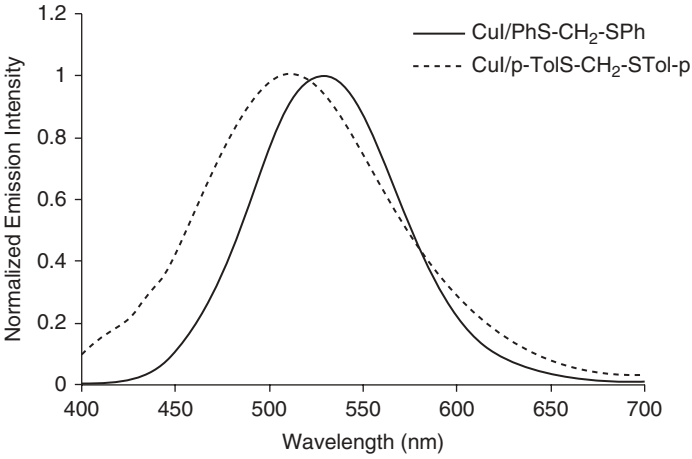

FIGURE 16. Normalized superimposed solid-state emission spectra recorded at room temperature for isostructural compounds **9** (*solid line*) and **10** (*dotted line*) after excitation at 360 nm.

in Figure 16. Upon excitation at 360 nm, a very strong unstructured emission band was observed for the tetranuclear dithioether-adduct **9** with a maximum at 532 nm, whereas isostructural **10** displays a blueshifted maximum at $\sim$508 nm. At present, it remains speculative to discuss the shift of the maxima noticed between **9** and **10**. The bis(*p*-tolylthio)methane ligand should behave as a slightly stronger donor ligand compared to bis(phenylthio)methane; however, it seems difficult to differentiate between the impact of electronic effects and packing forces on the subtle diverging Cu−Cu and Cu−S bond lengths between polymers **9** and **10**. Emissions in a similar spectral range have been observed for nitrogen-substituted $Cu_4I_4L_4$ clusters and were attributed to an emission from a triplet cluster-centered excited state (^{3}CC). As discussed for $[(Me_2S)_3\{Cu_4(\mu\text{-}I)_4\}]_n$ **4** and suggested for $[(Et_2S)_3\{Cu_4(\mu_3\text{-}I)_4\}]_n$ **1**, these broad emissions of CC-excited states have a mixed character with equal contributions of iodine to copper charge transfer (XMCT) and centered copper orbital (d$\rightarrow$s) transitions. Lifetime measurement performed on **10** yielded for τ 1.39 $\pm$ 0.05 μs at 298 K and 1.43 $\pm$ 0.03 μs at 77 K.

The colorless crystals obtained from the reaction of CuI with the 1,2-bis (tolylthio)ethane ligand in acetonitrile in a 1:1 molar ratio were identified by an X-ray study as the coordination polymer $[(CuI)_2\{\mu\text{-}PhS(CH_2)_2SPh\}_2]_n$ **11**. The framework consists of centrosymmetric $Cu_2(\mu_2\text{-}I)_2$ rhomboid dimers, connected to an adjacent unit via one μ_2-bridging dithioether ligand (Fig. 17). Each Cu atom is in a distorted tetrahedral environment, coordinated by two bridging iodo ligands and two thioether groups of two distinct ligands. The 2D network resulting from this coordination mode includes centrosymmetric 24-membered metallomacrocycles constituted by four dithioether ligands, six

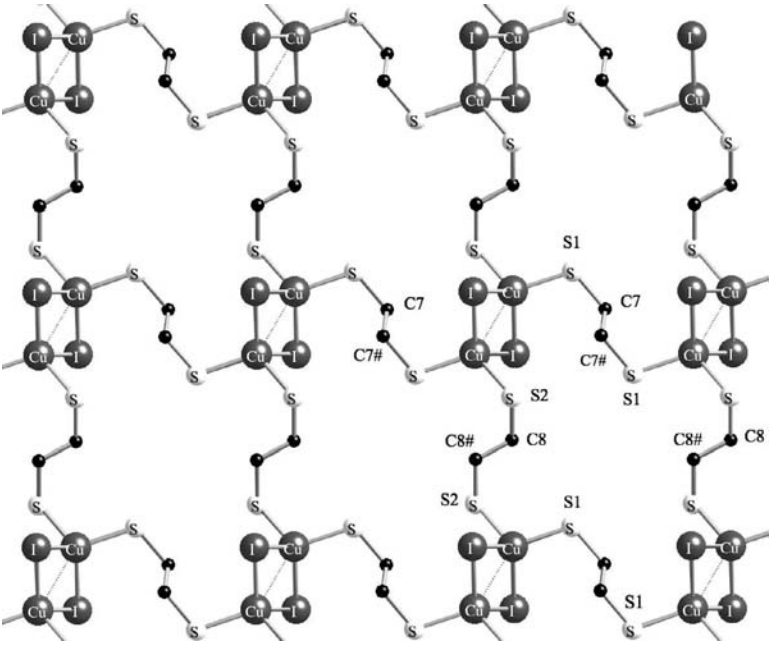

FIGURE 17. View of the core structure of **11** on the *ab* plane. H atoms and phenyl groups are omitted for clarity.

Cu atoms, and two iodo ligands (Fig. 16). The average distance of the two Cu-S bonds (2.3000(11) and 2.3855(10) Å) is just somewhat longer than the value in **9**. However, the Cu···Cu separation of 2.8058(11) Å is markedly longer than those observed in the earlier mentioned Cu_4I_4 unit of **9**.[145]

In contrast to **9** and **10**, the emission spectrum recorded for polymeric **11** containing the dinuclear Cu_2I_2 unit exhibits under similar experimental conditions a much weaker emission centered at 413 nm with a shoulder at 438 nm (Fig. 18). Although less studied than the tetranuclear systems, photophysical properties of some dinuclear Cu_2X_2 compounds have been reported in the literature but are currently limited to *N*-heterocyclic and phosphoros-donor ligands.[79] The observation of a shoulder suggests a different contribution originating from an XMCT and a Cu (d→s) transition. Solution measurements carried out in acetonitrile at room temperature show the disappearance of the luminescence properties for **9**, **10**, and **11**. This is probably due to a disassembly of the cluster units by this strongly coordinating solvent.

In contrast to the observation that substitution of -SPh by STol-*p* in $ArSCH_2SAr$ has no impact on the dimensionality and nuclearity of isostructural polymers **9** and **10**, replacement of phenyl substituents of PhS$(CH_2)_2$SPh by *p*-tolyl groups causes a profound change of the framework on reaction with copper iodide. Independently of the metal to ligand

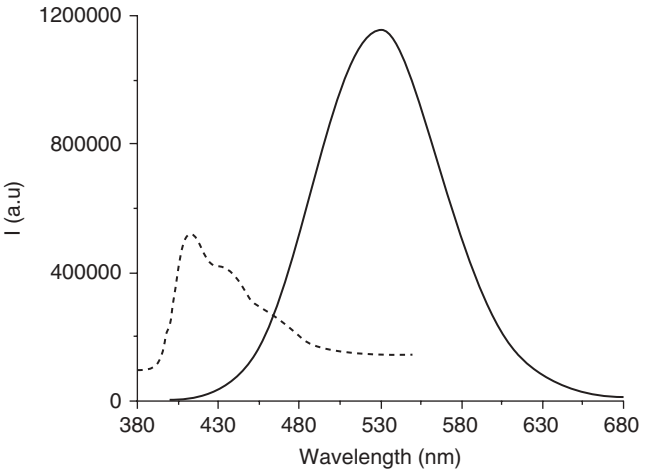

FIGURE 18. Superimposition of the solid-state luminescence spectra recorded at room temperature for compounds **9** (*solid line*) and **11** (*dotted line*).

ratio employed, a colorless material of composition $[(Cu_2I_2)\{\mu\text{-}p\text{-TolS}(CH_2)_2STol\}_2]_n$ **12**, crystallizing in the monoclinic space group P2(1)/*c*, was isolated. Figure 19a shows that the unusual inorganic core motif is best described as a corrugated 1D ribbon assembled by $Cu(\mu_2\text{-}I)_2Cu$ rhomboids with Cu···Cu interactions of 2.9073(11) Å, which are interconnected to the adjacent rhomboids through week Cu···Cu contacts of 2.9511(11) Å and two μ_3 bridging iodo ligands. In addition, each second $Cu(\mu_2\text{-}I)_2Cu$ unit is μ_2-spanned by a 1,2 bis(tolylthio)ethane ligand (Fig. 19b).

To probe the influence of the halide on the architecture of the network, 1,2-bis(phenylthio)ethane was also reacted with CuBr, according Scheme 9. Unexpectedly and regardless of the CuBr to ligand ratio, only the dinuclear complex $[Cu(\mu\text{-Br})\{p\text{-TolS}(CH_2)_2STol\}]_2$ **13** was produced. As corroborated by an X-ray diffraction study, the dithioether ligand is bound in a chelating manner on CuBr, forming a five-membered ring. The Cu···Cu separation of **13** is even more pronounced than that of **12** and reaches 3.0111(14) Å.

Polymeric material **12** is only weakly emissive compared to the Cu_4I_4 containing 1D chains of polymers **1**, **9**, and **10**, most probably due to the absence of strong Cu···Cu interactions. Upon excitation at 360 nm, a structured emission with maxima at 416 and 434 nm is observed (Fig. 20). The strong resemblance with the emission spectrum of the free ligand depicted in Figure 21 suggests that the luminescence of the polymer chain is essentially due to the dithioether ligand. The fact that the emission spectrum of $[Cu(\mu\text{-Br})\{p\text{-TolS}(CH_2)_2STol\}]_2$ **13** also displays two maxima in the same spectral range at an 419 and 430 nm (λ_{excit} 360 nm) indicates that the luminescence properties are mostly originating from the ligand.

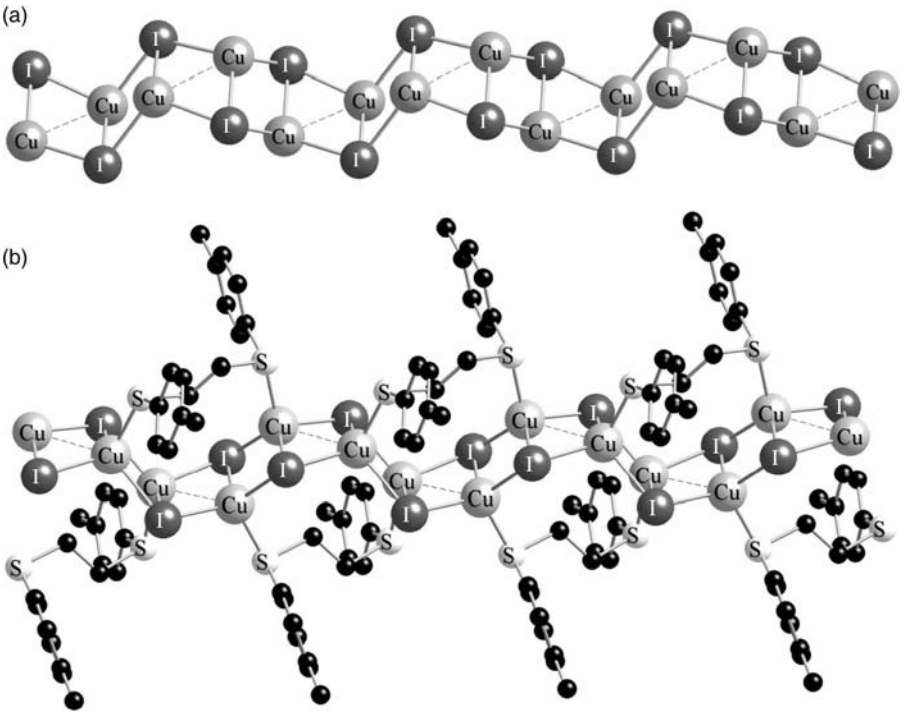

FIGURE 19. (a) View of the inorganic core 1D ribbon of **12** along the *c* axis. (b) View of the metal-organic framework of **12**. The H atoms are omitted for clarity.

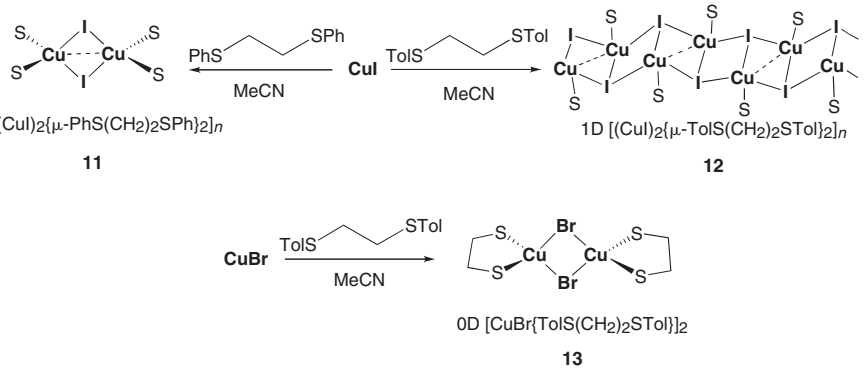

SCHEME 9

Upon treatment of a solution of 1,3-bis(phenylthio)propane in MeCN with an equimolar amount of CuI at ambient temperature, colorless crystals were formed. X-ray diffraction determination revealed the organization of coordination polymer $[(CuI)_2\{\mu\text{-}PhS(CH_2)_3SPh\}_2]_n$ **14** in form of a 2D sheet

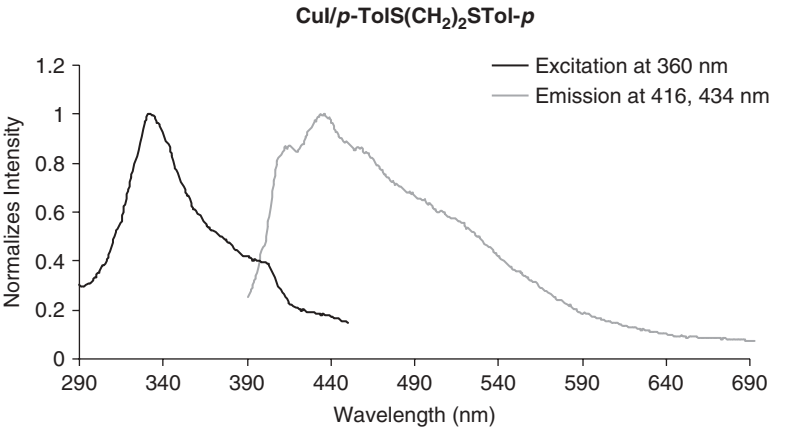

FIGURE 20. Excitation (left) and emission (right) of solid $[(Cu_2I_2)\{\mu\text{-}p\text{-TolS-}p(CH)_2STol\text{-}p\}_2]_n$ **12** at 298K.

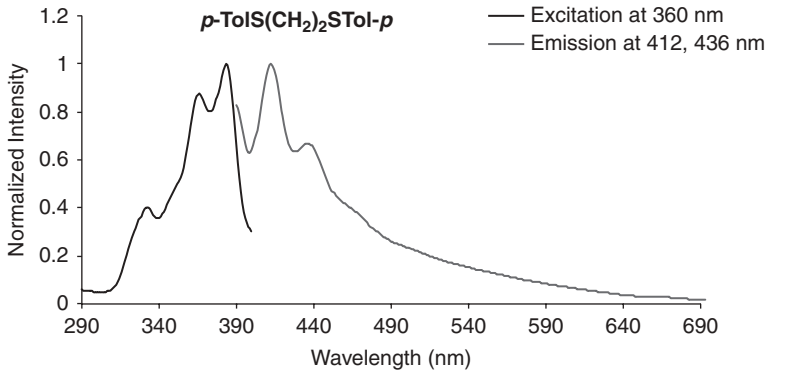

FIGURE 21. Excitation (left) and emission (right) of solid ligand p-TolS$(CH_2)_2$STol-p at 298 K.

structure. The framework consists of centrosymmetric $Cu_2(\mu_2\text{-}I)_2$ rhomboid dimers connected to an adjacent unit via one μ_2-bridging dithioether ligand (Fig. 22). Each Cu atom is in a distorted tetrahedral environment, coordinated by two bridging iodo ligands and two thioether groups of two distinct ligands. The 2D network resulting from this coordination mode includes centrosymmetric 28-membered metallomacrocycles constituted by four dithioether ligands, six Cu atoms, and two iodo ligands. Overall, the coordination mode is quite reminiscent of that encountered in coordination polymer $[(CuI)_2\{\mu\text{-PhS}(CH_2)_2SPh\}_2]_n$ **11**. The Cu$\cdots$Cu separation of **14** is similar to that observed in $[(CuI)_2\{\mu\text{-PhS}(CH_2)_2SPh\}_2]_n$ [2.826(10) vs. 2.8058(11) Å].

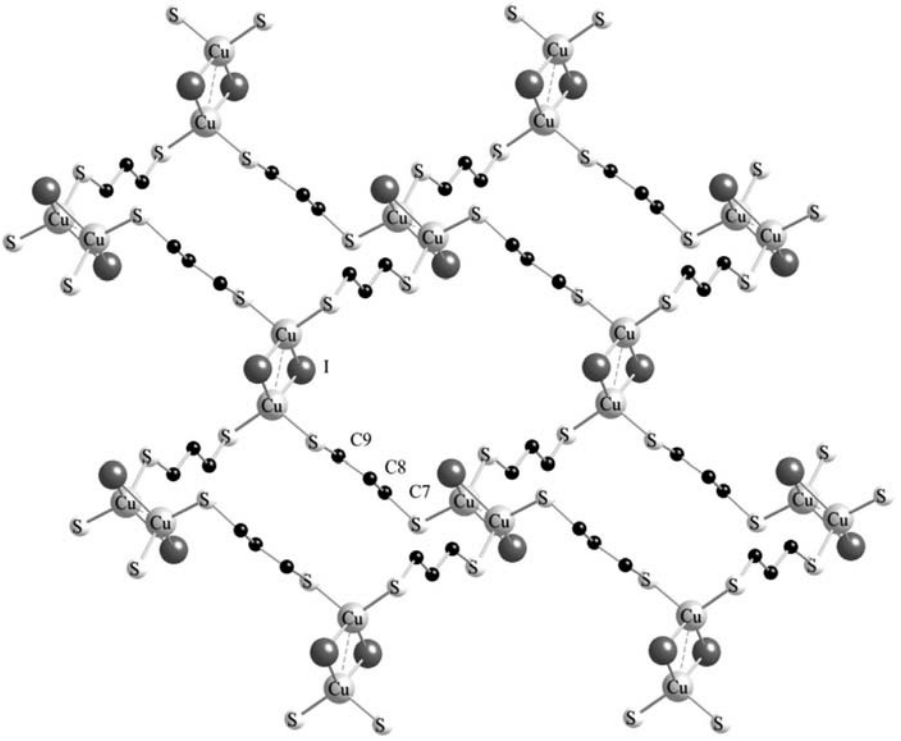

FIGURE 22. View of the core structure of **14** on the *ab* plane. H atoms and phenyl groups are omitted for clarity.

Changing the molar CuI to ligand ratio to 2:1 (using the same experimental conditions) has a dramatic effect on the composition of the colorless crystalline material **15**. Now elemental analyses were in accordance with the ligation of two CuI units per dithioether. Unfortunately, we failed to obtain X-ray-suitable crystals to elucidate the solid-state structure of this compound. However, comparison of the emission spectra of this extremely luminescent material with those of polymers **1**, **9**, **10, 16**, and **21** (see below), for which the occurrence of $Cu_4(\mu_3\text{-}I)_4$ clusters has been crystallographically established, suggests the existence of cubane-like $Cu_4(\mu_3\text{-}I)_4$ units in compound **15**.

It is not surprising that the emission spectrum of **14** resembles that of **11**. After excitation at 360 nm, it displays two emission maxima of medium intensity at 414 and 435 nm. In contrast, material **15** is strongly luminescent. In the solid state after excitation at 360 nm, it displays a broad featureless emission with λ_{max} at about 550 nm (Fig. 23).

Reaction of CuI with 1,4-bis(phenylthio)butane in acetonitrile in a 2:1 molar ratio gave air-stable crystals of the general formula $[Cu_4I_4\{\mu\text{-}PhS(CH_2)_4SPh\}_2]_n$ **16** (Scheme 10). Modification of the molar ratio to 1:1 had, in this case, no influence on the composition of the resulting material and only

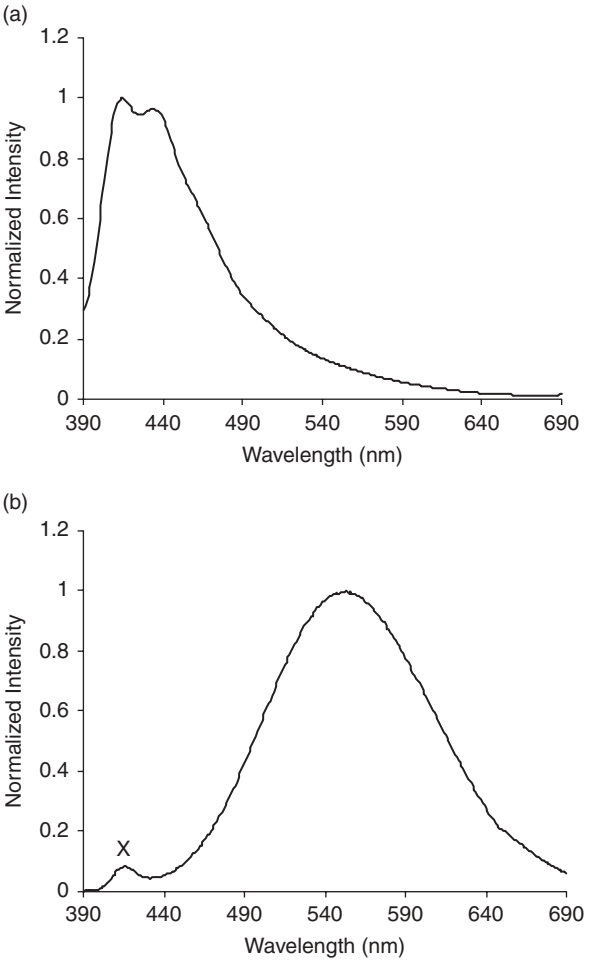

FIGURE 23. Normalized solid-state emission spectra of **14** (a) and **15** (b) recorded at ambient temperature, featuring maxima at 414, 435, and 550 nm, respectively (λ_{excit} = 360 nm). X denotes an emission at 414 nm due to some traces of compound **14** as impurity in the sample of **15**.

colorless material **16** was formed, crystallizing in the triclinic space group P1. Its crystal structure consists of cubane-like Cu_4I_4 clusters linked by bridging dithioethers, forming (in contrast to **9** and **10**) an infinite 2D network (Fig. 24). Its (4,4) topology can be described as undulated square grids, in which Cu_4I_4 clusters as secondary building units (SBUs) define the corners and the dithioether ligands, the edges. The side length of each 32-membered square-like macrocycle is $\sim$10.6 Å. Two of these grids are interpenetrated in such a manner that the square centers of a net plane are approximately located on the middle of the edges of the second one (Fig. 25). Each SBU is connected to four dithioether ligands, with

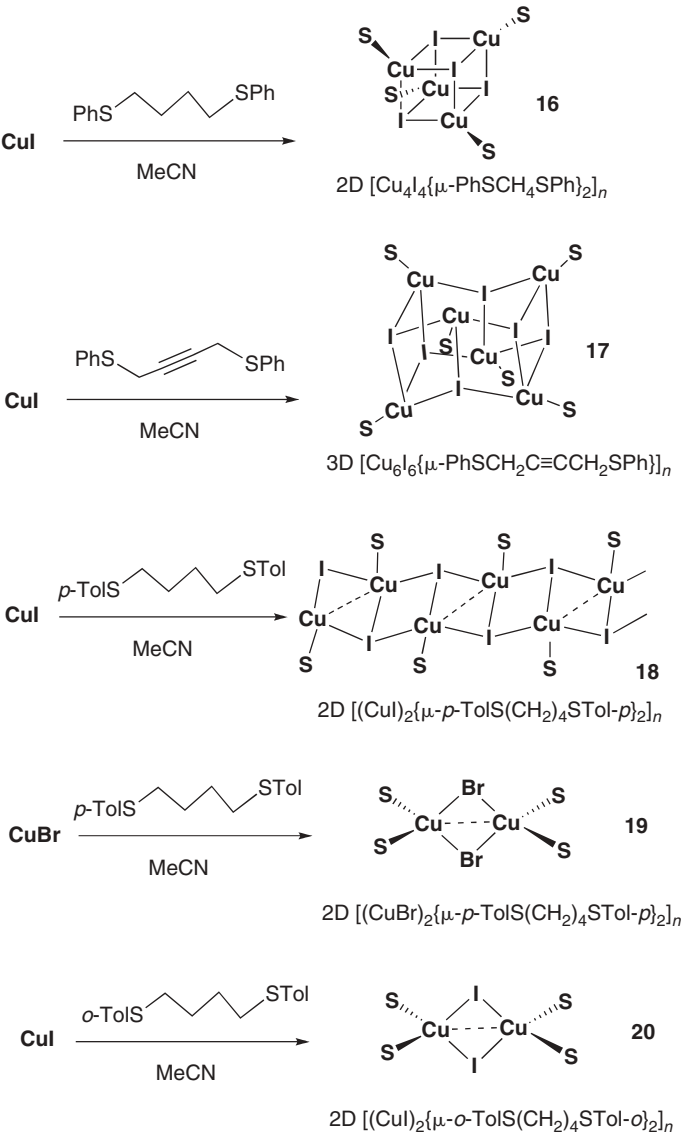

SCHEME 10

averaged Cu–S bond distances of 2.299(2) Å. The Cu–I bond lengths range between 2.6391(12) and 2.7745(14) Å. The Cu···Cu distances between the four nonequivalent Cu(I) centers [2.6505(16)–2.7431(16) Å] have at 173 K a mean value of 2.6942 Å, almost identical to that of the 1D polymer **9**.[146]

The photophysics of strongly luminescent **16** have been examined in detail in collaboration with the Harvey group.[146] After excitation at 360 nm, a

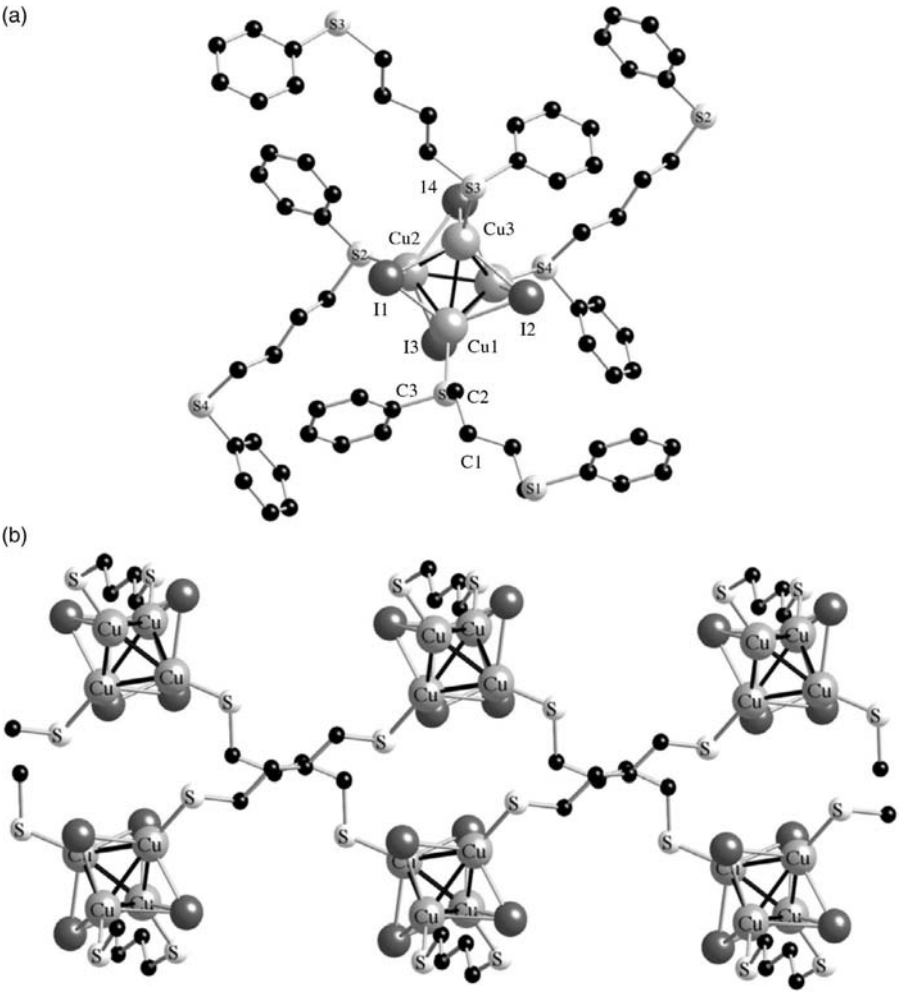

FIGURE 24. (a) View of the tetranuclear $Cu_4(\mu_3\text{-}I)_4$ core of **16** ligated by four PhS $(CH_2)_4SPh$ ligands. H atoms are omitted for clarity. (b) View of on the 2D network of **16** along the *bc* plane. The phenyl groups are omitted for clarity.

broad emission with maximum at 560 nm is observed in the solid-state spectrum (Fig. 26). At 77 K, an important red shift of the emission maximum to 590 nm is noticed. Furthermore, as reported earlier for thermoluminescent $Cu_4I_4(py)_4$, a high-energy band emerges. The data of the time-resolved emission spectra recorded at this temperature are depicted in Fig. 27.

The spacer rigidity of the dithioether ligand influences the resulting framework in a spectacular manner. Indeed, the unsaturated dithioether ligand 1,4-bis(phenythio)butyne, including a linear alkyne $-CH_2-C{\equiv}C-CH_2-$ array, reacts with CuI in MeCN to afford the colorless 3D polymer

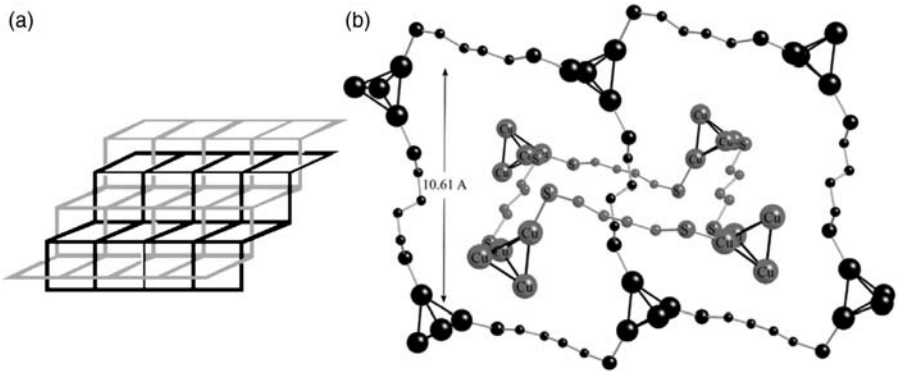

FIGURE 25. (a) The interwoven square grids of **16**. The interpenetrated layers are shown in two different colors. (b) Crystallographic presentation of two fused squares within the 2D network of **16**, which are interpenetrated by a square from a second orthogonal arranged layer. The phenyl groups, H atoms, and I atoms are omitted for clarity.

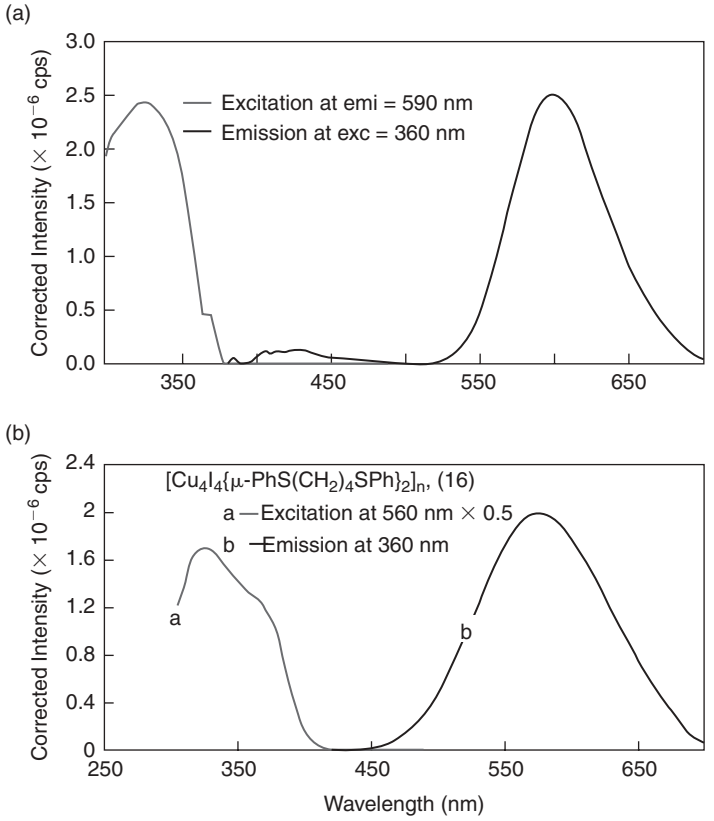

FIGURE 26. Emission and excitation spectra of solid **16** recorded at 77 K (a) and 298 K (b).

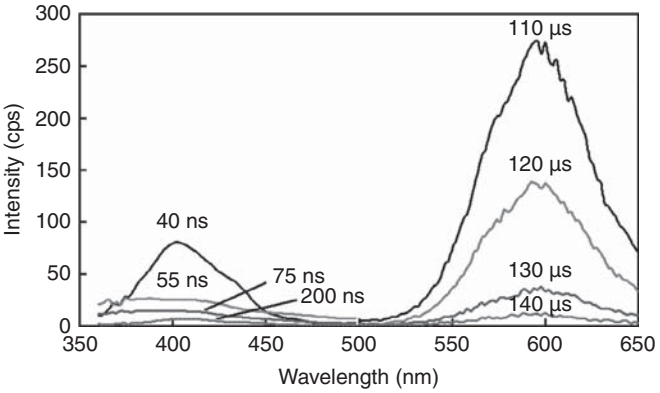

FIGURE 27. Time-resolved emission of $[Cu_4I_4\{\mu\text{-}PhS(CH_2)_4Ph\}_2]_n$ **16** at 77 K, $\lambda_{ex} = 350$ nm.

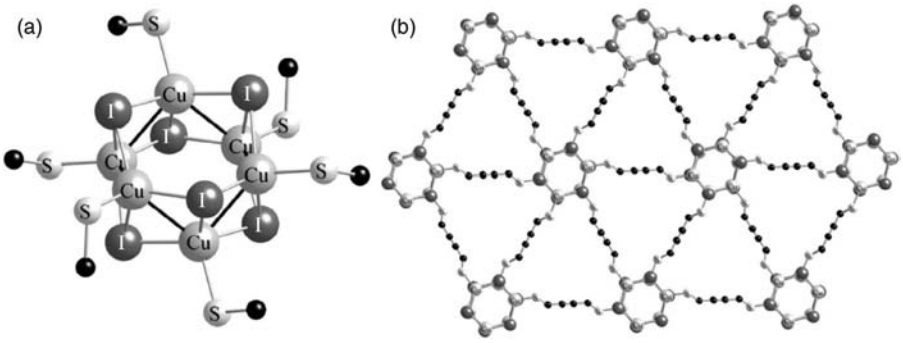

FIGURE 28. (a) Hexanuclear $Cu_6(\mu_3\text{-}I)_6$ core of **17** ligated by six unsaturated dithioether ligands. H atoms are omitted for clarity. (b) View on the 3D network of **17** along the *a,b* plane. The phenyl groups are omitted for clarity.

$[(Cu_6I_6)\{\mu\text{-}PhSCH_2C{\equiv}CCH_2SPh\}]_n$ **17**, crystallizing in the trigonal space group R_3 (Scheme 10).[146] The most salient feature of the framework is the presence of hexagonal $Cu_6(\mu_3\text{-}I)_6$ cluster units as connecting nodes (Figs. 28 and 29). The polymer composition is independent of on the CuI to ligand ratio. In contrast to some other thioether ligands possessing an alkyne function, no interaction between the copper centers and the triple bond is observed.[147] Compared to **16**, the Cu–S bond lengths [2.3655(8) Å] are somewhat elongated in **17**. In the hexagonal clusters of **17**, the Cu···Cu distance of 2.8484(6) Å is close to the sum of the van der Waals radii. Coordination polymers with discrete hexagonal $Cu_6(\mu_3\text{-}X)_6$ cluster are very scarce. To our knowledge, only two other coordination polymers—$[Cu_6(\mu_3\text{-}Br)_6(TTT)_2]_n$ (TTT = trisallyl-1,3,5-triazine-trione) and $[Cu_6(\mu_3\text{-}X)_6py_6]_n$ (X = Cl, Br, I)—involving this unusual motif have been reported

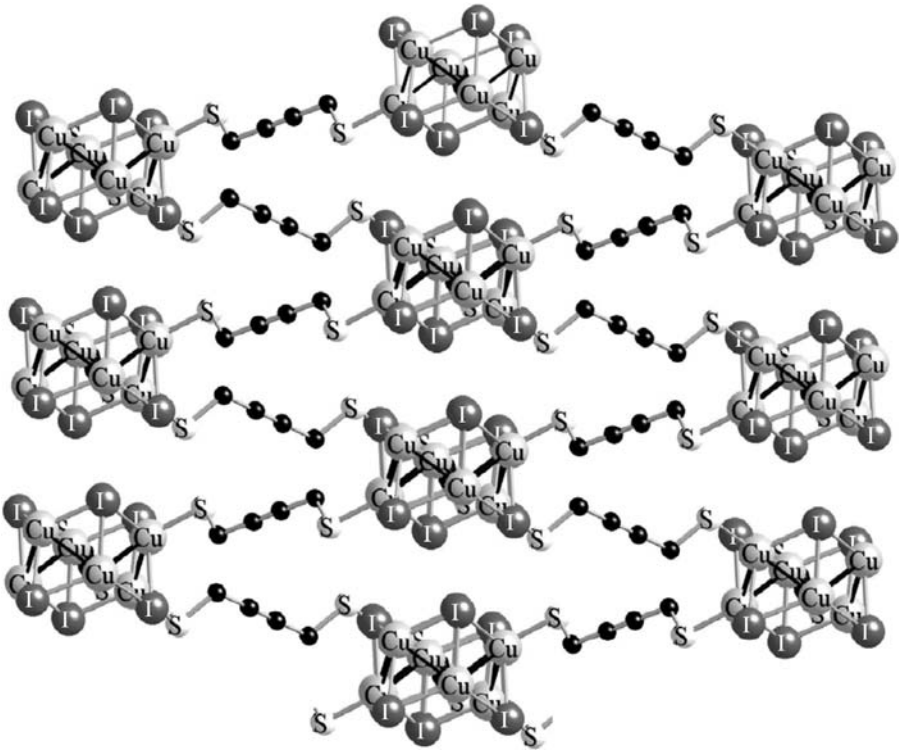

FIGURE 29. View of the hexanuclear $Cu_6(\mu_3\text{-}I)_6$ cores of **17** along the *b,c* plane.

so far.[148,149] In the latter luminescent material, a pyridine-functionalized triethyl-benzene spacer links the cluster nodes. However, there are some striking differences in the dimensionality (3D vs. 2D) and the Cu···Cu separations between **17** and the latter two compounds. The far longer Cu···Cu contacts amount to 2.9645(5) Å in $[Cu_6(\mu_3\text{-}I)_6py_6]_n$, and even reach 3.203 Å in $[Cu_6(\mu_3\text{-}Br)_6(TTT)_2]_n$.

Air-stable 3D material **17** is also strongly emissive at ambient temperature and gives rise to an unstructured band at 555 nm after excitation at 360 nm.[146] Although a little bit blue shifted compared to **16**, the resemblance of the emission spectra of **17** with that of **16** (Fig. 30; Table 1) and other Cu_4I_4-containing species seen in the literature is striking (where two bands are observed), giving us the temptation to propose similar assignments for the excited states responsible of the transitions in both clusters. Moreover, the long emission lifetimes and the large energy gap between the absorption (and excitation) and the emission bands indicate the presence of phosphorescence in **17** (Figs. 30 and 31). The observed emission of the alkyne ligand (**L17**) is blue shifted with respect of the low-energy emission of **17**, which indicates that the latter does not arise from the ligand itself (Table 1).

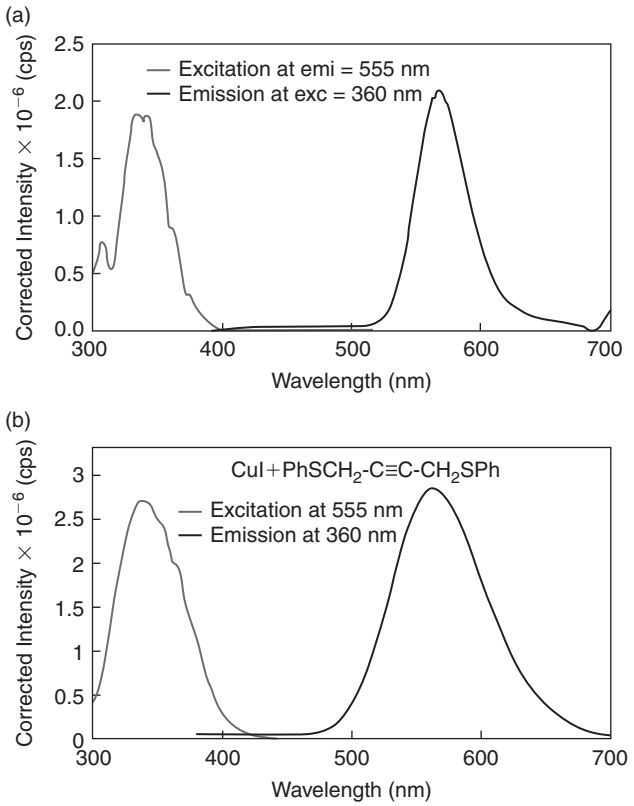

FIGURE 30. Emission and excitation spectra of solid $[(Cu_6I_6)\{\mu\text{-}PhSCH_2C{\equiv}CCH_2SPh\}]_n$ **17** recorded at 77 K (a) and 298 K (b).

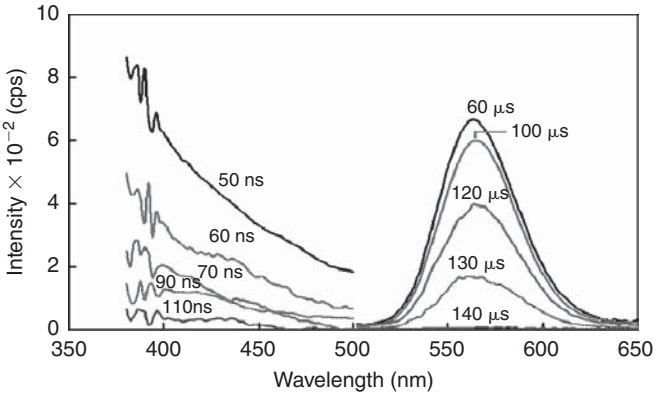

FIGURE 31. Time-resolved emissions of **17** recorded at 77 K, λex = 350 nm.

TABLE 1. Photophysical Data for Solid **16**, **17**, and $PhSCH_2C{\equiv}CCH_2SPh$ (**L17**) at 298 and 77 K

	298 K		77 K	
Compound	λ_{em} (nm)	τ_e (μs)(λ_{em} in nm)	λ_{em} (nm)	τ_e (μs)(λ_{em} in nm)
L17	540	1.35 ± 0.02 (540 nm)	545	1.42 ± 0.02 (545)
17	425	0.53 ± 0.02 (425 nm)	425	0.55 ± 0.03 (425)
	555	2.62 ± 0.03 (555 nm)	565	3.40 ± 0.06 (565)
16	—	—	430	0.60 ± 0.02 (430)
	575	0.85 ± 0.01 (575)	600	3.36 ± 0.01 (600)

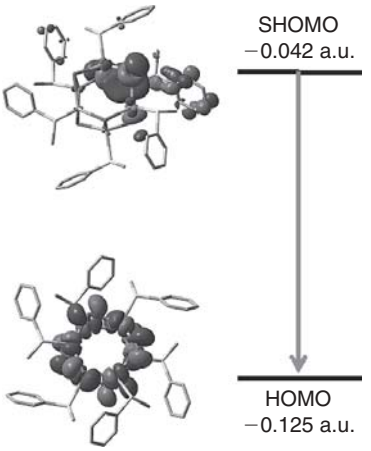

FIGURE 32. HOMO and LUMOs representations and their calculated energies for the model compound $Cu_6I_6(SPhMe)_6$ as well as the SHOMO of the corresponding triplet state.

DFT calculations on the model compound $Cu_6I_6(SPhCH_3)_6$ in its triplet state predict that the SHOMO localizes the spin density mainly on one Cu atom and its three iodo neighbors with the rest on one -SPh fragment, whereas it is rather delocalized over the Cu and I atoms in the HOMO (Fig. 32). The SHOMO is located at -0.042 a.u. above the HOMO (-0.125 a.u.). The simple arithmetic difference between the two levels suggests that the radiative relaxation should occur in the vicinity of 550 nm, which fits the experimentally observed maxima (Fig. 31). So the first theoretical study confirms a cluster-centered excited state as responsible for the observed emission, similar to other Cu_4I_4-containing species.[146]

To see the effect of an additional methyl substituent of the −SAr group on the architecture of the network, we treated CuI under analogous reaction conditions and metal to ligand ratio employed for the 1,4-bis(phenylthio)butane-linked derivative **16** with 1,4-bis(*p*-tolylthio)butane and with 1,4-bis(*o*-tolylthio) butane, respectively. In contrast to **9** and **10**, we noticed now a very sensible

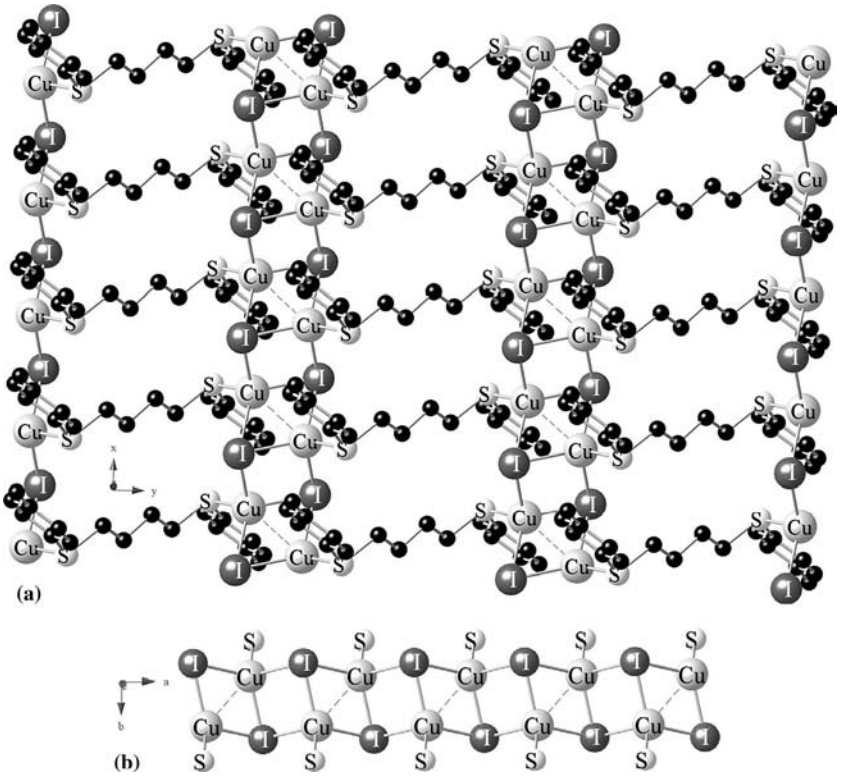

FIGURE 33. (a) View of the core structure of 2D polymer $[(CuI)_2\{\mu\text{-}p\text{-TolS}(CH_2)_4STol\text{-}p\}_2]_n$ **18** on the *ab* plane. H atoms groups are omitted for clarity. (b) Presentation of the inorganic staircase ribbon along the *a* axis.

influence of the aryl-substitution pattern on the topology of the resulting polymeric materials.

With 1,4-bis(*p*-tolylthio)butane, the 2D coordination polymer $[(CuI)_2\{\mu\text{-}p\text{-TolS}(CH_2)_4STol\text{-}p\}_2]_n$ **18** was isolated as the sole product (Scheme 10). Figure 33 shows that the sheets of **18** consist of parallel-arranged infinite inorganic staircase ribbons, which are interconnected through the dithioether ligands. These stepped ribbons are constructed by dinuclear $Cu(\mu_2\text{-}I)_2Cu$ units with a close Cu···Cu separation of 2.7976(18) Å, which are in loose contact [3.577 Å] with the neighboring rhomboids through μ_3-bridging iodo atoms. Although at first glance it is similar to the inorganic ribbon of 1D polymer $[(Cu_2I_2)\{\mu\text{-}p\text{-TolS}(CH_2)_2STol\text{-}p\}]_n$ **12** shown at the top of Figure 19, the comparison with the more symmetric inorganic ribbon of **18** presented in Figure 33b reveals the differences of the microstructures.

As noticed for compounds **12** and **13**, the nature of the halide ion is also decisive for the architecture of the framework. Using CuBr instead of CuI, the 2D character of the network is maintained, but the nuclearity of the CuX motif

switches from polymeric staircase CuI to discrete $Cu(\mu_2\text{-}Br)_2Cu$ dimers, which are kept together by bridging 1,4-bis(*p*-tolylthio)butane ligands, thus forming 32-membered macrocycles. The Cu···Cu contacts within a layer of $[(CuBr)_2\{\mu\text{-}p\text{-}TolS(CH_2)_4STol\text{-}p\}_2]_n$ **19** are significantly shorter than that of dinuclear complex **13** [2.8678(15) vs. 3.0111(14) Å]. (Fig. 34).

The position of the methyl substituent of 1,4-bis(tolylthio)butane plays also a major role for the control of the nuclearity. This was evidenced by mixing CuI with 1,4-bis(*o*-tolylthio)butane (Scheme 10). The 2D network of the reaction product $[(CuI)_2\{\mu\text{-}o\text{-}TolS(CH_2)_4STol\text{-}o\}_2]_n$ **20** (Fig. 35) contains discrete dinuclear $Cu(\mu_2\text{-}I)_2Cu$ rhomboids as connecting nodes, similar to the bonding situation encountered in $[(CuBr)_2\{\mu\text{-}p\text{-}TolS(CH_2)_4STol\text{-}p\}_2]_n$ **19**. The Cu···Cu separation of 2.796(3) Å matches closely with the sum of the van der Waals radii of two Cu atoms.

Both polymers **18** and **20** are luminescent in the solid state. In the case of compound **18**, the shape of the emission spectrum depends from excitation wavelength. Upon excitation at 320 nm, a broad featureless emission is observed at ~530 nm. After excitation at 380 nm, the emission spectrum exhibits a sharp maximum at ~429 and a broad hump centered at ~520 nm (Fig. 36). Three maxima at ~422, 505, and 542 nm are found in the emission spectrum of $[(CuI)_2\{\mu\text{-}o\text{-}TolS(CH_2)_4STol\text{-}o\}_2]_n$ **20** (Fig. 37b) after excitation at 360 nm. The resemblance of the band at 422 nm with the emission band of solid 1,4-bis(*o*-tolylthio)butane (Figure 37b) indicates that this emission is essentially

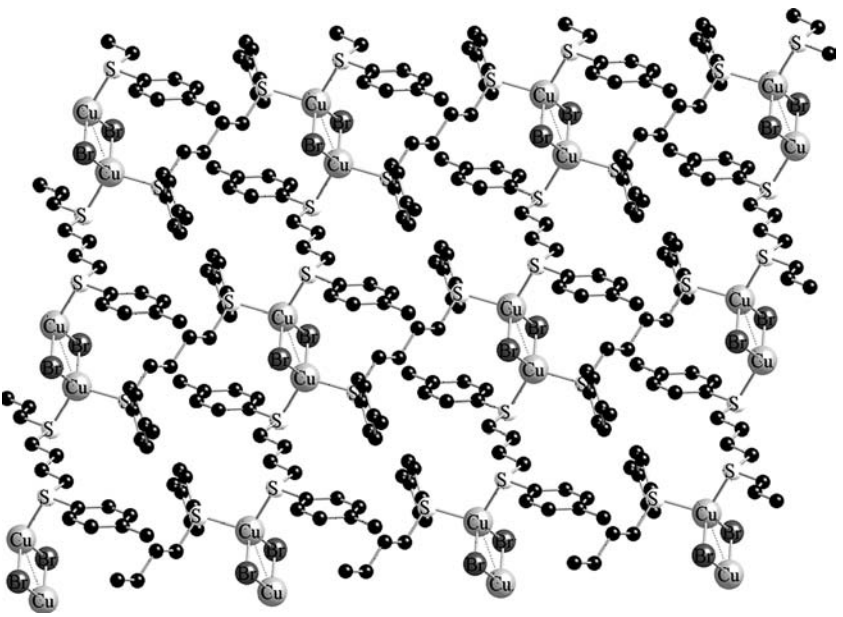

FIGURE 34. View of the sheet structure of 2D polymer $[(CuBr)_2\{\mu\text{-}p\text{-}TolS(CH_2)_4STol\text{-}p\}_2]_n$ **19**. H atoms are omitted for clarity.

ligand-centered. The CuBr-containing material **19** is only weakly emissive at ambient temperature and deserves no further comment.

The structural richness and diversity of the metal-organic networks obtained by reaction of CuI and CuBr with $ArSC_4SAr$ ($C_4 = (CH_2)_4$, $CH_2C{\equiv}CCH_2$) are summarized in Scheme 10.

Our studies revealed that, upon treatment of CuI with 1,5-bis(phenylthio) pentane in acetonitrile solution, the architecture of the resulting polymeric material depends in a crucial manner on the metal to ligand ratio employed. Performing the reaction in a 2:1 molar ratio gave air-stable crystals of general

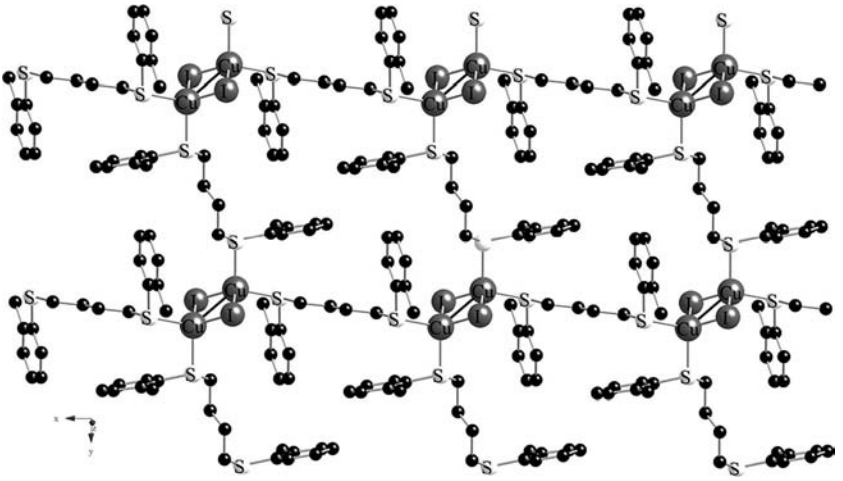

FIGURE 35. View of the core structure of 2D polymer **20** on the *ab* plane.

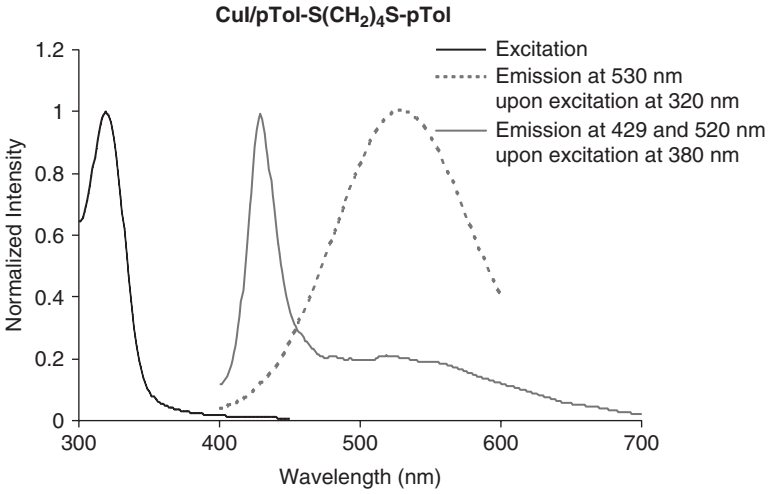

FIGURE 36. Excitation (left) and emissions (right) of solid 2D polymer **18** at 298 K.

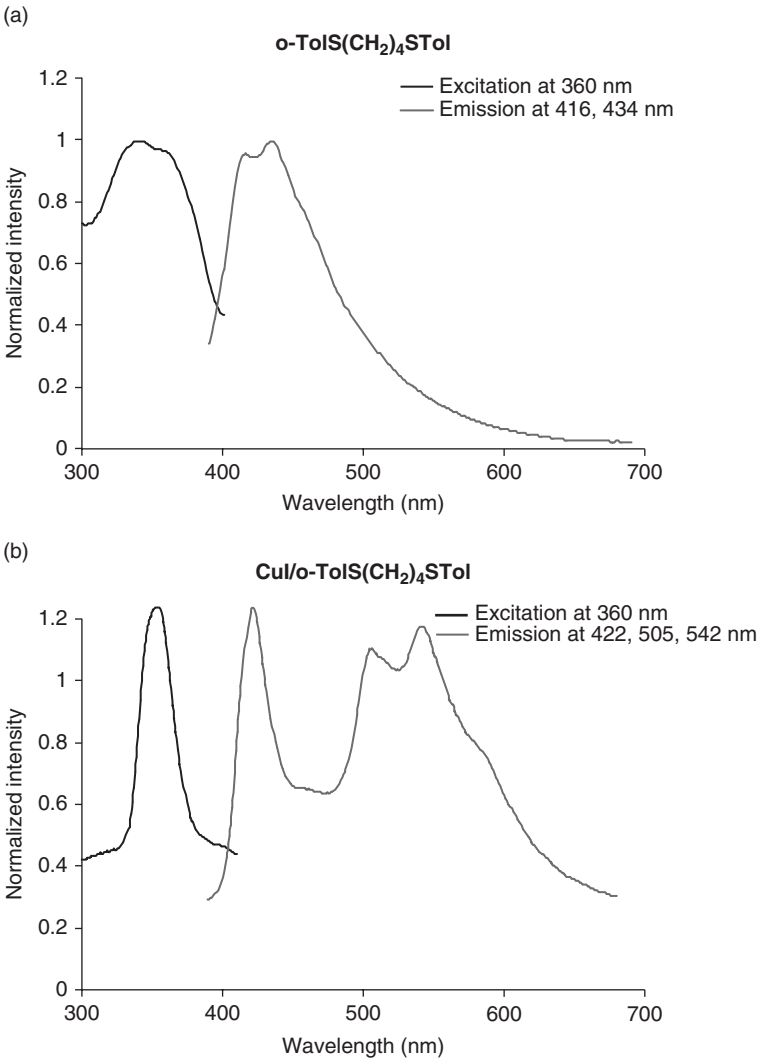

FIGURE 37. (a) Excitation (left) and emission (right) spectra of solid *o*-TolS$(CH_2)_4$STol-*o* at 298 K. (b) Excitation (left) and emission (right) of solid 2D polymer **20** at 298 K.

formula $[Cu_4I_4\{\mu\text{-PhS}(CH_2)_5SPh\}_2]_n$ **21**. In contrast to the 2D framework found for polymer **16**, the Cu_4I_4 units of **21** make up part of an infinite 1D chain, similar to 1D compounds **9** and **10**. Two neighboring clusters, whose centroids are separated by $\sim$12.5 Å, are doubly linked by two dithioether ligands, forming an 18-membered cycle. As can be seen from Figure 38, the adjacent macrocycle is situated in an orthogonal arrangement with respect to the first one. Each cluster core consists of four copper nuclei in close contact, with a mean Cu–Cu distance of 2.712 Å (at 193 K).

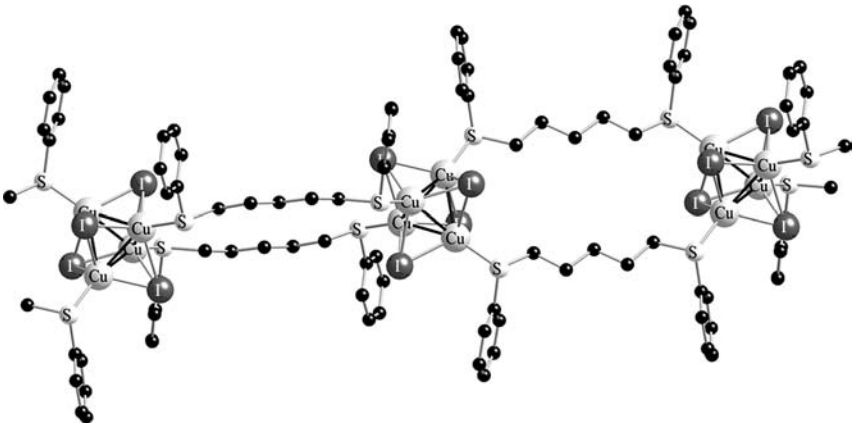

FIGURE 38. View of the 1D chain of **21**. H atoms are omitted for clarity.

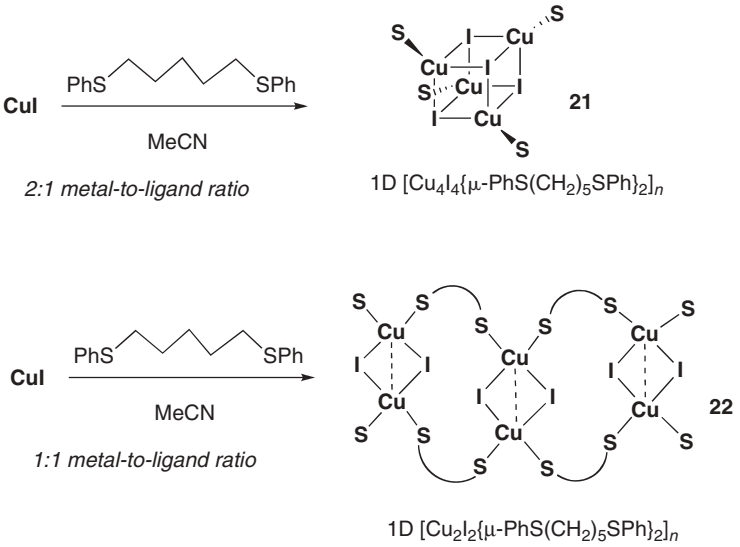

SCHEME 11

If the self-assembly reaction of CuI with bis(phenylthio)pentane is conducted in a 1:1 ratio, elemental analyses of the colorless blocks isolated from a concentrated MeCN solution were in accordance with the ligation of one dithioether ligand per copper center with composition $[(CuI)_2\{\mu\text{-PhS}(CH_2)_5SPh\}_2]_n$ **22** (Scheme 11). Alternatively, compound **22** is formed after addition of second equivalent of bis(phenylthio)pentane to a solution of **21**.

Crystallographic examination of **22** revealed the existence of infinite 1D ribbons (Fig. 39). These corrugated ribbons are constituted by two bridging dithioether ligands, with span rhomboid Cu_2I_2 units. Each copper center of

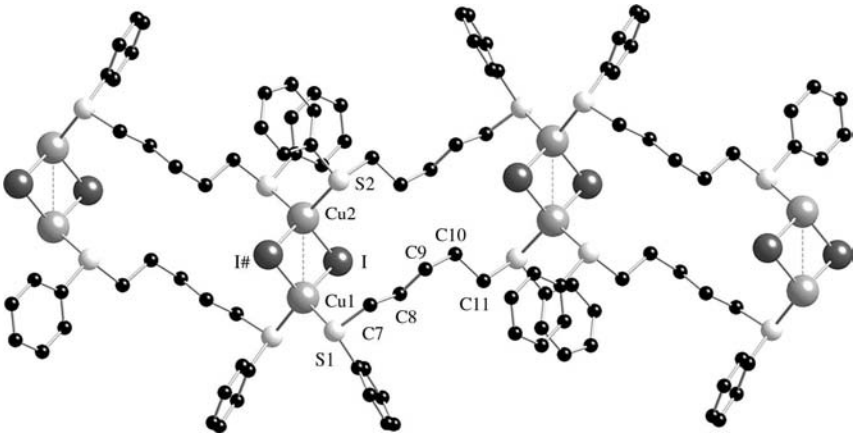

FIGURE 39. View of the 1D ribbon of **22** along the *a* axis.

these nodal Cu_2I_2 units is coordinated in a tetrahedral manner by two S atoms stemming from two different dithioether ligands and is symmetrically bridged by two μ-iodo ligands. As shown in Figure 39, 20-membered macrocycles comprising 10 carbon atoms, 4 copper atoms, 4 sulfur atoms, and 2 μ-I atoms result from this arrangement and are annelated along the a axis. Along with polymers **31**, **37**, and **45** (see below), compound **22** represents one of the rare cases in which Cu_2I_2 rhomboids make part of a 1D network.

The mean Cu−S distance of the two copper−thioether bonds of 1D polymer **22** is quite similar to the value found for 2D polymer **11** (2.3325 vs. 2.346 Å) but notably longer than the mean Cu−S distance of the 2D compound **14** (2.299 Å). Noteworthy is the weak Cu···Cu contact of 3.0089(15) Å, which is considerable elongated compared to those of **11** and **14**. Although this distance is significantly beyond the Van der Waals radius of 2.8 Å, a far longer Cu···Cu separation of 3.18 Å has been found in the 2D sheet structure of polymeric $[Cu_2I_2(dtpcp)2] \bullet thf$ (dtpcp = 2,11-dithia[3.3]paracyclophane).[150] This wide range of Cu···Cu separations experimentally observed in dinuclear Cu_2I_2 units ligated by thioether ligands indicates a certain degree of structural flexibility, which, in combination with the intrinsic flexibility of the dithioether ligands, may account for the richness of the structural motifs found in the solid-state structures of these compounds. In line with the elongation of the Cu···Cu distance, the Cu−I−Cu angle of **22** is markedly less acute than that of **11** [69.58(3) vs. 64.54(4)°]. The Cu−I distances of **22** and **11** are less affected by this phenomenon and lie in the range between 2.63 and 2.65 Å.

What are the limits of the number of spacer units between the two sulfur atoms of $ArS(CH_2)_nSAr$ dithioether ligands that still allow the self-assembly copper iodide and the build-up of metal-organic materials? To answer this question, we reacted CuI with both 1,6 bis(phenylthio)hexane and 1,7-bis (phenylthio)heptane in acetonitrile solution in a 2:1 ratio. In both cases,

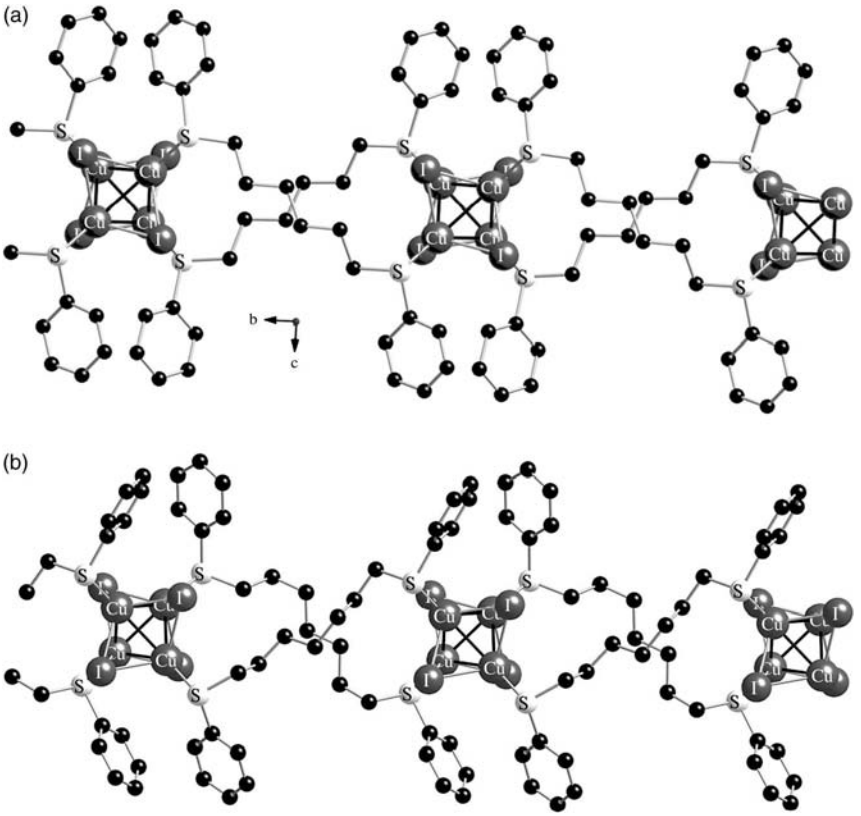

FIGURE 40. View of the 1D necklace chains of **23** (a) and **24** (b) along the *b* axis. H atoms are omitted for clarity.

exclusively 1D polymers $[Cu_4I_4\{\mu\text{-}PhS(CH_2)_6SPh\}_2]_n$ **23** and $[Cu_4I_4\{\mu\text{-}PhS(CH_2)_7SPh\}_2]_n$ **24**, with a necklace motif, were formed (Fig. 40). We failed, however, to isolate any product using 1,8-bis(phenylthio)octane or 1,10-bis (phenylthio)decane as starting material.

Again, the 1D chains of **23** and **24** are constructed by Cu_4I_4 cubanes as connecting nodes. The mean Cu···Cu distances amount to 2.711 and 2.750 Å (at 173 K), respectively. Probably due to the incorporation of supplementary methylene spacers between the sulfur donors and the enhanced flexibility of the alkane arrays, the spanning of the dithioether ligands is quite twisted, in contrast to the more linear spanning found in the related polymer $[Cu_4I_4\{\mu\text{-}PhS(CH_2)_5SPh\}_2]_n$ **21**. Like the other $ArS(CH_2)_nSAr$ derivates incorporating Cu_4I_4 building blocks, **23** and **24** are extremely emissive at 298 K. The superimposition of the solid-state emission spectrum of **23** with those of **16** and **21** reveals that the maximum is blue shifted to $\sim$520 nm (Fig. 41). A fluorescence thermochromism is also observed for compound **23**. As encountered for compound **16**, the

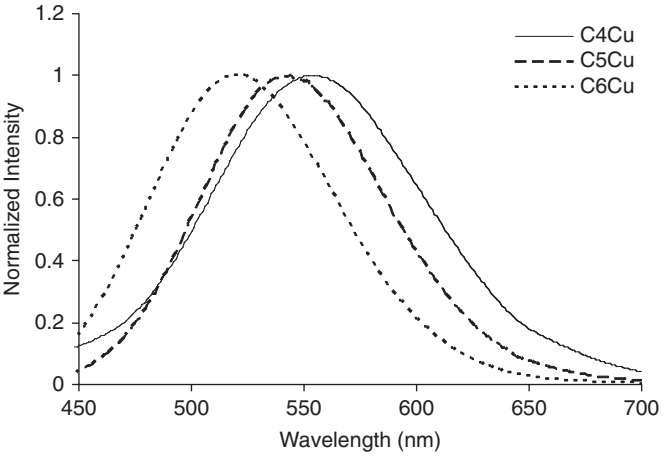

FIGURE 41. Corrected and normalized solid-state luminescence spectra recorded for compounds **16**, **21**, and **23** at room temperature.

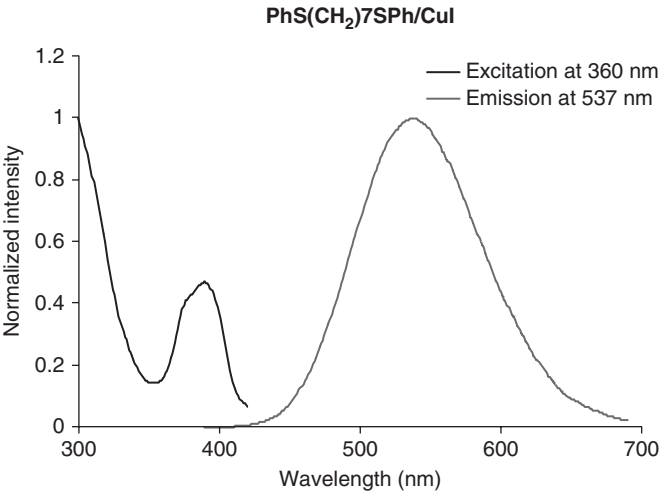

FIGURE 42. Excitation (left) and emission spectra (right) of solid **24** at 298 K.

unstructured emission with maximum at ~520 nm at 298 K undergoes a slight red shift to ~530 nm upon cooling to 77 K, an additional distinct high-energy band is found at ~425 nm. The same phenomenon has also been observed for the related polymer **43** (see below). The fact that the emission maximum of 1D compound **24** is centered at ~537 nm (Fig. 42) indicates, that no clear correlation between the number spacer units of $[Cu_4I_4\{\mu\text{-}ArS(CH_2)_xSAr\}_2]_n$ and the position of emission maxima exists.

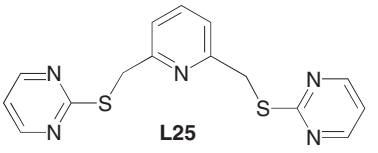

2,6-Bis(2-pyrimidinesulfanylmethyl)pyridine

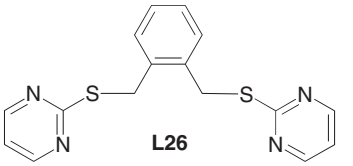

1,2-Bis(2-pyrimidinesulfanylmethyl)benzene

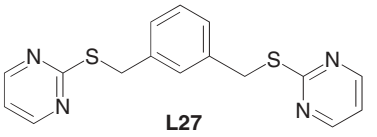

1,3-Bis(2-pyrimidinesulfanylmethyl)benzene

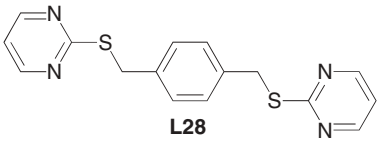

1,4-Bis(2-pyrimidinesulfanylmethyl)benzene

SCHEME 12

Parallel to our work with $RS(CH_2)_nSR$ ligands in this domain, the Li group underwent an interesting investigation of the reactivity of pyrimidine-functionalized dithioether ligands toward various copper(I) salts.[151,152] The ditopic ligands **L25**–**L28** incorporating an aromatic cycle in the spacer are illustrated in Scheme 12.

The thorough study of this group revealed (based on numerous X-ray diffraction studies, whose detailed description is renounced) that with these flexible ligands the outcome of the reaction depends from the substitution pattern of the central aromatic cycle. With the exception of the 1,4-bis(2-pyrimidinesulfanylmethyl)benzene ligand, which interacts with the Cu(I) centers both via its sulfur and nitrogen sites, all metal-ligand interactions occur exclusively through the *N*-donors. In addition, the nature of the counterion plays a crucial role in the formation and dimensionality (ranging from 0D to 3D) of the isolated compounds, some of which have very original frameworks. This systematic work is completed by the examination of the photophysics of some polymeric compounds, which display strong luminescence at room temperature in the solid state.

Particularly interesting is the comparison of the frameworks and luminescence properties of the materials obtained by reaction of CuI with bis(2-pyrimidinylthio)methane **L29** and bis(2-pyrimidinylthio)ethane **L30** and those of 1D polymer $[Cu_4I_4\{\mu\text{-}PhSCH_2SPh\}_2]_n$ **9** and **2**D polymer $[Cu_2I_2\{\mu\text{-}PhS(CH_2)_2SPh\}_2]_n$ **11** (Scheme 13).[153]

Like for polymer **9**, the framework of $[Cu_2I_2\{\mu\text{-}L29\}_2]_n$ **29** (Fig. 43) is monodimensional, but the dithioether ligand **L29** assembles dinuclear $Cu(\mu\text{-}I)_2Cu$ motifs (*d* Cu···Cu 3.131(2) Å) exclusively through the pyrimidine nitrogen atoms with formation of 16-membered macrocycles.

As noticed for **9** and **11**, the dimensionality of the framework depends on the number of spacer units of the $Ar(CH_2)_nAr$ ligand. When we employ the more flexible **L30** dithioether, the dimensionality of the framework increases.

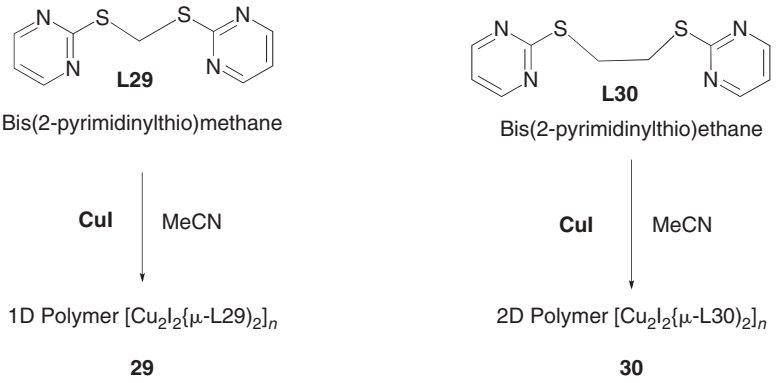

SCHEME 13

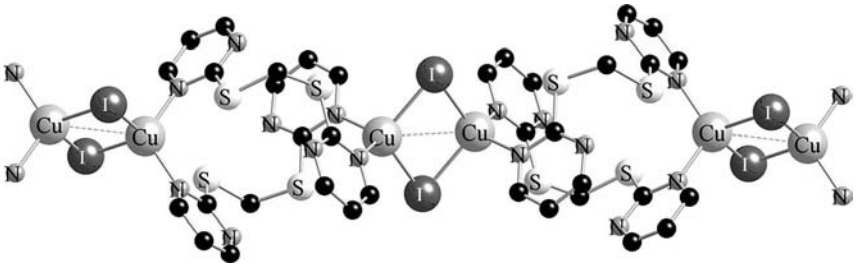

FIGURE 43. View of the 1D ribbon of polymer **29** incorporating dinuclear $Cu(\mu\text{-}I)_2Cu$ motifs.

However, the nuclearity is not affected. Figure 44 shows the 2D network of $[Cu_2I_2\{\mu\text{-}L30\}_2]_n$ **30**, in which the adjacent rhomboid $Cu(\mu\text{-}I)_2Cu$ units (*d* Cu···Cu 3.286 (4) Å) are linked by one **L30** ligand. The repeating 40-membered macrocycles of **30** are large enough to accommodate two free **L30** molecules as guests in the cavities.

Despite the nonbonding contacts between the copper centers of **29** and **30**, both compounds are reported to be luminescent, displaying broad structureless bands with maxima at ~533 and 543 nm, respectively. The strong emissions of the free ligands **L29** and **L30** are observed blue shifted at ~477 and 467 nm, respectively. The authors tentatively attribute the emission of the polymers to MC d→s excited states or MLCT states.

The same authors have also investigated the impact of the solvent during the self-assembly process in the reaction of CuI with the flexible ligand 3,4-bis(4 pyridinesulfanylmethyl)thiophene **L31**, which may adopt different conformations (Scheme 14).[154] Mixing a CuI/KI-saturated solution with a MeCN solution of **L31** produces the 1D polymer $[(Cu_2I_2)(L31)_2]_n$ **31** shown in Fig. 45, incorporating Cu_2I_2 rhomboids [*d* Cu···Cu 2.9531(19) Å] as SBUs. If CuI dissolved in aqueous MeCN is treated with a $CHCl_3$ solution of **L31**, the

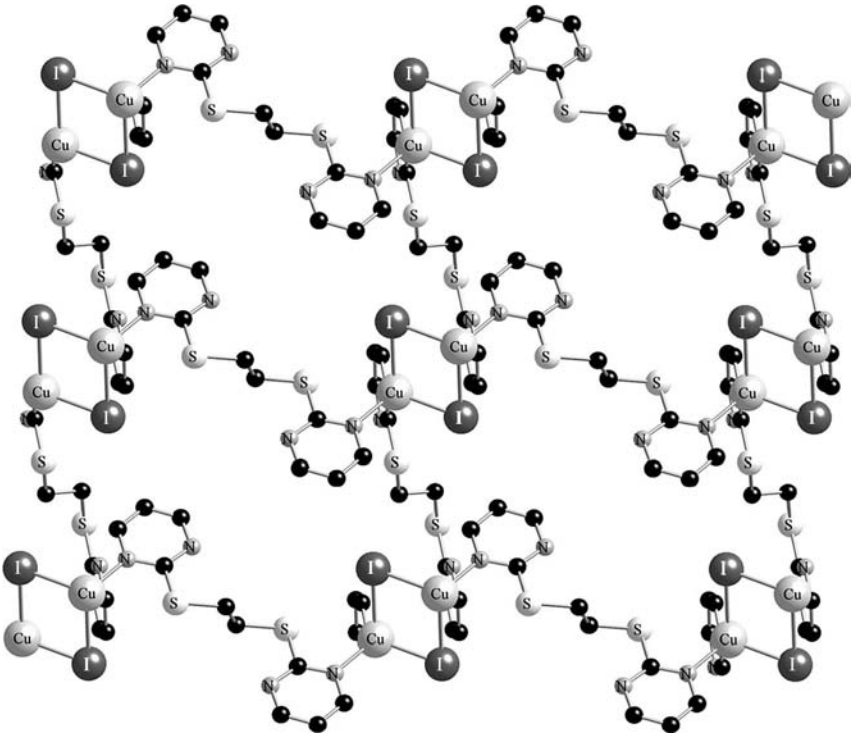

FIGURE 44. View of the 2D sheet of polymer **30** incorporating dinuclear $Cu(\mu\text{-}I)_2Cu$ motifs. The **L30** guest molecules within the channels are omitted for clarity.

topological isomeric 1D polymer $[(Cu_2I_2)(L31)_2]_n \bullet CHCl_3$ **31′** is formed. Within the Cu_2I_2 rhomboids of **31′**, the extremely close Cu-Cu bond length of only 2.5581(9) Å is remarkable. In the crystal packing of **31′**, disordered chloroform host molecules occupy the residual space. Additional weak C-H···Cl, C-H···I and C-H···S interactions give rise to a supramolecular network.

The most salient finding of this study is the fact, that using CH_2Cl_2 instead of $CHCl_3$ as solvent for **L31** causes a switch of the dimensionality of the metal-organic framework from 1D to 2D. In isomer **31″**, with composition $[(Cu_2I_2)(L31)_2]_n \bullet CH_2Cl_2$, the Cu−Cu distances of the Cu_2I_2 SBUs amount to 2.6587(12) Å. Within the (4,4) grids of **31″**, dichloromethane clathrate molecules are embedded (Scheme 14). As in the case of isomers **31** and **31′**, the coordination of functionalized dithioether **L31** on the Cu(I) ions occurs exclusively via the pyridine nitrogen atoms.

In contrast to nonemissive ligand **L31**, all three isomeric forms of polymer **31** show strong photoluminescence in the solid state at room temperature on irradiation with UV light. The authors of this study correlate the increasing red shift of the broad, structureless emissions from 493 nm (**31**), 532 nm (**31″**), to 540 nm (**31′**) with the decrease of the Cu···Cu separation.[154]

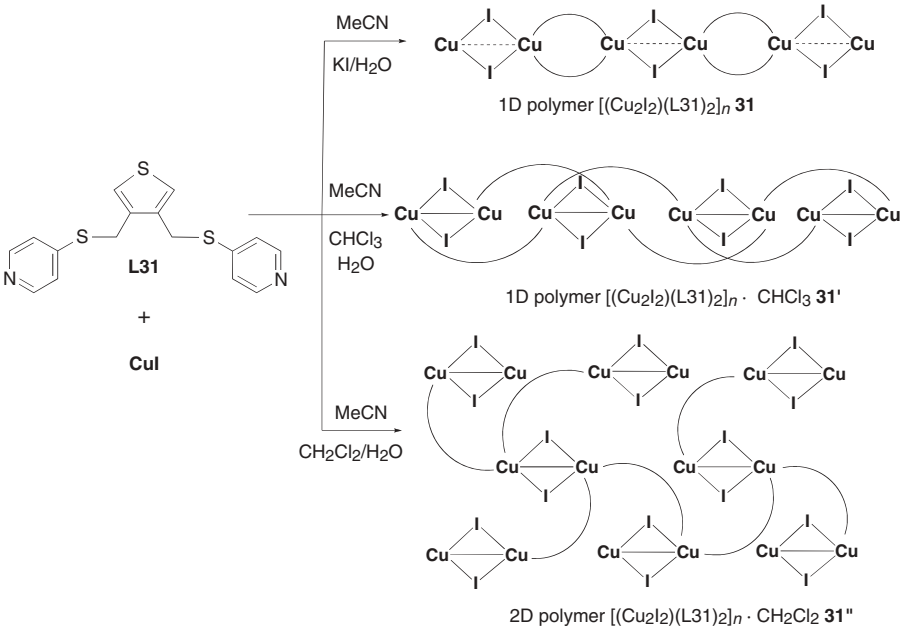

SCHEME 14

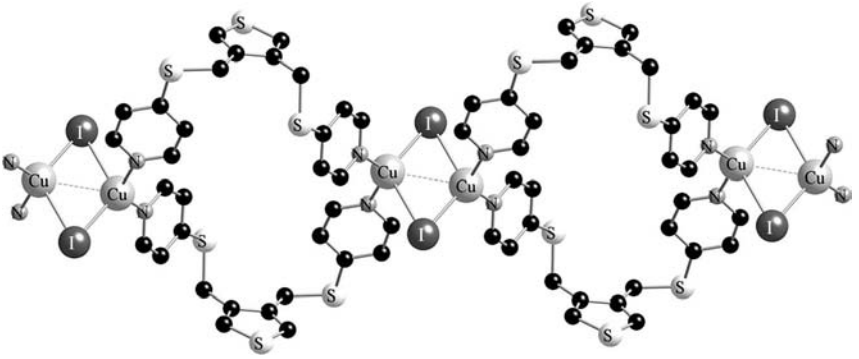

FIGURE 45. View of the 1D array of luminescent $[(Cu_2I_2)(L31)_2]_n$ **31** incorporating dinuclear $Cu(\mu\text{-}I)_2Cu$ motifs.

C. Copper Polymers Assembled by Aliphatic Dithioether and Polythioether Ligands

To evaluate the influence of the organic R group of the RS-thioether function and to allow a comparison with $ArS(CH_2)_4SAr$ (see above), CuI was reacted with 1,4 bis(cyclohexyl)butane $CyS(CH_2)_4SCy$. The colorless crystals obtained by reaction in a 1:1 metal to ligand ratio were found to be of composition

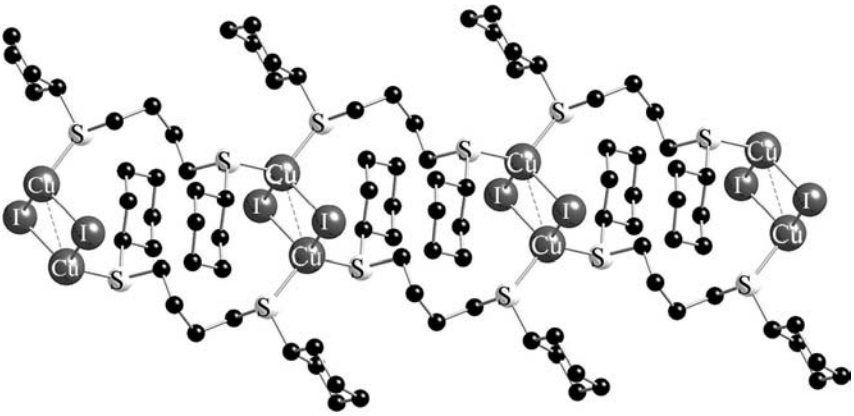

FIGURE 46. View of the 1D ribbon of $[(CuI)_2\{\mu\text{-}CyS(CH_2)_4SCy\}_2]_n$ **32** incorporating dinuclear $Cu(\mu\text{-}I_2)Cu$ motifs along the *a* axis.

$[(CuI)_2\{\mu\text{-}CyS(CH_2)_4SCy\}_2]_n$ **32**. X-ray diffraction analysis confirmed inded that replacement of -SPh by -SCy has a marked effect on the topology and nuclearity compared to the $PhS(CH_2)_4SPh$-linked 2D polymer **16**.

The overall topology of compound **31** is related to that of $[(CuI)_2\{\mu\text{-}PhS(CH_2)_5SPh\}_2]_n$ **22**, the infinite double-stranded ribbon consisting of $Cu(\mu_2\text{-}I)_2$ dimers, which are interconnected with the adjacent inorganic rhomboids through bridging dithioether ligands (Fig. 46). A striking difference, however, concerns the extreme long Cu···Cu separation, which exceeds even that reported for $[Cu_2I_2(dtpcp)_2] \cdot thf$ (dtpcp = 2,11 dithia[3.3]paracyclophane) [3.24 vs. 3.18 Å].[150]

With the objective to study the impact of the substitution pattern of a series of bis(cyclohexylthiomethyl)benzene ligands on the network topologies, Kim's group synthesized the 1,2-(**L33**), 1,3-(**L34**), and 1,4-bis(cyclohexylthiomethyl)benzene (**L35**) isomers and reacted them with CuI in MeCN solution according Scheme 15.[155] Whereas the reaction of the *ortho*-isomer **L33** afforded the dinuclear complex **33** (*d* Cu···Cu 2.9560(5) Å), reaction of CuI with the *meta*-isomer **L34** produced the 2D polymer **34**, incorporating rhomboid $Cu(\mu\text{-}I)_2Cu$ units with Cu–Cu separations of 2.7566(9) Å. In the case of the *para*-isomer **L35**, the 1D polymer **35** was isolated, in which cubane-like Cu_4I_4 clusters are located at the nodes of a loop-chain framework (Fig. 47).

In contrast to compounds **33** and **34**, the 1D polymer **35** exhibits a bright green emission at about 521 nm after excitation at 323 nm (Fig. 48). The position of λ_{max} is explained by the relatively high energy level of the LUMO and a bonding character owing to somewhat longer Cu–Cu distances in the range of 2.7719–2.8568 Å compared to other thioether and pyridine ligated cubane clusters with mean distances <2.8 Å.

The π-conjugated aromatic tetrakisthioether ligand 9,10-bis{[3,4-bis(methylthio)phenyl]ethynyl]}anthracene **L36** interacts with CuCN to form a 2D hybride network of composition **L36** · 2 CuCN, according Scheme 16.[156]

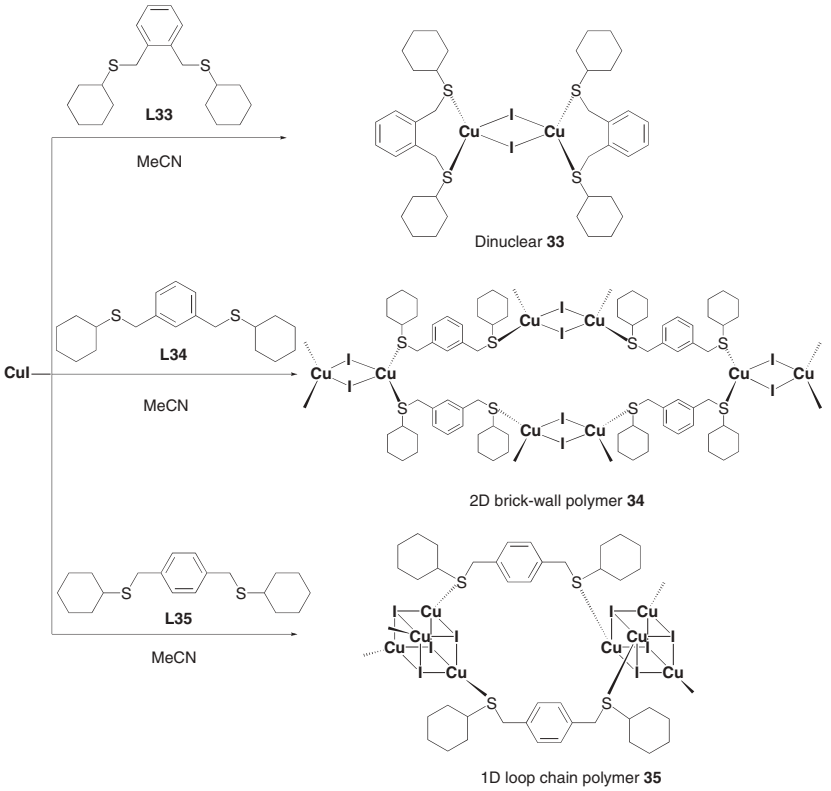

SCHEME 15

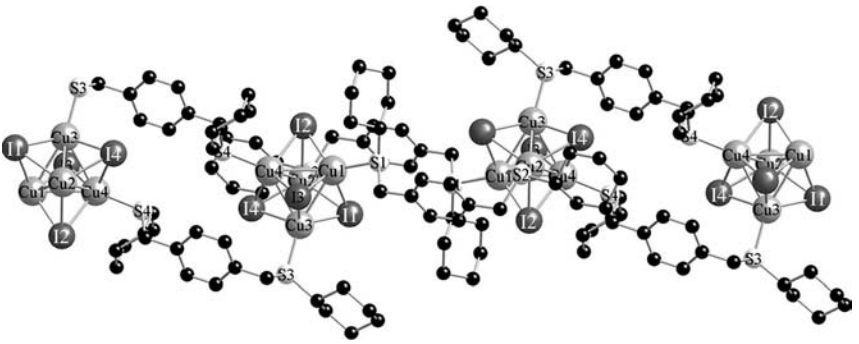

FIGURE 47. View of the 1D chain of $[Cu_4I_4\{\mu\text{-L35}\}_2]_n$ **35**. H atoms are omitted for clarity.

Figure 49 shows that CuCN forms cyanide-bridged Cu−CN−Cu zigzag chains as inorganic submotifs, which are linked by the **L35** ligands through thioether−Cu bonds with Cu−S distances of 2.537(8) and 2.6553 (8) Å, resulting in a distorted honeycomb net along the *bc* plane. The **L36** ligands,

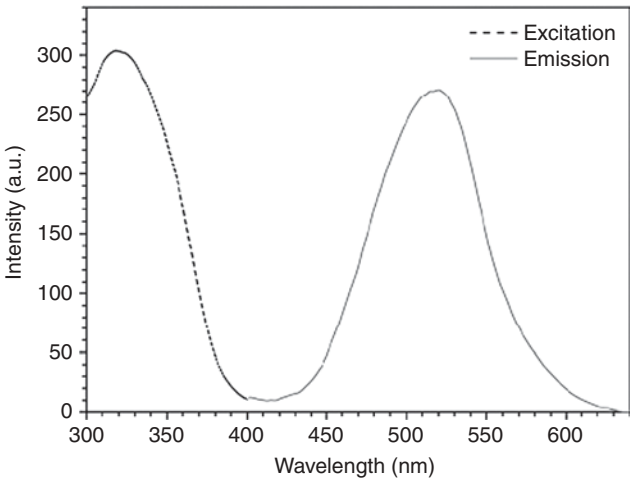

FIGURE 48. Solid-state excitation (*dashed line*) and emission spectra (*solid line*) of **35**, recorded at ambient temperature. (Modified from Ref. 155.)

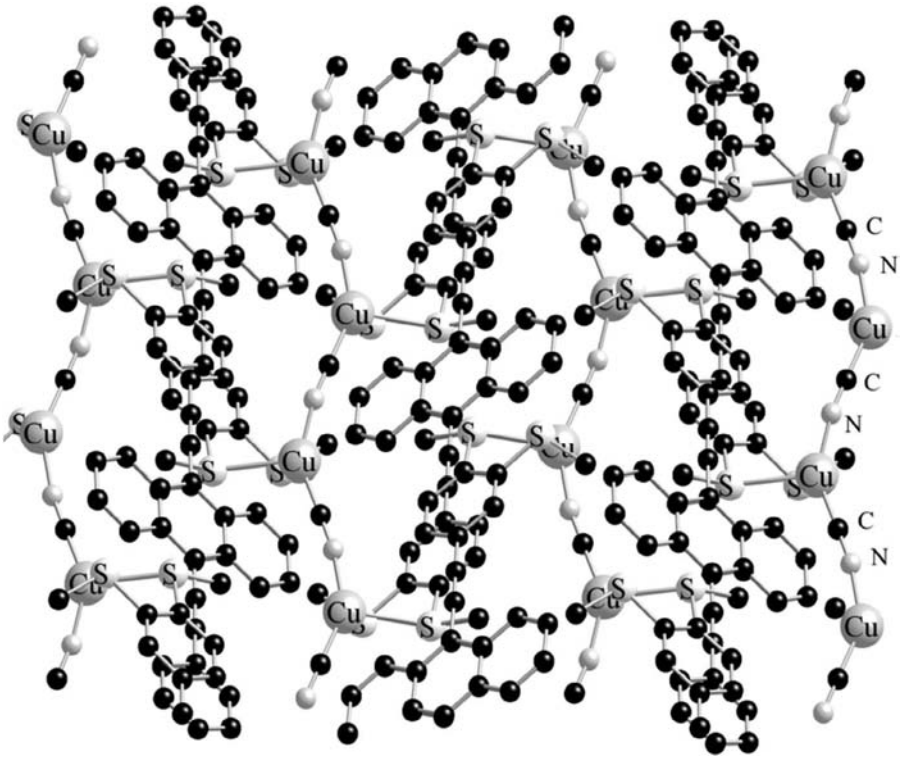

FIGURE 49. View of the *b,c* plane of the 2D network of **36**, showing the Cu−CN−Cu chains.

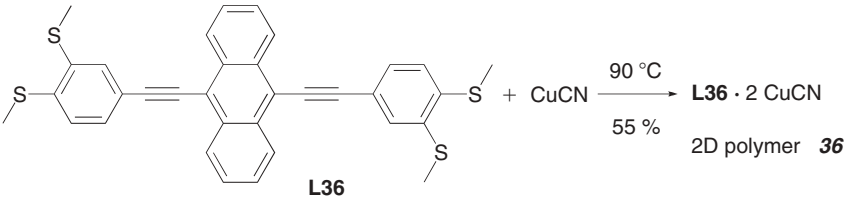

SCHEME 16

with an almost planar conformation, are organized into columns that are parallel and alternate with the CuCN chains within the honeycomb sheet.

The thioether ligand **L36** and CuCN in their separate solid-state forms feature emissions at 549 and 400 nm, respectively. The most intense emission of polymer **36** is observed red shifted at 614 nm, which is ascribed to the different packing of the **L36** linkers as well as the electronic interaction of across the **L36** unsaturated molecules and the Cu−CN−Cu chains.

D. Copper Polymers Assembled by Dithioether and Polythioether Ligands Bearing Heteroelements in the Spacer Unit

Several metal-organic polymers assembled by dithioether ligands, which are functionalized by heteroelements such as O, N, or Si in the spacer unit, have been recently described and reacted with Cu(I) salts. For example, the 2D square-grid coordination polymer **37** incorporating the 16-membered dithiaoxa crown-ether **L37** has been prepared by a self-assembly process involving the interaction of the dithiaoxa macrocycle with CuCN (Scheme 17); the parallel reaction of the dithiaoxa crown-ether with CuI afforded the 1D double-stranded coordination polymer **37**'. This example demonstrates, how the nature of the counterion can control the form of the network.[157]

When using the 18-membered thioxa-macrocycle **L38** as the assembling ligand for the construction of networks containing CuI-based connecting nodes, a mixture of coordination polymers was obtained (Scheme 18).[158] Crystallographically characterized 2D polymer $[Cu_2I_2(L38)_2]$ **38**, which is nonemissive, consists of dinuclear $Cu(\mu_2\text{-}I)_2Cu$ units with loose nonbonding Cu···Cu contacts. Each rhomboid core is bonded to four **L38** macrocycles via Cu−S bonds. The second compound, with composition $[Cu_4I_4(L38)_2]$ **38′**, was separated manually from **38**. In the solid state at ambient temperature, product **38′** exhibits a broad unstructured emission at ~570 nm after excitation at 360 nm; a cluster-centered excited state with mixed halide to metal charge transfer is thought to be origin of this band.

The same group has also investigated the reactivity of the related ligand calix[4]bis(thiacrown-5) **L39** (Fig. 48) with alternating conformation toward $AgPF_6$ and CuI.[159] In the latter case, two 3D polymers with different topologies co-crystallized from an acetonitrile solution. The monoclinic crystals **39**

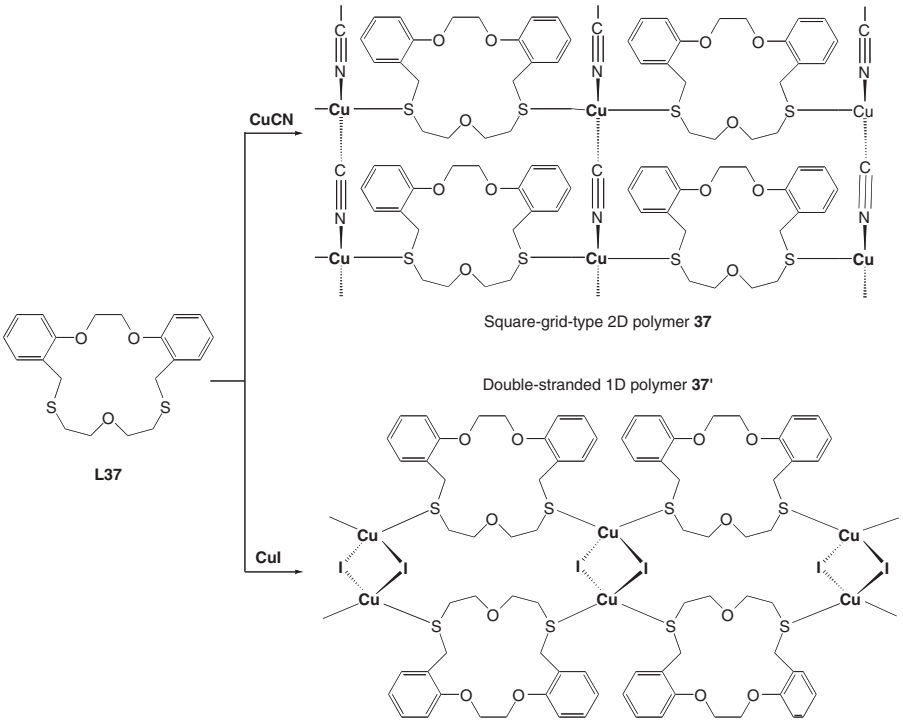

SCHEME 17

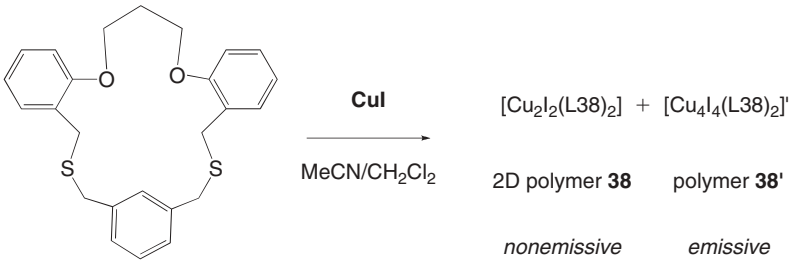

SCHEME 18

consist of 3D networks, in which $Cu(\mu_2I)_2Cu$ rhomboids with short Cu···Cu distances of 2.654(7) Å coordinate the functionalized calixarene ligands in an exocyclic manner. In the orthorhombic crystals, the 3D networks of composition $[Cu_4I_4(L39)]$ **39′** are assembled through closed cubane-like Cu_4I_4 clusters, which act as three-dimensional connecting nodes bound to four different tetrakisthioether ligands. The individual Cu···Cu distances within the cubes are variable and range from 2.607 to 2.995 Å, the mean value being 2.77 Å (at 173 K).

Whereas **39** is not emissive at room temperature, despite the short Cu···Cu distances, compound **39′** exhibits in the solid state a bright orange-yellow emission at 531 nm after excitation at 350 nm, arising from a CC-excited state with mixed XMCT character. Figure 50 shows also that a second high-energy band is present with a weaker maximum at ~420 nm.

A similar mixed oxa−thia macrocycle incorporating a rigid horseshoe-shaped aromatic moiety, 1,11,21-trioxa-8,14-dithia[2,9,2]paracyclophane, **L40**, has been synthesized and reacted with copper iodide in MeCN solution (Scheme 19).[160] Its polymeric copper iodide complex $[Cu_4I_4(L40)_2]$ **40** crystallizes, in a 2:1 metal: to ligand ratio, as an 1D infinite array of cubane-like units consisting of four copper atoms, four μ_3-iodine atoms, and four sulfur atoms, stemming from four different macrocycles. The Cu−Cu distances are about 2.731 Å. Unfortunately, the photophysics of this compound have not been studied.

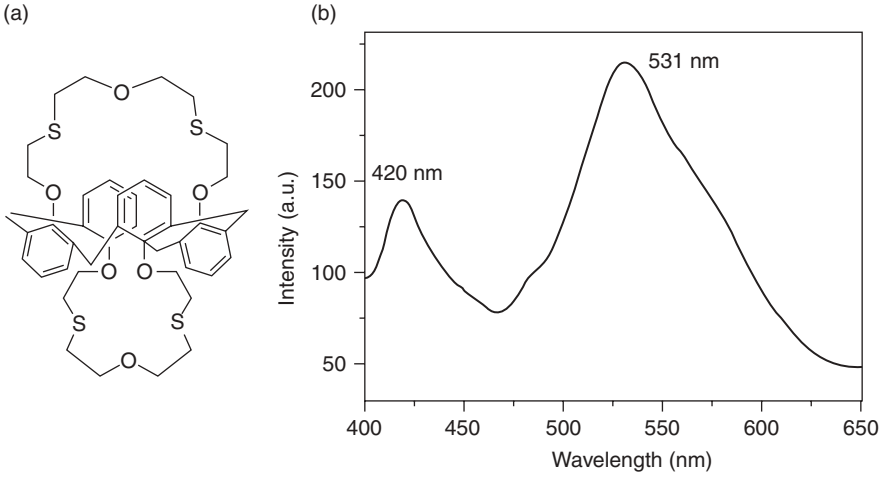

FIGURE 50. (a) Illustration of the calix[4]bis(thiacrown-5) ligand **L39**. (b) Solid-state emission spectrum of 3D polymer **39′** (298 K) incorporating closed Cu_4I_4 clusters as connecting nodes. (Modified from Ref. 159.)

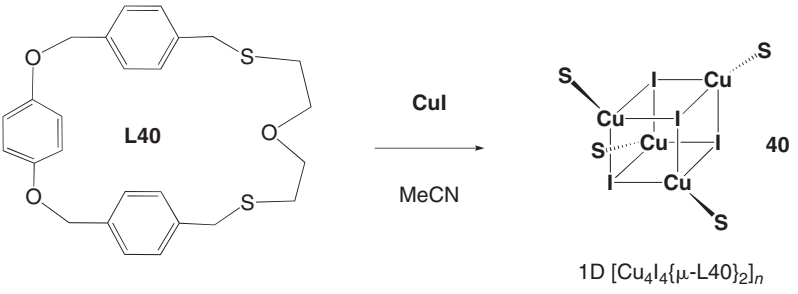

SCHEME 19

A nice example of a temperature-dependent self-assembly process providing three different networks, stemming from the reaction of CuI with the calix[4]-bisdithiacrown-6 ligand **L41** is presented in Schemes 20 and 21.[161] Mixing **L41** with CuI in a 1:2 ratio at room temperature yields the nonemissive 3D polymer of formula $[(Cu_3I_3)\mathbf{L41}(CH_3CN)]_n$ **41**, in which the thiacrown ethers macrocycles are connected via three-runged ladder-type units of type $Cu_3(\mu_3\text{-}I)(\mu\text{-}I)_2$. Two Cu_3I_3 building blocks bridge two **L41** macrocycles via Cu−S bonds to yield a 2D layer; then the adjacent 2D layers are bridged via Cu−S bonds to form the 3D framework. As shown in Figure 51, the Cu2 atom of the inorganic unit of **41** is tetrahedrally coordinated by three I atoms and one MeCN molecule; within this first example of such a coordination sphere, the Cu···Cu separations of 2.921 and 2.851 Å are significantly longer than the van der Waals radii (2.80 Å).[161]

Upon removal of the coordinated MeCN solvent molecule by heating at 175°C, the initial solvent-coordinated polymer **41** undergoes a unique

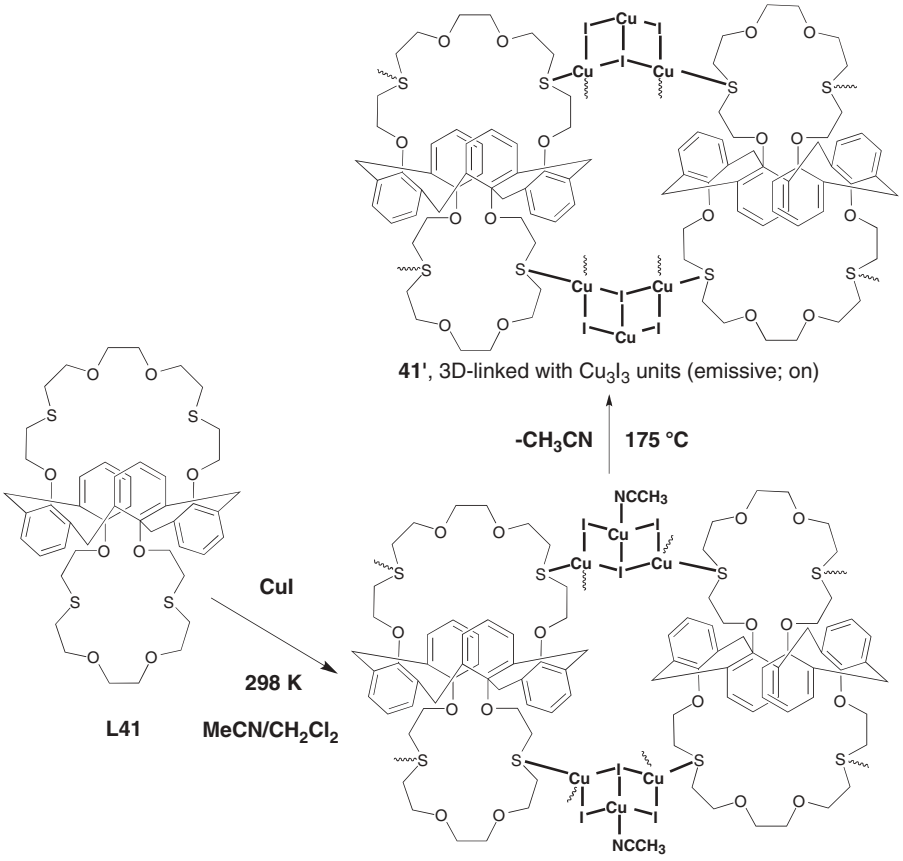

SCHEME 20

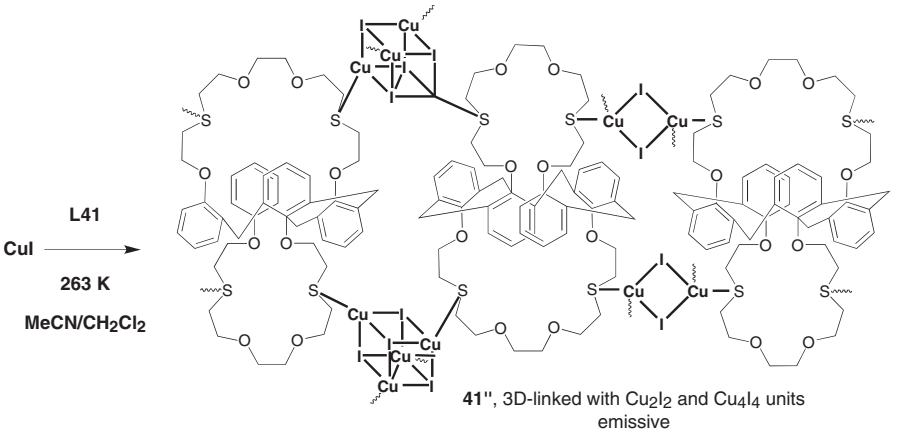

SCHEME 21

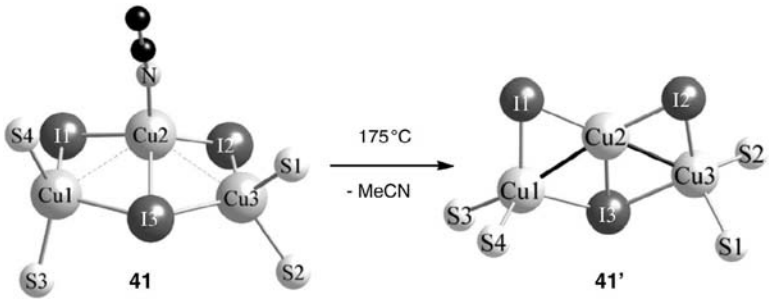

FIGURE 51. Crystallographic modification of the $Cu_3(\mu_3\text{-}I)(\mu\text{-}I)_2$ core units after single-crystal to single-crystal **41**→**41**′ transformation induced by evaporation of coordinated MeCN.

single-crystal to single-crystal transformation to yield the desolvated polymer **41**′ (Scheme 20). This elimination of MeCN was confirmed by a TGA study. Although the overall structure of **41**′ is similar to that of **41**, a marked change of metric parameters of the $Cu_3(\mu_3\text{-}I)(\mu\text{-}I)_2$ units was crystallographically evidenced. Loss of MeCN causes a flattening of the Cu_3I_3 unit and contraction of the bond lengths around the central Cu_2 atom to 2.729 and 2.685 Å, respectively.

As consequence of this cuprophilic interaction, desolvated polymer **41**′ shows photoluminescence behavior. The authors attribute the observation of bright yellow emission at 420 nm after excitation at 320 nm to an CC-excited state with mixed XMCT character; the term *solvato-photoluminescence* was coined for the off–on behavior caused by the **41**→**41**′ transformation.[161]

It is interesting that the reaction of **L41** in dichloromethane/MeCN with two equivalents of CuI at -10°C afforded crystals of a 3D polymeric product of formula $[(Cu_2I_2)(L41)_2(Cu_4I_4)]_n$ **41**″ (Scheme 21). X-ray analysis revealed that **41**″ incorporates both cubane-type Cu_4I_4 and rhomboid-type Cu_2I_2 units linked

alternately by **L41** ligands. Apart from our compound **2** (Fig. 3), material **41″** is a unique example of such a CuX complex; all other CuX complexes reported so far are linked by only a single type of CuX cluster. Polymer **41″** also exhibits an intense orange emission (531 nm) in the solid state arising from the Cu_4I_4 cubane units.

The Lee group also prepared three CuI coordination polymers using the calix[4]-bis monothiacrown ligand **L42**. If CuI in MeCN solution is reacted with **L42** in a 3:1 metal to ligand ratio, the colorless 1D polymer $[(Cu_4I_4)(CH_3CN)_2L4_2]_n$ **42** is obtained. In this material, each **L42** molecule is linked to two closed cubane-type Cu_4I_4 units through its thioether functions (Scheme 22). Two remaining copper(I) sites are ligated by MeCN molecules. Within the Cu_4I_4 cluster, the Cu-Cu distances vary (at 293 K) between 2.6652 (10) and 2.7892(8) Å. Upon excitation at 365 nm, polymer **42** exhibits at room temperature a bright yellow emission at 567 nm, attributed to CC-excited state with mixed iodide-to-metal charge transfer.[162] According TGA and DSC analysis, polymer **42** looses successively the Cu-bound MeCN molecules after heating at 150°C to yield the compound **42′**. If a microcrystalline sample of this acetonitrile-free compound **42′**, which displays an emission maximum around 600 nm, is exposed to MeCN, a reversible recoordination of acetonitrile occurs to give back **42**, as confirmed by TGA and XRPD analysis (Scheme 22). As

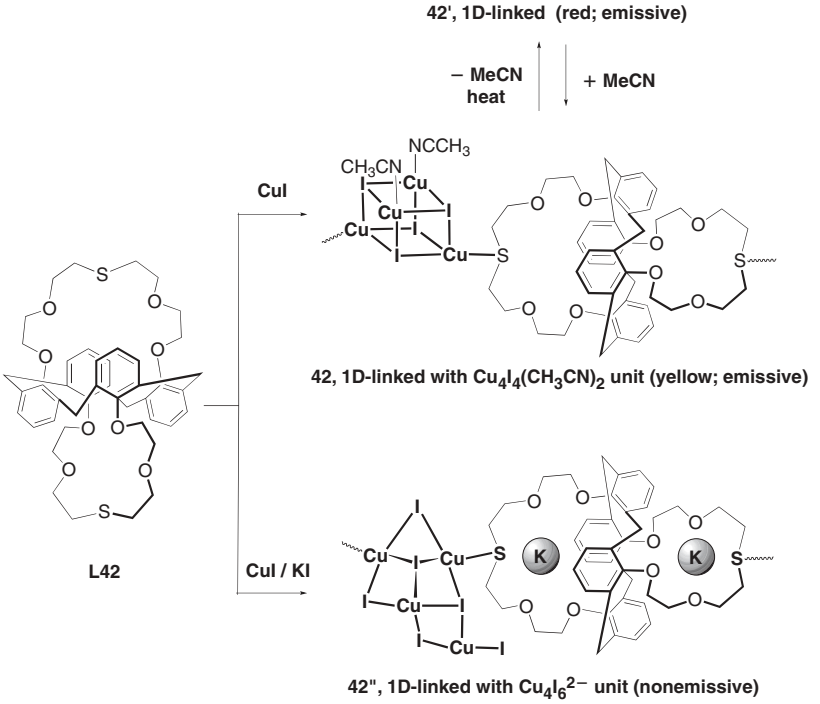

SCHEME 22

noticed in the case of the **41**→**41′** transformation, a photoluminescence switching behavior can be induced by removal of coordinated solvent.

Noteworthy also is the reaction between **L42** and CuI in the presence of KI. The crystal structure determination reveals the formation of hitherto unknown exocyclic $Cu_4I_6^{2-}$ clusters, which are linked by **L42** to generate a polymeric 1D array of composition $[K_2(Cu_4I_6)L42]_n$ **42″**. Within the crown ether cavities of **L42**, two potassium ions are trapped in an endocyclic manner. Also, upon inclusion of the K^+ ions the crown ring shrinks leading to opening of opposite aromatic rings in the host calixarene unit, a rare behavior for this class of compound.[162]

A luminescent 3D staircase coordination polymer of composition $[Cu_3I_3(L43)]_n$ **43**, based on planar Cu_3I_3 units, has been constructed by the reaction of CuI with 1,4-bis[(cyclohexylthio)acetyl)piperazine **L43** (Scheme 23).[163] The linear arrangement of the inorganic staircase ribbon is depicted in Figure 52. Within the Cu_3I_3 units, the Cu–Cu distances of 2.6175(9) Å are very short. In contrast, the loose Cu···Cu contact of 3.1686(17) Å with the adjacent units indicates very weak cuprophilic interactions between the Cu_3I_3 building blocks. The **L43** ligand links the staircase chains in a 3D manner by bonding through the thioether functions. Upon excitation at 325 nm, a broad emission with a maximum at 546 nm, which is temperature independent, is displayed. The authors assign the luminescence to a combination of XMCT and d→s transitions due to the short metal-metal interactions within the Cu_3I_3 motif.

Kim's group also prepared the 1,12-diphenyl-5,8-dioxa-2,11-dithidodecane ligand **L44** and reacted it with CuI.[164] Contrary to our failure to assemble a network with 1,8 bis(phenylthio)octane, **L44** containing eight spacer units between the sulfur atoms allowed the construction of a 2D square-grid-type coordination polymer **44**. This finding may be rationalized by the enhanced basicity of -*S*-benzyl vs. -*S*-phenyl (Scheme 23).

The 2D network contains cubane-like Cu_4I_4 clusters located at the nodes of the square grid and coordinated to four **L44** ligands by Cu–S bonds forming

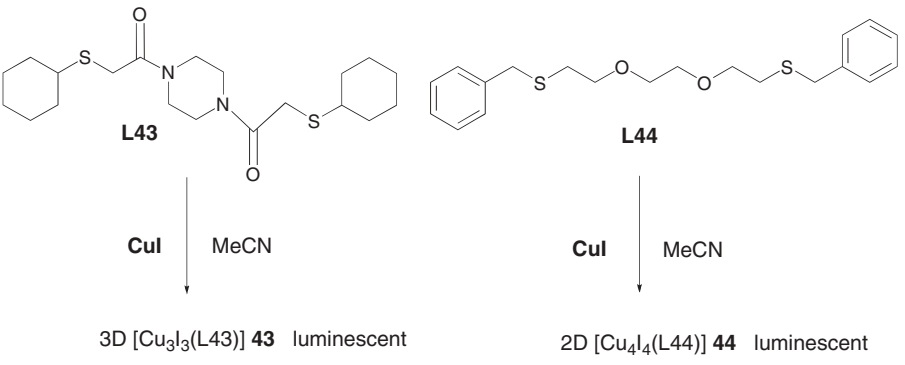

SCHEME 23

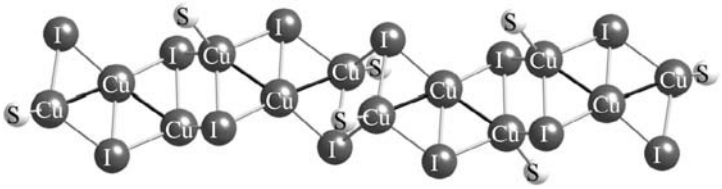

FIGURE 52. Projection of the inorganic 1D ribbon of the 3D polymer $[Cu_3I_3(L43)]$ **43**.

a layer structure. The layers are stacked with an ABAB sequence. The short Cu···Cu distances of 2.778(2) and 2.802 Å are certainly responsible for the strongly emissive character of this material. At 298 K, a broad emission band with a maximum at 565 nm ($\lambda_{excit} = 325$ nm) is observed. Like in the case of our structurally related compound **16**, coordination polymer **44** exhibits luminescence thermochromism. The maximum is red shifted to ~604 nm at 7 K; in addition, a second weaker high-energy band emerges at ~452 nm.

The same group also explored the reactivity of the two asymmetric dithioether ligands with cyclohexyl (**L45**) and phenyl (**L46**) end groups toward CuI.[164] Reaction of 2 (cyclohexylmethylthio)-1-thiomorpholinoethanone **L45** with copper(I) iodide afforded a 1D channel-type coordination polymer $[Cu_4I_4(L45)_2]_n$ **45**, interconnected by cubane-like tetranuclear Cu_4I_4 cluster units (Scheme 24). The mean Cu···Cu distance within the cluster cubes amounts to 2.749 Å at 173 K.

Upon irradiation by UV light ($\lambda_{excit} = 325$ nm), the metallopolymer **45** exhibits a bright green emission ($\lambda_{em} = 525$ nm) in the solid state. In contrast, a non-emissive 2D brick-wall type coordination polymer of composition $[Cu_2I_2(L46)_2]_n$ **46** with rhomboid dinuclear Cu−I_2−Cu nodes resulted from the reaction of 2-(benzylthio)-1-thiomorpholinoethanone **L46** with CuI. Compared to the short Cu···Cu distance in **45**, the metal···metal contacts within the rhomboids of **46** are much longer and reach 2.856(2) Å.

Another example of a single-crystal to single-crystal transformation has been observed in metallopolymers **47**, **47′**, and **47′′**, obtained by reaction of dithioether 2-(cyclohexythio)-1-thiomorpholinoethanone **L47** with copper(I) iodide.[165] The nonemissive 1D polymer $[Cu_2I_2(L47)_2]_n$ **47** is formed in the self-assembly process after mixing CuI and ligand **L47** in a 1:1 ratio using MeCN as solvent (Scheme 25). Within the monodimensional loop chain, rhomboid Cu_2I_2 units with loose metal···metal contacts of 2.98 Å act as connecting nodes. Treatment of **L47** with an excess of CuI in a MeCN/Et_2O mixture as reaction medium produces however the luminescent polymer $[Cu_4I_4(L47)_2]_n$ **47′**, in which the thioether groups of **L47** span tetranuclear Cu_4I_4 clusters giving rise to a 2D network. 2D polymer **47′** is also formed in MeCN solution by adding an excess of CuI to 1D polymer **47**. Alternatively, compound **47** can be converted to compound **47'** by heating a sample of **47** at 180° C in the solid state.

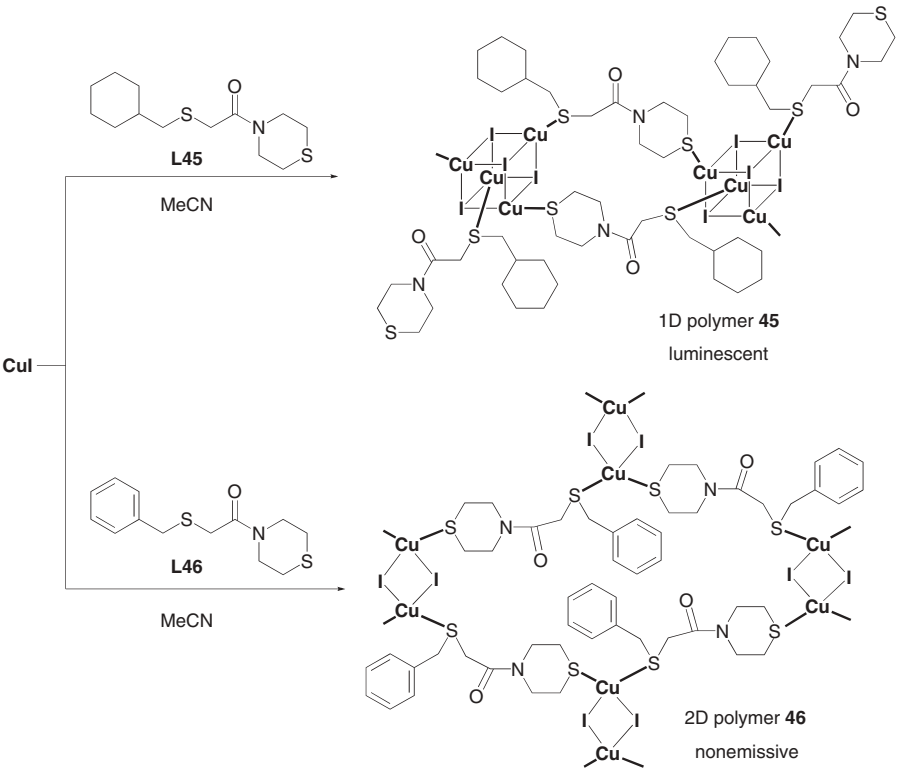

SCHEME 24

The nonnegligible influence of the polarity of the solvent mixture in this reaction is demonstrated by the observation that conducting the reaction of CuI with **L47** in MeCN/*n*hexane lead to the formation of a solvated 1D polymer with composition $[Cu_4I_4(L47)_2(MeCN)(C_6H_{14})]_n$ **47**″. This luminescent material incorporating closed-cubane $Cu_4(\mu_3\text{-}I)_4$ clusters undergoes a crystal to crystal transformation upon heating to 180°C in the solid state with extrusion of MeCN and *n*-hexane affording 2D material **47**′.

An important finding of Kim's group is the experimental correlation of the metric structural parameters within the Cu_4I_4 clusters of **47**′ and **47**″ and their luminescence thermochromism in function of the temperature. Table 2 presents the single-crystal X-ray data concerning the Cu···Cu distances of these two compounds, which have been recorded at four different temperatures. Analysis of these values reveals that the shorter Cu···Cu bond lengths do not contract much with decreasing temperature; however, the longer Cu···Cu contacts are much more affected and shrink below the sum of the Van der Waals radii.[166]

In other words, the bonding character increases, thus lowering the energy level, accompanied by a lowering of the energy difference between the excited

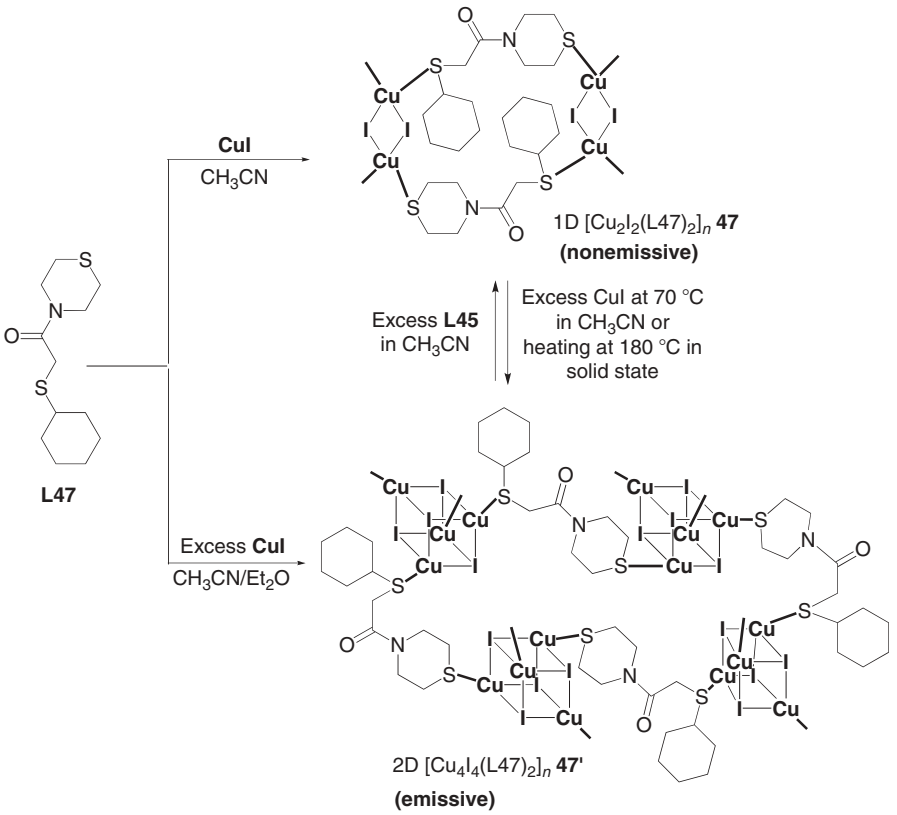

SCHEME 25

TABLE 2. Cu···Cu distances (Å) in **47**′ and **47**″ recorded at four different temperatures

	298 K	223 K	173 K	123 K
47′				
Cu1···Cu3	2.833(2)	2.8052(17)	2.7878(13)	2.7733(10)
Cu1···Cu2	2.789(2)	2.7642(17)	2.7513(13)	2.7403(11)
Cu3···Cu4	2.755(2)	2.7446(17)	2.7400(13)	2.7410(10)
Cu2···Cu3	2.740(2)	2.7267(17)	2.7182(13)	2.7111(11)
Cu1···Cu4	2.625(2)	2.6213(18)	2.6221(14)	2.6292(11)
Cu2···Cu4	2.631(2)	2.6169(17)	2.6107(13)	2.6079(11)
47″				
Cu2···Cu4	2.814(3)	2.7930(13)	2.7809(11)	2.7713(10)
Cu1···Cu2	2.815(3)	2.7871(13)	2.7752(11)	2.7652(10)
Cu3···Cu4	2.760(3)	2.7469(13)	2.7344(11)	2.7235(10)
Cu1···Cu4	2.748(3)	2.7321(12)	2.7175(11)	2.7030(10)
Cu2···Cu3	2.736(3)	2.7234(13)	2.7091(11)	2.6981(10)
Cu1···Cu3	2.672(3)	2.6594(12)	2.6501(10)	2.6432(10)

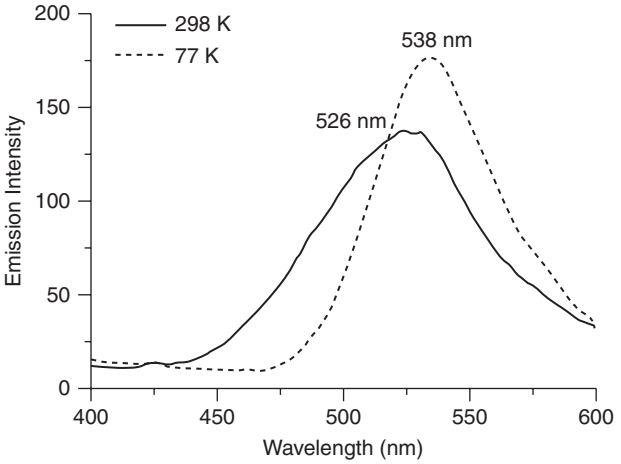

FIGURE 53. Solid-state emission spectra of 1D polymer $[Cu_4I_4(L47)_2(MeCN)(C_6H_{14})]_n$ **47′**, recorded at 298 K and 77 K after excitation at 286 nm. (Modified from Ref. 166.)

states and the ground state. (Note that according to theoretical studies, the Cu···Cu interactions in the excited state have LUMO character and are bonding).[67] The Cu–S bond lengths remain nearly constant within this temperature range.

In line with the variation of the Cu···Cu interaction in function of the temperature, the emission maximum in the solid-state luminescence spectrum ($\lambda_{excit} = 350$ nm) of **47′** appears considerably red shifted when the temperature is decreased from 298 K (538 nm) to 77 K (599 nm). The red shift is less pronounced in the case of compound **47″**; Figure 53 reveals that the low-temperature spectrum is somewhat less broadened than that recorded at room temperature.

We and Rabinovich's group have reported on the synthesis of silicon-based bidentate and tridentate thioethers $R_{4-n}Si(CH_2SR)_n$ ($n = 2$, 3; R = Me, Ph) and characterized a wide variety of complexes in which they act as either terminal or bridging ligands.[167–169] For example, reaction of CuX with the tridentate thioether ligand $MeSi(CH_2SMe)_3$ yielded the 1D coordination polymers $[Cu_3\{MeSi(CH_2SMe)_3\}_2X_3]$ (X = Cl, Br).[170] Our group reacted the dithioether ligand $Ph_2Si(CH_2SPh_2)$ **L48** with one equivalent of CuI, leading to the dinuclear 0D system $[CuI\{Ph_2Si(CH_2SPh)_2\}]_2$ **48** (Scheme 26). As corroborated by an X-ray diffraction study, the **L48** dithioether coordinates in a chelating manner at the Cu center, which is attached to a second moiety by two μ_2-I atoms. The Cu···Cu interaction in the resulting rhomboid motif is close to the sum of Van der Waals radii and amounts to 2.7964(6) Å. This complex exhibits a luminescence of only medium intensity; the emission spectrum shown

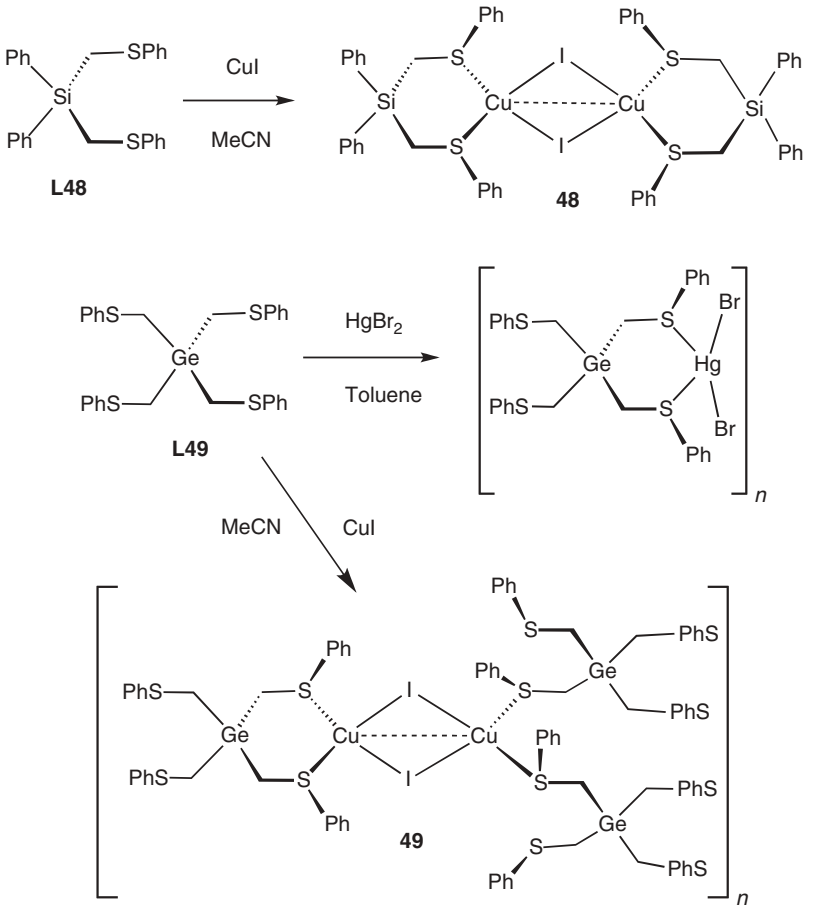

SCHEME 26

in Figure 54 displays two maxima at 417 and 435 nm after excitation at 360 nm. Overall, the emission spectrum of dinuclear compound **48** is very similar to that of 2D polymer **14** (Fig. 23).

We have demonstrated in a collaborative work that tetrathioether ligands of type $Si(CH_2SR)_4$ (R = Me, Ph) may be used as assembling ligands to construct monodimensional coordination polymers of type $[\{Si(CH_2SR)_4\}HgBr_2]_n$ upon reaction with $HgBr_2$.[171] Continuing our studies on multidentate thioethers, we set out to evaluate and compare the coordinative properties of the tetrakisthioether ligand $Ge(CH_2SPh)_4$ **L49** with those of its silicon analogue $Si(CH_2SPh)_4$.[172]

The reaction of CuI with 0.5 Eq of **L49** in MeCN gave colorless crystals of $[(CuI)_2\{Ge(CH_2SPh)_4\}]_n$ **49** (Scheme 26). This 2D coordination polymer is constructed by dinuclear $Cu_2(\mu_2\text{-}I)_2$ units, which are linked by the

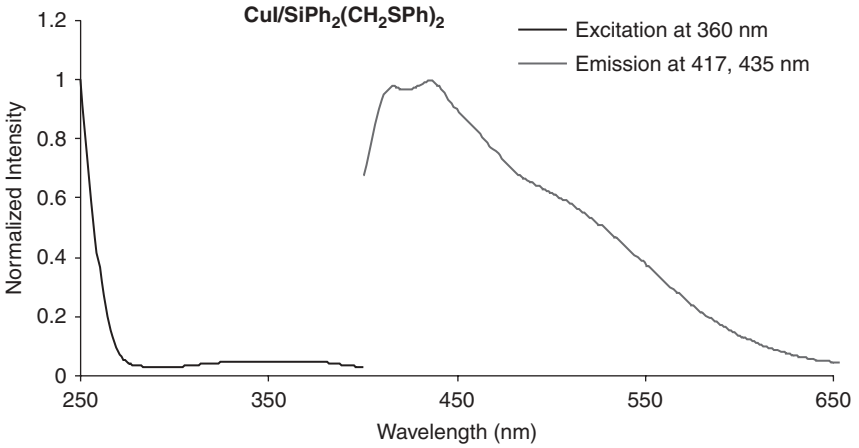

FIGURE 54. Excitation (left) and emission spectra (right) of solid dinuclear **48** at 298 K.

tetrakisthioether $Ge(CH_2SPh)_4$ ligand in a μ_3-coordination mode. Each copper (I) ion of the central dimeric Cu_2I_2 motif possesses a fourfold coordination to two iodine and two sulfur atoms, respectively, resulting in a distorted tetrahedral geometry. It is interesting that both Cu(I) ions of this motif are differently coordinated by the tetrakisthioether ligand **L49**. While Cu(1) is ligated by two sulfur atoms of a single ligand molecule, Cu(2) is coordinated by two different ligands **L49**, which are linked to the metal ion via only one sulfur atom (Fig. 55). The mean Cu–S bond length of 2.357(15) Å is close to that of 2D polymers **11** and **22**. The long Cu···Cu separation of 2.9433(9) Å reveals only a weak interaction between the two d^{10} ions within this material.[172]

Upon irradiation at 380 nm, ligand $Ge(CH_2SPh)_4$ exhibits an emission with a maximum at 440 nm in the solid state at 298 K (Fig. 56). A structureless emission is also observed in the solid state at 77 K, which is not shifted. When **L49** is excited at 260 nm in dichloromethane at room temperature, the emission maximum appears at 333 nm. The emissions recorded for the polymer **49** in the solid state at 298 K exhibit a pattern very similar to that of the ligand. We conclude that due to the absence of strong cuprophilic interactions in polymer **49**, the emission is essentially centered on the ligand.

Another dithioether ligand system, whose coordination chemistry and photophysics are currently being developed in our laboratory, is based on a π-conjugated 2-azabutadiene array.[173] For example, ligand **L50** has been coordinated to Re(I) leading to luminescent Re(I) *S,N* chelate complexes.[174] This ligand reacts with CuI to produce the dinuclear complex **50**, which is luminescent both in solution and in the solid state (Scheme 27). A recent X-ray diffraction study revealed that the Cu···Cu distance in the rhomboid motif is much beyond that of the related dinuclear compound **48** (2.673(6) vs. 2.7964(6) Å). Treatment of $[Cu(MeCN)_4][PF_6]$ with two equivalents **L50** afforded the

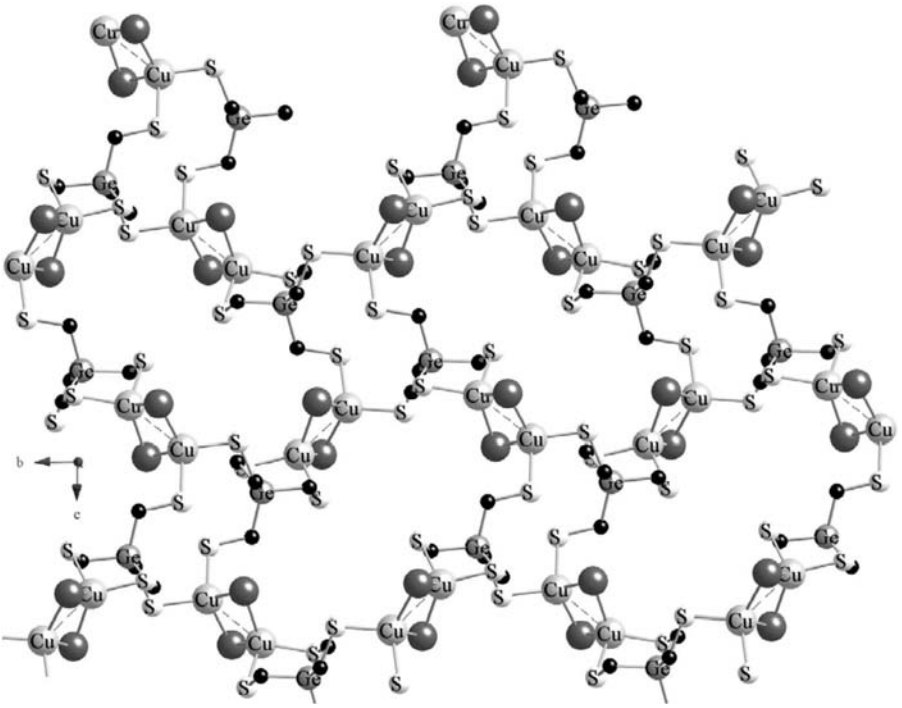

FIGURE 55. View of the 2D sheet-like network of **49**. The H atoms and phenyl groups are omitted for clarity.

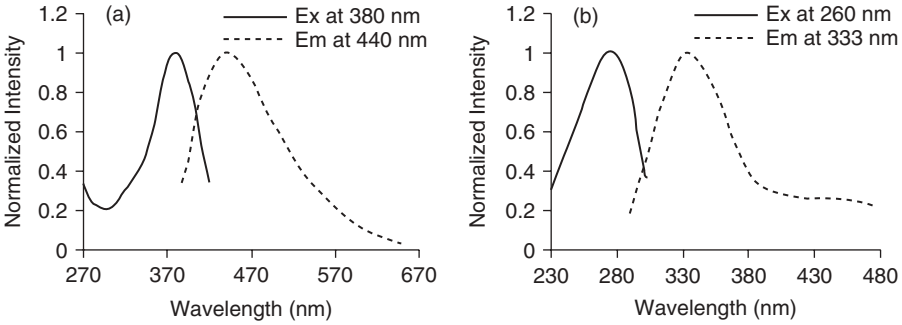

FIGURE 56. (a) Normalized solid-state excitation (*solid line*) and emission (*dotted line*) spectra of **L49** recorded at 298 K. (b) Normalized excitation (*solid line*) and emission (*dotted line*) spectra of $Ge(CH_2SPh)_4$ **L49** recorded in CH_2Cl_2 at 298 K.

mononuclear salt **51**, whose distorted tetrahedral *S,N* environment around the Cu center was confirmed by X-ray diffraction (Scheme 27). Deep-red **51** exhibits a strong emission peak at 685 nm in CH_2Cl_2 solution after excitation at 450 nm. The latter example demonstrates that in the case of thioether-ligated

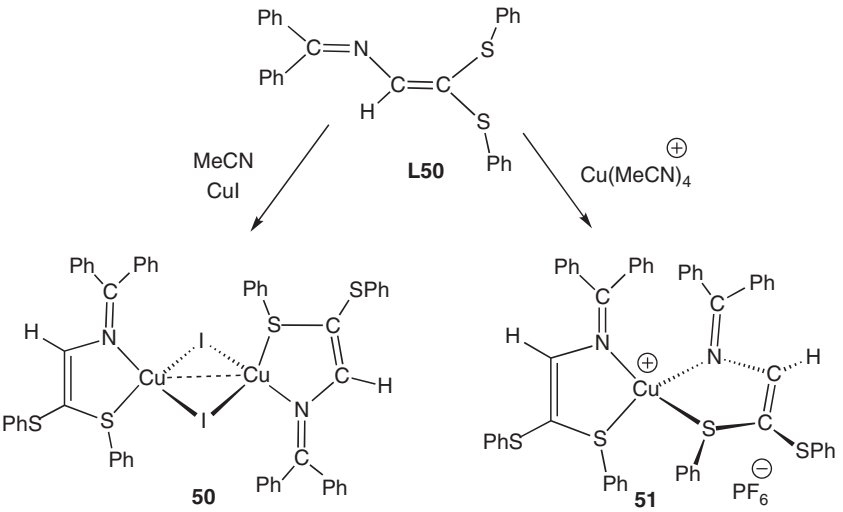

SCHEME 27

complexes a dinuclear or polynuclear metal core is not always mandatory to observe luminescence.

IV. CONCLUSION

This chapter focused on luminescent copper(I) complexes and materials bearing thioether ligands has shown that a rich structural diversity ranging from 0D to 3D exists, because copper halides and pseudohalides as inorganic components are prone to be part of a hybrid metal-organic network in the form of simple mononuclear connecting nodes, but also in form of dinuclear, trinuclear, tetranuclear, and even hexanuclear secondary building blocks. When dithioethers are used as assembling ligands, even a first glance reveals that innocent and subtle modifications of the substituents −SR may completely alter the topology of a network. Furthermore, the number and rigidity of the spacer units of the dithioether backbone may influence the dimensionality of the framework and the nuclearity of the inorganic core motifs. Other factors controlling these parameters are the nature of the anion, metal to ligand ratio, reaction temperature, and solvent polarities. Supported by the finding that in some reactions a mixture of polymeric material with different network topologies are formed, together with the recent observation of crystal to crystal transformations in the solid state, one may conclude that the energetic differences between different core motifs are relatively weak.

Some of these materials coordinated by thioether ligands presented herein are extremely luminescent at ambient temperature in the solid state and exhibit

reversible "luminescence thermochromism," a phenomenon that has been studied only on compounds ligated by nitrogen donors. To observe intense luminescence, there must be CuX motifs with at least three Cu centers possessing close interactions not greater than to the sum of the Van der Waals radii. If luminescence is observed in the case of networks incorporating mononuclear or dinuclear units, the emission often stems from the fluorescent ligand systems, the metallic contribution being less important. Although the origins of the luminescence properties of Cu_4I_4 cluster are now widely understood on a theoretical basis, other motifs deserve further theoretical study to interpret their photophysics.

V. ACKNOWLEDGMENTS

We thank Dr. A. Khatyr and Dr. A. S. Shawkat for performing the photophysical measurements and Dr. D. Fortin for the computations on $[(Cu_6I_6)\{\mu\text{-}PhSCH_2C{\equiv}CCH_2SPh\}]_n$. We are furthermore indebted to Professor C. Strohmann for the determination of numerous X-ray structures and Professor P. D. Harvey for fruitful discussions.

VI. REFERENCES

1. J. D. Brown, J. D. Dunitz, *Acta Cryst.,* **13,** *28* (1960).
2. G. S. Chandler, C. L. Raston, G. W. Walker, A. H. White, *J. Chem. Soc., Dalton Trans., 1797* (1974).
3. L. G. Warner, T. Ottersen, K. Seff, *Inorg. Chem.,* **13,** *2819* (1974).
4. J. S. Filippo, L. E. Zyontz, J. Potenza, *Inorg. Chem.,* **14,** *1667* (1975).
5. M. K. Ehler, S. J. Rettig, A. Storr, R. C. Thompson, J. Trotter, *Can. J. Chem.,* **67,** *1970* (1989).
6. L. Chen, L. K. Thompson, J. N. Bridson, *Can. J. Chem.,* **70,** *2709* (1992).
7. A. Escuer, M. Font-Bardia, E. Penalba, X. Solans, R. Vicente, *Polyhedron* **18,** *211* (1998).
8. Y. Garcia, P. J. V. Koningsbruggen, H. Kooijman, A. L. Spek, J. G. Haasnoot, O. Kahn, *Eur. J. Inorg. Chem., 307* (2000).
9. E. Colacio, R. Kivekäs, F. Lloret, M. Sunberg, J. Suarez-Varela, M. Bardají, A. Laguna, *Inorg. Chem.,* **41,** *5141* (2002).
10. L. Ping, W. Yao-Yu, L. Dong-Sheng, L. Xin-Jun, G. Song, S. Qi-Zhen, *Chin. J. Chem.,* **23,** *204* (2005).
11. M. Munakata, J. Han, M. Maekawa, Y. Suenaga, T. Kuroda-Sowa, A. Nabei, H. Ebisu, *Inorg. Chim. Acta,* **360,** *2792* (2007).
12. H. Chowdhury, S. H. Rahaman, R. Ghosh, S. K. Sarkar, H.-K. Fun, B. K. Ghosh, *J. Mol. Struct.,* **826,** *170* (2007).
13. X.-Y. Song, W. Li, L.-C. Li, D.-Z. Liao, Z.-H. Jiang, *Inorg. Chem. Commun.,* **10,** *567* (2007).

14. W. He, B. Wang, X. Bai, *Trans. Met. Chem.,* **33,** *399* (2008).
15. P. Sherwood, R. Hoffmann, *Inorg. Chem.,* **28,** *509* (1989).
16. A. J. Blake, R. L. Dorse, J. M. Rawson, R. E. P. Winpenny, *Polyhedron,* **13,** *2793* (1994).
17. H.-M. Hu, X.-Y. Huang, H.-S. Sun, D.-L. Long, J.-S. Huang, X.-Z. You, *J. Coord. Chem.,* **47,** *531* (1999).
18. D. M. Ciurtin, M. D. Smith, H.-C. Zur Loye, *Inorg. Chim. Acta,* **324,** *46* (2001).
19. J. Tao, Y. Zhang, M.-L. Tong, X.-M. Chen, Y. Tan, C. L. Lin, X. Huang, J. Li, *Chem. Commun., 1342* (2002).
20. X.-M. Zhang, X.-M. Chen, *Eur. J. Inorg. Chem., 413* (2003).
21. M.-L. Tong, L.-J. Li, K. Mochizuki, H.-C. Chang, X.-M. Chen, Y. Li, S. Kitagawa, *Chem. Commun., 428* (2003).
22. H.-Z. Kou, C. Z. Bei, R.-J. Wang, *J. Organomet. Chem.,* **689,** *369* (2004).
23. J.-M. Zheng, S. R. Batten, M. Du, *Inorg. Chem.* **44,** *3371* (2005).
24. X. Xu, X. Bai, Y. Lu, E. Wang, Y. Ma, *Inorg. Chem. Commun.,* **9,** *872* (2006).
25. W. Ouellette, A. V. Prosvirin, V. Chieffo, K. R. Dunbar, B. Hudson, J. Zubieta, *Inorg. Chem.,* **45,** *9346* (2006).
26. G. Fan, G. Xie, S. Chen, S. Gao, Q. Shi, *J. Coord. Chem.,* **59,** *791* (2006).
27. J. Y. Lu, A. B. Schauss, M. Julve, *Inorg. Chim. Acta* **359,** *2565* (2006).
28. Q. Yu, L.-G. Zhu, H.-D. Bian, J.-H. Deng, X.-G. Bao, H. Liang, *Inorg. Chem. Commun.,* **10,** *437* (2007).
29. C. J. Milios, C. P. Raptopoulou, A. Terzis, S. P. Perlepes, G. S. Papaefstathiou, *Bioinorg. Chem. Appl. 2007* (2007), Article ID 28508.
30. J. Y. Lu, *Coord. Chem. Rev.,* **246,** *327* (2003).
31. J.-H. Yu, Z.-L. Lü, J.-Q. Xu, H.-Y. Bie, J. Lu, X. Zhang, *New J. Chem.,* **28,** *940* (2004).
32. S. P. Anthony, T. P. Radhakrishnan, *Cryst. Growth Design.,* **4,** *1223* (2004).
33. J.-H. Yu, J.-Q. Xu, Y.-J. Song, H.-Y. Bie, J. Lu, T.-G. Wang, *Chin. J. Chem.,* **23,** *1030* (2005).
34. E. Cariati, D. Roberto, R. Ugo, P. C. Ford, S. Galli, A. Sironi, *Inorg. Chem.,* **44,** *4077* (2005).
35. Y. Niu, Y. Song, Q. Wang, X. Guo, Y. Zhu, H. Hou, *Chem. Lett.,* **35,** *650* (2006).
36. Y. Niu, Z. Li, Y. Song, M. Tang, B. Wu, X. Xin, *J. Solid State Chem.,* **179,** *4003* (2006).
37. X.-F. Huang, Y.-H. Li, Q. Wu, Q. Ye, R.-G. Xiong, *Inorg. Chim. Acta,* **358,** *2097* (2005).
38. Q.-F. Xu, Q.-X. Zhoua, J.-M. Lu, X.-W. Xia, L.-H. Wang, Y. Zhang, *Polyhedron,* **26,** *4849* (2007).
39. M. T. Buckner, D. R. McMillin, *J. Chem. Soc., Chem. Commun.,* **759 (**1978).
40. G. Blasse, D. R. McMillin, *Chem. Physics Lett.,* **70,** *1* (1980).
41. E. Eitel, D. Oelkrug, W. Hiller, J. Straehle, *Zeitschrift Naturforsch.,* **35B,** *1247* (1980).
42. P. A. Breddels, P. A. M. Berdowski, G. Blasse, D. R. McMillin, *J. Chem. Soc., Faraday Trans. 2*, 78, *595* (1982).
43. S.-M. Kuang, D. G. Cuttell, D. R. McMillin, P. E. Fanwick, R. A. Walton, *Inorg. Chem.,* **41,** *3313* (2002).
44. A. Vogler, H. Kunkely, *J. Am. Chem. Soc.,* **108,** *7211* (1986).
45. N. P. Rath, E. M. Holt, K. Tanimura, *J. Chem. Soc., Dalton Trans.,* **2303 (**1986).
46. N. P. Rath, J. L. Maxwell, E. M. Holt, *J. Chem. Soc., Dalton Trans.,* **2449 (**1986).
47. D. Li, C.-M. Che, W.-T. Wong, S.-J. Shieh, S.-M. Peng, *J. Chem. Soc., Dalton Trans., 653* (1993).
48. D. C. Lai, J. I. Zink, *Inorg. Chem.,* **36,** *2594* (1997).
49. M. Henary, L. Wootton, S. I. Khan, J. I. Zink, *Inorg. Chem.,* **36,** *796* (1997).

50. P. D. Harvey, M. Drouin, T. Zhang, *Inorg. Chem.,* **36,** *4998* (1997).
51. M. A. S. Goher, T. C. W. Mak, *Polyhedron,* **17,** *3485* (1998).
52. F. A. Mautner, M. A. S. Goher, *Polyhedron,* **18,** *553* (1998).
53. Y.-G. Ma, W.-H. Chan, X.-M. Zhou, C.-M. Che, *New J. Chem.,* **263 (**1999).
54. M. T. Miller, P. K. Gantzel, T. B. Karpishin, *J. Am. Chem. Soc.,* **121,** *4292* (1999).
55. C.-M. Che, Z. Mao, V. M. Miskowski, M.-C. Tse, C.-K. Chan, K.-K. Cheung, D. L. Phillips, K.-H. Leung, *Angew. Chem. Int. Ed. Engl.* **39,** *4084* (2000).
56. S. Parsons, Z. Pikramenou, G. A. Solan, R. E. P. Winpenny, *J. Cluster Sci.,* **11,** *227* (2000).
57. R.-H. Wang, M.-C. Hong, J.-H. Luo, R. Cao, J.-B. Weng, *Eur. J. Inorg. Chem., 3097* (2002).
58. C. Näther, J. Greve, I. Jeß, C. Wickleder, *Solid State Sci.,* **5,** *1167* (2003).
59. D. Li, Q. Feng, X.-L. Feng, J.-W. Cai, *Inorg. Chem. Comm.,* **6,** *361* (2003).
60. G. K. Patra, I. Goldberg, *Eur. J. Inorg. Chem., 969* (2003).
61. W.-W. Fu, X. Gan, C.-M. Che, Q.-Y. Cao, Z.-Y. Zhou, N. N.-Y. Zhu, *Chem. Eur. J.,* **10,** *2228* (2004).
62. Q. Zhang, Q. Zhou, Y. Cheng, L. Wang, D. Ma, X. Jing, F. Wang, *Adv. Mat.* **16,** *432* (2004).
63. V. Pawlowski, G. Knör, C. Lennartz, A. Vogler, *Eur. J. Inorg. Chem., 3167* (2005).
64. J.-K. Cheng, Y.-B. Chen, L. Wu, J. Zhang, Y.-H. Wen, Z.-J. Li, Y.-G. Yao, *Inorg. Chem.,* **44,** *3386* (2005).
65. X.-Q. Wang, J.-K. Cheng, Y.-H. Wen, J. Zhang, Z.-J. Li, Y.-G. Yao, *Inorg. Chem. Commun.,* **8,** *897* (2005).
66. M.-S. Wang, G.-C. Guo, M.-L. Fu, L. Xu, L.-Z. Cai, J.-S. Huang, *Dalton Trans., 2899* (2005).
67. F. D. Angelis, S. Fantacci, A. Sgamellotti, E. Cariati, R. Ugo, P. C. Ford, *Inorg. Chem.,* **45,** *10576* (2006).
68. C.-L. Chan, K.-L. Cheung, W. H. Lam, E. C.-C. Cheng, N. Zhu, S. W.-K. Choi, V. W. W. Yam, *Chem. Asian J.,* **1,** *273* (2006).
69. J.-X. Chen, Y. Zhang, Z.-G. Ren, J.-P. Lang, *J. Mol. Struct.,* **784,** *24* (2006).
70. W. L. Jia, T. McCormick, Y. Tao, J.-P. Lu, S. Wang, *Inorg. Chem.,* **44,** *5706* (2005).
71. S. H. Rahaman, H. Chowdhury, D. Bose, G. Mostafa, H.-K. Fun, B. K. Ghosh, *Inorg. Chem. Commun.,* **8,** *1041* (2005).
72. T. McCormick, J. Wen-Li, S. Wang, *Inorg. Chem.,* **45,** *147* (2006).
73. E. J. Fernández, A. Laguna, J. M. López-de-Luzuriaga, M. Monge, M. Montiel, M. E. Olmos, M. Rodríguez-Castillo, *Organometallics,* **25,** *3639* (2006).
74. S.-B. Zhao, R.-Y. Wang, S. Wang, *Inorg. Chem.,* **45,** *5830* (2006).
75. X.-X. Zhao, J.-P. Ma, Y.-B. Dong, R.-Q. Huang, T. Lai, *Cryst. Growth & Design.,* **7,** *1058* (2007).
76. H. Wang, M.-X. Li, M. Shao, X. He, *Polyhedron,* **26,** *5171* (2007).
77. Y. Niu, N. Zhang, H. Hou, Y. Zhu, M. Tang, S. Ng, *J. Mol. Struct.* **827,** *195* (2007).
78. A. Tsuboyama, K. Kuge, M. Furugori, S. Okada, M. Hoshino, K. Ueno, *Inorg. Chem.,* **46,** *1992* (2007).

79a. H. Araki, K. Tsuge, Y. Sasaki, S. Ishizaka, N. Kitamura, *Inorg. Chem.,* **44,** *9667* (2005)

79b. H. Araki, K. Tsuge, Y. Sasaki, S. Ishizaka, N. Kitamura, *Inorg. Chem.,* **46,** *10032* (2007).

80. I. Jeß, P. Taborsky, C. Näther, *Z. Naturforsch. B,* **62,** *501* (2007).
81. I. Jeß, P. Taborsky, J. Pospisil, C. Näther, *Dalton Trans.* **2263 (**2007).

82. T. A. Tronic, K. E. deKrafft, M. J. Lim, A. N. Ley, Pike, R. D. *Inorg. Chem.,* **46,** *8897* (2007).
83. R. D. Pike, K. E. deKrafft, A. N. Ley, T. A. Tronic, *Chem. Commun., 3732* (2007).
84. M. J. Lim, C. A. Murray, T. A. Tronic, K. E. deKrafft, A. N. Ley, J. C. deButts, R. D. Pike, H. Lu, H. Patterson, *Inorg. Chem.,* **47,** *6931* (2008).
85. J.-X. Zhang, J. He, Y.-G. Yin, M.-H. Hu, D. Li, X.-C. Huang, *Inorg. Chem.,* **47,** *3471* (2008).
86. C. Pettinari, C. D. Nicola, F. Marchetti, R. Pettinari, B. W. Skelton, N. Somers, A. H. White, W. T. Robinson, M. R. Chierotti, R. Gobetto, C. Nervi, *Eur. J. Inorg. Chem., 1974* (2008).
87. X. Gan, W.-F. Fu, Y.-Y. Lin, M. Yuan, C.-M. Che, S.-M. Chi, H.-F. J. Li, J.-H. Chen, Y. Chen, Z.-Y. Zhou, *Polyhedron,* **27,** *2202* (2008).
88. S.-W. Liang, M.-X. Li, M. Shao, X. He, *J. Mol. Struct.,* **875,** *17* (2008).
89. I. Kinoshita, A. Hamazawa, T. Nishioka, H. Adachi, H. Suzuki, Y. Miyazaki, A. Tsuboyama, S. Okada, M. Hoshino, *J. Chem. Phys. Lett.,* **371,** *451* (2003).
90. C. Kutal, *Coord. Chem. Rev.,* **99,** *213* (1990).

91a. P. C. Ford, *Coord. Chem. Rev.,* **132,** *129* (1994).

91b. P. C. Ford, E. Cariati, J. Bourassa, *Chem. Rev.,* **99,** *3625* (1999).

92. V. W.-W. Yam, K. K.-W. Lo, *Chem. Soc. Rev.,* **28,** *323* (1999).
93. N. Armaroli, G. Accorsi, F. Cardinali, A. Listorti, *Topics Curr. Chem.,* **280,** *69* (2007).
94. J. Zhang, R.-G. Xiong, J.-L. Zuo, X.-Z. You, *Chem. Commun.,* **20,** *1495* (2000).
95. J. Zhang, R.-G. Xiong, X.-T. Chen, C.-M. Che, Z. Xue, X.-Z. You, *Organometallics,* **20,** *4118* (2001).
96. J. Zhang, R.-G. Xiong, X.-T. Chen, Z. Xue, X.-Z. You, *Organometallics,* **21,** *235* (2002).
97. Y.-M. Song, J. Pang, K. Qian, X.-S. Wang, X.-N. Li, R.-G. Xiong, *J. Mol. Struct.,* **796,** *210* (2006).
98. E. Fournier, A. Decken, P. D. Harvey, *Eur. J. Inorg. Chem., 4420* (2004).
99. E. Fournier, F. Lebrun, M. Drouin, A. Decken, P. D. Harvey, *Inorg. Chem.,* **43,** *3127* (2004).
100. P. D. Harvey, *Macromol. Symposia,* **20,** *4887* (2004).
101. A. J. Blake, N. R. Brooks, N. R. Champness, L. R. Hanton, P. Hubberstey, M. Schröder, *Pure Appl. Chem.,* **70,** *2351* (1998).
102. A. J. Blake, N. R. Brooks, N. R. Champness, M. Crew, D. H. Gregory, P. Hubberstey, M. Schröder, A. Deveson, D. Fenske, L. R. Hanton, *Chem. Commun., 1432* (2001).
103. P. M. Graham, R. D. Pike, M. Sabat, R. D. Bailey, W. T. Pennington, *Inorg. Chem.,* **39,** *5121* (2000).

104a. N. R. Brooks, A. J. Blake, N. R. Champness, P. A. Cooke, P. Hubberstey, D. M. Prosperio, C. Wilson, M. Schröder, *J. Chem. Soc., Dalton Trans., 456* (2001).

104b. R. Peng, M. Li, D. Li, *Coord. Chem. Rev.,* **254,** *1* (2010).

105. J. C. Dyason, P. C. Healy, C. Pakawatchai, V. A. Patrick, A. H. White, *Inorg. Chem.,* **24,** *1957* (1985).
106. J. C. Dyason, L. H. Engelhardt, P. C. Healy, A. H. White, *Aust. J. Chem.,* **39,** *1043* (1986).
107. C. L. Raston, A. H. White, *J. Chem. Soc., Dalton Trans.,* **2153** (1976).
108. J. A. Campbell, C. L. Raston, A. H. White, *Aust. J. Chem.,* **30,** *1937* (1977).
109. H. D. D. Ahna, H. D. Hardt, *Z. Anorg. Allg. Chem.* **387,** *61* (1972).
110. H. D. Hardt, H. Gechnizdjani, *Naturwissenschaften,* **59,** *363* (1972).

111. H. D. Hardt, A. Pierre, *Z. Anorg Allg. Chem.,* **402,** *107* (1973).
112. H. D. Hardt, A. Pierre, *Inorg. Chim. Acta,* **25,** *L59* (1977).
113. G. A. Bowmaker, R. J. Knappstein, S. F. Tham, *Aust. J. Chem.,* **31,** *2137* (1978).
114. M. Radjaipour, D. Oelkrug, *Ber. Bunsen-Ges. Phys. Chem.,* **82,** *159* (1978).
115. E. Cariati, P. C. Ford, *Chem. Commun. 1623* (1998).
116. M. Vitale, P. C. Ford, *Coord. Chem. Rev.,* **219–221,** *3625* (2001).
117. B. Lv, C. Cheng, H. Yuan, D. Xiao, M. F. Choi, *J. Mat. Res.,* **23,** *1722* (2008).
118. P. K. Mehrotra, R. Hoffman, *Inorg. Chem.,* **17,** *2187* (1978).
119. G. Hu, G. J. Mains, E. M. Holt, *Inorg. Chim. Acta,* **240,** *559* (1995).
120a. M. Vitale, W. E. Palke, P. C. Ford, *J. Phys. Chem.,* **96,** *8329* (1992)
120b. J. A. Simon, W. E. Palke, P. C. Ford, *Inorg. Chem.* **35,** *6413* (1996).
121. A. Vega, J.-Y. Saillard, *Inorg. Chem.,* **43,** *4012* (2004).
122. C. Mealli, S. S. M. C. Godinho, M. J. Calhorda, *Organometallics.* **20,** *1734* (2001).
123. H. Mälger, F. Olbrich, J. Kopf, D. Abeln, E. Weiss, *Zeitschrift Naturforsch., B:* **47,** *12* (1992).
124. J. Zhou, G.-Q. Bian, J. Dai, Y. Zhang, Q.-Y. Zhu, W. Lu, *Inorg. Chem.,* **45,** *8486* (2006).
125. S. Muthu, Z. Ni, J. J. Vittal, *Inorg. Chim. Acta,* **358,** *595* (2005).
126. J. Wang, S.-L. Zheng, S. Hu, Y.-H. Zhang, M.-L. Tong, *Inorg. Chem.,* **46,** *795* (2007).
127. Z.-M. Hao, X.-M. Zhang, *Cryst. Growth & Des.,* **7,** *64* (2007).
128. J.-K. Cheng, J.-G. Yao, J. Zhang, Li Z.-J. Z.-W. Cai, X.-Y. Zhang, Z.-N. Chen, Y.-B. Chen, Y. Kang, Y.-Y. Qin, Y.-H. Wen, *J. Am. Chem. Soc.,* **126,** *7796* (2004).
129. Y.-B. Xie, Z.-C. Ma, D. Wang, *J. Mol. Struct.,* **784,** *93* (2006).
130. J. J. M. Amoore, L. R. Hanton, M. D. Spicer, *Dalton Trans., 1056* (2003).
131. R.-F. Song, Y.-B. Xie, J.-R. Li, X.-H. Bu, *CrystEngComm.,* **7,** *249* (2005).
132. P. L. Caradoc-Davies, L. R. Hanton, J. M. Hodgkiss, M. D. Spicer, *J. Chem. Soc., Dalton Trans.,* **1581** (2002).
133. M. Valderrama, R. Contreras, V. Arancibia, D. Boys, *J. Organomet. Chem.,* **620,** *256* (2001).
134. A. F. Chiffey, J. Evans, W. Levason, M. Webster, *J. Chem. Soc. Dalton Trans., 2835* (1994).
135. X.-H. Bu, W. Chen, M. Du, K. Biradha, W.-Z. Wang, R.-H. Zangh, *Inorg. Chem.,* **41,** *437*, (2002).
136. J.-R. Li, M. Du, R.-H. Zhang, X.-H. Bu, *J. Mol. Struct.,* **607,** *175* (2002).
137. J. R. Black, W. Levason, *J. Chem. Soc. Dalton Trans., 3225* (1994).
138. S. E. Dann, A. R. J. Genge, W. Levason, G. Reid, *J. Chem. Soc., Dalton Trans. 4471* (1996).
139. V. Miranda-Soto, M. Parra-Hake, D. Morales-Morales, R. A. Toscano, G. Boldt, A. Koch, D. B. Grotjahn, *Organometallics,* **24,** *5569* (2005).
140. A. R. Sanger, J. E. Weiner-Fedorak, *Inorg. Chim. Acta,* **42,** *101* (1980).
141. Y.-B. Xie, J.-R. Li, Y. Zheng, X.-H. Bu, R.-H. Zhang, *J. Mol. Struct.,* **645,** *227* (2003).
142. X.-H. Bu, W. Chen, W.-F. Hou, M. Du, R.-H. Zhang, F. Brisse, *Inorg. Chem.,* **41,** *3477* (2002).
143. M. O. Awaleh, F. Baril-Robert, C. Reber, A. Badia, F. Brisse, *Inorg. Chem.,* **47,** *2964* (2008).
144. M. Knorr, H. N. Peindy, F. Guyon, H. Sachdev, C. Strohmann, *Z. Anorg. Allg. Chem.,* **631,** *2397* (2005).
145. H. N. Peindy, F. Guyon, A. Khatyr, M. Knorr, C. Strohmann, *Eur. J. Inorg. Chem., 1823* (2007).

146. M. Knorr, F. Guyon, A. Khatyr, C. Däschlein, C. Strohmann, S. M. Aly, A. S. Abd-El-Aziz, D. Fortin, P. D. Harvey, *Dalton Trans., 948* (2009).
147. P. Schulte, G. Gröger, U. Behrens, *J. Organomet. Chem.,* **584,** *1* (1999).
148. X. Xue, X.-S. Wang, R.-G. Xiong, X.-Z. You, B. F. Abrahams, C.-M. Che, H. X. Ju, *Angew. Chem. Int. Ed. Engl.,* **41,** *2944* (2002).
149. H. Ohi, Y. Tachi, T. Kunimoto, S. Itoh, *Dalton Trans., 3146* (2005).
150. M. Munakata, L. P. Wu, T. Kuroda-Sowa, M. Maekawa, Y. Suenaga, S. Nakagawa, *J. Chem. Soc. Dalton Trans., 1525* (1996).
151. R. Peng, T. Wu, D. Li, *CrystEngComm.,* **7,** *595* (2005).
152. R. Peng, D. Li, T. Wu, X.-P. Zhou, S. W. Ng, *Inorg. Chem.,* **45,** *4035* (2006).
153. R. Peng, T. Wu, D. Li, *Cryst Eng Comm.,* **10,** *778* (2008).
154. R. Peng, S.-R. Deng, M. Li, D. Li, Z.-Y. Li, *Cryst Eng Comm.,* **10,** *590* (2008).
155. T. H. Kim, G. Park, Y. W. Shin, K.-M. Park, M. Y. Choi, J. Kim, *Bull. Korean Chem. Soc.,* **29,** *499* (2008).
156. Y.-Q. Sun, C.-K. Tsang, Z. Xu, G. Huang, J. He, X.-P. Zhou, M. Zeller, A. D. Hunter, *Cryst. Growth Des.,* **8,** *1468* (2008).
157. K.-M. Park, I. Yoon, J. Seo, J.-E. Lee, J. Kim, K. S. Choi, O.-S. Jung, S. S. Lee, *Cryst. Growth Design,* **5,** *1707* (2005).
158. J. H. Kim, M. R. Song, S. J. Lee, J. Y. Lee, S. S. Lee, *Eur. J. Inorg. Chem., 3532* (2008).
159. J. Y. Lee, S. Y. Lee, J. Seo, C. S. Park, J. N. Go, W. Sim, S. S. Lee, *Inorg. Chem.,* **46,** *6221* (2007).
160. P. R. Ashton, A. L. Burns, C. G. Claessens, G. K. H. Shimizu, K. Small, J. F. Stoddard, A. J. P. White, D. J. Williams, *J. Chem. Soc., Dalton Trans., 1493* (1997).
161. J. Y. Lee, S. Y. Lee, W. Sim, K.-M. Park, J. Kim, S. S. Lee, *J. Am. Chem. Soc.,* **130,** *6902* (2008).
162. J. Y. Lee, H. J. Kim, J. H. Jung, W. Sim, S. S. Lee, *J. Am. Chem. Soc.,* **130,** *13838* (2008).
163. T. H. Kim, Y. W. Shin, J. S. Kim, S. S. Lee, J. Kim, *Inorg. Chem. Commun.,* **10,** *717* (2007).
164. T. H. Kim, K. Y. Lee, Y. W. Shin, S.-T. Moon, K.-M. Park, J. S. Kim, Y. Kang, S. S. Lee, J. Kim, *Inorg. Chem. Commun.,* **8,** *27* (2005).
165. T. H. Kim, Y. W. Shin, S. S. Lee, J. Kim, *Inorg. Chem. Commun.,* **10,** *11* (2007).
166. T. H. Kim, Y. W. Shin, H. J. Jung, J. S. Kim, J. Kim, *Angew. Chem. Int. Ed. Engl.,* **47,** *685* (2008).
167. H. W. Yim, D. Rabinovich, K.-C. Lam, J. A. Golen, A. L. Rheingold, *Acta Cryst.,* **E59,** *556* (2003).
168. M. Knorr, F. Guyon, I. Jourdain, S. Kneifel, J. Frenzel, C. Strohmann, *Inorg. Chim. Acta,* **350,** *455* (2003).
169. M. Knorr, H. N. Peindy, F. Guyon, H. Sachdev, C. Strohmann, *Z. Anorg. Allg. Chem.,* **630,** *1955* (2004).
170. H. W. Yim, L. M. Tran, E. E. Pullen, D. Rabinovich, L. M. Liable-Sands, T. E. Concolino, A. L. Rheingold, *Inorg. Chem.,* **38,** *6234* (1999).
171. H. N. Peindy, F. Guyon, M. Knorr, A. B. Smith, J. A. Farouq, S. A. Islas, D. Rabinovich, J. A. Golen, C. Strohmann, *Inorg. Chem. Commun.,* **8,** *479* (2005).
172. H. N. Peindy, F. Guyon, A. Khatyr, M. Knorr, C. Strohmann, *Z. Anorg. Allg. Chem.,* **635,** *2099* (2009).
173. S. Jacquot-Rousseau, G. Schmitt, A. Khatyr, M. Knorr, M. M. Kubicki, E. Vigier, O. Blaque, *Eur. J. Org. Chem., 1555* (2006).
174. R. Kinghat, A. Khatyr, G. Schmitt, M. Knorr, M. M. Kubicki, E. Vigier, M. Villafane, *Inorg. Chem. Commun.,* **11,** *1060* (2008).

CHAPTER 4

Applications of Metal Containing Polymers in Organic Solar Cells

Chris S. K. Mak and Wai Kin Chan

Department of Chemistry, The University of Hong Kong, Pokfulam Road, Hong Kong

CONTENTS

Macromolecules Containing Metal and Metal-like Elements,
Volume 10: Photophysics and Photochemistry of Metal-Containing Polymers,
Edited by Alaa S. Abd-El Aziz, Charles E. Carraher Jr., Pierre D. Harvey, Charles U. Pittman Jr., Martel Zeldin.

I. INTRODUCTION

The search for an efficient and low-cost renewable energy source has been one of the most important research areas in modern science and technology. Solar light is a very reliable source of energy because it generates no harmful byproducts and is basically inexhaustive. The development of efficient organic photovoltaic (PV) cells has drawn the attention of materials scientists and engineers in recent years because organic photovoltaic cells are very promising alternatives to conventional silicon-based photovoltaic cells. Compared to silicon solar cells, organic solar cells have lower production and processing cost (especially for large area devices), higher structural flexibility, and better feasibility in material design and modification.[1–3] In 1986, Tang demonstrated the fabrication of efficient organic photovoltaic cells by a simple vacuum deposition technique.[4] The device was based on simple organic molecule-copper(II) phthalocyanine and perylene tetracarboxylic diimide derivatives. Thereafter, solar cells based on organic polymeric or molecular material and organic-inorganic hybrid material in the active layers were reported. Research in this topic has grown very rapidly in recent years. In this chapter, we first give a brief introduction of different types of organic solar cells and the materials involved in device fabrication. There are several review articles on pure organic materials in solar cell application.[5–7] However, no review on the use of metal containing polymers has been reported so far. In this chapter, the discussion mainly focuses on the use of metal containing polymers in the active layers in organic photovoltaic cells.

II. TYPES OF ORGANIC SOLAR CELLS

There are two major types of organic solar cells in terms of the device configuration: dye-sensitized solar cells and organic multilayer thin film devices. Although the major function of both types of devices is to convert light energy into electrical energy, their operating principles are different.

A. Dye-Sensitized Solar Cells

The dye-sensitized nanostructured solar cell (DSSC) was first developed by Grätzel's group in 1991.[8,9] The operating principle of DSSCs is shown in Figure 1. Light is harvested by an organic or organometallic sensitizer, which is anchored to the surface of a wide band gap inorganic semiconductor via a carboxylate, phosphonate, or hydroxamate group. Upon photosensitization and the formation of excitons, electrons are injected from the sensitizing molecules (the dye molecules) into the semiconducting metal oxides. Charge separation then occurs at the interface of the inorganic semiconductor and sensitizer, and the photo-excited electron is injected into the conduction band of the semiconductor in the subpicosecond region. Electrons then migrate to the back contact electrode via a network of semiconductor nanostructure. In the other end, the photo-sensitizers accept electrons from the redox mediator electrolyte. Hole transport is aided by the redox cycles in the electrolyte. The iodide/triiodide redox couple system is regarded as the best electrolyte in solvents containing DSSCs.

Polypyridyl ruthenium complexes have been extensively studied as the candidates for photosensitizers due to their high stability toward sunlight, excellent redox properties, and high versatility of turning the metal-to-ligand charge transfer (MLCT; $4d_{\pi}-\pi_{L}^{*}$) absorption over the visible spectrum by judicious manipulation of ligand chelation.[10,11] Metal oxides such as TiO_2, ZnO, SnO_2, and Nb_2O_5 are commonly used as the electron accepting and transport materials. The nanocrystalline structures provided huge surface area

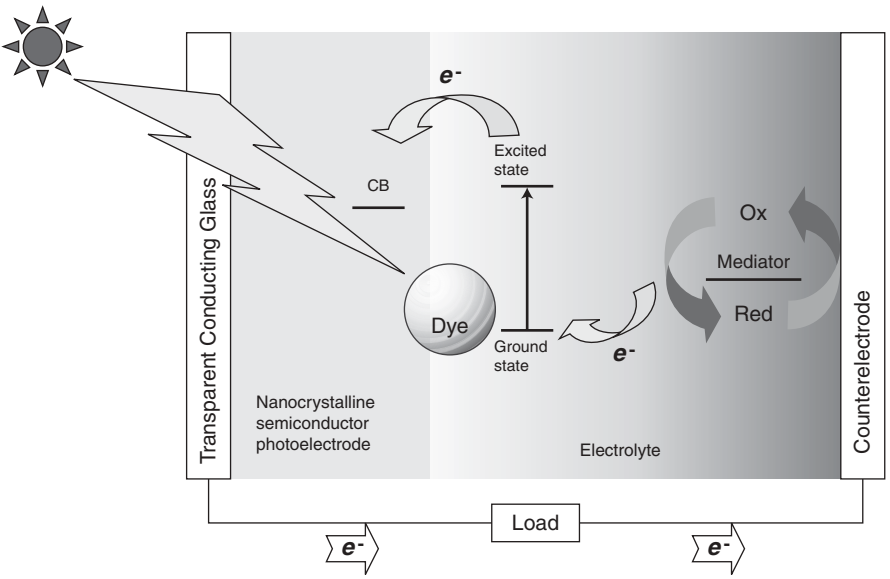

FIGURE 1. The operating principles of dye-sensitized solar cells.

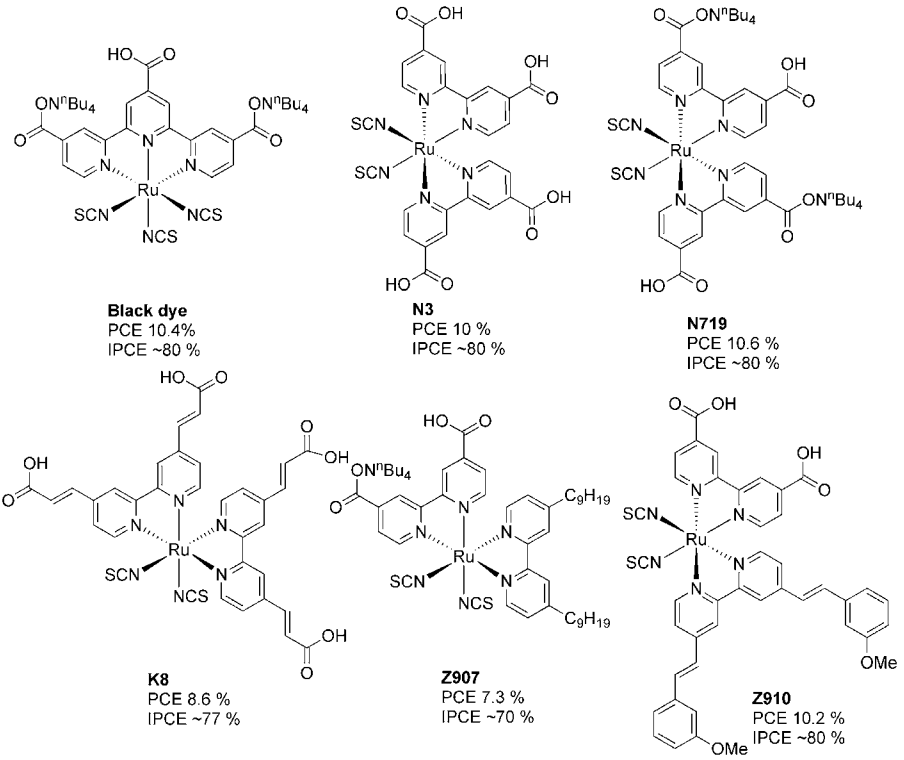

SCHEME 1.

for anchoring light-absorbing dye and enhance the absorption cross-section. The charges are transported to the electrodes and the external circuit to generate electricity through the conduction band of the semiconductor nanostructure. Excellent and comprehensive discussions on the advances in structure engineering of small molecule photosensitizers and inorganic semiconductor nanostructure of DSSC have been published.[8,9,12–17–20]

The cell is on the verge of commercialization, offering a potential alternative for the currently used silicon-based photovoltaic devices.[12] An unprecedented conversion efficiency of 11% could be manufactured from relatively cheap materials.[19] The most up-to-date efficient DSSCs are based on ruthenium complexes. Several representative ruthenium sensitizers possess high extinction coefficient and high photovoltaic performance are shown in Scheme 1.[15–19]

However, the presence of liquid electrolyte has the problems of leakage, robust sealing, and device stability, thus results in limited commercialization. Quasi-solid-state and solid-state DSSCs based on nonvolatile ionic liquid or organic hole-conducting material/polymer as the electrolyte are, therefore, developed to circumvent the sealing problem.

B. Organic Thin Film Solar Cells

DSSCs are not considered to be pure organic PV cells because the active layers are composed of organic-inorganic composite materials, which limit the fabrication of flexible solar cells. Another type of organic solar cells is based on pure organic materials in the active layers. The materials are introduced to the electrode substrate either by vacuum deposition (for small molecules) or by spin coating (for polymeric materials) techniques. Heterojunction and bulk-heterojunction cells are the two most popular device configuration. In a heterojunction PV cells (Fig. 2), the active layer is composed of two separate layers of sensitizer (the donor) and electron acceptor. Upon exciton generated by photoexcitation, charge separation mainly occurs near the donor-acceptor interface. Holes and electrons are then transported by the donor and accepting layers respectively, to the corresponding electrodes. In a bulk-heterojunction photovoltaic cell, the electron donors and acceptors are blended in the same layer. Due to the phase separation, different types of materials in the same layer may aggregate and form an interpenetrating network on a nanometer scale. The exciton generation and separation processes also happen at the donor-acceptor interface, but the contact surface between them is greatly increased when compared to heterojunction device. The holes and electrons formed are then transported via different percolated pathways to different electrodes separately.

Early examples of organic polymers used in PV devices include poly(*p*-phenylenevinylene) (PPV) and its derivatives,[21–25] while copper phthalocyanine, α-sexithiophene, and fullerene are typical examples of low molecular weight organic materials.[5,26] Recently, the efficiency of organic solar cells was improved by the design of new conjugated polymers with improved structural, optical absorption, and charge transport properties. Examples of these polymers are poly(3-hexylthiophene),[27–32] poly(fluorene-co-thiophene),[33]

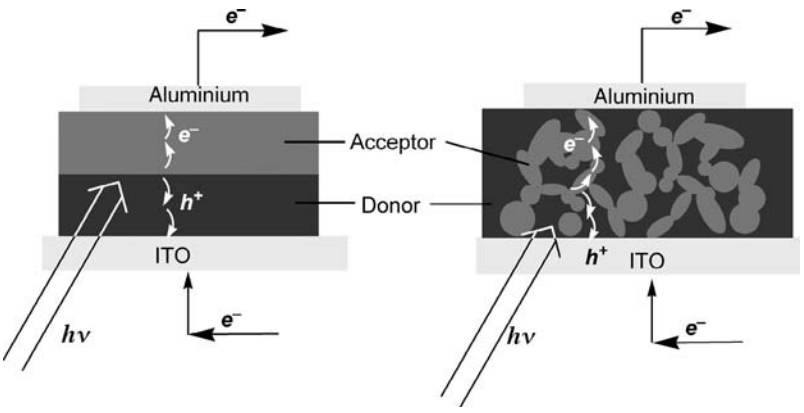

FIGURE 2. Device configuration for heterojunction (a) and bulk-heterojunction (b) organic thin film solar cells.

poly(phenylenevinylene)[34,35] and their derivatives, and low band gap conjugated polymers based on different heterocyclic moieties on the polymer main chain.[36–40] Other than developing new materials, the efficiency could also further enhanced by adopting new device architecture, such as insertion of an optical spacer layer.[41] In tandem polymer cells fabricated by solution processing, power conversion efficiency in excess of 6% was reported.[42]

III. SOLAR CELL CHARACTERIZATIONS

Under illumination with a light source, a typical solar cell exhibits the current-voltage characteristics shown in Figure 3. The current drawn by the cell when the terminals are connected to each other is the short circuit current (I_{sc}, in mA/cm^2). In the presence of an external load with infinite resistance (open circuit condition), the voltage developed is the open-circuit voltage (V_{oc}, in V).

The performance of a photovoltaic cell is characterized by the power conversion efficiency η_p, which is defined by:

$$\eta_p = \frac{V_{oc} \times I_{sc} \times FF}{P_{in}} \tag{1}$$

where P_{in} is the power of the incident light (mW/cm^2) and FF is the fill factor, which is defined as the ratio of the maximum power delivered by the cell

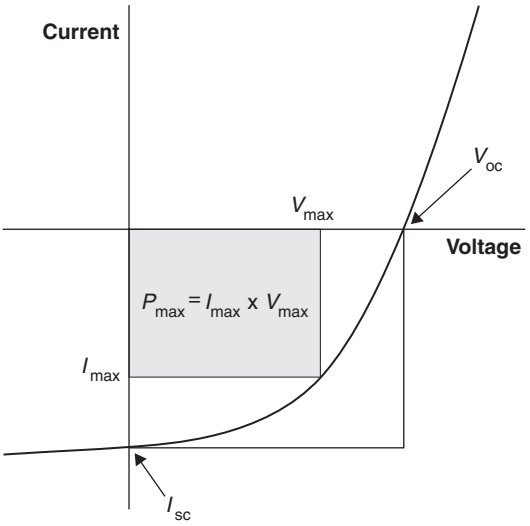

FIGURE 3. A typical current-voltage characteristic for a photovoltaic cell.

($V_{max} \times I_{max}$) to the theoretical maximum power ($V_{oc} \times I_{sc}$). This is equal to the ratio between the shaded rectangle and the larger rectangle shown in Figure 3. The most commonly used light source for photovoltaic cell characterization is simulated air mass (AM) 1.5 solar light with an intensity of 100 mW/cm^2 (= 1 sun). For the characterization of the conversion efficiency of a photon to electron at a particular wavelength λ(nm), the incident photon conversion to electron efficiency (IPCE), also known as the external quantum efficiency (EQE), is used. This is defined to be

$$IPCE(\lambda) = \frac{1240 \times I_{sc}}{\lambda P_{in}} \times 100\% \tag{2}$$

A plot of IPCE as the function of incident light wavelength usually reveals very important information regarding which functionalities in the sensitizing molecules are essential to the generation of excitons.

IV. METAL CONTAINING POLYMERS IN SOLAR CELLS

Although there are numerous reports on the use of transition metal complexes in DSSC, there are relatively fewer examples of using metal containing polymers in organic solar cells. Many transition metal complexes are highly promising photosensitizers because of their high optical absorptivity and relatively long-lived excited states, which may facilitate the exciton separation process. In addition, the optical absorption spectra of the complexes can be easily fine-tuned by modifying the structures of the ligand systematically. However, to introduce a metal complex sensitizer into the device active layer, the complex has to be doped into a polymer host. Many metal complexes are either ionic in nature or have very high molecular weight. They cannot be evaporated under high vacuum and have very low compatibility with the organic host materials. As a result, the amount of metal complex that can be doped in the organic host is limited.

Metal containing polymers offer the advantage that there is no limit to the metal content in the polymer host because the metal complexes are covalently attached to the polymer molecules. Therefore, phase separation of the complex will not be a problem. Moreover, multifunctional polymers can be easily designed and synthesized by incorporating photosensitizing metal complex into a charge transport polymer backbone. The resulting material exhibits high flexibility and can be processed by conventional techniques, such as spin-coating, solution casting, and dip coating. In the next two sections, examples of using metal containing polymers in the fabrication of photovoltaic cells are reviewed. The first part mainly concentrates on the use of metal containing polymers in DSSC, while

in the second part, the use of metal containing polymers in heterojunction or bulk-heterojunction photovoltaic cells is discussed. To limit the scope of the discussion, only polymeric materials functionalized with metal complexes are addressed; the use of organic polymers doped with metal complexes is not included in the section.

A. Dye-Sensitized Solar Cells

Several organic polymers have been used as the sensitizers in DSSCs.[43] Examples of metal containing polymers for DSSC are also mainly based on ruthenium complexes containing conjugated polymers. Conjugated polymers with $\pi-\pi^*$ electronic transitions generally have larger absorption cross-sections than that of metal complexes (commonly MLCT transitions). The combination of metal complex and conjugated polymer can enhance not only the charge transport properties of the photovoltaic devices but also the absorption range (both absorption from the MLCT transition of the complex and $\pi-\pi^*$ transition of the conjugated polymer). Coordination polymers **1-3** (Scheme 2) comprise a poly(*p*-phenylenevinylene) (PPV) building block with a donor or acceptor character and a ruthenium(II) bis(terpyridyl) chromophore as a spacer.[44] Fluorescence spectroscopy revealed the energy harvested by the polymer segments was efficiently transferred to the complex. Photovoltaic performances of two different types of solar cells, all-polymer solar cells obtained by spin-coating and DSSC with TiO_2 crystalline film, based on these polymers were compared. All the DSSC devices for the three different coordination polymers showed better performance than the all-polymer-based solar cells. Device efficiency close to 0.1% was obtained under AM 1.5 illumination (device configuration: FTO/TiO_2(anatase)/TiO_2(nanoporous)/polymer **3**/electrolyte/Pt/FTO) in spite of the lack of anchoring groups on the polymer to attach on the surface of TiO_2.[45] The use of $Co(btp)_3ClO_4$-based electrolyte [btp=(4,4-di-*tert*-butyl-2,2-dipyridyl)] instead of I^-/I_3^- avoids polymer degradation and thus increases cell performances.[44,46]

Similar studies have been carried out on a zwitterionic ruthenium bis(terpyridine) dye covalently linked to a thiophene conjugated polymer (Scheme 2, polymer **4)**. The zwitterionic ruthenium dye was functionalized with a phosphonic acid group on one of the terpyridine ligands, while another terpyridine ligand was conjugatively linked to the regioregular poly(hexylthiophene) by the Stille coupling reaction. The ruthenium dye anchored to the TiO_2 anatase enabled efficient electron injection, and the conjugated polymer served as light-harvesting antenna for the ruthenium complex and hole transport materials. Although the device efficiency was far from satisfaction ($\eta_p<0.05$ %), the material design demonstrated the efficient light-harvesting ability and energy transfer in the combination of Ru dye and polythiophene.[47]

In another report, layer-by-layer (LbL) self-assembly deposition was employed to prepare the acceptor-sensitizer dyad polyelectrolyte film in DSSC.[48] The viologen-containing polymer film with bromide as the counterions

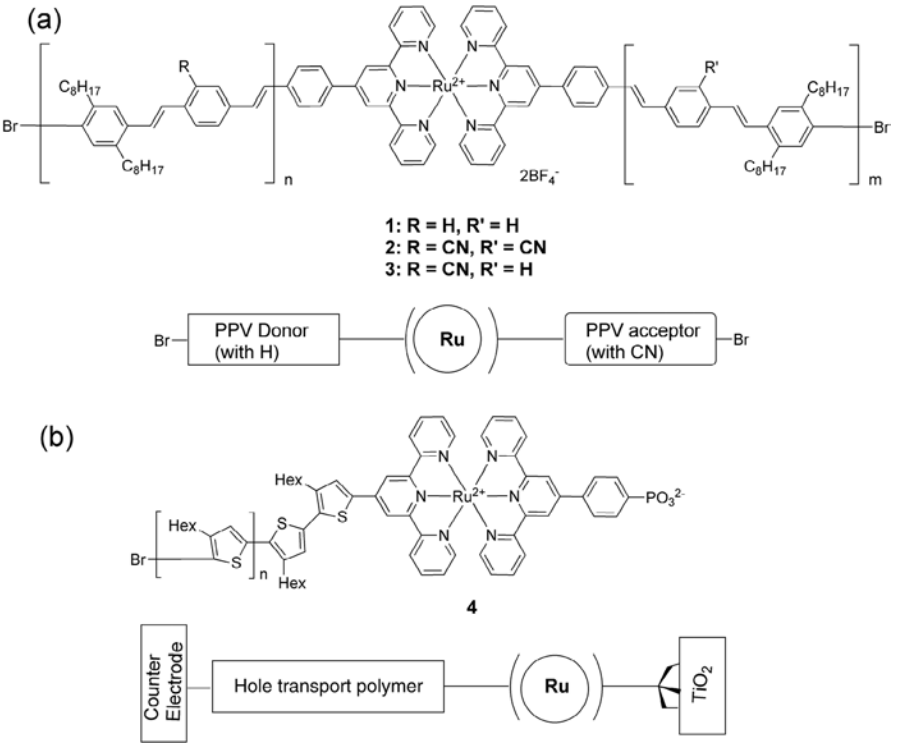

SCHEME 2.

of polypropylviologen (PPVG), which was coated on the ITO substrate by dipping. Poly(ethylenedioxythiophene)-polystyrene sulfonate (PEDOT:PSS) was deposited on top of the PPVG by the same method (Fig. 4). Successive layering of these two polymers alternatively formed a multilayer polyelectrolyte. The photosensitizer **N3** dye was incorporated into the multilayer by ion exchange with the bromide counterions of PPVG. A 4.5 bilayer device generated a photocurrent of I_{sc}=1.2 μA/cm^2 under AM 1.5 conditions, with a device configuration of ITO/multilayer/electrolyte (0.3 M LiI and 30 mM I_2 in CH_3CN)/Pt/ITO.

DSSCs with rodlike polymers as the sensitizer generally have poor efficiency due to their rigidity and incomplete infiltration into the void of the TiO_2 nanostructures. The loose contact between the polymer and the TiO_2 surface gives rise to poor electron injection and an increase in charge recombination. In situ photo-electrochemical polymerization (PEP) of hole conducting materials not only can provide better contact with sensitizers but also can replace the liquid electrolyte. Scheme 3 shows a series of novel ruthenium bipyridyl complexes functionalized with electropolymerizable hole transporting groups.[49–52] In situ PEP was carried out in the void of mesoporous structure after the ruthenium dyes were anchored on the labyrinthine surface of TiO_2.

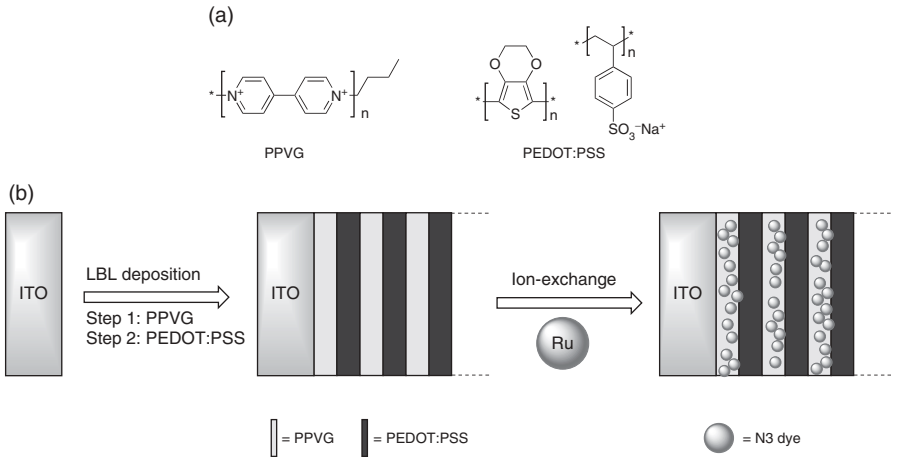

FIGURE 4. (a) Structures of PPVG and PEDOT:PSS. (b) The fabricating of the polyelectrolyte-organometallic multilayer film by the layer-by-layer deposition process.

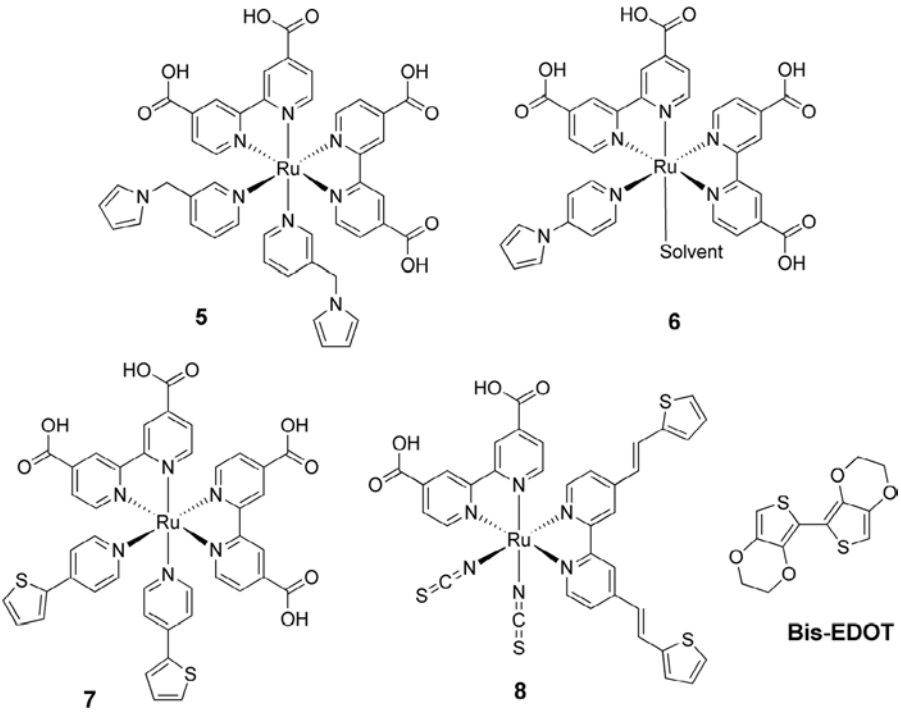

SCHEME 3.

The dyed TiO_2 film was immersed in an acetonitrile solution containing pyrrole or bis-EDOT monomer and lithium perchlorate. The applied potential of the film was referenced to the Ag/Ag^+ electrode and irradiated by a 500 W Xe lamp (22 mW/cm^2, $\lambda > 500$ nm).

A solid-state solar cell was assembled with an ionic liquid—1-ethyl-3-methylimidazolium bis(trifluoromethanesulfone)amide (EMITFSA) containing 0.2 M lithium bis(trifluoromethanesulfone)amide and 0.2 M 4-*tert*-butylpyridine—as the electrolyte and Au or Pt sputtered film as the cathode.[51,52] The in situ PEP of polypyrrole and PEDOT allows efficient hole transport between the ruthenium dye and the hole conducting polymer, which was facilitated by the improved electronic interaction of the HOMO of the ruthenium dye and the conduction band of the hole transport material. The best photovoltaic result (η_p=0.62 %, I_{sc}=104 μA/cm^2, V_{oc}=0.716 V, and FF=0.78) was obtained from the ruthenium dye **5** with polypyrrole as the hole transport layer and the carbon-based counterelectrode under 10 mW/cm^2 illumination. The use of carbon-based materials has improved the electric connectivity between the hole transport layer and the electrode.[51]

The same approach was adapted in a later study. An efficient solid-state DSSC was fabricated using hybridized ruthenium dye **8**. The hole conducting PEDOT was formed in situ via PEP. The thickness of the mesoporous TiO_2 layer of the solar cell was varied. The highest efficiency (2.6% under 100 mW/cm^2 illumination) was achieved by using a 5.8- μm-thick TiO_2 layer.[52]

Recently, a tris(2,2-bipyridyl) ruthenium(II) complex containing cyclodextrin (CD) supramolecule was applied to DSSC (Scheme 4).[53] Comparing to

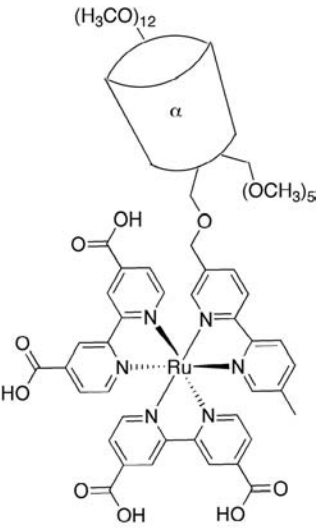

9

SCHEME 4.

the ruthenium complex without cyclodextrin moiety, the photovoltaic performance of polymer **9** revealed a 40% enhancement in efficiency (I_{sc}=4.21 mA/cm^2, V_{oc}=0.59 V, FF=0.59, η_p=1.6%). It was proposed that the CD moiety was able to act as a mediator and fine-tune the photoelectrode-electrode interface. There is a binding between the redox I^-/I_3^- couple and the CD cavity, resulting in the improvement in dye regeneration.

B. Organic Thin Film Solar Cells

i. Polyferrocenylsilanes

Polyferrocenylsilanes represent a major type of metal containing polymers with several interesting potential applications, such as ceramic materials, magnetic materials, redox activity, and sensing. On the other hand, relatively little work has been conducted regarding their applications in photovoltaic cells. Manners et al. have fabricated photovoltaic devices with the active layer composed of a blend of poly(ferrocenylmethylphenylsilane) (PFMPS; Scheme 5)[54] and PCBM or C_{60} with the device configuration of ITO/PFMPS:fullerene(PCBM or C_{60})/Mg/Ag/Au [PCBM=1-(3-methoxycarbonyl)propyl)-1-phenyl[6.6]C_{61}] with various fullerene contents. In the absence of fullerene, the device did not exhibit measurable photocurrent response. When the polymer was doped with 5 mol % C_{60} and a bias of -1 V was applied, a photo to dark current ratio of 15 was observed. Phase separation was observed when the C_{60} content was $>$ 8 mol %, while for PCBM, no observable phase separation was found even when the concentration was increased to 12 mol %. The generation of photocurrent was attributed to an intermolecular photoinduced electron charge transfer from the ferrocene donors to the fullerene acceptors. For the best device, the I_{sc}, V_{oc}, and FF measured were 3.8 nA, 0.44 V, and 0.28, respectively (incident light power=160 mW/cm^2).

ii. Polymeric Metal Complexes

A series of polymeric complexes with the general formula $\{M(dmb)_2Y\}_n$ (M=Cu(I), Ag(I); dmb=1,8-diisocyano-*p*-menthane; Y = BF_4^-, NO_3^-, PF_6^-, ClO_4^-) was prepared by Harvey et al. (Scheme 6).[55] The structures of some of the complexes

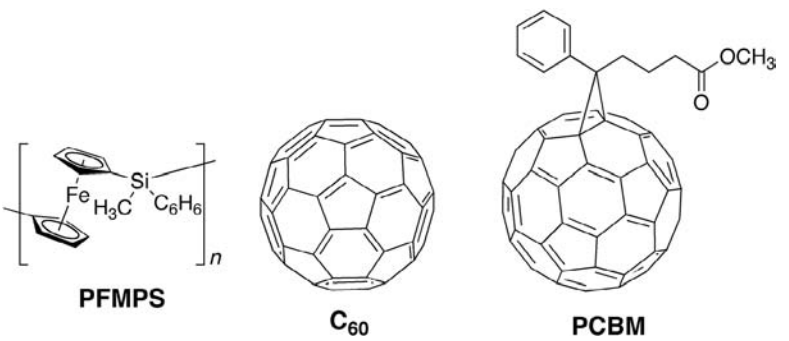

SCHEME 5.

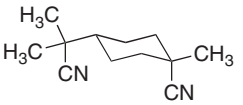

dmb

SCHEME 6.

were characterized by X-ray crystallography.[56] The silver complexes $[Ag(dmb)_2]Y$ ($Y = BF_4^-, NO_3^-, ClO_4^-$) exhibit a polymeric tubular structure in the solid state, and the silver atoms act as the bridge linking different dmb ligands in a distorted tetrahedral configuration. The weight average molecular weights of the copper complex were in the range of 1.27×10^5 to 1.92×10^5, while the silver complexes were suggested to be in oligomeric form. The counteranions may be replaced by tetracyanoquinodimethane(TCNQ), giving electrically insulating materials. Further doping with neutral TCNQ yielded conducting materials, of which the photoconducting properties were studied. A photoinduced electron transfer from the metal center to TCNQ was proposed.[57] Preliminary results on the photovoltaic properties of these materials were obtained by fabrication of photovoltaic cells based on $[Cu(dmb)_2]TCNQ_n$ by depositing the complex on tin oxide–coated glass substrates. Replacement of TCNQ by C_{60} yielded a lower photocurrent response, which was attributed to the poor π-stacking.

iii. Ruthenium/Rhenium Complexes Containing Conjugated Polymers

Despite the extensive application of ruthenium complexes in DSSC, transition metal containing polymers have received relatively little attention in the fabrication of polymeric photovoltaic cells. Most of the early works on ruthenium containing polymers were focused on the light-emitting properties.[58–60] Several examples of ruthenium terpyridine/bipyridine containing conjugated polymers and their photoconducting/electroluminescent properties were reported.[61,62]

Bisterpyridyl ruthenium(II) complex containing conjugated polymers were synthesized by the Heck coupling reaction. In the initial studies, it was found that the ruthenium complex could function as the photosensitizer. The photocurrent response of the polymer can be enhanced by the ruthenium complex. In addition, the metal complexes can also act as charge transport units, and the hole and electron carrier mobilities of the polymer depended on the metal content.[60,62,63] It was suggested that the charge transport process was due to the presence of both ruthenium-centered oxidation and the terpyridine/bipyridine ligand–centered reduction in the complex. The effect of metal complex content to the carrier mobilities was also observed in other examples of ruthenium containing polymers,[60,64–66].

Conjugated polymers incorporated with different heterocyclic moieties were reported. Examples of these conjugated main chains are poly(phenylene vinylene) (**10**)[60] and polybenzoxazole/polybenzthiazole (**11**)[64] (Scheme 7). In

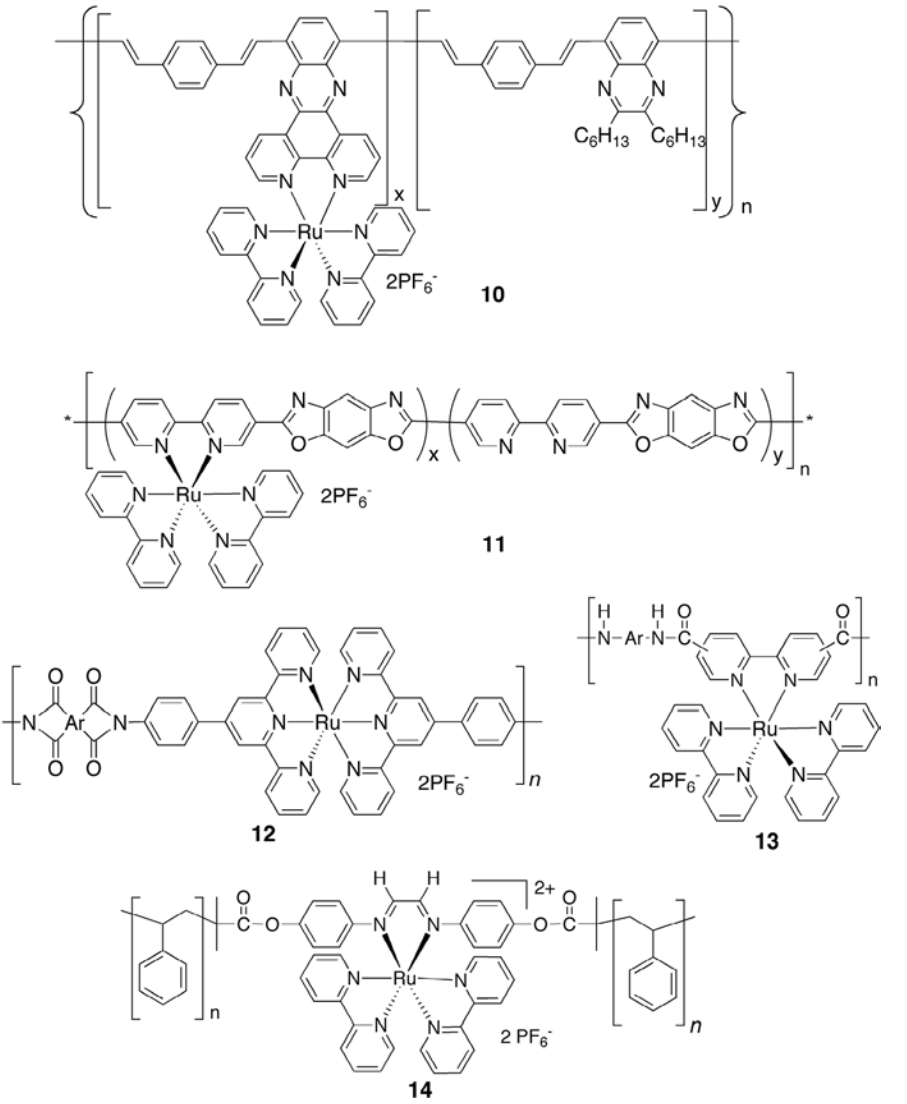

SCHEME 7.

these polymers, the ruthenium complex moieties can play the different functions, such as sensitizers, charge transporting species, and light-emitting groups. Other ruthenium containing polymers with a nonconjugated main chain—such as polyimide (**12**),[67] polyamide (**13**),[66] and polystyrene (**14**)[68]—derivatives were also synthesized. The photocharge generation and charge transport properties of these polymers were investigated.

All these polymers with ruthenium terpyridine/bipyridine complexes contain ionic ruthenium complex on the polymer main chain. Other than the

conventional spin-casting technique for polymer film formation, the polymers can be fabricated into multilayer films by the layer-by-layer (LbL) electrostatic self-assembly method.[69,70] This film forming technique involves the dipping of a suitable substrate into a polycation and a polyanion solution alternatively. This is a simple and versatile approach for fabricating multilayer polymer films because the polymer film thickness can be controlled accurately and the loss of material in the film forming process can be minimized. This technique has been adopted in the fabrication of photovoltaic cells by few research groups. [71,72] In these examples, pure organic polyelectrolytes were employed.

In 2004, Chan et al. reported the fabrication of photovoltaic cells based on polymer multilayers formed by ruthenium containing conjugated polymer **15** and partially sulfonated polyaniline (SPAN).[73] Scheme 8 shows the structures of the polymers and the schematic diagram of the deposition process. The design rationale was that SPAN functioned as the hole transport polymer and polymer **15** functioned as the sensitizing and electron transport polymers. It had been previously shown by the same group that some conjugated polymers functionalized with ruthenium complexes exhibited bipolar charge transport character.[62] In addition, in polymer multilayer thin films fabricated by the LbL process, the polymers formed interpenetrating polymer networks instead of stratified layers. Therefore, the polymer film may be considered to be a bulk heterojunction photovoltaic cell. Devices with the structure ITO/(SPAN/**15**)$_{20}$/Al and with an active layer thickness ranging from 9 to 58 nm were fabricated.[74] The thickness could be changed by varying the deposition conditions, such as the pH of the solution, the addition of different electrolytes, the concentration of salt in the solution, and the post film forming annealing processes. Multilayer films obtained from different conditions also showed significant differences in surface morphology. The best photovoltaic device showed a power conversion efficiency of 4.4×10^{-3}%., Although these devices exhibit lower efficiency compared to other bulk-heterojunction polymer based devices, this method provides a simple alternative approach for in the fabrication of polymeric photovoltaic cells based on ionic polymers.

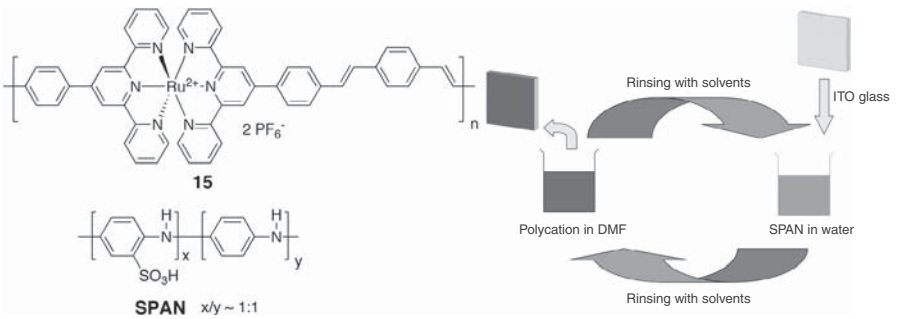

SCHEME 8.

Besides ruthenium complexes, rhenium complexes were also used as the photosensitizers in photovoltaic cells. Bulk heterojunction photovoltaic cells fabricated from sublimable rhenium complexes exhibited a power conversion efficiency of 1.7%.[75,76] The same rhenium complex moiety was incorporated into conjugated polymer chains such as polymer **16a–c** (Scheme 9). Fabrication of devices based on conjugated rhenium containing polymers **17a–c** and **SPAN** by the LbL deposition method was reported.[77] The efficiencies of the devices are on the order of 10^{-4}%.

The synthesis of a series of polyfluorene **18** incorporated with chlorotricarbonyl rhenium(I) 2,2-bipyridine complexes was reported (Scheme 10).[78] Suzuki cross-coupling reactions were used to construct the main chain, and the

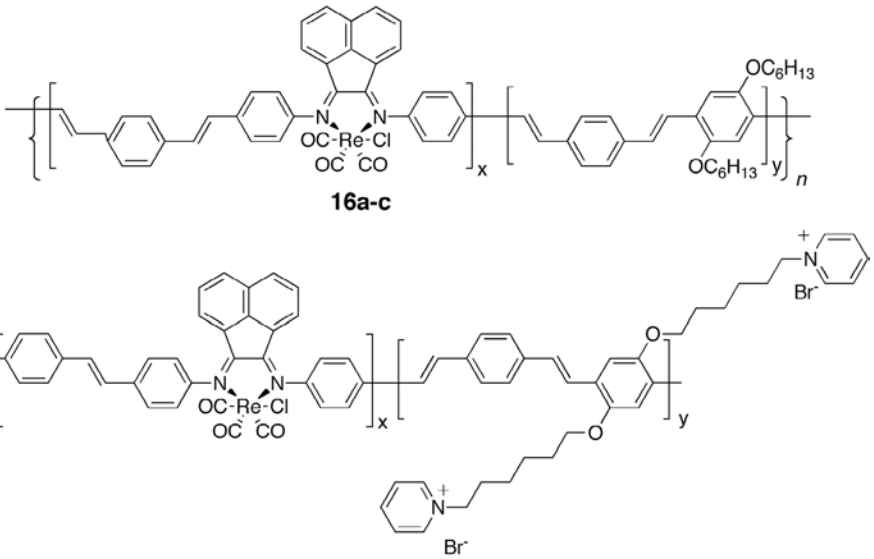

SCHEME 9.

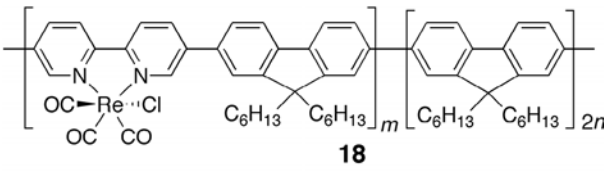

Rhenium complex content: $m/2(m+n) = 0.1, 0.2, 0.5$

SCHEME 10.

complexes were introduced into the polymer after the polymerization reaction. For the polymer with 50% rhenium complex, a lower energy absorption band centered at 420 nm was observed. The role of rhenium complexes in the photosensitization process was studied by measuring the field induced surface photovoltaic spectra. The generation of photovoltage was assigned to the π-π^* transitions.

iv. Hyperbranched Polymers

Besides liner polymers, hyperbranched metal containing polymers can also be used in the multilayer film deposition by the LbL process. Hyperbranched polymers **19**–**21** were synthesized from the corresponding AB_2 type monomer by the coordination reaction between the activated rhenium center and the pyridine *N*-donor ligand (Scheme 11). It was observed from AFM that the polymer molecules exhibited a globular shape when dispersed on a substrate.[79] The polymer can be used in the modification of the surface of nano- to micro-size ZnO tetrapods.[80] In the devices fabricated by the LbL process, sulfonated polythiophene derivative PTEBS was used as the hole transport polyanion.[81] A device with the structure ITO/(polymer **19**/PTEBS)$_{80}$/Al revealed a power conversion efficiency of 6×10^{-3}%. Detailed investigation of the transient photocurrent generated by the device revealed that the photocurrent rise and decay time constants are on the order of tens of seconds, which is much longer than those devices based on pure organic polymers. Due to the presence of counterions in the polymer multilayer films, the devices can be considered as capacitors (capacitance $\sim$ 0.16 μF). In other devices fabricated from polymers **20** and **21** by the LbL process, power conversion efficiencies of the same order of magnitude were obtained.[82]

v. Conjugated Polymers with Pendant Metal Complexes

One of the approaches in improving light harvest efficiency is to broaden the absorption spectrum of the active layer. This can be achieved by either designing a new compound with very broad absorption spectrum or by incorporating different photosensitizing units into the polymer. Chan et al. reported the synthesis of conjugated polymers **22**–**23** incorporated with a pendant ruthenium black dye analogue (Scheme 12) by a conventional palladium catalyzed coupling reaction.[83] Unlike other ruthenium/rhenium complex containing polymers that were synthesized from the metal complex monomers, the trithiocyanato ruthenium complex moieties were introduced after the synthesis of the polymer because the thiocyanato ligands are more labile in the presence of polar solvents. The polymer main chains are based on poly (phenylene-thiophene) or poly(fluorene-thiophene). The conjugated systems and the ruthenium complex absorb in different regions (400–550 nm and 600–700 nm, respectively), yielding polymers with very broad optical absorption in the visible to near IR regions (Fig. 5).

Photovoltaic cells with the simple device structure ITO/polymer/C_{60}/Al were fabricated. The power conversion efficiencies of the devices fabricated

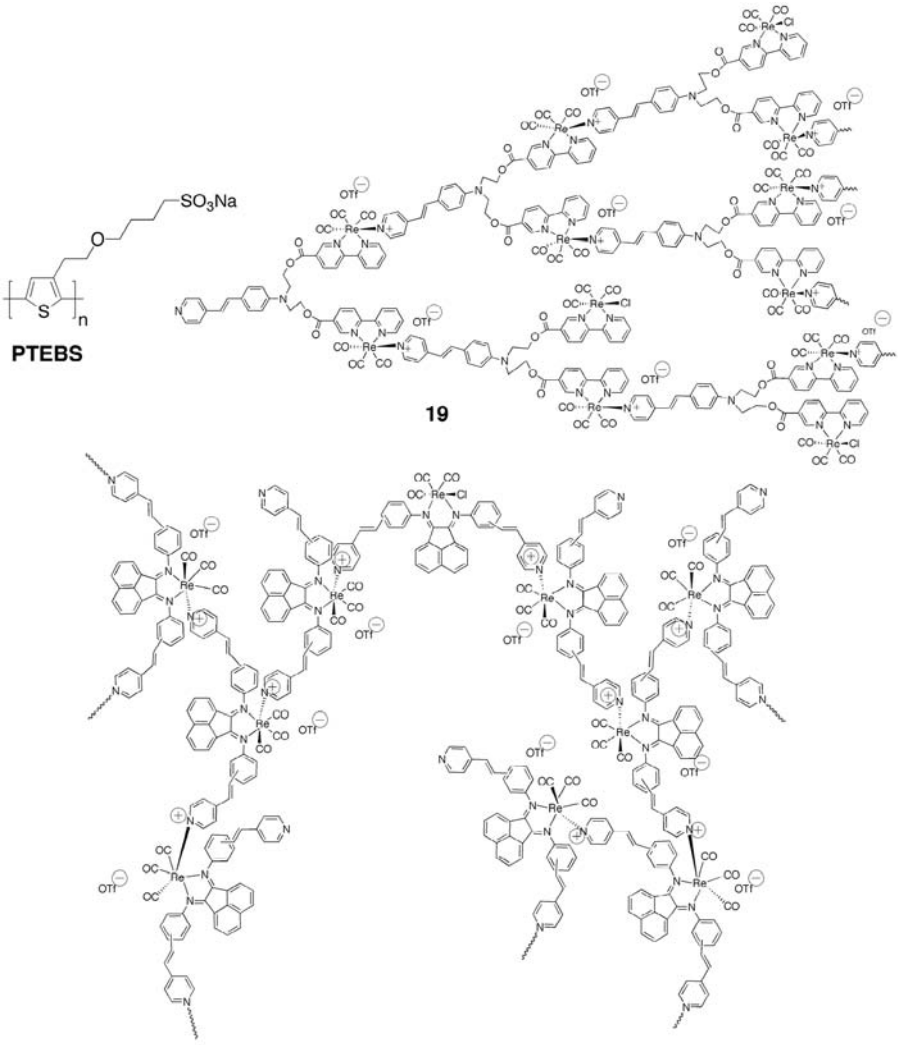

SCHEME 11.

from polymers **22** and **23** were 0.12 and 0.084%, respectively. The hole carrier mobilities of the polymers were measured to be on the order of 10^{-4} cm^2/Vs. This explains the modest efficiencies exhibited by these devices given the simple device structure. After photoexcitation, electrons are captured by the C_{60} near the interface, while holes migrate to the conjugated main chain. Unlike other polymer photovoltaic cells, insertion of a PEDOT:PSS layer between the ITO and polymer did not improve the device performance significantly.

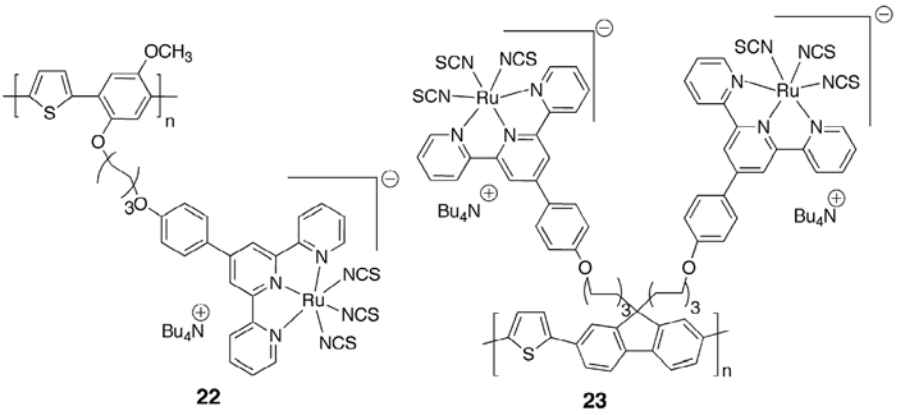

SCHEME 12.

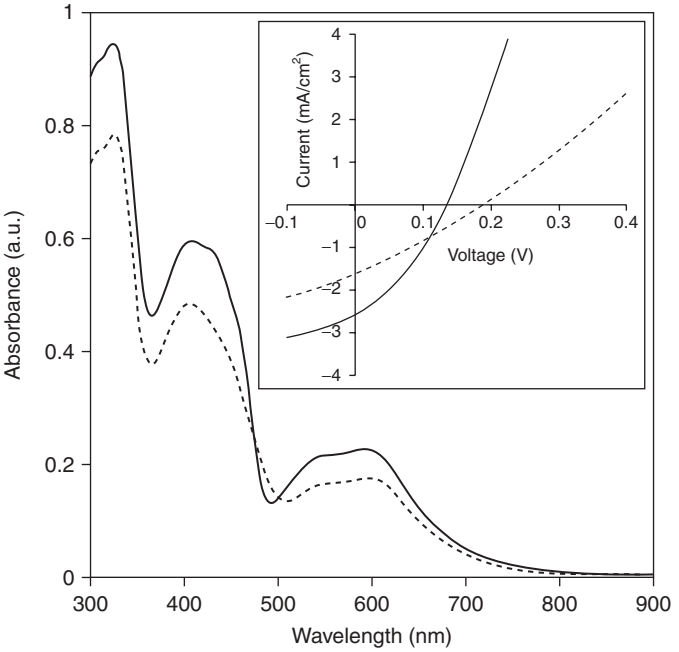

FIGURE 5. UV-VIS absorption spectra of polymer **22** (- - - - -) and **23** (———). *Inset:* The current-voltage characteristics of the ITO/polymer **22** and **23**/C_{60}/Al devices under illumination with simulated solar light (100 mW/cm^2).

vi. Platinum Acetylide Containing Conjugated Polymers

Platinum(II) bridged polyynes have been promising candidates for nonlinear optical materials.[84,85] They are characterized by the presence of $-C\equiv C$-Pt-$C\equiv C$ units on the polymer chains (Scheme 13). This functional unit has also been employed in the construction of supramolecules with various dimensions, shapes, and sizes.[86] In these types of polymers, π-conjugation is preserved due to the partial overlapping between the π-orbitals of the conjugated ligand and the Pt 5d orbitals. Early works on Pt-acetylide polymers were mainly focused on the synthetic methodology and the photophysical properties. Examples include conjugated Pt-acetylide polymers based on phenylene, thiophene,[87] pyridine, fluorene (polymer **25**),[88] and bithiazole (polymer **26**)[89] (Scheme 14).

The photosensitizing properties of some of these polymers under visible light irradiation were studied briefly.[89] Schanze et al. investigated the photophysical properties of the Pt-acetylide oligomers and polymers in more detail. A series of oligomer **24-*n*** (n = 2-5, 7) was synthesized by the successive coupling between the Pt-Cl moieties and the acetylide terminated building block using the convergent approach. These oligomers exhibit very rapid S_1-T_1 intersystem crossing, and it was suggested that the triplet excited state (T_1) was more localized than the singlet state (S_1).[90] Both experimental and theoretical results indicated that the triplet excited is localized within a single $-[PtL_2$-$C\equiv C$-C_6H_4-$C\equiv C$-$PtL_2]$ unit.[91] In another report, Pt-acetylide polymer **28** and its model compound **27** with thiophene moieties on the main chain were synthesized by similar methods. The polymer was blended with PCBM and fabricated into bulk heterojunction devices. The design rationale for devices based on these Pt based polymers is that the formation of a long-lived triplet state can lead to more efficient charge separation. Efficient quenching of the **28** emission from the triplet state by PCBM was observed, suggesting an electron (or energy) transfer process between these two moieties. Devices with the structure ITO/PEDOT:PSS/**28**:PCBM (1:4)/LiF/Al with different active layer thickness were fabricated. Under illumination of simulated solar light (AM1.5, 100 mW/cm^2), the highest power conversion efficiency was 0.27 %, and the I_{sc}, V_{oc}, and FF measured were 0.99 mA/cm^2, 0.64 V, and 0.43, respectively. In a later report, the synthesis of a thiophene-based Pt-acetylide **29** end capped with two C_{60} moieties was presented.[92] Results from transient absorption spectroscopy suggests that upon photo

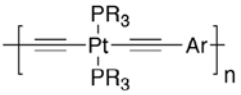

Ar = phenylene, pyridine, thiophene, or other heteroycles

SCHEME 13.

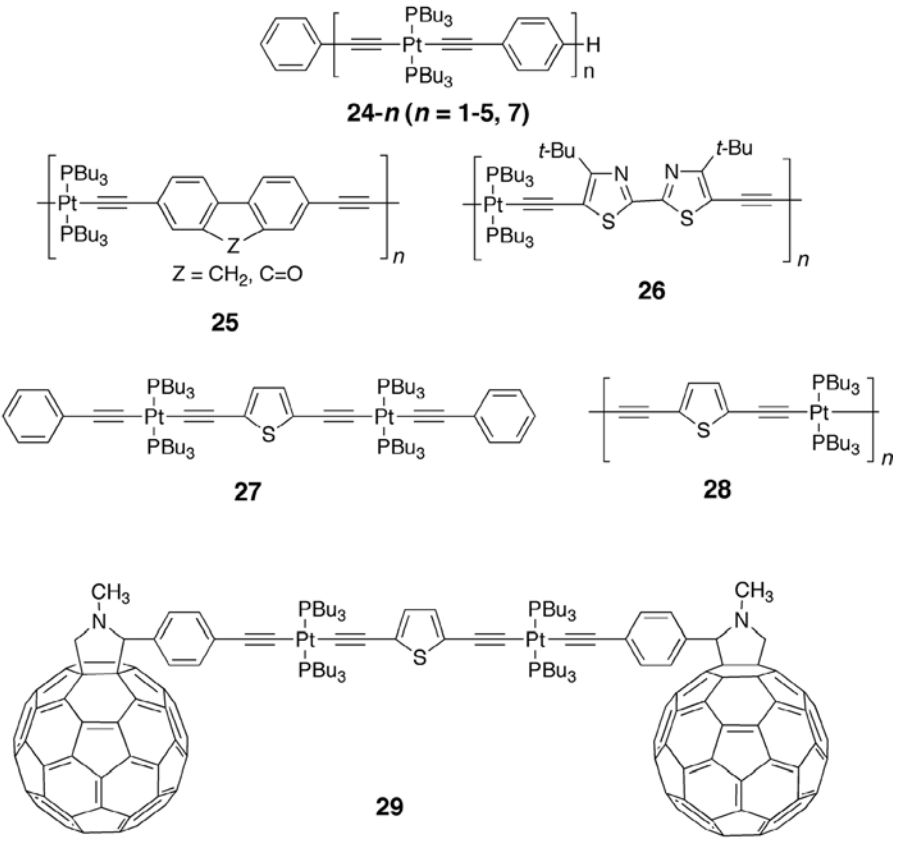

SCHEME 14.

excitation, a charge separated state is produced by photoinduced charge transfer process:

$$C_{60}\text{-}[Pt_2Th]^* - C_{60} \rightarrow C_{60}\text{-}[Pt_2Th^{+\bullet}] - C_{60}^{-\bullet} \quad (3)$$

Photovoltaic devices based on pure **29** and **29**:PCBM blend as the active layer is fabricated. It was interesting to observe that a device with pure **29** showed a higher power conversion efficiency (0.05%) compared to that consisting of a **29**/PCBM blend (0.0.0024% to 0.041%). The good performance in the photovoltaic cells with **29** only was attributed to the efficient charge separation process and that the material exhibits efficient hole and electron transport. The C_{60} moieties facilitated that electron transport, while the holes are transported via the hopping between Pt_2-thiophene units.

Another series of Pt acetylide based polymer **30** was synthesized by Wong et al. (Scheme 15).[93] The conjugated system is based on bithienyl benzothiadiazole,

and this polymer exhibits an strong absorption band centered at 554 nm, which is significantly lower than other phenylene or thiophene based Pt-acetylide polymers [**24-*n*** (n=7) exhibits an absorption peak maximum at 371 nm]. This absorption band was assigned to be the electronic transition to the charge transfer excited state, in which the -≡-Pt-≡- unit was the donor and the benzothiadiazole was the acceptor. As a result, it is possible to harvest the solar light in the red to near IR region more efficiently. Figure 6 shows the absorption and emission spectra of **30**. The polymer was blended with PCBM and fabricated into PV cell with the structure ITO/PEDOT:PSS/**30**:PCBM/Al. The current-voltage curve of the device is shown in Figure 7. A power conversion efficiency of 4.93% was measured (I_{sc}=15.43 mA/cm^2, V_{oc}=0.82 V, FF=0.39). The high efficiency was attributed to the enhancement in photosensitization in the longer wavelength region. This was confirmed by the plot of external quantum efficiency of the device as the function of wavelength (Figure 8).

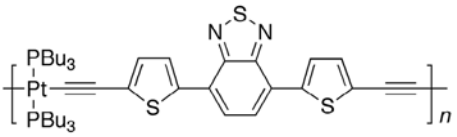

30

SCHEME 15.

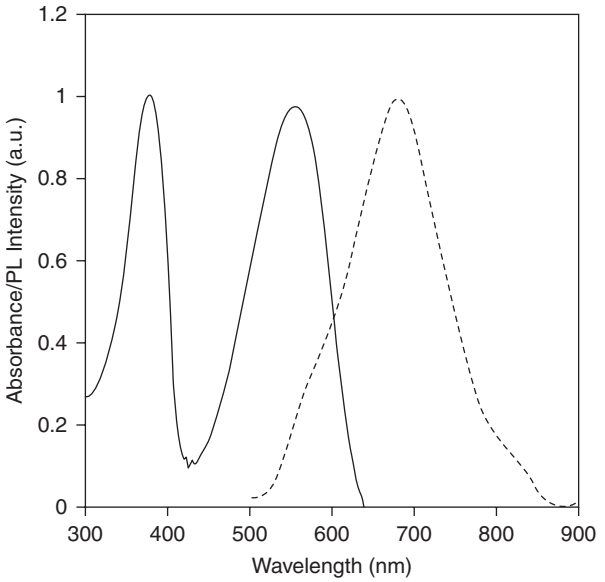

FIGURE 6. UV-VIS absorption and photoluminescence spectra of polymer **30**.

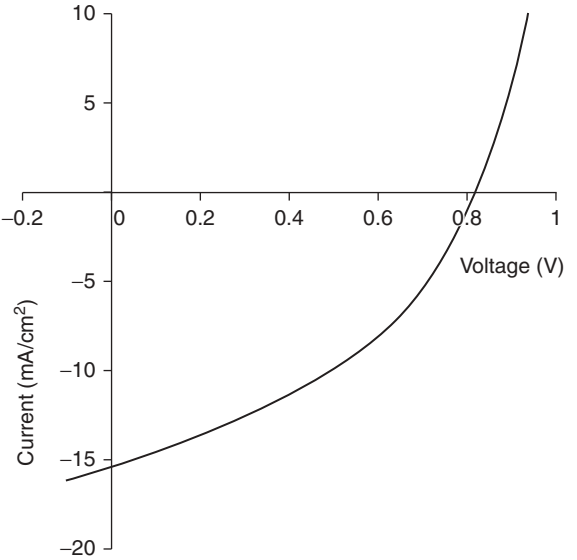

FIGURE 7. Current-voltage characteristic of the device ITO/PEDOT:PSS/polymer **3**0: PCBM/Al under illumination with simulated AM 1.5 solar light.

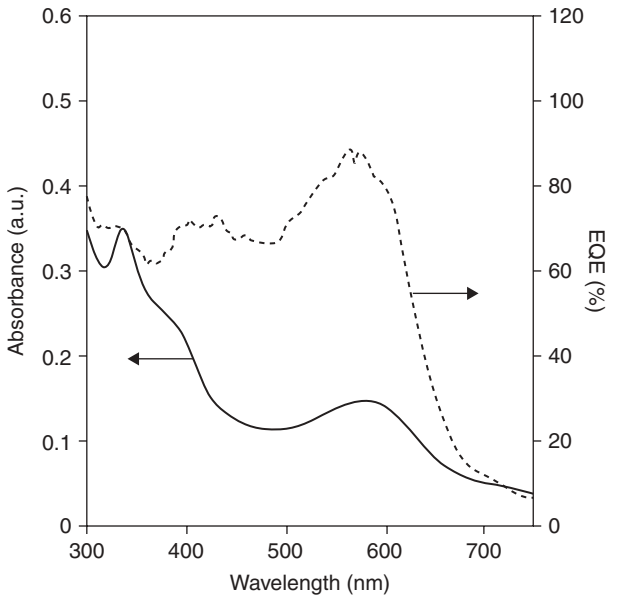

FIGURE 8. The external quantum efficiency of the device ITO/PEDOT:PSS/polymer **30**:PCBM/Al as a function of the incident light wavelength. The absorption spectrum of the device is shown for comparison.

The photovoltaic properties of other Pt-acetylide polymers **31** were published by the same group (Scheme 16). The aromatic linking units were modified, and the power conversion efficiency of the devices were in the range between 0.21% and 2.66%.[94] A review article dedicated to the optical properties of this group of Pt acetylide polymers has been published.[95]

vii. Other Metal Containing Polymers with Potential Photovoltaic Applications

In this section, some ruthenium complex containing polymers incorporated with charge transport functionalities are presented. Being incorporated with both photosensitizing and charge transport units in the same polymer molecule, they are considered promising candidates for polymeric photovoltaic cells. However, the photovoltaic properties have not been reported so far.

Polymer **32** (Scheme 17) was synthesized by the Stille coupling reaction between bis(tributyltin)quarterthiophene and the dibromo substituted ruthenium

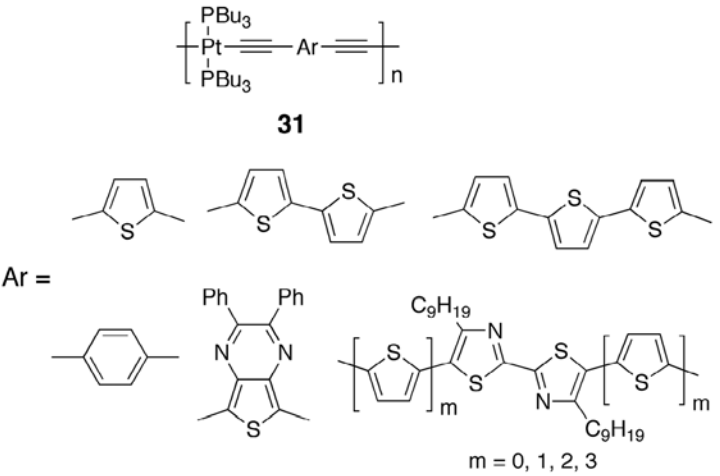

SCHEME 16.

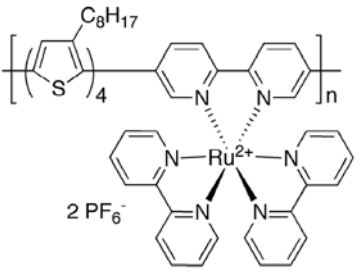

32

SCHEME 17.

complex.[96] The polymer exhibits broad absorption band spanning from 400 to 600 nm, which was explained to be due to the efficient delocalization of *p*-electrons on the main chain. Electrochemical experiments also revealed electronic interactions between the conjugated backbone and the ruthenium complexes.

Triphenylamine derivatives are known to be efficient hole transport materials and are widely used in organic light-emitting devices. Thelakkat et al. reported the synthesis of a 2,2-bipyridine ligand capped with poly(vinyltriphenylamine) at both ends.[97] The polymer chain was synthesized by the atom transfer radical polymerization of 4-bromostyrene using 4,4-bis (chloromethyl)bipyridine as the initiator (Scheme 18). The bromide groups were then replaced by diphenylamine in the presence of palladium catalyst. Polymer **33** was then obtained by the metalation reaction.

Schubert[98] proposed the potential use of several ruthenium containing polymers in photovoltaic devices. A ruthenium containing poly(ethylene glycol) derivative **34** was synthesized by the functionalization of 4-(3-aminopropyl)-4-methyl-2,2-bipyridine with poly(ethylene glycol) (M_n=2800, PDI=1.05), which was activated with *N,N*-carbonyldiimidazole (Scheme 19).[99] Applications in solid electrolytes for DSSC was proposed. Polyester **35** was incorporated with

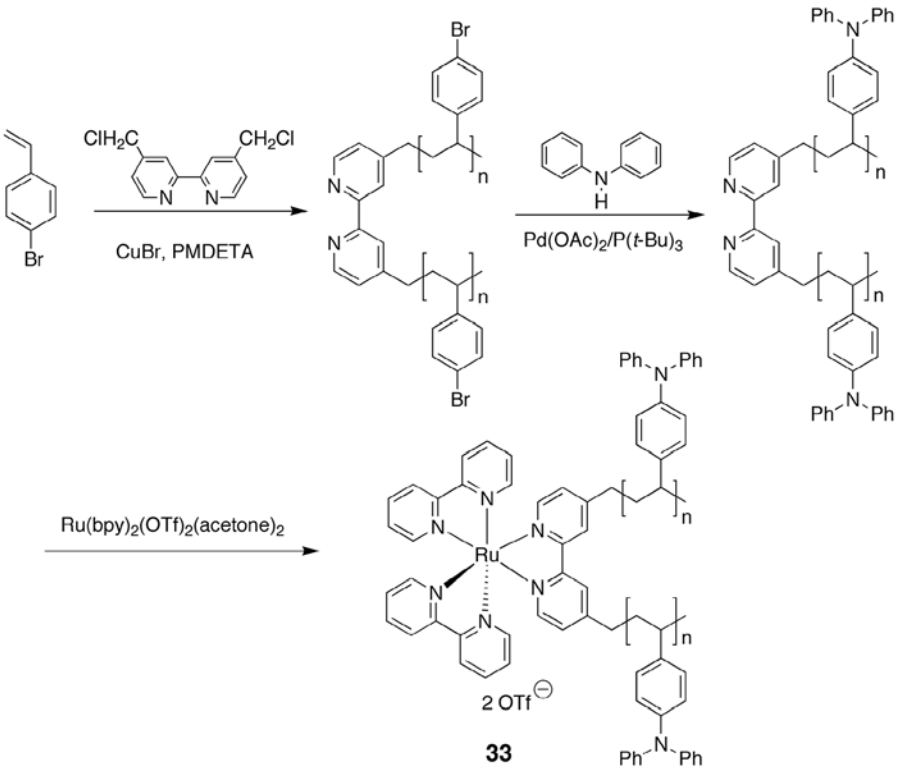

SCHEME 18.

ruthenium complex and was synthesized by the ring opening polymerization of ε-caprolactone.[100] In another report, methacrylate copolymers **36**–**38** with pendant ruthenium complexes were synthesized by radical chain copolymerization between the metal complex monomers and methyl methacrylate (Scheme 20).[101] All these polymers exhibit absorption originated from the MLCT transition of the

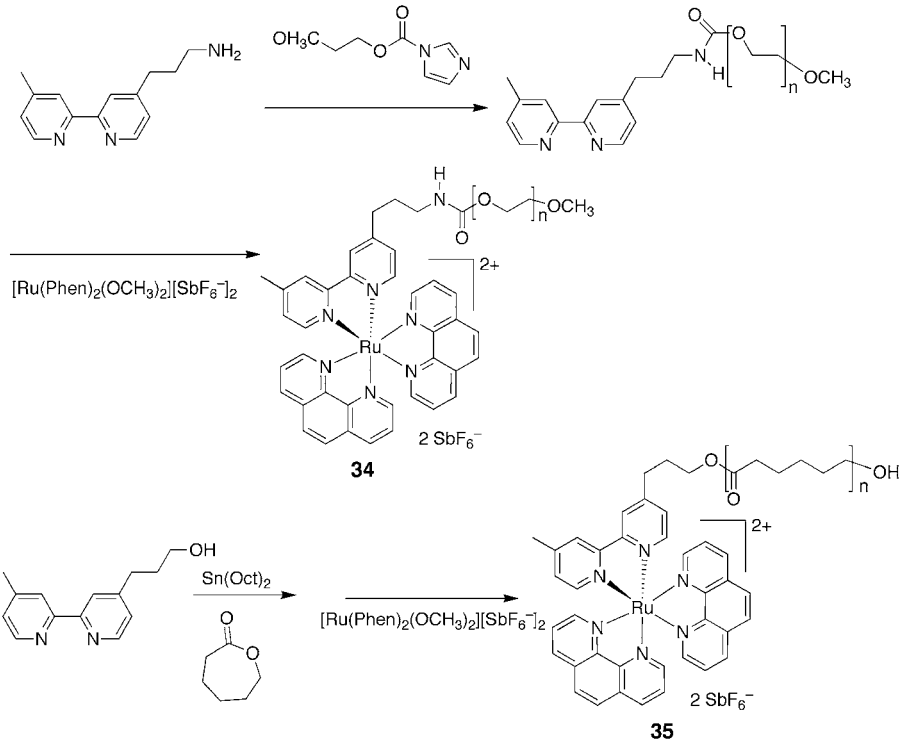

SCHEME 19.

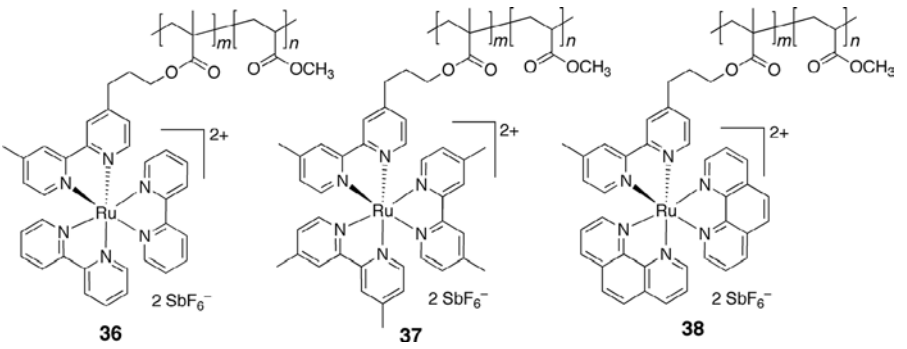

SCHEME 20.

Ru complexes, and it was suggested that they are potential candidates for active photovoltaic devices. However, the absence of charge transport units in the polymer also means that bilayer or multilayer polymers are required in the fabrication of the devices. Details of the photovoltaic properties were not presented.

V. SUMMARY

The application of metal containing polymers in dye-sensitized and organic thin film solar cells were reviewed. To date, the efficiencies of organic solar cells are still lower than those of the inorganic counterparts. The performance of organic solar cells is limited by several principal factors, such as spectral mismatch between the solar light spectrum and the absorption spectrum of polymers, lower charge carrier mobilities, and high charge recombination rate. At present, both DSSC and all organic solar cells have their own limitations. In DSSC, the nanocrystalline semiconductor facilitates the charge separation and transport process, but the rigidity of inorganic semiconductor and presence of electrolyte in the cell may impose a long-term stability problem. All-polymer solar cells provide large versatility and flexibility on the device fabrications. However, the long-term stability of organic molecules under exposure to sunlight may also be another critical issue to be considered. Development of new materials for the active layers, design of new device architecture, and fabrication of ordered electrode surface by nanotechnology may be the possible solutions to overcome these potential problems. Metal containing polymers possess both the advantages of molecular transition metal complexes and organic polymeric materials and are promising candidates for the multifunctional materials in the electrode modifying layer, charge transport layer, and sensitizing layers. Work done in this area is still sparse and more interdisciplinary research between science and engineering will be essential in the future.

VI. ACKNOWLEDGMENTS

Financial support from the Research Grants Council of The Hong Kong Special Administrative Region, China (project number 7008/07P and HKU7005/08P) is gratefully acknowledged.

VII. REFERENCES

1. N. S. Sariciftci, *Mater. Today,* **7,** *36* (2004).
2. R. A. J. Janssen, J. C. Hummelen, N. S. Saricifti, *MRS Bull.,* **30,** *33* (2005).
3. C. J. Brabec, N. S. Sariciftci, J. C. Hummelen, *Adv. Funct. Mater.,* **11,** *15* (2001).

4. C. Tang, *Appl. Phys. Lett.,* **48,** *183* (1986).
5. P. Peumans, A. Yakimov, S. R. Forrest, *J. Appl. Phys.,* **93,** *3693* (2003).
6. C. Brabec, *Sol. Energy Mater. Sol. Cells,* **83,** *273* (2004).
7. S. Günes, H. Neugebauer, N. S. Sariciftci, *Chem. Rev.,* **107,** *1324* (2007).
8. M. Grätzel, *Nature,* **414,** *338* (2001).
9. B. Oregan, M. Grätzel, *Nature,* **353,** *737* (1991).
10. A. Juris, V. Balzani, F. Barigelletti, S. Campagna, P. Belser, A. Von Zelewsky, *Coord. Chem. Rev.,* **84,** *85* (1988).
11. K. Kalyanasundaram, *Coord. Chem. Rev.,* **46,** *156*. (1982).
12. U. Bach, D. Lupo, P. Comte, J. E. Moser, F. Weissortel, J. Salbeck, H. Spreitzer, M. Grätzel, *Nature,* **395,** *583* (1998).
13. M. Grätzel, *J. Photochem. Photobio. C-Photochem. Rev.,* **4,** *145* (2003).
14. M. Grätzel, *MRS Bull.,* **30,** *23* (2005).
15. M. K. Nazeeruddin, P. Pechy, T. Renouard, S. M. Zakeeruddin, R. Humphry-Baker, P. Comte, P. Liska, L. Cevey, E. Costa, V. Shklover, L. Spiccia, G. B. Deacon, C. A. Bignozzi, M. Grätzel, *J. Am. Chem. Soc.,* **123,** *1613* (2001).
16. P. Wang, S. M. Zakeeruddin, R. Humphry-Baker, J. E. Moser, M. Grätzel, *Adv. Mater.,* **15,** *2101* (2003).
17. P. Wang, S. M. Zakeeruddin, J. E. Moser, R. P. Humphry-Baker, V. A. Comte, A. Hagfeldt, M. K. Nazeeruddin, M. Grätzel, *Adv. Mater.,* **16,** *1806* (2004).
18. C. Klein, M. K. Nazeeruddin, P. Liska, D. Di Censo, N. Hirata, E. Palomares, J. R. Durrant, M. Grätzel, *Inorg. Chem.,* **44,** *178* (2005).
19. M. K. Nazeeruddin, F. De Angelis, S. Fantacci, A. Selloni, G. Viscardi, P. Liska, S. Ito, B. Takeru, M. Grätzel, *J. Am. Chem. Soc.,* **127,** *16835* (2005).
20. Grätzel, M. *Inorg. Chem.* 2005, **44,** *6841*.
21. G. Yu, J. Gao, J. C. Hummelen, F. Wudl, A. J. Heeger, *Science,* **270,** *1789* (1995).
22. N. S. Sariciftci, D. Braun, C. Zhang, V. I. Srdanov, A. J. Heeger, G. Stucky, F. Wudl, *Appl. Phys. Lett.,* **62,** *585* (1993).
23. J. J. M. Halls, C. A. Walsh, N. C. Greenham, E. A. Marseglia, R. H. Friend, S. C. Moratti, A. B. Holmes, *Nature,* **376,** *498* (1995).
24. R. S. Smith, P. T. Jones, **34,** *16* (2009).
25. J. J. M. Halls, K. Pichler, R. H. Friend, S. C. Moratti, A. B. Holmes, *Appl. Phys. Lett.,* **68,** *3120* (1996).
26. M. Granstrom, K. Petritsch, A. C. Arias, A. Lux, M. R. Andersson, R. H. Friend, *Nature,* **395,** *257* (1998).
27. J. G. Xue, S. Uchida, B. P. Rand, S. R. Forrest, *Appl. Phys. Lett.,* **84,** *3013* (2004).
28. S. Berson, R. De Bettignies, S. Bailly, S. Guillerez, *Adv. Funct. Mater.,* **17,** *1377* (2007).
29. M. Koppe, M. Scharber, C. Brabec, W. Duffy, M. Heeney, I. McCulloch, *Adv. Funct. Mater.,* **17,** *1371* (2007).
30. Y. Kim, S. Cook, S. M. Tuladhar, S. A. Choulis, J. Nelson, J. R. Durrant, D. D. C. Bradley, M. Giles, I. McCulloch, C. S. Ha, M. Ree, *Nature Mater.,* **5,** *197* (2006).
31. W. L. Wang, H. B. Wu, C. Y. Yang, C. Luo, Y. Zhang, J. W. Chen, Y. Cao, *Appl. Phys. Lett.,* **90,** *183512* (2007).
32. M. Reyes-Reyes, K. Kim, D. L. Carroll, *Appl. Phys. Lett.,* **87,** *083506* (2005).
33. F. Padinger, R. S. Rittberger, N. S. Sariciftci, *Adv. Funct. Mater.,* **13,** *85* (2003).
34. Q. Zhou, Q. Hou, L. Zhang, X. Deng, G. Yu, Y. Cao, *Appl. Phys. Lett.,* **84,** *1653* (2004).
35. S. M. Tuladhar, D. Poplavskyy, S. A. Choulis, J. R. Durrant, D. D. C. Bradley, J. Nelson, *Adv. Funct. Mater.,* **15,** *1171* (2005).

36. S. E. Shaheen, C. J. Brabec, N. S. Sariciftci, F. Padinger, T. Fromherz, J. C. Hummelen, *Appl. Phys. Lett.,* **78,** *841* (2001).
37. C. J. Brabec, C. Winder, N. S. Sariciftci, J. C. Hummelen, A. Dhanabalan, P. A. van Hal, R. A. J. Janssen, *Adv. Funct. Mater.,* **12,** *709* (2002).
38. J. Peet, J. Y. Kim, N. E. Coates, W. L. Ma, D. Moses, A. J. Heeger, G. C. Bazan, *Nature Mater.,* **6,** *497* (2007).
39. C. Soci, I.-W. Hwang, D. Moses, Z. Zhu, D. Waller, R. Gaudiana, C. J. Brabec, A. J. Heeger, *Adv. Funct. Mater.,* **17,** *632* (2007).
40. D. Mühlbacher, M. Scharber, M. Morana, Z. Zhu, D. Waller, R. Gaudiana, C. C. Brabec, *Adv. Mater.,* **18,** *2884* (2006).
41. Z. Zhu, D. Waller, R. Gaudiana, M. Morana, D. Muhlbacher, M. Scharber, C. Brabec, *Macromolecules,* **40,** *1981* (2007).
42. J. Y. Kim, S. H. Kim, H.-H. Lee, K. Lee, W. Ma, X. Gong, A. J. Heeger, *Adv. Mater.,* **18,** *572* (2006).
43. J. Y. Kim, K. Lee, N. E. Coates, D. Moses, T.-Q. Nguyen, M. Dante, A. J. Heeger, *Science,* **317,** *222* (2007).
44. J. Boucle, P. Ravirajan, J. Nelson, *J. Mater. Chem.,* **17,** *3141* (2007).
45. V. Duprez, M. Biancardo, H. Spanggaard, F. C. Krebs, *Macromolecules,* **38,** *10436* (2005).
46. V. Duprez, M. Biancardo, F. C. Krebs, *Sol. Energy Mater. Sol. Cells,* **91,** *230* (2007).
47. S. A. Sapp, C. M. Elliott, C. Contado, S. Caramori, C. A. Bignozzi, *J. Am. Chem. Soc.,* **124,** *11215* (2002).
48. F. C. Krebs, M. Biancardo, *Sol. Energy Mater. Sol. Cells,* **90,** *142*(2006).
49. W. Lee, K. H. Hyung, Y. H. Kim, G. Cai, S. H. Han, *Electrochem. Commun.,* **9,** *729* (2007).
50. K. Murakoshi, R. Kogure, Y. Wada, S. Yanagida, *Chem. Lett., 471* (1997).
51. T. Kitamura, M. Maitani, M. Matsuda, Y. Wada, S. Yanagida, *Chem. Lett.,* **9,** *1054* (2001).
52. Y. Saito, T. Azechi, T. Kitamura, Y. Hasegawa, Y. Wada, S. Yanagida, *Coord. Chem. Rev.,* **248,** *1469* (2004).
53. A. J. Mozer, Y. Wada, K. J. Jiang, N. Masaki, S. Yanagida, S. N. Mori, *Appl. Phys. Lett.,* **89 (**2006).
54. J. Faiz, A. I. Philippopoulos, A. G. Kontos, P. Falaras, Z. Pikramenou, *Adv. Funct. Mater.,* **17,** *54* (2007).
55. P. W. Cyr, E. J. D. Klem, E. H. Sargent, I. Manners, *Chem. Mater.* **17,** *5770* (2005).
56. P. D. Harvey, *Coord. Chem. Rev.,* **219,** *17* (2001).
57. D. Fortin, M. Drouni, M. Turcotte, P. D. Harvey, *J. Am. Chem. Soc.,* **119,** *531* (1997).
58. P. D. Harvey, D. Fortin, *Coord. Chem. Rev.,* **171,** *351* (1998).
59. J. K. Lee, D. Yoo, M. F. Rubner, *Chem. Mater.,* **9,** *1710* (1997).
60. C. T. Wong, W. K. Chan, *Adv. Mater.,* **11,** *455* (1999).
61. W. K. Chan, P. K. Ng, X. Gong, S. J. Hou, *J. Mater. Chem.,* **9,** *2103* (1999).
62. W. Y. Ng, W. K. Chan, *Adv. Mater.,* **9,** *716* (1997).
63. W. K. Chan, X. Gong, W. Y. Ng, *Appl. Phys. Lett.,* **71,** *2919* (1997).
64. P. K. Ng, X. Gong, S. H. Chan, L. S. M. Lam, W. K. Chan, *Chem. J. Eur.,* **7,** *4358* (2001).
65. S. C. Yu, X. Gong, W. K. Chan, *Macromolecules,* **31,** *5639* (1998).
66. S. C. Yu, S. J. Hou, W. K. Chan, *Macromolecules,* **32,** *5251* (1999).
67. S. C. Yu, S. J. Hou, W. K. Chan, *Macromolecules,* **33,** *3259* (2000).
68. W. Y. Ng, X. Gong, W. K. Chan, *Chem. Mater.,* **11,** *1165* (1999).

69. S. H. Chan, L. S. M. Lam, C. W. Tse, K. Y. K. Man, W. T. Wong, A. B. Djurisic, W. K. Chan, *Macromolecules,* **36,** *5482* (2003).
70. G. Decher, J. D. Hong, J. Schmitt, *Thin Solid Films,* **210211,** *831* (1992).
71. G. Decher, *Science,* **277,** *1232* (1997).
72. H. Mattoussi, M. F. Rubner, F. Zhou, J. Kumar, S. K. Tripathy, L. Y. Chiang, *Appl. Phys. Lett.,* **77,** *1540* (2000).
73. J. K. Mwaura, M. R. Pinto, D. Witker, N. Ananthakrishnan, K. S. Schanze, J. R. Reynolds, *Langmuir,* **21,** *10119* (2005).
74. K. Y. K. Man, H. L. Wong, W. K. Chan, C. Y. Kwong, A. B. Djurisic, *Chem. Mater.,* **16,** *365* (2004).
75. K. Y. K. Man, H. L. Wong, W. K. Chan, A. B. Djurisic, E. Beach, S. Rozeveld, *Langmuir,* **22,** *3368*. (2006).
76. H. L. Wong, L. S. M. Lam, K. W. Cheng, K. Y. K. Man, W. K. Chan, C. Y. Kwong, A. B. Djurisic, *Appl. Phys. Lett.,* **84,** *2557* (2004).
77. H. L. Wong, C. S. K. Mak, W. K. Chan, A. B. Djurisic, *Appl. Phys. Lett.,* **90 (**2007).
78. K. Y. K. Man, C. W. Tse, K. W. Cheng, A. B. Djurisic, W. K. Chan, *J. Inorg. Organometal. Polym. Mater.,* **17,** *223* (2007).
79. M. Zhang, P. Lu, X. M. Wang, H. Xia, W. Zhang, B. Yang, L. L. Liu, L. Yang, M. Yang, Y. G. Ma, J. K. Feng, D. J. Wang, *Thin Solid Films,* **477,** *193* (2005).
80. C. W. Tse, K. W. Cheng, W. K. Chan, A. B. Djurisic, *Macromol. Rapid Commun.,* **25,** *1335* (2004).
81. C. W. Tse, Y. H. Leung, K. H. Tam, W. K. Chan, A. B. Djurisic, *Nanotechnology,* **17,** *3563* (2006).
82. C. W. Tse, K. Y. K. Man, K. W. Cheng, C. S. K. Mak, W. K. Chan, C. T. Yip, Z. T. Liu, A. B. Djurisic, *Chem. Eur. J.,* **13,** *328* (2007).
83. C. W. Tse, K. W. Cheng, W. K. Chan, *J. Inorg. Organometal. Polym. Mater.,* **18,** *59* (2008).
84. K. W. Cheng, C. S. K. Mak, W. K. Chan, A. M. C. Ng, A. B. Djurisic, *J. Polym. Sci. Part A: Polym. Chem.,* **46,** *1305* (2008).
85. C. C. Frazier, S. Guha, W. P. Chen, M. P. Cockerham, P. L. Porter, E. A. Chauchard, C. H. Lee, *Polymer,* **28,** *553* (1987).
86. P. L. Porter, S. Guha, K. Kang, C. C. Frazier, *Polymer,* **32,** *1756* (1991).
87. P. Siemsen, U. Gubler, C. Bosshard, P. Günter, F. Diederich, *Chem. Eur. J.,* **7,** *1333* (2001).
88. N. Chawdhury, A. Kohler, R. H. Friend, M. Younus, N. J. Long, P. R. Raithby, J. Lewis, *Macromolecules,* **31,** *722* (1998).
89. J. Lewis, P. R. Raithby, W.-Y. Wong, *J. Organomet. Chem.,* **556,** *219* (1998).
90. W. Y. Wong, S. M. Chan, K. H. Choi, K. W. Cheah, W. K. Chan, *Macromol. Rapid Commun.,* **21,** *453* (2000).
91. Y. Liu, S. Jiang, K. Glusac, D. H. Powell, D. F. Anderson, K. S. Schanze, *J. Am. Chem. Soc.,* **124,** *12412* (2002).
92. K. Glusac, M. E. Kose, H. Jiang, K. S. Schanze, *J. Phys. Chem. B,* **111,** *929* (2007).
93. F. Q. Guo, K. Ogawa, Y. G. Kim, E. O. Danilov, F. N. Castellano, J. R. Reynolds, K. S. Schanze, *Phys. Chem. Chem. Phys.,* **9,** *2724* (2007).
94. W. Y. Wong, X. Z. Wang, Z. He, A. B. Djurisic, C. T. Yip, K. Y. Cheung, H. Wang, C. S. K. Mak, W. K. Chan, *Nature Mater.,* **6,** *521* (2007).
95. W. Y. Wong, *Macromol. Chem. Phys.,* **209,** *14* (2008).
96. W. Y. Wong, *Dalton Trans., 4495* (2007).
97. L. Trouillet, A. De Nicola, S. Guillerez, *Chem. Mater.,* **12,** *1611* (2000).
98. K. Peter, M. Thelakkat, *Macromolecules,* **36,** *1779* (2003).

99. V. Marin, E. Holder, R. Hoogenboom, U. S. Schubert, *Chem. Soc. Rev.,* **36,** *618* (2007).
100. V. Marin, E. Holder, M. A. R. Meier, R. Hoogenboom, U. S. Schubert, *Macromol. Rapid Commun.,* **25,** *793* (2004).
101. V. Marin, E. Holder, R. Hoogenboom, U. S. Schubert, *J. Polym. Sci. Part A: Polym. Chem.,* **42,** *4153* (2004).
102. V. Marin, E. Holder, U. S. Schubert, *J. Polym. Sci. Part A: Polym. Chem.,* **42,** *374* (2004).

CHAPTER 5

Functional Silole-Containing Polymers

Junwu Chen,[1] Yong Cao,[1] and Ben Zhong Tang[2]

[1]*Institute of Polymer Optoelectronic Materials & Devices, South China University of Technology, Guangzhou, China, 510640*

[2]*Department of Chemistry, The Hong Kong University of Science & Technology, Clear Water Bay, Kowloon, Hong Kong, China*

CONTENTS

Macromolecules Containing Metal and Metal-like Elements,
Volume 10: Photophysics and Photochemistry of Metal-Containing Polymers,
Edited by Alaa S. Abd-El Aziz, Charles E. Carraher Jr., Pierre D. Harvey, Charles U. Pittman Jr., Martel Zeldin.

I. INTRODUCTION

Semiconducting polymers have drawn broad attention due to their important applications in polymeric light-emitting diodes (PLEDs),[1,2] photovoltaic cells (PVCs),[3] field-effect transistors (FETs),[4] and chemosensing abilities to various targets.[5] Solution processing of the semiconducting polymers, such as spin coating and printing, is the attracting advantage for the fabrications of large area optoelectronic devices. Semiconducting polymers are the best candidates to be used to fabricate flexible optoelectronic devices.[6] A notable feature of semiconducting polymers also lies in the enormous versatility of synthetic methodology, which affords wide space to construct new polymers with improved properties.

Siloles[7,8] or silacyclopentadienes are a group of five-membered silacyclics that possess $\sigma^*-\pi^*$ conjugation arising from the interaction between the σ^* orbital of two exocyclic σ-bonds on the silicon atom and the π^* orbital of the butadiene moiety.[9] The calculated LUMO level of a silole ring is lower than those of other heterocyclopentadienes, such as pyrrole, furan, and thiophene.[7,9] The unique aromaticity and the low-lying LUMO level endue siloles with intriguing optoelectronic properties. Siloles, in terms of their structures, may be simply and arbitrarily classified as two types, substituted siloles **1** and siloles fused with other aromatic rings (Fig. 1).[10] Up to six substituents can be attached to the silole ring of **1**, which opens a big room to tune the optoelectronic properties; 2,3,4,5-tetraarylsiloles, normally possessing noncoplanar geometry, are the widely studied and the most important group of **1**.[11–17]

Many important photophysical properties, such as aggregation-induced emission (AIE),[11,12] blue shift of PL emission in the crystal state relative to that of amorphous solid,[13] extremely high photoluminescence (PL) quantum yields

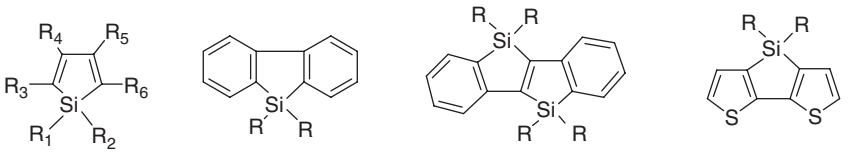

1 **2** **3** **4**

FIGURE 1. Chemical structures of siloles.

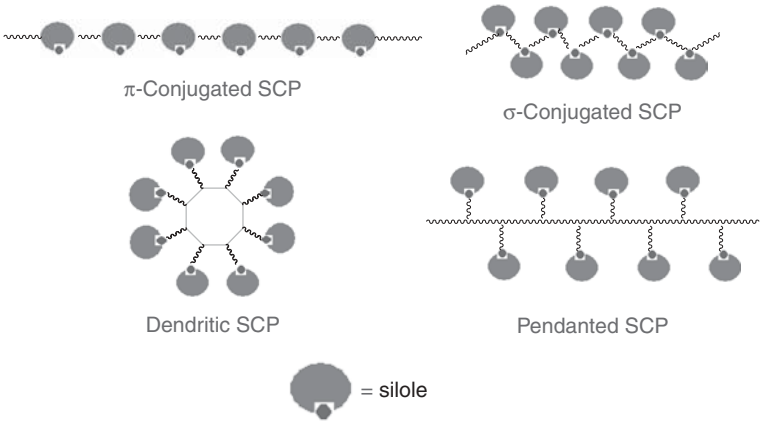

FIGURE 2. Schematic constructions of SCPs.

even in a crystalline form,[13] high external quantum efficiency (η_{EL}) up to 8% in electroluminescence (EL) devices,[14] high electron mobility of 2×10^{-4} $cm^2/(V\ s)$,[15] and fluorescent chemosensor for explosives and organic solvent vapors,[16,17] have been reported for 2,3,4,5-tetraarylsiloles. As shown in Figure 1, dibenzosilole or 9-silafluorene **2**,[18] bis-silicon-bridged stilbene **3**,[19] and dithienosilole or silicon-bridged bithiophene **4**,[20] with enlarged coplanar skeletons, are the typical examples of siloles fused with other aromatic rings.

The incorporation of siloles in polymers is of interest and importance in chemistry and functionalities. Some optoelectronic properties, impossible to obtain in silole small molecules, may be realized with silole-containing polymers (SCPs). The first synthesis of SCPs was reported in 1992.[21] Since then, different types of SCPs, such as main chain type π-conjugated SCPs catenated through the aromatic carbon of a silole, main chain type σ-conjugated SCPs catenated through the silicon atom of a silole, SCPs with silole pendants, and hyperbranched or dendritic SCPs (Fig. 2), have been synthesized.[10] In this chapter, the functionalities of SCPs, such as band gap, photoluminescence, electroluminescence, bulk-heterojunction solar cells, field effect transistors, aggregation-induced emission, chemosensors, conductivity, and optical limiting, are summarized.

II. ELECTRONIC TRANSITION AND BAND GAP

Polydibenzosiloles are wide band gap SCPs. Poly(3,6-dibenzosilole)s **5** (Fig. 3) show absorptions peaks (λ_{ab}) at $\sim$283 nm and absorption edges at $\sim$310 nm in solutions as well as in thin films.[22] The calculated optical band gaps of poly(3,6-dibenzosilole)s are 4.0 eV, which is the widest band gap so far

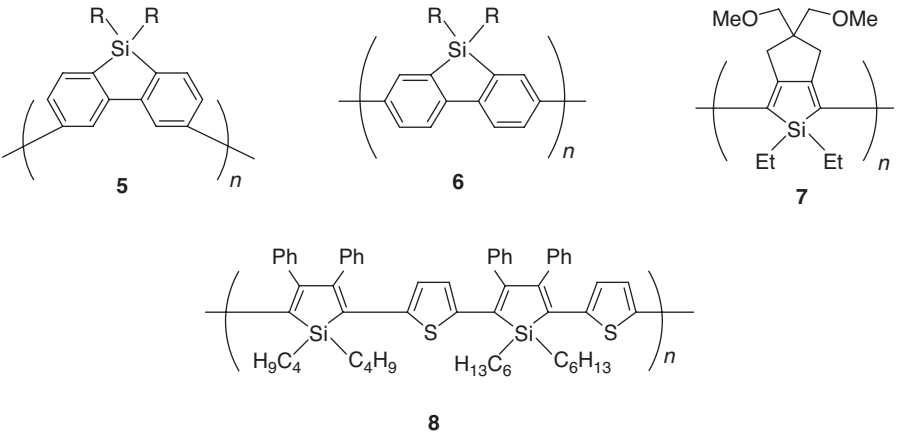

FIGURE 3. Chemical structures of **5**–**8**.

reported for conjugated polymers. The results also suggest that poly(3,6-dibenzosilole)s possess high triplet energy levels. The oxidation onsets of poly(3,6-dibenzosilole)s are at 1.7 V in CV scans, giving estimated HOMO levels of −6.1 eV. The film of poly(2,7-dibenzosilole) **6** shows a λ_{ab} of 390 nm, which is comparable to that of poly(9,9-dioctyl-2,7-fluorene) (PF8).[23] Compared with poly(3,6-dibenzosilole), poly(2,7-dibenzosilole) possesses longer conjugation length.

Poly(2,5-silole) **7** shows a λ_{ab} of 482 nm at room temperature.[24] A band gap of the polymer, if calculated with the absorption edge (650 nm), is 1.9 eV. A silole-thiophene alternating copolymer **8** can show a further decreased band gap.[25] The copolymer displays a broad absorption spectrum with λ_{ab} at 648 nm in chloroform. The calculated band gap from the absorption edge is only 1.55 eV, a very small value so far reported for the synthesized SCPs.

Other SCPs, including many types of copolymers, possess band gaps between 4.0 and 1.55 eV. The largely varied electron transitions and band gaps of SCPs imply that the optoelectronic properties of SCPs could be tuned.

III. LIGHT EMISSION

A. Photoluminescence

The photoluminescence spectra of SCPs can be greatly tuned through the molecular design of their chemical structures. The photoluminescence can vary from a UV light to a red light.

Because they have the largest band gap among SCPs, poly(3,6-dibenzosilole)s **5** are expected to show fluorescence at the shortest wavelength. Under

excitations at 325 nm, poly(3,6-dibenzosilole)s emit UV lights with emission maxima (λ_{PL}) of 355–360 nm in solutions as well as in films.[22] Under the same excitation, the film of poly(2,7-dibenzosilole) **6** can show stable blue light (CIE coordinates $x = 0.15$, $y = 0.11$) with a λ_{PL} at 425 nm.[23] The photoluminescence is quite efficient, with the absolute PL quantum yield of 62%. A random copolymer **9** (Fig. 4) derived from 3,6- and 2,7-dibenzosiloles also shows a λ_{PL} at ~425 nm, with a absolute PL quantum yield of 83%.[26] Similar stable blue fluorescence can also, be achieved from copolymers **10** derived from 3,6-dibenzosilole and 2,7-fluorene.[27]

Highly efficient green photoluminescence has also been realized from SCPs. Copolymers **11** (Fig. 5) derived from 2,7-fluorene and 2,3,4,5-tetraphenylsilole show absolute PL quantum yields up to 84%.[28] A well-defined alternating copolymer **12** with a repeating unit made up of ter-(2,7-fluorene) and 2,5-silole possesses an absolute PL quantum yield > 80%.[29] SCPs **13** with a main chain structure of 3,6-carbazole-2,7-fluorene-2,5-silole also show absolute PL quantum yields up to 86%.[30] An energy transfer copolymer **14** of 2,7-dibenzosilole and

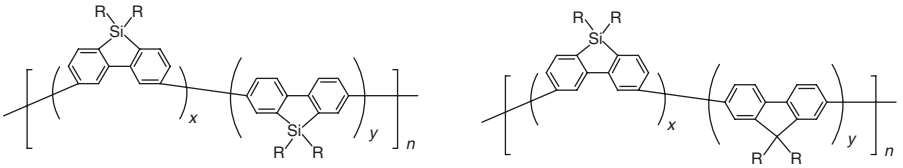

FIGURE 4. Chemical structures of **9** and **10**.

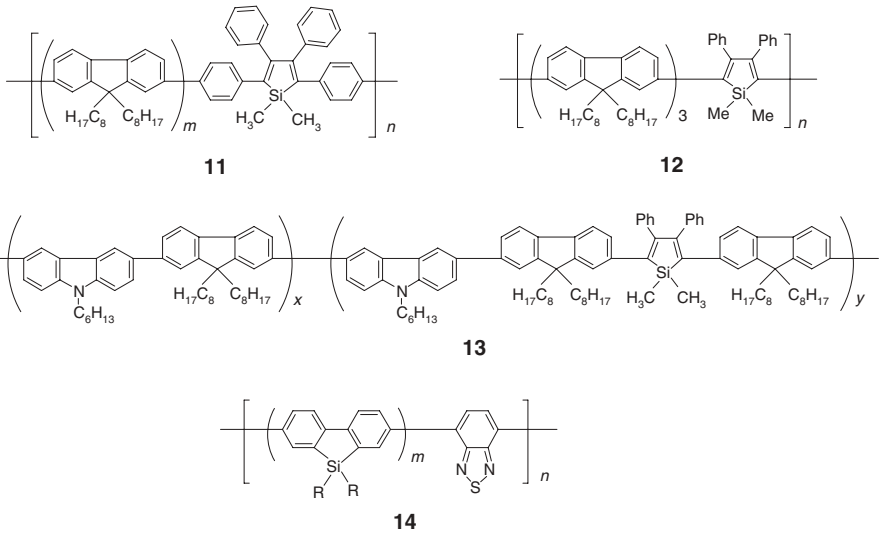

FIGURE 5. Chemical structures of **11**–**14**.

2,1,3-benzothiadiazole displays a green emission with an absolute PL quantum yield of 52%.[26]

Copolymers **15** (Fig. 6) derived from 2,7-fluorene and 2,5-dithienylsilole show red fluorescence via an energy transfer process.[31] The λ_{PL} could be 591 nm for copolymers with higher contents of 2,5-dithienylsilole. The absolute PL quantum yields (<30%) of the copolymers are somewhat lower than the green fluorescent SCPs. A copolymer **16** derived from 2,7-dibenzosilole and 4,7-dithienyl-2,1,3-benzothiadiazole show a better red fluorescence.[26] The λ_{PL} of the copolymer is at 629 nm, with an absolute PL quantum yield of 53%.

B. Electroluminescence

Due to the large band gap and high triplet energy level of the poly(3, 6-dibenzosilole) **5**, the copolymer is an excellent host for the fabrication of blue polymer phosphorescent light-emitting diodes. A high external quantum efficiency (η_{EL}) of 4.8% and a luminance efficiency of 7.2 cd/A at 644 cd/m^2 have been achieved for blue phosphorescence devices (emission peak (λ_{EL}) at 462 nm, CIE coordinates $x = 0.15$, $y = 0.26$). The performances of the devices are much better than those reported for blue phosphorescent devices with poly(*N*-vinylcabarzole) (PVK) as the host.[32]

Copolymers **10** derived from 3,6-dibenzosilole and 2,7-fluorene are blue electroluminescent SCPs.[27] When the copolymers are used as the emissive layer in EL devices, highly efficient pure blue emissions with CIE coordinates of ($x = 0.16$, $y = 0.07$), a η_{EL} of 3.34%, and a luminance efficiency of 2.02 cd/A at 326 cd/m^2 are achieved from the copolymer with 90% fluorene content. The blue color matches the NTSC blue standard ($x = 0.14$, $y = 0.08$) quite well. The EL spectral stability of the devices is quite good, even under operation at elevated temperatures. Copolymer **9** derived from 3,6- and 2,7-dibenzosiloles also exhibits high performance with a η_{EL} of 1.95%, a luminous efficiency of 1.69 cd/A, and a maximal brightness of 6000 cd/m^2, with the CIE coordinates of ($x = 0.162$, $y = 0.084$).[26]

Copolymers **11** derived from 2,7-fluorene and 2,3,4,5-tetraphenylsilole are green electroluminescent SCPs.[28] The EL spectra of the copolymers show exclusive green emissions (λ_{EL} ~528 nm) from the silole units, which are almost not changed with the copolymer compositions. A maximum η_{EL} of 1.51% can be achieved with the copolymers as the emissive layer in EL devices.

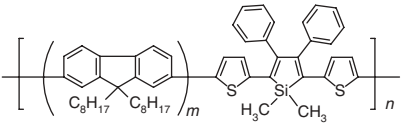

15

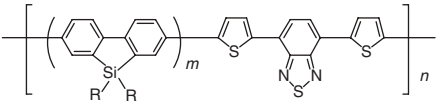

16

FIGURE 6. Chemical structures of **15** and **16**.

Green electroluminescence is also achieved from the well-defined alternating copolymer **12** with a repeating unit made up of ter-(2,7-fluorene) and 2, 5-silole.[29] With its neat film as the emissive layer, the EL device shows a maximum η_{EL} of 0.47%, but the device performance can be largely improved to a maximum η_{EL} of 1.99% when using a copolymer/PF8 blend film as the emissive layer. Copolymer **14** derived from 2,7-dibenzosilole and 2,1,3-benzothiadiazole is also an excellent green EL polymer.[26] A maximum η_{EL} of 3.81% can be realized in EL devices.

Copolymers **17** (Fig. 7) derived from 3,6-carbazole and 2,3,4,5-tetraphenylsilole possess HOMO levels between −5.15 eV and −5.34 eV, matching good hole injections from ITO anode (work function about −4.7 eV).[33] Single-layer green EL devices with a simple configuration of ITO/copolymer/Ba/Al show η_{EL} of 0.77% at a practical brightness of 333 cd/m^2. Copolymers **13** derived from 3,6-carbazole, 2,7-fluorene, and 2,5-silole possess HOMO levels of about −5.35 eV.[30] Since the HOMO level of 1,3,5-tris(*N*-phenylbenzimidizol-2-yl)benzene (TPBI) is −6.2 eV,[34] it is expected that effective hole blocking may be achieved in a device configuration of ITO/PEDOT/copolymer/TPBI/Ba/Al. The hole blocking by the TPBI layer can significantly improve the EL efficiency, a high maximum η_{EL} of 3.03% and maximum luminous efficiency (LE_{max}) of 7.59 cd/A can be achieved from the device configuration, compared to a η_{EL} of 0.48% and a LE_{max} of 1.20 cd/A for an EL device without the TPBI layer.[30]

Copolymers **15** derived from 2,7-fluorene and 2,5-dithienylsilole are red electroluminescent SCPs.[31] The EL devices with the copolymers as the emissive layer can display red light emissions with λ_{EL} up to 638 nm. The maximum η_{EL} of the devices can reach 0.89%. Copolymer **18** derived from 2,7-fluorene and

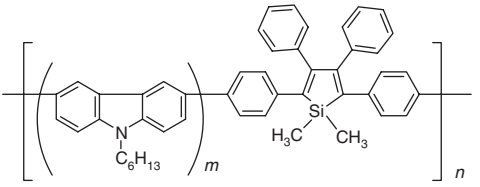

17

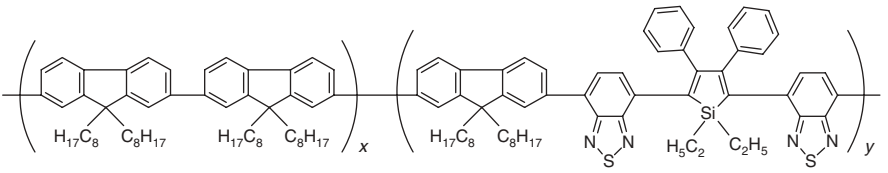

18

FIGURE 7. Chemical structures of **17** and **18**.

bis(2,1,3-benzothiadiazolyl)silole displays red light emissions with λ_{EL} of 601 nm.[35] With its neat film as the emissive layer, the EL device shows a maximum η_{EL} of 0.51%, but the device performance can be improved to a maximum η_{EL} of 1.37% when using a copolymer/PF8 blend film as the emissive layer. With the copolymer **16** derived from 2,7-dibenzosilole and 4,7-dithienyl-2,1,3-benzothiadiazole as the emissive layer, good device performance with a maximum η_{EL} of 2.89% is achieved for a saturated red EL ($\lambda_{EL} = 643$ nm).[26]

White electroluminescence from a single polymer that can display simultaneous blue, green, and red (RGB) emission is a promising candidate for use in a full-color display with a color filter and a backlight for a liquid-crystal display (LCD). Three-color white electroluminescence has been reported for an SCP (Fig. 8).[36] When small amounts of a green-emissive 2,5-diphenylsilole and a red-emissive 2,5-dithienylsilole are incorporated in the blue-emissive PF8 backbone, efficient and stable white light EL from a single polymer with a simultaneous RGB emission can be realized. The CIE coordinates ($x = 0.33$, $y = 0.36$) of the white light EL spectra are very close to ($x = 0.33$, $y = 0.33$) for pure white light. The relative intensities for the three RGB peaks, at 450, 505, and 574 nm, are 0.94, 1, and 0.97, respectively, showing a balanced simultaneous RGB emission. The EL device displays a maximum luminous efficiency of 2.03 cd/A for a brightness of 344 cd/m^2 and a luminous efficiency of 1.86 cd/A for a more practical brightness of 2703 cd/m^2.

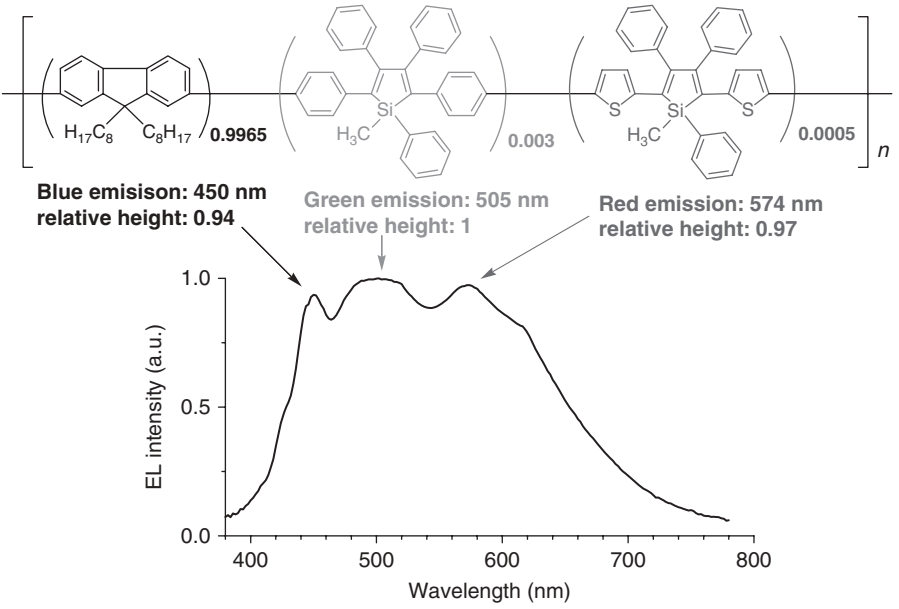

FIGURE 8. A SCP showing three-color white electroluminescence and its electroluminescent spectrum.

IV. BULK-HETEROJUCTION PHOTOVOLTAIC CELLS

In a bulk-heterojunction photovoltaic cell with methanofullerene [6,6]-phenyl C61-butyric acid methyl ester (PCBM) as an electron acceptor, alternating copolymer **19** (Fig. 9), derived from 2,7-fluorene and 2,5-dithienylsilole, can show impressive performance as the electron donor.[31] In a device configuration of ITO/PEDOT/active layer/Ba/Al, the dark current density−bias curve shows a small leakage current, suggesting a continuous, pinhole-free active layer in the device. Under illumination of an AM1.5 solar simulator at 100 mW/cm^2, a high short-circuit current of 5.4 mA/cm^2, an open-circuit voltage of 0.7 V, and a fill factor of 31.5% are achieved. The calculated energy conversion efficiency is 2.01%.

Alternating copolymer **20** derived from 2,7-dibenzosilole and 4,7-dithienyl-2,1,3-benzothiadiazole is an outstanding polymeric electron donor in photovoltaic cells.[37] With an active layer made up of copolymer to PCBM in a 1:2 ratio, the solar cell displays a high short-circuit current of 9.5 mA/cm^2, an open-circuit voltage of 0.9 V, and a fill factor of 50.7%, under illumination of an AM1.5 solar simulator at 80 mW/cm^2. The calculated energy conversion efficiency is 5.4%, which is one of the highest efficiencies so far reported for polymeric photovoltaic cells.

V. FIELD EFFECT TRANSISTORS

Carrier mobilities play an important role in bulk-heterojunction photovoltaic cells. The alternating copolymer **19**, should possess enough high hole mobility based on its good electron donor performance in the photovoltaic cell.[31] In a FET device with a top contact configuration of ITO/polyacrylonitrile (PAN)/copolymer/Au, the drain current of the device could reach saturation along with drain voltage, at different gate voltages. From the transfer characteristics of the device, the hole mobility of the copolymer is estimated to be 4.5×10^{-5} cm^2/V s.

In a FET device with highly doped Si as the gate and SiO_2 as the gate insulator, the hole mobility of the alternating copolymer **20** was measured.[37]

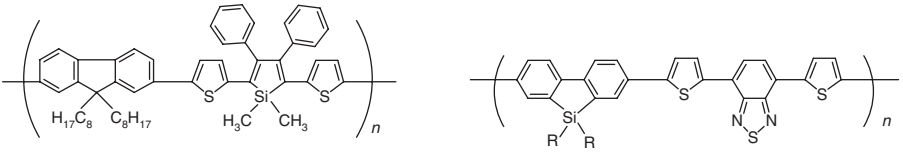

19 **20**

FIGURE 9. Chemical structures of **19** and **20**.

The hole mobility of the copolymer is 1×10^{-3} cm^2/V s, which well supports its outstanding photovoltaic performance.

Dithienosilole-thiophene copolymers **21** (Fig. 10) can show excellent FET performances.[38] With the copolymers as the active layer, remarkably high hole mobility from 0.02 to 0.06 cm^2/(V s) can be achieved. Furthermore, the FET devices possess high current on/off ratios of $\sim 10^5 - 10^6$. The FET devices also display impressive stabilities under repeated on/off cycles up to 2000 in air.

VI. AGGREGATION-INDUCED EMISSION

2,3,4,5-Tetraphenylsiloles **22** (Fig. 11) are the prototype that exhibit aggregation-induced emission (AIE) behavior.[12] They are virtually nonemissive in solution, but their aggregates or solid films are highly luminescent, several hundreds times enhancement of the fluorescence of the aggregated phase to the solution can be found. 2,3,4,5-Tetraphenylsilole-containing polyacetylenes **23** are the only examples of polymers that replay the AIE behavior.[39] Under excitation, the polymers emit faint lights in chloroform solutions, with PL quantum yields as low as 0.5%, but the PL quantum yields for nanoaggregates formed in the 90% methanol mixture can be elevated to 9.25%, which is ~ 46 times that of the chloroform solution. The long flexible spacer of the non-anyloxy group decoupled the silole pendants from the rigid polyacetylene

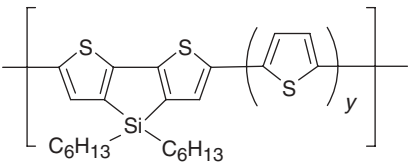

21 $y = 1, 2$

FIGURE 10. Chemical structure of **21**.

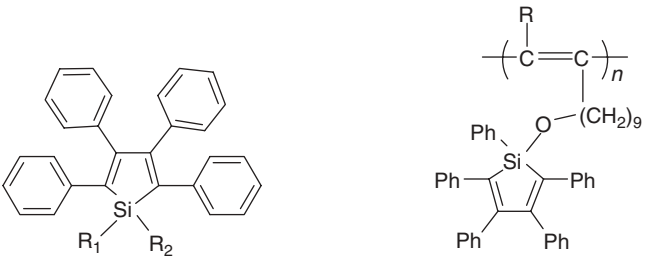

22 **23**

FIGURE 11. Chemical structures of **22** and **23**.

backbone and enabled the silole groups to pack during aggregate formations, otherwise no AIE behavior could be observed.[39,40] The mechanism for the AIE behavior has been revealed by the observations of cooling-enhanced emissions of the polymer solutions, from which a model of restricted intramolecular rotations of the peripheral phenyls on the silole ring could be proposed.[11,39]

VII. CHEMOSENSORS

Poly(1,1-silole)s, SCPs catenated through the ring silicon atom, can be regarded as a new class of polysilanes. It was found that PL intensities of the toluene solution of a poly(1,1-silole) **24** (Fig. 12) could be quenched by the addition of tiny amounts of 2,4,6-trinitrotoluene (TNT), 2,4,6-trinitrophenol (picric acid), 2,4-dinitrotoluene (DNT), and nitrobenzene, demonstrating that poly(1,1-silole)s are potential chemosensors for explosives.[41] TNT could also be detected using the polymer film. In an air stream containing 4 ppb TNT, 8.2% decrease of the PL intensity was found from the film. PL quenching can also be detected when the film contacts a 50 ppb TNT-water solution.

VIII. CONDUCTIVITY

Dithienosilole-thiophene alternating copolymer **21** is the important example for the electrical conduction of SCPs.[42] When the copolymer is doped with iodine, a high electrical conductivity of 400 S cm^{-1} can be achieved. This value is the highest among SCPs and is also close to that of well-defined poly(3-alkylthiophene).

IX. OPTICAL LIMITING

A hyperbranched polysilole **25** (Fig. 13) is nonlinear and optically active and can strongly attenuate the optical power of intense laser pulses.[43]

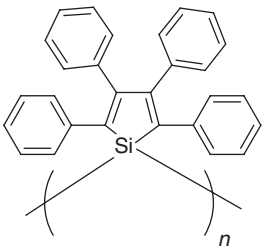

24

FIGURE 12. Chemical structure of **24**.

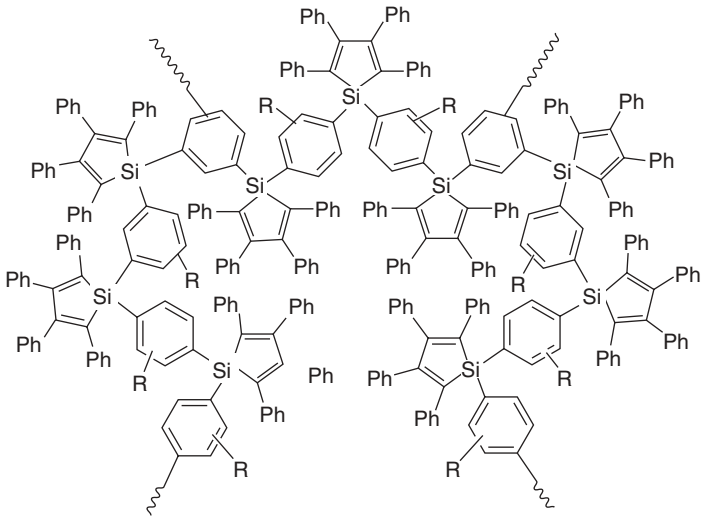

25

FIGURE 13. Chemical structure of **25**.

The dichloromethane solution of the polysilole (0.7 mg/mL) starts to limit the optical power at a low threshold of 185 mJ/cm^2 and suppresses the optical signals to a great extent (81% power cutoff).

X. SUMMARY

The diverse chemical structures of siloles and the largely tunable band gaps from 4.0−1.55 eV of SCPs imply SCPs would exhibit many functionalities. For the fluorescence, the widely variable fluorescent colors from UV light to blue, green, and red lights have been realized. Fluorescent chemosensing of TNT-type explosives, aggregation-induced emission, and attenuation of strong laser power, reveal the attracting features of SCPs. The highly efficient electroluminescence including blue, green, red, and three-color white lights, phosphorescent hosts with high triplet energy level, very efficient solar cells, and stable FETs with high hole mobility in air, are the important applications of SCPs in optoelectronic film devices. Thus SCPs will become an important group of polymeric semiconductors.

XI. ACKNOWLEDGMENTS

This work was partly supported by the National Science Foundation of China, the Ministry of Science and Technology of China, and the Research Grants Council of Hong Kong, China.

XII. REFERENCES

1. J. H. Burroughes, D. D. C. Bradley, A. R. Brown, R. N. Marks, K. Mackay, R. H. Friend, P. L. Burns, A. B. Holmes, *Nature (London)*, **347**, *539* (1990).
2. A. Kraft, A. C. Grimsdale, A. B. Holmes, *Angew. Chem., Int. Ed.*, **37**, *402* (1998).
3. K. M. Coakley, M. McGehee, *Chem. Mater.*, **16**, *4533* (2004).
4. Z. Bao, A. Dodabalapur, A. J. Lovinger, *Appl. Phys. Lett.*, **69**, *4108* (1996).
5. S. W. Thomas III, G. D. Joly, T. Swager, *T. M. Chem. Rev.*, **107**, *1339* (2007).
6. G. Gustafsson, Y. Cao, G. M. Treacy, F. Klavetter, N. Colaneri, A. J. Heeger, *Nature (London)* **357**, *477* (1992).
7. S. Yamaguchi, K. Tamao, *J. Chem. Soc., Dalton Trans.*, **3693** (1998).
8. M. Hissler, P. W. Dyer, R. Reau, *Coord. Chem. Rev.*, **244**, *1* (2003).
9. S. Yamaguchi, K. Tamao, *Bull. Chem. Soc. Jpn.*, **69**, *2327* (1996).
10. J. Chen, Y. Cao, *Macromol. Rapid Commun.*, **28**, *1714* (2007).
11. J. Chen, C. C. W. Law, J. W. Y. Lam, Y. Dong, S. M. F. Lo, I. D. Williams, D. Zhu, B. Z. Tang, *Chem. Mater.*, **15**, *1535* (2003).
12. J. Luo, Z. Xie, J. W. Y. Lam, L. Cheng, H. Chen, C. Qiu, H. S. Kwok, X. Zhan, Y. Liu, D. Zhu, B. Z. Tang, *Chem. Commun.*, *1740* (2001).
13. J. Chen, B. Xu, K. Yang, Y. Cao, H. H. Y. Sung, I. D. Williams, B. Z. J. Tang, *Phys. Chem. B*, **109**, *17086* (2005).
14. H. Y. Chen, J. W. Y. Lam, J. D. Luo, Y. L. Ho, B. Z. Tang, D. B. Zhu, M. Wong, H. S. Kwok, *Appl. Phys. Lett.*, **81**, *574* (2002).
15. H. Murata, G. G. Malliaras, M. Uchida, Y. Shen, Z. H. Kafafi, *Chem. Phys. Lett.*, **339**, *161* (2001).
16. S. J. Toal, K. A. Jones, D. Magde, W. C. Trogler, *J. Am. Chem. Soc.* **127**, *11661* (2005).
17. J. Chen, Y. Cao, *Sens. Actuators. B*, **114**, *65* (2006).
18. H. Gilman, R. D. Gorsich, *J. Am. Chem. Soc.*, **80**, *1883* (1958).
19. S. Yamaguchi,; C. Xu, K. Tamao, *J. Am. Chem. Soc.*, **125**, *13662* (2003).
20. J. Ohshita, M. Nodono, H. Kai, T. Watanabe, A. Kunai, K. Komaguchi, M. Shiotani, A. Adachi, K. Okita, Y. Harima, K. Yamashita, M. Ishikawa, *Organometallics*, **18**, *1453* (1999).
21. K. Tamao, S. Yamaguchi, M. Shiozaki, Y. Nakagawa, Y. Ito, *J. Am. Chem. Soc.*, **114**, *5867* (1992).
22. Y. Mo, R. Tian, W. Shi, Y. Cao, *Chem. Commun.*, *4925* (2005).
23. C. K. Chan, M. J. Mckiernan, C. R. Towns, A. B. Holmes, *J. Am. Chem. Soc.*, **127**, *7662* (2005).
24. S. Yamaguchi, R. Z. Jin, Y. Itami, T. Goto, K. Tamao, *J. Am. Chem. Soc.*, **121**, *10420* (1999).
25. S. Yamaguchi, T. Goto, K. Tamao, *Angew. Chem. Int. Ed.*, **39**, *1695* (2000).
26. E. Wang, C. Li, W. Zhuang, J. Peng, Y. Cao, *J. Mater. Chem.*, **18**, *797* (2008).
27. E. Wang, C. Li, J. Peng, Y. Cao, *J. Polym. Sci. Part A: Polym. Chem.*, **45**, *4941* (2007).
28. F. Wang, J. Luo, J. Chen, F. Huang, Y. Cao, *Polymer*, **46**, *8422* (2005).
29. Z. Liu, L. Wang, J. Chen, F. Wang, X. Ouyang, Y. Cao, *J. Polym. Sci. Part A: Polym. Chem.*, **45**, *756* (2007).
30. Z. Liu, J. Zou, J. Chen, L. Huang, J. Peng, Y. Cao, *Polymer*, **49**, *1604* (2008).
31. F. Wang, J. Luo, K. Yang, J. Chen, F. Huang, Y. Cao, *Macromolecules,* **38**, *2253* (2005).
32. X. Zhang, C. Jiang, Y. Mo, Y. Xu, H. Shi, Y. Cao, *Appl. Phys. Lett.*, **88**, *629* (2006).

33. Y. Wang, L. Hou, K. Yang, J. Chen, F. Wang, Y. Cao, *Macromol. Chem. Phys.*, **206**, *2190* (2005).
34. K. R. J. Thomas, J. T. Lin, Y. T. Tao, C. H. Chuen, *Chem. Mater.*, **16**, *5437* (2004).
35. Y. Liu, Z. Chen, J. Chen, F. Wang, Y. Cao, *Polym. Bull.*, **59**, *31* (2007).
36. F. Wang, L. Wang, J. Chen, Y. Cao, *Macromol. Rapid Commun.*, **28**, *2012* (2007).
37. E. Wang, L. Wang, C. Luo, W. Zhuang, J. Peng, Y. Cao, *Appl. Phys. Lett.*, **92**, *033307* (2008).
38. H. Usta, G. Lu, A. Facchetti, T. J. Marks, *J. Am. Chem. Soc.*, **128**, *9034* (2006).
39. J. Chen, Z. Xie, J. W. Y. Lam, C. C. W. Law, B. Z. Tang, *Macromolecules*, **36**, *1108* (2003).
40. J. Chen, H. S. Kwok, B. Z. Tang, *J. Polym. Sci. Part A: Polym. Chem.*, **44**, *2487* (2006).
41. H. Sohn, R. M. Calhoun, M. J. Sailor, W. C. Trogler, *Angew. Chem. Int. Ed.*, **40**, *2104* (2001).
42. W. Chen, S. Ijadi-Maghsoodi, T. J. Barton, *Polym. Prepr. Am. Chem. Soc., Div. Polym. Chem.*, **38**, *189* (1997).
43. J. Chen, H. Peng, C. C. W. Law, Y. Dong, J. W. Y. Lam, I. D. Williams, B. Z. Tang, *Macromolecules*, **36**, *4319* (2003).

CHAPTER 6

Photophysics and Photochemistry of Polysilanes for Electronic Applications

Starr Dostie, Cetin Aktik, and Mihai Scarlete

Department of Chemistry, Bishop's University, Sherbrooke, Québec, Canada

CONTENTS

Macromolecules Containing Metal and Metal-like Elements,
Volume 10: Photophysics and Photochemistry of Metal-Containing Polymers,
Edited by Alaa S. Abd-El Aziz, Charles E. Carraher Jr., Pierre D. Harvey, Charles U. Pittman Jr., Martel Zeldin.

I. INTRODUCTION

Polysilanes are hybrid inorganic-organic polymers based on sp^3-hybridized silicon backbones and organic substituents. For most applications, tailoring of polysilanes' properties is obtained by grafting alkyl and aryl side chains, siloxanes, methoxy units, or through copolymerization. Some of the properties that have received more attention are the intense near-UV absorption, electroluminescence, photoluminescence, and semiconducting properties (due to observed high hole mobility). The interesting characteristics of polysilanes are due to the specific delocalization of the σ electrons along the silicon backbone, known as σ-conjugation, which is responsible for electric conductance, photoconduction, and charge transport. Physical properties of polysilanes vary greatly, depending on the nature of the side groups.[1] Polysilanes with small alkyl substituents tend to be highly crystalline and insoluble.[1] Lengthening an alkyl chain changes the properties rapidly. For example, polymethylpropylsilane is a soluble solid and polymethylhexylsilane is an elastomeric, rubbery material.[1] Aryl groups normally raise the glass-transition temperature (T_g) of the polymer. Polymethylphenylsilane (PMPS) is a glassy solid that flows only at temperatures $>200°C$. The T_g varies from $>-50°C$ for elastomeric polysilanes to $>120°C$ for aryl compounds.[1,2] The band structure resulting from the σ delocalization is responsible for the UV-VIS, electron beam, and X-ray absorption within antireflection and grating layers is increasingly used in nanolithography of (opto)electronic devices.

II. SYNTHESIS OF ELECTRONIC-GRADE POLYSILANES

A comprehensive review of the progress in the general synthesis of polysilanes is presented in Koe.[2] Only a brief selection of the advancements in

the synthesis of polysilanes that have made possible the deposition of polysilane thin films for electronic applications will be presented herein. Increased UV resolution has been obtained by absorption of polarized UV light in epitaxially grown thin polydimethylsilane (PDMS) films, via the observed discrimination of the optical properties function of the relative orientation to the substrate.[3] Consequently, highly ordered thin films of tactic polysilanes with a low index of polydispersity (PDI) have been deposited on substrates such as single crystal silicon and gallium arsenide. Ordered PDMS single crystal thin films have been obtained by physical vapor deposition,[4] and the properties of the primitive translation vectors have been obtained from the X-ray diffraction pattern. As early as 1997, epitaxial (110) films of PDMS have been deposited on highly oriented poly(tetrafluoroethylene).[5] The small size of the methyl side groups in PDMS has been used for the epitaxial deposition of an all-trans rigid conformation polymer at room temperature.[5] The crystal and electronic structures of this material have been determined.[6] The observations from these preliminary studies on the folding and self-orientation of 1D silicon chains brought interest in preservation of the long-range order at increased 2D/3D reticulation degrees, in correlation with lithographic applications. It has been observed that at low deposition rates on amorphous substrates, silicon chains tend to align normally to the substrate surface with little coherence between the silicon chains.[5] At high deposition rates, silicon chains have a tendency to lie parallel to the surface.[5] By employing highly tactic polymer layers on cleaved crystalline substrates, crystalline PDMS films have been formed with the *c*-axis either normal or parallel.[5] Structure determination indicates that PDMS has a monoclinic unit cell with $a = 7.45$Å, $b = 7.24$Å, and $c = 3.89$Å and $\gamma = 67.1°$.[5]

To produce these highly ordered films, the synthesis methods had to evolve over the years from the initial 1920 Wurtz-Fittig-Kipping method that produced intractable, insoluble materials (strongly limiting the applications of those materials) to new regioselective synthesis methods capable of providing highly tactic polysilanes. Continuous improvement in the Wurtz method is observed today, with the objectives of increased yield and molecular mass, and decreased PDI. Increased yields are obtained if the reductive coupling reaction is activated by 15-crown-5 ether as a phase transfer catalyst.[7–10] Grignard reagents have also been tested, but only as an alternative way to control the substitution pattern.[11] Poly(phenylsilane) has been synthesized by polymerization of phenylsilane with a variety of zirconocene catalyst precursors and with an average degree of polymerization of 30–40 silicon atoms.[11] Upon treatment of poly(phenylsilane) with CCl_4 under room light exposure, chlorination of the Si-H bonds occurs forming poly(chlorophenylsilane). Substitution of the Si-Cl bonds with MeMgBr produces PMPS. Substitution of the Si-Cl bonds with MeOH in the presence of NEt_3 and dimethylaminopyridine at room temperature yields poly(methoxyphenylsilane).These reactions are illustrated in Figure 1.

Ultrasound has been used for efficient and clean synthesis of polysilanes as well as further conversion of polysilanes to SiC by combining a reducing

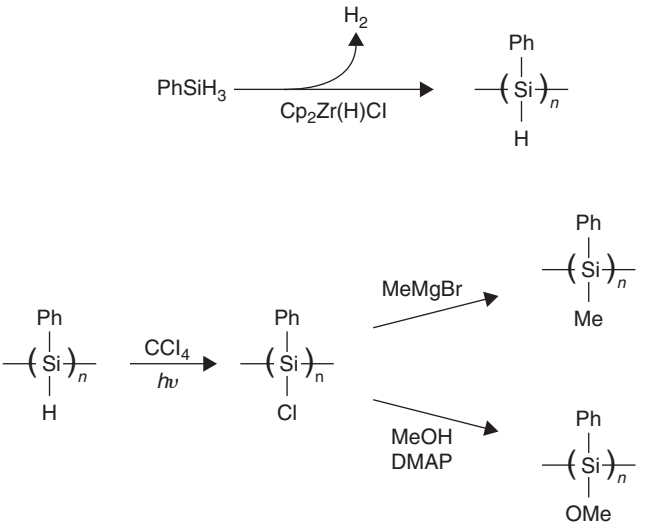

FIGURE 1. Synthesis of substituted poly(phenylsilane)s. (Reprinted from Ref. 11.)

agent and a polysilane precursor, followed by exposure of the mixture to ultrasonic waves.[12] Sonication can take place at room temperature, avoiding solvent removal and reflux conditions, which typically result in less control over the molecular weight of the polysilane.

In 1949, one of the most important polymers of the class, PDMS, was obtained and characterized by Burkhard as being an intractable solid.[13] In the late 1970s, due to the perceived application of PDMS as SiC ceramic precursors,[14] photoresist materials, and photoinitiators for vinyl polymerization, efforts were mainly devoted to increasing molecular weight.[1] Soluble low molecular weight polysilanes were obtained in the early 1980s[15–17] by phenyl grafting procedures. Increased molecular weights have been obtained by Miller and collaborators.[18] Kumada observed the rearrangement of PDMS to meltable polycarbosilane at 400°C.[14] This observation resulted in the industrial production of polysilanes mainly to support the demand for shaped bulk SiC and shifted the main interest toward polysilanes as ceramic precursors rather than their optical properties for a couple of decades. The random scission of polysilane backbones induced by high temperature during Kumada rearrangement frequently leads to materials with structural irregularities and altered (opto)electronic properties. Sacarescu reported new low-temperature restructuring processes in soluble polysilanes obtained by copolymerization of methylphenyldichlorosilane or diphenyldichlorosilane with methyl(H)dichlorosilane following the mechanism in Figure 2.[19]

This work is consistent with the previously observed low temperature (200°C) onset of the Kumada rearrangement in polymethylsilane.[20] The lower

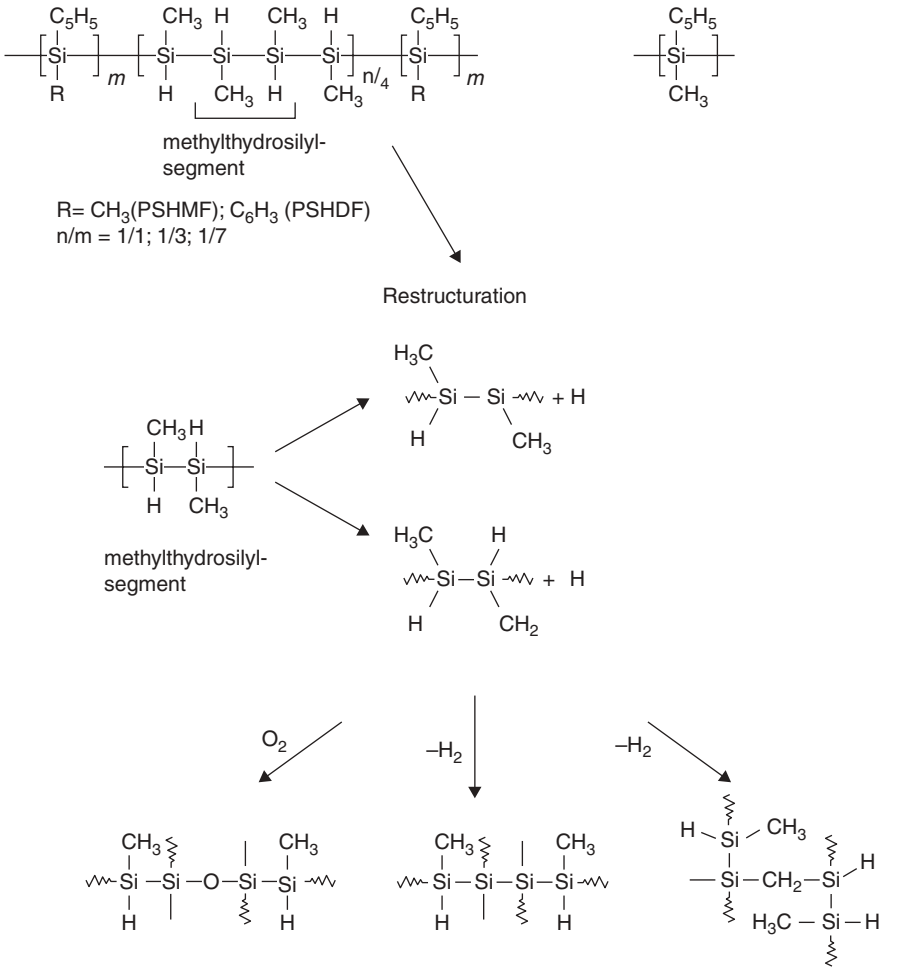

FIGURE 2. Restructuring process of the methylhydrosilyl segment within the main polyhydrosilane chain. (Reprinted from Ref. 19.)

activation energy involved by the Kumada rearrangement at 200°C has found application in the sonication procedure for the synthesis of ceramic materials.[12] Polymerization via catalytic dehydrogenation using titanocene and zirconocene was reported by Harrod et al. in 1984,[21,22] and the process has been adapted for the preparation of polycarbosilanes used as SiC precursors.[23] Tilley studied the coordination polymerization of silanes to polysilanes by σ-bond metathesis in an effort to provide conditions for increased molecular mass of polysilanes.[24] Polymethylsilane with molecular weights up to 19,000 were produced by dehydrogenation using Wilkinson's catalyst by Mechtler and Marschner.[25]

Optimization of the latter reaction is an object of current study.[26] Electrosynthesis of polysilanes has undergone a transformation from laboratory research experiments[27–32] to industrial production of imaging polysilanes for microlithography.[33] Anionic polymerization of masked disilenes was established as a new synthetic route to polysilanes of highly ordered structure.[34] A functional polysilane with an ethereal group, poly[1-(6-methoxy-hexyl)-1,2,3-trimethyldisilanylene] ($M_n = 7.2 \times 10^3$) was prepared by the mask disilene method.[35]

Tacticity is required for the synthesis of crystalline thin polysilane films used for optical and semiconductor devices. Modern synthetic routes allow control over the conformation and tacticity of polysilane molecules used as precursors for thin layers of photoresists, photoconductors and nonlinear optical phases in complex semiconductor and (opto)electronic devices. These properties can be exploited only if the synthesis method ensures a minimal level of contamination, especially with oxygen and metals, and special care is taken to limit electronic-grade polysilanes to a level of contamination on the order of a few ppm in the case of oxygen and in the ppb range for metals. The reactivity of polysilane toward oxygen has forced placing the devices in a helium environment during measurement procedures.[36]

It has been observed that insertion of Si-H groups within the main polymer chain has allowed for the possibility of obtaining polysilane films with predetermined electronic and mechanical properties.[19] However, the high reactivity of the methylhydrosilyl segments produced during the restructuring of the Si-H free backbone at 200°C leads to in situ increased reactivity of the polysilane and requires appropriate handling procedures. The quantitative determination of the extent of oxidation has been followed via the kinetics of the IR absorption of the Si-O-Si asymmetric stretch[20] of thin films deposited on silicon single crystal wafers with a known concentration of interstitial oxygen (15 ppma) used for calibration purposes, as shown in Figure 3.

The 30% quantum efficiency of the photoluminescence (PL) of polysilanes, together with sufficient hole mobility of the order 10^{-4} cm^2/sV,[37,38] has made them interesting materials for LED applications. Polysilane electroluminescence (EL) diodes have been obtained using PMPS as the active emission layer.[36] Short diode lifetimes due to thermal instability of the PMPS conformation required that they be studied at low operating temperatures. In 1996, Hattori obtained UV EL at room temperature by using a film of PDMS in the all-trans rigid conformation of the silicon side chain as the emission layer. The tacticity of the polymeric precursor allowed the deposition of layers with high crystallinity and a $T_g > 160$°C.[39] The orientation of the PDMS molecules in the deposited films can be manipulated by regular parameters controlling the physical vapor deposition process, such as pressure (10^{-6} torr) and source temperature (300°C).[36] The UV component has a major feature at 350 nm, while the visible component is observed as a continuous emission up to 700 nm. The UV emission has been linked to the direct σ- σ * transition in the PDMS, leading to an external quantum efficiency of 1.6×10^{-4}, which is low

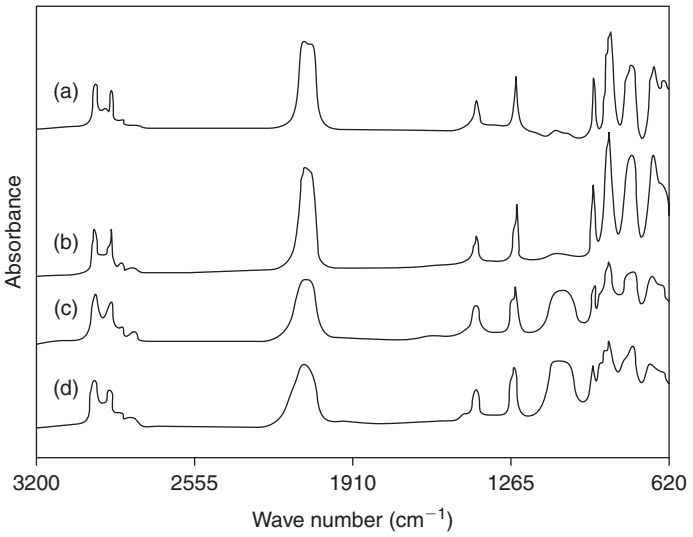

FIGURE 3. IR spectra of poly(methylsilane) during oxidation at room temperatures: (a) 1 min, (b) 5 min, (c) 10 min, and (d) 20 min. (Reprinted from Ref. 20.)

due to limitations of the diode design rather than to the intrinsic properties of the polysilane. The visible component was loosely related to a perceived increase in the degree of disorder in the film activated even at low temperature as well as to other defects at the interfaces of the polymer with the indium-tin-oxide (ITO) layer, and with the glass substrate. Network polysilanes have been synthesized with methoxy (MeO) functionalized polysilanes as the starting material.[40] Network polysilanes are used for their charge-transfer interactions with organic electron acceptors and for photogeneration of carriers, explaining the observed photoconductivity in a system consisting of 42% network polysilanes, 8% dicyanoanthracene as a sensitizer, and 50% polybutyral as a phototransparent binder.

Highly oriented self-assembled PDMS thin films have been synthesized by evaporation and source melting.[41] In the evaporated film, the chains are parallel to the substrate surface, whereas they are inclined from the substrate surface in the powder-melted films. Twin-like crystals were observed and explained using the structural model. At the molecular level, polymer chains align themselves perpendicular to the surface via chain folding.[42] Due to the very small thickness of the crystallites along the chain direction, a single polymer chain must traverse the crystallite from which it originates several times. Two types of models can describe the polymer chain folding. One is a random model in which the polymer chains give rise to an amorphous overlayer and the other is the adjacent reentry model in which the polymer chains fold regularly, making hairpin turns at the surface. The surface structure of

PDMS that adopts an all-trans packing arrangement revealed rod-like features corresponding to chain folds at the single crystal surface, consistent with the regular reentry model.[42]

The exponential increase of device density in ULSI circuits has prompted development of resists that could operate under lower wavelength excitation, such as UV, double photon, and e-beam exposure. In 1985 and 1988, Miller, Michl and Zeigler observed that some polysilanes can be used as self-developing resists (no solvent necessary to remove the exposed areas).[43–46] In 1995, free-radical hydrosilation of polyphenylsilane or poly(*p-tert*-butylphenylsilane) led to the formation of polysilanes that were spin coated onto a silicon wafer and investigated for lithographic behavior.[47] The synthesis was based on a Harrod-type catalyst, zirconocene chloride hydride.[47] The advantages of these polysilane photoresists were the use of inexpensive tools for exposure (a Hg/Xe lamp), their high-yield two-step synthesis from commercially available starting materials, and use of environmentally friendly developing solvents.[47,48] Addition of peroxide compounds to the polysilane has resulted in increased photoresist sensitivity through a photoinduced electron transfer reaction,[48] confirming previous observations.[49] Photoresist applications were expanded in 1998 to include a new method for the preparation of metal patterns on polysilane films[50] by exposing a PMPS film to UV light through a photomask, treating with $PdCl_2$, and contacting via electroless deposition of copper or nickel.

E-beam resists have been synthesized by photopolymerization using PMPS with $M_n > 1.32 \times 10^4$ as a macromolecular photoradical initiator.[51] Tetraethoxysilane (TEOS), propylene glycol 1-monomethyl ether 2-acetate (PEGMA) solutions of the polymer, together with a catalytic amount of HCl were spin-coated on a quartz plate, followed by annealing at 120°C for 2 h under air, resulting in a film with a thickness of 0.05–0.2 μm. Various polysilane-acrylic block copolymers have been prepared by photopolymerization of vinyl monomers using PMPS as the macromolecular photoradical initiator land have been applied to positive resists for EB lithography.[52] The inversion of the behavior of polysilanes from positive (chain scission) to negative (cross-linking) was reported (Fig. 4).[53] Polysilanes have been previously confirmed to show positive-type resist properties from UV light, EB and X-rays under all conditions. However, the cross-linking reaction of the polymer becomes dominant in the polysilane with Si-branchings upon irradiation with UV light, EB and ion beams.[54]

Another type of negative resist consisting of polyhydrosilane with Si-H bonding and vinyl groups was designed[54] by using hydrosilylation between Si-H and vinyl groups, and improvement in the sensitivity of the polymer as a negative resist was observed. Low absorption coefficients are required for high-resolution resists. Polysilanes have been used in 193 nm immersion lithography, 3D two photon lithography, and molecular glass-type photoresists under extreme ultraviolet (EUV) exposure.[55] Negative-tone, oxygen-free poly (trimethylsilylstyrene-co-chloromethylstyrene), showed excellent transparency,

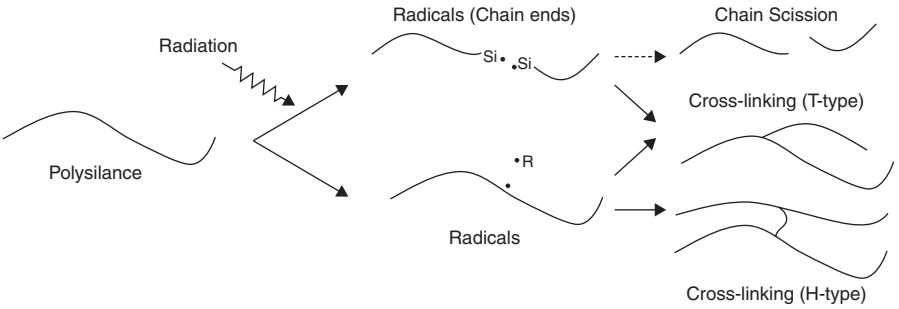

FIGURE 4. The formation of cross-lining points in PMPS-based polysilanes. (Reprinted from Ref. 54.)

with an absorption coefficient of 1 μm^{-1}. Pattern distortion caused by swelling limited the resolution of this system.

PMPS films (6400 amu by GPC) synthesized by Wurtz have been used as pattern masks in UV lithography.[56] UV absorption in air by the material led to a large decrease of the refractive index from 1.70 to 1.56 as a result of the photodecomposition accompanying the cleavage of the Si backbone and the elimination of the π-conjugation moieties of the side groups.

It was found that 5-nm-thick resist-mask polysilane films worked well in a direct lithography process on silicon substrates, resulting into a line width of 40 nm prepared by scanning probe microscope lithography, using a carbon nanotube tip.[57] Thin PMPS films of 6–8 nm, with a molecular weight of 30,000 were prepared by spin casting and cured at 150°C to obtain a smooth surface. It has been interpreted that moisture was essential for the oxidation of the polysilane. The proposed mechanism involved dissociation of Si-Si bonds in polysilane by the electron injection from the carbon nanotube tip catalyzed by moisture.

Antireflective polysilane layers have been considered due to absorption by the Si-Si bond in the deep UV.[58,59] These layers have been used in LSI lithographic processes when the line width is under 0.2 μm and are necessary for preventing critical dimension variations caused by multireflection in both the resist and the substrate.[58] For this purpose, cross-linked diphenylsilane thin films, with an average M_W of 12,000 produced by Wurtz synthesis, were deposited by spin coating and cured at 190°C for 60 s.[59] Loosely cross-linked poly(diphenyl)silane-based copolymers have been used to address problems related to optical interference in the resists and lack of resist thickness during underlying substrate etching appearing during deep UV lithography by Sato.[59,60] Improved results were obtained by increasing the degree of reticulation in the thin bottom antireflective coating (BARC) films of highly cross-linked diphenylsilane (PDPS) copolymers with poly(phenylmethylsilane-co-methylhydrosilane-comethylsilyne) with *m*-diethynylbenzene.[61] The superior properties resulting from increased reticulation have been manifested in the

optical properties of the films: Their reflection was reduced by 0.9%, the refractive index is $n = 1.93$ and $k = 0.32$, and there was improvement in the homogeneity of the film. The resulting advantages were reduced footing and decreased residue directly related to solubility of the homogeneous film. Sato et al. observed that the networked polysilanes containing high amounts of silicon were the most suitable structures for increasing the etch selectivity against the resist without losing antireflection property.[62]

III. BAND STRUCTURE

Properties such as photoconductivity, induction of charge carriers via UV exposure, and the possibility of tailoring optical constants such as refractive index and dielectric constant have all been under close scrutiny for LED, EL, PL, lithographic, and antireflection applications. The electronic structure of polysilanes has been extensively reviewed by Miller[63] and Koe.[2] The molecular weight dependence of the absorption spectra of polysilane provided the first indication that the excited states in polysilanes are delocalized.[64] In the case of oligomeric chains, the MO bonding model for an all-trans oligosilane shows that d-orbitals are not involved to any significant extent in the ground or the low-energy occupied states.[63] The bonding in polysilanes uses Si sp^3 hybrid orbitals. The resonance integral between two sp^3 orbitals located on adjacent silicons and pointing toward each other (β_{vic}) is responsible for SiSi σ bond formation. This vicinal interaction splits each pair of basis orbitals into a strongly bonding σ_{SiSi} and a strongly antibonding σ^*_{SiSi} A less strongly negative integral β_{gem} between two sp^3 hybrids on the same silicon is responsible for the interaction between localized orbitals. A linear chain of mutually interacting localized orbitals results, and the molecular orbitals are delocalized over the whole silicon backbone. This basis set is known as the Sandorfy C model as seen in Figure 5.

The Sandorfy model H results when substituent orbitals are also taken into consideration. The degree of electron delocalization in the silicon backbone is a function of the ratio of β_{gem} to β_{vic}. The bonding orbitals do not have nodes at the bond midpoints and can be seen as a Huckel-type linear combination of localized σ-orbitals separated by an increasing number of nodes as their energy increases. The HOMO consists of a node at every Si atom. The antibonding MOs are a linear combination of localized σ^{*SiSi} orbitals, which are separated by an increasing number of nodes on the Si atoms as the energy increases. The LUMO consists of nodes located at each bond midpoint. The two sp^3 hybrids of each Si that are used for bonding to the substituents combine with the orbitals of the substituents into low-energy bonding σ_{SiH} and high-energy antibonding σ^*_{SiH} orbtials. In a long all-trans chain, the effect of the mixing with σ-symmetry combinations of the σ_{SiH} and σ^*_{SiH} orbitals on the HOMO is negligible, while the effect on the LUMO is large. The HOMO is essentially a pure backbone orbital for which the Sandorfy model C is

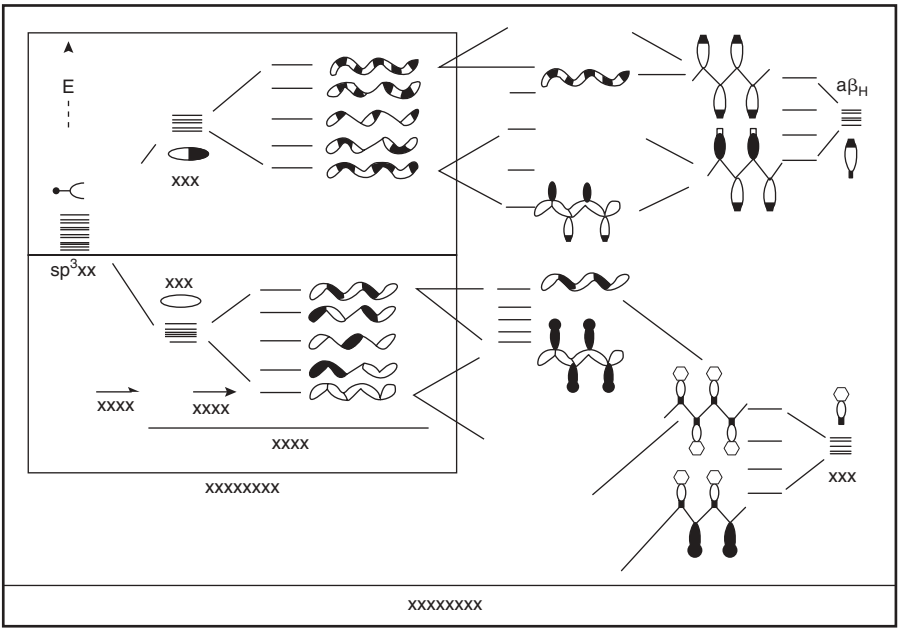

FIGURE 5. The σ-symmetry orbitals of a long, all-trans polysilane chain showing backbone orbitals (left), orbitals of the SiH bonds (right), and the result of their mutual interaction (center). (Reprinted from Ref. 63.)

appropriate, whereas the LUMO is better described by the Sandorfy H model. At those Si atoms where a backbone MO has a node, the two sp^3 hybrids enter with opposite signs and their 3s components cancel so at these atoms the MO has a purely $3p_z$ character as is the case for the HOMO. At those Si atoms where the two hybrids enter with equal signs, their 3s components add up and the p components add to a $3p_y$ orbital so the MO at these atoms has a strong 3s, $3p_y$ character, as in the LUMO. Substitution effects with methyl can be rationalized based on the fact that it can act both as a π-donor and a π-acceptor because it has occupied and empty orbitals of π-symmetry. The $3p_z$ nature of the HOMO is perfect for hyperconjugation with the methyl donor so that destabilization of the HOMO is expected, which is revealed by photoelectron spectra with methyl substituents. The σ-symmetry SiSi antibonding orbital of the backbone with 3s and $3p_y$ character has the wrong orientation for interaction with the methyl substituent. The π-symmetry SiC antibonding orbital has better symmetry and will be stabilized. If the substituent effect is strong enough this orbital may become the LUMO, and there is ambiguity in the assignment of the nature of the LUMO of alkylated oligosilanes.

Stronger effects than those of hyperconjugation can be expected for substituents with stronger interacting power. The effect of aryl substituents will depend on their orientation relative to the plane of the silicon backbone.[63]

When the aromatic plane is orthogonal to the backbone, the π-orbital will be able to interact with the HOMO but not with the π-symmetry SiC antibonding orbital. Upon a 90° rotation of the aryl group, the opposite interactions will occur. In neither case will the interaction of the aryl group be ideal with the LUMO. Orthogonal geometry of the aryl group is preferred sterically so destablalization of the HOMO is expected.

Orbital energies of polysilanes are very sensitive to molecular conformation. Structured PDMS layers have been deposited by epitaxy on various substrates inducing various conformations via self-arrangement of the polymeric chains, either normal or parallel to the surface of the substrate, such as PTFE layers or freshly cleaved crystalline surfaces of KBr, NaCl, or KCl.[5] Highly crystalline PDMS layers have been deposited on substrates and the UV absorption spectra are found to depend on the orientation of the crystal with respect to the substrate, as shown in Figure 6.

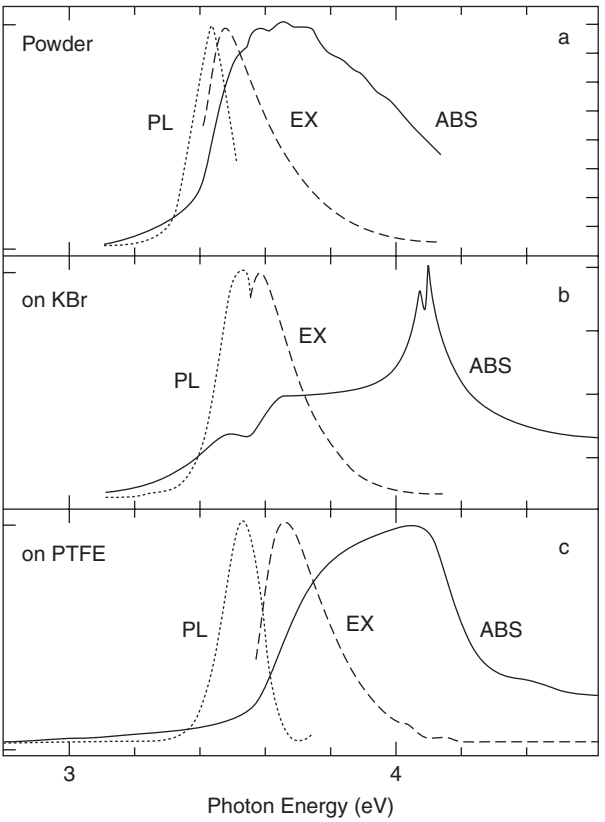

FIGURE 6. Room temperature PL, EX, and ABS of (a) PDMS powder, (b) PDMS film evaporated on PTFE layer, and (c) on KBr cleaved surface. (Reprinted from Ref. 5.)

Absorption spectra of the epitaxial films show a characteristic peak at 4.1 eV (300 nm) and a broad absorption tail in the low energy region, (b) and (c), while the powder material shows a broad peak at 3.6 eV (344 nm), (a). The PL and absorption in polysilanes are associated with the σ-σ^* band gap transition of the silicon backbone. The broad absorption is related to the distribution of delocalized electrons along the Si backbone. The absorption peak energy of 4.1 eV corresponds to the number of silicon atoms in the delocalized region (cluster size) of 10. The UV absorption changes were interpreted as a result of induced orientation of the PDMS crystal on the surface to accommodate the exposed crystalline plane to the existent "sticking" centers on the substrate. For example, on the PTFE substrate, the PDMS layer is exposing its (110) crystalline plane parallel to the substrate, while in the KBr substrate, the plane parallel to the substrate becomes the 6.7-Å-spaced (010) PDMS plane, best accommodating the 6.6 Å of the exposed KBr lattice. The sensitivity to twisting that a given MO displays depends significantly on the degree of 3s and 3p character.[63] Thus the HOMO, which is nearly purely of $3p_z$ character, is very sensitive, whereas the LUMO, which has more 3s character, is less sensitive.

As the number of silicon atoms in the backbone increases, the number of HOMO and LUMO states increases, resulting in a band structure for high molecular weight polysilanes. Electronic absorptions from the HOMO (σ) to LUMO (essentially σ^*) give the characteristic UV absorption of polysilanes observed between 300 and 400 nm. The longest wavelength maximum occurs for the all-trans conformation with a Si-Si-Si-Si dihedral angle of 180°. Red shifting occurs when unsaturated side chains are connected to the main chain due to mixing of σ and π orbitals resulting in a smaller HOMO-LUMO gap.[2] Ab initio HF calculations for Si_2 to Si_8 permethylated compounds showed that the HOMO destabilizes as the dihedral angle increases up to all-trans. It is expected that with the introduction of gauche-turns into an all-trans chain, delocalization is interrupted and concentrated in the longer segments.[2,63] Although ab initio studies and experimental data on the influence of the conformation sequence in a polysilane chain on electron delocalization were not initially in agreement, a proposed GT3GT sequence theoretically indicated preservation of delocalization.[65] Conformational studies of solid-state polysilanes indicate that the UV absorption of the all-trans conformer with a dihedral angle of 180° should have a UV absorption in the range 330−370 nm.[66−68] The 7/3 helix, with a dihedral angle of about 154°, has a UV absorption in the 310−320 nm range[69] and the conformations with alternating anti and gauche angles have absorptions around 350 nm.[70−72]

Fine-tuning of the UV absorption can be accomplished through moderate reticulation. This effect has been observed in the synthesis of PDPS thin films used for bottom antireflecting coatings for deep UV lithography to improve durability during SiO_2 etching.[61] The promising results of experiments using a low reticulation degree prompted further experimentation at increased reticulation. Optimal refractive index, T_g, and UV-VIS absorption have been

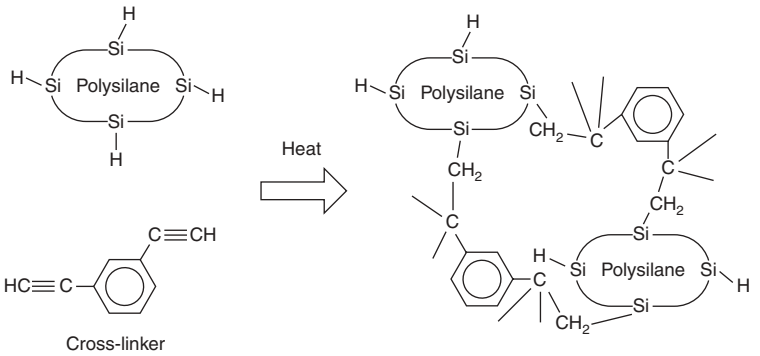

FIGURE 7. Thermal cross-linking reaction of polysilane. (Reprinted from Ref. 6.)

obtained by copolymerizing poly(phenylmethylsilane-co-methylhydrosilane-co-methylsilyne) with *m*-diethylnylbenzene.[61] The cross-linking, obtained via Si-H groups and ethynyl groups (Fig. 7) has resulted in a layer with a refractive index of $n = 1.93$ and $k = 0.32$.

Completely networked polysilanes show a variation of n and k with the degree of cross-linking compared to parent linear polysilanes.

IV. PHOTOPHYSICS

A. Influence of the Backbone Structure

The broadness of the PL emission is caused by a cluster of a minimum of three adjacent Si-Si bonds. This effect is linked to 1D or 2D branching of the polymer, as the PL of large polymeric chains retains its sharpness. The PL becomes broad in branched or reticulated polysilanes even for Si-Si bond clustering as low as 4 silicon atoms. Branch and ladder Si polymers whose backbones are constructed of organosilicon units having three Si-Si bonds exhibit broad PL spectra, which is different from the sharp PL observed in chain structures constructed of organosilicon units with only two Si-Si bonds.[73] The structures of chain-like Si polymers adopt a variety of conformations such as trans-planar, trans-gauche, 7/3 helical, and disordered forms, depending on the organic substituent. However, the PL band is very sharp for all conformations. In the branch and ladder structures, broad PL spectra are observed. In these structures excitons are strongly localized on two or three Si atoms, but in the chain structure excitons are delocalized over about 30 Si atoms. It is considered that broad PL bands observed in the branch and ladder

structures and Si network polymers are closely related to the existence of Si atoms having three or four Si-Si bonds.

Linear PMPS and branched poly(phenyl-dimethyl)silane and poly (phenylmethylphenyl)silane synthesized by Wurtz reductive coupling show that the absorption band for the branched polysilanes tails into the visible region. The corresponding emission peaks have a red shift compared with linear PMPS, indicating that branched polysilanes have a lower energy band gap.[74] Linear PMPS has two major absorption peaks around 272 nm and 332 nm, whereas the branched polysilanes has only one absorption peak between 283 nm and 287 nm. The peak at 332 nm is due to the σ-σ* transition of the Si backbone, while the peak at 272 nm is due to the interaction between a π-orbital and a σ-orbital of Si-C. The difference in UV absorption spectra between the two branched polysilanes and the linear polysilane is due to the fact that introduction of branched points in the Si backbone extends the σ-σ* conjugation of the system. The absorption bands of the two branched polysilanes tail into the visible region and are red shifted with respect to the linear polysilane, the tail of which ends at 360 nm, as shown in Figure 8.

Most linear polysilanes show bright resonant luminescence in the UV region but network and branched polysilanes show luminescence in the visible

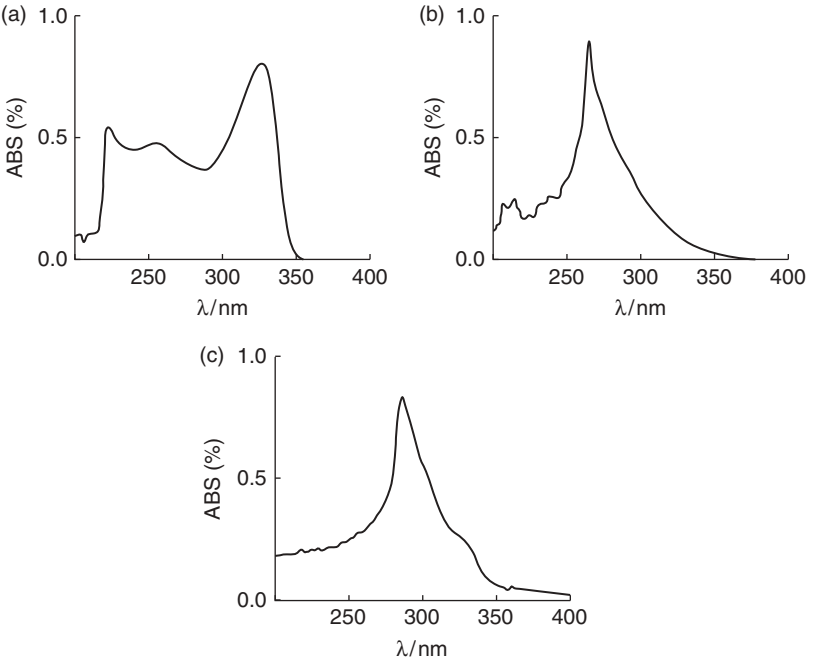

FIGURE 8. UV absorption spectra of (a) linear PMPS, (b) branched PPDMS, and (c) branched PPMS. (Reprinted from Ref. 74.)

region. The linear PMPS shows a sharp single emission peak at 352 nm as the mirror image of the σ-σ* absorption with a 20 nm Stokes shift, indicating that the geometry of the linear PMPS in the ground state resembles the excited state as shown in Figure 9.

The branched polysilanes show a broad emission peak around 450 nm, where the large red shift in the fluorescence spectra is due to the influence of aryl substituents and the introduction of branched points. For (opto)electronic applications, the UV irradiation and thermal stability are crucial to device stability. Branched polysilanes have better thermostability and are more resistant to UV irradiation than are linear polysilanes.

B. Side Groups

The absorption maximum of alkyl-substituted polysilanes shifts linearly to lower energies with increasing substituent size. This shift comes from steric interference of the substituents, resulting in straining of the Si-Si backbone and a change in backbone conformation.[75]

Free radical chlorination of poly(phenylsilane) to produce poly (chlorophenylsilane) and then substitution with MeOH or MeMgBr

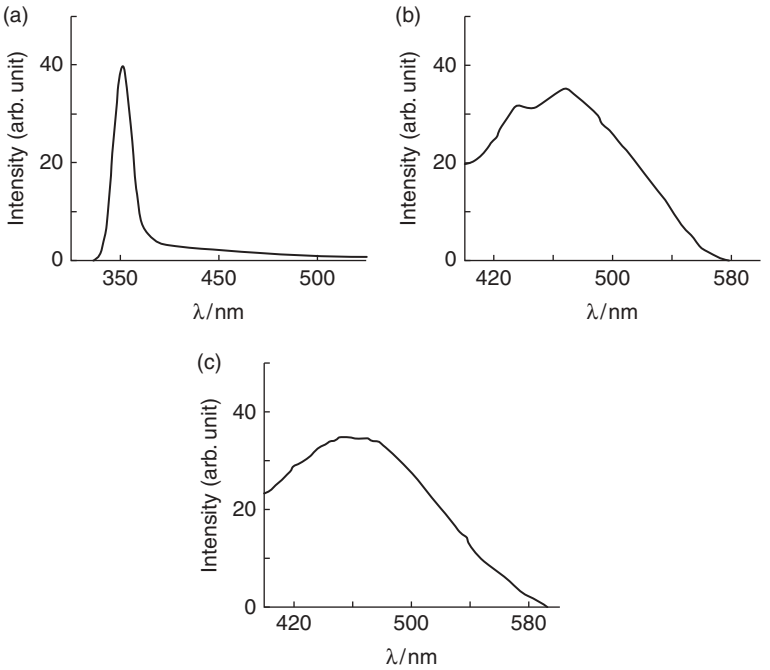

FIGURE 9. Fluorescence spectra of (a) PMPS, (b) PPDMS, and (c) PPMS. (Reprinted from Ref. 74.)

nucleophiles (Fig. 1) has lead to observation of substituent effects on the UV absorption of σ-conjugated polysilanes.[11] From the data in Table 1 and the UV spectra in Figure 10, it can be seen that the UV absorption spectrum of poly (phenylsilane) contains a weak transition at 294 nm, assigned to the Si (σ- σ*) transition with phenyl (π- π*) character.

Fluorescence of poly(phenylsilane) at room temperature was not detected. Poly(chlorophenylsilane) has a long wavelength tail out to 380 nm with a transition centered at 330 nm. Substitution of the Si-Cl bonds of the

TABLE 1. Properties of Substituted Poly(phenylsilanes)s[11]

R	%[a]	M_n[b]	M_w/M_n[b]	M_n[c]	DP[d]	λ (nm)[e]	$\varepsilon_{Si\text{-}Si}$[f]
H		2590	1.70	4855	46	294	2489
Cl	85	2371	1.67	3329	25	330	1561
Me	75	2781	1.89	4890[g]	42	328	4539
MeO	80	2262	1.89	1563	12	348	2710

[a] Percentage of substitution on the polymers.
[b] Values obtained from GPC.
[c] Values obtained from vapor pressure osmometry.
[d] Degree of polymerization.
[e] Si(σ-σ*) absorption maximum.
[f] Values obtained from deconvoluted spectrum. Extinction coefficient in $cm^{-1}M^{-1}$.
[g] Sample was washed with MeOH to remove magnesium salts.

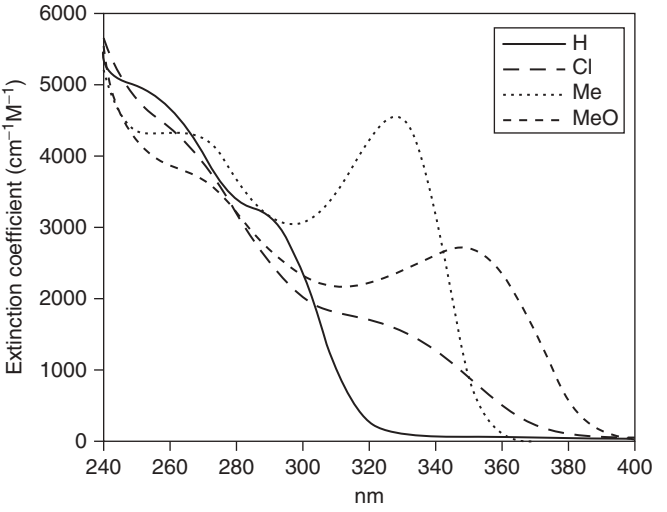

FIGURE 10. UV spectra of polysilane with various side groups. (Reprinted from Ref. 11.)

chlorinated polymer with methyl groups results in a red shift of the UV absorption relative to the original poly(phenylsilane), with an increase in the intensity of the Si (σ- σ*)transition. The absorption spectrum of PMPS prepared in this way is blue shifted but comparable to the absorbance spectrum observed for high molecular weight PMPS prepared by Wurtz coupling (λ = 343nm, $\varepsilon_{Si\text{-}Si}$ = 12,000 $cm^{-1}M^{-1}$).[63] PMPS fluoresces at room temperature in THF at 360 nm.[11] Substitution of the Si-Cl bonds by MeOH leads to a red shift relative to the other polysilanes, with a slight decrease in the extinction coefficient relative to PMPS. Poly(methoxyphenylsilane) fluoresces at room temperature at 394 nm. The difference in the absorption spectra of the hydro- and methyl-substituted polymers can be explained by conformational effects, in that the smaller hydrogen substituent allows for a large number of gauche or eclipsed conformations, causing the polymer to exist in a tight random coil with few extended segments. The methyl substituent would stiffen the polymer chain, resulting in extended trans segments and thus a red shift in the absorption spectrum. The red shift upon incorporation of the methoxy groups is due to both conformational and electronic effects. Interaction of the oxygen lone pairs with the orbitals of the silicon backbone increases the energy of the HOMO more than that of the LUMO, leading to lower transition energy. As a result, in spite of lower molecular weights produced by dehydrogenative coupling, polysilanes can exhibit electronic behavior similar to the high molecular weight materials produced by Wurtz coupling.

Optical absorption, PL and EL in poly[(tetraalkyldisilanylene)-*p*-oligophenylene]s (PDSiOP) were found to depend on the length of the oligophenylene and not on the length of the short alkyl substituents, such as methyl and ethyl groups.[76]

Poly[(tetramethyldisilanylene)-*p*-terphenylene](PMe$_4$DSiTP), poly[(tetraethyldisilanylene)-*p*-terphenylene](PEt$_4$DSiTP), poly[(tetramethyldisilanylene)-*p*-quarterphenylene](PMe$_4$DSiQP) and poly[(tetraethyldisilanylene)-*p*-quarterphenylene] (PEt$_4$DSiQP) have the structures shown in Figure 11 and were synthesized by a nickel-catalyzed dehalogenative coupling reaction. It is observed that the absorption spectra depend on the oligophenylene units and not on the alkyl substituents. PL peaks of PMe$_4$DSiTP and PEt$_4$DSiTP are located at higher energies compared to those of PMe$_4$DSiQP and PEt$_4$DSiQP. The blue EL peaks of these polymers coincide with the PL peaks. Quenching of PL and the enhancement of photoconductivity upon C_{60} doping is observed in PEt$_4$DSiQP and is interpreted in terms of highly efficient photoinduced charge transfer (CT) between the oligophenylene unit and C_{60}.[76]

Helical polysilanes where the side groups are partly substituted with Rhodamine B dye molecules and chiral groups (Fig. 12) have been synthesized and spread onto quartz plates by vertical dipping.[77] A weak absorption peak due to the dye is observed around 2 eV in addition to the sharp exciton peak at 3.85 eV. The PL spectrum shows a new peak at 2 eV, while the original peak at 4 eV for the polysilane without the dye is greatly decreased. Strong red PL is observed. The introduction of only a few percent of dye modifies the absorption

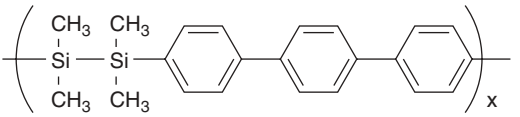

Poly [(tetramethyldisilanylene)-*p*-terphenylene]: PMe_4DSiTP

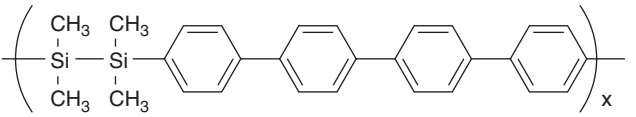

Poly [(tetramethyldisilanylene)-*p*-quaterphenylene]: PMe_4DSiQP

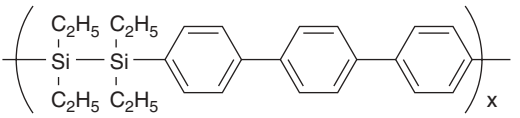

Poly [(tetraethyldisilanylene)-*p*-terphenylene]: PEt_4DSiTP

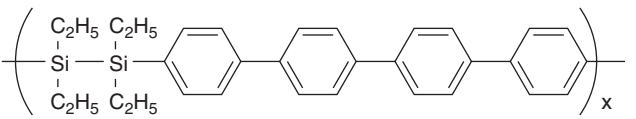

Poly [(tetraethyldisilanylene)-*p*-quaterphenylene]: PEt_4DSiQP

FIGURE 11. Molecular structures of poly[(tetraalkyldisilanylene)-*p*-oligophenylene] polymers. (Reprinted from Ref. 76.)

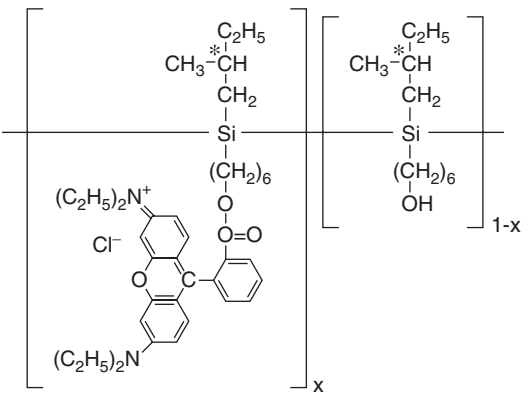

PS : x = 0

PS-dye : x = 0.015

FIGURE 12. Helical polysilane bearing Rhodamine B. (Reprinted from Ref. 77.)

spectrum very little from the original spectrum of the polysilane, but readily quenches the resonant exciton emission around 4 eV, making the dye luminescence band around 2 eV dominant. It has been shown that the photogenerated free excitons on the Si backbone with the helical conformation are the dominant contribution to the PL band around 2 eV, as opposed to the dye. This approach will open the way to fabricating wavelength-tunable luminous devices by using the exciton transport in Si chains.

Diphenyl-methylphenyl polysilane copolymer films synthesized by the Wurtz reaction were spin casted on silicon substrates.[78] The copolymer shows a narrow PL at room temperature in the NUV region, which can be used for LEDs. PL shows a sharp peak at 368 nm with a FWHM of 24 nm. The potential of the high-purity material as a source of blue or NUV emitter is necessary to obtain a low value for the FWHM. Although all emissions are at 369 nm, the PL intensity is a function of the concentration of the polymer in the solvent related to the thickness of the film.

Wurtz coupling of dibutylaminotrimethyl-1-2-dichlorodisilane forms a partially networked polymer.[79] This networked polymer shows an absorption maximum at 360 nm, that is 30 nm red shifted relative to the absorption of poly (dialkylsilanes). The shift is due to the nonbonding electron pair of the amino substituents extending the σ-conjugation of the silicon backbone. Two broad emission bands at 440 nm and 400 nm are observed and assigned to the network silicon units and the linear silicon chains, respectively. The unusual photophysical properties arise from both the amino side groups and the networked structure.

Specific properties of polysilanes have been linked to the method of synthesis.[35] For example, in the case of anionic polymerization of poly[1-(6-methoxy-hexyl)-1,2,3-trimethyldisilanylene] a new type of chromism was induced in the polysilane film by the difference in the surface properties of substrates and was termed a *surface-mediated chromism*. The polysilane exhibited thermochromism with an absorption maximum at 306 nm at 23°C, but $<$15°C a band at 328 nm began to appear. A monolayer of the polysilane was transferred onto both a clean hydrophilic quartz plate and a hydrophobic one treated with hexamethyldisilazane by the vertical dipping method. With the hydrophobic plate, a broad UV absorption at 306 nm is obtained, whereas the absorption on a hydrophilic plate shifts to 322 nm. The conformation of the polysilane is preserved by hydrogen bonding between the silica surface and the ether section of the substituent on the hydrophilic plate. The polysilane is attached to the hydrophobic surface only by van der Waals forces, and this weaker interaction would not sustain the thermodynamically unstable conformational state that is attained on the water surface.

Detailed information on the conformation and orientation of polysilane thin films has been obtained by anisotropic PL.[80] The alignment of poly (methylphenylsilane-co-methacryloxypropyltriethoxysilane) [P(MPS-co-MPTES)] adsorbed on silica substrates has been studied at 14 K using an attenuated He-Cd polarized laser beam (λ = 325 nm) as the excitation source. Laser irradiation decreases the PL intensity, blue shifts the PL peak position

and induces the anisotropy of PL in thin films of different proportions of the polysilane fraction in the copolymer. The photoinduced anisotropy of PL is due to the transition-dipole-orientation-dependent photodecomposition of the polysilane segments in hybrid thin films. The polysilane segments whose transition dipole is not perpendicular to the polarization of the UV light are photodecomposed, whereas the polysilane segments whose transition dipole is perpendicular to the UV-polarization are relatively unaffected.

C. Nanostructured Polysilanes

Polysilane-based nanostructured composites were synthesized by the inclusion of poly(di-*n*-hexylsilane) (M_w = 53,600) into mesoporous, Si-OH-rich silica with a pore size of 2.8 nm.[81] Two PL bands are observed for the composite. A narrow band at 371 nm, assigned to a PDHS film on a quartz substrate is blue shifted by 20 nm, a shift attributed to the polymer being incorporated into the pores.[82] The size of the monomeric unit of the PDHS is about 1.6 nm, so only one polymer chain can be incorporated into a mesopore with a diameter of 2.8 nm. The narrow PL band at 350 nm is due to the reduction of the intermolecular interactions between polymer chains. This narrow PL band at 350 nm is assigned to the excited state of the linear polymer chain.[81] Also, a new broad band of visible fluorescence at 410 nm appeared, which is assigned to localized states induced by conformational changes of the polymer chains caused by its interaction with the silanol (Si-OH) covered pore surface. Visible luminescence in nanosize PDHS is observed only when the polymer was incorporated in hexagonal pores of 2.8 nm and is not seen for the polymer incorporated into cubic pores of 2.8 nm diameter or hexagonal pores of 5.8 nm diameter.

Helical polysilane rods are regarded as a soluble polymeric model of a quantum wire with a width of 5 Å.[83] The helical organopolysilanes used were synthesized by the Wurtz reaction using both (S)-2-methylbutyl and *n*-alkyl substituents. Poly(*n*-hexyl-((S)-2-methylbutyl)silane) (250 Å of wire length) showed a UV absorption band at 3.85 eV, and the PL spectral profile at 3.79 eV is a complete mirror image. Although the spectroscopic features of this polysilane are very similar to those of poly(*n*-decyl((S)-2-methylbutyl)silane) (ε = 55,000cm^{-1}, 3000 Å), its absorptivity (ε = 38,000 cm^{-1}) is slightly lower. The discrepancy arises from the difference in the wire length and not from the side-chain length. Phenomena such as thermochromism, piezochroism, ionochroism, and solvatochroism are caused by the conformational dependence of the electronic structure.[84]

D. PL Quenching by Doping

PL of polysilanes with aromatic side groups has been found to be strongly quenched by doping with fullerene (C_{60}), whereas quenching does not occur in polysilanes with alkyl side chains.[85] Poly(methylpropylsilane)

(PMPrSi), poly(methyphenylsilane)(PMPSi), poly(naphthylphenylsilane) (PNPSi), poly(dihexylsilane) (PDHSi), and poly(biphenylphenylsilane) (PBPSi) were synthesized by Wurtz condensation of organodichlorosilanes, prepared by the reaction of *p*-substituted phenyl magnesium bromide with alkyltrichlorosilane. Films were obtained by casting a C_{60}/polysilane solution on quartz plates. The PL spectra of PNPSi and C_{60} doped PNPSi show that the shape of the emission spectrum at 405 nm does not change with introduction of C_{60}, but its intensity is significantly decreased. Similar quenching effects are observed for PMPSi[85,86] and PBPSi. However, in PMPrSi and PDHSi with saturated hydrocarbon chains, PL quenching is not observed. The differences in quenching between polysilanes with aromatic side chains and those with aliphatic side chains is due to a CT between the C_{60} and the polysilanes governed by the energy and overlap of the electronic levels. If the side group is aromatic, a high degree of overlapping is expected due to the geometry of the π-orbitals. The aromatic group plays the role of a mediator in photo-induced CT. Upon C_{60} doping, an enhancement of photoconductivity can be observed due to the fact that the polysilane transfers electrons to C_{60}, and the remaining holes can then migrate along the chains.[85,86] The highest photocarrier generation yield is observed for fullerene-doped PMPS (φ = 40%) at an applied field of 100 V/μm upon exposure of 340 nm and fullerene-doped poly(*N*-vinylcarbozole) (φ = 10%).[87] Studies in 1998, indicated that PL quenching by C_{60} doping was observed for polysilanes not only with aromatic side groups but also with saturated hydrocarbon side groups.[88]

E. Energy Transfer

An intermolecular energy transfer process between Wurtz synthesized PDHS (M_W = 12,000), PDPS, and their mixture in powder form has been shown to occur only by their mixture in a mortar.[89] The PL spectrum of PDHS has a single peak at 3.18 eV with a FWHM of 0.16 eV, which originates from the free exciton recombination of σ-delocalized electronic states. In the excitation spectrum of PDHS, two peaks at 3.65 eV and 3.28 eV are observed, as shown in Figure 13. The former corresponds to the 7/3-helix conformation and the latter to the all-trans conformation. Since the excitation energy absorbed in the 7/3-helix region is relaxed rapidly to the more stable trans region, PDHS powder emits only from the trans region at room temperature. When heated to $>40^{\circ}$C, phase transition from trans to all 7/3-helix yields an emission from the helix region. The PL spectrum of PDPS shows a single peak at 2.98 eV with a FWHM of 0.16 eV. The excitation spectrum has a peak energy at 3.10 eV with a shoulder around 3.60 eV. The peak energy of PL in PDHS coincides with the main peak of PL excitation in PDPS. This coincidence was thought to be advantageous for the intermolecular energy transfer. It was found that both the intensity and lifetime of the PDHS emission decreased, while those of PDPS emission increased in the mixed sample. In pure PDHS, excited energy is relaxed rapidly to the lowest excited state and then to the ground state, with the

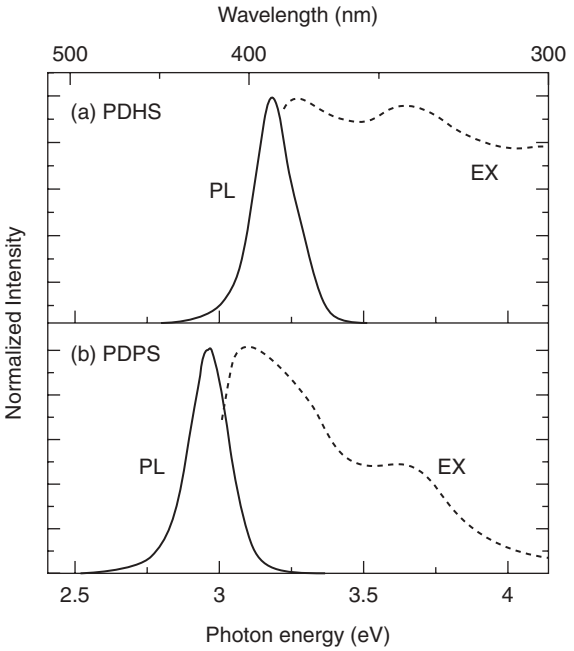

FIGURE 13. PL(*solid curve*) and PL excitation (*dashed curve*) spectra of (a) PDHS and (b) PDPS. (Reprinted from Ref. 89.)

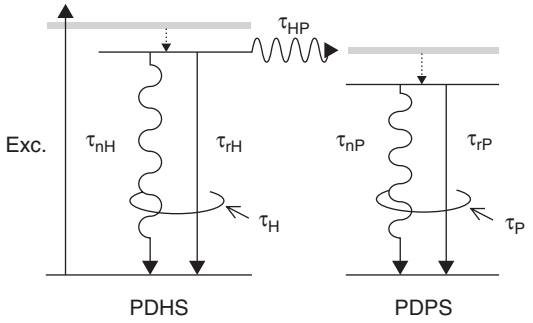

FIGURE 14. The recombination and resonant energy transfer processes in the PDHS/PDPS sample. (Reprinted in Ref. 90.)

recombination lifetime τ_H composed of radiative and nonradiative components, τ_{rH} and τ_{nH}. In the mixed samples however, the lifetime of the resonant energy transfer τ_{HP} from the excited state of PDHS to that of PDPS must also be considered, as shown in Figure 14. This indicates that intermolecular

interaction plays an important role in spectrally matched polysilanes, which provides a wider possibility of optimizing molecular pairs toward future application.

An interesting application of energy transfer involving poly(3,3,3-trifluoropropylmethylsilane) (PTFPMS) is the detection of explosives containing nitroaromatic compounds due to a quenching of the 355 nm polysilane fluorescence.[90] The PTFPMS used either in THF solution or as a solid film is more sensitive to nitroaromatic compounds than nonfluorinated poly (methylproylsilane) due to the electron-withdrawing CF_3 groups, which stabilize the HOMO and LUMO and increase the positive charge on silicon, thereby increasing its ability to interact with the nitro groups of the explosive. A noncovalent interaction between the silicon and the nitro group facilitates electron transfer from the electron-rich polysilane to the electron-accepting nitroaromatic-enhancing PL quenching around 335 nm as shown in Figure 15.

F. Electroluminescence

Polysilanes have a quantum efficiency of >30% and show a hole mobility of 10^{-4} $cm^2s^{-1}V^{-1}$ at room temperature, independent of the side groups.[37,38] Due to sufficient hole mobility, polysilanes are considered to be suitable materials for the hole-transporting layer in injection-type organic EL diodes.[36] It is also known that polysilanes themselves can be efficient emission materials in the UV and visible regions.

UV EL diodes with a Al/PDMS/ITO glass structure operating at room temperature have been prepared using evaporated PDMS as an emission layer.[36] The deposition rate of the PDMS film is low enough to ensure that the PDMS molecules are aligned normal to the substrate surface. To avoid oxidation of the PDMS film during measurement, the diodes are placed in a helium environment. A sharp emission band exists in the UV region (330 nm at 77 K, 355 nm for RT) in both the EL and PL spectra originating from the σ-σ* transition. This coincidence between the EL and the PL peaks suggests a similarity between the irradiative recombination mechanisms. The wavelength of the UV emission band is suitable for exciting phosphors in the visible region. Combination with phosphors may lead to the development of full-color display

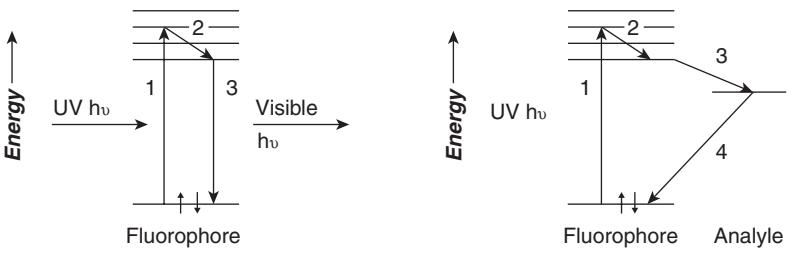

FIGURE 15. Electron-transfer fluorescence quenching. (Reprinted from Ref. 90.)

panels, which are driven by a single UV light source. The EL spectra have a broad emission band in the visible region, which is not detected in the PL spectra. A possible source of the visible emission is the ITO and glass substrate or perhaps the PDMS film itself emitting visible light associated with the presence of defects in the film. The EL intensity decreases gradually with time, due to Si-Si bond breaking and the oxidation or degradation of the Al electrode. Nevertheless, PDMS EL diodes have the advantages of room temperature operation and a lifetime exceeding PMPS by several thousands of seconds. PMPS's short life is attributed to the thermal instability of the 7/3 helical conformation. The stable operation at room temperature with PDMS is due to the high glass-transition temperature (160°C) and the aligned configuration of the rigid all-trans conformation.

PMPS, poly(phenylsilyne) (PPS), poly(2-naphtyl-phenylsilane) (PNPS), and poly(phenyl-*p*-biphenylsilane) (PBPS) were used in EL diodes.[91] The absorption spectra of the polysilanes all exhibited strong absorption in the UV region, except for PPS as, shown in Figure 16. Their PL spectra exhibited a sharp peak, as shown in Figure 17.

In the spectra for PMPS and PPS, broad peaks also exist around 472 nm. The FWHM (0.21 eV) of the sharp emission peak is similar for all polysilanes. The peak wavelengths of the sharp emissions of PMPS, PPS, PNPS, and PBPS are 357 nm, 378 nm, 409 nm, and 409 nm. The origin of the broad emission peak at 472 nm is the radiative transition of excitons localized at branching points or a CT from phenyl π*-orbitals to Si σ-orbitals. The spectrum of PNPS is almost the same as that of PBPS, which may be due to the energetic equivalence of biphenyl and naphtyl substituents. Although both PMPS and PPS possess a phenyl substituent, their emission peaks differ due to the fact that PMPS has a linear structure and PPS has Si-branching. The EL spectra are

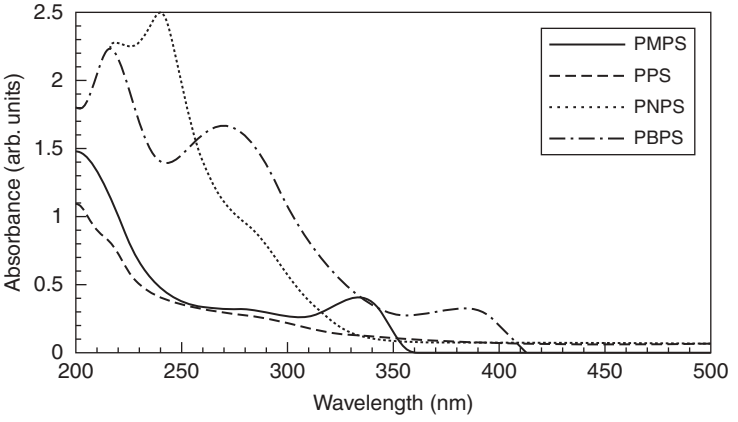

FIGURE 16. Absorption spectra of polysilane films on quartz substrates at room temperature. (Reprinted from Ref. 91.)

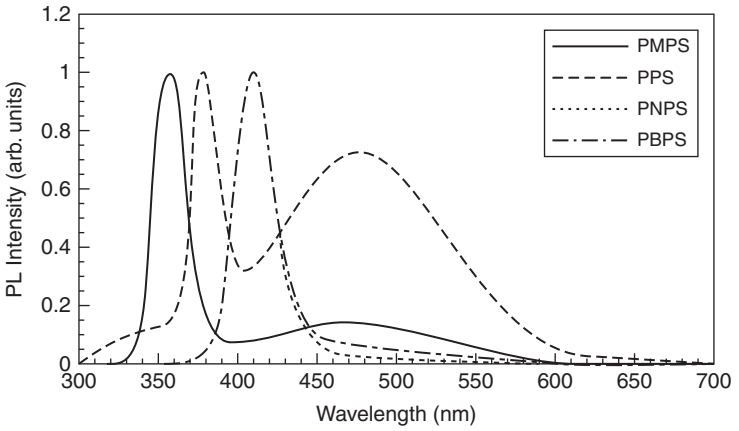

FIGURE 17. PL spectra of polysilane films on quartz substrates at room temperature. (Reprinted from Ref. 89.)

almost independent of the applied voltage and of the thickness of the polysilane films. The emission colors of PNPS and PBPS are violet, and that of PPS is white. The emission of PMPS contains a mixture of UV and visible blue. The peaks in the EL spectra of PMPS, PNPS and PBPS almost coincide with those in the PL spectra at room temperature. The 353 nm, 405 nm, and 405nm EL spectra of PMPS, PNPS, and PBPS, respectively, correspond to σ^*- σ transitions similar to the PL bands. The FWHM for PMPS PNPS, and PBPS are 0.14 eV, 0.18 eV, and 0.17 eV, respectively and are narrower than those of the PL bands due to the lower temperature of the EL measurements. In the case of PPS, a sharp peak corresponding to the band-gap energy is not observed, instead a broad spectrum with the maximum at 595 nm is obtained, attributed to a radiative transition originating at localized exciton states, as shown in Figure 18. The current required to obtain the same emission intensity is observed to decrease in the order of PPS > PMPS > PBPS > PNPS. Therefore, it is suggested that a polysilane with a 1D system and with side groups with π-conjugation greater than napthyl substituents may exhibit efficient emission in an EL diode.

PDHS ($M_W = 9.3 \times 10^5$) exhibits an EL identical to its NUV PL.[92] In contrast, PDBS ($M_W = 1.2 \times 10^5$) exhibits EL in both the visible and NUV regions. Although these two polysilanes differ only in their substituent groups, their device characteristics vary considerably. The PDBS-LED exhibits a larger device current, inferior rectifying behavior, and lower turn-on voltage than the PDHS-LED. This observation is inconsistent with predictions based on the hypothetical band diagrams of these two LEDs. The peak position of the PL spectrum is 371 nm for PDHS and 343.5 nm for PDBS. This means that the excitons of PDHS and PDBS have different energy levels. Since electronic perturbations caused by alkyl substituents for the electronic state of the Si

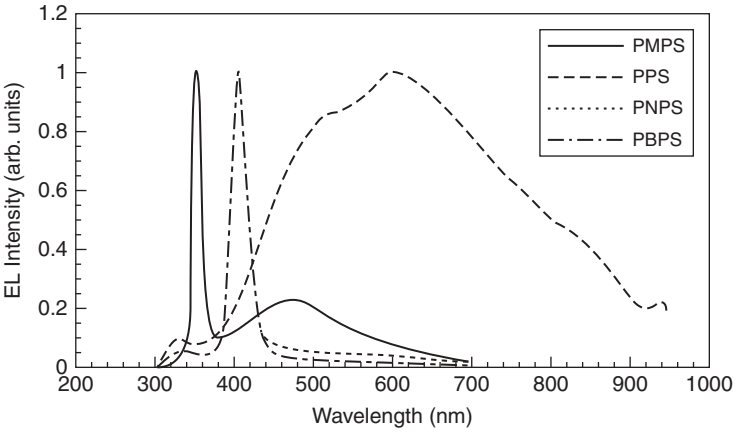

FIGURE 18. EL spectra of the polysilane EL diodes at 77 K. (Reprinted from Ref. 91.)

backbone are small regardless of the alkyl chain length, the energy difference in the excitons is assigned to the variation in backbone conformations. The emission of PDHS originates from the excitons delocalized along the polymer backbone with a trans-planar conformation. The PL spectrum in the NUV region is broader for PDBS than PDHS, indicating that there is a distribution in the energy of excitons in PDBS. It was revealed that the 7/3 helical structure is the most probable backbone conformation of PDBS, below the disordering temperature of 358 K. However, the PL excitation spectrum of the PDBS film exhibits a maximum around 320 nm and is similar to the absorption spectrum of a PDBS film with a disordered phase. Therefore, the NUV PL is ascribed to 1D-excitons delocalized along the disordered backbone. Weak VIS-PL emission of PDBS is assigned to branching, catalyzing the recombination of localized excitons.

The EL spectrum of the PDHS-LED is composed only of NUV emission around 368 nm almost identical to the PL spectrum. The EL spectrum of the PDHS-LED is thus due to the radiative recombination of excitons delocalized along a polymer backbone with a trans-planar conformation. The EL spectrum of the PDBS-LED is composed of NUV-EL, peaking at 341 nm and broad VIS-EL. The NUV-EL originates from the excitons that are the origin of the NUV-PL, but the VIS-EL was different from the PL observed in the VIS region in terms of intensity and spectral shape. The recombination sites for the VIS-EL are again assigned to branching points generated during synthesis.

It has been shown that the EL of polysilane-based LEDs is emitted near the interface between the polysilane and the electron injecting electrode, because of the strong unipolar (hole conductive) nature of polysilanes. Defect levels existing at the interface are considered to play an essential role in the emission of EL in the visible region,[93] and have both positive and negative effects on the LED characteristics. The positive space charges generated by

TABLE 2. PL and EL Characteristics of Linear Polysilanes[93]

	PL		EL					
polynitane	λ nm (ev)	VIS	λ nm (ev)	VIS	φ % photons/ electron	E_{tb} MV/cm	τ min	T_{op} K
PDBS	347 (3.57)	O	341 (3.64)	O	(10^{-4})	1.8	5–10	200
PDHS	379 (3.27)	×	368 (3.37)	×	(10^{-4})	3.0	5–10	200
PMPS	355 (3.49)	O	353 (3.51)	O	$<10^{-5}$	1.7	5–10	270
PBPS	406 (3.05)	×	407 (3.05)	×	<0.1	0.68	>720	RT

holes trapped at these defect levels facilitate the injection of electrons, which is crucial to improving the device characteristics of polysilane-based LEDs. Defect levels also act as efficient radiative recombination centers and energy acceptors for singlet excitons; therefore, the efficiency of the UV-EL is reduced. It was suggested that improvements could be achieved for the LED characteristics by using polysilanes carefully synthesized to prevent formation of defect levels, with high T_g and stability against light exposure. NUV LEDs emitting at 407 nm with an efficiency of 0.1% photons/electron and a spectral bandwidth of <15 nm have been obtained by optimizing the emissivity of the polysilane emitter layer. The Table 2 summarizes PL and EL characteristics of PDBS, PDHS, PMPS, and poly[bis-(*p*-butylphenyl)sialne] (PBPS).

Bilayered polysilane LEDs have been obtained by inserting a SiO_x thin layer between the cathode and a Wurtz synthesized PMPS emitter film.[94] The SiO_x layers were prepared by O_2 plasma treatment of the PMPS film surfaces. It was found that the external quantum efficiency was significantly enhanced by this treatment. This enhancement has been attributed to an increased electron injection via tunneling, resulting in a reduced hole current caused by the blocking effect of the thin SiO_x layer. The weak visible emission observed from single-layer polysilane LEDs is almost completely eliminated. It was concluded that the visible emission is caused by the erosion of the PMPS surfaces due to the collision with hot metal particles during the vacuum deposition of the cathode, and this erosion process is avoided by the SiO_x layer.

Poly[(*p*-butoxyphenyl)phenylsilane] (PBPPS) has been employed as an emissive layer of an organic EL device.[95] PBPPS was spin coated onto an uniaxially oriented poly(diethylsilane) (PDES) ultrathin film. Polarized NUV-EL was observed and the polarization direction was found to be identical with the drawing direction of the friction-transfer process for the PDES film, indicating that PBPPS in the emissive layer was aligned parallel to the uniaxial orientation of PDES.

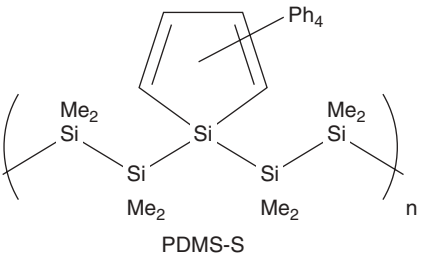

PDMS-S

FIGURE 19. Molecular structure of silole-incorporated polysilane (PDMS-S). (Reprinted from Ref. 96.)

An EL device using a polysilane that incorporates siloles with a high electron affinity, poly(2′,3′,4′,5′-tetraphenyl-1′-silacyclopenta-2′,4′-diene-1′, 1′-ylidene-1,1,2,2,3,3,4,4-octamethyltetrasilanylene (PDMS-S), as shown in Figure 19, exhibits blue emission with a maximum at 488 nm and better electrical properties compared to the device using PMPS without silole rings.[96] PDMS-S has a better injection balance of holes and electrons, and the silole derivative with low-lying LUMO levels are useful as electron-transporting materials. The maximum quantum external efficiency of the device with PDMS-S was 0.001%.

EL of perylene (blue), coumarin 6 (green), 4-(dicyanomethylene)-2-methyl-6-(*p*-dimethylaminostyryl)-4H-pyran and zinc tetra-phenylporphyrin (red) have been observed via an efficient intermolecular energy transfer from Wurtz synthesized poly(*m*-hexoxyphenyl)phenylsilane (PHPPS).[97] The EL device has a single layer, which was prepared by spin-casting the mixed solution of PHPPS and the energy-matched dye molecules. PHPPS films show a PL peak at 411 nm with a FWHM of 0.13 eV while the PHPPS/coumarin 6 film show a broad emission of coumarin 6 around 2.5 eV with a reduced PHPPS emission. Because no current was measured in the EL device without PHPPPS, the distinct green emission of coumarin 6 implies that the energy transfer from conducting PHPPS to coumarin 6 took place in the EL device. A white EL is observed from the mixture of PHPPS and the four dyes. The combination of a conducting polysilane and energy-matched dye molecules opens a field of Si-based EL devices through wet processes.

G. Cathodoluminescence

Wurtz-synthesized PMPS was selected as the material to be studied when subjected to cathodoluminescence (CL).[98] The CL method of the study of PMPS is based on the measurement of CL intensity of emitted light after its passage through the specimen, as shown in Figure 20. For the PMPS degradation measurements, electron beam energy of 10k eV was used. The PL emission spectrum consists of two emission bands. The maximum of the

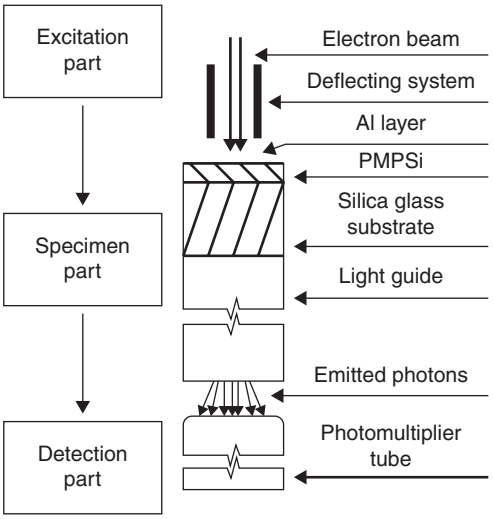

FIGURE 20. Layout of the experimental arrangement of the study of CL properties of polysilanes. (Reprinted in Ref. 98.)

weaker broad band in the visible region is 470 nm, whereas the narrow UV band is located at 356 nm. The layers were prepared from toluene solution by the spin-coating technique in two thicknesses (2.29 μm and 3.23 μm). The CL intensity of the thicker layer is proportional to the energy absorbed and converted to photons. The remaining electrons passed through the material in the specimen substrate, without PMPS excitation. A decrease of the CL intensity with irradiation time is attributed to material degradation. The interaction of electrons with PMPS is linked to the progressive scission of Si-Si bonds in the main chain, leading to the formation of radicals. After 150 min excitation, the specimens were left in a vacuum chamber at room temperature without excitation. After 20 h of such relaxation, the specimens were again excited under the same conditions. A partial recovery in intensity was observed, which was attributed to a reverse recombination reaction of silyl radicals in vacuum. The CL spectrum of PMPS is in good agreement with the PL spectrum. The unirradiated sample has a UV band at 357 nm along with a broad visible band from 420 nm to 570 nm, as shown in Figure 21.

Si-Si bond scission, cross-linking, and weakened bond formation are possible, depending on the conditions of excitation. This degradation of PMPS can be exploited in electron beam lithography.

H. Interaction with Photoelectrons

The interaction of polysilanes with X-ray photoelectrons (XPS) has been used for theoretical studies[99] and for analytical purposes.[19] Seven polymers with silane, carbosilane, and siloxane fragments—$(\text{-Si}(\text{CH}_3)_2\text{-})_n$ (PDMS),

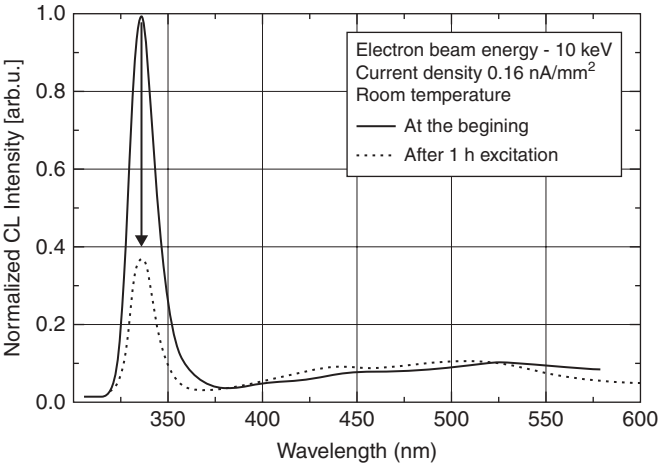

FIGURE 21. Change of the CL emission spectra of PMPS with electron beam irradiation time. (Reprinted from Ref. 98.)

$(\text{-Si}(C_6H_5)(CH_3)\text{-})_n$ (PMPS), $(\text{-Si}(\text{n-}C_6H_{13})_2\text{-})_n$ (PDHS), $(\text{-Si}(CH_3)_2\text{-O-})_n$ (PDMSO), $(\text{-Si}(C_6H_5)(CH_3)\text{-O-})_n$ (PMPSO), $(\text{-Si}(CH_3)(C_6H_5)\text{-}CH_2\text{-})_n$ (PMPSM), and $(\text{-Si}(C_6H_5)_2\text{-}CH_2\text{-})_n$ (PDPSM)—have been studied by deMon DFT, and the results have been compared with the observed spectra of the polymers between 0 and 40eV.[99] DFT by energy shift (*WD*) was used to account for solid-state effects and accurate core-electron binding energies (CEBEs) of eight polymers involving C, N, O, F, S, and Cl, calculated to simulate the valence XPS in a previous study.[100] The simulated and observed spectra of PDMS, PMPS, and PDHS are shown in Figure 22.

Characteristic spectra are observed in the range of 12−22 eV and are linked to oxidation states induced by the side groups. The intense peak from PDMS, as shown in Figure 22a is attributed to s-σ (C_{2s}-Si_{3s}) bonding orbitals, and the shoulder peak between 10 eV and 12.5 eV is attributed to the p-σ (Si_{3s}-Si_{3p}) bonding orbitals. As shown in Figure 22b for PMPS, three peaks at 19.5 eV, 17.0 eV, and 13.0 eV are seen for s- σ (C_{2s}-C_{2s}), s-σ (C_{2s}-Si_{3s}), and for p-σ (Si_{3s}-Si_{3p}) bonding orbitals. For PDHS as shown in Figure 22c, characteristic double peaks at 19.5 eV and 14.0 eV, which depend on the s-σ (C_{2s}-C_{2s}) and p-σ (C_{2s}-C_{2p}) bonding orbitals of the *n*-hexyl side groups, are seen. Similar comparisons were made between calculated and experimental spectra for PMPSM, PDPSM, PDMSO, and PMPSO polymers. The computed CEBEs of the seven polymers are in good agreement with the observed values. The energy shifts for these polymers are calculated as 6.2−6.8eV for silylene polymers, 7.1−7.2eV for silamethylene, and 5.7−5.8 eV for siloxythane polymers. Experimentally, XPS analysis has been performed on poly[methyl(H)-co-diphenyl]silane (PSHDF) (sample #1), polymethylphenylsilane (PSMF) (sample #2), and on the low molecular weight portion of PSHDF (sample #3),[19] as shown in Figure 23.

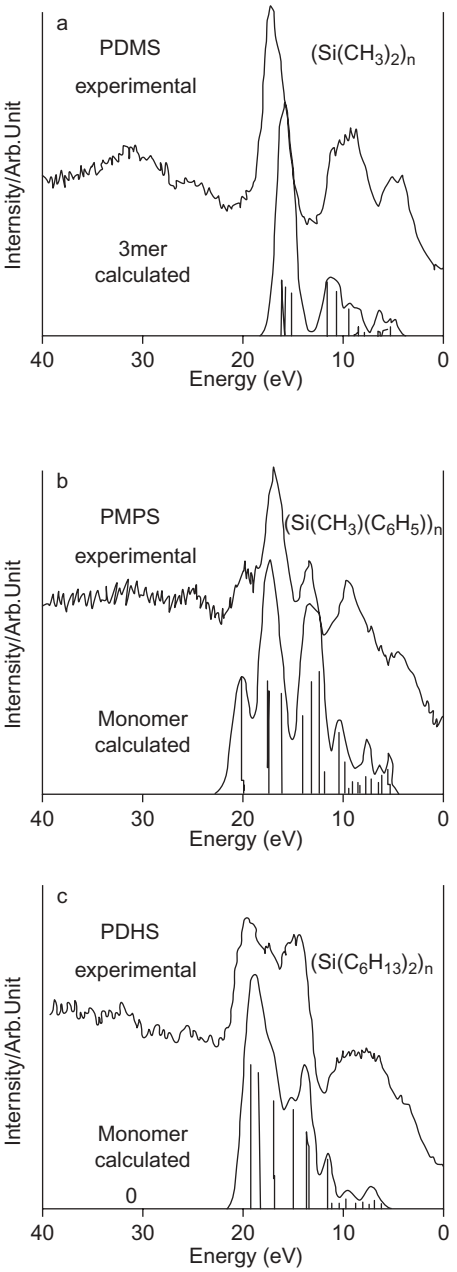

FIGURE 22. Valence XPS of (a) PDMS, (b) PMPS, and (c) PDHS with the simulated spectra of the model molecule using deMon. (Reprinted from Ref. 99.)

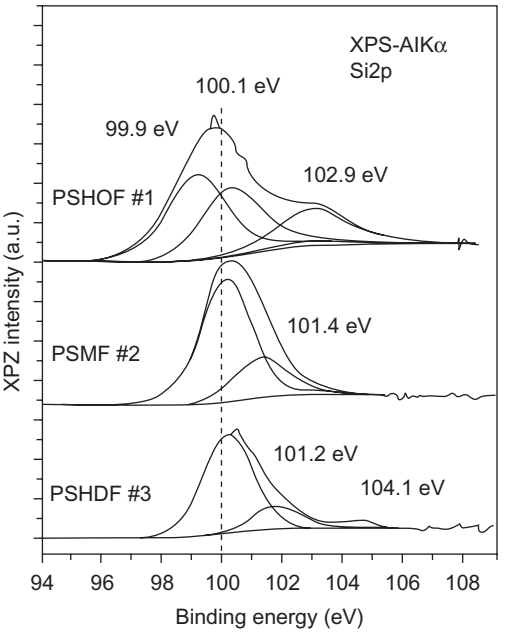

FIGURE 23. Si_{2p} spectra of polysilanes. (Reprinted from Ref. 19.)

XPS analysis confirms the effects of the restructuring process in polyhydrosilanes. The experimentally observed BE of 100.1 eV for sample #2 is assigned to a Si atom coordinated to two other silicon atoms, a phenyl and a methyl group. The second Si_{2p} at 101 eV is due to one of the Si neighbors being replaced by oxygen. The Si_{2p} spectrum for sample #3 shows a component at 104.4 eV originating from completely oxidized silicon atoms and a component at 101.8 eV from partially oxidized Si atoms. The Si_{2p} spectrum of sample #1 shows four components at 99, 100, 102, and 103.6 eV. The main difference with sample #3 is the appearance of the peak at 99 eV, which represents elemental Si. The increased O/Si atomic ratios obtained for PSHDF results from the contribution of the methylhydrosilyl segments, which participate in oxidative restructuring, even at low temperatures.

V. PHOTOCHEMISTRY

Time-dependent emission spectra from Wurtz-synthesized PMPS ($M_w = 1.1 \times 10^4$), poly(methylpropylsilane) (PMPrS, $M_w = 4.1 \times 10^4$) and

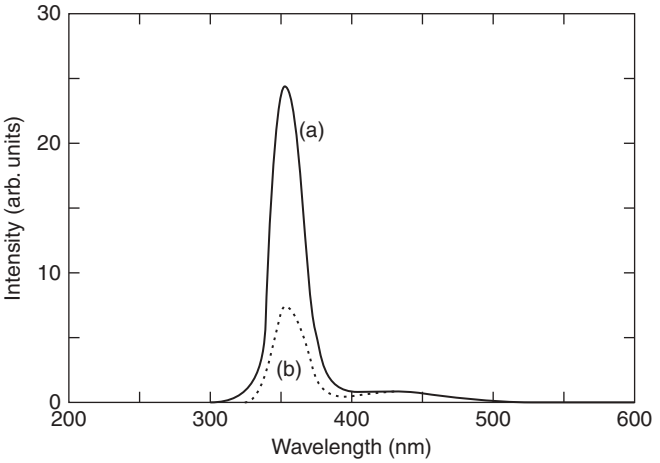

FIGURE 24. Time-dependent emission spectra of PMPS (a) 100 s irradiation and (b) 1000 s irradiation. (Reprinted from Ref. 19.)

PDHS (M_w = 2.9x 10^4), spin coated on Si substrates were measured at room temperature under 2.0M eV He^+ irradiation.[101] Emission spectra of PMPS were obtained after 100 s and 1000 s of irradiation. Two emission bands at 355 nm and 440 nm are observed, as shown in Figure 24.

The 355 nm emission is sharp and intense at the start of irradiation, and the intensity decreases with prolonged irradiation time. The 440 nm emission is weak and broad, and the intensity does not change with the irradiation time. Emission spectra of PMPrS obtained at ion fluences of 0.15, 0.76, and 1.53 $\mu C/cm^2$ shows emission bands at 350 nm and 440 nm. The decrease in the intensity of the main peak indicates that main chain scission (photolysis) occurs under ion beam irradiation. Intense and sharp emission at 340 nm and weak broad emission at 440 nm for PDHS at 354 K are observed at the beginning of the irradiation and decrease on further irradiation. At 313 K and 270 K, sharp intense main emissions at 385 nm are seen. The 340 nm and 385 nm emission bands are assigned to σ^*- σ fluorescence. Experimental results have shown the presence of a phase transition at 313 K for PDHS.[102,103] Below 313 K, the backbone conformation of PDHS is trans-planar, and above the solid-solid phase change temperature, a disordered conformation is seen. Fluorescent σ^*-σ transitions occur at 355 nm for PMPS, 350 nm for PMPrS, and 385 nm and 340 nm for PDHS. Emissions around 440 nm are observed at all temperatures examined and are assigned to defect and network structures induced by ion beams.

UV irradiation causes photodegradation of poly[methylcyclohexyl-co-methyl(β-tri-methylsilyl)ethyl]silane and PMPS solutions.[104] It was found that branching of PMPS is induced by light exposure. The photochemistry of both pure solids and their toluene solutions has been studied. The UV absorption of the copolymer in solution has a maximum at 308 nm and at 303 nm for the

film. UV irradiation of the copolymer causes a rapid decrease of the main absorption band. An interesting effect accompanying the degradation of the polymer is that with a decrease in the optical density of the absorption maximum, λ_{max} shifts to shorter wavelengths. The blue shift is related to reduced length of the chain fragment having the trans-planar conformation. It is concluded that the UV irradiation of polysilane solutions causes their photodegradation, whereas long-term exposure to visible light causes photochemical branching and further cross-linking of the polymer.

Light-induced degradation of PL occurs not only for Wurtz-synthesized PMPS (M_W = 114,500) with aromatic substituents but also for poly(cyclohexylmethylsilane) (PHMS) (M_W = 120,000) without aromatic substituents.[105] PMPS shows a sharp PL peak at 360 nm with a FWHM of 0.16 eV and a broad peak at 530 nm with a FWHM of 0.6 eV. PHMS gives PL spectra with a single peak at 350 nm and a FWHM of 0.15 eV. The peaks at 350−360nm for both polysilanes are due to the σ*-σ emission, while the broad peak for PMPS is assigned to the aromatic substituents. The PL spectra degradation is attributed to annihilation of σ bonds. The variation of the PL intensity with time shows that each curve has a clear kink separating two components. This two step decay of the PL intensity is a universal phenomenon for polysilane films and is independent of the substituents. The first decay is explained in terms of an interaction of excitons with trapped carriers. The second decay corresponds to a decrease in the absorption of excitation light.

A. Photo-Oxidation

One of the most serious problems for the practical applications of polysilanes is the photooxidation of the Si main chain under UV light irradiation.[106] Suppression of the photooxidation has been attempted by embedding polysilanes into SiO_2 glass networks by coupling hydrophobic polysilanes to hydrophilic molecules.[107] Water-soluble poly-*n*-hexyl(((*N,N*-dimethyl-3-methylpentan-1-ol-2-ammonio)methyl)phenyl)silane chloride (HSC), poly-*n*-propyl((triethylammonio)methylpehnyl)silane chloride (PSC), and poly-*n*-hexyl (((triethylammonio)methyl)phenyl)propylsilane chloride (HTSC) were synthesized by the Wurtz reaction and a Fridel-Crafts chloromethylation, as shown in Figure 25.

Through sol-gel processes, ethanol-diluted polysilanes were added to the starting solution of TEOS and the solution was spin coated on quartz substrates. The PL spectrum of HTSC embedded into sol-gel glass is identical to that of spin-coated HTSC films, indicating that the main chain is sufficiently relaxed even inside the glass network. PL quenching of the HTSC spin-coated film to 10% of its initial intensity after 30 min of UV exposure is observed. The PL intensity of the glass film with HTSC is quenched during the initial 10 min, but the intensity is kept at 70%, with no additional decrease observed after 30 min. This distinct difference is attributed to an effective protection of the surrounding SiO_2 glass network against free oxygen and water.

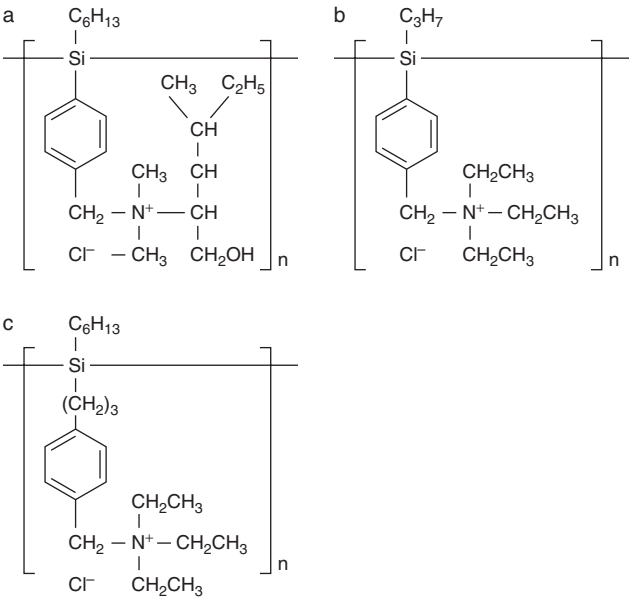

FIGURE 25. Molecular structure of synthesized water-soluble polysilane: (a) HSC, (b) PSC, and (c) HTSC. (Reprinted from Ref. 106.)

VI. POLYSILANE THIN FILMS FOR ELECTRONIC DEVICES

A. LED

The properties of polysilanes can be used in the development of (opto) electronic devices due to their potential as UV and NUV emitters. There are few materials that have been demonstrated to be good UV-emitters.[108] Single crystal nitride-semiconductors, SiC, and few oxides are some of the inorganic materials that have been used to make solid-state UV-LEDs, but making single crystals of even limited dimensions of these materials is relatively expensive. A proposed alternative to this problem is the use of organic LEDs with emission in the UV-NUV range. Organic polymers are not suitable due to a low π-π^* band gap as well as to a large Stokes shift, leading to emission with even longer wavelengths.[109] The easy synthesis of polysilane films allows design of large area and low-cost UV emitters.

UV-EL diodes were fabricated based on a Al/polysilane/ITO/glass structure.[36] Glass or quartz plates coated with indium-tin-oxide (ITO) were used as substrates. The EL diodes operate at room temperature.[36] A typical representation of the structure is shown in Figure 26.[93] The device comprises a heterojunction forming a Schottky diode, with the polysilane film being the p-type layer, the ITO acting as an ohmic contact, and the Al being the Schottky

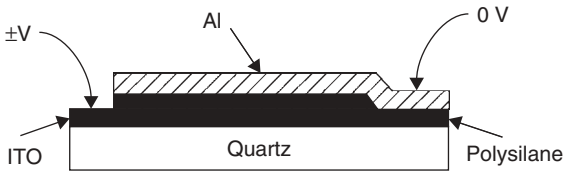

FIGURE 26. Structure of single-layer LEDs. (Reprinted from Ref. 93.)

barrier. Hattori used a PDMS film deposited onto ITO by evaporating a PDMS source at about 300°C under high vacuum (1.0×10^{-6} torr).[36] An Al top electrode with a thickness of 1000 Å was then evaporated in another evaporator. Temporal exposure of the PDMS surface to air before Al evaporation was observed to induce surface oxidation and/or contamination. A low deposition rate of 7 Å/min was observed to ensure that the PDMS molecules aligned normal to the substrate surface. The thickness of the film was 4000 Å. PDHS based UV-LED was prepared by adding *n*-dichlorodihexyl to sodium in *n*-octane at 383 K to give a 10% yield of crude PDHS (M_W = 300,000) as a flexible hard white elastomer.[110] The crude polymer was purified by reprecipitation from benzene-ethanol. The polysilane in xylene was then spin coated as thin films between ITO and aluminum electrodes with a thickness of 500 nm. The EL is emitted in most cases from singlet excited states of the emissive material, although they are generated in different ways: direct photoexcitation for the PL and recombination of electrons and holes for the EL.[111] EL covering the whole visible spectrum can be observed by doping polysilanes with organic dyes.[97]

Polarized organic LEDs of the type ITO glass/photodegraded PMPS/phthalocyanines/Al were prepared by using PMPS films exposed to polarized UV light.[112] The device structure consisted of the hole injection ITO electrode, the hole transporting PMPS film, the emissive phthalocyanine layer, and the Al electrode. The EL films of phthalocyanines deposited on PMPS surfaces from solution or vacuum evaporation showed oriented structures, which produced polarized EL.

B. Photoconductors

Photoconductive cells have been prepared using fullerene doped PMPS.[113] With 1.6% of fullerene as dopant, its photoinduced discharge rate is enhanced by orders of magnitude.[113] Wavelength selectivities of organic photoconductive films can be obtained by varying the dopant.[114] The device uses a double-layer structure with zinc phthalocyanine/tris-8-hydroxyquinoline aluminum. The doping of polysilane can be obtained using the CT interaction between networked polysilanes and substituents, such as alkyls, aryls or iodine.[40] With MeO-functionalized polysilanes as the starting material, networked polysilanes $[MeSi(OMe)_x(R)_y]_n$ have been obtained with various R

groups as the side chains by the action of the corresponding Grignard reagents RMgX. Among these polysilanes, those having *N,N*-dialkylaminophenyl groups as side chains exhibit electrical conductivities on the order of 10^{-3} Scm^{-1} upon iodine doping, which are essentially stable under oxidative conditions because of their network structures.[40] Although linear polysilanes generally show high hole mobility or photorecepting ability due to their electrical characteristics, no studies regarding such properties for network polysilanes has appeared so far. The CT between iodine and polysilane has been used to produce photoconductor thin films.[40] Organic polysilane-TiO_2 thin films prepared by a sol-gel process show lower PL quantum efficiency than PS-silica hybrid thin films[115] and higher photoconductivity.[116] This is explained by the fact that the photogenerated excitons are dissociated at the PS/TiO_2 nanointerface because of electron transfer from PS to TiO_2 in the excited states and/or due to photoinduced CT.

C. Photovoltaics

Fullerene/PMPS photovoltaic cells were fabricated with various concentrations of C_{60}.[117] The structure of the device is shown in Figure 27. The ITO glass substrate with a sheet resistance of $10\Omega/cm^2$ was cleaned by an ultrasonic bath of isopropyl alcohol, toluene, acetone and methanol followed by air plasma treatment. As a buffer layer, poly(3,4-ethylenedioxythiphene): poly(4-styrenesulfonate) (PEDOT:PSS, Baytron P) was spin coated with a thickness of 40 nm on the ITO glass substrate to decrease contact resistance between ITO and the photoactive layer. The photoactive layer was prepared by spin coating a C_{60}/PMPS solution in chlorobenzene to a thickness of 80 nm on the PEDOT:PSS buffer layer. After drying at 40°C for 12 h, a 0.6-nm LiF layer was vacuum deposited on the photoactive layer at 10^{-5} torr to ensure a good ohmic contact between the metal and organic layer. A 100-m Al electrode was then vacuum deposited. The photoactive area of the device was 4 mm^2.

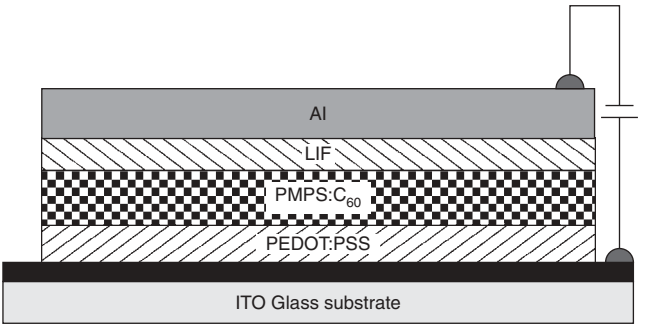

FIGURE 27. C_{60}/PMPS device. (Reprinted from Ref. 117.)

Poly[*p*-(methylphenylsilanylene)anthrylene] (PMPSA) with anthracene units incorporated into the backbone of poly(methylphenylsilanylene) was synthesized.[118] Schottky barrier photovoltaic cells consisting of semi-transparent aluminum and phthalocyanine (H_2Pc) dispersed in PMPSA were fabricated (H_2Pc-PMPSA). The conductivity of H_2Pc-PMPSA films increased by the introduction of anthracene units and annealing, which improved the photovoltaic properties. The power conversion efficiency presented a maximum for H_2Pc-PMPSA with a copolymerization ratio of (1:1) at the annealing temperature of 160°C for 2 h.

Quasi-solid state dye-sensitized solar cells (DSCs) have been constructed using a new polymeric ionic fluid as the electrolyte.[119] The electrolyte was synthesized by the sol-gel route using $MTMSPI^+I^-$ as the precursor that was made by derivatizing methylimidazolium with triethyoxysilane. Condensation of this material in the presence of formic acid and in the absence of water led to Si-O-Si-O-type polymerization and formation of a polysilsesquioxane-type structure. When this material was mixed with iodine, it served as a redox electrolyte for DSCs. The DSCs made this way are robust and easy to assemble but their efficiency of 3.1% is relatively low. However, possible improvement lies in modification of the organic groups attached to the polysilsesquioxane backbone.

D. Lithography

The near-UV absorption (300–400 nm) properties of polysilanes originally attracted attention because of their possible applications as photoresists for high-resolution lithography.[46] The proposed mechanism of polydialkylsilane photodegradation by Michl[46] involves two concurrent and competitive reactions. One of these is silylene extrusion, which shortens the polymer chain by only one unit and does not affect the molecular weight significantly, as shown in reaction 1. The other is homolytic cleavage, which cuts the average molecular weight approximately in half, as shown in reaction 2.

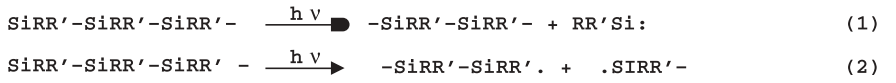

A third process proposed by Michl to be involved in photodegradation is chain cleavage by reductive elimination according to reaction 3:

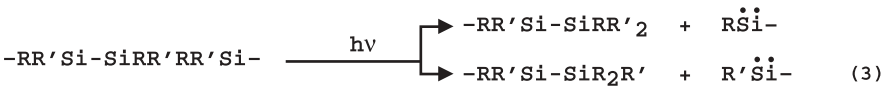

The degradation mechanism makes polysilanes choice materials for the fabrication of patterns with very high resolution, because polysilanes are easily converted to materials having completely opposite properties when exposed to UV and high-energy beams.[120] Polysilanes are dry etched at a lower rate than usual electronic substrates such as SiO_2 and silicon layers under plasma gas and are also different from the dry-etching rates of polysiloxane layers formed by irradiation followed by photo-oxidation of the polysilane. A special advantage of the polysilane as photoresist materials is the fact that the Si atoms forming the backbone are not recognized as being impurities by the Si substrate host, while carbon or metal atoms cause serious contamination problems in the Si layer. Bilayer resists using polysilanes became important for deep UV exposures, wavelength <200 nm, because they eliminate the problem of penetration depth of the light. Anti-reflection layers for deep UV lithography is another interesting application of polysilanes, which are better than the conventional organic anti-reflecting coatings (ARC). Advantages for polysilane ARC are that the resist thickness can be reduced, and the ARC thickness can be increased. The etching selectivity and optical properties make polysilanes the most promising anti-reflection films for lithography.[120] Exposure of a polymethylsilyne film with a thickness of 120–170 nm, plasma polymerized with a 240-nm light, results in an etching selectivity coefficient of 3 between the exposed area (flux = 100 mJ/cm^2) and the unexposed area, which is a good value for the lithographic process. The efficient photooxidation of the polysilane allows fabrication of patterns of 200 nm resolution, via the selected production of thin oxide hard masks. The dry development has been carried out in Cl or HBr plasmas, and the unexposed polysilane area, is etched faster than the photooxided area, providing negative images.[121–127] Polybutylsilylene has the highest sensitivity toward HBr etching and shows photooxidation by exposure to 193 nm. Larger substituents such as phenyl and cyclohexyl groups decrease the sensitivity.[123] Table 3 summarizes the positive and negative photoresist behavior of some polysilanes.

Copolymers between polysilanes and OH/COH bearing organic polymers have been used for developing procedures in aqueous solutions.[47,128]

E. Electron Beam

Increased resolution of the LSI patterning can be obtained by e-beam lithography. Polysilanes can be used as analogue-type positive resists, defined as materials that have properties (thickness, solubility, T_g) developed proportionally with the UV exposure, desirable for the fabrication of optical elements by direct writing, such as masks.[51] Photopolymerization using PMPS with an average molecular mass of 1.32×10^4 and $M_w/M_n = 1.94$ as a macromolecular photoradical initiator has been used to produce a polysilane-acryl block copolymer ($M_n = 1.02 \times 10^4$, $M_w/M_n = 1.78$).[129] A series of thin films were irradiated with a 50 kV e-beam. The test pattern was developed in 2-propanol and 2-buatone solution as well as reactive ion etching (RIE)

TABLE 3. Polysilane Resists and Development Methods[120]

Polymer Structure	Preparation	Exposure	Development	Location
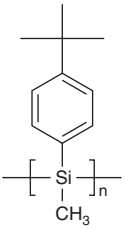	Spin coating	313 248 248	Methylcyclohexane Isopropylalcohol (P) Ablation (P) Ablation (P)	IBM/Wisconsin Unversity Sandia, N.L.
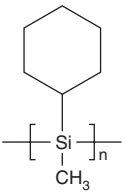	Spin coating	248	THF/isopropanol (P) Cyclohexanol Butylacetate Isopropanol	ATT/Sandia, N.L. IBM/University of Texas
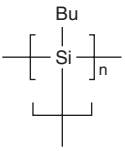	Spin coating	193	Methanol, Acetone (N) Toluene (P) Cl_2,HBr plasma (P)	MIT/Penn State University
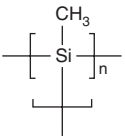	Plasma	193	Toluene (N) HBr, Cl_2 RIE (N) Ablation	MIT
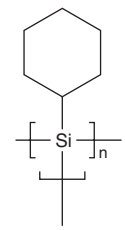	Spin coating	193	HBr plasma (N)	MIT/IBM/Penn State University
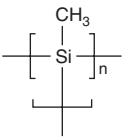	Plasma Plasma	248 193 193	Cl_2 (N) NH4F/HF (P) Cl_2 (N)	ATT MIT

P, positive; *N*, negative.

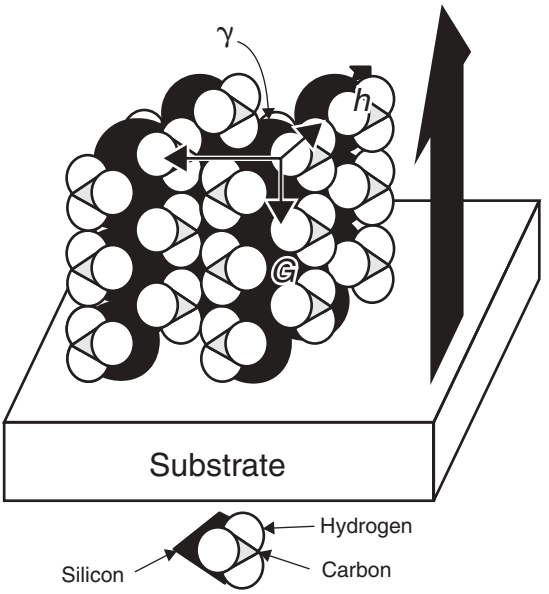

FIGURE 28. Structural model of the evaporated film. (Reprinted from Ref. 30.)

in fluorocarbon/O_2 plasma.[51] On the positive pattern, Al was then vacuum deposited without any deformation although similar deposition of polymethylmethacralyate gave a rough surface. This result is attributed to the higher heat resistance of the copolymer than that of polymethylmetacrylate.[51] Similarly, PMPS has been used as a macromolecular photoinitiator to produce block polysilanemethyacrylate copolymer.[52] The product has been spin coated from a toluene solution and irradiated with 50 kV electron beam with the conclusion that the copolymer is more suitable for e-beam lithography than the organic counterpart due to the high heat resistance, dry-etching resistance, and good sensitivity to electron beam irradiation.

By e-beam irradiation onto a highly oriented PDMS film in which the polymer's backbone is perpendicular to the substrate surface, submicron patterns were obtained after the etching process.[130] PDMS was synthesized by the Wurtz-type method from dimethylchlorosilane, and oriented films were prepared by vacuum evaporation on fused silica. Figure 28 shows the structural model of the evaporated film. The oriented character and the high density of the film are advantageous for high resolution. The fabrication process for obtaining submicron patterns using the oriented films is shown in Figure 29.

The first step (Fig. 29a) is the evaporation of the polysilane material and recrystallization on the substrate. The film is then irradiated by the electron beam (Fig. 29b). In the irradiated area of the film, C-O-C, Si-O-C, and Si-O-Si bonds are formed between nearest-neighbor polysilane chains. Thus the

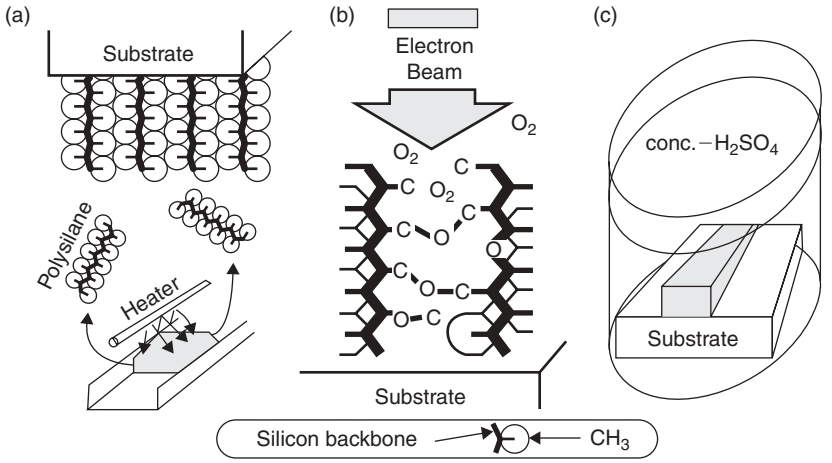

FIGURE 29. Process for the fabrication of the submicron pattern. (Reprinted from Ref. 130.)

irradiated film is hardened and has durability against etching. The specimen is then dipped in concentrated H_2SO_4 so that only the irradiated part of the films remains and forms the negative-tone pattern on the substrate surface. The estimated dose values obtained with acceleration voltages of 15 kV, 10 kV, and 5 kV with beam currents of 200 pA, 130 pA, and 60 pA and irradiation times of 15 min are 7.2×10^{-2} C/cm^2, 3.3×10^{-2} C/cm^2, and 1.1×10^{-2} C/cm^2. The electron beam could be made narrower with higher acceleration voltage so the narrowest pattern is obtained at about 0.5 μm Patterns with irradiation times of 20 and 30 min, with voltage and beam current kept constant at 15 kV and 200 pA, have dose values of 9.6×10^{-2} C/cm^2 and 1.4×10^{-2} C/cm^2. These show an increase in the width of the pattern and are explained by the effects of mechanical vibrations and backscattering of the electron.[130]

VII. POLYSILANE FILMS FOR OPTICAL DEVICES

Pure optical applications are found in the use of PMPS grating layers as an alignment layer for liquid crystal cells.[131] A toluene solution of Wurtz-synthesized PMPS was spin coated to 100 nm thickness on glass and ITO substrates. Gratings were fabricated by either a holographic method or a phase-mask method using a He-Cd laser. The sandwich-type liquid crystal cells were prepared by parallel arrangement of two PMPS gratings on ITO substrates, as shown in Figure 30. The thickness of the liquid crystal cells was about 19 μm and liquid crystalline compound, 4-cyano-4′-*n*-pentylbiphenyl was introduced into the cells.

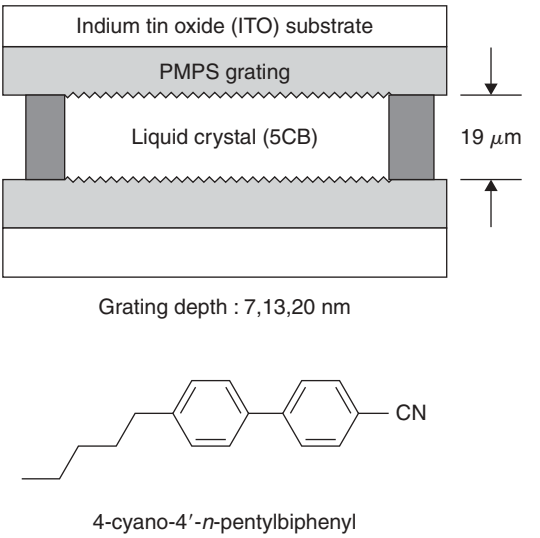

FIGURE 30. Structure of liquid crystal cells. (Reprinted from Ref. 131.)

It was found that liquid crystal molecules are aligned parallel to the grating grooves and that even 20-nm grating depths are effective for alignment of liquid crystal molecules. Photoinduced surface relief gratings on PMPS thin films are thus applicable to the alignment layers for liquid crystal cells with weak anchoring energy whose (opto)electronic properties were improved in comparison with conventional liquid crystal display devices. The operating voltage of liquid crystal cells with weak anchoring energy is considerably reduced.

An array of 10-μm microlenses was fabricated from the adhesion of an aminated silicasol on a poly[methyl(phenyl)silane-co-methyl(3,3,3-trifluoropropyl)silane] (CF_3PMPS) film patterned by UV light irradiation.[132] By soaking the UV-patterned polysilane film into the sol-gel solution, a convex xerogel layer adhered only to the UV-exposed polysilane, which was cured to form a glass that functioned as a condensing lens.

Electrically active PMPS, known as a good hole transporting material, and poly[bis(*p*-*n*-butylphenyl)silane] (PBPS), known as NUV EL materials, were end grafted directly on a crystalline silicon surface.[133] The cut and graft technique used involved a one-to-one chemical reaction between a reactive anchor built on a substrate, and an end-lithiated polysilane prepared by the scission reaction of a Si-Si bond in polysilane using methyllithium in a polar organic solvent. End-grafted single molecules of PMPS were observed as dots, while end-grafted PBPS appeared as worms due to the rigidity of the PBPS resulting from the intramolecular stacking forces between the phenyl rings.

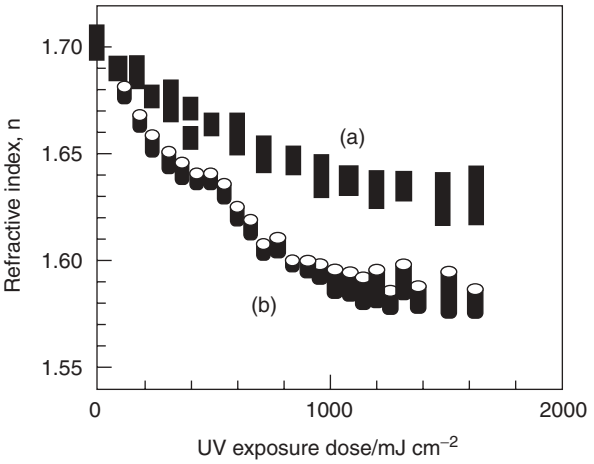

FIGURE 31. The refractive index variation in the PMPS film by UV-light irradiation using different light sources: (a) excimer lamp (308 nm) and (b) mercury-arc lamp (185, 254, 303 nm). (Reprinted from Ref. 134.)

A. NLO

The development of phase masks using the refractive index variation due to the UV-photodecomposition of the polysilane was examined.[134] The refractive index due to UV-photodecomposition of PMPS changes from 1.70 to 1.56. The refractive index variation in PMPS films by UV-light irradiation is shown in Figure 31.

When the excimer lamp of 308 nm is used for the irradiation light source, the refractive index lowers from 1.70 to 1.63. With the mercury-arc lamp the refractive index lowers to 1.58. The larger reduction of the refractive index with the shorter wavelength light derives from the elimination of the side-chain phenyl group.

UV light induced refractive index change has been observed in organic polysilane (PS)-silica and PS-titania hybrid thin films prepared by the sol-gel method.[135] The magnitude of the refractive index change was found to be 0.16 for 50 wt % PS-silica and 0.18 for 50 wt % PS-titania hybrid thin films. It was demonstrated that the refractive index change of the hybrid thin films is due to the photodecomposition of PS. These findings indicate potential usefulness of the hybrid thin films as optical devices with refractive index modulated structures.

VIII. SUMMARY

The σ-σ^* conjugation along Si-Si bonds in linear and reticulated polysilanes results in valuable optical and charge transport properties, with broad

applications in (opto)electronic devices. A high degree of ordering in molecules, self-assembled thin films on various substrates of interest for the electronic industry (ITO, SiO_2, Si, TiO_2), as well as the high-crystallinity in 3D structures, can significantly change the behavior of the polysilanes. Control of the absorption and emission properties of the polysilane structures, used either as active or passive components in the design of devices is obtained via specific synthesis methods coupled to classic thin film deposition procedures. Polysilane layers are used as photoconductors, photoresists, antireflective layers, photomasks, emissive and transport layers in LEDs, and photovoltaic devices among many others. Current research in the field is devoted to improve the homogeneity of the materials to reach ULSI resolution, to control photolysis and photo-oxidation at the 0.1-μm spatial resolution, and to induce chemical and steric homogeneity, consistent with the synthesis of nanowires and future derived nanostructures.

IX. REFERENCES

1. R. West, *J. Organometall. Chem.,* **300,** *327* (1986).
2. J. R. Koe, D. M. P. Mingos, R. H. Crabtree, eds., Elsevier Organopolysilanes, Oxford, 2007.
3. K. Ishida, D. Sasaki, T. Horiuchi, K. Matsushige, *Synth. Metals,* **91,** *371* (1997).
4. S. Furukawa, H. Ohta, *Thin Solid Films,* **438-439,** *48* (2003).
5. R. Hattori, T. Sugano, J. Shirafuji, *Appl. Surface Sci.,* **113/114,** *472* (1997).
6. S. Furukawa, K. Takeuchi, *Solid State Commun.,* **87,** *931* (1993).
7. S. Gauthier, D. Worsfold, *Macromolecules,* **22,** *2213* (1989).
8. R. G. Jones, R. E. Benfield, R. H. Cragg, A. C. Swain, *J. Chem. Soc. Chem. Commun,* **112 (**1992).
9. R. G. Jones, R. E. Benfield, R. H. Cragg, A. C. Swain, S. J. Webb, *Macromolecules,* **26,** *4878* (1993).
10. R. G. Jones, U. Budnik, S. J. Holder, W. K. C. Wong, *Macromolecules,* **29,** *8036* (1996).
11. Y. Hsiao, J. P. Banovetz, R. M. Waymouth, *ACS Symp. Ser.,* **572,** *55* (1994).
12. D. Seyferth, T. Sugimoto, P. Czubarow, US Pat., **6,020,** *447* (2000).
13. C. A. Burkhard, *J. Am. Chem. Soc.,* **71,** *963* (1949).
14. M. Kumada, K. Tamao, *Adv. Organometal. Chem.,* **6,** *19* (1968).
15. K. S. Mazdyasni, R. West, L. D. David, *J. Am. Ceram. Soc.,* **61,** *504* (1978).
16. J. D. Wesson, T. C. Williams, *J. Polym. Sci. Polym. Chem. Ed.,* **18,** *959* (1980).
17. R. E. Trujillo, *J. Organomet. Chem.,* **198,** *C27* (1980).
18. R. D. Miller, R. Sooriyakumaran, *J. Poly. Sci. Part A, Pol. Chem.,* **25,** *321* (1987).
19. L. Sacarescu, A. Siokou, R. Ardeleanu, G. Sacarescu, M. Simionescu, *Macromol. Rapid Commun.,* **27,** *1054* (2006).
20. M. Scarlete, S. Brienne, I. S. Butler, J. F. Harrod, *Chem. Mater.,* **6,** *977* (1994).
21. C. T. Aitken, J. F. Harrod, E. Samuel, *J. Am. Chem. Soc.,* **108,** *4059* (1986).
22. C. Aitken, J. F. Harrod, E. Samuel, *Can. J. Chem.,* **64,** *1677* (1986).

23. R. J. P. Corriu, M. Enders, S. Huille, J. J. E. Moreau, *Chem. Mater.,* **6,** *15* (1994).
24. T. D. Tilley, *Acc. Chem. Res.,* **26,** *22* (1993).
25. C. Mechtler, C. Marschner, *Organosilicon Chemistry IV: From Molecules to Materials,* Wiley-VCH Verlag, Weinheim, (2000).
26. L. Rosenburg, *Macromol. Symp.,* **196,** *347* (2003).
27. E. Hengge, G. Litscher, *Angew. Chem.,* **88,** *414* (1976).
28. E. Hengge, G. Litscher, *Monatsh. Chem.,* **109,** *1217* (1978).
29. E. Hengge, H. Firgo, *J. Organomet. Chem.,* **212,** *155* (1981).
30. R. J. P. Corriu, G. Dabosi, M. Martineau, *J. Chem. Soc., Chem. Commun., 457* (1979).
31. R. J. P. Corriu, G. Dabosi, M. Martineau, *J. Organomet. Chem.,* **188,** *63* (1980).
32. R. J. P. Corriu, G. Dabosi, M. Martineau, *J. Organomet. Chem.,* **222,** *195* (1981).
33. X. Wang, Y. Yuan, I. Cabasso, *Electrochem. Solid State Lett.,* **9,** *D34* (2006).
34. K. Sakamoto, M. Yoshida, H. Sakurai, *Macromolecules,* **23,** *4494* (1990).
35. M. Yoshida, T. Seki, F. Nakanishi, K. Sakamoto, H. Sakurai, *Chem. Commun., 1381* (1996).
36. R. Hattori, T. Sugano, J. Shirafuji, T. Fujiki, *Jpn. J. Appl. Phys.,* **35,** *L1509* (1996).
37. R. G. Kepler, J. M. Zeigler, L. A. Harrah, S. R. Kurtz, *Phys. Rev.,* **B35,** *2818* (1987).
38. Y. Majima, H. Nishizawa, T. Hiraoka, Y. Nakano, S. Hayase, *Jpn. J. Appl. Phys.,* **34,** *3820* (1995).
39. L. A. Leites, S. S. Bukalov, T. S. Yadritzeva, M. K. Mokhov, B. A. Antipova, T. M. Frunze, V. V. Demoentev, *Macromolecules,* **25,** *2991* (1992).
40. T. Kobayashi, H. Shimura, S. Mitani, S. Mashimo, A. Amano, T. Tankano, M. Abe, H. Wantanabe, M. Kijima, H. Shirakawa, H. Yamaguchi, *Angewandte Chem.-Int. Ed.,* **39,** *3110* (2000).
41. S. Furukawa, K-I. Takeuchi, *Solid State Communi.,* **87,** *931* (1993).
42. R. D. Boyd, J. P. S. Badyal, *Adv. Mater.,* **9,** *895* (1997).
43. R. D. Miller, D. Hofer, D. R. McKean, C. G. Willson, R. West, P. T. Trefonas, *Materials for Microlithography ACS Symposium Series,* American Chemical Society, Washington, DC, **266 (**1984).
44. R. D. Miller, D. Hofer, G. N. Fickes, C. G. Wilson, E. Marinero, P. Trefonas, R. West, *Photopolymers: Principles, Processes, and Materials* Mid-Hudson Section of Society of Plastics Engineers, Ellenville, N.T. (1985).
45. J. M. Zeigler, L. A. Harrah, A. W. Johnson, *SPIE Proc.,* **539,** *166* (1985).
46. J. Michl, J. W. Downing, T. Karatsu, A. J. McKinley, G. Poggi, G. M. Wallfraff, R. Sooriyakymaran, R. D. Miller, *Pure Appl. Chem.,* **60,** *959* (1988).
47. J. V. Beach, D. A. Loy, Y. Hsiao, R. M. Waymouth, *ACS Symp. Ser.,* **614,** *355* (1995).
48. R. Kani, Y. Nakano, H. Yoshida, S. Mikoshiba, S. Hayse, *J. Polym. Sci. Part A Polym. Chem.,* **35,** *2355* (1997).
49. E. Watanabe, H. Tsushima, *Preparation Polymer Material Forum,* The Society of Polymer Science, Tokyo, **4,** *97* (1995).
50. M. Fukushima, N. Noguchi, M. Aramata, Y. Hamada, E. Tabei, S. Mori, Y. Yamamoto, *Synth. Metals,* **97,** *273* (1998).
51. T. Tamai, Y. Matsuura, K. Matsukawa, H. Inoue, T. Hamamoto, H. Toyota, K. Satho, *Journal of Photopolym. Sci. Technol.,* **14,** *185* (2001).
52. Y. Matsuura, T. Tamai, K. Matsukawa, H. Inoue, T. Hamamoto, H. Toyota, K. Sato, *Journal of Photopolym. Sci. Technol.,* **14,** *175* (2001).
53. S. Seki, et al. *J. Phys. Chem.,* **B102,** *8367* (1998).
54. S. Seki, Y. Sakurai, K. Maeda, Y. Kunimi, S. Tagawa, *Jpn. J. Appl. Phys.,* **39,** *4225* (2000).

55. D. Bratton, D. Yang, J. Dai, C.K. Ober, *Polym. Adv. Technol.,* **17,** *94* (2006).
56. T. Sato, N. Nagayama, M. Yokoyama, *Jpn. J. Appl. Phys.,* **43,** *8064* (2004).
57. A. Okazaki, S. Akita, Y. Nakayama, *Jpn. J. Appl. Phys.,* **41,** *4973* (2002).
58. S. Hayase, Y. Nakano, S. Yoshikawa, H. Ohta, Y. Sato, E. Shiobara, S. Miyoshi, Y. Onishi, M. Abe, H. Matsuyama, Y. Ohiwa, *Chem. Mater.,* **13,** *2186* (2001).
59. Y. Sato, E. Shiobara, S. Miyoshi, M. Asano, H. Matsuyama, Y. Onishi, Y. Nakano, S. Hayase, *J. Vac. Sci. Technol. B,* **17,** *3398* (1999).
60. Y. Onishi, at al. *Proc. SPIE,* **3678,** *205* (1999).
61. Y. Sato, E. Shiobara, Y. Onishi, S. Yoshikawa, y. Nakano, S. Hayase, Y. Hamada, *J. Vac. Sci. Technol. B.,* **20,** *909* (2002).
62. Y. Sato, H. Matsuyama, Y. Onishi, Y. Nakano, S. Hayase, *Jpn. J. Appl. Phys.,* **41,** *6351* (2002).
63. R. D. Miller, J. Michl, *Chem. Rev.,* **89,** *1359* (1989).
64. J. M. Zeigler, L. A. Harrah, A. W. Johnson, *Polym. Preprints,* **28,** *424* (1987).
65. T. Schepers, J. Michl, *J. Phys. Org. Chem.,* **15,** *490* (2002).
66. A. J. Lovinger, D. D. Davis, F. C. Schilling, F. J. Padden, Jr., F. A. Bovey, J. M. Zeigler, *Macromolecules,* **24,** *132* (1991).
67. A. J. Lovinger, D. D. Davis, F. C. Schilling, F. A. Bovey, J. M. Zeigler, *Polym. Commun.,* **30,** *356* (1989).
68. L. A. Leites, S. Bukhalov, T. Yadritseva, R. Menescal, R. West, *Macromolecules,* **27,** *5885* (1994).
69. F. C. Schilling, A. J. Lovinger, J. M. Zeigler, D. D. Davis, F. A. Bovey, *Macromolecules,* **22,** *3055* (1989).
70. E. K. KariKari, A. J. Greso, B. L. Farmer, R. D. Miller, J. F. Rabolt, *Macromolecules,* **26,** *3937* (1993).
71. J. Michl, R. West, R. G. Jones, W. Ando and J. Chojnowski, eds., in *Silicon-Based Polymers: The Science and Technology of Their Synthesis and Application,* Kluwer, Dordrecht, **4990 (**2000).
72. R. West, Zvi Rappoport and Yitzhak Apeloig eds., in *The Chemistry of Organic Silicon Compounds, Wiley,* **3,** *541* (2001).
73. K. Suzuki, Y. Kanemitsu, S. Kyushin, H. Matsumoto, *ACS Symp. Ser.* **579,** *425* (1994).
74. N. Ma, Y. Yu, Z. Sun, S. Huang, *J. Luminesc.,* **126,** *827* (2007).
75. L. A. Harrah, J. M. Zeigler, *Macromolecules,* **20,** *601* (1987).
76. K. Yoshino, K. Tada, M. Hirohata, R. Hidayat, S. Tatsuhara, M. Ozaki, A. Naka, M. Ishikawa, *Jpn. J. Appl. Phys.,* **36,** *L1548* (1997).
77. H. Tachibana, H. Kishida, Y. Tokura, *Appl. Phys. Lett.,* **77,** *2443* (2000).
78. A. Sharma, S. Deepak, Kumar, M. Katiyar, A. K. Saxena, A. Ranjan, R. K. Tiwari, *Synth. Metals,* **139,** *835* (2003).
79. N. Kameta, H. Hiramatsu, T. Sanji, H. Sakurai, *J. Inorg. Organomet. Polym.,* **17,** *589* (2007).
80. A. Kobayashi, H. Naito, Y. Matsuura, K. Matsukawa, H. Inoue, Y. Kanemitsu, *Jpn. J. Appl. Phys.,* **41,** *L1467* (2002).
81. N. Ostapenko, N. Kotova, V. Lukashenko, G. Telbiz, V. Gerda, S. Suto, A. Watanabe, *J. Luminesc.,* **112,** *381* (2005).
82. N. Ostapenko, N. Kotova, V. Lukashenko, G. Telbiz, S. Suto, A. Watanabe, *Mol. Cryst. Liq. Cryst.,* **426,** *149* (2005).
83. M. Fujiki, *Appl. Phys. Lett.,* **65,** *3251* (1994).
84. T. Schepers, J. Michl, *J. Phys. Org. Chem.,* **15,** *490* (2002).

85. K. Yoshino, K. Yoshimoto, M. Hamaguchi, T. Kawai, A. A. Zakhidov, H. Ueno, M. Kakimoto, H. Kojima, *Jpn. J. Appl. Phys.,* **34,** *L141* (1995).
86. A. Acharya, S. Seki, A. Saeki, S. Tagawa, *Synth. Metals,* **156,** *293* (2006).
87. Y. Wang, *Nature,* **356,** *585* (1992).
88. S. Ninomiya, Y. Ashihara, Y. Nakayama, K. Oka, R. West, *J. Appl. Phys.,* **83,** *3652* (1998).
89. S. Aihara, N. Kamata, W. Ishizaka, M. Umeda, A. Nishibori, D. Terunuma, K. Yamada, *Jpn. J. Appl. Phys.,* **37,** *4412* (1998).
90. S. J. Toal, W. C. Trogler, *J. Mater. Chem., 2871* (2006).
91. A. Fujii, K. Yoshimoto, M. Yoshida, Y. Ohmori, K. Yoshino, H. Ueno, M. Kakimoto, H. Kojima, *Jpn. J. Appl. Phys.,* **35,** *3914* (1996).
92. S. Hoshino, H. Suzuki, M. Fujiki, M. Morita, N. Matsumoto, *Synth. Metals,* **89,** *221* (1997).
93. H. Suzuki, S. Hoshino, C. Yuan, M. Fujiki, S. Toyoda, N. Matsumoto, *IEEE J. Select. Top. Quant. Electron.,* **4,** *129* (1998).
94. Y. Xu, T. Fujino, S. Watase, H. Naito, K. Oka, T. Dohmaru, *Jpn. J. Appl. Phys.,* **38,** *2609* (1999).
95. Y. Ichino, N. Takada, N. Tanigaki, A. Kaito, M. Yoshida, S. Yokokawa, H. Sakurai, *Thin Solid Films,* **376,** *220* (2000).
96. A. Adachi, H. Yasuda, T. Sanji, H. Sakurai, K. Okita, *J. Luminesc.,* **87–89,** *1174* (2000).
97. N. Kamata, R. Ishii, S. Tonsyo, D. Terunuma, *Appl. Phys. Lett.,* **81,** *4350* (2002).
98. P. Horak, P. Schauer, *Nucl. Instr. Meth. Phys. Res. B,* **252,** *303* (2006).
99. S. Kuroki, K. Endo, S. Maeda, D. P. Chong, P. Duffy, *Polym. J.,* **30,** *142* (1998).
100. K. Endo, Y. Kaneda, H. Okada, D. P. Chong, P. Duffy, *J. Phys. Chem.,* **100,** *19455* (1996).
101. H. Shibata, S. Seki, S. Tagawa, Y. Yoshida, K. Ishigure, *Nucl. Instr. Meth. Phys. Res. B,* **105,** *42* (1995).
102. R. D. Miller, D. Hofer, R. F. Rabolt, G. N. Fickes, *J. Am. Chem. Soc.,* **107,** *2172* (1985).
103. J. F. Rabolt, D. Hofer, R. D. Miller, G. N. Fickes, *Macromolecules,* **19,** *611* (1986).
104. T. A. Larina, E. E. Said-Galiev, I. I. Tverdokhlebova, V. V. Men'shov, S. A. Bashkirova, V. V. Ivanov, *Polym. Sci. Ser. A,* **37,** *385* (1995).
105. Y. Nakayama, H. Hayashi, T. Kurando, K. Oka, T. Dohmaru, R. West, *Jpn. J. Appl. Phys.,* **35,** *913* (1996).
106. N. Kamata, D. Terunuma, R. Ishii, H. Satoh, S. Aihara, Y. Yaoita, S. Tonsyo, *J. Organomet. Chem.,* **685,** *235* (2003).
107. K. Matsukawa, S. Fukui, N. Higashi, M. Niwa, H. Inoue, *Chem. Lett.,* **1073 (**1997).
108. M. Katiyar, A. Sharma, Deepak. *Proc. ASID,* **8-12,** *84* (2006).
109. H. Suzuki, S. Hoshino, K. Furukawa, C. Ebata, H. Yuan, I. Bleyl, *Polym. Adv. Technol.,* **11,** *460* (2000).
110. K. Ebihara, S. Koshihara, T. Miyazawa, M. Kira, *Mol. Cryst. Liq. Cryst.,* **285,** *567* (1996).
111. H. Suzuki, S. Hoshino, C. Yuan, M. Fujiki, S. Toyoda, N. Matsumoto, *Thin Solid Films,* **331,** *64* (1998).
112. S. Nespurek, G. Wang, D. Rais, J. Rakusan, M. Karaskova, J. Stumpe, Y. Zakrevskyy, *Mol. Cryst. Liq. Cryst.,* **448,** *1* (2006).
113. Y. Wang, R. West, C. Yuan, *J. Am. Chem. Soc.,* **115,** *3844* (1993).
114. S. Aihara, Y. Hirano, T. Tajima, K. Tanioka, M. Abe, N. Saito, N. Kamata, D. Terunuma, *Appl. Phys. Lett.,* **82,** *511* (2003).

115. A. Kobayashi, H. Naito, Y. Matsuura, K. Matsukawa, S. Nihonyanagi, Y. Kanemitsu, *J. Non-Cryst. Solids,* **299-302,** *1052* (2002).
116. S. Miura, H. Naito, Y. Kanemitsu, Y. Matsuura, K. Matsukawa, H. Inoue, *Thin Solid Films,* **438-439,** *253* (2003).
117. J. Lee, C. Seoul, J. Park, J.H. Youk, *Synth. Metals,* **145,** *11* (2004).
118. Y. Haga, Y. Harada, *Jpn. J. Appl. Phys.,* **40,** *855* (2001).
119. E. Stathatos, V. Jovanovski, B. Orel, I. Jerman, P. Lianos, *J. Phys. Chem. C,* **111,** *6528* (2007).
120. S. Hayase, *Prog. Polym. Sci.,* **28,** *359* (2003).
121. R. R. Kunz, M. W. Horn, R. B. Goodman, P. A. Bianconi, D. A. Smith, C. A. Freed, *J. Vac. Sci. Technol. B.,* **8,** *1820* (1990).
122. M. W. Horn, S. W. Pang, M. Rothschild, *J. Vac. Sci. Technol. B.,* **8,** *1493* (1991).
123. R. R. Kunz, M. W. Horn, G. M. Wallraff, P. A. Bianconi, R. D. Miller, W. Goodman, D. A. Smith, J. R. Eshelman, E. J. Ginsberg, *Jpn. J. Appl. Phys.,* **31,** *4327* (1992).
124. T. W. Weidman, A. M. Joshi, *Appl. Phys. Lett.,* **62,** *372* (1993).
125. M. W. Horn, B. E. Maxwell, R. R. Kunz, M. S. Hibbs, L. M. Eriksen, S. C. Palmateer, A. R. Forte, *Proc. SPIE,* **2438,** *760* (1995).
126. T. W. Weidman, O. Joubert, A. M. Joshi, R. L. Kostelak, *Proc. SPIE,* **2438,** *496* (1995).
127. O. Joubert, T. Weidman, A. Joshi, R. Cirelli, S. Stein, J. T. C. Lee, S. Vaidya, *J. Vac. Sci. Technol. B.,* **122,** *3909* (1994).
128. R. Horiguchi, Y. Onishi, S. Hayase, *Macromoleucles,* **21,** *304* (1988).
129. K. Matsukawa, S. Fukui, N. Higashi, M. Niwa, H. Inoue, *Chem. Lett.,* **1073 (**1999).
130. K. Takeuchi, S. Furukawa, *Jpn. J. Appl. Phys.,* **34,** *L195* (1995).
131. K. Matsukawa, T. Nanba, Y. Matsuura, H. Naito, *J. Photopolym. Sci. Technol.,* **16,** *97* (2003).
132. Y. Sakurai, S. Okuda, N. Nagayama, M. Yokoyama, *J. Mater. Chem.,* **11,** *1077* (2001).
133. K. Furukawa, K. Ebata, *Appl. Phys. Lett.,* **77,** *4289* (2000).
134. N. Nagayama, M. Shimono, T. Sato, M. Yokoyama, *Mol. Cryst. Liq. Cryst.,* **349,** *119* (2000).
135. S. Miura, A. Kobayashi, H. Naito, Y. Matsuura, K. Matsukawa, H. Inoue, *Synthe. Metals,* **137,** *1405* (2003).

CHAPTER 7

Polymers with Metal-Metal Bonds as Models in Mechanistic Studies of Polymer Photodegradation

David R. Tyler, Bevin C. Daglen, and Ginger V. Shultz

Department of Chemistry, University of Oregon, Eugene, Oregon

CONTENTS

Macromolecules Containing Metal and Metal-like Elements,
Volume 10: Photophysics and Photochemistry of Metal-Containing Polymers,
Edited by Alaa S. Abd-El Aziz, Charles E. Carraher Jr., Pierre D. Harvey, Charles U. Pittman Jr., Martel Zeldin.

I. INTRODUCTION

Polymer chemists have spent enormous time and effort researching ways to prevent their materials from degrading.[1–3] It may seem peculiar therefore that some plastics are designed to degrade.[4] However, there are compelling economic, environmental, and social reasons for using degradable plastics in selected applications, and considerable research is being devoted to devising photodegradable plastics. The biggest use for photodegradable plastics is in the technique of farming called plasticulture.[5] In plasticulture, the ground is covered with plastic sheeting (typically a polyolefin), which acts as a mulch to prevent the growth of weeds (thus requiring the use of fewer herbicides), to decrease water demand, and to extend the growing season. By making these agricultural films out of degradable plastics, considerable labor and money can be saved in the plastics recovery phase of the technique. In the environmental area, photodegradable plastics are finding increased use as packaging materials in items that have a high probability of becoming litter.[6] The idea is that if such materials should end up as litter they will degrade rather quickly and not be an eyesore.

There are two basic methods for making polymer materials photochemically degradable.[1,2] One method is to chemically incorporate a chromophore into the polymer chains. One commercially successful chromophore is the carbonyl group.[1,2,7] Absorption of UV radiation leads to degradation by the Norrish type I and II processes or by an atom abstraction process (Scheme 1). Note that once radicals are introduced into the system, chain degradation occurs by the autoxidation mechanism (Scheme 2).

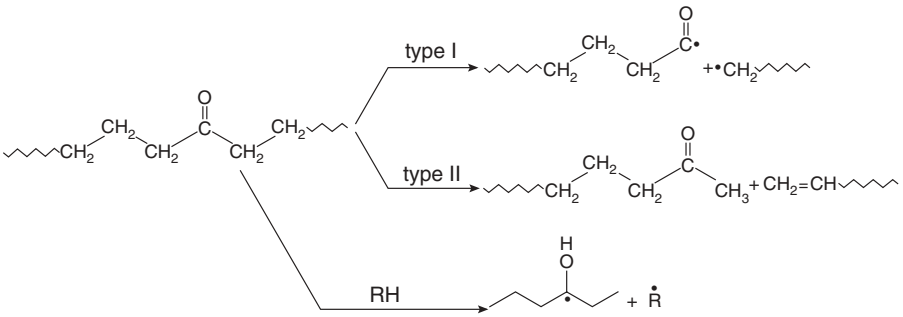

SCHEME 1. Photochemical degradation pathways for polymers containing carbonyl groups.

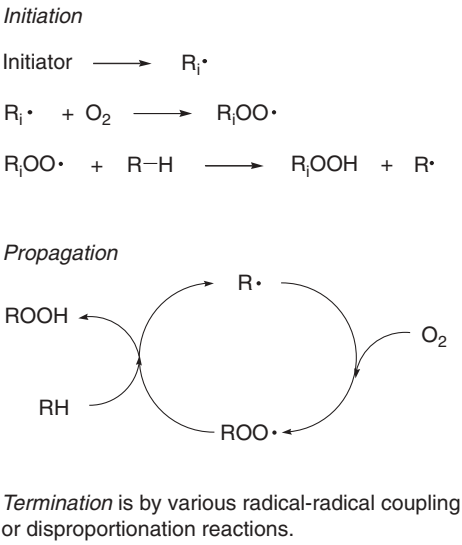

SCHEME 2. The autoxidation mechanism for hydrocarbon materials.

The second general method for making polymer materials photochemically degradable is to mix a radical initiator into the polymer. Once carbon-based radicals have formed, the chains degrade by the autoxidation cycle (Scheme 2). Numerous radical initiators have been investigated, and a partial list includes metal dithiocarbamates,[8] metal oxides (e.g., TiO_2, ZnO, CuO), metal chlorides (e.g., LiCl, $FeCl_3$), $M(acac)_n$ complexes, $M(stearate)_n$ complexes, benzophenone, quinones, and peroxides.[1,2]

To improve the performance of photodegradable plastics, it is necessary to understand the photochemical decomposition mechanisms so that appropriate features and properties can be incorporated into the polymers to make

them suitable as photodegradable materials. In this regard, it is noted that the ideal photodegradable polymer has (at least) two essential properties.[4] First, the onset of degradation should be tunable. This property makes practical sense, but it is difficult to achieve in practice because light intensities vary, as do temperatures and a host of other environmental variables that affect the onset of degradation. The second essential property is that the polymer should degrade completely and quickly once degradation starts (Fig. 1). This characteristic is important because small amounts of degradation can drastically decrease the molecular weight (and thus the mechanical properties) of a plastic, yet to all appearances, the plastic piece is visually unchanged. In essence, the plastic is still present, but it is not structurally sound—and hence useless and perhaps dangerous. Under such circumstances, it may as well be completely degraded.

To design photodegradable polymers with tunable degradation onsets and rapid degradation rates, it is necessary to understand the environmental and experimental parameters that can affect polymer lifetimes and degradation rates. A number of factors have been shown to affect the lifetimes of photodegradable polymers. Among these factors are temperature, humidity, light intensity, chromophore concentration, molecular weight, morphology, tensile stress, and compressive stress.[9] However, very little is known in a quantitative sense about how these parameters affect polymer photodegradation rates and how they affect the onset of polymer degradation. To increase our understanding, we have been systematically studying how these parameters impact the kinetics of polymer degradation and the mechanistic reasons for the observed effects. This chapter presents an overview of our findings on the mechanistic aspects of how the various parameters affect polymer photodegradation rates. As explained below, we use polymers with metal-metal bonds along their backbones in these studies. It is important to emphasize that our research is not intended to arrive at new commercial photodegradable polymers containing metal-metal bonds but rather to explore the photochemical mechanisms of decomposition so that we and other workers will

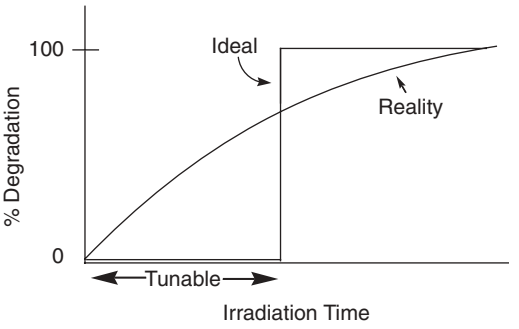

FIGURE 1. The properties of an ideal photochemically degradable polymer—namely, tunable onset of degradable and rapid degradation.

know what features and properties need to be incorporated into polymers to make them suitable as photodegradable materials.

II. EXPERIMENTAL STRATEGIES

Several challenging experimental problems hinder the rigorous experimental mechanistic exploration of how the various environmental and experimental parameters affect polymer photodegradation. The major problem is that polymer degradation reactions are mechanistically complicated.[10] This is not to say that the mechanisms are not understood; in fact, they are understood in detail.[10] Rather, the mechanisms are intricate, often involving multiple steps, cross-linking, and side-reactions; this makes pinpointing the effects of the various experimental parameters difficult. Another complication is that oxygen diffusion is sometimes the rate-limiting step in the photooxidative portion of the degradations.[11,12] This can add to the intricacy of the kinetics analysis because cracks and fissures develop in the polymer as degradation proceeds; these fractures provide pathways for direct contact of the polymers with oxygen, which will then no longer degrade at a rate controlled by oxygen diffusion. To circumvent these experimental and mechanistic complexities and therefore make it less difficult to interpret data and obtain fundamental insights, we use three key experimental strategies in our investigations.

First, we study the problem using photodegradable polymers that contain metal-metal bonds along the backbone.[13–18] The visible light induced photochemistry of organometallic complexes with metal-metal bonds involves homolytic cleavage of the metal-metal bond (eq. 1) and this photochemistry is also observed when these types of complexes are incorporated into polymer backbones. Thus these polymers degrade with visible light by a straightforward mechanism involving metal-metal bond homolysis followed by capture of the metal radicals with an appropriate radical trap (typically an organic halide or molecular oxygen; Scheme 3). By studying these "model" systems, we have been able to extract information without the mechanistic complications inherent in the degradation mechanisms of organic radicals. (For example, metal radicals do not lead to cross-linking, so we can avoid this complicating feature found with organic

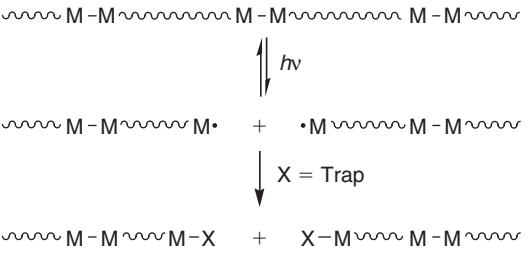

SCHEME 3. Photochemical degradation of a polymer with metal-metal bonds along its backbone.

radicals.) A second key experimental strategy we use when necessary is to study polymers with built-in radical traps—namely, C-Cl bonds.[19,20] By eliminating the need for external oxygen to act as a trap, we an exclude the complicating kinetic features of rate-limiting oxygen diffusion. The third experimental strategy is to use the distinctive M-M bond chromophore to spectroscopically monitor the photodegradation reactions of the polymers. This allows us to compare the efficiencies of the photodegradations by measuring the quantum yields of the reactions. (The quantum yield, Φ, is defined as the rate of a photoreaction divided by the absorbed light intensity; i.e., Φ = rate/absorbed intensity.) The use of quantum yields to quantify and compare the various degradation rates is a crucial advance because polymer degradation reactions have typically been monitored by stress testing, molecular weight measurements, or attenuated total reflection (ATR) spectroscopy,[21] all of which can be laborious and time-consuming. Relative to these techniques, quantum yield measurements are straightforward. Of course, quantum yields in regular carbon-chain polymers cannot be measured conveniently by UV-VIS spectroscopy because there are generally no suitable chromophores.

$$L_nM{-}ML_n \xrightarrow{h\nu} L_nM\bullet + \bullet ML_n$$

$$\bullet MLn = CpMo(CO)_3\ (Cp = \eta^5{-}C_5H_5),\ CpW(CO)_3,\ Mn(CO)_5,\ Re(CO)_5,\ CpFe(CO)_2 \quad (1)$$

III. SYNTHESIS OF POLYMERS WITH METAL-METAL BONDS ALONG THEIR BACKBONES

A. Step-Growth Polymers

A general synthetic route for incorporating metal-metal bonds into polymer backbones is based on the step-growth polymerization strategy used for incorporating ferrocene into polymer backbones.[22–28] Step-growth polymers of ferrocene can be made by substituting the cyclopentadienyl (Cp) rings with appropriate functional groups, followed by reaction with appropriate difunctional organic monomers (e.g., eq. 2).[29–31]

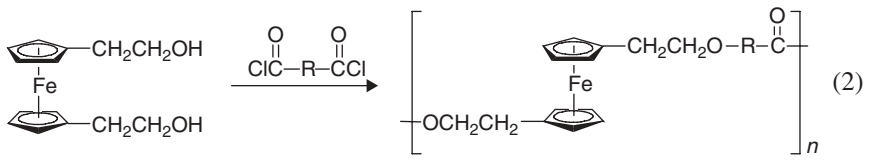

(2)

The analogous strategy for synthesizing metal-metal bond-containing polymers also uses difunctional, cyclopentadienyl-substituted metal dimers. A sample step-growth polymerization reaction is shown in equation 3, which

illustrates the reaction of a metal-metal bonded dialcohol with hexamethylene diisocyanate (HMDI) to form a polyurethane.[15]

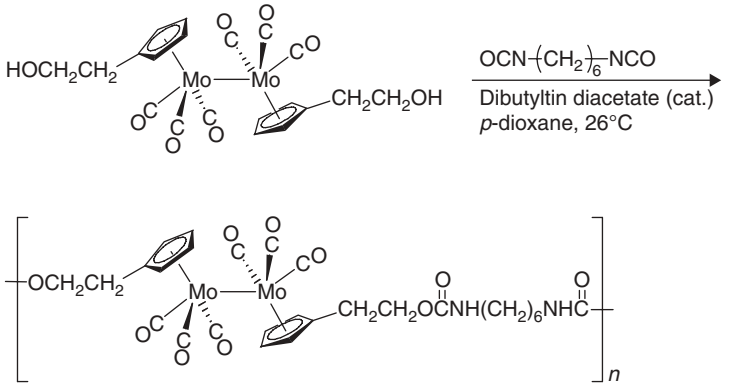

(3)

This step-growth polymerization strategy is general, and a number of metal-metal bond-containing polymers have been made from monomers containing functionalized cyclopentadienyl ligands.[13] In principle, step polymers could be synthesized from monomers containing other derivatized ligands, but in practice not many other ligands have been derivatized for this purpose.

The comparatively weak metal-metal bonds (e.g., $D_{\text{Mo-Mo}}$ 32 kcal mol^{-1}) pose problems for the synthesis of the polymers. In particular, the relative weakness of the metal-metal bonds makes them more reactive than the bonds found in standard organic polymers, thus under many standard polymerization reaction conditions, metal-metal bond cleavage would result. For example, metal-metal bonds react with acyl halides to form metal halide complexes. Therefore, the synthesis of polyamides using metal-metal bonded "diamines" and diacyl chlorides would simply lead to metal-metal bond cleavage rather than polymerization. Likewise, metal-metal bonded complexes are incompatible with many Lewis bases because the Lewis bases cleave the metal-metal bonds in disproportionation reactions.[32] This type of reactivity thus rules out many standard condensation polymerization reactions in which bases are used to neutralize any acids produced. Similar reasons prevent the use of acyl chlorides in the synthesis of polyamides. Polymerization strategies must therefore be carefully designed to avoid cleaving the metal-metal bond during the polymerization process.

A sample polymerization reaction, showing the synthesis of a polyurethane, is shown equation 3. Using similar synthetic strategies, various polyurethanes, polyureas (eq. 4), and polyamides (eq. 5) have been synthesized.[14–17] Note that the step polymers in these reactions have a metal-metal bond in every repeat unit. Copolymers are straightforwardly synthesized by adding appropriate difunctional organic molecules into the reaction mixture (e.g., eq. 6).

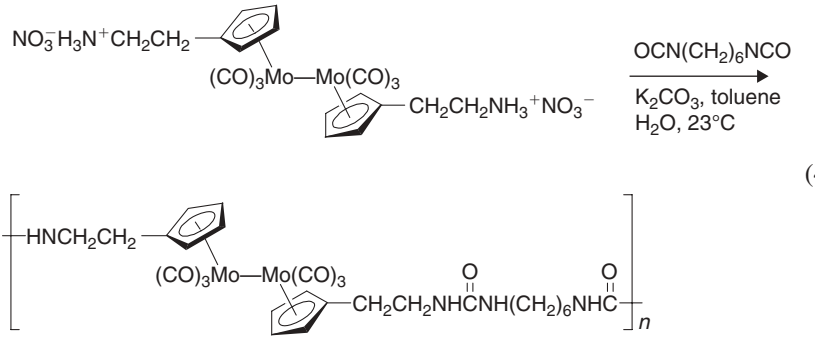

(4)

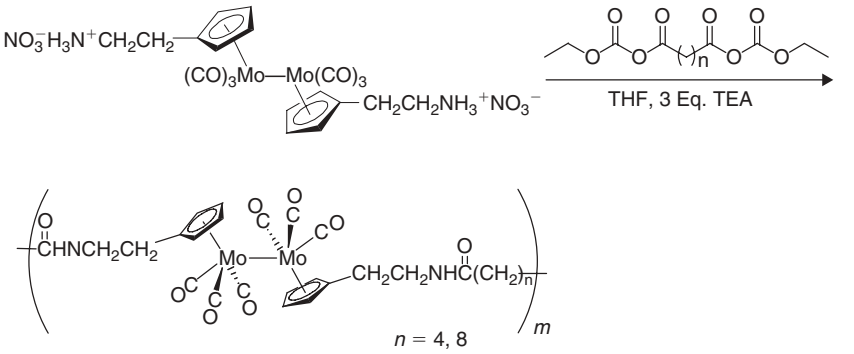

(5)

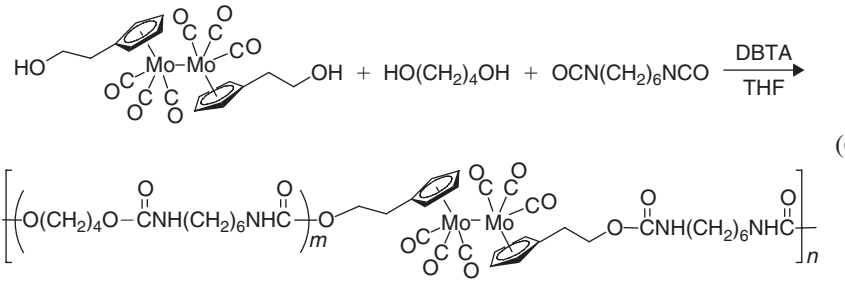

(6)

Yet another step-growth synthesis strategy is to react the difunctional dimer molecules with prepolymers. Equation 7 shows an example of this technique.[16] (As received from the manufacturer, prepolymers are often ill-defined

materials. In this instance, analysis of the prepolymer sample showed it to contain, on average, three tolyl isocyanate end groups; M_n was $\sim$ 2000.)

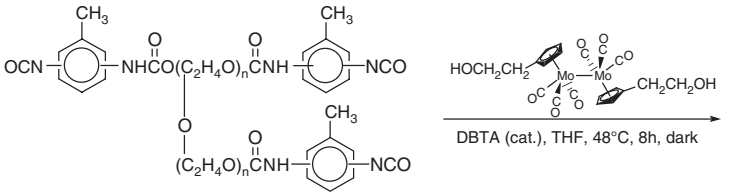

(7)

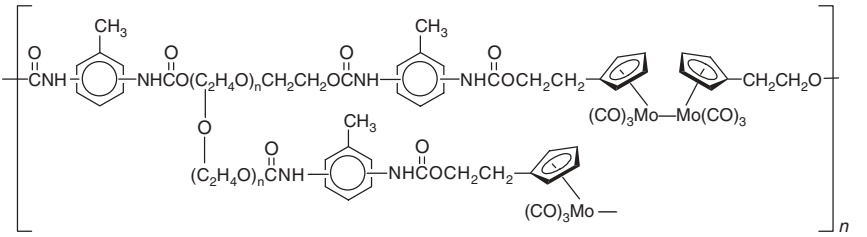

1

Again, copolymers can likewise be synthesized by using prepolymers and another organic difunctional molecule (eq. 8).[33]

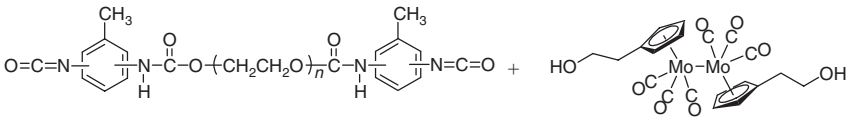

(8)

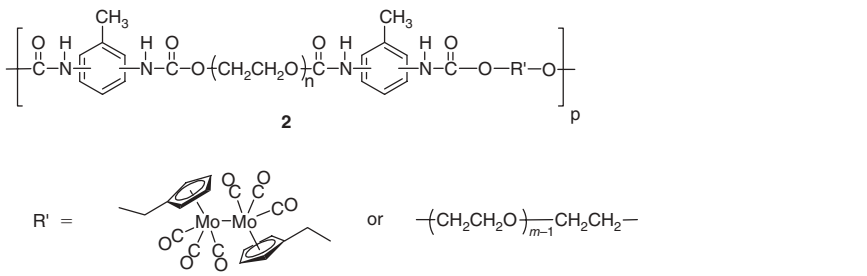

2

In another example of a step-growth polymerization reaction that yielded polymers containing metal-metal bonds, Moran and co-workers reported the

synthesis of a number of polysiloxanes that contain Fe-Fe bonds in their backbones. Their syntheses start with the derivatized $Cp_2Fe_2(CO)_4$ dimer:[34]

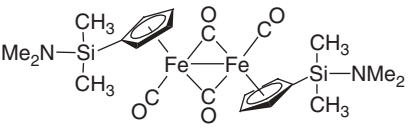

Reaction of this molecule with disilanols gave siloxanes (eqs. 9 and 10).

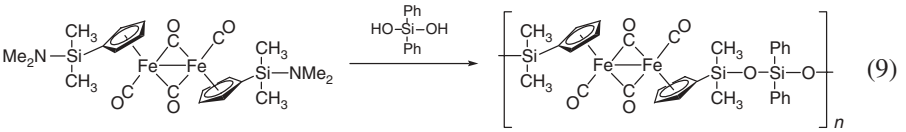

(9)

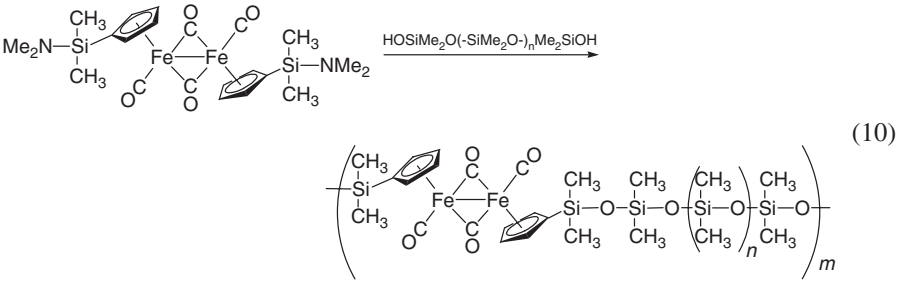

(10)

The step-growth polymerization strategy used to incorporate metal-metal bonded units into polymers can also be used to incorporate metal clusters into polymers. One of only a few examples of this type of reactivity is shown by equation 11.[35] It is noteworthy that metal clusters also undergo photochemical reactions.[36,37] These reactions should also occur when the clusters are incorporated into polymer backbones. If polymers containing metal clusters can be shown to have unusual properties or applications (photochemical or otherwise), then the synthesis of these polymers will likely burgeon in coming years.

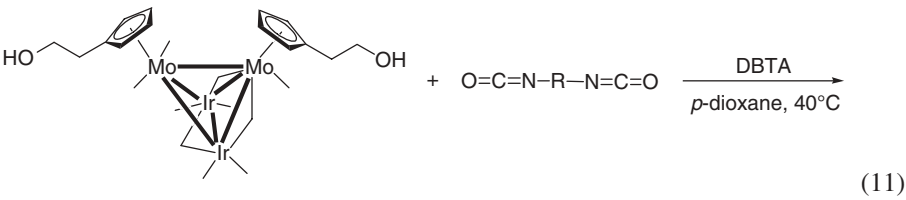

(11)

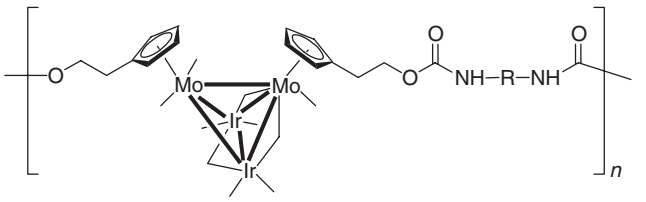

B. ADMET Polymerization

As noted above, the syntheses of polymers containing metal-metal bonds is challenging because the metal-metal bonds are relatively weak and will not stand up to many of the conditions typically used for the synthesis, isolation, and purification of organic polymers. To avoid the problems associated with normal step polymerization methods, new synthetic routes to these polymers are being investigated. For example, ADMET polymerization (acyclic diene metathesis polymerization; eq. 12) of α,ω-dienes is another step-growth method that is potentially useful for the synthesis of polymers with metal-metal bonds (eq. 13). First demonstrated by Wagener in 1990 with organic monomers, ADMET is a versatile method used to synthesize a broad range of organic polymers with varying functionality and intriguing architectures.[38–41]

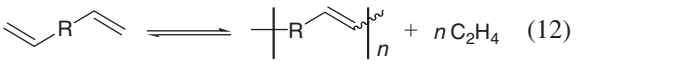

(12)

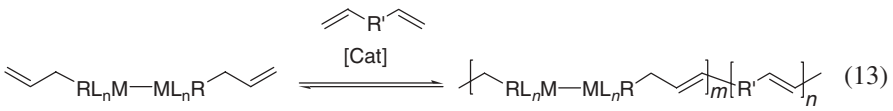

(13)

Overall, ADMET polymerization is an advantageous strategy for synthesizing transition metal-containing polymers because of the functional group tolerance of the metathesis catalysts employed, the mild conditions under which it operates, the wide range of accessible architectures, and the precise structural control afforded by the method.

One strategy to obtain organometallic α,ω-dienes for ADMET is to substitute phosphine ligands containing terminal alkene substituents onto metal-metal bonded dimers.[42] An example of one such dimer is shown in equation 14.

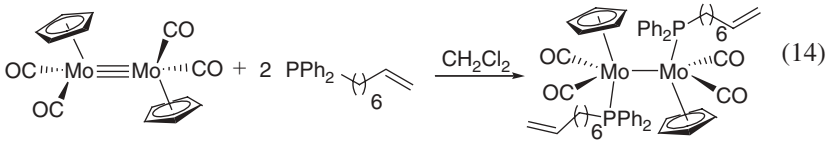

(14)

3

Unfortunately, no ADMET polymerization of complex **3** was achieved with Grubbs generation 1, Grubbs generation 2, or Schrock's catalysts.[42] Control experiments showed that the lack of reactivity of the Grubbs catalysts toward $Cp_2Mo_2(CO)_4(Ph_2P(CH)_6CH=CH_2)_2$ (**1**) is not related to catalyst decomposition by the phosphine or to deactivation due to $Ph_2P(CH)_6CH=CH_2$ coordination on the catalyst. Presumably, the inability of complex **3** to polymerize is due to its sterically demanding nature. For example, in the step polymerization of related complexes reported by Humphrey and Lucas,[35] the length of the alkyl chain between the complex and the reacting group was found to significantly effect the extent of polymerization. Specifically, they found that methylene chain lengths of at least 10 carbons were required before step polymerization reactions could occur in materials with

Cp-substituted reactants. It is not clear why such long chain lengths are required to alleviate steric interactions in the Humphrey-Lucas molecules, but similar steric effects may be acting in the polymerizations of complex **3**, where two molecules of **3** and a catalyst molecule all need to interact to carry out the polymerization. Nevertheless, despite this one setback, ADMET remains an attractive method for synthesizing new polymers with metal-metal bonds along their backbones.

C. Chain-Growth Polymers

Few chain growth polymers with metal-metal bonds have been reported. The general synthetic route to these materials is to substitute a ligand on a metal-metal bonded dimer with a polymerizable olefin. In the case of $Cp_2M_2(CO)_n$-type molecules (M = Mo, W, Fe), it is difficult to synthesize a dimer that has only one substituted Cp ring, and hence both Cp rings are substituted with polymerizable olefins. This leads to cross-linked polymers with metal-metal bonds in the chain. Examples of this reactivity are shown in Scheme 4.[43]

An example of a chain-growth polymer that uses an olefin-substituted ligand other than cyclopentadienyl is shown in equation 15.[44] The electrons in this reduction reaction are provided electrochemically. This polymer is particularly interesting because the metal-metal bond can be reformed by electrochemical reduction following photochemical cleavage in the presence of CCl_4 radical trap (Scheme 5). It was demonstrated that the reversibility of the Re-Re bond cleavage (and similar reactivity in other systems) may be useful in applications involving reversible imaging.

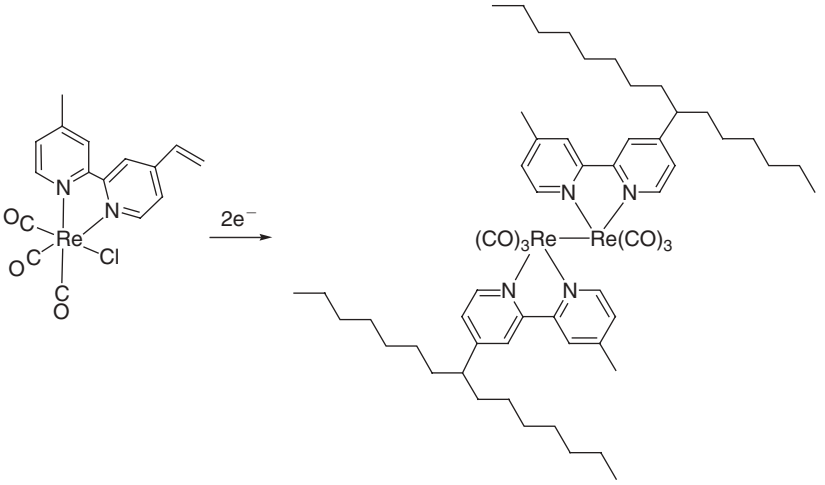

(15)

IV. PHOTOCHEMICAL REACTIONS OF THE POLYMERS IN SOLUTION

The photochemistry in solution of the polymers with metal-metal bonds in their backbones is qualitatively similar to the reactions of the discrete metal-metal

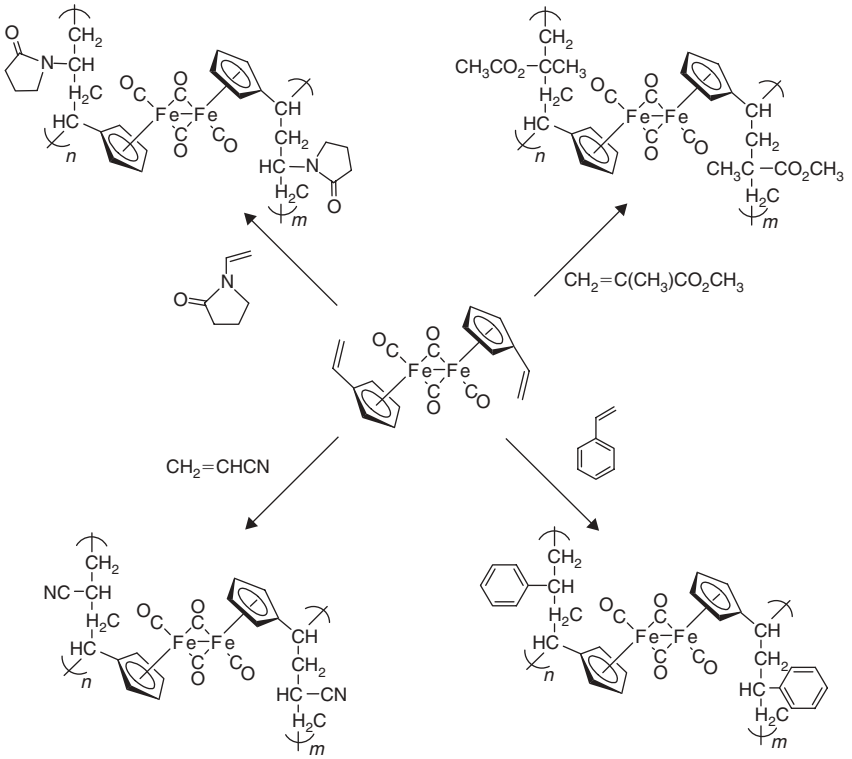

SCHEME 4. Synthesis of chain-growth polymers containing metal-metal bonds along their backbones.

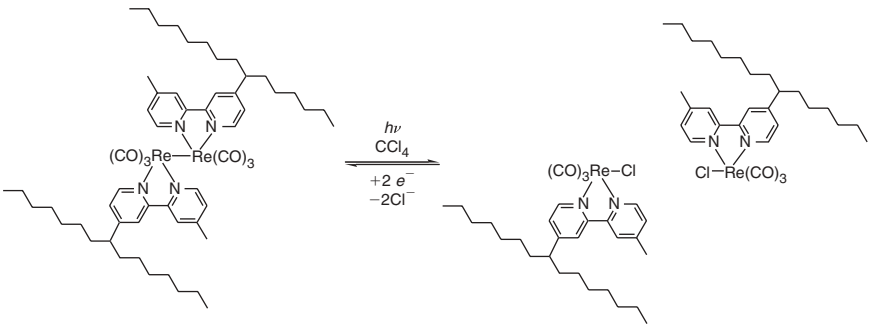

SCHEME 5. Photochemical cleavage of the Re-Re bond and electrochemical formation of the Re-Re bond in poly[(vbpy)$Re(CO)_3$]$_2$.

bonded dimers in solution.[15,45,46] Irradiation of metal-metal bonded complexes into their lowest energy absorption band (500 nm) generally leads to one of four fundamental types of reactivity:[15,45,46]

1. The metal radicals produced by photolysis react with radical traps to form monomeric complexes (e.g., eq. 16).

2. The complexes react photochemically with ligands to form ionic disproportionation products (e.g., eq. 17).
3. The complexes react with oxygen to form metal oxides (eq. 18). This reaction is likely a radical trapping reaction but may involve excited state electron transfer.
4. With higher energy excitation, M-CO bond dissociation occurs (e.g., eq. 19). This type of reactivity does not necessarily lead to polymer backbone degradation.

$$Cp_2Mo_2(CO)_6 + 2\,CCl_4 \xrightarrow{h\nu} 2\,CpMo(CO)_3Cl + 2\,[\cdot CCl_3] \quad (16)$$

$$Cp_2Mo_2(CO)_6 + 2\,PR_3 \xrightarrow{h\nu} CpMo(CO)_3^- + CpMo(CO)_2(PR_3)_2^+ + CO \quad (17)$$

$$Cp_2Mo_2(CO)_6 \xrightarrow[O_2]{h\nu} \text{Mo(V) and Mo(VI) oxides} \quad (18)$$

$$Cp_2Mo_2(CO)_6 \xrightarrow{h\nu} Cp_2Mo_2(CO)_5 + CO \quad (19)$$

Reactions analogous to these are observed with the polymers that contain metal-metal bonds along their backbones. Because the metal-metal bond chromophore absorbs in the visible region, the photochemical reactions of the polymers can be conveniently monitored by electronic absorption spectroscopy. The quantum yields for the reactions are in the range 0.1 to 0.6, depending on the specific polymer and the M-M bond.[14] Sample reactions of the polymers are shown in equations 20–22.

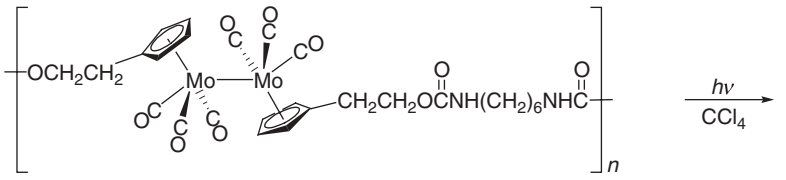

(20)

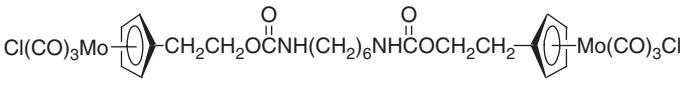

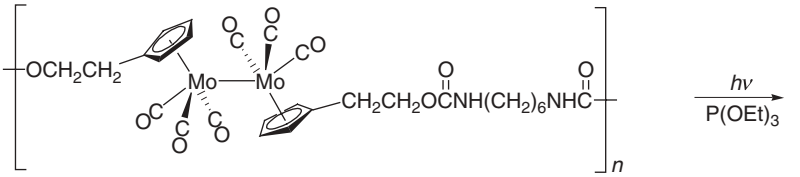

(21)

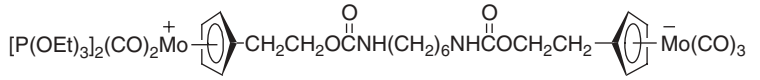

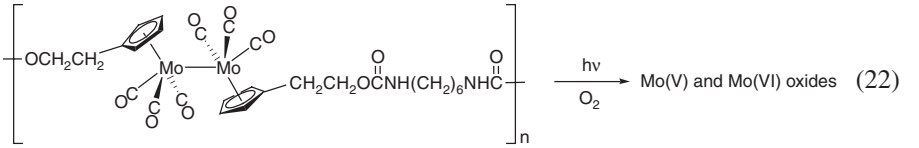

(22)

As mentioned, photochemical M-CO bond dissociation increases in efficiency relative to M-M photolysis as the radiation energy increases.[45] In solution, this type of reactivity generally leads to substitution. However, in the case of the $Cp_2Mo_2(CO)_6$ molecule, the reaction in equation 23 occurs.[14] (Among the dimers, this reaction to form a triply bonded product is unique to the Mo and W species.)

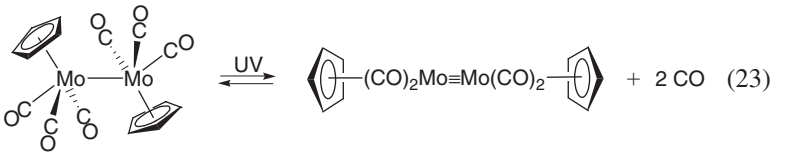

(23)

An analogous photoreaction occurs with polymers containing the Mo-Mo unit (eq. 24).

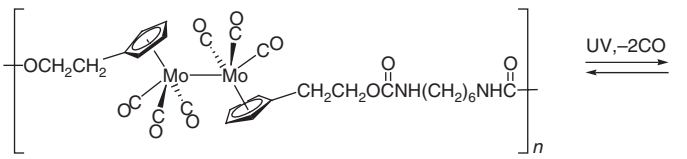

(24)

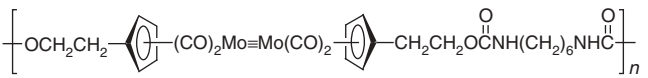

In both equations 23 and 24, addition of CO to the product solution causes the system to back-react to reform the starting materials. Once again, the main point to be made is that the solution photochemistry of the polymers is analogous to the solution photochemistry of the discrete metal-metal bonded dimers.

Photochemical reactivity in the absence of exogenous radical traps is possible in the case of polymers that have carbon-halogen bonds along their backbones. (Recall, the use of an internal radical trap is used in experiments to avoid rate-limiting O_2 diffusion.) For example, irradiation of polymers **4**–**6** in solution in the absence of CCl_4 or O_2 led to net metal-metal bond cleavage.[33] Spectroscopic monitoring of the reaction showed that metal-metal bond cleavage is accompanied by an increase in the concentration of CpMo $(CO)_3Cl$ units. Photochemical reactions analogous to that in Scheme 6 were proposed.

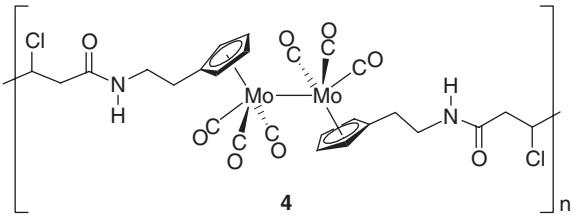

4

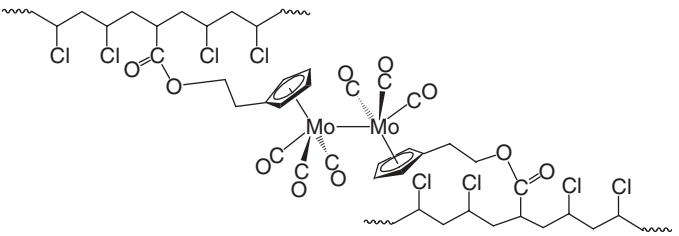

5

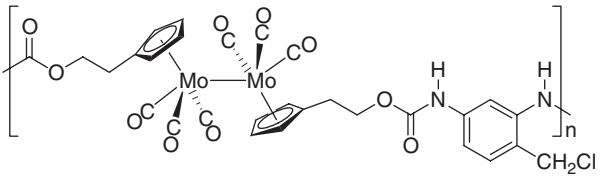

6

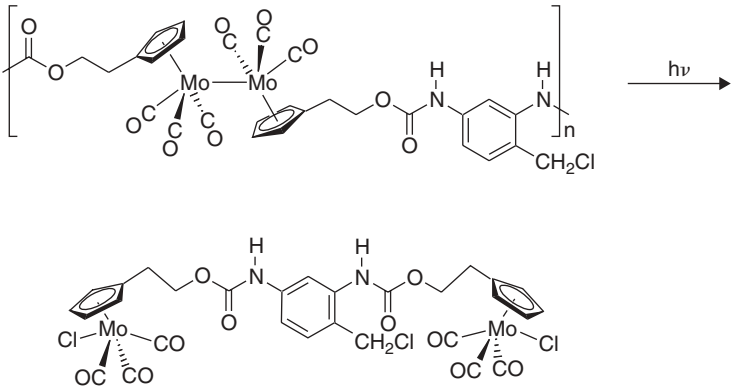

SCHEME 6. Photochemical reaction of polymer **6** in the absence of an external trapping reagent.

V. PHOTOCHEMISTRY IN THE SOLID STATE

Thin films (0.05 mm in thickness) of the polymers with metal-metal bonds in their backbone reacted when they were exposed to *visible* light, whether from the overhead fluorescent lights in the laboratory, from sunlight, or from the filtered output of a high-pressure mercury arc lamp.[14] All of the films were irradiated both in the presence and absence of oxygen. The degradation reactions are conveniently measured by UV-VIS spectroscopy using the $d\pi \rightarrow \sigma^*$ absorption band near 500 nm. Figure 2 is a plot of absorbance at 508 nm versus time for the polyurethane in equation 3 under the various experimental conditions. As indicated in the figure, the polymer film that was exposed to sunlight in air completely decomposed in 2 months. (The $\sigma_{M\text{-}M} \rightarrow \sigma^*_{M\text{-}M}$ electronic absorption band[45] at 390 nm disappeared during this time, confirming that the Mo-Mo bond was not intact.) Thin films stored in the dark in air or irradiated under nitrogen showed only a slight loss of absorbance at 508 nm over a 1-year period (Fig. 2). From these data, it was concluded that the decomposition of the polymers requires both light and air (oxygen). (The small amount of reaction for those slides stored in the glovebox in the light is probably due to reactions with solvent vapors.) Infrared spectra of the decomposition products showed the absence of products with CO ligands, as indicated by the absence of any stretches in the region 1600–2200 cm^{-1}. As mentioned previously, oxide complexes form in the solution phase reactions of $Cp_2Mo_2(CO)_6$ with O_2, and it was proposed that the metal-containing decomposition product of the polymer is a metal oxide.

These data suggest that oxygen is necessary for the solid-state photochemical reaction to occur. It was proposed that oxygen traps the metal radicals produced in the photolysis of the metal-metal bonds, thereby preventing radical recombination (eq. 25). If oxygen diffusion is rate limiting then

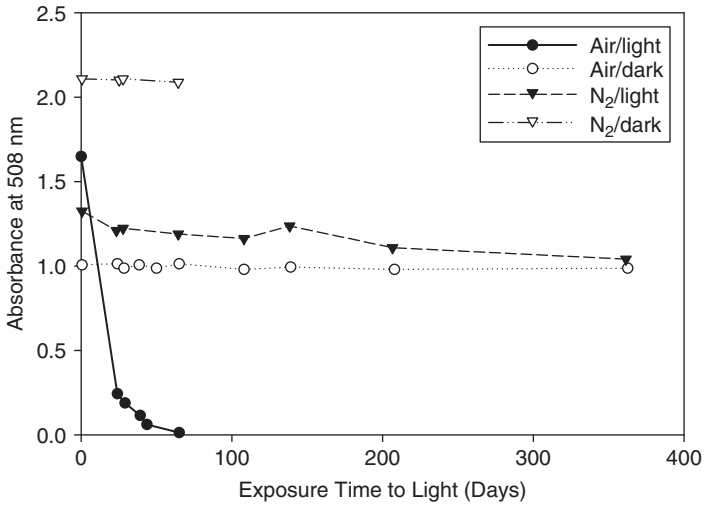

FIGURE 2. The absorbance at 508 nm vs. time for four thin films of the polyurethane synthesized by equation 3. Only the sample exposed to both light and air degraded. The absorbance at 508 nm is characteristic of the metal-metal bond. The differences in absorbance at time = 0 are due to different thicknesses of the various samples.

the relative rates of oligomer photochemical decomposition in the solid-state would reflect the oxygen diffusion rate.

(25)

An especially interesting degradation is that of polymer **2**.[33] (This polymer was synthesized by the route in equation 8. The isocyanate prepolymer is Hypol 2000, and the diol prepolymer is PEG-1000.) The solid polymer was readily degraded by ambient laboratory light over the course of 5 h, and as degradation occurred the solid polymer was converted back into the liquid prepolymers!

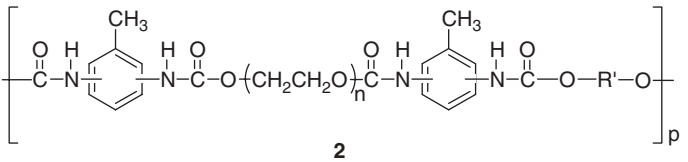

2

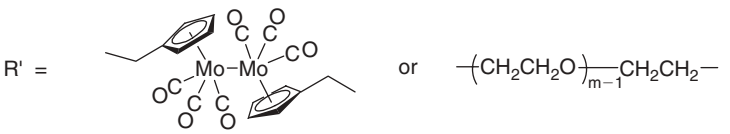

VI. FACTORS CONTROLLING THE RATE OF POLYMER PHOTOCHEMICAL DEGRADATION IN THE SOLID STATE

A. Temperature Effects

The effect of temperature on the thermal degradation rates of polymers has been extensively explored because of the need to predict the service lifetime of consumer plastics. However, considerably less is known about the effect of temperature on the photochemical degradation rates of polymers. It is important to know the effect of temperature on photochemical reactions because the exposure of plastics to sunlight is generally accompanied by (solar) heating of the plastic, which will affect the degradation rate relative to irradiation alone. Prior studies are inconclusive with respect to a general model for predicting the dependence of photodegradation rates on temperature. Several studies found that the results are consistent with an Arrhenius relationship,[47,48] but other studies found non-Arrhenius behavior.[49–51] There is some indication that the non-Arrhenius behavior is due to the complex degradation pathways referred to earlier. Consequently, the relatively straightforward degradation process of polymers with metal-metal bonds is ideally suited in this case to provide fundamental insights that could not have been obtained with standard carbon-chain polymers.

In one study,[52] the temperature dependence of quantum yields was investigated using polymer **5** (prepared by the route in equation 26). Thin films of polymer **5** are photochemically reactive ($\lambda =$ 532 or 546 nm) in the absence of oxygen, giving the products shown in Scheme 7.[19] The reaction is thus similar to the photochemical radical trapping reactions of the $Cp_2Mo_2(CO)_6$ dimer that take place in solution in the presence of an alkyl halide, and an analogous mechanism was proposed (Scheme 7).

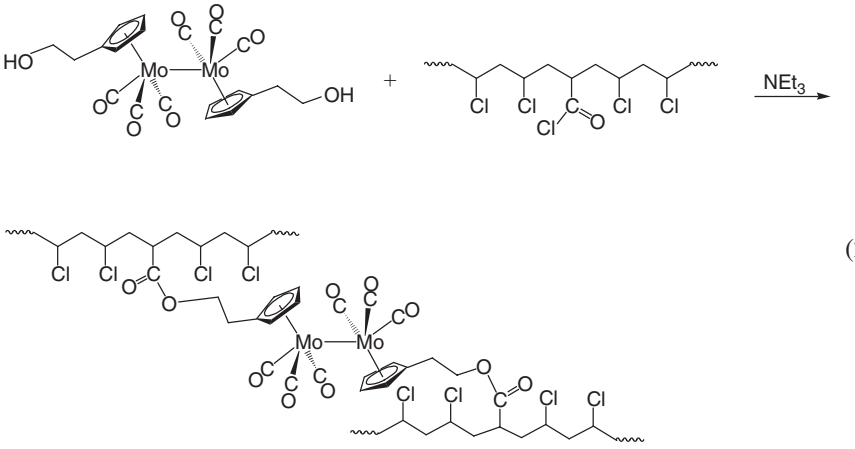

(26)

5

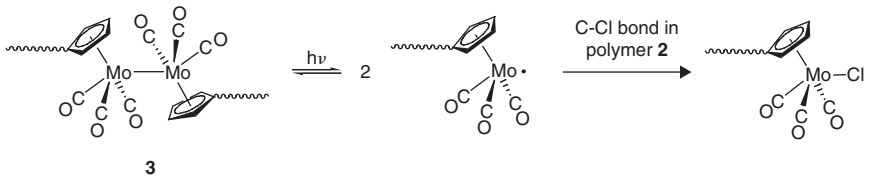

3

SCHEME 7. Photochemical reaction of a polymer with metal-metal bonds along its backbone.

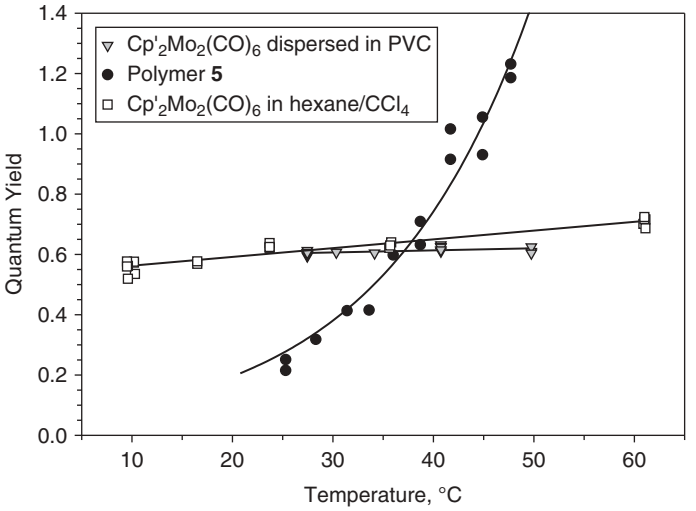

FIGURE 3. Plots of the quantum yields for disappearance of the $Cp'_2Mo_2(CO)_6$ unit in polymer **5**, $Cp'_2Mo_2(CO)_6$ dispersed in PVC, and $Cp'_2Mo_2(CO)_6$ in hexane/CCl_4 ($Cp' = \eta^5$-$C_5H_4CH_3$).

The temperature dependence of the quantum yields for the degradation of polymer **5** could depend on (1) the inherent temperature dependence of the photolysis and radical trapping reaction of the $Cp_2Mo_2(CO)_6$ unit, (2) the temperature-dependent behavior of the polymer morphology, or (3) a temperature-dependent dynamical property of the photogenerated radicals in the polymer. To differentiate among these possibilities, two control experiments were carried out—namely, the photolysis of $Cp'_2Mo_2(CO)_6$ ($Cp' = \eta^5$-$C_5H_4CH_3$) dispersed in a PVC polymer matrix and the photolysis of $Cp'_2Mo_2(CO)_6$ in hexane/CCl_4 solution. The quantum yields for the disappearance of the $Cp'_2Mo_2(CO)_6$ unit in polymer **5**, for $Cp'_2Mo_2(CO)_6$ dispersed in PVC, and for $Cp'_2Mo_2(CO)_6$ in hexane/CCl_4 solution are plotted versus temperature in Figure 3. Note that all of the solid-state data were collected below the glass-transition temperatures of the polymer films (T_g = 65–72 °C). The plots showed there is a significant increase in the quantum yields for

polymer **5** with increasing temperature. In contrast, for $Cp'_2Mo_2(CO)_6$ dispersed in PVC and for $Cp'_2Mo_2(CO)_6$ in hexane/CCl_4 solution (in which the Mo-Mo chromophores are unattached to the polymer chains) there are only slight increases in the quantum yields over this temperature range.

An immediate conclusion from the preceding data is that the large increase in the quantum yield with temperature for polymer **5** is not attributable to an inherent temperature dependence of the photolysis and subsequent radical trapping reaction of the $Cp'_2Mo_2(CO)_6$ unit. (Otherwise, the quantum yields for $Cp'_2Mo_2(CO)_6$ in the hexane/CCl_4 solution would also show a sizable temperature dependence.) Also, because the quantum yields for $Cp'_2Mo_2(CO)_6$ dispersed in PVC showed only a slight temperature dependence, the temperature dependence observed for polymer **5** cannot be ascribed solely to changes in PVC morphology. (Otherwise, the $Cp'_2Mo_2(CO)_6$ dispersed in PVC and polymer **5** would show a similar temperature dependence because the morphologies of PVC and polymer **5** are similar in regard to crystallinity, modulus (1300 ± 100 vs. 1200 ± 50 MPa), and glass-transition temperature (65 ± 4 vs. 72 ± 3°C).) As an aside it is noted that, for the $Cp'_2Mo_2(CO)_6$ dispersed in PVC, the small increase in quantum yields with increasing temperature was attributed to an increase in the free-volume.[2] This explanation was based on a suggestion by Guillet to explain a similarly small temperature dependence in the quantum yields for degradation of poly(vinyl ketone), PVK.[53]

To get better insight into what parameter is controlling the temperature dependence of Φ in polymer **5**, it was necessary to look in more detail at the mechanism of $Cp'_2Mo_2(CO)_6$ photolysis and the subsequent radical capture reaction. (Recall from the discussion above that the increase in Φ with increasing temperature in polymer **5** cannot be attributed to either an intrinsic temperature-dependent reactivity property of the $Cp'_2Mo_2(CO)_6$ molecule or to changes in PVC morphology.) At 25.4°C, the quantum yields for disappearance of the Mo-Mo chromophore were reported as follows: polymer **5**, $\Phi = 0.20$; $Cp'_2Mo_2(CO)_6$ dispersed in PVC, $\Phi = 0.07$; and $Cp'_2Mo_2(CO)_6$ in hexane/CCl_4 solution, $\Phi = 0.35$. As is normal in such comparisons, the quantum yield in solution is considerably higher than that for $Cp'_2Mo_2(CO)_6$ dispersed in the PVC polymer because the solution state is considerably less viscous than the solid state. Perhaps surprising, however, is the much larger quantum yield for polymer **5** (0.20) compared to $Cp'_2Mo_2(CO)_6$ dispersed in the PVC polymer (0.07). The substantial difference in the two quantum yields was proposed to be attributable to a difference in the radical-radical recombination efficiencies (the "cage effect")[54] in the two polymers. The cage effect is illustrated in Scheme 8, which shows the

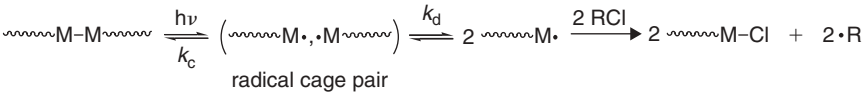

SCHEME 8. Reaction of a photoreactive species to form a caged radical pair followed by a radical trapping reaction.

elementary steps involved in the photochemical generation of metal radicals and their subsequent capture reactions with a trapping molecule.

It was proposed that the temperature dependence of polymer **5** arises from the temperature dependence of the k_d step. Specifically, it was suggested that the polymer segments to which the radicals are attached are conformationally stressed. There are two possible modes for the newly formed radicals to relax and become separated: They can rotate or recoil away from each other (Scheme 9). These secondary motions of the polymer arise from the relaxation of unfavorable bond conformations that are formed during the polymer casting process. The increased thermal energy facilitates the rotation and recoil relaxation processes, which effectively increases the rate constant for diffusion of the radicals out of the cage, k_d. This leads to decreased radical-radical recombination and consequently an increase in photodegradation efficiency.

The quantum yield data for polymer **5** in Figure 3 has an exponential dependence on the inverse temperature, and activation parameters were

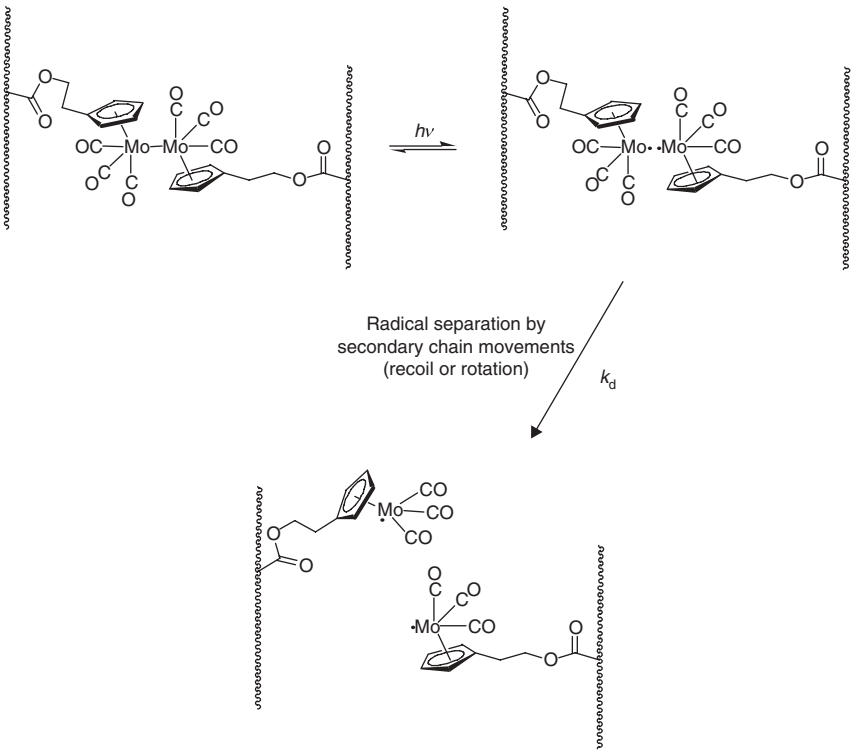

SCHEME 9. Pathway for the increased separation efficiency of the radicals formed by irradiation of polymer **5**. A rotation process is shown, but radical recoil will also lead to increased radical-radical separation. Relaxation of the polymer chains leads to an increase in k_d and a subsequent increase in the quantum yield for degradation.

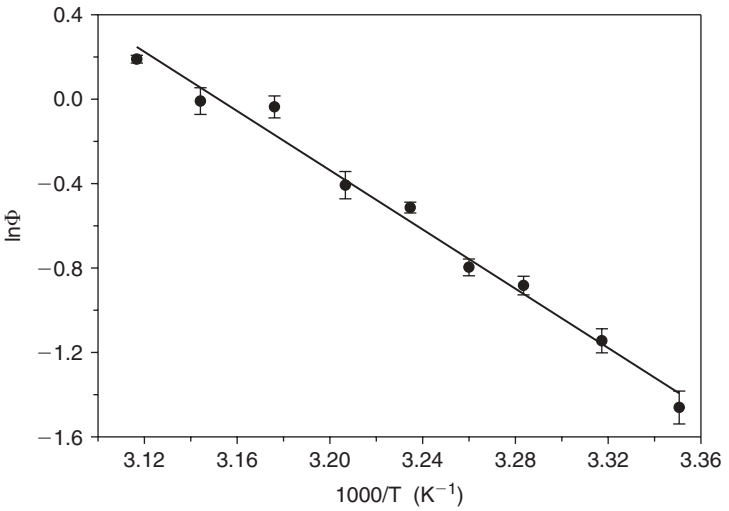

FIGURE 4. Plot of ln Φ versus T^{-1} for polymer **5**.

extracted from the natural log plots of quantum yield versus inverse temperature (Fig. 4). The relationship between the temperature and activation parameters in a photochemical reaction is a complex one,[55] and the apparent activation energies thus obtained were interpreted with care. The activation energy obtained from the lnΦ versus T^{-1} plot (Fig. 4) was 14.1 ± 0.3 kcal mol^{-1}. This value is typical for secondary relaxation chain movements in polymers (which generally fall in the range of 10–20 kcal mol^{-1}) [56–58] and is consistent with the proposal that the temperature dependence of **Φ** results from chain movements involved in recoil and rotation processes.

In summary, the quantum yields for degradation of the $Cp_2Mo_2(CO)_6$ unit in a polymer chain are strongly temperature dependent. When a polymer chain is cleaved at the Mo-Mo bond, the chains relax by secondary chain movements. It was proposed that increased thermal energy facilitates the rotation and recoil relaxation processes, which effectively increases the rate constant for diffusion of the radicals out of the cage, k_d. In effect, the cage recombination efficiency is decreased, and this leads to an increase in the efficiency of degradation. The apparent activation energy obtained from the temperature dependence of the quantum yield of polymer **5** (14.1 ± 0.3 kcal mol^{-1}) is consistent with secondary relaxation chain movements in polymers.

B. Interpreting the Kinetics of Polymer Degradation in the Solid State

Concentration versus time data for the photodegradation of polymer **7** as a function of irradiation time are shown in Figure 5.[59] (The data in the figure were normalized by dividing the concentration values by the initial

concentration.) Note that the traces in the figure exhibit biphasic character, showing a relatively fast rate during the first 1–2% of the reaction but a slower rate at longer times. Typically, photochemical reactions are simple zero-order reactions. (The reaction is zero-order after the initially high reaction rate during the first 1–2% of the reaction.) The plot in Figure 5 does not fit first-order kinetics ($C/C_0 = Ae^{-kt}$), second-order kinetics, or the kinetics for any of several diffusion models. Instead, the decay data were shown to fit a model based on so-called Perrin kinetics.[60,61] The Perrin kinetics model was originally proposed to explain the nonexponential phosphorescence decay in solid polymers, but the kinetics also apply to the trapping reactions of radicals in the solid state. The key feature of the model is that, for phosphorescence decay, when an acceptor is in the quenching sphere of an electronically excited donor molecule, the fluorescence will be quenched. The observed rate of phosphorescence decay is therefore a combination of the decay rate of excited molecules in the presence of the quencher and the natural decay rate of molecules in the absence of the quencher. A mechanistic analogy can be made for photogenerated radical species in solid-state polymers: The observed rate of radical decay will be the combination of the rate when a radical trapping agent is in the reactive sphere of the radical and the rate when no radical trapping agent is present. (The term *reactive sphere* is equivalent to the term *quenching sphere* used in the case of the original Perrin model.) Under such conditions, the concentration of reactive species is given by equation 27.

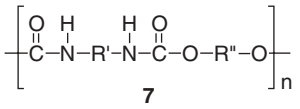

7

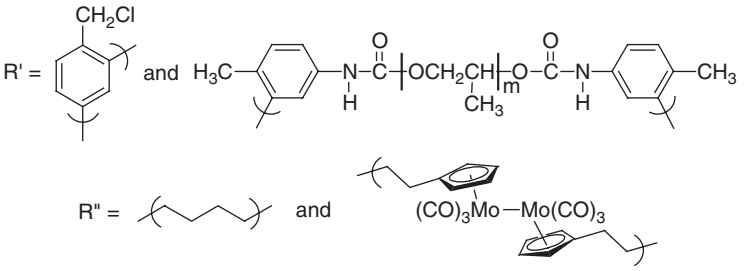

$$[A] = X_0 + k_1 t + Y_0 e^{-k_2 t} \tag{27}$$

The Perrin-like expression in equation 27 was used to fit the kinetic decay trace of polymer **7**; the fit is illustrated in Figure 5.

The biphasic kinetics curve for the reactions of polymers is very typical and is found frequently in the polymer literature. Daglen and Tyler showed[62] that equation 27 gave excellent fit to these systems as well, which suggests the presence of reaction spheres is common in the mechanism of solid-state polymer photodegradation.

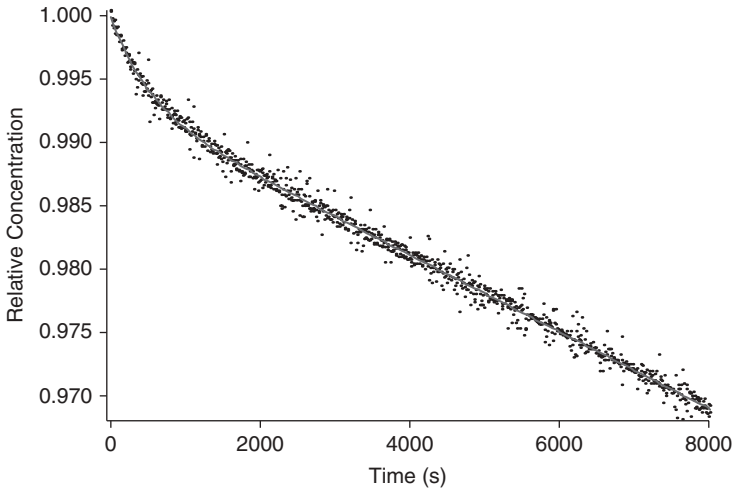

FIGURE 5. Kinetics plot showing the disappearance of polymer **7** as a function of time in seconds.

SCHEME 10. A generalized reaction scheme showing photolysis of a bond along the backbone in a polymer (*M*, a generic atom, carbon or otherwise).

C. Photodegradation Rate Dependence on Polymer Curing Time

Experiments with the metal-metal bonded polymers showed that the degradation rates depended on the curing time. For example, experiments showed that an increase in curing time of polymer **7** led to a decrease in the rate of photodegradation.[62] This result was attributed to an increase in the fraction of the sample that is crystalline. It is well known that an increase in polymer crystallinity leads to a decrease in diffusion of particle or radicals in the polymer. It was hypothesized that the resulting decrease in diffusion (and the consequent increase in radical-radical recombination; Scheme 10) leads to a decrease in the net rate of degradation.

D. The Effects of Stress on Polymer Degradation

i. The Effect of Radical-Radical Recombination

An interesting outcome of photodegradation studies on polymers is the finding that tensile and shear stress can accelerate the rate of photochemical degradation.[9,19,63] For example, recent studies of this phenomenon showed

that tensile stress will accelerate the photodegradation of numerous polyolefins as well as polycarbonates, nylon, and acrylic-melamine coatings. Conversely, compressive stress will generally retard photodegradation reactions.[64] These observations are of practical importance because most polymers are subjected to light and some form of temporary or permanent stress during their lifetime. In order to control the onset of degradation and the rate of degradation in polymers, it is important to understand the mechanistic origin of the synergism between light and stress in these systems. Furthermore, it is important to understand the photochemical degradation reactions of polymers to develop new light stabilizers, to predict the service lifetime of polymers, and to design environmentally friendly degradable materials.

Polymers with metal-metal bonds played a key role in the investigation of the stress effects. As discussed in the introduction, the reason is that polymers generally photodegrade by a photo-oxidative pathway involving the autoxidation radical chain mechanism.[10] The photo-oxidative mechanism, while well understood, is intricate, involving multiple steps, cross-linking, side reactions, and sometimes rate-limiting oxygen diffusion. These features make pinpointing the effects of stress difficult. To circumvent these experimental and mechanistic complexities and therefore make it less difficult to interpret data and obtain fundamental insights, polymer **3** was studied because this polymer photochemically degrades in the absence of oxygen.[19,20] By eliminating the need for external O_2 to act as a radical trap, the complicating kinetics features of diffusion-controlled oxidation reactions were eliminated.

Infrared spectroscopic analysis demonstrated that the chlorine atoms along the polymer backbone did act as built-in traps for Mo-centered radicals formed by photolysis of the Mo-Mo bonds. The effect of stress on the degradation quantum yield of **5** is shown in Figure 6. Note that stress initially increased the quantum yields for degradation, but the quantum yields reached a maximum value and then decreased with higher stress. These results support the decreased radical recombination efficiency (DRRE) hypothesis, one of several hypotheses that have been proposed in the literature to explain the effect of stress on polymer photodegradation rates and efficiencies. Specifically, the DRRE hypothesis proposes that the function of stress is to increase the initial separation of the photochemically generated radical pair, which has the effect of decreasing their recombination efficiency and thus increasing the degradation efficiency (Scheme 8).[65–69] The hypothesis predicts an eventual downturn in degradation efficiency because of polymer chain ordering; the increased order hinders diffusion apart of the radicals and thus increases their probability of recombination. Wide-angle X-ray diffraction and infrared spectroscopy confirmed that chain orientation increased with increasing stress in polymer **5**.[19]

ii. More Details on Stress-Induced Changes in $k_{\text{recombination}}$

A number of authors[65–69] have proposed theories for explaining the stress dependence of polymer photochemical degradation rates that are based on the

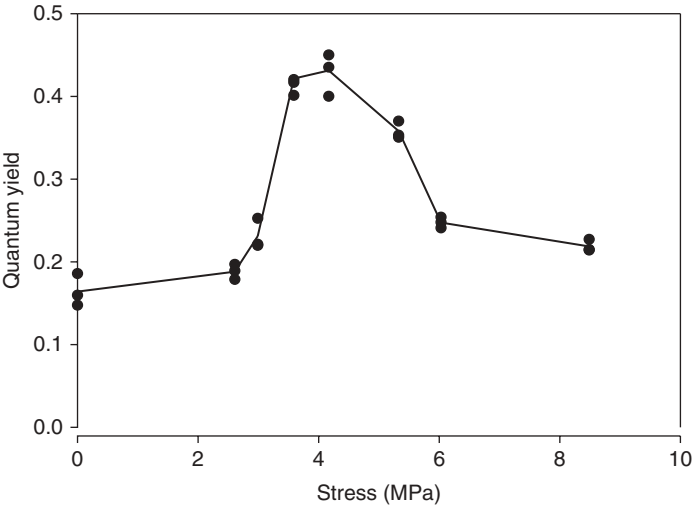

FIGURE 6. Quantum yields for degradation of polymer **5** versus applied tensile stress.

concept of stress affecting the ability of geminate radical pairs, formed in bond cleavage reactions, to recombine. These various theories differ slightly in their details, but they are similar overall and are discussed together here. For convenience these theories, are referred to as the decreased radical recombination efficiency hypothesis. In the DRRE hypothesis, the effect of stress on the photochemical reactions of polymers is divided into four stages (Figure 7). Stage one is the low-stress domain. In this stage, there is little or only slight deformation of the original polymer structure, and the rate of photodegradation is not greatly affected.

In stage two, higher stress causes significant morphological changes, including the straightening of the polymer chains in the amorphous regions. These straightened chains contain taut tie molecules. (Tie molecules are the interlamellar- or intercrystal-fibrils.) When bonds in the taut tie molecules are cleaved by light, the probability of radical recombination is decreased relative to nonstressed samples because entropic relaxation of the chain drives the radicals apart and prevents their efficient recombination because of their increased separation. At slightly higher stresses (stage three), the chains are not only straightened but also stretched, and mechanical recoil also aids in the separation of the radicals (much like the midpoints of a stretched spring would fly apart if it were cut in the middle). According to this model, the role of stress is to increase the separation of the radical fragments produced by photolysis. An increased separation leads to slower radical-radical recombination, which increases the probability of radical trapping and thus of degradation.

In stage four (not shown in Figure 7), a strong stress is present, which gives the polymer a fibrillar structure with a higher degree of orientation and

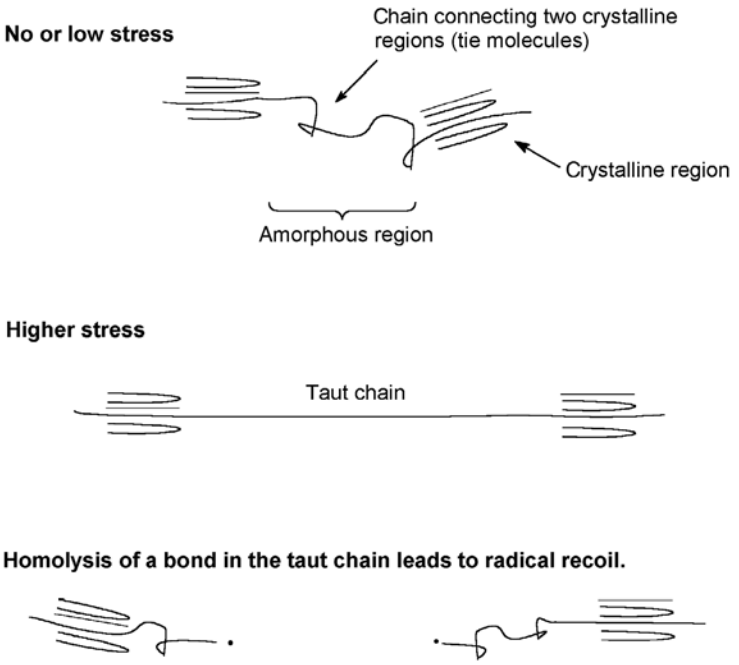

FIGURE 7. The proposed effect of stress in the several stages of the decreased radical recombination efficiency hypothesis.

crystallinity. (In this stage, ordered regions develop as segments of different chains align.) Diffusion in a crystalline structure is retarded relative to the amorphous material, and the efficiency of degradation is expected to decrease because of decreased diffusion apart of the radical pair and decreased radical-trap mobility. Overall, the DRRE theory predicts that tensile stress will initially increase the quantum yield of degradation, and then further increases in stress will decrease the quantum yield (Fig. 8). A note of caution when interpreting data is that, if one experimentally observes a decrease in the quantum yield as predicted for stage four behavior, it is important to establish that the origin of the decrease is in fact a higher degree of orientation and crystallinity. An alternative explanation is that microcracks and fissures have formed in the sample and these are acting to relieve the stress, which in turn would also decrease the quantum yields. This alternative mode of action was detected by Nguyen and Rogers in their study of acrylic-melamine coatings.[70]

VII. KINETICS OF POLYMER FORMATION

Two frequently asked questions are (1) How do the metal-metal bonded species affect the kinetics and mechanisms of polymerization compared to

analogous reactions with traditional organic-only monomers? and (2) How are the physical properties of the polymers affected by the presence of the metal-metal bonds? To study these questions, the kinetics of the dibutyltin diacetate (DBTA)-catalyzed polymerization reactions of $(\eta^5\text{-}C_5H_4CH_2CH_2OH)_2Mo_2(CO)_6$ with Hypol 2000 (eq. 7) and of Hypol 200 with 1,4-butanediol (Scheme 11) were studied, as were the kinetics of a copolymerization involving $(\eta^5\text{-}C_5H_4CH_2CH_2OH)_2Mo_2(CO)_6$ and PEG-1000 (a poly(ethylene glycol)) with Hypol 2000 (eq. 8).[71] The results showed that $(\eta^5\text{-}C_5H_4CH_2CH_2OH)_2Mo_2(CO)_6$ did not significantly alter the time scale of the polymerization reactions and that the same reaction mechanism (Scheme 12) is used as with the 1,4-butanediol and PEG-1000. Some slight differences in the rate constants of the elementary steps were observed, but these differences were attributed to the increased steric crowding caused by the bulkier $(\eta^5\text{-}C_5H_4CH_2CH_2OH)_2Mo_2(CO)_6$ diol compared to 1,4-butanediol and PEG-1000.

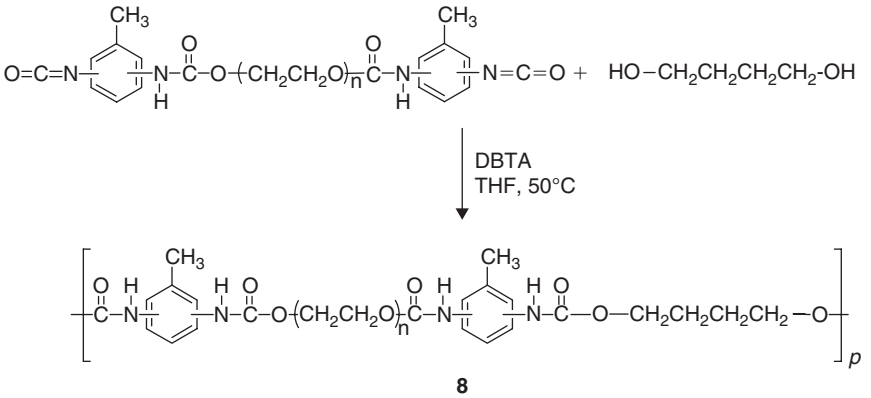

8

SCHEME 11

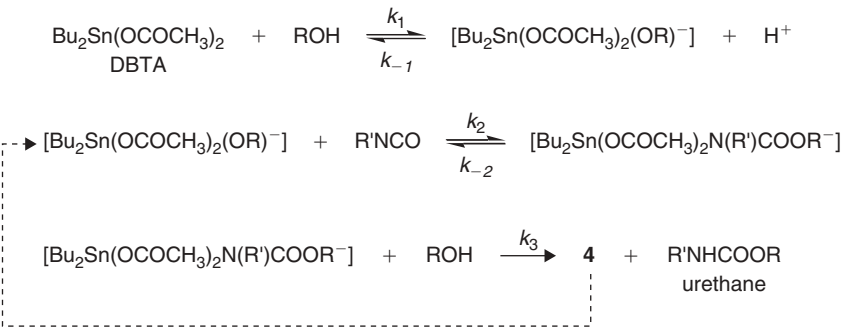

SCHEME 12. Proposed mechanism for the DBTA-catalyzed reaction of an isocyanate with an alcohol.

The effect of the $(\eta^5\text{-}C_5H_4CH_2CH_2OH)_2Mo_2(CO)_6$ on the polymers' physical properties was also investigated.[71] The polymers in equations 7 and 8 and in Scheme 11 (polymers **1**, **2**, and **8**, respectively) are segmented polyurethanes—that is, block copolymers consisting of alternating soft and hard segments. The polyether chains are soft, and the hard segments consist of the urethane group and the diol structural unit, if the diol structural unit is of low molecular weight, as in the case of polymers **1** and **8**. Two important features of segmented polyurethanes are that (1) the lengths of the hard and soft segments and their relative proportions affect the morphology and properties of the segmented polyurethanes,[72,73] and (2) the polar nature of the hard urethane segments leads to domain formation through hydrogen bonding. Generally, the longer the soft segment and the more of it, the softer the character of the polyether.[74,75] Thus polymer **2**, which has proportionally more soft, polyether components, is a sticky and soft material, and polymers **1** and **8**, with less polyether content, are stiff and tough.

The hard domains in a segmented polyurethane provide both physical cross-link sites and filler-like reinforcement to the soft-segment matrix, which is responsible for the elastomeric behavior of these polyurethanes. The extent of hydrogen bonding between hard segments is expressed by the hydrogen bonding index (HBI),[76] which is defined as the ratio of the absorbance for the hydrogen bonded C = O peak[77] at 1701 cm^{-1} to the absorbance for the free C = O peak at 1732 cm^{-1} in the infrared spectrum. In general, the HBI value increases with increasing hard segment content. The HBI values for the polymers **1**, **2**, and **8** are 0.707, 0.555, and 0.786. The physical differences discussed above are quantitatively reflected in the HBI values of the three polymers: polymer **2** has the lowest HBI value, indicating it has the highest content of soft segments, consistent with the soft, sticky nature of this polymer and its low strength. Polymers **1** and **8** have fewer soft segments and concomitant larger HBI values, which is apparent in their increased stiffness. The conclusion is that the hydrogen bonding index (HBI) and the relative amount of soft segments of the $(\eta^5\text{-}C_5H_4CH_2CH_2OH)_2Mo_2(CO)_6$-containing polyurethane correlate in a general way with the physical properties of the polymer.

VIII. CONCLUDING REMARKS ON THE IMPORTANCE OF RADICAL-RADICAL RECOMBINATION ON THE EFFICIENCY OF POLYMER PHOTOCHEMICAL DEGRADATION

The ability of two geminate radicals to escape from each other and thereby avoid radical-radical recombination is a key mechanistic feature that determines the rate of polymer degradation (Scheme 10). As shown in the discussion, the existence of a photochemically generated radical pair containing

two radicals in close proximity explains: (1) the effect of tensile stress on the rate of polymer degradation, (2) the effect of temperature on photodegradation rates, and (3) the effect of polymer curing on degradation rates. In each of these situations, the efficiency of radical diffusion affects the net efficiency of radical-radical recombination, which affects the efficiency of photodegradation. The concept of radical-radical recombination also manifests itself in the biphasic kinetics observed for polymers in many photodegradations. In this situation, the initial high rate of decay is interpreted as being due to radical capture within a matrix cage.

IX. ACKNOWLEDGMENTS

Acknowledgment is made to the National Science Foundation and to the Petroleum Research Fund, administered by the American Chemical Society, for the support of the authors' work described in this chapter.

X. REFERENCES

1. N. Grassie, G. Scott, *Polymer Degradation and Stabilization,* Cambridge University Press, New York, 1985.
2. J. Guillet, *Polymer Photophysics and Photochemistry: An Introduction to the Study of Photoprocesses in Macromolecules,* Cambridge University Press: New York, 1985.
3. J. F. Rabek, *Mechanisms of Photophysical Processes and Photochemical Reactions in Polymers,* Wiley, New York, 1987.
4. J. E. Guillet, in S. A. Barenberg, J. G. Brash, R. Narayan, A. E. Redpath, eds., *Degradable Materials,* CRC Press, Boston, 1990, p *55*.
5. R. Leaversuch, *Modern Plastics,* **78,** *72* (2001).
6. G. Scott, D. M. Wiles, *Degradable Hydrocarbon Polymers in Waste and Litter Control,* Kluwer Academic Publishers, Dordrecht, Netherlands, 2002.
7. P. J. Hocking, *J. Macromol. Sci. Rev. Macromol. Chem. Phys.,* **C32,** *35* (1992).
8. S. Al-Malaiaka, A. Marogi, G. Scott, *Polym. Degrad. Stab.,* **18,** *89* (1987).
9. D. R. Tyler, *J. Macromol. Sci. Poly. Rev.,* **44,** *351* (2004).
10. G. Geuskens, *Compr. Chem. Kinet.,* **14,** *333* (1975).
11. A. Huvet, J. Philippe, J. Verdu, *Eur. Polym. J.,* **14,** *709* (1978).
12. A. V. Cunliffe, A. Davis, *Polym. Degrad. Stab.,* **4,** *17* (1982).
13. D. R. Tyler, *Coord. Chem. Rev.,* **246,** *291* (2003).
14. S. C. Tenhaeff, D. R. Tyler, *Organometallics,* **10,** *1116* (1991).
15. S. C. Tenhaeff, D. R. Tyler, *Organometallics,* **10,** *473* (1991).
16. S. C. Tenhaeff, D. R. Tyler, *Organometallics,* **11,** *1466* (1992).
17. G. F. Nieckarz, D. R. Tyler, *Inorg. Chim. Acta,* **242,** *303* (1996).
18. G. F. Nieckarz, J. J. Litty, D. R. Tyler, *J. Organomet. Chem.,* **554,** *19* (1998).

19. R. Chen, D. R. Tyler, *Macromolecules,* **37,** *5430* (2004).
20. R. Chen, M. Yoon, A. Smalley, D. C. Johnson, D. R. Tyler, *J. Am. Chem. Soc.,* **126,** *3054* (2004).
21. B. E. Krisyuk, A. A. Popov, G. E. Zaikov, *Vysokomolek. Soedineniya, Ser. A,* **22,** *329* (1980).
22. C. U. Pittman Jr., M. D. Rausch, *Pure Appl. Chem.,* **58,** *617* (1986).
23. K. Gonsalves, L. Zhan-Ru, M. D. Rausch, *J. Am. Chem. Soc.,* **106,** *3862* (1984).
24. K. E. Gonsalves, R. W. Lenz, M. D. Rausch, *Appl. Organomet. Chem.,* **1,** *81* (1987).
25. F. W. Knobloch, W. H. Rauscher, *J. Polym. Sci.,* **54,** *651* (1961).
26. C. U. Pittman, Jr., *J. Polym. Sci., Polym. Chem. Ed.,* **6,** *1687* (1968).
27. K. E. Gonsalves, M. D. Rausch, *J. Polym. Sci. Part A: Polym. Chem.,* **26,** *2769* (1988).
28. W. J. Patterson, S. P. McManus, C. U. Pittman Jr., *J. Polym. Sci., Polym. Chem. Ed.,* **12,** *837* (1974).
29. P. Nguyen, P. Gomez-Elipe, I. Manners, *Chem. Rev.,* **99,** *1515* (1999).
30. I. Manners, *Adv. Organomet. Chem.,* **37,** *131* (1995).
31. I. Manners, *Coord. Chem. Rev.,* **137,** *109* (1994).
32. A. E. Stiegman, D. R. Tyler, *Coord. Chem. Rev.,* **63,** *217* (1985).
33. R. Chen, J. Meloy, B. C. Daglen, D. R. Tyler, *Organometallics,* **24,** *1495* (2005).
34. M. Moran, M. C. Pascual, I. Cuadrado, J. Losada, *Organometallics,* **12,** *811* (1993).
35. N. T. Lucas, M. G. Humphrey, A. D. Rae, *Macromolecules,* **34,** *6188* (2001).
36. F. W. Grevels, *NATO ASI Ser. Ser. C: Math. Phy. Sci.* **376,** *141* (1992).
37. P. C. Ford, *J. Organomet. Chem.,* **383,** *339* (1990).
38. J. E. Schwendeman, A. C. Church, K. B. Wagener, *Adv. Synth. Catal.* **344,** *597* (2002).
39. T. W. Baughman, K. B. Wagener, *Adv. Polym. Sci.,* **176,** *1* (2005).
40. M. D. Watson, K. B. Wagener, *Macromolecules,* **33,** *8963* (2000).
41. J. C. Sworen, J. A. Smith, J. M. Berg, K. B. Wagener, *J. Am. Chem. Soc.* **126,** *11238* (2004).
42. G. V. Shultz, O. B. Berryman, L. N. Zakharov, D. R. Tyler, *J. Inorg. Organomet. Poly. Mater.,* **18,** *149* (2008).
43. D. R. Tyler, J. J. Wolcott, G. F. Nieckarz, S. C. Tenhaeff, *ACS Symp. Ser.,* **572,** *481* (1994).
44. T. R. O'Toole, B. P. Sullivan, T. J. Meyer, *J. Am. Chem. Soc.* **111,** *5699* (1989).
45. T. J. Meyer, J. V. Caspar, *Chem. Rev.,* **85,** *187* (1985).
46. G. L. Geoffroy, M. S. Wrighton, *Organometallic Photochemistry,* Academic Press, New York, 1979.
47. R. Mishra, S. P. Tripathy, D. Fink, K. K. Dwivedi, *Radiat. Eff. Defects Solids,* **159,** *569* (2004).
48. R. Mishra, S. P. Tripathy, D. Fink, K. K. Dwivedi, *Radiat. Measurements,* **40,** *754* (2005).
49. M. Celina, K. T. Gillen, R. A. Assink, *Polym. Degrad. Stab.,* **90,** *395* (2005).
50. T. Yamashita, H. Tomitaka, T. Kudo, K. Horie, I. Mita, *I. Polym. Degrad. Stab.,* **39,** *47* (1993).
51. L. Audouin, S. Girois, L. Achimsky, J. Verdu, *Polym. Degrad. Stab.,* **60,** *137* (1998).
52. B. C. Daglen, J. D. Harris, D. R. Tyler, *J. Inorg. Organomet. Polym. Mater.,* **17,** *267* (2007).
53. E. Dan, J. E. Guillet, *Macromolecules,* **6,** *230* (1973).
54. J. P. Lorand, *Prog. Inorg. Chem.,* **17,** *207* (1972).

55. V. Balzani, V. Carassiti, *Photochemistry of Coordination Compounds,* Academic Press, New York, 1970.
56. J. R. Fried, *Polymer Science and Technology,* Prentice Hall, Upper Saddle River, NJ, 1995.
57. A. Elicegui, J. J. Del Val, J. L. Millan, C. Mijangos, *J. Non-Cryst. Solids,* **235–237,** *623* (1998).
58. L. David, C. Girard, R. Dolmazon, M. Albrand, S. Etienne, *Macromolecules,* **29,** *8343* (1996).
59. D. R. Tyler, B. C. Daglen, *Polym. Prepr. Am. Chem. Soc. Div. Polym. Chem.,* **49,** *919* (2008).
60. F. Perrin, *Compt. Rend.,* **178,** *1978* (1924).
61. N. J. Turro, *Modern Molecular Photochemistry,* Addison-Wesley, Reading, MA, 1978.
62. B. C. Daglen, D. R. Tyler, in preparation.
63. J. R. White, N. Y. Rapoport, *Trends Polym. Sci.,* **2,** *197* (1994).
64. L. Tong, J. R. White, *Polym. Degrad. Stab.,* **53,** *381* (1996).
65. W. K. Busfield, M. J. Monteiro, *Mat. Forum,* **14,** *218* (1990).
66. D. Benachour, C. E. Rogers, *ACS Symp. Ser.,* **151,** *263* (1981).
67. T. L. Nguyen, C. E. Rogers, *Polym. Mater. Sci. Eng.,* **53,** *292* (1985).
68. E. Baimuratov, D. S. Saidov, I. Y. Kalontarov, *Polym. Degrad. Stab.,* **39,** *35* (1993).
69. Y. A. Shlyapnikov, S. G. Kiryushkin, A. P. Marin, *Antioxidative Stabilization of Polymers,* Taylor & Francis, Bristol, PA, 1996.
70. T. L. H. Nguyen, C. E. Rogers, *Polym. Sci. Technol.,* **37,** *431* (1988).
71. R. Chen, E. Spence, D. R. Tyler, *J. Inorg. Organomet. Polym. Mater.,* **15,** *221* (2005).
72. C.-C. M. Ma, H.-C. Hsia, D.-S. Chen, Y.-S. Li, M.-S. Li, *Polym. Int.,* **35,** *361* (1994).
73. H.-D. Kim, T.-J. Lee, J.-H. Huh, D.-J. Lee, *J. Appl. Polym. Sci.,* **73,** *345* (1999).
74. M. J. O'Sickey, B. D. Lawrey, G. L. Wilkes, *J. Appl. Polym. Sci.,* **84,** *229* (2002).
75. J. Liu, D. Ma, Z. Li, *Eur. Polym. J.,* **38,** *661* (2002).
76. T. Gupta, D. De, B. Adhikari, *Polym. Int.,* **52,** *938* (2003).
77. V. V. Zharkov, A. G. Strikovsky, T. E. Verteletskaya, *Polymer,* **34,** *938* (1993).

CHAPTER 8

Optical Properties and Photophysics of Platinum-Containing Poly(aryleneethynylene)s

Wai-Yeung Wong

Department of Chemistry and Centre for Advanced Luminescence Materials, Hong Kong Baptist University, Waterloo Road, Kowloon Tong, Hong Kong, P. R. China

CONTENTS

Macromolecules Containing Metal and Metal-like Elements,
Volume 10: Photophysics and photochemistry of metal-containing polymer,
Edited by Alaa S. Abd-El Aziz, Charles E. Carraher Jr., Pierre D. Harvey, Charles U. Pittman Jr., Martel Zeldin.

I. INTRODUCTION

Incorporation of transition metal elements into macromolecular organic structures allows the hybridization of the interesting physical characteristics of metals such as electronic, optical, and magnetic properties with the solubility and processability of traditional carbon-based polymers.[1–5] Transition metal centers with a large variety of ligand environments, oxidation states, and structural geometries may offer distinct physical, optoelectronic, and structural properties on these purely organic polymers. Within the framework of synthetic metal-containing polymers, polymers with metal–carbon σ-bonds in the main chain represent one of the attractive and important subsets of these materials.[1–4] Rigid-rod transition metal acetylide polymers, or polymetallaynes in short, have spurred tremendous worldwide interest at the forefront of many metallopolymer investigations.[6]

The development of synthetic methodologies toward transition metal acetylide oligoynes and polyynes of the form *trans*-[−M(L)$_2$C≡C(R)C≡C−]$_n$ (L=auxiliary ligands, R=spacer unit) has shown much progress following the initial reports by the Japanese group in the 1970s on the synthesis of polymeric Pt and Pd acetylides,[7–10] and the interest has been principally stimulated from their applications in molecular electronics and materials science (Fig. 1).[1,2] In the early 1990s, there were also a couple of reports on the synthesis of rigid-rod metal-containing polyynes of groups 8 and 10 by Lewis and co-workers based on bis(trimethylstannylacetylide) synthons.[11–14] Since then, these organometallic-based oligomeric and polymeric functional materials have become famous for their unique properties, such as electrical conductivities, rich luminescence and nonlinear optical properties, liquid crystallinity and photovoltaic effect.[6] The prototypical polymer for much of this work is *trans*-[−Pt(PBu$_3$)$_2$C≡C(*p*-C$_6$H$_4$)C≡C−]$_n$ (**1**). To date, a large series of derivatives containing various conjugated carbocyclic and heteroaromatic ring systems are known.[1,6] All of these materials are organic soluble, and the solubility and polymer length can be adjusted by an appropriate selection of Ar or L units (Fig. 1). The advances in chemical synthesis have also resulted in the preparation of a library of application-oriented conjugated polymers of this kind that can display diverse optical and photophysical properties. This chapter provides a comprehensive overiew on this topic for platinum-containing poly(aryleneethynylene)s.

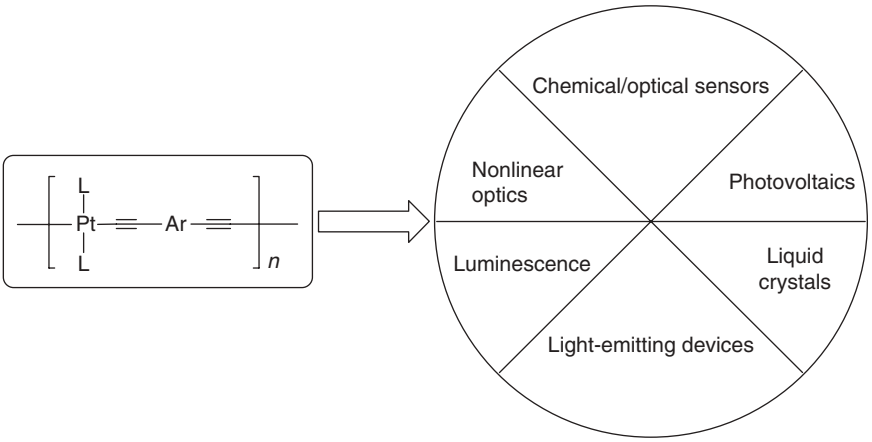

FIGURE 1. Polyplatinynes in different areas of material applications.

II. SYNTHETIC METHODS AND MATERIALS CHARACTERIZATION

Since the pioneering work by Hagihara et al. on the prototype compound of group 10 metals spaced by the phenylene ring in polymer **1** followed by the synthetic extension of the method to group 8 metals,[7–10] there has been a large body of literature on the chemical syntheses, spectroscopic and structural aspects, material properties as well as potential applications of organometallic polyyne polymers of the late transition metals. Long and others have provided leading references to the modern literature of the synthesis and mechanism of metal polyynes, and these topics will not be included here.[1,2,4,6] In general, a series of diethynyl-derived spacers can be used as versatile precursors to produce dinuclear and polymeric compounds of platinum by the most common copper(I)-catalyzed dehydrohalogenative coupling procedures in an amine solvent (e.g., diethylamine or diisopropylamine) at room temperature. The $Me_3SiC{\equiv}CRC{\equiv}CSiMe_3$ derivatives can be obtained in good yields from the Sonogashira coupling of $Me_3SiC{\equiv}CH$ with the appropriate dibromo species, which upon deprotection with a suitable base such as K_2CO_3 in MeOH or Bu_4NF in THF readily afford the diterminal alkyne compounds $HC{\equiv}CRC{\equiv}CH$ (Fig. 2). The feed mole ratios of the platinum chloride precursors and the active diethynyl ligands are 2:1 and 1:1 for the model complex and polymer syntheses, respectively. As summarized in Figure 3, the spacers adopted can range widely from common organic carbocyclic rings (**1**–**27** and **75**) to various heterocyclic moieties (**28**–**51**) and even the inorganic units, such as some main group (**52**–**74**) and transition metal elements (**17** and **27**). Purification of the polymers was effected by column chromatography on silica

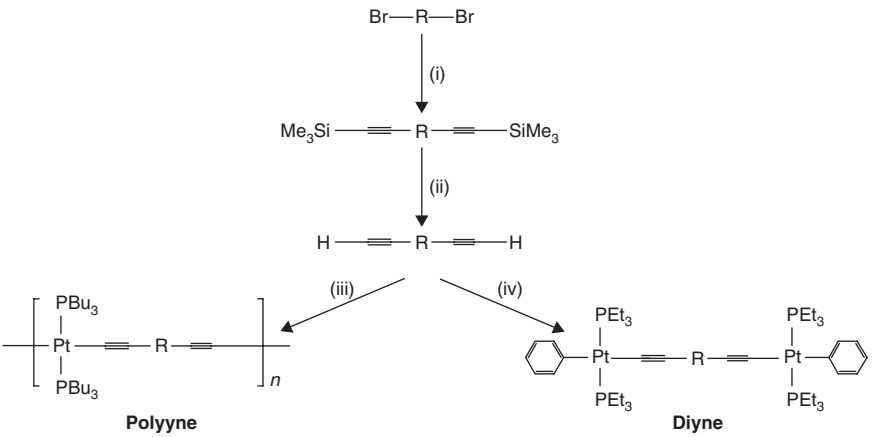

FIGURE 2. Synthetic schemes for polyplatinynes and their molecular model compounds. Reagents and conditions: (i) Trimethylsilylacetylene, $Pd(OAc)_2$, CuI, PPh_3, amine; (ii) K_2CO_3 in MeOH or Bu_4NF in THF; (iii) *trans*-$[PtCl_2(PBu_3)_2]$ (1 equiv.), CuI, amine; (iv) *trans*-$[PtCl(Ph)(PEt_3)_2]$ (2 equiv.), CuI, amine.

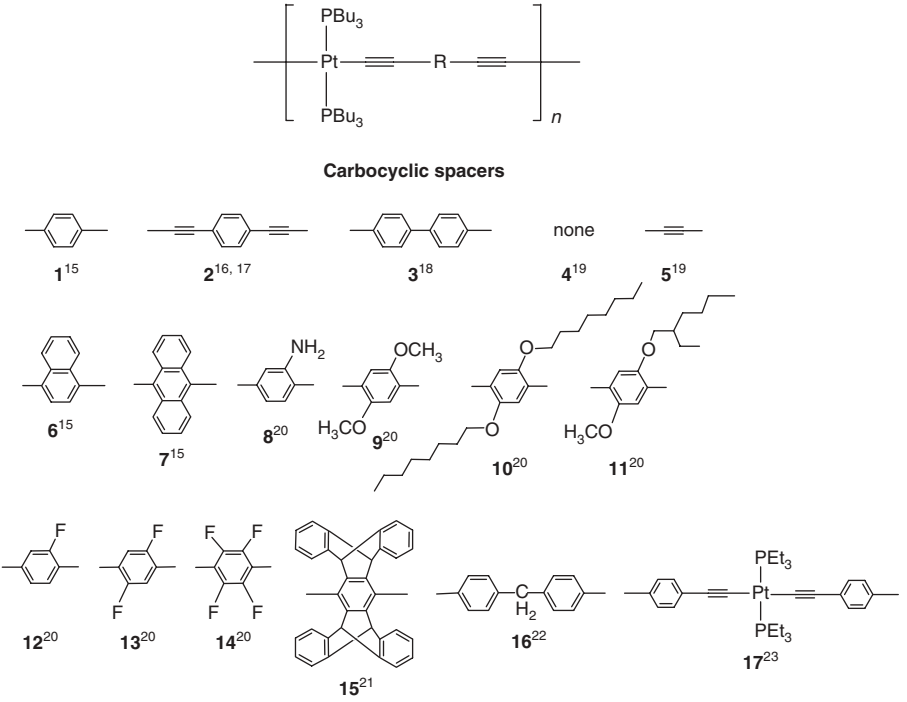

FIGURE 3. Chemical structures of platinum(II) polyyne polymers **1**–**75**.

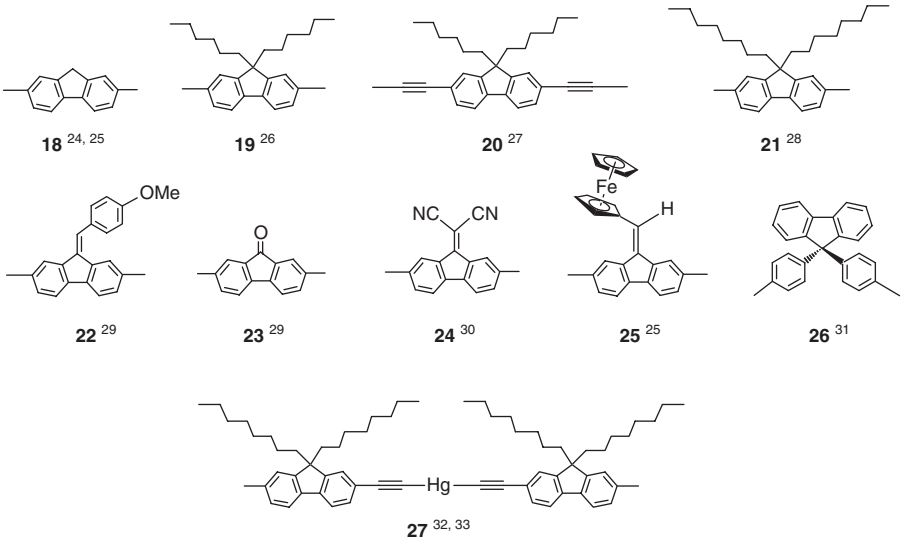

18 [24, 25] **19** [26] **20** [27] **21** [28]

22 [29] **23** [29] **24** [30] **25** [25] **26** [31]

27 [32, 33]

Heterocyclic spacers

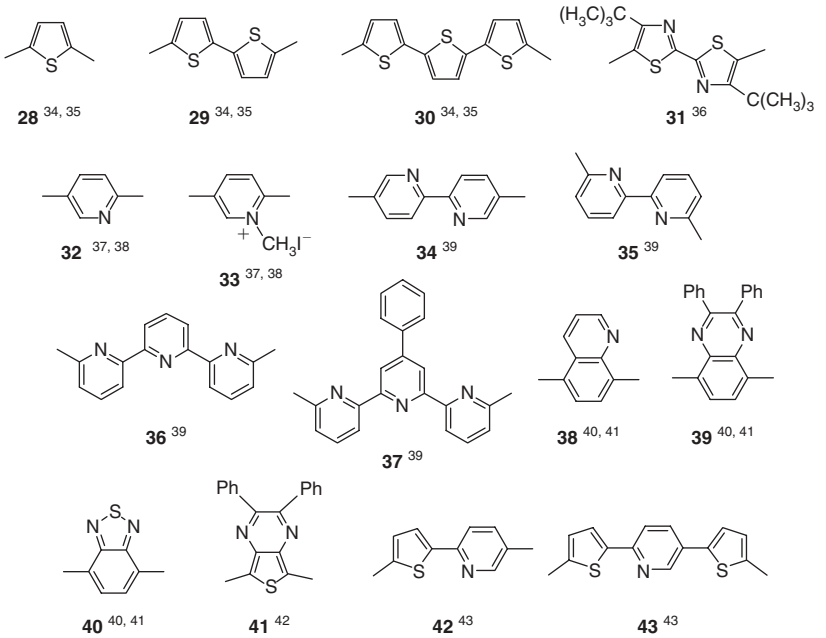

28 [34, 35] **29** [34, 35] **30** [34, 35] **31** [36]

32 [37, 38] **33** [37, 38] **34** [39] **35** [39]

36 [39] **37** [39] **38** [40, 41] **39** [40, 41]

40 [40, 41] **41** [42] **42** [43] **43** [43]

FIGURE 3. (Continued)

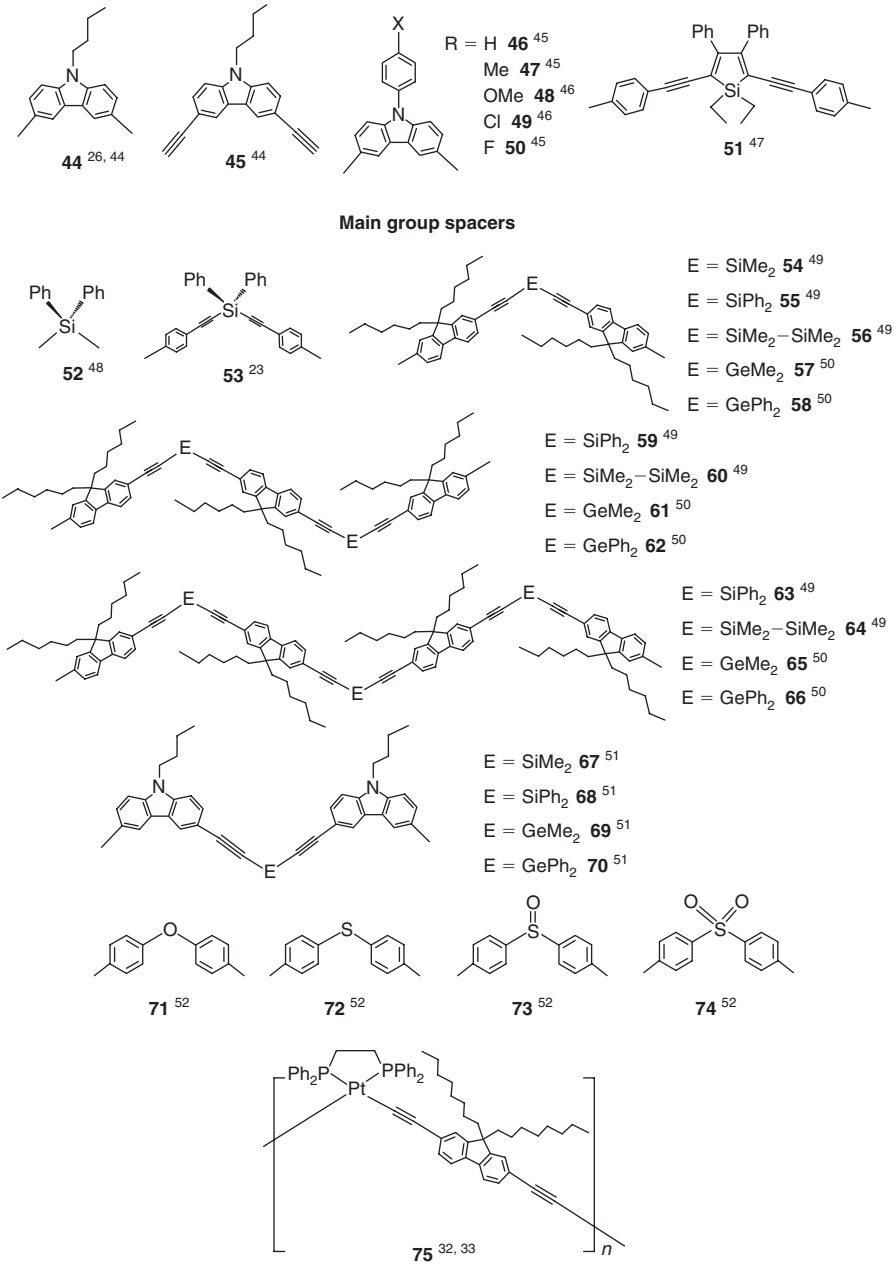

FIGURE 3. (Continued)

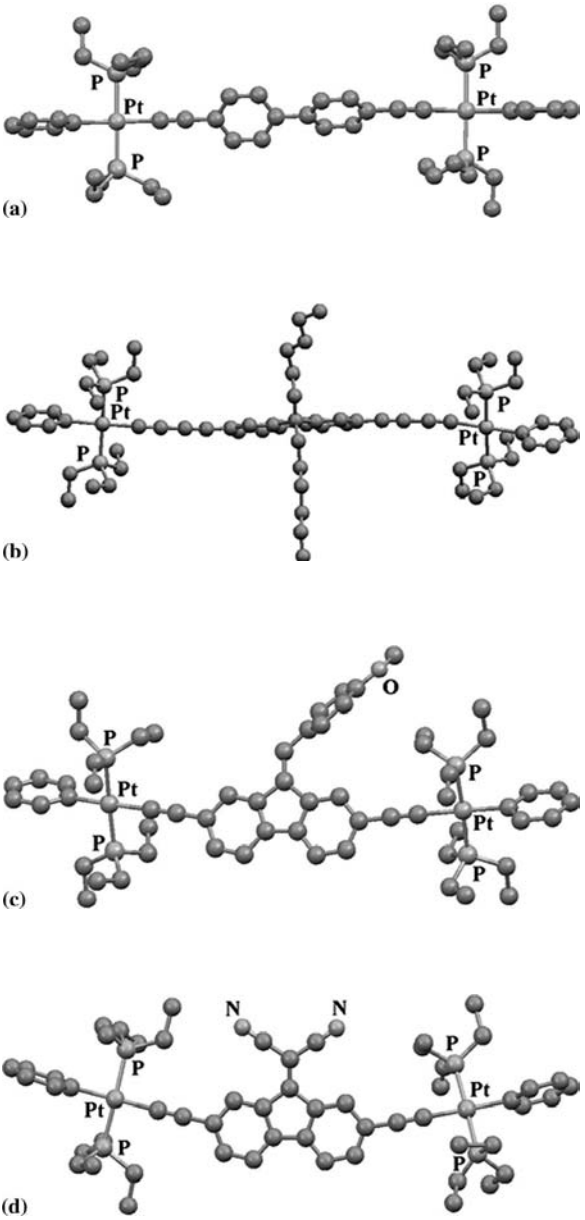

FIGURE 4. X-ray structures of model complexes for (a) **3**, (b) **20**, (c) **22**, (d) **24**, (e) **29**, (f) **31**, (g) **48**, (h) **52**, (i) **72**, and (j) **74**. In each case, the carbon labels are omitted for clarity.

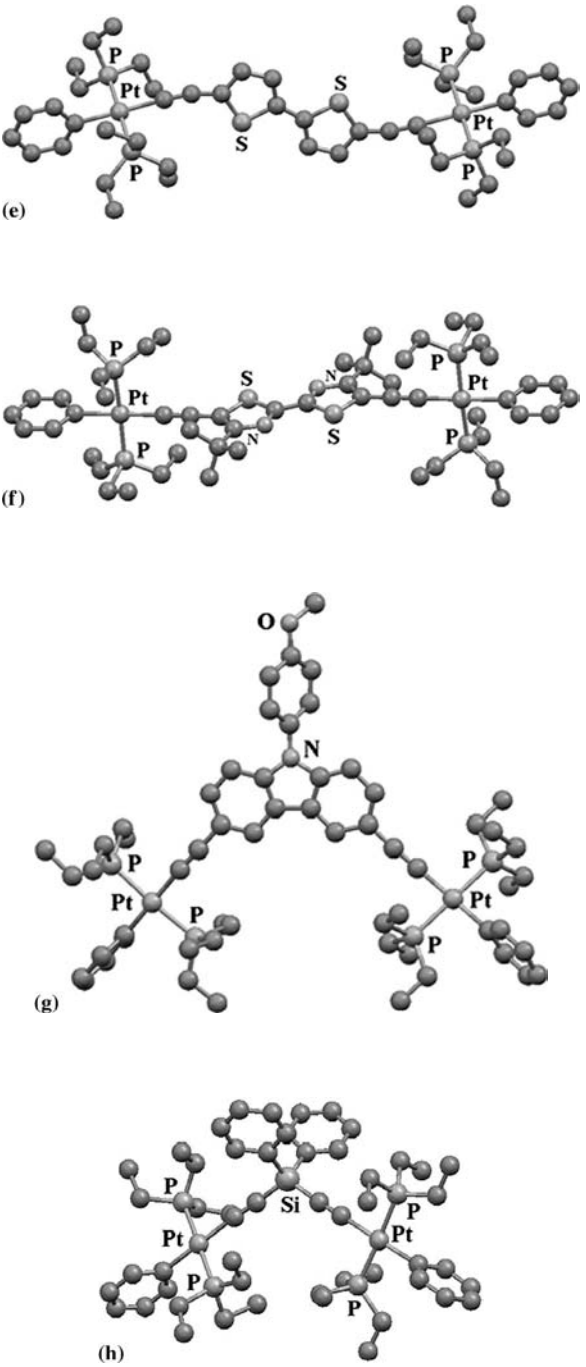

FIGURE 4. (Continued)

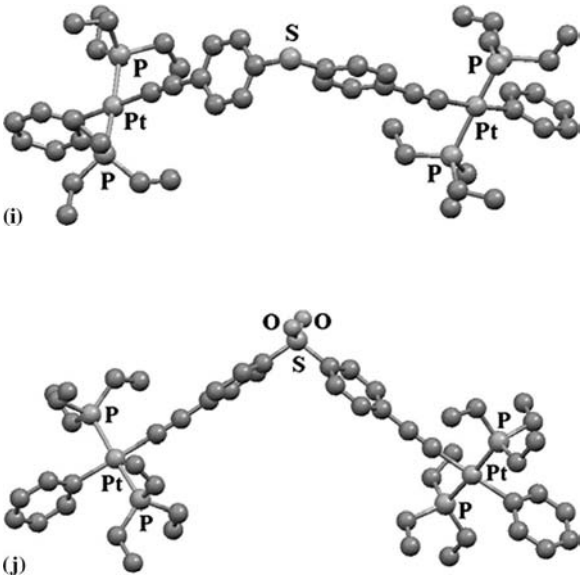

FIGURE 4. (Continued)

or alumina using appropriate solvent combinations. Typically, the enhanced solubility associated with metallopolyynes favors these organometallic polymers over purely organic polymers when it comes to preparing optical-quality thin films for detailed optical characterizations.

All of the metal polyynes and their corresponding oligomeric molecular model systems were fully characterized by a combined use of elemental analyses, FAB-MS, IR and NMR spectroscopies. The metal diynes can be considered building blocks for the high molecular weight polymers from which valuable insights for the polymer properties can be attained. The progress in synthetic methodologies has resulted in numerous methods producing a large series of conjugated polymers of this kind that can display highly tunable functional properties. While the IR spectroscopy is useful for identifying the acetylenic functional group in the complexes, there is little change in its position over a range of metals or spacer groups, and so it does not provide much information as to the electronic properties of the coordinating units. The 3D structures of the model complexes were unambiguously confirmed by single-crystal X-ray analyses in many instances. Some representative examples are portrayed in Figure 4.

The molecular weights of most of the soluble polymers were predicted by gel permeation chromatography (GPC) analyses against polystyrene calibration. While GPC does not give absolute values of molecular weights but provides a measure of hydrodynamic volume, there is probably some differences in

the hydrodynamic behavior of rigid-rod type polymers in solution from those for flexible polymers, leading to certain systematic errors in the GPC measurements.[1] But, the end group analysis in the NMR spectra can also help in examining the degree of polymerization. As studied by thermogravimetric analyses, all of the polymers exhibit very good thermal stability.

III. OPTICAL AND PHOTOPHYSICAL PROPERTIES

A. Energy Gap Law for Triplet States

It is well known that metallopolyynes are good luminescent and functional materials, typically exhibiting both fluorescence and phosphorescence. The synthetic modification of the organometallic acetylide polymers to produce materials of variable bandgaps and phosphorescent energy states can be categorized according to the types of metal groups and their auxiliary ligands, and the central spacer units.[53–55] The nature and energy of the excited state of Pt polyynes can be manipulated easily by deliberate chemical synthesis.[56]

Figure 5 illustrates the classical Jablonski energy level diagram for a simple photoluminescence (PL) system. Upon absorption of photons by a molecule, there are two main radiative decay processes—namely, fluorescence ($S_1 \rightarrow S_0$) and phosphorescence ($T_1 \rightarrow S_0$). The relative positions of the singlet and triplet excited states strongly affect the intersystem crossing (ISC) rate into the triplet manifold. This provides a major nonradiative decay mechanism for organic systems, thereby reducing the luminescence efficiency. Detailed studies of π-conjugated polymers over the past decades have already clarified some fundamental issues about the nature of the singlet excited states,[57–59] yet much

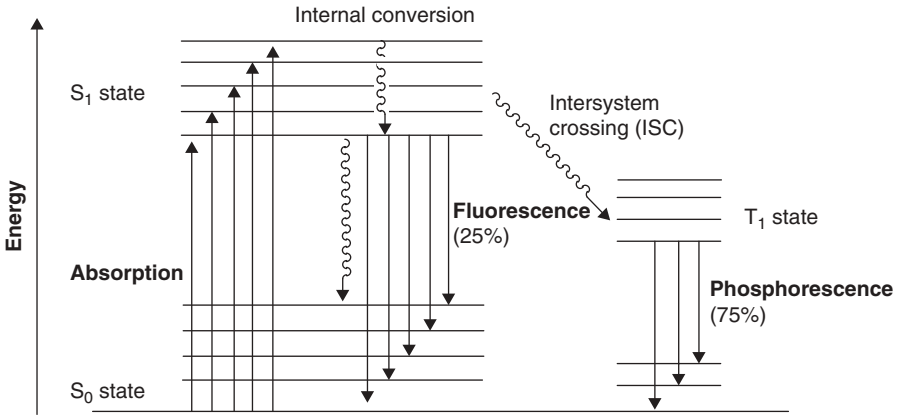

FIGURE 5. A typical Jablonski diagram for a PL system.

would still be expected about the nature of the corresponding triplet excited states.

Considerable work has shown that triplet states play an important role in optical and electrical processes within conjugated organic polymers with direct technological implications in electrooptics.[60–68] The ultimate efficiency of organic light-emitting diodes (OLEDs) is largely controlled by the fraction of triplet states generated or harvested, in which a ratio of 3:1 for the generation of nonemissive triplet to emissive singlet excitons would be anticipated according to the spin statistics.[69–73] While it is important to control the relative energy levels of the singlet and triplet excitons for the chemical tuning of singlet–triplet energy gap, a vast body of transition metal–containing polyynes have been extensively employed to explore the triplet excited states in conjugated polymers directly, in which the presence of heavy-metal centers can increase the spin-orbit coupling, thus partially enabling the spin-forbidden triplet emission.[53–55] This can also open up a versatile venture toward phosphorescence emission color tuning in these materials for meeting the target of full-color flat-panel displays and low-cost lighting sources.

In another context, researchers have paid a growing attention to the exploition of conjugated organic polymers and metallopolyynes in polymer solar cells.[74] Considerable effort has been made to optimize the spectral response of polymer photovoltaic cells by extending the absorption to longer wavelengths, since absorption of the active layer must cover the major part of the solar spectrum. Typically, in the design of low band gap polymer solar cells, a good control of the HOMO and LUMO levels of the polymer is crucial, and a lowering of the band gap (E_g) of the polymer is predicted to result in enhanced photovoltaic cell efficiency. However, the photovoltaic application of this type of material is usually hampered by their wide band gaps, and most of these platinum(II) polyynes compare unfavorably with those of some conjugated organic polymers with alternating electron donor (D) and acceptor (A) units (<1 eV).[75] New synthetic strategies for creating narrow band gap metallopolyynes would thus be desirable. A thorough consideration and a good compromise of the triplet photophysics and the associated band gap in the polymer are essential for affording highly active materials displaying tunable emission and photovoltaic properties.

A number of reports have shown that the nonradiative decay of the triplet states in a series of platinum-containing conjugated polyynes and their model complexes can be described by the energy gap law. In this context, the nonradiative decay rate from the triplet state increases exponentially with decreasing triplet–singlet energy gap, according to the expression $(k_{nr})_P \propto \exp(-A\Delta E_{S-T})$, where ΔE_{S-T} is the energy gap for the T_1-S_0 transition and A is a term controlled by the molecular parameters and vibrational mode.[56] There is always a trade-off between the band gap and the rate of phosphorescence emission in such metallopolymeric system. In other words, a high band gap polymer with a high triplet state energy will normally favor the observation of triplet emission,

whereas the low band gap congener will probably not be phosphorescent, even at low temperatures.

The optical and PL spectroscopies have been undertaken to understand the structure-property correlations of this important family of triplet-emitting polymers. The red shift in the absorption features upon coordination of the metal groups is consistent with there being an increase in conjugation length over the molecule through the metal center. The trade-off relationship between the phosphorescence parameters (such as emission wavelength, quantum yield, rates of radiative and nonradiative decay) and the optical gap will be formulated. For systems with third-row transition metal chromophores in which the ISC efficiency is close to 100%,[76–78] the phosphorescence radiative $(k_r)_P$ and nonradiative $(k_{nr})_P$ decay rates are related to the measured lifetime of triplet emission (τ_P) and the phosphorescence quantum yield (Φ_P) by equations 1 and 2:

$$(k_{nr})_P = (1 - \Phi_P)/\tau_P \tag{1}$$

$$(k_r)_P = \Phi_P/\tau_P \tag{2}$$

i. Effect of π-Conjugation and Interruption

With the phenylene ring as the spacer in **1**, the delocalization of electrons along the polymer chain will not be disrupted by the metal units because π-conjugation can be maintained between the orbitals of metal and ligands. Doubling the number of C≡C units on each side of the phenylene ring in **2** leads to a red shift in the phosphorescence wavelength with respect to **1** and **17**.[16,17] A similar shift of about 0.12 eV is also observed for **3** as we change from a single phenyl to a biphenyl moiety.[18] Rigid-rod Pt(II) acetylide polymers **4** and **5** show very different phosphorescence energies, depending on the number of acetylenic units.[19] The substitution of the acetylenic linkage in **5** with a phenylene group spacer reduces the extent of π-conjugation.

Synthetic derivatization to the oligothiophene system represents a good means of making sulfur-containing π-conjugated polymetallaynes. With increasing chain length of the thiophene segment from **28** to **30**, the optical gap and emission data are shifted to lower energy.[34] We attribute this to an increased delocalization of π-electrons along the polymer chain. However, this reduction in E_g tends to reach saturation up to three rings. The singlet peaks at 2.85, 2.44, and 2.28 eV for **28**–**30**, respectively, involve the mixed ligand–metal orbitals, dominated either by the intraligand HOMO–LUMO π–π* transition or charge-transfer type transition. The triplet emission peak at 2.05 eV in **28** increases in intensity strongly as the temperature is lowered. For **29**, there is a weak triplet emission shoulder centered at about 1.67 eV at room temperature, but it is totally absent for **30** over the measured range (1.2–3.0 eV). At 18 K, the triplet emissive bands become more clear at 2.05, 1.67, and 1.53 eV for **28**–**30**, respectively, and they all lie at 0.80–0.88 eV below the S_1 level. The

measured S_1-T_1 separations lie essentially constant at 0.75–0.80 eV (Fig. 6). The intensity of this triplet emission drops rapidly with an increase in the number of thienyl rings. This can be anticipated because the bigger ring size in the ligand reduces the influence of the heavy platinum effect. Also, in the oligothiophene systems, ISC is reduced with increasing number of thienyl rings, as the energy of the singlet excited state drops below the corresponding resonance state for ISC in those systems.[79] The energy of the triplet emission also experiences a bathochromic shift when the ligand contains more thiophene rings, suggesting that the triplet excited state should be extended over three or more thiophene rings. Such shift of the T_1 energy in **28**–**30** is consistent with the calculations by Beljonne and co-workers on the evolution of the triplet excitation energy in purely organic oligothiophene systems.[79,80]

For the Pt-acetylide polymer **32** with 2,5-diethynylpyridine moiety and its stable quaternized counterpart **33**,[37,38] quaternization of the pyridyl nitrogen leads to a strong red shift in the UV-VIS absorption spectrum and an increase in the emission quantum yield. There is also an improved π-electron delocalization along the backbone upon quaternization. Both of these are insulators in the undoped state. Upon doping with iodine vapor, they become semiconducting, and the conductivity of **33** (3.4×10^{-3} S cm^{-1}) was found to be higher than that for **32** (2.5×10^{-3} S cm^{-1}). The dependence of ISC and the spatial extent of singlet and triplet excited states in **1**, **28**, and **32** as a function of π-electron delocalization in the spacer group was examined.[38] From their optical absorption and PL data, conjugation is increased, but ISC rate is reduced by the electron-rich thiophene ring, whereas the opposite trend was observed for the electron-deficient pyridine group relative to the phenylene

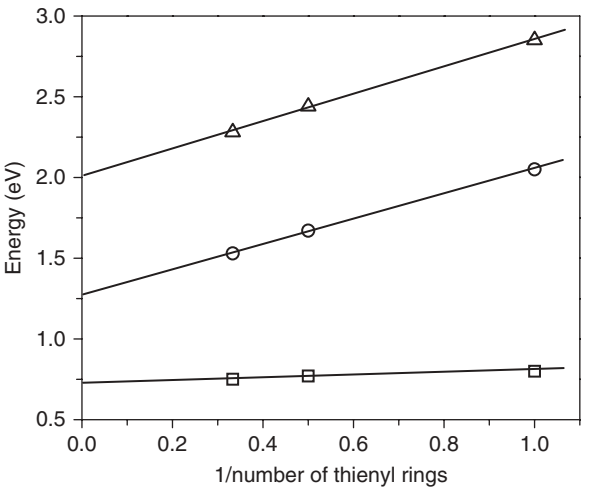

FIGURE 6. Energy versus chain length dependence of **28**–**30** for S_1-S_0 (Δ), T_1-S_0 (○) and S_1-T_1 (□) separations.

unit. The T_1 state remains strongly localized and the T_n state is strongly delocalized even more than the delocalized S_1 state. A series of oligopyridine-linked Pt(II) polyynes **34**–**37** can be compared to those for **32**.[39] For **34**, the inclusion of a second pyridine unit shifts the band gap to the red by 0.1 eV relative to **32**, while for **35**–**37**, the band gap experiences a blue shift of 0.3 eV compared to **32**. This agrees with the fact that polymer **34** with the alkynyl groups at the 5,5′-positions is fully conjugated, whereas in **35**–**37**, the alkynyl units at the 6,6′- or 6,6″-positions can hinder conjugation between the pyridine rings. Apparently, the phosphorescence spectra for **34**–**37** show some excimer formation at room temperature. There is no fluorescence band but only the phosphorescence band at 10 K for the kinked bipyridine and terpyridine-containing compounds **35** and **36**. The reduced conjugation in **35** and **36** shifts the triplet peak to the blue by 0.3 eV as compared to **34**. Polyynes **35** and **36** also constitute a novel class of materials with high-energy T_1 states giving reduced $(k_{nr})_P$.

With reference to the energy gap law, it is preferred to work on polymers with high-energy triplets to avoid competition with nonradiative decay. Various approaches have been successfully adopted to enhance the phosphorescence emission efficiency. The excited-state transitions can be tuned by localizing electron density in discrete regions of the molecule or by partially destroying ligand aromaticity. This approach is well manifested in the formation of polymer **16**, which contains the conjugation-breaking diphenylmethane chromophoric spacer.[22] The T_1 level can be effectively elevated by the CH_2 interrupter in the organic spacer to accommodate higher E_g. The sp^3-carbon site of the diphenylfluorene in **26** is an effective conjugation-interrupter to limit the conjugation length in metal polyynes, leading to materials with high E_g and high-energy T_1 states.[31] At 11 K, there is virtually no fluorescence band but only the phosphorescence band in **26**. The hindered conjugation in **26** shifts the T_1 state to the blue by 0.45 eV as compared to **3**. The order of ISC efficiency is $\mathbf{26} > \mathbf{3} \approx \mathbf{1}$. The heavy-atom effect of Pt can increase the $(k_r)_P$ value for the triplet emission by 4 orders of magnitude and incorporation of the diphenylfluorene group in metal polyynes with larger T_1-S_0 gaps can speed up $(k_r)_P$ with respect to **1**.

Apart from the (hetero)aromatic or carbon-rich spacer unit, recent work has also proliferated on the exploitation of some main group elements in the buildup of polymetallaynes. Such study represents a significant step forward in the development of triplet-emitting materials for OLEDs. Although sp^3-silicon unit is generally not as good as sp- or sp^2-carbon structural motif in facilitating electronic conjugation, inclusion of conjugation-interrupting silyl units can help in improving the phosphorescence properties of these conjugated compounds.[48] The degree of electronic conjugation roughly follows the order $\mathbf{5} \geq \mathbf{28} > \mathbf{1} > \mathbf{32} > \mathbf{52}$, indicating that acetylene and thiophene units are better electron transmitters. While the silyl moiety can interrupt electron movement, the energy of the S_1 state is the highest for **52**. These results, in conjunction with computational data, have facilitated and expedited the design of active phosphorescent polymers.[48] We

note a very high efficiency of triplet emission for **53**, and the order of S_1-T_1 crossover efficiency is **53** > **17**.[23]

As observed in Figure 7, the ratio of integrated intensities of phosphorescence to fluorescence is greater than unity for **53** but is less than unity for **17** at 290 K. In essence, the use of conjugation-interrupting silyl component in such metal polyynes can fine-tune the effective conjugation length and gives rise to efficient crossover between S_1 and T_1 states. The reduced conjugation in **52** shifts the phosphorescence to the blue by 0.06 and 0.38 eV, respectively, as compared to **1** and **28**. After the propitious results for the silyl-tethered systems, work was then focused on the metallopolyynes with heavier group 14 germanium element of even lower ionization energy (I.E.) (first I.E.: 791 versus 762 kJ mol^{-1} for Si and Ge, respectively). Pt(II) metallopolyynes **54**–**66** serve this purpose and can display very high $(k_r)_P$ values.[49,50] Inclusion of a conjugation-breaking sp^3-Ge linker into the organic bridge can limit the effective conjugation length and triggers the triplet light emission by taking advantage of the heavy-atom effect of Ge atoms. The triplet energy does not vary much with the oligomer chain length—that is, the lowest T_1 state is confined to a single repeat unit. Alternation of the R group will not affect this strong confinement. Insertion of conjugation hindered GeR_2 group in these polymers

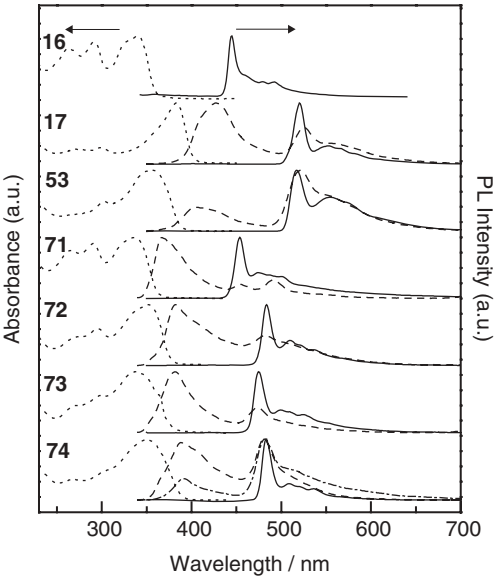

FIGURE 7. The absorption and PL spectra of **16**, **17**, **53**, and **71**–**74**. The absorption spectra are the higher energy *dotted lines* measured at 290 K. PL spectra were taken at both 290 (*dashed lines*, in CH_2Cl_2) and 20 K (*solid lines*, as thin films). For **74**, the PL spectrum (*dashed/dotted line*) as thin film at 290 K is also included.

shifts the phosphorescence bands to the blue relative to **19**. The measured Φ_P values are relatively insensitive to the oligomer chain length, but they notably change with the ER_2 group (E=Si, Ge). The $GeMe_2$ systems are about two times more phosphorescent than the $GePh_2$ congeners. However, substitution of $GePh_2$ by $SiPh_2$ reduces Φ_P by almost half ($\Phi_P \sim 10-13\%$ for the $SiPh_2$ assembly), which is likely caused by the heavy-atom effect of Ge in the former case. The $(k_r)_P$ values at 20 K are $(2.1-3.5) \times 10^5\ s^{-1}$ for **57**, **61**, and **65** and $(1.3-1.7) \times 10^5\ s^{-1}$ for **58**, **62**, and **66**. Relative to **19** ($(k_r)_P \sim 4.4 \times 10^4\ s^{-1}$), insertion of the germylene segment can significantly boost $(k_r)_P$ by ~ 10 times. It is encouraging that it is possible to get comparable orders of magnitude for $(k_{nr})_P$ and $(k_r)_P$. Hence heavy-atom derivatization using Pt and Ge atoms together with conjugation interruption by the latter can greatly increase $(k_r)_P$ values by ~ 5 orders of magnitude.[81] The high energy benzene stretching modes of Ph group can facilitate $(k_{nr})_P$ for **58**, **62**, and **66**, giving rise to smaller Φ_P and $(k_r)_P$ values than those observed in **57**, **61** and **65**.

Another system for circumventing the problem of the triplet state being nonemissive is to use polymers **71–74,** which contain some non-π-conjugated group 16 chalcogen units; the conjugation path is controlled by an insulating spacer, akin to the role played by the group 14 silylene unit in **53**.[52] These materials can also give an attractive combination of physical, optical, and mechanical properties, and the harvesting of organic triplet emissions harnessed through the heavy-atom effects of Pt can be accomplished. These metal-containing aryleneethynylenes spaced by chalcogen units were found to have large E_g values and high-energy T_1 states. The use of good conjugation-interrupting chalcogen units greatly boosts the phosphorescence decay, and one could readily observe room temperature phosphorescence for **71–74** (Fig. 7).

Comparable orders of magnitude for $(k_{nr})_P$ and $(k_r)_P$ can be obtained, which is rarely the case for the more π-conjugated polymetallaynes. The absorption energy of the oxygen-linked metal compound is the largest, whereas the sulfone-containing counterpart shows the lowest absorption energy. Relative to **3** (λ_{abs}=372 nm in CH_2Cl_2), it was shown that the non-π-conjugated chalcogen unit between the two phenyl rings hinders conjugation and causes a blue shift in the absorption wavelength (λ_{abs}=343–361 nm for **71–74**). At 20 K, there is almost no fluorescence band but only the prominent phosphorescence band from the central ligand chromophore. The emission maxima depend much on the nature of the chalcogenide ligand. With our long-term interest in rendering the observation of triplet emission under ambient conditions, this work certainly represents an important milestone toward our goal. Presumably due to the internal heavy-atom effect of the sulfone group, polyyne **74** shows the most intense phosphorescence band at 290 K within this series, and we can even observe very strong solid-state triplet emission for **74**, in which the ratio of integrated intensities of phosphorescence to fluorescence exceeds unity.

Figure 8 displays the energy level scheme for the lower-lying excitations for **16**, **53**, and **71–74**. All of them exhibit T_1-S_0 gaps of 2.5 eV or above,

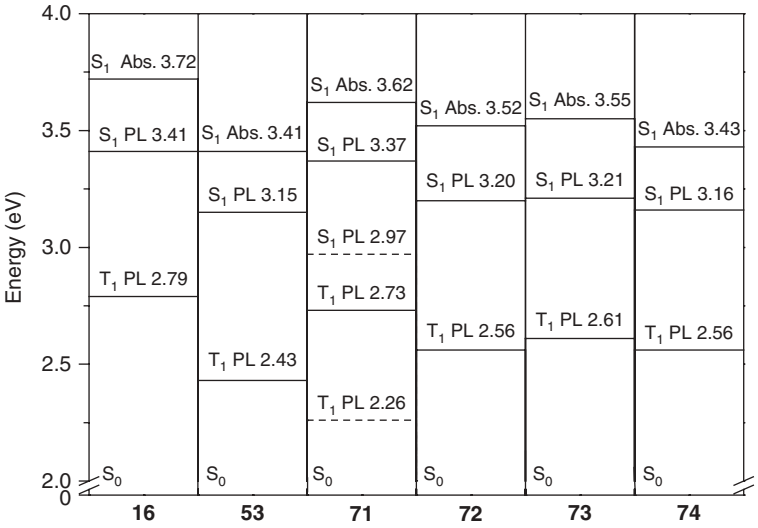

FIGURE 8. Electronic energy level diagram of Pt polyynes with group 14 and 16 main group elements based on absorption and PL data. *Dashed lines* represent the levels for **P3**. The S_0 levels are arbitrarily shown to be of equal energy, and all energy values are quoted in eV.

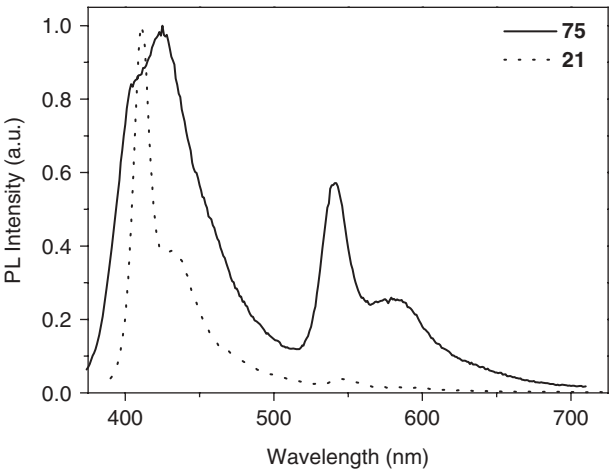

FIGURE 9. PL spectra for **21** and **75** in CH_2Cl_2 at 290 K.

which correspond to $S_1(PL)-S_0$ gaps of $\sim$ 3.13–3.57 eV. The measured S_1-T_1 gaps are constant at around 0.7 $\pm$ 0.1 eV, corresponding closely to the S_1-T_1 energy splittings estimated for some organic conjugated polymers.[82,83] The one with the diphenylether linkage has the highest T_1 state, which was shown to

TABLE 1. Optical and Photophysical Data for Platinum(II) Metallopolyynes

Polymer	E_g (eV)[a]	Energy states[b]	Φ_P (%)[c]	$(k_{nr})_P$ (10^4 s^{-1})[d]	$(k_r)_P$ (10^4 s^{-1})[e]	References
1	2.98	405 (S_1) 521 (T_1) [2.38]	30.0	1.4	0.6	15
2	2.60	569 (T_1) [2.17]				16,17
3	3.10	418 (S_1) 549 (T_1) [2.26]	23.9			18
4	2.88	475 (T_1) [2.61]				19
5	2.63	523 (T_1) [2.37]				19
6	2.80	443 (S_1) 633 (T_1) [1.96]				15
7	2.35	564 (S_1)				15
8		428 (S_1) 528 (T_1) [2.35]				20
9		435 (S_1) 551 (T_1) [2.25]				20
11		415 (S_1) 551 (T_1) [2.25]	20.0	7.1	0.18	20
12						20
13						20
14		539 (T_1) [2.30]				23
16	3.42	364 (S_1) 445 (T_1) [2.79]	51.5	20.5	21.7	22
17	3.05	402 (S_1) 520 (T_1) [2.38]				23
18	2.90	427 (S_1) 549 (T_1) [2.26]				24,25
19	2.92	416 (S_1) 554 (T_1) [2.24]	13.9	2.8	4.4	26
20	2.87	584 (T_1) [2.12]	1.54	1.2	1.9	27
21	2.92	428 (S_1) 551 (T_1) [2.25]				28
22	2.17	530 (S_1)				29
23	2.10	646 (S_1)				29
24	1.58	680 (S_1)[f]				30
25	2.10					25
26	3.38	458 (T_1) [2.71]	25.0	9.5	2.5	31
27	3.01	409 (S_1) 542 (T_1) [2.29]				32,33
28	2.80	435 (S_1) 605 (T_1) [2.05]	2.0	6.0	0.1	34
29	2.55	508 (S_1) 742 (T_1) [1.67]	~ 0	2.9	~ 0	34
30	2.40	544 (S_1) 810 (T_1) [1.53]	0.07	6.0	0.04	34

(*Continued*)

TABLE 1. (Continued)

Polymer	E_g (eV)[a]	Energy states[b]	Φ_P (%)[c]	$(k_{nr})_P$ (10^4 s^{-1})[d]	$(k_r)_P$ (10^4 s^{-1})[e]	References
31	2.35	539 (S_1)				36
32	3.00	387 (S_1)				37,38
		523 (T_1) [2.37]				
34	2.90	426 (S_1)				39
		569 (T_1) [2.18]				
35	3.30	463 (T_1) [2.68]				39
36	3.30	461 (T_1) [2.69]				39
38	2.60	470 (S_1)	1.0	3.0	0.03	40,41
		667 (T_1) [1.86]				
39	2.25	556 (S_1)	0.3	4.0	0.1	40,41
		747 (T_1) [1.66]				
40	2.20	577 (S_1)	0.02	5.6	0.1	40,41
		832 (T_1) [1.49]				
41	1.77	715 (S_1)[g]				42
42	2.67	460 (S_1)				43
		646 (T_1) [1.92]				
43	2.55	485 (S_1)				43
		691 (T_1) [1.79]				
44	3.10	403 (S_1)	5.9	12.0	4.8	26,44
		462 (T_1) [2.68]				
45	3.06	438 (S_1)	2.6	28.0	0.75	44
		497 (T_1) [2.49]				
46	3.22	462 (T_1) [2.68]				45
47	3.21	462 (T_1) [2.68]				45
48	3.23	462 (T_1) [2.68]				46
49	3.21	461 (T_1) [2.69]				46
50	3.23	461 (T_1) [2.69]				45
51	2.10	537 (S_1)[g]				47
52	3.70	419 (S_1)				48
		508 (T_1) [2.44]				
53	3.10	394 (S_1)				23
		512 (T_1) [2.42]				
54	2.95	414 (S_1)	35.0	23.6	12.7	50
		550 (T_1) [2.25]				
55	2.99	417 (S_1)	10.3	42.3	4.84	50
		550 (T_1) [2.25]				
56	2.98	414 (S1)	16.3			50
		549 (T_1) [2.26]				
57	3.05	412 (S_1)	45.0	43.0	35.0	49
		547 (T_1) [2.27]				
58	3.00	414 (S_1)	17.0	63.0	13.0	49
		548 (T_1) [2.26]				
59	3.00	417 (S_1)	12.3	29.1	4.06	51
		549 (T_1) [2.26]				

(*Continued*)

TABLE 1. (Continued)

Polymer	E_g (eV)[a]	Energy states[b]	Φ_P (%)[c]	$(k_{nr})_P$ (10^4 s^{-1})[d]	$(k_r)_P$ (10^4 s^{-1})[e]	References
60	2.97	413 (S_1) 548 (T_1) [2.26]	18.7			51
61	3.04	411 (S_1) 544 (T_1) [2.28]	43.0	27.0	21.0	49
62	3.00	411 (S_1) 545 (T_1) [2.27]	18.0	68.0	15.0	49
63	3.00	415 (S_1) 547 (T_1) [2.27]	13.5	15.3	2.39	50
64	2.98	413 (S_1) 547 (T_1) [2.27]	21.8			50
65	3.04	410 (S_1) 544 (T_1) [2.28]	45.0	39.0	32.0	49
66	3.00	411 (S_1) 545 (T_1) [2.27]	20.0	69.0	17.0	49
67	3.20	459 (T_1) [2.70]	15.8	6.5	34.6	51
68	3.21	460 (T_1) [2.70]	2.08	0.37	17.3	51
69	3.20	460 (T_1) [2.70]	22.6	2.74	9.41	51
70	3.22	459 (T_1) [2.70]	11.0	3.54	28.6	51
71	3.40	454 (T_1) [2.73]	45.8	8.5	7.18	52
72	3.26	484 (T_1) [2.56]	48.6	8,5	8.08	52
73	3.28	475 (T_1) [2.61]	51.3	6.7	7.06	52
74	3.18	484 (T_1) [2.56]	46.3	6.3	5.41	52
75	3.05					32,33

[a] Optical band gap as estimated from the onset wavelength of solid-state absorption spectrum.
[b] As thin film at 11–20 K or in frozen CH_2Cl_2 at 77 K; the lowest triplet states (T_1) in eV are shown in parentheses.
[c] Phosphorescence quantum yield relative to **P1** (Φ_P=30%).
[d] Nonradiative decay rate constant for phosphorescence.
[e] Radiative decay rate constant for phosphorescence.
[f] As thin film at 290 K.
[g] In CH_2Cl_2 at 290 K.

exceed that of the sulfide analogue, owing to the higher degree of conjugation for the more polarizable S over O atoms. These findings are in agreement with some simple organic aromatic molecules ArEAr (Ar = aryl, E = S, SO, SO_2).[84] Hindered conjugation by using different group 16 element-derived units shifts the phosphorescence to the blue as compared to **3**; the largest blue shift is encountered for **7**1 (0.48 eV). But Φ_P does not vary much with the type of E groups. It can be seen that the values for $(k_{nr})_P$ are comparable to those for $(k_r)_P$ for **71**–**74**. Incorporation of the group 16 conjugation interruptors in the Pt polyyne systems results in $(k_r)_P$ values of (5.4–8.1) $\times$ 10^4 s^{-1}, which are more efficient relative to **19** by $\sim$ 1 order of magnitude.

By changing from a *trans*- to a *cis*-configured Pt(II) unit (i.e., from **21** to **75**), the conjugation chain in **75** is disturbed (λ_{max}=364 nm for **75** versus 391 nm for **21**), resulting in a much stronger triplet emission at room temperature (Fig. 9).[32,33] However, the solubility of **75** notably decreases relative to **21**, resulting in a lower molecular weight for the soluble fraction of the polymer.

ii. Effect of Fused Ring

Based on the results for Pt(II) polyynes containing naphthalene and anthracene condensed carbocyclic systems **6** and **7**, the use of fused-ring spacers is an effective strategy to produce low band gap conjugated polymers.[15] The electron-rich naphthalene and anthracene rings create strong intramolecular interactions between the Pt(II) units and conjugated organic groups along the rigid polyyne backbone. The E_g values decrease as the size of the aromatic spacer increases, in line with there being greater π-delocalization within the anthryl group relative to the phenylene spacer. For compounds that contain an anthracene unit, there is no evidence of observing any phosphorescence in thin films.

The work has also been extended to the platinum polyynes and diynes with thienothiophene and dithienothiophene entities.[85] The design rationale lies in the fact that the self-rigidification of these cores, due to the fused ring system, and the delocalized π-systems extending over the fused rings confer them novel optoelectronic properties. The band gap is related more to the conjugation length through the oligothiophene system than to whether the thiophene is fused or not.

The effect of aggregation or interchain interaction on the triplet excited state in Pt-acetylide polymers was investigated by comparing the optical properties of **1** with the pentiptycene-bridged polymer **15**.[21] The interchain interaction is prevented by the sterically demanding pentiptycene moiety in **15**, and its photophysics is being dominated by the intrachain triplet exciton.

iii. Effect of Ring Substitution

Fluorene derivatives have been extensively explored for various functional properties in various domains of optoelectronic and photonic applications,[86–92] and a series of 2,7-fluorene-based polyplatinynes **18**–**25** have also been investigated. By changing the substituents at C-9 position of fluorene ring, the optoelectronic properties of these metal-containing polymers can be chemically modified. These materials can display a variety of colors and E_g values in the solid state (Table 1). Hence the energy of the S_1 state varies significantly with the fluorene structure and is highest for **18** and its alkylated derivatives **19** and **21**. The inductive influence of strongly electron-withdrawing moieties will lower the S_1 state to a significant extent (vide infra). The butyl side chains on the Pt atoms also help decrease aggregation effects.

Among the heterocyclic derivatives, carbazole ring has emerged as a vital building block in the synthesis of many useful optoelectronic materials.[93–96]

We have recently widened our scope to form a new series of platinum arylacetylide polymers **44**–**50** containing carbazolyl functional groups. These represent remarkable model systems to evaluate how the carbazole rings would limit the effective conjugation length of polymetallaynes. It was shown that the S_1 state extends over more than a repeat unit, while the T_1 state remains localized to less than one repeat unit. The band gaps measured are 3.06–3.23 eV. It was found that the employment of carbazole unit leads to high-energy triplet states and presents a good approach in enhancing the ISC rate.[26] We were able to tune the molecular functional properties such as absorption and photoluminescence by changing the length of the acetylenic chain between the metal and the central spacer group as observed in **44** and **45**.[44] Upon increasing the C≡C chain length (*m*) from one to two (i.e. **19** versus **20** and **44** versus **45**), the following trends can be observed: (1) the energy of the S_1 excited state reduces, (2) the energy of triplet emission decreases rapidly (i.e., there is a red shift in the emission energy), (3) the S_1-T_1 energy gap remains constant at 0.7 $\pm$ 0.1 eV, (4) in accordance with the energy gap law for nonradiative decay, the phosphorescence emission efficiency is significantly reduced with decreasing triplet state energy as a result of increasing nonradiative recombination sites. The dependence of E_g as a function of the acetylenic chain length in such Pt system was well probed by both optical spectroscopy and computational calculations in which an inverse square law was established (Fig. 10), and the results are similar to those found for linear oligomers of polyene, poly(paraphenylene)s, and poly(paraphenylenevinylene)s.[27]

iv. Effect of Donor-Acceptor Interaction

A new family of Pt(II) polyyne polymers functionalized with substituted 1,4-diethynylbenzene derivatives **8**–**14** were synthesized and optically characterized by absorption and PL studies.[20] In regard to the emission properties, it is interesting to see that the relative intensity of triplet emission increases strongly with the electronegative fluorine content in such system.

Relative to **18**, the lowest energy absorption peak in **24** with two strong electron-accepting cyano groups exhibits an exceptionally large red shift, showing the importance of donor-acceptor (D-A) interaction in this class of polymetallaynes,[30] typical of those reported in the literature for the production of low band gap organic congeners.[97] The estimated E_g value of **24** is 1.58 eV, which is the lowest among any of the polyplatinynes known to date and represents a new avenue toward the development of low band gap materials. It is clear that electron-withdrawing substituents at the periphery exert a more significant electronic effect on narrowing the band gaps of these polymers than electron-donating groups. The presence of significant D-A interaction also results in a low E_g at 2.10 eV for a mixed-metal polymer of ferrocenylfluorene **25** (versus 2.90 eV for **18**).[25]

By virtue of the electron-donating and electron-accepting features of the thiazole ring (generally regarded as a hybrid of the thiophene and pyridine groups) as compared to the thienyl analogue, a luminescent bithiazole-bridged

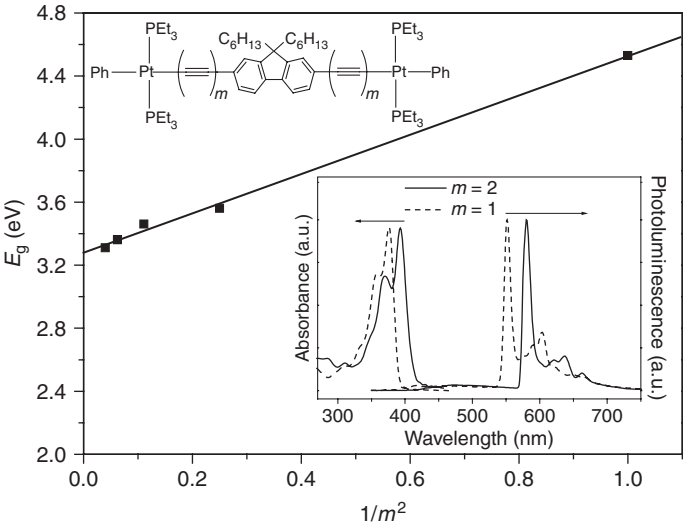

FIGURE 10. A plot of E_g against $1/m^2$ for complexes with different acetylenic chain length.

polyyne **31** was also made.[36] For **31**, the absorption peaks show a significant spectral red shift as compared to **29**, due to the electron-withdrawing effect of the imine nitrogen atoms. No phosphorescence band was, however, detected for **31**, even at low temperatures in the experimental spectral range.

A range of Pt polyynes **38**–**40** functionalized with quinoline, quinoxaline and benzothiadiazole units have been reported, which provide an excellent system to study the evolution of the singlet and triplet excited states with electronegativity of the spacer groups.[40] The absorption spectra of **38**–**40** reveal substantial D-A interaction between the platinum center and the conjugated spacer. Both the singlet and triplet emissions as well as the absorption bands decrease in energy with increasing electronegativity of the ligands along the series from **38** to **40**. In other words, the more electron-withdrawing the spacer unit is, the lower is the E_g value between the S_0 and S_1 excited states. The triplet excited state properties of **1**, **11** and **38**–**40** were examined as a function of optical gaps by means of optical steady-state and time resolved spectroscopy. The S_1-T_1 energy gap is, however, independent of the spacer, such that the T_1 state is typically 0.7 ± 0.1 eV below the S_1 state.[41] With decreasing optical gap, the lifetimes and intensities of phosphorescence are dramatically reduced, and the $(k_{nr})_P$ value increases exponentially with decreasing T_1-S_0 gap. The soluble blue polymer containing the thieno[3,4-b]pyrazine spacer **41** was similarly designed by using the concept of alternating D and A units.[42] Polymer **41** shows a low band gap of 1.77 eV, attributable to the push-pull interaction between the electron-donating metal acetylene group and the electron-withdrawing thieno[3,4-b]pyrazine unit.

Two interesting Pt(II) polyynes that possess mixed heterocyclic groups consisting of both thienyl and pyridyl rings **42** and **43** were also reported.[43] The E_g values for **42** and **43** are 2.67 and 2.55 eV, respectively, which can be compared to the gaps of 2.55 and 2.40 eV for **29** and **30**, and the corresponding blue shifts of 0.12 and 0.15 eV are consistent with a reduction in the D-A interaction between the metal and ligand.

A soluble silole-containing polyplatinayne **51** was prepared.[47] As compared to 2,5-dibromo-1,1-diethylsilole (λ_{max} = 326 nm), the positions of the low-lying shoulder bands (λ_{max} = 504 nm in CH_2Cl_2) are remarkably red-shifted by $\sim$178 nm for **51** after the inclusion of heavy-metal chromophores. This is possibly due to the intramolecular D-A interaction between the electron-rich metal ethynyl unit and the electron-poor silole ring. The E_g value is impressive at 2.10 eV for **51**, and it is significantly lowered by $\sim$ 1.0 eV relative to **53** (3.10 eV).[48] Compound **51** is photoluminescent with the singlet emission band at 537 nm. No room temperature emission from the T_1 state was detected over the measured spectral window.

v. Effect of Temperature

Variation of temperature has a great effect on the phosphorescence emission intensity of a metallopolyyne. As the temperature is cooled down from 290 K to 11 K, we detect virtually no fluorescence band but only the organic-based phosphorescence band at the lower-lying spectral regime in the majority of cases, especially for those with high-energy T_1 states. Interpretation of the emission assignment can be made in terms of the observed temperature dependence of the PL data, typical of earlier work on platinum(II) polyynes.[53,54] Representative examples of the temperature dependencies of the PL spectra for **47** and **53** are displayed in Figures 11 and 12. With decreasing temperature, the triplet emission band increases in intensity, which is characterized by a well-resolved vibronic structure with most weight in the 0-0 vibrational peak. We consider that the strong dependence of the triplet exciton arises from the fact that it is a long-lived triplet excited state and as such is more sensitive to thermally activated nonradiative decay mechanisms. This increase in nonradiative decay with temperature can be attributed to thermally activated diffusion of triplet excitons along the polymer chain, which can lead to triplet-triplet annihilation or an increased sampling of dissociation sites or nonradiative sites.

B. Phosphorescence Color Tuning of Metallopolyynes

The results of optical investigations showed that the HOMO, LUMO, and energy gap of polyplatinynes can easily be modified or tuned by the use of various central aryl cores that include carbocyclic, heterocyclic, and inorganic main group chromophores showing various extents of π-conjugation. Practically, we are able to tune the triplet emission wavelength of the polyyne from blue to red by simply changing the structure of the spacer, even though these emissions were observed only at low temperatures in a variety of cases.

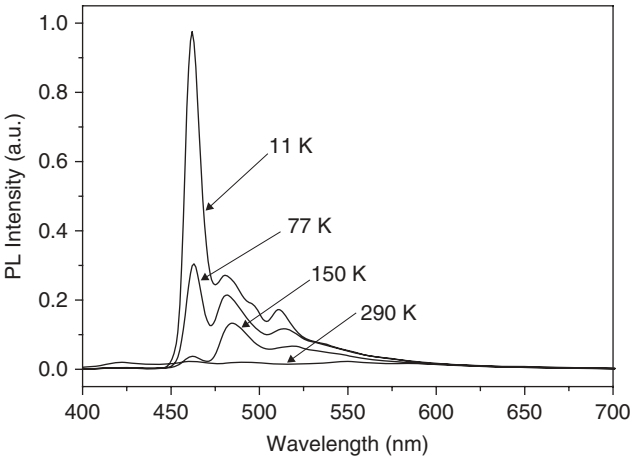

FIGURE 11. Temperature dependence of the PL spectra of **47**.

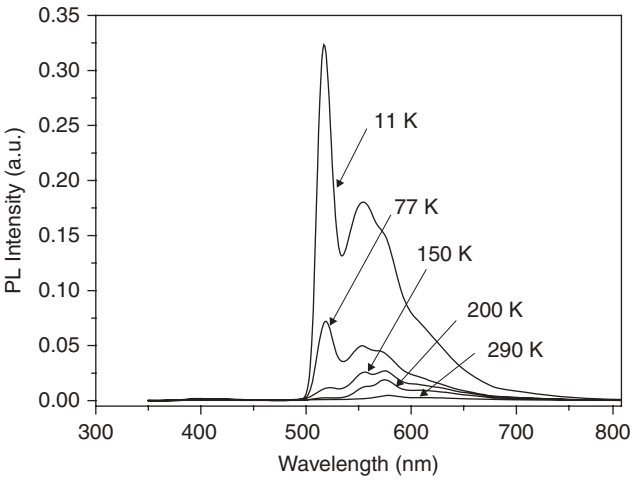

FIGURE 12. Temperature dependence of the PL spectra of **53**.

As a result, their emission bands in the solution or frozen state can cover the full UV-VIS spectrum from 462 to 832 nm. The large Stokes shifts of these triplet emissive peaks from the dipole-allowed absorptions, together with their long emission lifetimes in the microsecond range at 77 K, indicate their triplet parentage, and they can thus be ascribed to the $^3(\pi\pi^*)$ excited states of the metalated conjugated units. By a judicious choice of the ligand structure, we can fine-tune the phosphorescence wavelength effectively to fulfil the requirements (Fig.13). On the other hand, the optical band gaps can vary over a wide range of 1.58−3.70 eV in the group of polymetallaynes reported, and

accordingly, the triplet energy levels are tunable from 1.49 to 2.68 eV, essentially spanning the whole visible spectrum and even extending to the near-IR regime. Therefore, this kind of organometallic polyyne may serve as a good emitter in displays due to the potential of achieving full-color emission spectrum through modification of the electronic structure of the conjugated ligand segment.

C. Roles of Metallopolyynes in Optoelectronic and Photonic Devices

Owing to the intrinsic optical and photophysical features discussed for metallopolyynes, it is expected that they have great potential as active materials in optical and photonic devices. Over the years, numerous studies have shown that these metallopolymers can be exploited for a collection of electronic and optoelectronic applications.

i. Light-Emitting Devices

A seminal paper on the spin-dependent exciton formation in the platinum polyyne **39** was reported to realize the key role of this class of organometallic polyyne materials in practical OLEDs. Electrophosphorescence from the triplet state can be observed in an OLED structure of ITO/PEDOT-PSS/39/Ca:Al (Fig. 14, PEDOT=poly(3,4-ethylenedioxythiophene; PSS=poly(styrenesulphonate)).[61] The average singlet generation fraction of 57 ± 4% for **39** was determined, suggesting that a spin-dependent process, favoring singlet formation, predominates in the

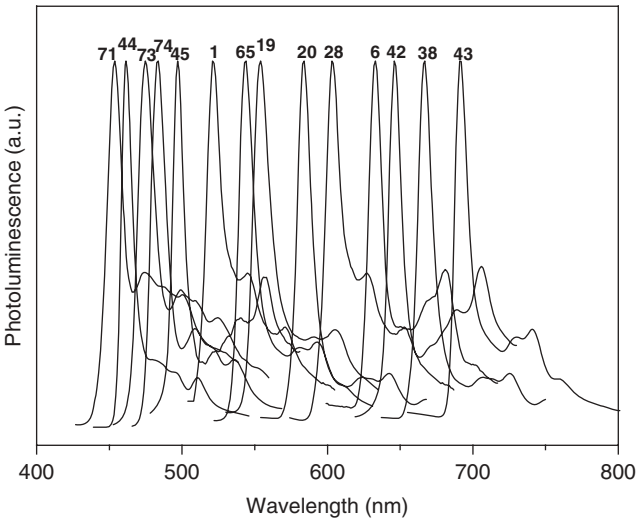

FIGURE 13. Phosphorescent emission color tunability observed in polyplatinyes.

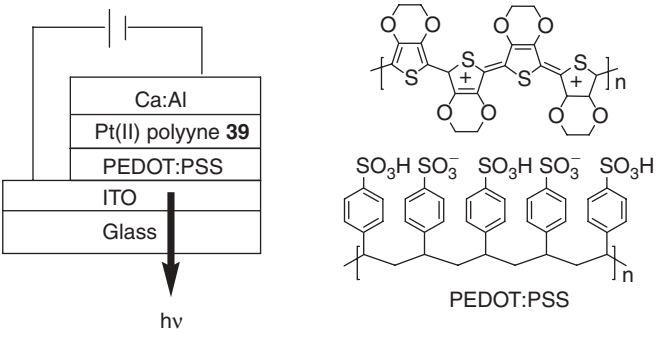

FIGURE 14. Polymer-based OLED structure based on **39**.

polymer film. The value is more than double the value expected from simple spin statistics and is above the lower limit for the singlet generation fraction of 35−50% measured for poly(*p*-phenylenevinylene) (PPV) derivatives. The results demonstrate that singlets are favored over triplets. The value for the corresponding diplatinum model complex is $\sim$ 22 $\pm$ 1%, which is close to 25% expected from simple spin statistics and in agreement with the value of 22 $\pm$ 3% measured for tris(8-hydroxyquinolinato)aluminium. This implies that recombination of holes and electrons is spin independent.

ii. Photovoltaic Cells

Bulk heterojunction solar cells have been extensively studied due to their great potential for cost-effective photovoltaic devices as an alternative for renewable energy sources. Although recent advances are largely based on conjugated organic polymers, one possible approach that has not been commonly explored involves the use of robust organometallic polymers. Although organometallic donor materials are commonly used in small-molecule solar cells,[98,99] soluble π-conjugated organometallic polyyne polymers have rarely been used in polymer solar cells.[100−104] Previous literature data indicated that the maximum photocurrent quantum efficiencies (PCQE) in single-layer neat platinum polyyne cells were $\sim$ 0.04−1%,[42,101] while quantum efficiencies of $\sim$ 1−2% could be achieved for these cells with the addition of 7 wt.% of C_{60}.[101]

It was also shown that **28**−**30** are good photoconductors in suitably fabricated single-layer configurations (Fig. 15a).[34] The photocurrent spectra of the Au/**28**/Al, ITO/**29**/Al and ITO/**30**/Al photocells show two peaks, one at the onset of absorption [2.92 (**28**), 2.64 (**29**), and 2.43 eV (**30**)] and one at higher energies [3.81 (**28**), 3.56 (**29**), and 3.38 eV (**30**)]. The second photocurrent peaks were probably due to absorption into the higher-lying absorption bands. Polymers **28**−**30** show a short-circuit quantum efficiency of $\sim$ 0.04% at the first photocurrent peak, which is a common value for single-layer devices. We observe no great difference in PCQE with variation of the

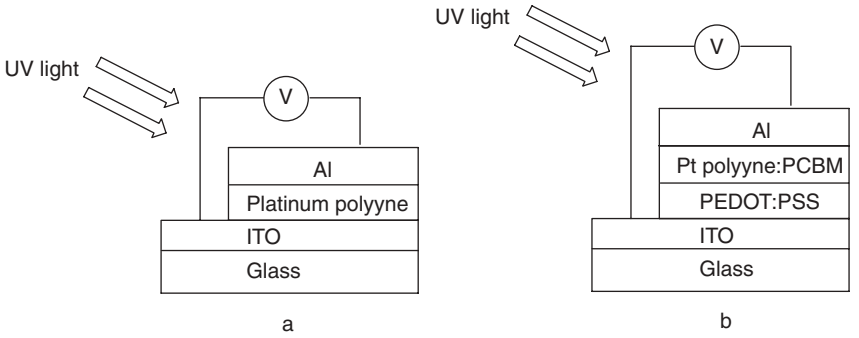

FIGURE 15. A platinum(II) polyyne-based photocell in (a) single-layer and (b) bulk heterojunction structures.

thiophene content in these Pt-containing polymers. The quantum efficiency of the second peak is different among **28**–**30** and is very sensitive to air.[102] The overall photocurrent increases when exposed to air and is reduced after annealing under vacuum. The *I-V* characteristics at the first peak in the spectral response show open-circuit voltages of 0.50, 0.75, and 0.47 V and fill-factors of 0.32, 0.35, and 0.30 for **28**–**30**, respectively. More recently, an external quantum efficiency of $\sim$ 9% has been achieved in bulk heterojunction cells using the **28**:PCBM composite (PCBM=[6,6]-phenyl C_{61}-butyric acid methyl ester), resulting in a power conversion efficiency of 0.27%.[104] The polymer absorbed only in the blue-violet spectral region with a maximum efficiency at 400 nm, and consequently the efficiency was low due to low coverage of the solar spectrum, although the charge separation was shown to occur via triplet state of the polymer. Although **41** does not show phosphorescence in the visible region, it can show an unusually high PCQE of up to 1% at 400 nm for single-layer photovoltaic cells in air. A photocell in a single-layer structure of ITO/**53**/Al was also fabricated with 0.01% efficiency,[23] a typical value for single-layer devices that is also comparable to that for the ITO/**1**/Al cell.[103] The photocurrent was found to increase with an increase in bias voltage. Similar to **1**, the excited states are mostly strongly bound triplet excitons in such Pt polyyne upon photoexcitation, and these are confined to one monomer unit.

The photoconductive properties of the fluorene-derived polymers **19**, **23**, and **24** were studied by the single-layer photocells in the configuration of ITO/Pt polyyne/Al. These polymers show moderate photoconductivity. A PCQE of $\sim$0.01% was estimated in these cases, which does not vary much with variation of the central fluorene ring.[26,30] Likewise, polymer **44** was also shown to be a photoconducting material in a similar architecture with a PCQE of $\sim$ 0.01% in the forward bias mode.

The very recent breakthrough in this area focused on the fabrication of highly efficient organometallic photovoltaic cells based on **76**.[105] The bulk

heterojunction cells (Fig. 15b) consisting of this strongly absorbing donor-acceptor metallopolyyne and [6,6]-phenyl C_{61}-butyric acid methyl ester (PCBM) exhibit substantial photovoltaic responses, which outperform the majority of solar cells made from the state-of-the-art organic polymers and can compete with the best reported efficiencies of fully optimized devices based on poly(3-hexylthiophene) (P3HT).[106] A lower band gap contributes to a wide solar spectral coverage, so that highly efficient polymer solar cells based on a bulk heterojunction of **76** and PCBM could be obtained, which showed an average power-conversion efficiency of 4.1%, even without annealing or the use of spacer layers needed to achieve comparable efficiency with P3HT. From the spectroscopic ellipsometry measurements, the extinction coefficient of **76**:PCBM blend was shown to be higher above 550 nm, leading to improved absorption of the incident solar radiation. The **76**:PCBM blends exhibit balanced charge transport, as required for efficient solar cell performance. We anticipate that this new strategy represents a novel prototype for cheap, large-area cells.

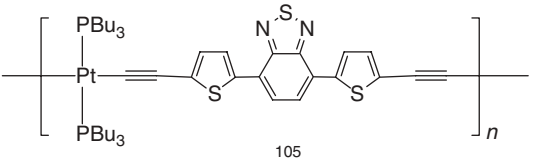

76 [105]

iii. Optical Power Limiters

In the era of laser technology used in many electronic devices and instruments, lasers are well known to be effective threats against optical sensors. To tackle this problem, research on sensor protection devices through optical power limiting is steadily progressing. Optical power limiters (OPL) are devices that strongly attenuate optical beams at high intensities while exhibiting higher transmittance at low intensities.[107] Such devices are useful for the protection of human eye and other delicate optical sensors from intense laser beams. At present, materials practically employed for optical limiting are largely small molecules[108–111] but the optical limiting properties of metal-containing polyyne polymers are less explored. Many of the dyes exhibiting nonlinear absorbing properties, such as porphyrins and fullerenes, are strongly colored; consequently these dyes have obvious limitations for use as sensor protection within the visible wavelength region. Platinum(II) acetylides, on the other hand, are only slightly colored and well known to possess strong excited state absorption, giving rise to efficient nonlinear absorbing properties.

A series of solution-processible and tractable polymetallaynes of Pt and their mixed-metal analogues were demonstrated to be excellent OPL materials to nanosecond laser pulses at 532 nm, with optimized optical transparency/nonlinearity trade-offs. The optical-limiting behavior of selected platinum(II) polyynes was investigated by the Z-scan technique. Polyynes **19**, **21**, **22**, **27**, **29**,

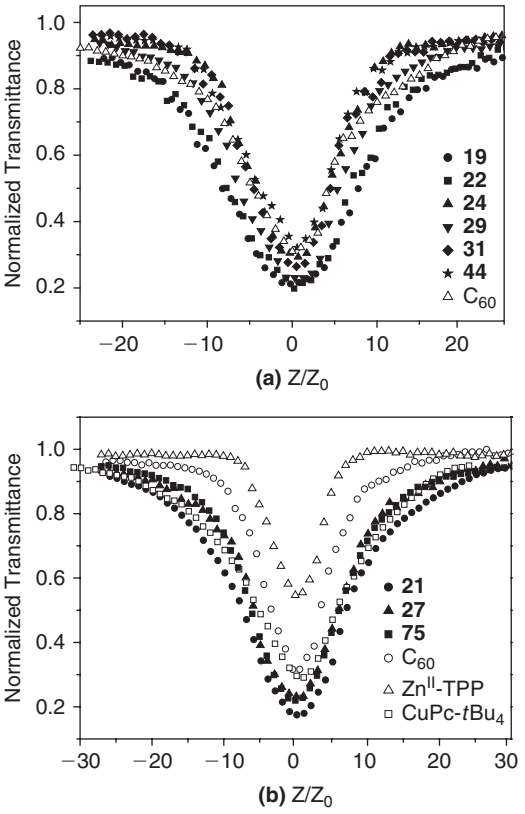

FIGURE 16. The open aperture Z-scan results for (a) **19**, **22**, **24**, **29**, **31**, **44**, and C_{60} solutions at the same linear transmittance of 82% and (b) **21**, **27**, **75**, and some benckmark OPL materials.

31, and **44** have OPL performance comparable or superior to those of the state-of-the-art reverse saturable absorption dyes, such as fullerene C_{60} and metallophthalocyanine dyes (Fig. 16). To improve the transparency window of **21** further for developing OPL materials for human eye protection, it is necessary to get rid of the dragged absorption tail behind 400 nm by reducing the π-conjugation. In this context, introduction of a Hg unit into the Pt polyyne will endow better transparency to the material and offer nearly no impairment to the OPL properties of the parent polymer (Fig. 17).[32,33] Copolymers with a Hg ion in the polyyne backbone will shorten the conjugation length of the chromophore, resulting in a higher energy triplet state accompanied by an increase in Φ_P, in accordance with the energy gap law.[56] This is also partly indicated by the lower fluorescence quantum yield of **27** compared with that of **21**. Pertaining to the reverse saturable absorption mechanism, the contribution of increased Φ_P of **27** to OPL can compensate for

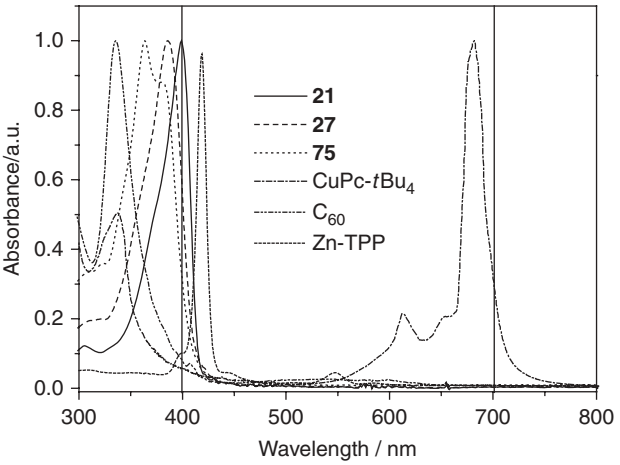

FIGURE 17. Transparency region for selected platinum polyynes and some benchmark optical limiters (Cu-Pc-tBu$_4$=Cu^{II}-tetrakis(*tert*-butyl)phthalocyanine; Zn-TPP=Zn^{II}-tetrakis(4-phenyl)porphyrin).

the loss in OPL due to interruption of conjugation by Hg, and hence **27** still shows comparable OPL to that of **21**. In addition, **27** has an improved transparency window for optimizing the properties of OPL materials of this kind (λ_{max} = 386 nm for **27** versus 399 nm for **21**) (Fig. 17). Using a similar conjugation-breaking strategy to increase Φ_P upon switching the metal geometry from the *trans*- to the *cis*-configured Pt(II) unit in **75**,[32,33] the conjugation chain is markedly disturbed (λ_{max} = 364 nm for **75**). Remarkably, **75** shows almost the same OPL as that of **21** (Fig. 16b), indicating that the negative effect caused by conjugation-interruption to OPL can be retrieved effectively by the positive contribution of increased Φ_P. This was supported by the much stronger triplet emission at 298 K (Fig. 9) and much lower fluorescence quantum yield for **75** compared to that of **21**. So a suitable molecular engineering of the $PtP_2(C{\equiv}CAr)_2$ geometry can help in solving the critical optical nonlinearity/transparency trade-off problem.

The optical-limiting thresholds for these polymetallaynes range from 0.06 to 0.13 J/cm^2. The light energy transmitted starts to deviate from Beer's law with increasing input light fluence, and the polymer solution becomes increasingly less transparent as the fluence rises. So the transmittances of the samples are found to decrease as the laser fluence increases, characteristic of optical limiting. To investigate the effect of heavy metal on the optical-limiting action of poly(aryleneethynylene)s, the purely organic polyyne polymer was prepared, and the optical-limiting behavior was also studied.[29] The organic polyynes have OPL responses weaker than those of the corresponding organometallic congeners. Thus the OPL of the organic polyyne can be enhanced by metal ion addition.

IV. SUMMARY

In conclusion, platinum(II)-containing metallopolyynes represent an interesting class of phosphorescent materials. These metal-based macromolecular materials have been recognized for their exciting optical and photophysical properties. We can study the evolution of singlet and triplet excited states with the chemical and electronic structures of the polymer by using a range of functionalized spacers in the main chain. The relationship between triplet energy and the rate of nonradiative decay can be shown to follow the energy gap law. Impressive progress in phosphorescent polymetallaynes was spurred by the search for new materials with high-energy triplet levels to avoid competition with nonradiative decay pathways and recent attempts to harvest room-temperature triplet-state energy were fruitful.

In such research platform, the successes obtained in the synthetic tailoring of the phosphorescence color emission of this class of polymetallaynes demonstrate the significance of these polymeric materials as triplet emitters in light-emitting applications and as semiconductors in organometallic photovoltaics. The in-depth exploration of using these metallized compounds as semiconducting and optical limiting materials in the fabrication of photovoltaic cells and sensor protectors is also worthy of serious investigation. The performance of these polymeric materials in such roles is generally governed by their excited-state properties and optical band gaps. There exists different approaches for the phosphorescence color tuning and addressing the emission efficiency/band gap trade-off problem. Current activity in this exciting area will focus on the development of new narrow-band gap Pt polyynes, but new materials showing intense room-temperature phosphorescence are still in a great demand. There are pros and cons on the use of conjugated versus nonconjugated spacers in these metal polyyne systems. Lower bandgaps are generally attained at the expense of other important properties (e.g., excited-state lifetime and phosphorescence intensity). This trade-off issue must be considered before further predictions can be made about the real practical applications. The optical and photophysical properties of these materials will likely act as a benchmark for future optoelectronically-active polymer design. Similar materials of the form $[-MC{\equiv}CRC{\equiv}C-]_n$ (M = Au, Hg) for group 11 and 12 metals[112–116] should provide another scope for their experimental and theoretical investigations in optoelectronic applications.

V. ACKNOWLEDGMENTS

Financial support from the Research Grants Council of the Hong Kong SAR (Grant no. HKBU202709) and the Hong Kong Baptist University (FRG2/08-09/111) is gratefully acknowledged. The author is also indebted to his postgraduate students, postdoctoral associates and collaborators whose names appear in the references.

VI. REFERENCES

1. I. Manners, *Synthetic Metal-Containing Polymers,* Wiley, Weinheim, Germany, 2004.
2. P. Nguyen, P. Gómez-Elipe, I. Manners, *Chem. Rev.,* **99,** *1515* (1999).
3. I. Manners, *Angew. Chem. Int. Ed. Engl.,* **35,** *1602* (1996).
4. A. S. Abd-El-Aziz, *Macromol. Rapid Commun.,* **23,** *995* (2002).
5. V. W.-W. Yam, *J. Organomet. Chem.,* **689,** *1393* (2004).
6. N. J. Long, C. K. Williams, *Angew. Chem. Int. Ed,* **42,** *2586* (2003).
7. Y. Fujikura, K. Sonogashira, N. Hagihara, *Chem. Lett., 1067* (1975).
8. K. Sonogashira, S. Takahashi, N. Hagihara, *Macromolecules,* **10,** *879* (1977).
9. S. Takahashi, M. Kariya, T. Yatake, K. Sonogashira, N. Hagihara, *Macromolecules,* **11,** *1063* (1978).
10. K. Sonogashira, S. Kataoka, S. Takahashi, N. Hagihara, *J. Organomet. Chem.,* **160,** *319* (1978).
11. S. J. Davies, B. F. G. Johnson, M. S. Khan, J. Lewis, *J. Chem. Soc. Chem. Commun.,* **187 (**1991).
12. Z. Atherton, C. W. Faulkner, S. L. Ingham, A. K. Kakkar, M. S. Khan, J. Lewis, N. J. Long, P. R. Raithby, *J. Organomet. Chem.,* **462,** *265* (1993).
13. B. F. G. Johnson, A. K. Kakkar, M. S. Khan, J. Lewis, *J. Organomet. Chem.,* **409,** *C12* (1991).
14. S. J. Davies, B. F. G. Johnson, J. Lewis, P. R. Raithby, *J. Organomet. Chem.,* **414,** *C51* (1991)
15. M. S. Khan, M. R. A. Al-Mandhary, M. K. Al-Suti, F. R. Al-Battashi, S. Al-Saadi, B. Ahrens, J. K. Bjernemose, M. F. Mahon, P. R. Raithby, M. Younus, N. Chawdhury, A. Köhler, E. A. Marseglia, E. Tedesco, N. Feeder, S. J. Teat, *Dalton Trans., 2377* (2004).
16. R. D. Markwell, I. S. Butler, A. K. Kakkar, M. S. Khan, Z. H. Al-Zakwani, J. Lewis, *Organometallics,* **15,** *2331* (1996).
17. J. Lewis, M. S. Khan, B. F. G. Johnson, T. B. Marder, H. B. Fyfe, F. Wittmann, R. H. Friend, A. E. Dray, *J. Organomet. Chem.,* **425,** *165* (1992).
18. L. Liu, S.-Y. Poon, W.-Y. Wong, *J. Organomet. Chem.,* **690,** *5036* (2005).
19. B. F. G. Johnson, A. K. Kakkar, M. S. Khan, J. Lewis, A. E. Dray, R. H. Friend, F. Wittmann, *J. Mater. Chem.,* **1,** *485* (1991).
20. M. S. Khan, M. R. A. Al-Mandhary, M. K. Al-Suti, T. C. Corcoran, Y. Al-Mahrooqi, J. P. Attfield, N. Feeder, W. I. F. David, K. Shankland, R. H. Friend, A. Köhler, E. A. Marseglia, E. Tedesco, C. C. Tang, P. R. Raithby, J. C. Collings, K. P. Roscoe, A. S. Batsanov, L. M. Stimson, T. B. Marder, *New J. Chem.,* **27,** *140* (2003).
21. X. Zhao, T. Cardolaccia, R. T. Farley, K. A. Abboud, K. S. Schanze, *Inorg. Chem.,* **44,** *2619* (2005).
22. W.-Y. Wong, S.-Y. Poon, *J. Inorg. Organomet. Polym. Mater.,* **18,** *155* (2008).
23. W.-Y. Wong, C.-K. Wong, G.-L. Lu, A. W.-M. Lee, K.-W. Cheah, J.-X. Shi, *Macromolecules,* **36,** *983* (2003).
24. J. Lewis, P. R. Raithby, W.-Y. Wong, *J. Organomet. Chem.,* **556,** *219* (1998).
25. W.-Y. Wong, W.-K. Wong, P. R. Raithby, *J. Chem. Soc. Dalton Trans.,* **2761 (**1998).
26. W.-Y. Wong, G.-L. Lu, K.-H. Choi, J.-X. Shi, *Macromolecules,* **25,** *3506* (2002).
27. L. Liu, W.-Y. Wong, S.-Y. Poon, J.-X. Shi, K.-W. Cheah, Z. Lin, *Chem. Mater.,* **18,** *1369* (2006).
28. M. S. Khan, M. R. A. Al-Mandhary, M. K. Al-Suti, B. Ahrens, M. F. Mahon, L. Male, P. R. Raithby, C. E. Boothby, A. Köhler, *Dalton Trans., 74* (2003).

29. G.-J. Zhou, W.-Y. Wong, D. Cui, C. Ye, *Chem. Mater.,* **17,** *5209* (2005).
30. W.-Y. Wong, K.-H. Choi, G.-L. Lu, J.-X. Shi, *Macromol. Rapid Commun.,* **22,** *461* (2001).
31. W.-Y. Wong, L. Liu, S.-Y. Poon, K.-H. Choi, K.-W. Cheah, J.-X. Shi, *Macromolecules,* **37,** *4496* (2004).
32. G.-J. Zhou, W.-Y. Wong, Z. Lin, C. Ye, *Angew. Chem. Int. Ed.,* **45,** *6189* (2006).
33. G.-J. Zhou, W.-Y. Wong, C. Ye, Z. Lin, *Adv. Funct. Mater.,* **17,** *963* (2007).
34. N. Chawdhury, A. Köhler, R. H. Friend, W.-Y. Wong, J. Lewis, M. Younus, P. R. Raithby, T. C. Corcoran, M. R. A. Al-Mandhary, M. S. Khan, *J. Chem. Phys.,* **110,** *4963* (1999).
35. J. Lewis, N. J. Long, P. R. Raithby, G. P. Shields, W.-Y. Wong, M. Younus, *J. Chem. Soc. Dalton Trans., 4283* (1997).
36. W.-Y. Wong, S.-M. Chan, K.-H. Choi, K.-W. Cheah, W.-K. Chan, *Macromol. Rapid Commun.,* **21,** *453* (2000).
37. K. A. Bunten, A. K. Kakkar, *J. Mater. Chem.,* **5,** *2041* (1995).
38. N. Chawdhury, A. Köhler, R. H. Friend, M. Younus, N. J. Long, P. R. Raithby, J. Lewis, *Macromolecules,* **31,** *722* (1998).
39. M. S. Khan, M. R. A. Al-Mandhary, M. K. Al-Suti, A. K. Hisahm, P. R. Raithby, B. Ahrens, M. F. Mahon, L. Male, E. A. Marseglia, E. Tedesco, R. H. Friend, A. Köhler, N. Feeder, S. J. Teat, *J. Chem. Soc. Dalton Trans., 1358* (2002).
40. M. S. Khan, M. K. Al-Suti, M. R. A. Al-Mandhary, B. Ahrens, J. K. Bjernemose, M. F. Mahon, L. Male, P. R. Raithby, R. H. Friend, A. Köhler, J. S. Wilson, *Dalton Trans., 65* (2003).
41. J. S. Wilson, A. Köhler, R. H. Friend, M. K. Al-Suti, M. R. A. Al-Mandhary, M. S. Khan, P. R. Raithby, *J. Chem. Phys.,* **113,** *7627* (2000).
42. M. Younus, A. Köhler, S. Cron, N. Chawdhury, M. R. A. Al-Mandhary, M. S. Khan, J. Lewis, N. J. Long, R. H. Friend, P. R. Raithby, *Angew. Chem. Int. Ed.,* **37,** *3036* (1998).
43. M. S. Khan, M. R. A. Al-Mandhary, M. K. Al-Suti, N. Feeder, S. Nahar, A. Köhler, R. H. Friend, P. J. Wilson, P. R. Raithby, *J. Chem. Soc. Dalton Trans.,* **2441 (**2002).
44. L. Liu, W.-Y. Wong, S.-Y. Poon, K.-W. Cheah, *J. Inorg. Organomet. Polym. Mater.,* **15,** *555* (2005).
45. L. Liu, W.-Y. Wong, J.-X. Shi, K.-W. Cheah, *J. Polym. Sci. Part A, Polym. Chem.,* **44,** *5588* (2006).
46. L. Liu, W.-Y. Wong, J.-X. Shi, K.-W. Cheah, T.-H. Lee, L. M. Leung, *J. Organomet. Chem.,* **691,** *4028* (2006).
47. W.-Y. Wong, C.-K. Wong, S.-Y. Poon, A.W.-M. Lee, T. Mo, X. Wei, *Macromol. Rapid Commun.,* **26,** *376* (2005).
48. W.-Y. Wong, C.-K. Wong, G.-L. Lu, K.-W. Cheah, J.-X. Shi, Z. Lin, *J. Chem. Soc. Dalton Trans.,* **4587 (**2002).
49. W.-Y. Wong, S.-Y. Poon, J.-X. Shi, K.-W. Cheah, *J. Polym. Sci. Part A, Polym. Chem.,* **44,** *4804* (2006).
50. W.-Y. Wong, S.-Y. Poon, A. W.-M. Lee, J.-X. Shi, K.-W. Cheah, *Chem. Commun.,* **2420 (**2004).
51. W.-Y. Wong, S.-Y. Poon, J.-X. Shi, K.-W. Cheah, *J. Inorg. Organomet. Polym. Mater.,* **17,** *189* (2007).
52. S.-Y. Poon, W.-Y. Wong, K.-W. Cheah, J.-X. Shi, *Chem. Eur. J.,* **12,** *2550* (2006).
53. W.-Y. Wong, *J. Inorg. Organomet. Polym. Mater.,* **15,** *197* (2005).
54. W.-Y. Wong, C.-L. Ho, *Coord. Chem. Rev.,* **250,** *2627* (2006).
55. A. S. Abd-El-Aziz, I. Manners, eds., *Frontiers in Transition Metal-Containing Polymers,* Wiley, New Jersey, 2007, *Ch. 6*.

56. J. S. Wilson, N. Chawdhury, M. R. A. Al-Mandhary, M. Younus, M. S. Khan, P. R. Raithby, A. Köhler, R. H. Friend, *J. Am. Chem. Soc.,* **123,** *9412* (2001).
57. J. L. Brédas, J. Cornil, A. J. Heeger, *Adv. Mater.,* **8,** *447* (1996).
58. N. S. Sariciftci, ed., *Primary Photoexcitations in Conjugated Polymers: Molecular Exciton vs Semiconductor Band Model,* World Scientific, Singapore, 1997.
59. T. A. Skotheim, J. R. Reynolds, R. L. Elsenbaumer, eds., *Handbook of Conducting Polymers,* 2nd ed., Marcel Dekker, New York, 1998.
60. R. H. Friend, R. W. Gymer, A. B. Holmes, J. H. Burroughes, R. N. Marks, C. Taliani, D. D. C. Bradley, D. A. Dos Santos, J. L. Brédas, M. Lögdlund, W. R. Salaneck, *Nature,* **397,** *121* (1999).
61. J. S. Wilson, A. S. Dhoot, A. J. A. B. Seeley, M. S. Khan, A. Köhler, R. H. Friend, *Nature,* **413,** *828* (2001).
62. A. Köhler, J. S. Wilson, R. H. Friend, *Adv. Mater.,* **14,** *701* (2002).
63. C. Adachi, M. A. Baldo, M. E. Thompson, S. R. Forrest, *J. Appl. Phys.,* **90,** *5048* (2001).
64. J. M. Lupton, A. Pogantsch, T. Piok, E. J. W. List, S. Patil, U. Scherf, *Phys. Rev. Lett.,* **89,** *167401* (2002).
65. Y. V. Romanovskii, A. Gerhard, B. Schweitzer, U. Scherf, R. I. Personov, H. Bässler, *Phys. Rev. Lett.,* **84,** *1027* (2000).
66. X. Gong, J. C. Ostrowski, G. C. Bazan, D. Moses, A. J. Heeger, M. S. Liu, A. K.-Y. Jen, *Adv. Mater.,* **15,** *45* (2003).
67. R. C. Evans, P. Douglas, C. J. Winscom, *Coord. Chem. Rev.,* **250,** *2093* (2006).
68. J. L. Brédas, R. R. Chance, eds., *Conjugated Polymeric Materials: Opportunities in Electronics, Optoelectronics and Molecular Electronics,* Kluwer Academic Publishers, Dordrecht, 1990.
69. P. K. H. Ho, J. S. Kim, J. H. Burroughes, H. Becker, S. F. Y. Li, T. M. Brown, F. Cacialli, R. H. Friend, *Nature,* **404,** *481* (2000).
70. Y. Cao, I. D. Parker, G. Yu, C. Zhang, A. J. Heeger, *Nature,* **397,** *414* (1999).
71. V. Cleave, G. Yahioglu, P. Le Barny, R. H. Friend, N. Tessler, *Adv. Mater.,* **11,** *285* (1999).
72. M. A. Baldo, D. F. O'Brien, Y. You, A. Shoustikov, S. Sibley, M. E. Thompson, S. R. Forrest, *Nature,* **395,** *151* (1998).
73. M. A. Baldo, M. E. Thompson, S. R. Forrest, *Nature,* **403,** *750* (2000).
74. Y. Kim, S. Cook, S. M. Tuladhar, S. A. Choulis, J. Nelson, J. R. Durrant, D. D. C. Bradley, M. Giles, I. McCulloch, C. S. Ha, M. Ree, *Nature Mater.,* **5,** *197* (2006).
75. M. Karikomi, C. Kitamura, S. Tanaka, Y. Yamashita, *J. Am. Chem. Soc.,* **117,** *6791* (1995).
76. S. D. Cummings, R. Eisenberg, *J. Am. Chem. Soc.,* **118,** *1949* (1996).
77. H. F. Wittmann, R. H. Friend, M. S. Khan, J. Lewis, *J. Chem. Phys.,* **101,** *2693* (1994).
78. N. J. Demas, G. A. Crosby, *J. Am. Chem. Soc.,* **92,** *7262* (1970).
79. J. Cornil, D. Beljonne, D. A. dos Santos, Z. Shuai, J. L. Brédas, *Synth. Met.,* **78,** *209* (1996).
80. D. Beljonne, J. Cornil, J. L. Brédas, R. H. Friend, *Synth. Met.,* **76,** *61* (1996).
81. N. J. Turro, *Modern Molecular Photochemistry,* University Science Books, Mill Valley, CA, 1991.
82. D. Hertel, S. Setayesh, H. G. Nothofer, U. Scherf, K. Mullen, H. Bässler, *Adv. Mater.,* **13,** *65* (2001).
83. A. P. Monkman, H. D. Burrows, L. J. Hartwell, L. E. Horsburgh, I. Hamblett, S. Navaratnam, *Phys. Rev. Lett.,* **86,** *1358* (2001).
84. W. S. Jenks, W. Lee, D. Shutters, *J. Phys. Chem.,* **98,** *2282* (1994).
85. P. Li, B. Ahrens, N. Feeder, P. R. Raithby, S. J. Teat, M. S. Khan, *Dalton Trans., 874* (2005).

86. W.-Y. Wong, *Coord. Chem. Rev.,* **249,** *971* (2005).
87. D. Neher, *Macromol. Rapid Commun.,* **22,** *1365* (2001).
88. B. Tsuie, J. L. Reddinger, G. A. Sotzing, J. Soloducho, A. R. Katritzky, J. R. Reynolds, *J. Mater. Chem.,* **9,** *2189* (1999).
89. K.-T. Wong, Y.-Y. Chien, R.-T. Chen, C.-F. Wang, Y.-T. Lin, H.-H. Chiang, P.-Y. Hsieh, C.-C. Wu, C. H. Chou, Y. O. Su, G.-H. Lee, S.-M. Peng, *J. Am. Chem. Soc.,* **124,** *11576* (2002).
90. W.-Y. Wong, G.-J. Zhou, X.-M. Yu, H.-S. Kwok, B. Z. Tang, *Adv. Funct. Mater.,* **16,** *838* (2006).
91. X.-M. Yu, H.-S. Kwok, W.-Y. Wong, G.-J. Zhou, *Chem. Mater.,* **18,** *5097* (2006).
92. W.-Y. Wong, G.-J. Zhou, X.-M. Yu, H.-S. Kwok, Z. Lin, *Adv. Funct. Mater.,* **17,** *315* (2007).
93. N. D. McClenaghan, R. Passalacqua, F. Loiseau, S. Campagna, B. Verheyde, A. Hameurlaine, W. Dehaen, *J. Am. Chem. Soc.,* **125,** *5356* (2003).
94. P. Kunda, K. R. Justin Thomas, J. T. Lin, Y.-T. Tao, C.-H. Chien, *Adv. Funct. Mater.,* **13,** *445* (2003).
95. K. R. Justin Thomas, J. T. Lin, Y.-T. Tao, C.-W. Ko, *J. Am. Chem. Soc.,* **123,** *9404* (2001).
96. F. Sanda, T. Nakai, N. Kobayashi, T. Masuda, *Macromolecules,* **37,** *2703* (2004).
97. J. Roncali, *Chem. Rev.,* **97,** *173* (1997).
98. N. Robertson, *Angew. Chem. Int. Ed.,* **45,** *2338* (2006).
99. B. O'Regan, M. Grätzel, *Nature,* **353,** *737* (1991).
100. W.-Y. Wong, *Macromol. Chem. Phys.,* **209,** *14* (2008).
101. A. Köhler, H. F. Wittman, R. H. Friend, M. S. Khan, J. Lewis, *Synth. Met.,* **77,** *147* (1996).
102. N. Chawdhury, M. Younus, P. R. Raithby, J. Lewis, R. H. Friend, *Opt. Mater.,* **9,** *498* (1998).
103. A. Köhler, H. F. Wittmann, R. H. Friend, M. S. Khan, J. Lewis, *Synth. Met.,* **67,** *245* (1994).
104. F. Guo, Y.-G. Kim, J. R. Reynolds, K. S. Schanze, *Chem. Commun., 1887* (2006).
105. W.-Y. Wong, X.-Z. Wang, Z. He, A. B. Djurišić, C.-T. Yip, K.-Y. Cheung, H. Wang, C. S. K. Mak, W.-K. Chan, *Nature Mater.,* **6,** *521* (2007).
106. J. Y. Kim, S. H. Kim, H. H. Lee, K. Lee, W. Ma, X. Gong, A. J. Heeger, *Adv. Mater.,* **18,** *572* (2006).
107. C. W. Spangler, *J. Mater. Chem.,* **9,** *2013* (1999).
108. J. W. Perry, K. Mansour, I.-Y. S. Lee, X. L. Wu, P. V. Bedworth, C.-T. Chen, D. Ng, S. R. Marder, P. Miles, T. Wada, M. Tian, H. Sasabe, *Science,* **273,** *1533* (1996).
109. L. W. Tutt, A. Kost, *Nature,* **356,** *225* (1992).
110. B. Z. Tang, H. Y. Xu, *Macromolecules,* **32,** *2569* (1999).
111. R. Vestberg, R. Westlund, A. Eriksson, C. Lopes, M. Carlsson, B. Eliasson, E. Glimsdal, M. Lindgren, E. Malmström, *Macromolecules,* **39,** *2238* (2006).
112. W.-Y. Wong, L. Liu, J.-X. Shi, *Angew. Chem. Int. Ed.,* **42,** *4064* (2003).
113. H. Y. Chao, W. Lu, Y. Li, M. C. W. Chan, C. M. Che, K. K. Cheung, N. Zhu, *J. Am. Chem. Soc.,* **124,** *14696* (2002).
114. W. Lu, H.-F. Xiang, N. Zhu, C.-M. Che, *Organometallics,* **21,** *2343* (2002).
115. C.-M. Che, H.-Y. Chao, V. M. Miskowski, Y. Li, K.-K. Cheung, *J. Am. Chem. Soc.,* **123,** *4985* (2001).
116. W.-Y. Wong, *Coord. Chem. Rev.,* **251,** *2400* (2007).

CHAPTER 9

Luminescence in Polymetallic Gold-Heteronuclear Derivatives

Antonio Laguna[1] and José M. López-de-Luzuriaga[2]

[1]*Department of Inorganic Chemistry, ICMA, University of Zaragoza, Zaragoza, Spain*

[2]*Department of Chemistry, UA-CSIC, University of La Rioja, Logroño, Spain*

CONTENTS

Macromolecules Containing Metal and Metal-like Elements,
Volume 10: Photophysics and Photochemistry of Metal-Containing Polymers,
Edited by Alaa S. Abd-El Aziz, Charles E. Carraher Jr., Pierre D. Harvey, Charles U. Pittman Jr., Martel Zeldin.

I. INTRODUCTION AND BACKGROUND

Gold is a noble metal of very special characteristics that make it unique. It displays a reddish yellow color; it is soft, ductile, manageable, and a good conductor of heat and electricity. With exception of its color, we can find similar macroscopic properties in many other metals of the Periodic Table. Nevertheless, it has been present in man's life since the earliest civilizations and has occupied an important place in the history of mankind for >7000 years.

The reason for it is not obvious since gold is not a very rare element on earth, and other metals, for example, platinum, rhodium, osmium, and rhenium, are less abundant and more expensive. Its yellow color cannot be the reason either, since other metals, such as copper, and its alloys as bronze or brass, have different colors from the bright silver of most of the metals. Probably, the reason resides in its noble character. In fact, gold does not tarnish with time, and coins and jewelry remain indefinitely unalterable even after long exposure to extremely aggressive conditions.

This chemical inertia is, probably, also the reason for which its chemistry has played a minor role for many years. In fact, initially all its known chemistry was that related to the concentration, recovery, and purification of this element.[1] Moreover, the chemistry of gold was merely regarded as an art to recover and convert gold metal into all possible forms for ornamental, monetary, anticorrosive, or electrical usage. It is therefore no surprise that the chemistry of gold, which is so clearly dominated by the metallic state, remained undeveloped for so long.

But, in addition to the conventional characteristics that everybody relates with gold, we can point out some unusual properties that condition its chemical and physical behavior:

1. The value of its electrochemical potential is lower than in any other metal. The main consequence is that gold in any cationic form will accept electrons from virtually any reducing agent to form metallic gold.
2. Gold is the most electronegative of all the metals.[2]
3. Gold has the possibility of having a mononegative oxidation state, and, for instance, it is known an ionic compound of formula CsAu with a cesium iodide like structure.
4. In vapor state, gold is formed by diatomic molecules (Au_2), whose dissociation energy is higher than those of many other diatomic non-metal elements, such as halogens.[3]

In fact, these characteristics give an explanation of the commented chemical inertia and the difficulties in developing a chemistry of this metal comparable to those of the metals in its neighborhood. In addition, also in the last point, a preliminary clue about what has been a constant in its chemical behavior in the last two decades is given: The marked tendency of gold atoms to aggregate themselves, not only in the gas phase but also in their compounds, forming dimers, trimers, or generically, oligomers of different length and dimensionality. This strange interatomic attractive force seems to determine, at least in part, the molecular configurations and crystal lattices of these compounds. This phenomenon already appeared in gold metal, in which the gold-gold distance is even shorter than the corresponding silver-silver one in metallic silver, and this effect cannot be considered just as a consequence of the lanthanide contraction.

The collection of these new observations has attended a revived interest in the theoretical chemistry to explain the behavior of the heaviest elements of the Periodic Table on the basis of relativistic effects, which are specially important for elements with a high nuclear charge.[4–6] It is only through the consideration of the relativistic effects that a deeper understanding of the chemistry of gold has emerged.[7]

From a theoretical point of view, the electronic configuration of gold(I) would justify the relative stability of gold(I) compounds with 10 electrons in the *5d* orbitals, but it does not help to understand the predominance of the metallic form. In the post-lanthanide elements, where there is a great number of protons in the atomic nuclei, the electrons must move at a speed close to the speed of light, and they cannot be treated in terms of classical physics, instead the relativity assigned a relativistic mass that is larger than the mass of the electron at rest. The net effect on the *6s* electrons in those elements is that the orbital radius is contracted and the distance of the electron from the nucleus is reduced. As can be seen in Figure 1, it reaches a pronounced local minimum for gold.[8]

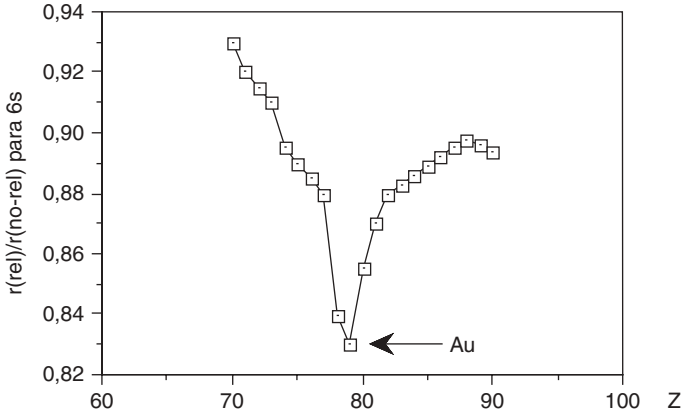

FIGURE 1. Relativistic contraction of 6s orbitals for heavy elements (atomic number from $Z = 70$ to 90).

The consequences of this effect in gold chemistry are the following:[9]

1. Gold is more difficult to ionize and, in consequence, to obtain cations. This situation also explains the high electron affinity and the possibility to accept electrons to give anions.
2. A shortening of the energy gap between the *6s* and the *5d* orbitals, which makes both states available for bonding. As a consequence, the closed shell $5d^{10}$ is no longer chemically inert and can interact with other elements—that is, with other gold atoms in molecules—or, as we will see in the next pages, with other closed shell atoms. It also becomes possible to rationalize the bonding between two gold(I) centers with equal charge and a closed shell configuration, which is a very difficult fact to explain in terms of classical bonding.
3. The small difference of energy among the *s*, *p*, and *d* orbitals leads to the efficient formation of *s*/*d* or *s*/*p* hybridizations, which are important to explain the pronounced tendency of gold(I) to form linear two-coordinate complexes.
4. The destabilization of the *5d* orbitals permits us to explain the ease of formation of the oxidation state III, almost absent in copper and silver.

In addition, the great availability and development of the X-ray diffraction analyses has allowed us to show that gold(I) is not an exception in the Periodic Table and that other metal atoms with closed shell configurations can display the same tendency to aggregate themselves. Thus examples of interactions between centers with d^{10}-d^{10} (Ag(I)-Ag(I),[10] Cu(I)-Cu(I),[11] Hg(II)-Hg(II),[12] Pt(0)-Pt(0),[13] Pd(0)-Pd(0),[14]), d^8-d^8 (Pt(II)-Pt(II)[15]), or s^2-s^2 (Tl(I)-Tl(I)[16], Pb(II)-Pb(II)[17]) configurations or even between centers with different configurations, such as s^2-d^8 (Tl(I)-Pt(II),[18] Tl(I)-Pd(II),[19] Tl(I)-Ir(I)[20]), s^2-d^{10} (Tl(I)-Au(I), Pb(II)-Au(I)), or d^8-d^{10} (Pt(II)-Au(I) Pd(II)-Au(I),[21] Pt(II)-Hg(II)[22], Pt(II)-Ag(I)[23]) have been reported. Theoretical studies of selected examples have been carried out.[4] In these complexes, whose number is increasing every day, the metallophilicity promoted by gold seems to be a key factor. In fact, the well-known aurophilicity that justifies the aggregation in gold complexes seems not to be an isolated phenomenon; instead, the presence of gold in the complexes seems to increase the metallophilicity of the other metals and, consequently the presence of metal-metal interactions.[24]

As we will see in the next pages, this bonding interaction between the metals is responsible for important associated properties. Thus, for instance, one of the most studied in the last years is the luminescence that appears in many gold-containing complexes. This property, originally found in gold in the trinuclear complex $[AuCl(PPh_3)_2]$ by Dori and co-workers in 1970[25] led a number of groups to synthesize and study luminescent gold molecules, demonstrating that the three-coordination is not a necessary condition to produce luminescent gold complexes and that in selected examples a moderate deviation from the linearity produced the same phenomenon. In addition, the

ligands bonded to the different metals are of capital importance since the luminescence of the complexes can have its origin in those molecules. Also, the presence of metal-metal interactions in the complexes often produces excited states that lead to emissions of light. More precisely, the luminescence can be produced by transitions between orbitals exclusively of the gold or in the heterometal or as a result of the interaction between them, in orbitals of the ligands, or in transitions involving both metals and ligands (charge transfer transitions).[26]

Another very important factor that should be considered is the expected large spin-orbit effect promoted by a heavy atom as gold. The heavy-metal-induced spin-orbit coupling favors an effective emission from the triplet excited states that leads to a phosphorescence, which generally is not observed for linear molecules.[27]

Consequently, the formation of extended chain complexes of gold and other heterometal leads to a promising class of luminescent materials because, in addition to the special characteristics of gold, its interactions with other metal centers deviates its environment from the linearity, which favors the luminescence of this center. In addition, this interaction can modify the relative energy of the frontier orbitals of gold and create new orbitals as a consequence of the new gold-metal interaction, multiplying the possibilities of electronic transitions between them or between the metals and the ligands (charge transfer (CT) transitions). These also favor phosphorescent transitions. All of these characteristics can make these complexes appropriate for practical applications such as selective sensors for organic or inorganic materials, imaging technology, environmental safety, and in the OLED industry.

In the next pages we describe examples of luminescent gold containing materials with a polymeric structure and built through weak metal-metal interactions. We will not consider those in which formal metal-metal bonds appear, and we divide the discuss by the heterometal interacting with the gold. The type and number of the ligands, the coordination environments around the metal centers, the temperature, the heterometal, the metal-metal distances, and so on increase the possibilities of electronic transitions and hence multiply the factors that affect the energy and number of emissions observed, which makes it a fascinating area of research.

II. LUMINESCENT GOLD-SILVER DERIVATIVES

In spite of being one of its group congeners, the number of materials containing gold and silver is very limited today compared to the total amount of heterometal-silver complexes. It is a surprising situation since one would expect that a similar electronic configuration and even covalent radius (gold is 0.07 Å smaller than silver[28]) would favor the synthesis of complexes in which both atoms were part of the same molecule. Nevertheless, the number of these structurally characterized derivatives does not exceed 80 complexes from a

total of Ag-M of 1200 examples.[29] From them, the number of extended systems (mono-, bi-, or three-dimensional) is more limited (see below), and the number of luminescent studies carried out on these systems is still less. Therefore, undoubtedly, more work is needed in this area, especially where the reported optical properties indicate a very promising area of research with promising practical applications.

Thus, in the next examples, we comment on supramolecular entities, including linear chains, two-dimensional sheets, and even three-dimensional networks. From them, perhaps the most common structural arrangement is that in which the metals form extended linear systems, usually built from mononuclear units, dinuclear, using polydentate donor ligands; and polymetallic units. It is worth mentioning that in this part and also in the following we consider only structures built by gold-heterometal interactions, not bonds; thus formal clusters will not be considered.

We will divide this part, taking into account the unit that is repeated and that forms the supramolecular entity.

A. Supramolecular Gold-Silver Complexes with Bidentate Ligands

The most common strategy in the synthesis of heteronuclear complexes is the use of bidentate donor ligands bearing different donor centers. In that way both donor atoms can be coordinated selectively to two different metal centers in a consecutive way. If the space between the donor atoms of the ligands is short, interactions between both metals usually appear, normally intramolecular. Sometimes, albeit not very often, the bidentate units bind to one another, leading to extended structures through metallophilic interactions. As we have commented, in the case of gold-silver derivatives the number of luminescent studies of these derivatives is very scarce.

One example is the case of the complex $[AuAg(MTP)_2]_n$ (MTP = diphenylmethylenethiophosphinate), reported by Fackler's laboratory. The synthesis of this polymeric Au-Ag complex is achieved by reaction of the gold complex $[PPN][Au(MTP)_2]$ (PPN = bis(triphenyl-phosphoranylidene)ammonium) with $AgNO_3$ in equimolecular amounts.[30] The structure of this derivative consists of a one-dimensional chain structure, with the MTP ligands bridging the gold and silver centers, which keep a short contact of 2.9124(13) Å. In each unit, both carbon atoms are bonded to gold, while both sulfur atoms are bonded to silver. The dinuclear units are bound together through gold-silver interactions between different units of 3.635 Å. In this structure, it can be observed a deviation of the S-Ag-S angle from the linearity (171.7°) with the Ag atom directed toward the Au center, indicating that the intramolecular interaction is not forced by the ligand architecture; instead, it is promoted by the relativistic effects between these two metals (Fig. 2).

In its absorption spectrum, a band at 275 nm with a large extinction coefficient appears, which depends on concentration and also appears in the

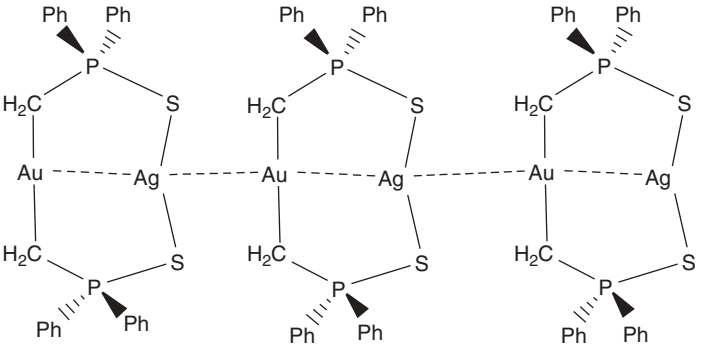

FIGURE 2. The $[AuAg(MTP)_2]_n$ chain.

homologous homonuclear gold and silver species $[Au_2(MTP)_2]_n$ and $[Ag_2(MTP)_2]_n$, respectively. Consequently, the authors assigned it to a permitted intraligand transition between the π-π* orbitals in the MTP ligand. It is interesting that an increase of the concentration in the solutions of this heteronuclear complex leads to a shift of the edge of the band (7800 cm^{-1}), therefore breaking Lambert-Beer's law, which suggests the molecular aggregation of these dinuclear units into oligomers. Nevertheless, the fact that the maximum in its excitation spectrum appears at lower energy (~320 nm) than the band edge of the absorption spectrum in solution, indicates that these oligomers formed in solution contain few dinuclear units even in concentrations near saturation.

The emission of this complex appears at 424 nm, and the DFT calculations suggests an excited state that results from *argento-aurophilic* bonding. The homologous gold and silver dinuclear species showed bands at lower energies at 493 and 466 nm, respectively, and not at lower and higher energies, respectively, as was expected according with the absorption data.

In the case of the ligand Meimpy (1-methyl-3-(2-pyridinyl)imidazolate), both donor atoms, carbon and nitrogen, bind to gold and silver, respectively. Thus, starting from the complex $[Au(Meimpy)_2]PF_6$, in which gold is bonded to both imidazolate groups through the carbon atoms, the reactions with equimolecular amounts of silver salts such as $AgBF_4$ or $AgNO_3$ in acetonitrile, benzonitrile, or benzylnitrile gave rise to the synthesis of the polymeric species $\{[AuAg(Meimpy)_2L]X\}_n$ ($X = PF_6$, $L = CH_3CN$, C_6H_5CN, $C_6H_5CH_2CN$; $X = NO_3$, $L = NO_3$ (CH_3CN solvate)).[31] In all cases, the complexes exhibit alternate sequences of gold and silver atoms with interactions in a range between 2.8125(2) and 2.9428(2) Å (Fig 3). The silver atoms are bonded to two pyridine groups of different Meimpy ligands and to one L (nitrile or NO_3^-), showing a distorted trigonal planar environment.

The absorption spectra of the complexes were similar to those of the precursor $[HMepyim]PF_6$ (1-methyl-3-(2-pyridinyl)imidazolium hexafluorophosphate), which exhibited bands between 260 and 270 nm, attributed to π-π*

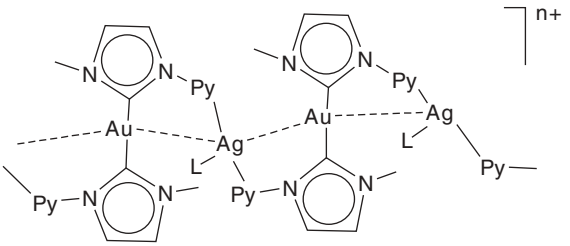

FIGURE 3. The $\{[AuAg(Meimpy)_2L]^+\}_n$ chain.

transitions. It was proposed that this result indicated that the extended chain dissociates in solution, leading to monomeric species. The solid-state emission spectra of the nitrile containing polymers displayed intense bands at 480 (CH_3CN), 474 (C_6H_5CN), and 522 ($C_6H_5CH_2CN$) nm. The nitrate containing polymer showed a band at 469 nm. The effect of cooling the samples prompted the bands to sharpen and shift to blue, 450, 480, 453, and 466 nm, respectively, in all cases. In solution, all showed the same emissions, which were also the same as those of the precursor gold complex, which is again in accordance with the existence of monomeric species in solution. Taking into account that the identified order of the increasing energy of the emissions for the complexes of benzylnitrile < acetonitrile < benzonitrile did not correlate to decreasing Au-Ag separation or to the nitrile donor ability as measured by the nitrile-Ag sepration, the authors proposed that the origin of the emissions resides in a combination of metal chain geometry and ancillary ligand electronic and steric properties.

B. Supramolecular Gold-Silver Complexes with Tridentate Ligands

Although not common, tridentate ligands can lead to heteronuclear extended systems. For instance, with the related imidazolium salt 1,3-bis(2-pyridinyl)imidazolium (py_2im), Catalano et al. reported the synthesis of heteronuclear gold silver materials. The reaction was carried out between the gold-imidazolium precursor $[Au(py_2im)_2][BF_4]$ with silver tetrafluoroborate in acetonitrile. That led to the helical polymer $\{[AuAg(py_2im)_2(CH_3CN)][BF_4]\}_n$ (see Fig. 4). The chiral nature of this material was confirmed by the authors with the resolution of the crystal structures of both enantiomers. The extended structures displayed very short alternating Au-Ag separations of 2.8359(4)−2.9042(4) Å.[32]

This complex, like the carbene precursor, is luminescent in solution and in the solid state. In acetonitrile solution, it displays an emission at 345 nm, which originates from an electronic state centered at 284 nm, which is attributed to an intraligand fluorescent process. In the solid state, the gold-silver complex emitts at 515 nm, and the ligand precursor, $[H(py)_2im]BF_4$, at 514 nm. Consequently, the remarkable similarity between the emissions of the ligand

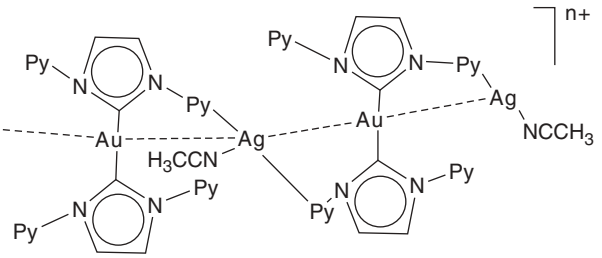

FIGURE 4. The polymer $\{[AuAg(py_2im)_2(CH_3CN)]^+\}_n$.

and the metal salt in both solid state and solution, suggests a ligand-centered emission.

C. Supramolecular Gold-Silver Complexes Built with Metallic Cationic and Anionic Counterparts

Probably the most useful method for preparing polymeric materials through unsupported metallophilic interactions is an acid-base reaction. In these, basic gold(I) precursors react with metallic Lewis acids, forming supramolecular networks via acid-base stacking. The stability of these systems can be related to the ionic interactions; nevertheless, the dispersion forces and relativistic effects can also be invoked to explain the formation of these systems, and in some occasions, these effects are even more important than the electrostatic attractions in determining the structural motifs.

The first reported case is that of the $[Au(CN)_2]^-$ anion. In it, the gold center can itself act as a donor because since the negative charge of each cyanide ligand increases the electronic density on this metal, making it a potential donor center. To a certain degree, it is a potential tridentate complex making use of their nitrogen donor atoms and the gold center. Nevertheless, in the first study, the complex $K[Au(CN)_2]$ consisted of $[Au(CN)_2]^-$ linear ions, alternating with layers of K^+ ions. In that case, the gold centers and the potassium cations were placed at distances larger than the sum of their van der Waals radii.[33–35] However, the presence of another heavier element acting as countercation facilitated the presence of interactions between the metals. For instance, the silver-gold mixed metal systems of stoichiometry $M[Ag_xAu_{1-x}(CN)_2]_3 \cdot 3H_2O$ ($x = 0.25, 0.50, 0.75, 0.90$) (M = La,[36] Eu[37]) were obtained and studied by Patterson et al. and exhibited tunable photoluminescence, depending on the Au/Ag stoichiometric ratio in the complexes.

The lanthanum or europium atoms had no interaction with the gold and silver centers, and the determined crystal structures exhibited hexagonal arrays of metal-metal interactions with diagonal interactions in the layer and the lanthanoids in the middle of the hexagonal prisms. In both examples, the lanthanum and the europium salts were isostructural (Fig. 5).

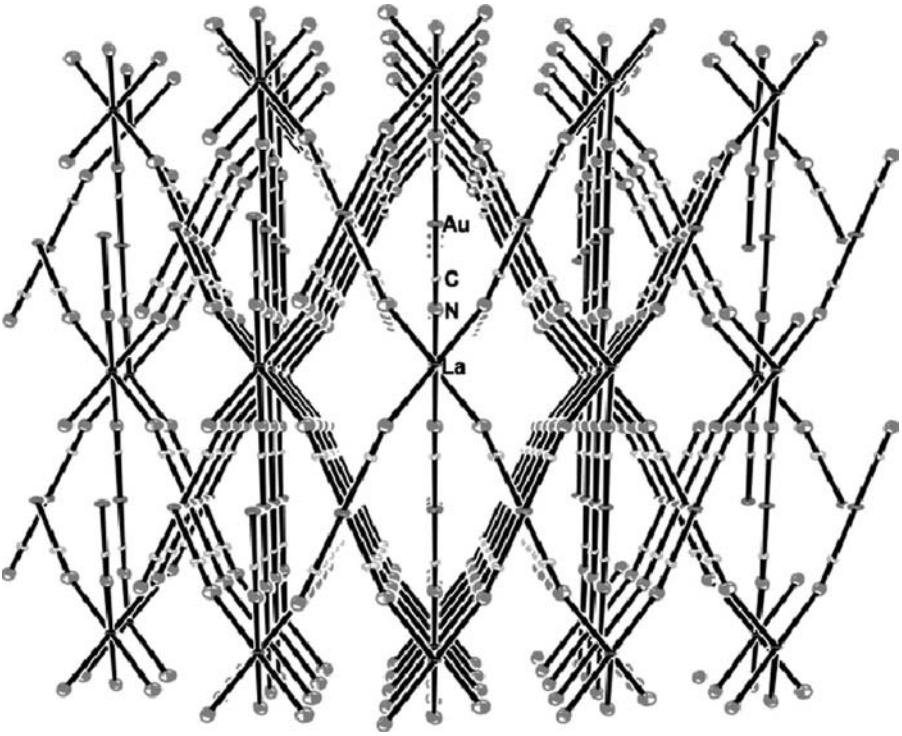

FIGURE 5. The structure of the $La[Ag_xAu_{1-x}(CN)_2]_3 \cdot 3H_2O$ complexes.

These complexes were prepared by slow crystallization of pure gold and silver dicyanide complexes in different molar ratios; therefore, they were not prepared by a conventional acid-base reaction.

In the case of the two lanthanum derivatives, the exact compositions established by X-ray diffraction studies gave empirical formula in which the silver centers were in a ratio $x = 0.33$ and 0.78. For the europium complexes, only when $x = 0.14$ the structural characterization was performed.

In all cases the complexes were strongly luminescent at room temperature, in contrast to the precursor homonuclear derivatives, and at an energy that was tunable, displaying a site-selective excitation that depended on the Au:Ag molar ratio, lying between the emission bands of the pure Ag and Au compounds. For instance, while the homonuclear derivative $La[Ag(CN)_2]_3$ emitted at 77 K at 345 and 470 nm (exc. 310 nm) and the gold complex $La[Au(CN)_2]_3$ at 431 and 493 nm (exc 310 nm), the mixed metal systems tended toward Ag or Au peak positions, depending on loading.

Therefore, the excited states responsible for the emissions were throughout to be located on the gold and silver atoms in each complex. The theoretical TD-DFT calculations coincided with these results and showed

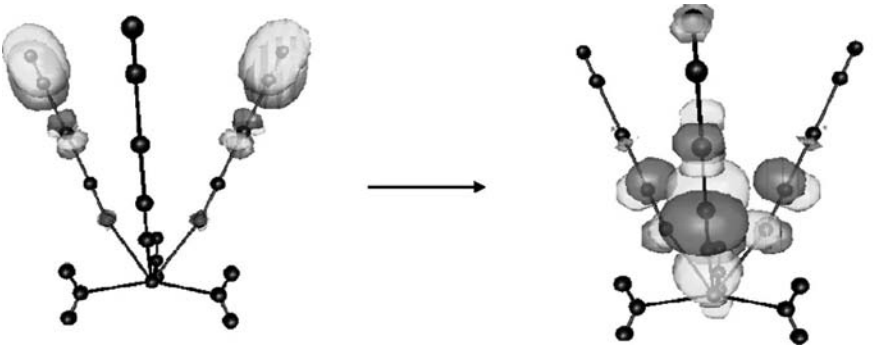

FIGURE 6. The HOMO-LUMO transition for the model $La[Ag_2Au(CN)_2]_3 \cdot 3H_2O$.

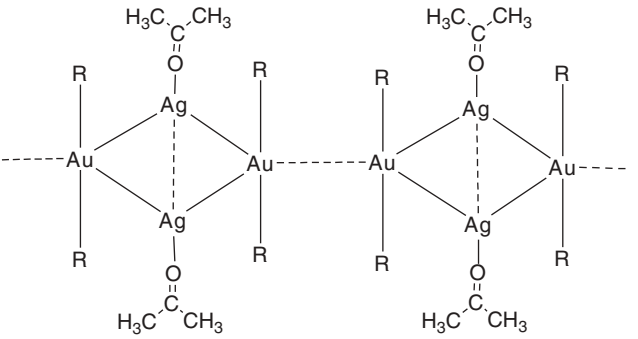

FIGURE 7. $[Au_2Ag_2(C_6F_5)_4(Me_2CO)_2]_n$ ($R=C_6F_5$).

higher oscillator strengths for the mixed systems than for the pure precursors, possibly making them better candidates for photoluminescence applications.

Another type of reaction, for instance, those between perhalophenylgold (I) complexes and different silver salts, can also lead to classic acid-base stacking through interactions between the metals present in the precursors. Among these, perhaps the best-known Lewis basic precursor is the electron-rich bis(pentafluorophenyl)aurate(I) anion. For example, the reaction between $NBu_4[Au(C_6F_5)_2]$ and $AgClO_4$ in acetone leads to a heterometallic extended linear chain of formula $[Au_2Ag_2(C_6F_5)_4(Me_2CO)_2]_n$.[38] Its crystal structure consists of an extended polymeric chain of tetranuclear Au_2Ag_2 units formed through short gold-gold contacts of 3.1674(11) Å (Fig. 6). The gold-silver distances are 2.7903(9) and 2.7829(9) Å, and both silver atoms keep a short interaction of 3.1810(13) Å (Fig. 7).

The product is emissive; it was unexpected that it would display a single emission band, in spite of the different metal-metal interactions that appear in

the complex. Thus, in solid state, it displays a band at 546 nm that shifts to 554 nm at 77 K. Its behavior is different in solution because in dilute solutions (5×10^{-4} M) it is also luminescent at a different wavelength (em = 405 nm by excitation at 332 nm), and changes in the concentration of the sample give rise to changes in the emission wavelengths and, therefore, a deviation from Lambert-Beer's law. This result is interpreted in terms of isolated tetranuclear units as responsible for the luminescence behavior observed in dilute solutions, while the increase in concentration produces an oligomerization process of tetranuclear $[Au_2Ag_2(C_6F_5)_4(Me_2CO)_2]$ units through gold-gold contacts. In that case, as the number of gold-gold interactions increases, the emissions should shift to lower energies. The representation of the emission wavelengths versus the inverse of concentration is a simple linear fit, in which the extrapolation to infinite concentration (547.04 nm), zero in x axis, clearly matches the solid-state emission (Fig. 8). This fact allows us to establish a clear correlation between the aggregation process through gold-gold contacts in solution and the emissive behavior in solid state.

Density functional theory (DFT) calculations were also carried out to assign the molecular orbitals involved in the transitions that lead to luminescence, concluding that metal centered $(d\sigma^*)^1(p\sigma)^1$ or $(d\sigma^*)^1(p\sigma)^1$ excited states are responsible for the luminescence in the solid state, while in dilute solutions the luminescence arises from $\pi\pi^*$ excited states in the pentafluorophenyl ligands or from π-MMCT transitions.

A recent work from Laguna's and Fackler's laboratories goes further in the use of these tetranuclear systems. Although the synthesis of polymeric Au-Ag materials of the type $[Au_2Ag_2(C_6F_5)_4L_2]_n$ (L = neutral ligand) was

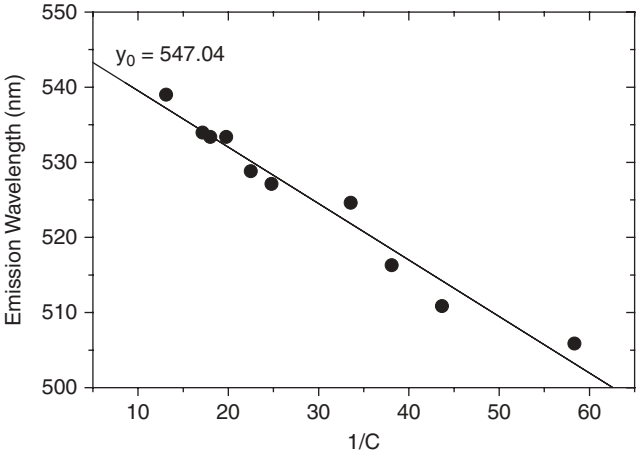

FIGURE 8. The linear fit of the emission wavelengths versus the inverse of concentration for complex $[Au_2Ag_2(C_6F_5)_4(Me_2CO)_2]_n$ (R=C_6F_5).

reported by our laboratory more than 20 years ago,[39] it was only at the beginning of this century that their study was reinstated, as we saw in the previous example. In addition, and very interesting, they are promising VOCs sensors because of the lability of some ligands, such as Et_2O, in the coordination sphere of silver.[40]

For example, the polymeric compound $\{[AuAg(C_6F_5)_2(Et_2O)]_2\}_n$, obtained in the reaction between the metallic precursors in presence of diethyl ether, was used as starting material for the synthesis of a series of complexes with the stoichiometry $\{[AuAg(C_6F_5)_2(L)]_2\}_n$ (L = Me_2CO, THF or CH_3CN), all of them showing the same polymeric nature that we have noted. This synthesis is achieved not only in solution but also in solid/vapor phase when the starting ether product is exposed to vapors of the rest of the ligands. Thus the exposure of $\{[AuAg(C_6F_5)_2(Et_2O)]_2\}_n$ in the solid state at room temperature to vapors of the volatile organic compounds leads to a quick, perceptible change in the color of the samples. The thermogravimetric analyses reveal that the variations in the temperature and percentage of VOC ligands loss are due to their different boiling points and the strengths of the interactions between the ligands and the silver centers. Similarly, powder X-ray diffraction studies are in accord with a complete substitution of the very labile Et_2O ligand by the vapors of acetone, THF, or CH_3CN, rather than to absorption processes. Nevertheless, some exchange processes are not reversible, which suggests that similar behaviors described in the literature for related systems as VOCs sensors probably should be revisited. In Scheme 1, we can observe the transformations in solid/vapor phase of the four complexes.

Finally, as in the previous example, all the complexes are luminescent in solid state at room temperature and at 77 K. A plausible origin of the emission spectra in these complexes is that the excited states responsible for the emissions are localized in the tetranuclear $[Au_2(C_6F_5)_2Ag_2L_2]$ core, with an energy which is influenced by the gold-gold or gold-silver interactions and by molecular aggregation, in accordance with the DFT and TD-DFT calculations carried out previously (Fig. 9).[38, 41]

Although, the anionic nature of this gold precursor could be the origin of its donor characteristics, our research group has found that the presence of only one perhaplophenyl group in the gold precursor produces similar potential in their reactions with silver salts. For instance, the neutral species [AuR(tht)] (R = C_6F_5, 3,5-$C_6Cl_2F_3$, C_6Cl_5) have been investigated in their reactions with silver trifluoroacetate. These lead to $[AgAu(C_6F_5)(CF_3CO_2)(tht)]_n$, $[Ag_2Au(3,5\text{-}C_6Cl_2F_3)(CF_3CO_2)(tht)]_n$, or $[AgAu(C_6Cl_5)(CF_3CO_2)(tht)]_n$, respectively.[42] The three structures have a polymeric nature, the first one being two-dimensional and the other two mono-dimensional (Fig. 10). They all are formed by association of almost linear [AuR(tht)] units and eight-membered $[Ag_2(CF_3CO_2)_2]$ rings join together through Au-Ag interactions. In the pentafluorophenyl complex, in addition to the Au-Ag interactions that build the polymer and the intramolecular Ag-Ag of the carboxylate dimers, Au-Au interactions also appear. In all the complexes, the metal-metal interactions are

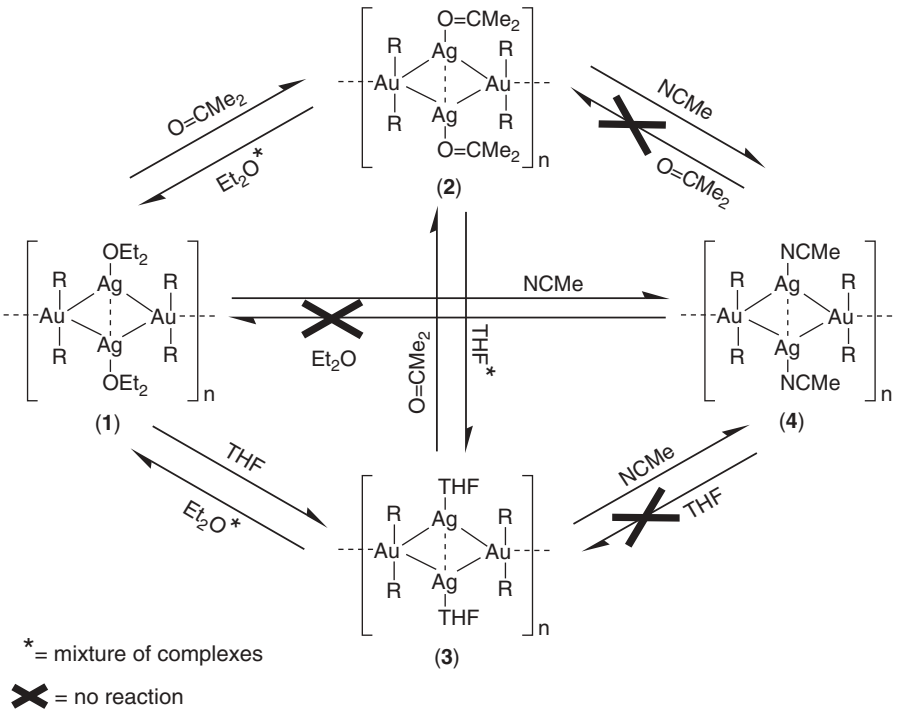

SCHEME 1. Vapochromic bahavior of complexes $\{[AuAg(C_6F_5)_2L]_2\}_n$.

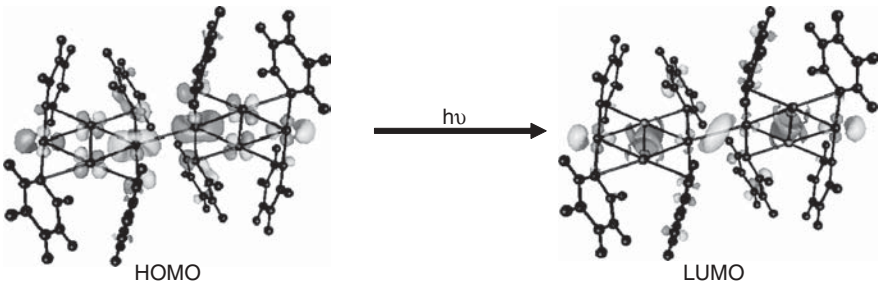

FIGURE 9. HOMO-LUMO molecular orbitals for the model $[Au_2(C_6H_5)_2Ag_2]_2$.

shorter than the sum of the van der Waals radii and have approximately the same magnitude.

The three complexes are luminescent in the solid state at room temperature and at 77 K or in frozen solutions of dichloromethane or acetone. The optical behavior in frozen solution is similar for the three complexes and also similar to that of the precursor gold derivatives [AuR(tht)], but not in the solid state. The differences in this state are attributed to the different number and types of metal-metal interactions present in each complex. In agreement with this assumption,

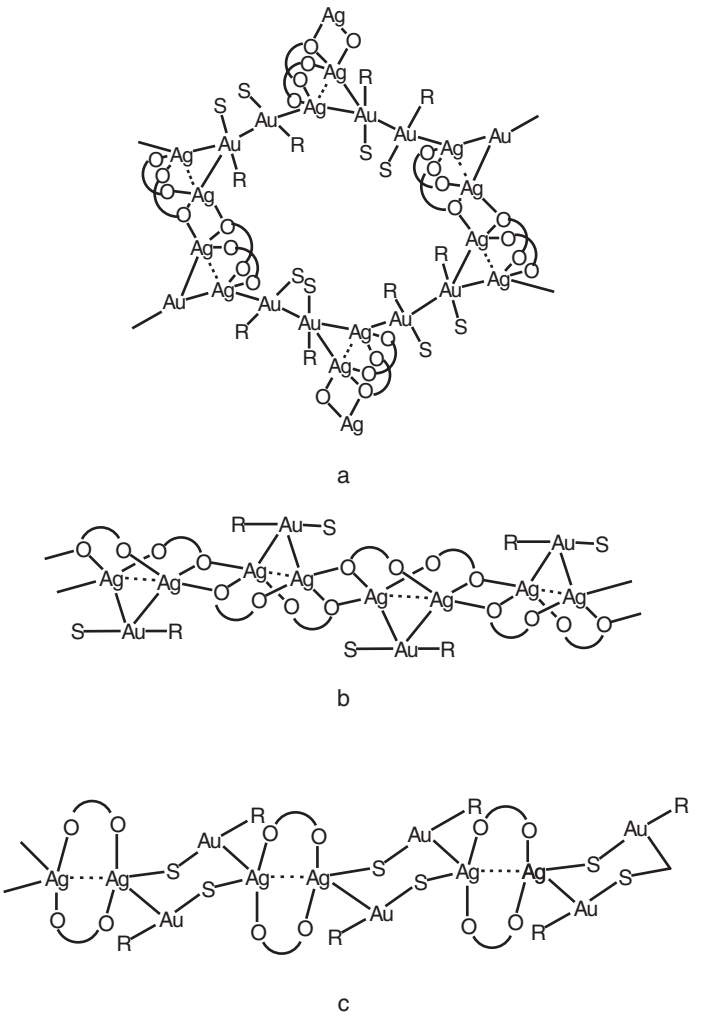

FIGURE 10. The polymeric structures of (a) $[AgAu(C_6F_5)(CF_3CO_2)(tht)]_n$, (b) $[Ag_2Au(3,5\text{-}C_6Cl_2F_3)(CF_3CO_2)(tht)]_n$, (c) and $[AgAu(C_6Cl_5)(CF_3CO_2)(tht)]_n$.

the complexes do not show luminescence in fluid solutions at room temperature, where the metal-metal interactions are not present. Thus, for instance, at 77 K, the pentafluorphenyl derivative shows two emissions at 430 and 480 nm, which are not observed in the case of the other perhalophenyl complexes, which show emissions at 590 and 495 nm, respectively. All of the emissions show lifetimes in the microsecond range, suggesting phosphorescent processes. The DFT calculations carried out for the $C_6Cl_2F_3$- and C_6Cl_5-derivatives indicate that the highest occupied molecular orbitals (HOMOs) are placed at the perhalophenyl groups with some contribution of the gold centers, while the lowest unoccupied

molecular orbitals are mainly located at gold and silver centers. Therefore, a ligand metal to metal charge transfer (LMMCT) is suggested.

Finally, the two emissions observed for the pentafluorophenyl complex are assigned to the different types of metal-metal interactions present in the complex: gold-gold and gold-silver. In this case, the DFT calculations suggested a cooperative contribution of both gold centers ($(C_6F_5)Au\cdots Au(C_6F_5)\rightarrow Ag$) and a charge transfer to the acidic silver (Fig. 11).

The same strategy was also used in the Fackler's laboratory employing the trinuclear complex $[Au(\mu\text{-}C^2,N^3\text{-bzim})]_3$ (bzim = benzylimidazolate) (Fig. 12). This gold complex is able to react, for example, with acid silver

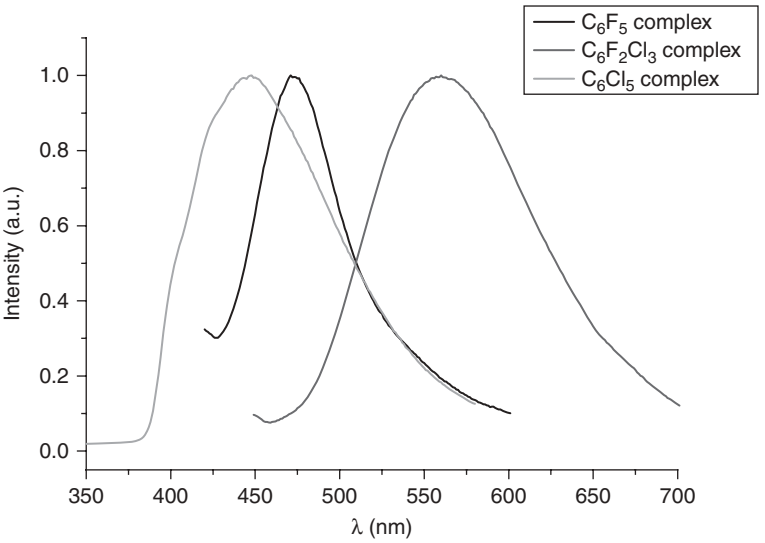

FIGURE 11. Emission spectra of $[AgAu(C_6F_5)(CF_3CO_2)(tht)]_n$, $[Ag_2Au(3,5\text{-}C_6Cl_2F_3)(CF_3CO_2)(tht)]_n$, and $[AgAu(C_6Cl_5)(CF_3CO_2)(tht)]_n$.

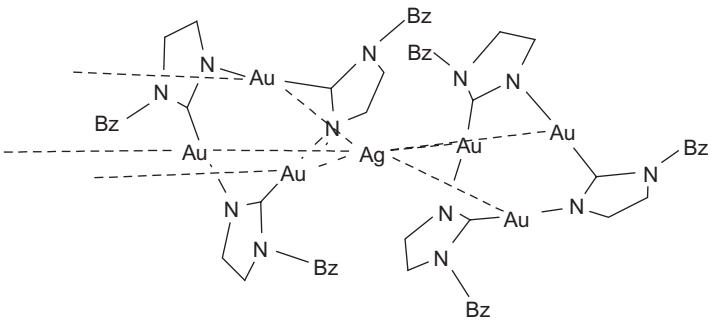

FIGURE 12. $\{Ag([Au(\mu\text{-}C^2,N^3\text{-bzim})]_3)_2\}_n$.

salts.[43,44] Thus its reaction with $AgBF_4$ leads to a luminescent complex that shows a structure in which each silver atom is bonded to two nine-membered rings of bzim to form sandwich units. The Au-Ag distances range from 2.731(2) to 2.922(2) Å, indicating relatively strong metal-metal bonding, and the Au_3AgAu_3 prisms interact through gold-gold interactions (average distance of 3.19 Å) between molecular units forming a chain.

This complex shows low energy visible emission at room temperature (535 nm), changing to an orange glow ($\lambda_{max} \sim 570$ nm at 77 K), with lifetimes of 115 and 550 ns at room temperature that change to 200 and 1100 ns at 77 K, which is attributed to phosphorescence. This low-energy phosphorescent emission is consistent with the extended-chain structure observed and assigned to an excited state that is delocalized along the crystallographic axis of the chain. The sift to red with decreasing temperature is in agreement with a thermal contraction that leads to a reduction of the intermolecular distances and to a reduction of the band gap energy.

III. LUMINESCENT GOLD-COPPER DERIVATIVES

The number of gold-copper supramolecular systems is very low, and the starting point to achieve their synthesis was the gold-silver complex $[Au_2Ag_2(C_6F_5)_4(MeCN)_2]_n$. The reaction of this material with CuCl in acetonitrile leads to $[Au_2Cu_2(C_6F_5)_4(MeCN)_2]_n$.[41] Both of them consist of extended linear chains formed by tetranuclear Au_2Ag_2 or Au_2Cu_2 units joined through gold-gold interactions, structures with a similar characteristics of the tetranuclear gold-silver compound $[Au_2Ag_2(C_6F_5)_4(Me_2C{=}O)_2]_n$, described previously.[38] It is interesting that the copper and the silver derivatives are isostructural, and the comparison between them allows us to conclude that it is the influence of the heterometal in the structure and hence in the optical properties of both complexes.

For example, similar to the other tetranuclear gold-silver complexes discussed, an important bonding interaction between the gold centers of different tetranuclear units (2.8807(4) Å for the gold-silver derivative and 2.9129 (3) Å for the gold-copper one) appears. Nevertheless, as expected in accordance with the relativistic effects for both metals, the gold-silver distances are 2.7577 (5) and 2.7267(5) Å, while the gold-copper ones are 2.5741(6) and 2.5876(5) Å, which suggests a stronger bonding interaction in the silver derivative than in the copper one. In addition, there is a silver-silver interaction of 3.1084(10) Å, but the copper-copper distance (3.0197(11) Å) is more than twice the copper Van der Waals radius.

Both complexes emitt in solid state at room temperature: 547 nm (max. exc. 397) for the silver complex, and 570 nm (max. exc. 366 nm) for the copper one (Fig. 13). The emissions shift to lower energies when the temperature is lowered to 77 K (567 nm and 594 nm, respectively), suggesting that the

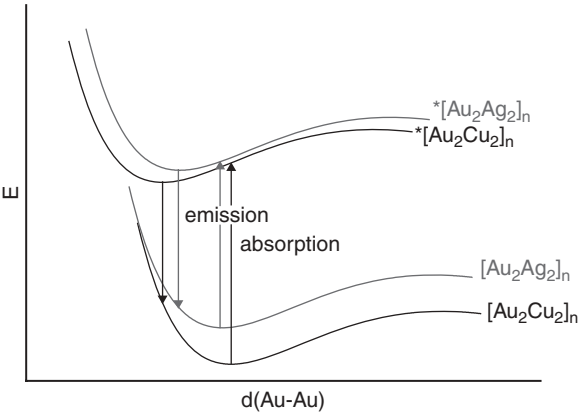

FIGURE 13. Proposed photophysical model for the $[Au_2M_2(C_6F_5)_4(MeCN)_2]_n$ (M=Ag, Cu) complexes.

thermal contraction influence the orbitals responsible for the emissions. As in the other related complexes, their lifetimes in the nanoseconds range suggest fluorescence.

The complexes loose their emissive properties in solution, which is interpreted in terms of the rupture of the metal-metal interactions. Nevertheless, the evaporation of the solvent regenerates their original emissive properties. This situation is not observed in glassy solutions at 77 K because, whereas the gold-silver complex shows three concentration-dependent emission bands at 470, 501, and 540 nm, (explained by the presence of oligomers of different length in solution as a function of the concentration), the gold-copper complex is not luminescent. The last observation is justified as a quench of the emission by formation of exciplexes with solvents of donor characteristics. In fact, when the measurement is carried out in CH_2Cl_2 or toluene at 77 K, the quench is not produced, and the complex shows luminescence.

Finally, the time-dependent DFT calculations agreed with the experimental results, showing that the transition responsible for the luminescent behavior is that from an antibonding occupied orbital, mainly centered in the gold interacting atoms with a contribution from the heterometals, to a bonding virtual orbital located between the gold and the silver (or copper) centers.

When the previous reaction is carried out in the same solvent (acetonitrile) with the addition of one equivalent of pyrimidine, the polymeric species $[CuAu(C_6F_5)_2(MeCN)(\mu_2\text{-}C_4H_4N_2)]_n$ is obtained in high yield.[45] In this case, the chain of metals is different from the previous case, and polymerization is produced by covalent copper-pyrimidine bonds with pairs of gold-copper interactions (2.8216(6) Å). The environment of the copper centers is tetrahedral, with one acetonitrile molecule occupying the fourth position (Fig. 14).

This complex is luminescent in the solid state at 525 nm (exc. 390 nm) at room temperature, and at 529 nm (exc. 371 nm) at 77 K. The lifetime, 10 μs, suggests a phosphorescent process. It is interesting that, in solution, its

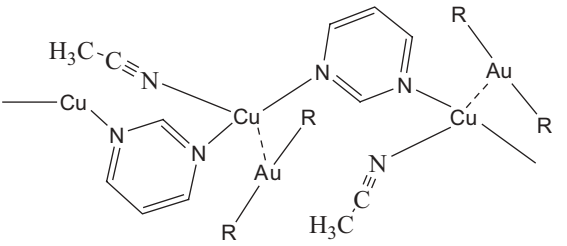

FIGURE 14. The polymeric complex $[CuAu(C_6F_5)_2(MeCN)(\mu_2\text{-}C_4H_4N_2)]_n$.

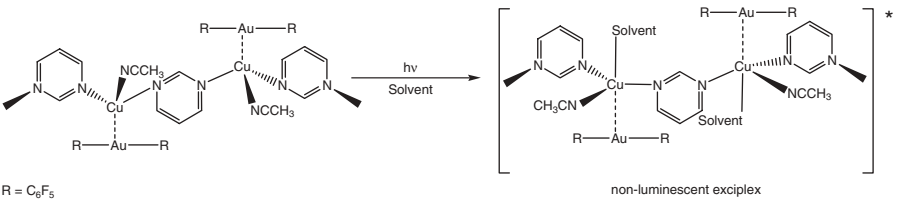

SCHEME 2. Quenching mechanism of complex $[CuAu(C_6F_5)_2(MeCN)(\mu_2\text{-}C_4H_4N_2)]_n$ in donor solvents.

luminescence shows a solvent dependence. Thus, while the high energy emissions ($\sim$360 nm) that are observed in MeOH or in CH_3CN are assigned to intraligand transitions in the pyrimidine ligand, in CH_2Cl_2 a dual emission at 394 (exc. 263 nm) and 530 (exc. 369 nm) is observed. The low-energy emission is assigned to arise from a^3 (MLCT) excited state. The reason this emission is not observed in the other solvents is in agreement with an exciplex quenching mechanism where the copper centers coordinate nucleophiles, forming non-luminescent exciplexes trough an associative attack by the solvent (Scheme 2).

IV. LUMINESCENT GOLD-THALLIUM DERIVATIVES

As described above, among the several closed-shell metal ions that form luminescent supramolecular entities with gold, thallium(I) forms the most numerous examples. While aurophilic attractions can be considered the upper extreme of the metallophilic interactions (with values up to 46 kJ mol^{-1}), intermetallic contacts involving Tl(I) centers appear as the weakest ones (even $<$20 kJ mol^{-1}),[46] which is explained by the enhancement of the Au$\cdots$Au interactions and the weakening of the Van der Waals attractions between the s^2 metal atoms produced by the relativistic effects.[47] Nevertheless, the complexes in which this interaction appears are surprisingly stable, with additional electrostatic, packing forces, or the ligand architecture, responsible for this fact.

For instance, the strength of the Au(I)···Tl(I) contacts in extended linear chains with an average metal-metal separation of 3.03 Å is estimated at ~276 kJ mol^{-1}, of which 80% consists on ionic interaction.[48] Consequently, the rationalization of the bonding in these species still remains as a challenge for synthetic and theoretical chemists.

Another challenge is now to tune the emissive properties of these compounds, which implies the study of all the factors that modify them, such as the intemetallic distance, the coordination number and geometry around the metal centers—which in the case of Tl(I) is variable[49]—or the donor characteristics of the ligands.

Although there are luminescent gold-thallium complexes of different nuclearity, in this part we deal only with polymeric species containing Au···Tl contacts. Such complexes have been prepared following two different strategies:

1. The use of asymmetric bridging ligands, which permits a selective coordination of the different donor atoms to the metal centers and leads to supported gold-thallium interactions forced by the ligand.
2. Reactions between basic gold(I) complexes and acid thallium(I) salts, which give rise to supramolecular networks formed via acid-base stacking containing unsupported gold-thallium interactions.

A. Supramolecular Gold-Thallium Complexes with Bidentate Ligands

The first luminescent polymeric Au/Tl chain and the only example of this strategy, $[AuTl(MTP)_2]_n$ (MTP = μ-$CH_2P(S)Ph_2$), was reported by Fackler et al. in 1988.[50] It was obtained by reaction of Tl_2SO_4 with $PPN[Au(MTP)_2]$, which leads to the coordination of both sulfur atoms of the starting gold(I) complex to the thallium(I) center. The result is the formation of an eight-membered ring with the P,S-donor ligands doubly bridging the metal centers, which are located at a distance as short as 2.959(2) Å. The extended system appears as a result of the unidirectional polymerization of dinuclear units through unsupported Au···Tl interactions of 3.003(2) Å (Figure 15).

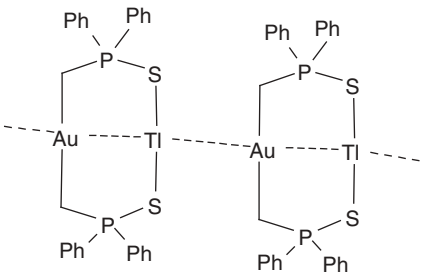

FIGURE 15. $[AuTl(MTP)_2]_n$.

Its absorption spectrum shows one band at 320 nm ($\varepsilon = 2900\ M^{-1}cm^{-1}$), assigned to the $\sigma_1^* \rightarrow \sigma_2$ transition localized in the Au-Tl moiety. The emission spectrum in the solid state at 77 K shows a band at 602 nm, which is attributable to a transition between orbitals that appear as a result of the metal-metal interaction. In this sense, Fenske-Hall molecular orbital calculations indicate that the ground state is the result of the mixing of the empty 6*s* and 6*pz* orbitals of gold(I) with the filled 6*s* and the empty 6*pz* orbitals of thallium(I). In frozen solution, this derivative shows a shift of the emission to 536 nm, which has been explained by a higher aggregation of $[AuTl(MTP)_2]$ units in the solid state if compared to the situation in solution.

B. Supramolecular Gold-Thallium Complexes through Acid-Base Reactions

A specially productive method for preparing extended heteronuclear systems through metallophilic interactions is the acid-base process, in which basic gold(I) precursors react with metallic Lewis acids forming supramolecular networks via acid-base stacking. The cation/anion interactions assist the formation of extended chains.

For instance, take the case of the gold−thallium complex $Tl[Au(CN)_2]$,[51] by reaction of $TlNO_3$ and $K[Au(CN)_2] \cdot 2H_2O$ in the early 1990s and studied by Patterson et al. This group carried out a pioneering study of the luminescence properties of this complex and their theoretical interpretations. The structural data reported showed two thallium-gold interactions of 3.474 and 3.491 Å in one of the three crystallographically distinct Au sites in the crystal, with the rest of Au-Tl distances being longer than the sum of their Van der Waals radii (3.62 Å).

It is interesting that the emission of the complex is thermochromic and thus the temperature influences emission energies and lifetimes. For instance, two bands at 575 and 518 nm appear at 5 K, but at 300 K the former disappear when temperature increases. This was attributed to luminescent traps. In contrast, the most energetic band shifts to blue under the same conditions; it appears at 509 at 40 K and at 483 nm at 360 K.

Similarly, the dependence of lifetime on temperature is also very pronounced, changing from 176 μs at 1.7 K to about 50 ns at 400 K. The analyses of the theoretical calculations indicated that the composition of the HOMO remained the same, independent of the Au-Tl distance since it had a 60% gold and 25% CN^- character. The LUMO has mostly a CN^- character, with a small contribution of $Tl(6p_z)$ and gold, with a greater contribution of the thallium orbital when the distance diminishes. The authors concluded that the absorptions and emissions result from the gold−thallium interactions, influencing the energies, intensities and rates of deactivation because the homologous $Cs[Au(CN)_2]$,[52] which contained only Au-Au interactions, did not exhibit similar optical behavior.

The first contribution of our group to this field of research was the synthesis of the complex $[AuTl(C_6F_5)_2(OPPh_3)_2]_n$ in 1998, which represents

the first extended unsupported gold-thallium polymer.[53] It was prepared by reaction between triphenylphosphine oxide, thallium nitrate and lithium bis (pentafluorophenyl)aurate(I) as represented in equation 1.

$$2\ OPPh_3 + TlNO_3 + Li[Au(C_6F_5)_2] \rightarrow [AuTl(C_6F_5)_2(OPPh_3)_2]$$

This complex consists of an extended unsupported linear chain of alternate gold and thallium centers at distances of 3.0358(8) and 3.0862(8) Å. Taking into account the stereochemically active inert pair of thallium(I), the environment can be described as pseudo-trigonal-bipyramidal. As described below, the environment around thallium is one of the main factors that affects the optical properties of these mixed systems.

This complex exhibits luminescence in the solid state at room temperature (494 nm) and at 77 K (494 and 530 nm), but it is not emissive in acetone solution, recovering its optical properties when the solvent is evaporated, suggesting that the emission is the result of the interactions between the metals. It is interesting that when the process of dissolution is carried out in a halogenated solvent and it is irradiated with UV light, the luminescence is quenched and the evaporation of the solvent gives rise to a luminescent uncharacterized grey solid. Nevertheless, if it is not irradiated, the original complex is recovered without any change. These facts allowed us to conclude (1) that the emission arises from interactions between the metals, (2) that the gold-thallium interactions are broken in dilute solutions, and (3) that the excited state reached by UV-radiation is able to react with halocarbons in an electron transfer reaction, perhaps making this product appropriate as an irreversible sensor for halocarbons.

When fluorine is replaced by chlorine in the gold precursor, the same reaction with the thallium salt and triphenylphosphine oxide in tetrahydrofuran or acetone leads to products of stoichiometry $\{[Tl(OPPh_3)][Tl(OPPh_3)L][Au(C_6Cl_5)_2]_2\}_n$ (L = THF, Me_2CO).[48] Their crystal structures also display extended linear chains with alternating metal centers in a zigzag disposition, with Au-Tl distances between 3.0529(3) and 3.3205(3) Å (L = tetrahydrofuran) or between 3.0937(3) and 3.2705(4) Å (L = acetone). It is interesting that in these cases the environments around the thallium atoms, considering the stereochemically active lone pair, are alternatively pseudotetrahedral and distorted trigonal-bipyramidal (Fig. 16).

Both complexes are not luminescent in solution but show a temperature-dependent strong luminescence in the solid state, displaying a single band at 497 nm (exc. 400 nm) for L = THF or at 501 nm (exc. 390 nm) for L = Me_2CO at room temperature. At 77 K, they show a site-selective excitation, and each displays two independent bands at 461 nm (exc. 330 nm) and 510 nm (exc. 412 nm) in the former and 465 nm (exc. 335 nm) and 526 nm (exc. 410 nm) in the latter. The first conclusion that can be drawn from the lack of luminescence in solution is that it seems

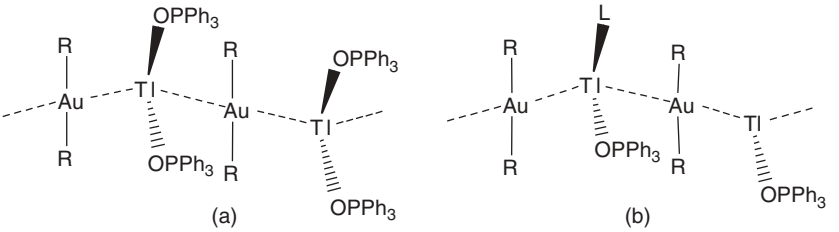

FIGURE 16. Linear chains showing the different environments at the thallium centers. (a) L = $OPPh_3$, R = C_6F_5; (b) L = $OPPh_3$, L′ = acetone or tetrahydrofuran, R = C_6Cl_5.

to indicate that the metal-metal interactions are no longer present in these conditions. Furthermore, the four different metal-metal distances in each complex do not seem to be responsible for the different emissions found in the solid state at room temperature and at 77 K because a more complicated pattern would be expected. Finally, the fact that in both complexes the pairs of excitation and emissions appear at similar energies allows us to conclude that the coordinating solvents do not significantly influence the excited states from which the emissions are produced.

Theoretical calculations helped to establish the nature of the intermetallic interaction as well as the origin of the excited states responsible for the emissions. As regards the former, ab-initio calculations revealed that the energy associated with the Au-Tl interaction reaches an impressive value of 275.7 kJ/mol, from which almost 20% is due to Van der Waals and 80% to ionic interactions. This result, far from being theoretically unusually indicates a very strong metallophilic interaction between both extremes of metallophilicity. In terms of the unusual optical behavior, the TD-DFT calculations revealed that, as observed experimentally, the excited states are not determined by the length of the gold-thallium interactions. Instead, what seemed likely was that those states are related to a charge transfer transition between the electron rich $\{Au(C_6Cl_5)_2\}^-$ units and the thallium atoms in different coordination modes, existing simultaneously in each complex. Thus the tetrahedral thallium atoms account for the low energy emissions and the trigonal-bipyramidal thallium centers, with very different gold thallium interactions (3.05 and 3.32 Å), accounting for the high energy ones. Therefore, the main conclusion that can be drawn from these studies is that the importance of the environment is greater than the metal-metal distances in gold-thallium extended systems. Similar conclusions were separately drawn by Che et al. for d^{10}-d^{10} metal complexes.[54–56]

The strong influence of the environment is also evident in the 1D, 2D and 3D supramolecular assemblies $\{[Tl(4,4'\text{-bipy})(THF)][AuR_2]\}_n$, $\{[Tl(1,10\text{-phen})][AuR_2]\}_n$, $\{[Tl(py)_2][AuR_2]\}_n$, and $\{[Tl(2,2'\text{-bipy})][AuR_2]\}_n$ (R = C_6F_5).[57] The crystal structures of all of them display an alternating arrangement of gold and thallium centers, exhibiting a wide range of metal-metal separations, even within the same complex. In spite of this situation, and as in the previous case, since all the Tl(I) centers display a similar environment in a given product, each

complex shows a single emission in the solid state both at room temperature and at 77 K.

Nevertheless, the environment around the metals and the metal-metal distances are not the only factors that influence the optical properties in such complex systems. For instance, the experimental conditions of the reaction may also condition the structure in many cases and, therefore, the luminescence of the product. For example, the reaction between the pentachlorophenyl derivative $[AuTlR_2]_n$ ($R = C_6Cl_5$) and 2,2′-bipyridine affords different two- and three-dimensional polymeric species, depending on the solvent employed in the reaction or the crystallization process; thus a series of complexes of stoichiometry $[AuTlR_2(2,2'\text{-bipy})_{0.5}]_n$, $[AuTlR_2(2,2'\text{-bipy})]_n$, $\{[Tl(2,2'\text{-bipy})][Tl(2,2'\text{-bipy})_{0.5}(THF)][AuR_2]_2\}_n$, $\{[Tl(2,2'\text{-bipy})][Tl(2,2'\text{-bipy})_{0.5}(THF)][AuR_2]_2 \cdot THF\}_n$ and $\{[AuTlR_2(2,2'\text{-bipy})] \cdot 0.5\text{toluene}\}_n$ were isolated and structurally characterized.[58] All of them contain 2,2′-bipyridine and/or solvent molecules coordinated to thallium, but crystals with different ratio of ligands appeared even within the same crystallization tube.

As commented above, different compositions lead to different emission energies, and these systems emit at 646, 609, 620, 606, and 683 nm, respectively, by excitation at $\sim$550 nm. Furthermore, there is no correspondence of the emissions with the gold-thallium lengths since all of them range from 2.9 to 3.1 Å or with the environment around the thallium centers. As a plausible explanation it was reported that each 2D or 3D network could probably lead to different excited states, and the formation of such networks might be influenced by the presence or absence of coordinating solvents in their structures.

The influence of the basic character of the gold precursor, which should affect the number of ancillary ligands bonded to thallium and hence the structure of the complex, was also analyzed by varying the nature of the aryl groups bonded to gold. The reaction of $NBu_4[AuR_2]$ ($R = C_6F_5$, C_6Cl_5) with $TlPF_6$ in the presence of 4,4′-bipyridine and in tetrahydrofuran leads to highly luminescent materials of stoichiometry $[Tl(bipy)]_2[Au(C_6F_5)_2]_2$ or $[Tl(bipy)][Tl(bipy)_{0.5}(thf)][Au(C_6Cl_5)_2]$, respectively.[59] The X-ray diffraction analyses shows tetrameric Tl-Au-Au-Tl units ($R = C_6F_5$) (Fig. 17a) or polymeric Tl-Au-Tl′-Au chains ($R = C_6Cl_5$) (Fig. 17b), which again display metal-metal distances shorter than the sum of their Van der Waals radii. The presence of bridging 4,4′-bipy ligands bonded to thallium atoms of different tetramers or polymers, respectively, results in two-dimensional polymers. While in the former, the layers are associated via Tl$\cdots$F contacts between different planes, in the latter, two polymeric layers are linked through additional bridging bipy molecules.

It is interesting that in contrast to other gold thallium chains, the pentafluorophenyl derivative (Fig. 17a) exhibits a nonalternating sequence of formal charges ($+\ -\ -\ +$), which is at variance with the classical Coulomb rules that would give a more stable ($+\ -\ +\ -$) arrangement.

As before, both materials display a strong fluorescence in the solid state both at room temperature and at 77 K, but not in solution, indicating that the metal-metal contacts are the responsible of the emissions. Nevertheless, the dependence of the emission on the temperature is different,

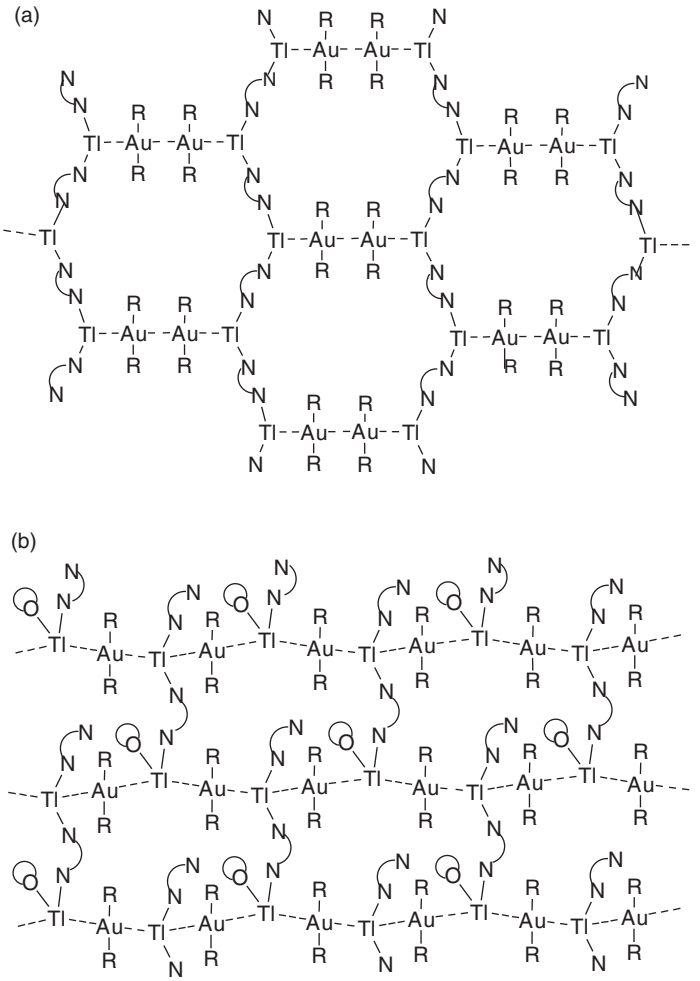

FIGURE 17. (a) The crystal structure of $\{[Tl(bipy)]_2[Au(C_6F_5)_2]_2\}_n$. (b) The crystal structure of $\{[Tl(bipy)][Tl(bipy)_{0.5}(thf)][Au(C_6Cl_5)_2]\}_n$.

which is likely to be related to the different metal arrangements in both species. Thus, while the pentachlorophenyl derivative shows an usual shift to red (from 620 to 642 nm) when decreasing the temperature, in the case of the pentafluorophenyl complex this emission shifts to higher energies (from 525 to 507 nm). This blue shift has also been observed in other luminescent complexes[50,60] and has been explained as a substantial dependence of the emission maxima on environmental rigidity. TD-DFT calculations carried out for $\{[Tl(bipy)]_2[Au(C_6F_5)_2]_2\}_n$ show a good agreement between theoretical and experimental excitations (Fig. 18), and the analyses of these theoretical transitions indicate a LMMCT from an antibonding orbital of the

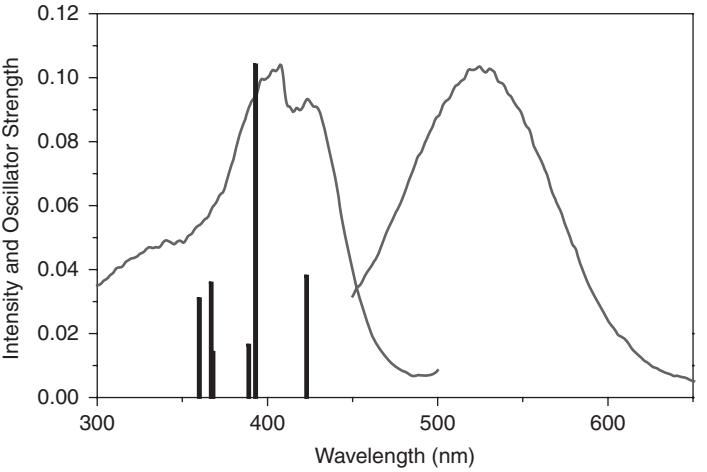

FIGURE 18. Corrected experimental excitation and emission spectra and theoretical oscillator strengths (*vertical lines*) for $\{[Tl(bipy)]_2[Au(C_6F_5)_2]_2\}_n$.

$[Au(C_6F_5)_2]^-$ groups to an antibonding orbital with the contribution of the four metallic centers.

The reaction between the one-dimensional polymer $[AuTlR_2]_n$ ($R = C_6F_5$, C_6Cl_5) and [Tl(acac)] is another example of the influence of the basicity of the gold precursor in the solid state structure of the resulting complex. This reaction leads to complexes with the stoichiometries $[AuTl_3(acac)_2(C_6F_5)_2]_n$ or $[AuTl_2(acac)(C_6Cl_5)_2]_n$,[61] whose crystal structures revealed a polymeric chain for the former or a two-dimensional network for the pentachlorophenyl derivative. They both contain $Tl_2(acac)_2$ units acting as connections between $[AuTl(C_6F_5)_2]$ units (Fig. 19a) or between $[AuTl(C_6Cl_5)_2]_n$ linear chains (Fig. 19b), respectively. Within the $Tl_2(acac)_2$ units each Tl(I) links four oxygen atoms of the two acetylacetonate groups. It is very interesting that, in addition to the expected Au···Tl interactions of 3.0963(7) and 3.2468(7) Å for the pentachlorophenyl derivative, and of 3.0653(4) Å for the pentafluorophenyl one, both of them display $Tl^I \cdots Tl^I$ contacts of 3.6774(11) Å in the former and between 3.6688(4) and 3.7607(4) Å in the latter.

Therefore, a new structural characteristic appears in these complexes, which has also consequences in their optical properties. As expected, both complexes are luminescent in the solid state at room temperature, showing a single band, but at 77 K they display two independent emissions at 463 and 588 nm for the pentachlorophenyl derivative and at 427 and 507 nm for pentafluorophenyl one. This last profile was repeated in glassy solutions at the same temperature (Fig. 20). In addition, and unlike the results found for other polymeric gold-thallium systems, the products exhibit luminescence in dilute solutions, showing similar profiles and energies (390 nm). The proposed origin for these high-energy emissions, which appear both in solution and in solid state at low temperature, are the $Tl_2(acac)_2$

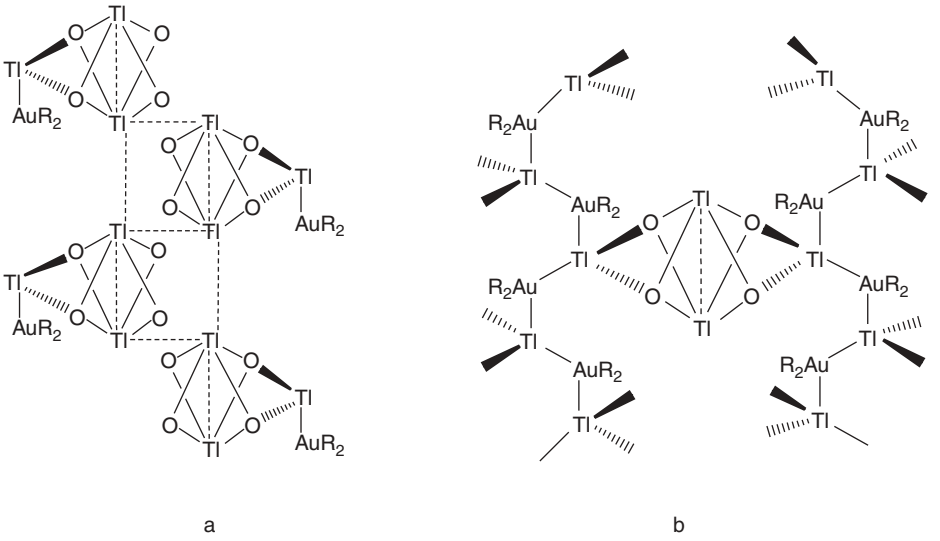

FIGURE 19. (a) $[AuTl_3(acac)_2(C_6F_5)_2]_n$. (b) $[AuTl_2(acac)(C_6Cl_5)_2]_n$.

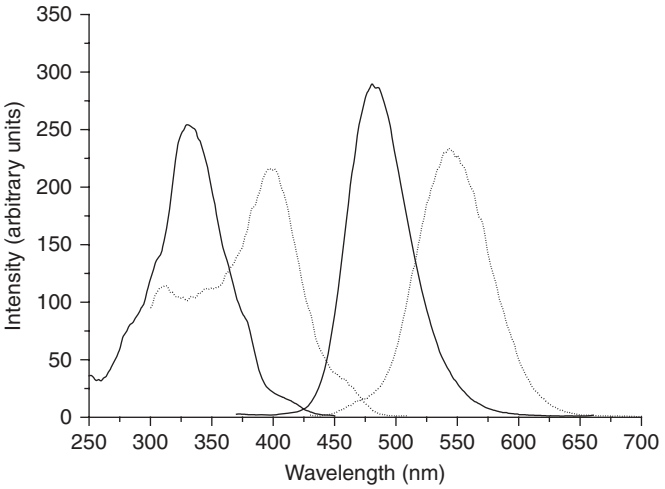

FIGURE 20. Glassy luminescence spectra of $[AuTl_2(acac)(C_6Cl_5)_2]_n$ at 77 K showing two pairs of independent excitation and emissions (*solid lines, dashed lines*).

units, which seem to remain even in solution. In fact, Tl(acac) showed a similar behavior, and in this case, TD-DFT calculations showed that the transitions arise from ligand-based (acac) orbitals to Tl-based molecular orbitals.

Another couple of related perhalophenyl compounds are obtained by reaction of the same gold starting materials $[AuTlR_2]_n$ ($R=C_6F_5$,

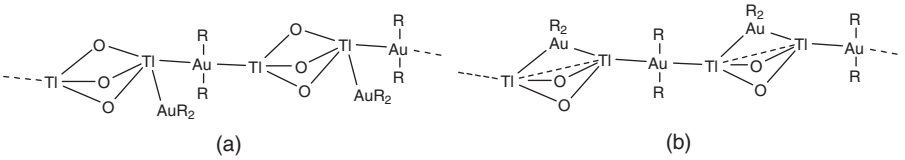

FIGURE 21. The crystal structures of (a) $[Tl_2\{Au(C_6F_5)_2\}_2\{\mu\text{-DMSO}\}_3]_n$ and (b) $[Tl_2\{Au(C_6Cl_5)_2\}_2\{\mu\text{-DMSO}\}_2]_n$.

C_6Cl_5) with dimethylsulfoxide (DMSO), which leads to the synthesis of $[Tl_2\{Au(C_6F_5)_2\}_2\{\mu\text{-DMSO}\}_3]_n$ or $[Tl_2\{Au(C_6Cl_5)_2\}_2\{\mu\text{-DMSO}\}_2]_n$, respectively.[62] The crystal structure of the complex with fluorine shows a monodimensional polymer formed by repetition of $[Au\cdots Tl(\mu\text{-}O{=}SMe_2)_3Tl]$ units, with gold-thallium interactions of 3.2225(6)-3.5182(8), while the pentachlorophenyl derivative contains two bridging DMSO molecules and an additional $[Au(C_6Cl_5)_2]^-$ anion. In addition, a thallium-thallium interaction of 3.7562(6) Å appears in the latter (Fig. 21).

Similar to the results observed in previous cases, the structural differences affect the optical properties of the complexes. While in the former, a single emission is observed in the solid state, both at room temperature (440 nm, exc. 390 nm) and at 77 K (460 nm, exc. 360 nm); the latter shows one band (510 nm, exc. 450 nm) and one shoulder (560 nm) at room temperature and two independent emissions (510 nm, exc. 370 nm; 550 nm, exc. 480 nm) at 77 K. Furthermore, the C_6Cl_5 derivative is also luminescent in solution, displaying a band at 530 nm (exc. 345 nm), which is not present in the precursor complexes or in the pentafluorophenyl derivative. This fact indicates, as in the previous case, that the Tl-Tl interaction present in the solid state remains even in solution and is the responsible for the luminescence observed in this state.

The reactions discussed above, which afford polymeric Au/Tl systems, highlight the role of bis(perhalophenyl)aurate anions as electron density donors to thallium(I) and can be considered Lewis neutralizations. In such reactions, the thallium centers incorporate additional electron donor molecules to their coordination sphere, which sometimes includes the solvent employed in the reaction. Therefore, one could think that bis(perhalophenyl)aurates themselves could act as the only electrons source—that is, they could behave as metalloligands giving rise to anionic instead of neutral polymers. Indeed, the heteropolynuclear complexes $[AuTlR_2]_n$ (R = 3,5-$C_6Cl_2F_3$, C_6Cl_5) react with $NBu_4[AuR_2]$, leading to the first anionic heteropolymetallic chains with the stoichiometries $\{NBu_4[Tl_2\{Au(C_6Cl_5)_2\}\{\mu\text{-}Au(C_6Cl_5)_2\}_2]\}_n$, $\{NBu_4[Tl\{Au(3,5\text{-}C_6Cl_2F_3)_2\}\{\mu\text{-}Au(C_6Cl_2F_3)_2\}]\}_n$ or $\{NBu_4[Tl\{Au(C_6Cl_5)_2\}\{\mu\text{-}Au(3,5\text{-}C_6Cl_2F_3)_2\}]\}_n$, which have incorporated a half (in the former) or one (in the two latter) additional gold center per thallium, as shown in Figure 22.[63]

The gold-thallium interactions in these complexes are of approximately the same strength, because that they show no dependence on the behavior of the $[AuR2]^-$ fragments as angular or linear bridges in the former or as linear

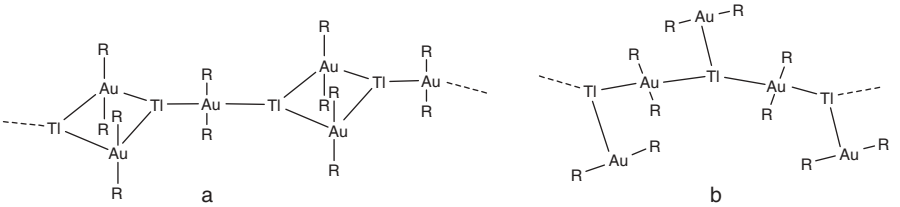

FIGURE 22. The crystal structures of (a) $\{NBu_4[Tl_2\{Au(C_6Cl_5)_2\}\{\mu\text{-}Au(C_6Cl_5)_2\}_2]\}_n$ and (b) $\{NBu_4[Tl\{Au(3,5\text{-}C_6Cl_2F_3)_2\}\{\mu\text{-}Au(C_6Cl_2F_3)_2\}]\}_n$ and $\{NBu_4[Tl\{Au(C_6Cl_5)_2\}\{\mu\text{-}Au(3,5\text{-}C_6Cl_2F_3)_2\}]\}_n$.

bridging or terminal metallo ligands in the two latter. Therefore, the Au-Tl lengths seem not to be responsible for their different optical properties. Instead, the emissions are probably influenced by the number and type of Au···Tl interactions, as well as by the aryl groups bonded to gold. In the solid state each complex displays two emissions at low temperature: 560 and 612 nm for $\{NBu_4[Tl_2\{Au(C_6Cl_5)_2\}\{\mu\text{-}Au(C_6Cl_5)_2\}_2]\}_n$, 470 and 520 nm for $\{NBu_4[Tl\{Au(3,5\text{-}C_6Cl_2F_3)_2\}\{\mu\text{-}Au(C_6Cl_2F_3)_2\}]\}_n$, and 580 and 620 nm for $\{NBu_4[Tl\{Au(C_6Cl_5)_2\}\{\mu\text{-}Au(3,5\text{-}C_6Cl_2F_3)_2\}]\}_n$, which are probably related to the presence of a different type of metal-metal interaction. The high-energy bands can be assigned to excited states arising from the new Au-Tl interactions formed by the addition of $[AuR_2]^-$ groups to the extended chains, while the low-energy emissions are likely assigned to delocalized excitons along the main axis. The difference between the isostructural complexes $\{NBu_4[Tl\{Au(3,5\text{-}C_6Cl_2F_3)_2\}\{\mu\text{-}Au(C_6Cl_2F_3)_2\}]\}_n$ and $\{NBu_4[Tl\{Au(C_6Cl_5)_2\}\{\mu\text{-}Au(3,5\text{-}C_6Cl_2F_3)_2\}]\}_n$ could be related to the different aryl groups present in each complex. As expected, none of these complexes is luminescent in solution at room temperature, again confirming that the metal-metal interactions are the origin of the emissive behavior, and a mixture of MMCT and LMCT is proposed to be the origin of these emissions.

An extension of this work was the attempt of preparing extended linear chains using the acid-base synthetic strategy but in the absence of ligands that could affect the atom environments, which, as we have seen, greatly affects the luminescence. This allowed us to know another essential factor in the synthesis of unsupported gold-thallium complexes: the solvent used in the process, which affects the final structure and hence the optical properties of the materials prepared. Thus, for instance, the reaction between $NBu_4[Au(C_6Cl_5)_2]$ and $TlPF_6$ in acetone leads to the tetranuclear complex $[Au_2Tl_2(C_6Cl_5)_4]\cdot$ acetone,[64] while the same reaction in tetrahydrofuran affords the polymeric $[AuTl(C_6Cl_5)_2]_n$.[65] It is surprising that the latter does not contain THF molecules bonded to the thallium centers, instead, its crystal structure consists of a perfectly linear chain (180°) that runs parallel to the crystallographic *z*-axis built via unsupported Au···Tl interactions of 3.0045(5) and 2.9726(5) Å (Fig. 23a). The unsaturated thallium atoms keep up to eight contacts with chlorine atoms

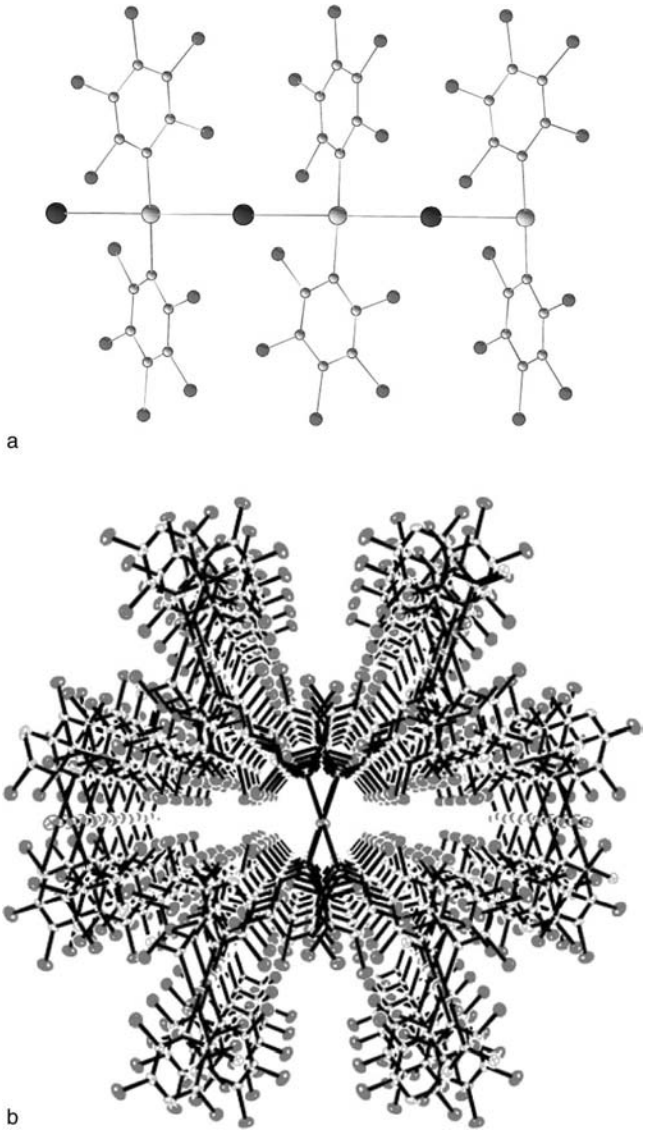

FIGURE 23. Crystal structure of (a) $[AuTl(C_6Cl_5)_2]_n$ and (b) packing viewed down the crystallographic z axis.

of adjacent chains, which contribute to the stability of the system and leads to a 3D structure containing holes parallel to the z-axis of $\sim$10 Å (Fig. 23b).

The solid shows a strong luminescence in the solid state at room temperature and at 77 K, but not in solution, where the interactions between the metal centers no longer exist, as in other extended systems discussed. It is

interesting that the emission at room temperature depends on the particle size, which is interpreted in terms of a certain degree of semiconductivity in the complex. In fact, SEM images taken of the solid without coating with a conductor appear clear, suggesting that the material is not an insulator.

On the other hand, perhaps the most striking characteristic of this material is its ability to act as a VOC sensor; thus the thallium-chlorine contacts between neighboring chains can be easily replaced by stronger bonds with donor molecules, which occurs even with such molecules in the gas phase, changing its color and luminescence properties. In fact, it reacts with molecules of THF, tetrahydrothiophene (THT), acetylacetone (acacH), 2-fluorpyridine, NEt_3, py, CH_3CN, or acetone, producing very evident changes in color that are reversible when the sample is heated for a few minutes. This change is even greater under UV radiation, and for example, the emission of the complex without VOCs (531 nm) shifts when exposed to different vapors to 507 nm (THF), 567 nm (THT), 650 nm (acacH), 627 nm (2-Fpy), 511 nm (NEt_3), 646 nm (py), 513 nm (CH_3CN) or 532 nm (acetone), which is easily detectable to the human eye (Fig. 24). In addition, all of them shift to red when the measurements are carried out at 77 K.

The mechanism responsible for this unusual behavior is interpreted based on the information obtained from the products prepared through conventional reactions between the starting materials in solution. Thus, comparison of the structure and the optical properties of the materials formed with the vapors with the products obtained in solution from the reaction of $[AuTl(C_6Cl_5)_2]_n$ with the same ligands, leads us to conclude that the vapor molecules penetrate through the tunnels into the structure, bind to some of the thallium centers and produce a variation of the Au-Tl distances. Therefore, different band gaps result in different emissions. Reversibility is achieved because the molecules do not interact with the whole of the thallium centers but with some of them, thus preventing the supramolecular structure from collapsing. It is important to note that if all the thallium atoms were involved in the bonds with the vapor

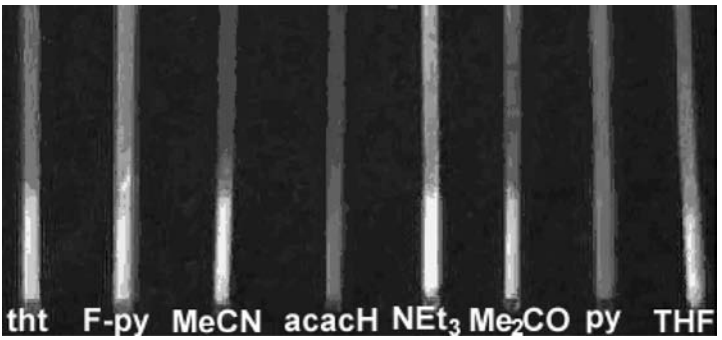

FIGURE 24. Color changes of $[AuTl(C_6Cl_5)_2]_n$ with vapors of donor molecules under UV light.

molecules, the contacts between different chains would have disappeared, together with the holes, and the reaction would have been irreversible.

Another possible practical application of this heteropolynuclear system in organic synthesis was recently reported in a study of the gold-thallium interaction as an assistant in the synthesis of imines.[66] Treatment of $[AuTlR_2(en)]_n$ ($R = C_6Cl_5$, C_6F_5) with ketones (even in the gas phase) leads to the rapid conversion of ehtylenediamine into imine or diimine, with loss of water. Thus its reaction with acetone or phenylmethylcetone affords $[AuTlR_2\{(CH_3)_2C{=}N(CH_2)_2NH_2\}]_n$, $[AuTlR_2\{((CH_3)_2C{=}N)_2(CH_2)_2\}]_n$, or $[AuTlR_2\{((PhCH_3)C{=}N)_2(CH_2)_2\}]_n$.

The importance of the metal-metal contacts in these reactions is confirmed when ethylenediamine is treated with the same ketones in the absence of one of the metals, a process from which the starting materials are recovered unaltered; neither imine nor diimine can be prepared under these conditions. In this sense, it is interesting to note that the methods previously reported for the synthesis of imines always require high temperatures, prolonged reaction periods, and the presence of dehydrating agents. In contrast, the reaction between $[AuTlR_2(en)]_n$ and the ketones takes place even in the gas phase and in a few seconds.

As an example, Figure 25 shows the step-by-step transformation of $[AuTl(C_6F_5)(en)]_n$ subjected to acetone vapors. As shown in the figure, both the starting material and the imine derivative are strongly luminescent under UV light. The starting ethylenediamine products display emissions at 515 or 505 nm for the pentachloro- or pentafluoro-phenyl complexes, respectively, while the resulting products of their reactions with ketones shift the emissions to 670 or 625 nm for $[AuTlR_2\{(CH_3)_2C{=}N(CH_2)_2NH_2\}]_n$ (C_6Cl_5 or C_6F_5, respectively), 640 or 675 nm

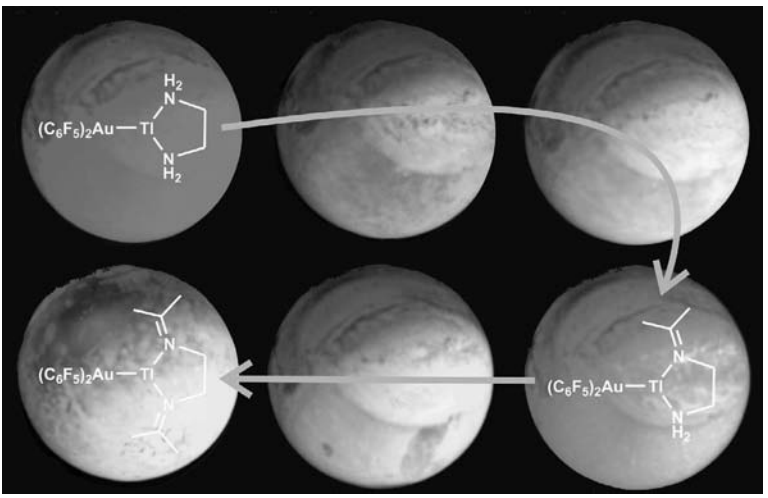

FIGURE 25. Conversion of $[AuTl(C_6F_5)_2(en)]_n$ by exposure to vapors of acetone under UV light.

for $[AuTlR_2\{((CH_3)_2C{=}N)_2(CH_2)_2\}]_n$, and 560 or 575 nm for $[AuTlR_2\{((PhCH_3)C{=}N)_2(CH_2)_2\}]_n$. None of the complexes exhibits luminescence in solution; consequently, the excited states that origin the emissions are likely to be similar to those described for other polymetallic chains with similar donor centers, that is, delocalized excitons along the chains influenced by the coordination environment of thallium. Furthermore, this explanation is consistent with the shift of the emission maximum to lower energies observed when $[AuTl(C_6Cl_5)_2(en)]$, whose crystal structure shows discrete dinuclear molecules with an unique Au···Tl contact of 3.1 Å (intermolecular Au-Tl distance 4.04 Å), is transformed in any of the imine polymeric complexes.

Finally, and also following the acid-base strategy that we discussed in the case of the gold-silver complex, Fackler, Burini, and co-workers reported in 2000 the reaction of $[Au(\mu\text{-}C^2,N^3\text{-bzim})]_3$ (bzim=1-benzylimidazolate) or $[Au(\mu\text{-}C(OMe){=}NCH_3)]_3$ with the acid cation Tl^+, which afford a series of sandwich derivatives formed by interaction of the π-base gold(I) complexes. These complexes, of stoichiometry $[Tl\{[Au(\mu\text{-}N^3,C^2\text{-bzim})]_3\}_2]^+$ or $[Tl\{[Au(\mu\text{-}C(OEt){=}NC_6H_4CH_3)]_3\}_2]^+$, contain $[Au_3TlAu_3]$ units (Fig. 26), whose polymerization through gold-gold interactions leads to infinite chains [44].

The thallium ion center is bonded to six gold atoms, forming a distorted trigonal prism. The gold-thallium distances range from 2.9711(7) to 3.0448(7) Å in $[Tl\{[Au(\mu\text{-}N^3,C^2\text{-bzim})]_3\}_2]^+$ and from 3.0673(4) to 3.1075(4) Å in $[Tl\{[Au(\mu\text{-}C(OEt){=}NC_6H_4CH_3)]_3\}_2]PF_6$. These units polymerize by gold-gold interactions from 3.0525(4) to 3.1089(7) Å in both complexes.

The emission spectra of these compounds display low-energy phosphorescence exhibiting thermochromism (red shifts) when cooling the crystals to 77K. The authors assigned the observed luminescence from excited states delocalized along the crystallographic axis of the chain. This is in agreement with the observed thermochromism since the cooling produces a thermal contraction and, consequently, a reduction in the intermolecular metal-metal distances along the chain reducing the band gap energy. In addition, complex $[Tl\{[Au(\mu\text{-}N^3,C^2\text{-bzim})]_3\}_2]^+$ depended on the excitation

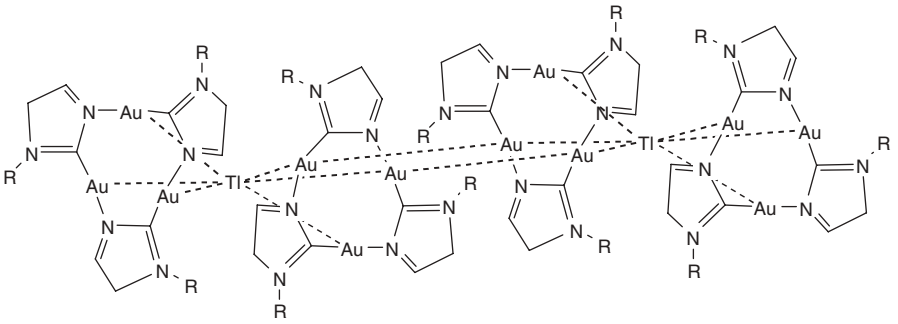

FIGURE 26. The structure of $[Tl\{[Au(\mu\text{-}N^3,C^2\text{-bzim})]_3\}_2]^+$.

wavelength. For instance, at 77 K a strong green emission is observed upon excitation with 420 nm, whereas a yellow emission is seen upon excitation with 475 nm. The authors attribute this behavior to the presence of two electronically uncoupled luminescent sites.

V. LUMINESCENT GOLD-LEAD DERIVATIVES

As far as we know, the only example of a supramolecular gold-lead complex described that exhibits luminescence was reported by Fackler's laboratory in 1989.

Similar to what happened with the commented MTP gold-thallium dinuclear system, in this case, the extended system appears as a result of the polymerization in one direction, but, in this case, of trinuclear units through metal-metal interactions. This compound is prepared by reaction of the gold precursor [PPN][$Au(MTP)_2$] with $Pb(NO_3)_2$ in a 2:1 molar ratio, which leads to $[Au_2Pb(MTP)_4]_n$.[50b] This gold-lead derivative consists of an extended linear chain formed by the interactions between trinuclear units through the gold centers (Fig. 27). The gold-lead distances within the trinuclear unit are 2.896(1) and 2.963(2) Å. The intermolecular distance between the gold centers is 3.149(2) Å.

The absorption spectrum of the gold-lead complex shows two bands at 290 nm ($\varepsilon = 28598\ M^{-1}cm^{-1}$) and 385 nm ($\varepsilon = 7626\ M^{-1}cm^{-1}$), while the emission spectrum in the solid state shows only one band at 752 nm at room temperature. It was assigned to a transition between orbitals that appear as a result of the gold-lead interaction. Thus Fenske-Hall molecular orbital calculations indicated that the HOMO is constituted from the 6*pz* orbital of gold and 6*s* orbital of lead and the LUMO is entirely constituted from the 6*pz* orbitals of these atoms.

The behavior of this complex in solution is interesting since its emission spectrum shows a strong dependence on the aggregation state and temperature. Thus the emission band in THF solution, which appears at 555 nm (298 K) ($\tau = 57$ ns), is shifted to 480 nm in frozen solution ($\tau = 2.3\ \mu s$) or appears at 752

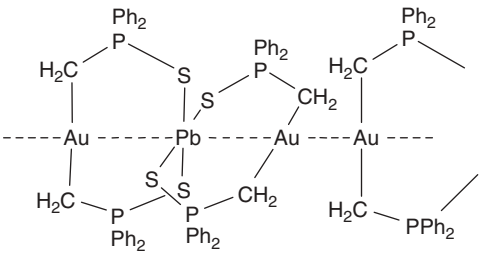

FIGURE 27. A portion of the structure of complex $[Au_2Pb(MTP)_4]_n$.

nm in the solid state (τ = 22 ns). The observed shift to high energy in THF solution may be related to the break of the polymeric structure of the complex in solution, in contrast to what happens in the solid state. A similar result was obtained in the case of the related $[AuTl(MTP)_2]_n$, which shows a shift to low energy in solid state if compared to the situation in solution.

VI. LUMINESCENT GOLD-PLATINUM DERIVATIVES

As far as we are aware, the number of luminescent extended systems with gold-platinum interactions is reduced to only one report. This is a puzzling situation since the situation of platinum in the periodic table suggests considerable relativistic effects for this atom and extended chains of squared-planar Pt(II) cation-anion complexes built by metal-metal interactions are not strange. In fact, salts such as $\{[Pt(CNR)_4][Pt(CN)_4]\}_n$,[67] which are luminescent and display vapochromic behavior, and the modified form of the Magnus salt $\{[Pt(NH_3)_4][Pt(CN)_4]\}_n$,[68] which shows semiconducting properties, are examples of this type of supramolecular systems. Therefore, the stable combination of gold and platinum in cation/anion-acid/base systems should be anticipated.

The report from Balch's laboratory describes the synthesis of the complex $[Pt(NH_3)_4][Au(CN)_2]$ $1.5(H_2O)$.[69a] Its structure displays two $[Au(CN)_2]$ ions above and bellow the plane of one $[Pt(NH_3)_4]^{2+}$ cation, with Pt···Au interactions of 3.2804(4) and 3.2794(4) Å. These units are arranged into extended chains through short gold-gold interactions of 3.1902(4) Å. Additional cross-linking of these chains occur through Au···Au contacts of similar lengths.

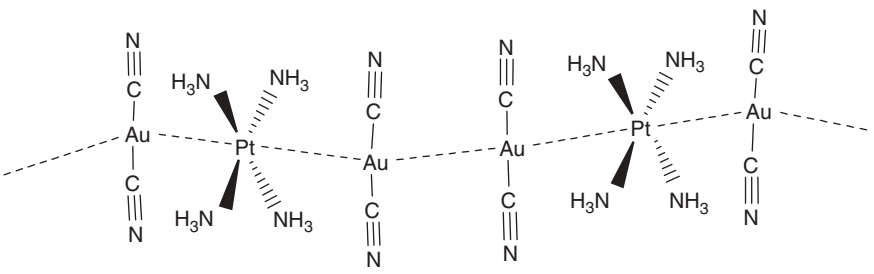

The complex is nonluminescent at room temperature, but becomes luminescent in the solid state upon cooling at 77 K, showing an unstructured emission at 443 nm. This emission is independent of the excitation wavelength over the range 300−370 nm, and it is attributed to the gold centers or to the interaction between the gold and the platinum ions. In agreement with this, the isostructural product $[Pt(NH_3)_4][Ag(CN)_2] \cdot 1.4(H_2O)$ is not luminescent,

and similarly, the corresponding nickel complex $[Ni(NH_3)_2][Au(CN)_2]_2$, whose structure shows only gold-gold interactions (3.0830(5) Å), does not show luminescence at room temperature or at 77 K. Also, chains of alternating gold and platinum metals of the type $[Pt(L\text{-}L)_2][Au(CN)_2]$ (L-L=ethylenediamine, bipyridine)[69b] are not luminescent either.

VII. LUMINESCENT GOLD-MERCURY DERIVATIVES

Similar to silver or thallium, the trinuclear pirazolate complex $[Au(\mu\text{-}C^2,N^3\text{-bzim})]_3$ (bzim = benzylimidazolate) and the carbeniate $[AuC(O\text{-}R)=NR']_3$ (R = Et; R′ = $C_6H_4CH_3$) complexes can also lead to luminescent extended chains by reaction with acid trimer complex $[Hg(\text{-}C,C\text{-}C_6F_4)]_3$, leading to the hexanuclear complexes $\{[Hg(\text{-}C,C\text{-}C_6F_4\ ]_3([AuC(O\text{-}R)=NR']_3)_2\}_n$ or $\{[Hg(\text{-}C,C\text{-}C_6F_4]_3([Au(\mu\text{-}C^2,N^3\text{-bzim})]_3)_2\}_n$, where the repeating motif is the $Au_3Hg_3Au_3$ unit.[70] The Hg(II) atoms interact with the Au(I) atoms in adjacent rings, with Hg···Au distances of 3.24 and 3.27 Å, respectively. The DFT calculations revealed the electrostatic nature of the interactions between the mercury ring and the gold rings, with the former bearing the positive charge and the later the negative one.

All of these complexes display a strong visible luminescence under UV excitation, which is sensitive to the interaction of the gold atoms with the mercury centers. Thus in $\{[Hg(\text{-}C,C\text{-}C_6F_4\ ]_3([AuC(O\text{-}R)=NR']_3)_2\}_n$ and $\{[Hg(\mu\text{-}C,C\text{-}C_6F_4)_3([Au(\mu\text{-}C^2,N^3\text{-Rim})]_3)_2\}_n$ an increase of the intensity upon coordination of mercury to the starting gold materials was observed.

For example, the spectrum of the precursor gold carbeniate complex at 77 K shows a fluorescent blue emission with a vibronic structure. This has an average spacing of $(1.4\pm0.2)\cdot10^3$ cm^{-1}, corresponding to a progression in the ν (C=N) vibrational mode of the carbeniate ligand that also appears in the in the infrared spectrum at 1500 cm^{-1}. This vibronic pattern indicates that the orbital in the ground state has a strong C-N ligand character. By contrast, in the case of the imidazolate gold-mercury complex, a strong green luminescence appears at ambient temperature with vibronic progression, but it is less resolved than in the case of the precursor. The formation of the stacking adduct shifted the emission to the red, which indicates an increased metallophilic bonding in the ground and excited states as happened in the homologous complexes with thallium and silver commented in the previous sections.

VIII. CONCLUSION

As we have seen, in the last years it has been shown that gold is an element that allows the formation of supramolecular structures built through

metal-metal contacts not only between gold atoms (thanks to the well-known aurophilicity) but also between gold and other metals by promoting relativistic interactions with them that help the stability of the species. In fact, the relativistic effects reach a maximum in gold and increase these effects in the metal that interacts with it. Among the consequences of these interactions, the complexes usually show interesting luminescent properties. In spite of this, however, few examples have been reported. Clearly, this is a very promising area in which the design of strategies that lead to modifications in the number of types of interaction with different metals, the number of the ligands and the donor centers, the geometry of the coordination environments around the metals, the temperature, the metal-metal distances, and so on can determine not only the structural motifs but also the energy and type of emissions that can be observed. Certainly, more effort in this topic is needed and surely this will bring us advances in, for example, imaging technology, sensors, and light-emitting devices, areas that currently have an increasing demand of materials with this property.

IX. REFERENCES

1. (a) J. W. Hill, T. A. Lear, *J. Chem. Educ.,* **65,** *802* (1988). (b) J. D. Bradley, M. Brand, J. A. M. Loulie, *J. Chem. Educ.,* **61,** *634* (1984). (c) T. Tran, *Int. Sci. Rev.,* **17,** *356* (1992).
2. N. N. Greenwood, A. Earnshaw, *Chemistry of the Elements,* 2nd ed., Butterworth-Heinemann: Woburn, MA, *1173* (1997).
3. T. G. Spiro, *Prog. Inorg. Chem.,* **11,** *1* (1970).
4. P. Pyykkö, *Chem. Rev.,* **97,** *597* (1997).
5. P. Pyykkö, *Angew. Chem.,* **43,** *4412* (2004).
6. P. Pyykkö, *Inorg. Chim. Acta,* **358,** *4113* (2005).
7. H. Schmidbaur, ed., *Gold: Progress in Chemistry, Biochemistry and Technology,* John Wiley & Sons, Ltd., Chichester, 1999.
8. (a) P. Pyykkö, *Chem. Rev.,* **88,** *563* (1988). (b) P. Pyykkö, J. P. Desclaux, *Acc. Chem. Res.,* **12,** *276* (1979).
9. M. Bardají, A. Laguna, *J. Chem. Educ.,* **76,** *201* (1999).
10. (a) See, for example: H. H. Karsch, U. Schubert, *Z. Naturforsch.,* **37b,** *186* (1982). (b) T. Tsuda, S. Ohba, M. Takahashi, M. Ito, *Acta Crystallogr. C,* **45,** *887* (1989). (c) M. Jansen, *Angew Chem. Int. Ed. Engl.,* **26,** *1098* (1987).
11. See, for example: A. Heine, R. Herbst-Irmer, D. Stalke, *J. Chem. Soc. Chem. Commun.,* **1729 (**1993).
12. See, for example: H. Schmidbaur, H.-J. Öller, D. L. Wilkinson, B. Huber, G. Müller, *Chem. Ber.,* **122,** *31* (1989).
13. See, for example: S. Otsuka, *J. Organomet. Chem.,* **200,** *191* (1980).
14. Y.-L. Pan, J. T. Mage, M. J. Fink, *J. Am. Chem. Soc.,* **115,** *3842* (1993).
15. (a) See, for example: T. Tanase, Y. Kudo, M. Ohno, K. Kobayashi, Y. Yamamoto, *Nature,* **344,** *526* (1990). (b) N. M. Boag, M. Green, J. A. K. Howard, F. G. A. Stone, H. Wadepohl, *J. Chem. Soc. Dalton Trans.,* **862 (**1981).

16. (a) See, for example: R. Blom, H. Werner, J. Wolf, *J. Organomet. Chem.,* **354,** *293* (1988). (b) H. Pritzkow, P. Jennische, *Acta. Chem. Scan.,* **A29,** *60* (1975). (c) B. Krebs, H. Greiwing, *Z. Anorg. All. Chem.,* **616,** *145* (1992).
17. See, for example: L. A. Bengtsson, R. Hoffmann, *J. Am. Chem. Soc.,* **115,** *2666* (1993).
18. See, for example: J. K. Nagle, A. L. Balch, M. M. Olmstead, *J. Am Chem. Soc.,* **110,** *319* (1988).
19. A. L. Balch, B. J. Davis, E. Y. Fung, M. M. Olmstead, *Inorg. Chim. Acta.,* **212,** *149* (1993).
20. A. L. Balch, J. K. Nagle, M. M. Olmstead, P. E. Reedy, Jr., *J. Am. Chem. Soc.,* **109,** *4123* (1987).
21. O. Crespo, A. Laguna, E. J. Fernández, J. M. López-de-Luzuriaga, P. G. Jones, M. Teichert, M. Monge, P. Pyykkö, N. Runeberg, M. Schütz, H.-J. Werner, *Inorg. Chem.,* **39,** *4786* (2000).
22. T. F. Carlson, J. P. Fackler Jr., R. J. Staples, R. E. P. Winpenny, *Inorg. Chem.,* **34,** *426* (1995).
23. H.-K. Yip, H.-M. Lin, Y. Wang, C.-M. Che, *J. Chem. Soc. Dalton Trans.,* **2939 (**1993).
24. E. J. Fernández, J. M. López-de-Luzuriaga, M. Monge, M. A. Rodríguez, O. Crespo, M. C. Gimeno, A. Laguna, P. G. Jones, *Chem. Eur. J.,* **6,** *636* (2000).
25. R. F. Ziolo, S. Lipton, Z. Dori, *Chem. Commun.,* **1124 (**1970).
26. J. M. Forward, D. M. Roundhill and J. P. Fackler Jr. eds., J. P. Fackler Jr., Z. Assefa, in *ptoelectronic Properties of Inorganic Compounds,* Plenum Press, New York, *195*–226 (1999).
27. H. Yersin, Ed., *Highly Efficient OLEDs with Phosphorescent Materials,* Wiley-VCH, Weinheim, *1* (2008).
28. A. Bayler, A. Schier, G. A. Bowmaker, H. Schmidbaur, *J. Am. Chem. Soc.,* **118,** *7006* (1996).
29. The Cambridge Structural Data Base (2007).
30. M. A. Rawashdeh-Omary, M. A. Omary, J. P. Fackler Jr., *Inorg. Chim. Acta,* **334,** *376* (2002).
31. V. J. Catalano, A. O. Etogo, *J. Organomet. Chem.,* **690,** *6041* (2005).
32. V. J. Catalano, M. A. Malwitz, A. O. Etogo, *Inorg. Chem.,* **43,** *5714* (2004).
33. N. Nagasundaram, G. Roper, J. Biscoe, J. W. Chai, H. H. Patterson, N. Blom, A. Ludi, *Inorg. Chem.,* **25,** *2947* (1986).
34. M. A. Rawashdeh-Omary, M. A. Omary, H. Patterson, *J. Am. Chem. Soc.,* **122,** *10371* (2000).
35. M. A. Rawashdeh-Omary, M. A. Omary, H. Patterson, J. P. Fackler Jr., *J. Am. Chem. Soc.,* **123,** *11237* (2001).
36. (a) J. C. F. Colis, C. Larochelle, E. J. Fernández, J. M. López-de-Luzuriaga, M. Monge, A. Laguna, C. Tripp, H. Patterson, *J. Phys. Chem. B.,* **109,** *4317* (2005). (b) J. C. F. Colis, C. Larochelle, R. Staples, R. H. Irmer, H. Patterson, *Dalton Trans.,* **675 (**2005). (c) C. Larochelle, H. Patterson, *Chem. Phys. Lett.,* **429,** *440* (2006).
37. J. C. F. Colis, R. Staples, C. Tripp, D. Labrecque, H. Patterson, *J. Phys. Chem. B.,* **109,** *102* (2005).
38. E. J. Fernández, M. C. Gimeno, A. Laguna, J. M. López-de-Luzuriaga, M. Monge, P. Pyykkö, D. Sundholm, *J. Am. Chem. Soc.,* **122,** *7287* (2000).
39. (a) R. Usón, A. Laguna, M. Laguna, P. G. Jones, G. M. Sheldrick, *Chem. Commun.,* **1097 (**1981); (b) R. Usón, A. Laguna, M. Laguna, B. R. Manzano, P. G. Jones, G. M. Sheldrick, *J. Chem. Soc. Dalton Trans., 285* (1984).
40. E. J. Fernández, A. Laguna, J. M. López-de-Luzuriaga, M. Monge, Spanish Pat. P200001391, (2003).

41. E. J. Fernández, A. Laguna, J. M. López-de-Luzuriaga, M. Monge, M. Montiel, M. E. Olmos, M. Rodríguez-Castillo, *Organometallics,* **25,** *3639* (2006).
42. E. J. Fernández, P. G. Jones, A. Laguna, J. M. López-de-Luzuriaga, M. Monge, M. E. Olmos, R. C. Puelles, *Organometallics,* **26,** *5931* (2007).
43. A. Burini, J. P. Fackler Jr., R. Galassi, B. R. Pietroni, R. J. Staples, *J. Chem. Soc. Chem. Commun.,* **95 (**1998).
44. A. Burini, R. Bravi, J. P. Fackler Jr., R. Galassi, T. A. Grant, M. A. Omary, B. R. Pietroni, R. J. Staples, *Inorg. Chem.,* **39,** *3158* (2000).
45. E. J. Fernández, A. Laguna, J. M. López-de-Luzuriaga, M. Monge, M. Montiel, M. E. Olmos, *Inorg. Chem.,* **44,** *1163* (2005).
46. (a) P. Schwerdtfeger, *Inorg. Chem.,* **30,** *64* (1991); (b) G. Treboux, J. C. Barthelat, *J. Am. Chem. Soc.,* **115,** *4870* (1993); (c) C. Janiak, R. Hoffmann, *J. Am. Chem. Soc.,* **112,** *5024* (1990).
47. P. Pyykkö, M. Straka, T. Tamm, *Phys. Chem. Chem. Phys.,* **1,** *3441* (1999).
48. E. J. Fernández, A. Laguna, J. M. López-de-Luzuriaga, F. Mendizábal, M. Monge, E. Olmos, J. Pérez, *Chem. Eur. J.,* **9,** *456* (2003).
49. F. Weisbrock, H. Schmidbaur, *J. Am. Chem. Soc.,* **125,** *3622* (2003), and references therein.
50. (a) S. Wang, J. P. Fackler Jr., C. King, J. C. Wang, *J. Am. Chem. Soc.,* **110,** *3308* (1988). (b) S. Wang, G. Garzón, C. King, J. C. Wang, J. P. Fackler Jr., *Inorg. Chem.,* **28,** *4623* (1989).
51. (a) Z. Assefa, F. DeStefano, M. A. Garepapaghi, J. H. LaCasce Jr., S. Oulette, M. R. Corson, J. K. Nagle, H. H. Patterson, *Inorg. Chem.,* **28,** *2868* (1991). (b) P. Fischer, J. Mesot, B. Lucas, A Ludi, H. Patterson, A. Hewat, *Inorg. Chem.,* **36,** *2791* (1997).
52. N. Blom, A. Ludi, H. B. Bürgi, K. Tichy, *Acta Cristallogr.,* **C 40,** *1767* (1984).
53. O. Crespo, E. J. Fernández, P. G. Jones, A. Laguna, J. M. López de Luzuriaga, A. Mendía, M. Monge, E. Olmos, *J. Chem. Soc. Chem. Commun., 2233* (1998).
54. W. F. Fu, K. C. Chan, V. M. Miskowsky, C. M. Che, *Angew. Chem. Int. Ed.,* **38,** *2783* (1999).
55. W. F. Fu, K. C. Chan, K. K. Cheung, C. M. Che, *Chem. Eur. J.,* **7,** *4656* (2001).
56. H. X. Zhang, C. M. Che, *Chem. Eur. J.,* **7,** *4887* (2001).
57. E. J. Fernández, P. G. Jones, A. Laguna, J. M. López-de-Luzuriaga, M. Monge, M. Montiel, M. E. Olmos, J. Pérez, *Z. Naturforsch.,* **59b,** *1379* (2004).
58. E. J. Fernández, A. Laguna, J. M. López-de-Luzuriaga, M. E. Olmos, J. Pérez, *Dalton Trans., 1801* (2004).
59. E. J. Fernández, P. G. Jones, A. Laguna, J. M. López-de-Luzuriaga, M. Monge, M. E. Olmos, J. Pérez, *Inorg. Chem.,* **41,** *1056* (2002).
60. (a) A. Lees, *J. Chem. Rev.,* **87,** *711* (1987); (b) M. K. Itokazu, A. S. Polo, N. D. M. Iha, *J. Photochem. and Photobiol. A: Chem.,* **160,** *27* (2003).
61. E. J. Fernández, A. Laguna, J. M. López-de-Luzuriaga, M. Monge, M. Montiel, M. E. Olmos, J. Pérez, *Organometallics,* **23,** *774* (2004).
62. E. J. Fernández, A. Laguna, J. M. López-de-Luzuriaga, M. Montiel, M. E. Olmos, J. Pérez, *Inorg. Chim. Acta,* **358,** *4293* (2005).
63. E. J. Fernández, A. Laguna, J. M. López-de-Luzuriaga, M. Montiel, M. E. Olmos, J. Pérez, *Organometallics,* **24,** *1631* (2005).
64. E. J. Fernández, J. M. López-de-Luzuriaga, M. Monge, M. E. Olmos, J. Pérez, A. Laguna, *J. Am. Chem. Soc.,* **124,** *5942* (2002).
65. (a) E. J. Fernández, J. M. López-de-Luzuriaga, M. Monge, M. E. Olmos, J. Pérez, A. Laguna, A. A. Mohamed, J. P. Fackler Jr., *J. Am. Chem. Soc.,* **125,** *2022* (2003). (b) E. J. Fernández, J. M. López-de-Luzuriaga, M. Monge, M. Montiel, M. E. Olmos,

J. Pérez, A. Laguna, F. Mendizábal, A. A. Mohamed, J. P. Fackler Jr., *Inorg. Chem.,* **43,** *3573* (2004).

66. E. J. Fernández, A. Laguna, J. M. López-de-Luzuriaga, M. Montiel, M. E. Olmos, J. Pérez, *Organometallics,* **25,** *1689* (2006).
67. (a) J. W. Grate, L. K. Moore, D. E. Janzen, D. J. Veltkamp, S. Kaganove, S. M. Drew, K. R. Mann, *Chem. Mater.,* **14,** *1058* (2002). (b) C. E. Buss, C. E. Anderson, M. K. Pomije, C. M. Lutz, D. Britton, K. R. Mann, *J. Am. Chem. Soc.,* **120,** *7783* (1998). (c) C. A. Daws, C. L. Exstrom, J. R. Sowa, K. R. Mann, *Chem. Mater.,* **9,** *363* (1997).
68. W. R. Caseri, H. D. Chanzy, K. Feldman, M. Fontano, P. Smith, T. A. Tervoort, J. G. P. Goossens, E. W. Meijer, A. P. H. J. Schenning, I. P. Dolbyna, M. G. Debije, M. P. de Haas, J. M. Warman, A. M. van de Craats, R. H. Friend, H. Sirringhaus, N. Stutzmann, *Adv. Mater.,* **15,** *125* (2003).
69. (a) M. Stender, R. L. White-Morris, M. M. Olmstead, A. L. Balch, *Inorg. Chem.,* **42,** *4504* (2003); (b) R. L. White-Morris, M. M. Olmstead, S. Attar, A. L. Balch, *Inorg. Chem.,* **44,** *5021* (2005).
70. A. Burini, J. P. Fackler Jr., R. Galassi, T. A. Grant, M. A. Omary, M. A. Rawashdeh-Omary, B. R. Pietroni, R. J. Staples, *J. Am. Chem. Soc.,* **122,** *11264* (2000).

CHAPTER 10

Functional Self-Assembled Zinc(II) Coordination Polymers

Chi-Chung Kwok and Chi-Ming Che

Department of Chemistry, Institute of Molecular Functional Materials, and HKU-CAS Joint Laboratory on New Materials, The University of Hong Kong, Pokfulam Road, Hong Kong SAR, P. R. China

CONTENTS

I. INTRODUCTION

There has been a considerable interest to develop metal coordination polymers due to their unique electronic and spectroscopic properties. Metal coordination polymers have been reported to have applications in nonlinear

Macromolecules Containing Metal and Metal-like Elements,
Volume 10: Photophysics and Photochemistry of Metal-Containing Polymers,
Edited by Alaa S. Abd-El Aziz, Charles E. Carraher Jr., Pierre D. Harvey, Charles U. Pittman Jr., Martel Zeldin.

optics,[1] development of magnetic materials,[2] and molecular sensing.[3] Metal ions can be electrostatically or covalently bonded on the main chain or side chain of polymers. Self-assembled polymerization is a reaction in which coordinatively labile metal ions act as a template to connect organic building blocks via coordination of ligands, producing a polymer backbone containing both the ligand and metal ion. In contrast to other polymerization methods such as Wittig[4] or Heck coupling reactions,[5] the polymerization procedures described in this work proceed through metal ion coordination with minimal quantities of reagents and require no catalyst. This kind of reaction was introduced in 1968, in which zinc(II) polymers were prepared by the reaction of methylenebis-[2-(*N*-butylformimidoyl)phenyl] with diethyl zinc.[6] Schiff base coordination polymers containing VO^{2+}, Mn^{2+}, Cr^{3+}, and Fe^{3+} ions were also prepared in 1980 by Karampurwala.[7] Due to their insolubility, it is difficult to purify, characterize, and make use of these polymers.

In 1995, Constable proposed that coordination polymers can be obtained on addition of metal ions to terpyridine functionalized monomers.[8] Terpyridine based coordination polymers containing Fe^{2+}, Ru^{2+}, and Zn^{2+} template ions were subsequently synthesized by El-Ghayoury,[9] Constable,[10] and Würthner,[11] respectively. These polymers are soluble, emissive, and exhibit charge transporting properties, rendering them to have potential application in optoelectronic devices such as polymer light-emitting devices (PLEDs).

PLEDs generally give superior performance, including low turn-on voltage, easy fabrication in the context of large displays, and greater stability without the recrystallization problem commonly encountered with OLEDs fabricated through thermal deposition of small molecules.[12] However, the practical applications of aromatic π-conjugated polymers, such as polyphenylene vinylene (PPV), poly(*p*-phenylene) (PPP), polythiophene (PT), and polyfluorene (PFO), in PLED are limited by their intrinsic properties. Although PPV-based materials demonstrate high photoluminescence (PL) and electroluminescence (EL) efficiencies as well as color-turning properties, long-term stability of the EL devices fabricated with PPV-based materials are obstructed by photo-oxidative degradation.[13] For PPP, its relative insolubility poses a problem. While PT and related compounds have been shown to display EL in the blue to near infrared spectra region, devices fabricated from these materials generally exhibit low EL efficiencies. PFO, a blue EL emitter, shows good thermal stability and high efficiency, but chain aggregation and keto defect sites in the polymer can induce degradation of the EL device.[14,15]

The use of transition or rare earth metal complexes as emitting materials for OLED has attracted much attention recently because of the enhancement in EL efficiency from triplet excited state.[16] Chan and co-workers demonstrated that incorporation of ruthenium bipyridyl complexes into conjugated polymers would enhance the charge carrier mobilities.[17] Through attachment of different transition metal complexes onto polymer chains, tuning of light-emitting properties could be achieved.[18]

In this chapter, we describe the synthesis of a series of self-assembled metal coordination polymers that show various color emissions from the violet to red spectral region with high PL quantum yields and good OLED efficiencies.

II. ZINC(II) TERPYRIDINE POLYMERS

The synthesis of 2,2′:6′,2″-terpyridine was first described by Morgan and Burstall in 1931.[19] Subsequently, metal-terpyridine complexes have become an area of active research. In 1995, Constable proposed a concept of using terpyridine functionalized monomer to give coordination polymers upon addition of metal ions (Fig. 1).[8]

A large number of works on the construction of linear-rod polymers based on terpyridine ligands have been reported in the literature. Kimura et al. developed helical coordination polymers by self-assembling reaction involving twisted bridging terpyridine ligand and Fe(II) ion.[20] The ligand is composed of two terpyridine chelating units connected by a pair of binaphthol enantiomers, and it reacts with $FeCl_2$ to form Fe(II) coordination polymer (Fig. 2). The ligand to Fe(II) ratio was determined by UV-VIS absorption titration experiment using the metal to ligand charge transfer (MLCT) absorption band at 576 nm as reference.

Ru(II) based terpyridine polymers were prepared by Houston et al. in 2003.[21] The polymers were prepared by reacting *bis*-terpyridine monomers with $Ru(DMSO)_4Cl_2$ in hot ethanol (Fig. 3). To improve the solubility of the coordination polymers, pinene moieties are attached to the monomers. The degree of polymerization of the polymers was studied by elemental analyses, gel permeation chromatography, vapor phase osmometry, STM and electrospray ionization mass spectrometry. However, no precise result was obtained, and the size of the polymers was estimated to be between 40 and 60 repeating units.

In 2002, Würthner et al. reported a Zn(II) terpyridine polymer showing a rod-like structure (Fig. 4).[11] The polymer exhibits a strong fluorescence, with an emission quantum yield of 0.61 in DMF solution.

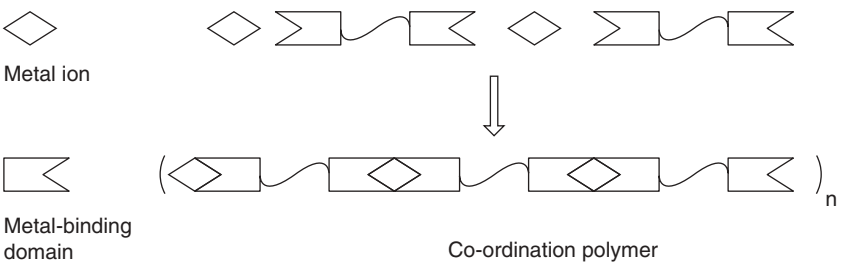

FIGURE 1. Terpyridine coordination polymer proposed by Constable.[8]

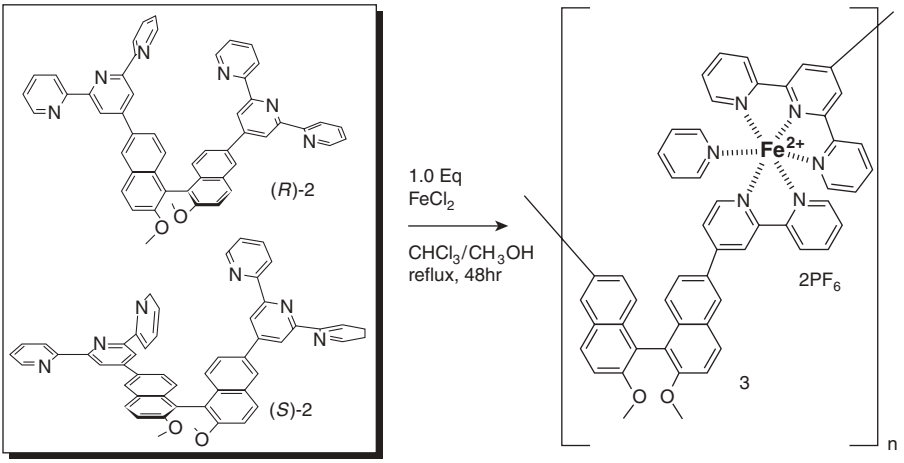

FIGURE 2. Synthetic scheme for self-assembled Fe(II) terpyridine polymer.[20]

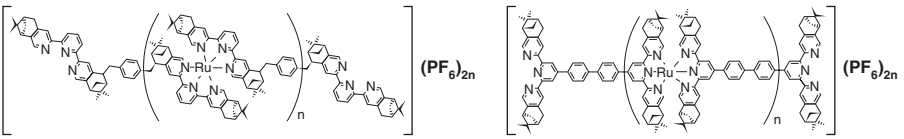

FIGURE 3. Ru(II) terpyridine self-assembled polymer prepared by Houston.[21]

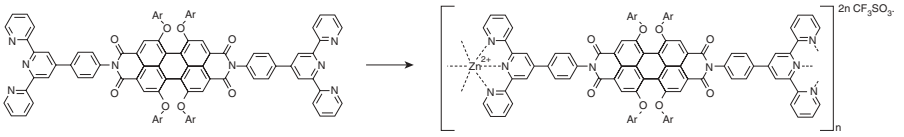

FIGURE 4. Zn(II) terpyridine self-assembled polymer prepared by Würthner.[11]

In 2003, we first used self-assembled zinc(II) terpyridine polymers in the fabrication of PLEDs.[22] We synthesized a series of monomers containing two terpyridine as chelating units, which are at opposite ends and separated by a spacer group (R) (Fig. 5). The self-assembled zinc(II) coordination polymers were easily prepared by the addition of $Zn(OAc)_2$ into solution of monomers. The product yields were up to 80%, and the inherent viscosities of the polymers were in the range of 0.48 to 1.21 dL/g, as determined using an Ubbelohde viscometer in NMP at 30 ± 0.1°C.

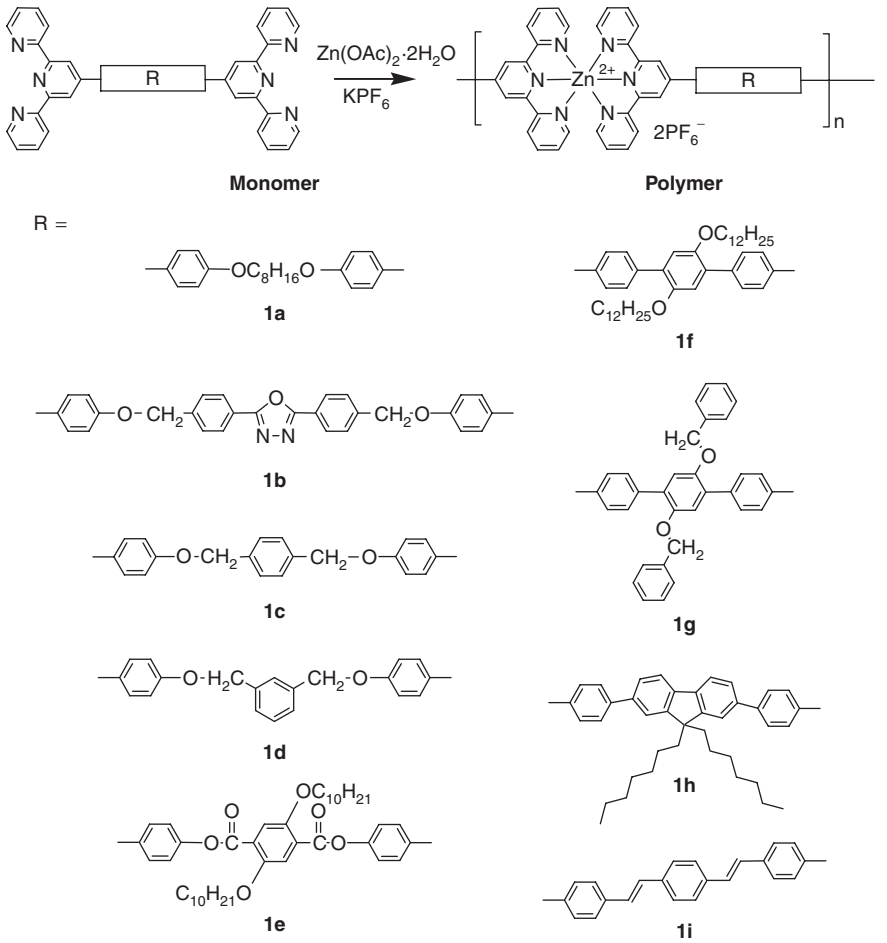

FIGURE 5. Synthetic scheme for Zn(II) terpyridine polymers **1a**–**1i**.

Thermal stability is an important issue for materials used in PLEDs. As metal cathode of PLED is fabricated by thermal deposition, materials used in PLEDs must have a good thermal stability to stand for this fabrication process. Recrystallization is one of the major factors affecting the lifetime of PLEDs, and the material used must stay in amorphous state throughout the device fabrication process and during operation. In other words, the material must possess a high decomposition temperature (T_d) and glass-transition temperature (T_g). The self-assembled zinc(II) terpyridine polymers by us show good thermal stability. Their T_d values ranged from 336° (**1e**) to 433°C (**1h**) (Table 1). No phase transition was observed in differential scanning calorimetry (DSC) study up to 300°C for all the polymers, revealing their high T_g values.

TABLE 1. Physical Properties for Polymers **1a**–**1i**

Polymer	η_{inh} (dLg^{-1})[a]	Yield (%)	T_d/°C
1a	0.70	78	374
1b	0.68	69	354
1c	0.77	67	357
1d	0.54	74	358
1e	0.48	65	336
1f	1.10	75	424
1g	0.62	70	368
1h	1.21	80	433
1i	0.75	69	394

[a]Inherent viscosity measured in NMP at 30 ± 0.1°C, using Ubbelohde viscometer.

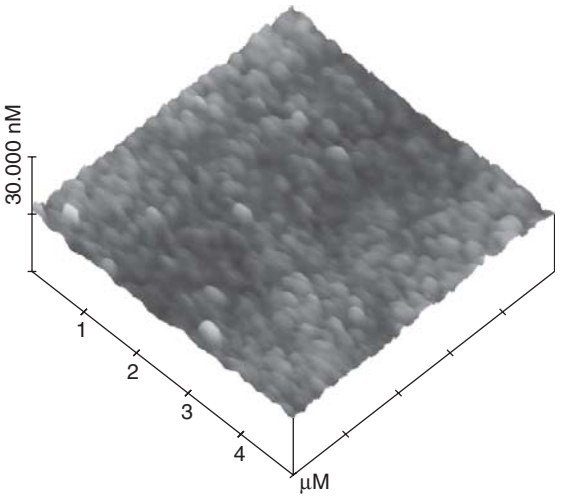

FIGURE 6. AFM (topographic) image of **1a** on ITO glass.

Optical transparency, surface smoothness of the thin film, and the absence of pin holes affect both the efficiency and the lifetime of PLEDs. To study the surface morphology of the thin films, the polymers were spin coated on ITO glass and examined using atomic force microscopy (AFM). Figure 6 shows the topographic images of the film from **1a**. This thin-film sample has a surface roughness of 2 nm (R. M. S) in the 5 × 5 μm^2 scan area. The morphological smoothness revealed that only a limited number of pin holes were introduced into the device layers with this polymer. This film has good optical quality and provides good contact with the next layer of deposited material.

Spectroscopic data of **1a**–**1i**, monomers of **1a**–**1i**, and model compound **1** (zinc(II) *bis*(*N*-phenyl salicylaldiminato) are listed in Table 2. The absorption spectra of these zinc(II) terpyridine polymers are similar, with absorption maxima at 286–290 and 320–391 nm. PL of these polymers span violet, blue, green, and yellow color. The PL quantum yields (Φ_{PL}) range from 25% for **1b** and **1e** to 77% for **1f** in DMAc. The Φ_{PL} values of the polymer thin films were determined using integrating sphere,[23] which were found to vary from 0.15 to 0.55 ± 0.05 (Table 2).

Figure 7 shows the UV-VIS absorption and emission spectra of **1a** and monomer of **1a** in DMAc solution, both of them exhibit a strong absorption band at λ_{max} 287 nm (a_{max}=73.9 g^{-1} dm^3 cm^{-1} for **2a**). Because zinc(II) adopts a d^{10} electronic configuration and is difficult to be oxidized or reduced and because there would be no metal to ligand charge transfer (MLCT) or ligand to metal charge transfer (LMCT) transition in the UV-VIS spectral region, we assign the transitions to ligand-centered (LC) π–π^* transition of the aryl groups. A shoulder at $\sim\lambda_{max}$ 328 to 342 nm (a_{max}=36.5 to 28.8 g^{-1} dm^3 cm^{-1}), which is absent for the monomer, was also found for **1a**. Similar observations were reported in the literature,[24] and the absorption spectra are similar to those of the doubly protonated terpyridine ligands.

The optical band gaps of the polymers **1a**–**1i**, determined from the absorption spectra, are in the range of 2.64 to 3.26 eV. The polymers with $-OCH_2-$ linkage (**1a**–**1d**) have a larger band gap than the others. In the case of **1a**–**1d**, the two terpyridine units are separated by a $-OCH_2-$ linkage, resulting in a decrease of π-conjugation. Among the monomers, **1e**–**1i**, the optical band gap of **1i** is the smallest.

The PL spectra of **1a** both in thin film and in solution exhibit blue emission at λ_{max} 450 nm. Figure 8 shows the MO diagram of 4-phenylterpyridine,[25] which may be applicable to the polymer system discussed here. The HOMO and LUMO, denoted by π_{tpy} and π^*_{tpy}, respectively, of the 4-phenylterpyridine unit are localized on the terpyridine unit exclusively. The blue emission is attributed to intraligand $^1(\pi_{tpy}^*-\pi_{tpy})$ fluorescence. The terpyridine polymers exhibit higher PL quantum (Φ_{PL}) yields than their monomer counterparts. For example, **1a** shows solution Φ_{PL} of 0.45 and 0.20 in DMAc and as thin film, respectively; these values are higher than those of 0.18 for **1a** in solution under the same conditions. The increase in Φ_{PL} may be due to decrease in nonradioactive decay of the terpyridine unit upon coordination to zinc(II). Indeed, increase in fluorescence quantum yield of terpyridine ligand upon coordination to zinc(II) has been reported.[26]

The spacer between terpyridine units affects PL of the zinc(II) polymers. The emission colors are blue ($\Phi_{PL,film}$=0.20), green (0.50), green (0.20), green (0.55), and yellow (0.40) with λ_{max} at 450, 546, 530, 535, and 567 nm, respectively. The difference in the emission colors could be attributed to the difference in conjugation length of the terpyridine ligands.

Polymers **1a** and **1h** were fabricated into electroluminescent devices A and B, respectively, with the following configuration: ITO/PEDOT:PSS/polymer/Ca/Al.

TABLE 2. Photophysical data of model compound 1, monomers of **1a**–**1i** and polymers **1a**–**1i**

Monomer	λ_{max} $_{abs}$[a] (nm)	$\lambda_{max,\ PL\ sol}$ (nm)/ $\Phi_{PL\ sol}$[b,c,d]	Polymer	λ_{max} $_{abs}$[a] (nm)	$\lambda_{max,\ PL\ sol}$ (nm)/ $\Phi_{PL\ sol}$[b,c,d]	$\lambda_{max,\ PL\ film}$ (nm)/ $\Phi_{PL\ film}$[d,e,f]
1a	287, 327	419/0.18	**1a**	287, 328, 342(sh)	450/0.45	450/0.20
1b	288	419/0.05	**1b**	290, 320, 343(sh)	439/0.25	436, 489/0.30
1c	285, 345	419/0.11	**1c**	287, 328, 345(sh)	457/0.50	465/0.40
1d	288	420/0.10	**1d**	288, 326, 344(sh)	441/0.44	430/0.25
1e	286, 319	425/0.07	**1e**	287, 328, 342(sh)	422/0.25	488/0.15
1f	285, 324	383, 412/0.18	**1f**	289, 328, 346, 373(sh)	457/0.77	546/0.50
1g	288, 334	447/0.13	**1g**	288, 346, 372(sh)	456/0.34	530/0.20
1h	285, 354	420/0.12	**1h**	287, 328, 342(sh)	434, 518/0.32	535/0.55
1i	282, 392	460/0.63	**1i**	286, 327, 391, 413(sh)	440, 461, 556/0.49	567/0.40
Model compound 1	288, 327, 344	447/0.62				

[a]Concentration at 1×10^{-5} mol dm^{-3} in DMAc.
[b]Concentration at 1×10^{-5} g dm^{-3} in DMAc.
[c]Quinine sulfate in 0.1 N sulfuric acid was used as reference for determination of PL quantum yields.
[d]Excitation wavelength was 330 nm.
[e]The thickness of films was 38–70 nm.
[f]The deviation of PL quantum yield on thin film is ± 0.05.

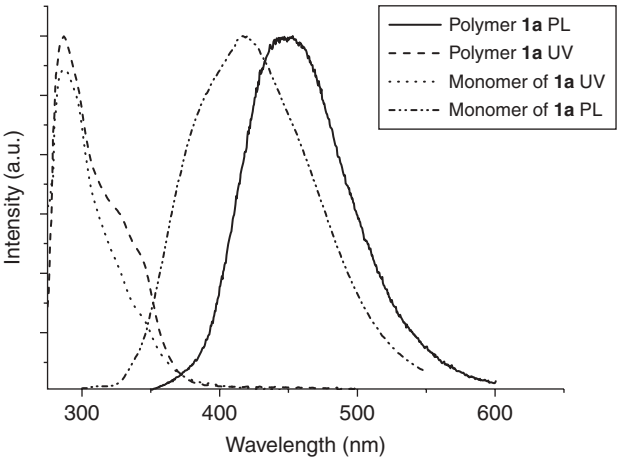

FIGURE 7. Absorption and emission spectra of polymer and monomer **1a** in DMAc.

The EL spectrum of device A at a bias voltage of 10 V shows an emission with peak maxima at 450 nm (Fig. 9). This is similar to the emission of spin-coated **1a** film. We suggest that the same excited state could be responsible for both EL and PL emission. The current density-voltage-luminance characteristic curves of device A are shown in Figure 10. The blue-light EL intensity is augmented with increasing bias voltage. The turn-on voltage is around 6 V, and the maximum efficiency of the device is 0.8 cd/A. The maximum luminance of 1700 cd/m^2 was obtained under a driving voltage of 13 V. The emission color of device A is blue (CIE_1931 coordinates: $x = 0.15$, $y = 0.21$). Figure 10 shows the current density-voltage-luminance characteristic curves of devices B. Device B exhibits an intense EL emission peak with λ_{max} at 572 nm. The onset voltage is approximately 6 V, and the maximum efficiency and luminance are 1.1 cd/A and 2380 cd/m^2 at 13 V, respectively. The EL color of device B is yellow (CIE_1931 coordinates: $x = 0.46$, $y = 0.50$). Attempts such as reducing the thickness of the emissive layer were made to enhance the performance of EL devices. However, similar turn-on voltages and luminance were observed despite these attempts.

After publication of our work,[22] new self-assembled Zn(II) terpyridine polymers were prepared and used in PLEDs. Following the methodology reported by us, Lin et al. similarly prepared a series metallopolymers by self-assembled reaction containing Zn(II) terpyridine units, including a metallo-homopolymer and metallo-*alt*-copolymer containing carbazole pendants attached to the C-9 position of fluorene by long alkyl spacers.[27]

The polymers prepared by Lin show good thermal stability (T_d up to 422°C), have high quantum efficiencies (Φ up to 0.23 in DMF), and form good quality thin film by spin coating (Fig. 11). Green EL emission with a

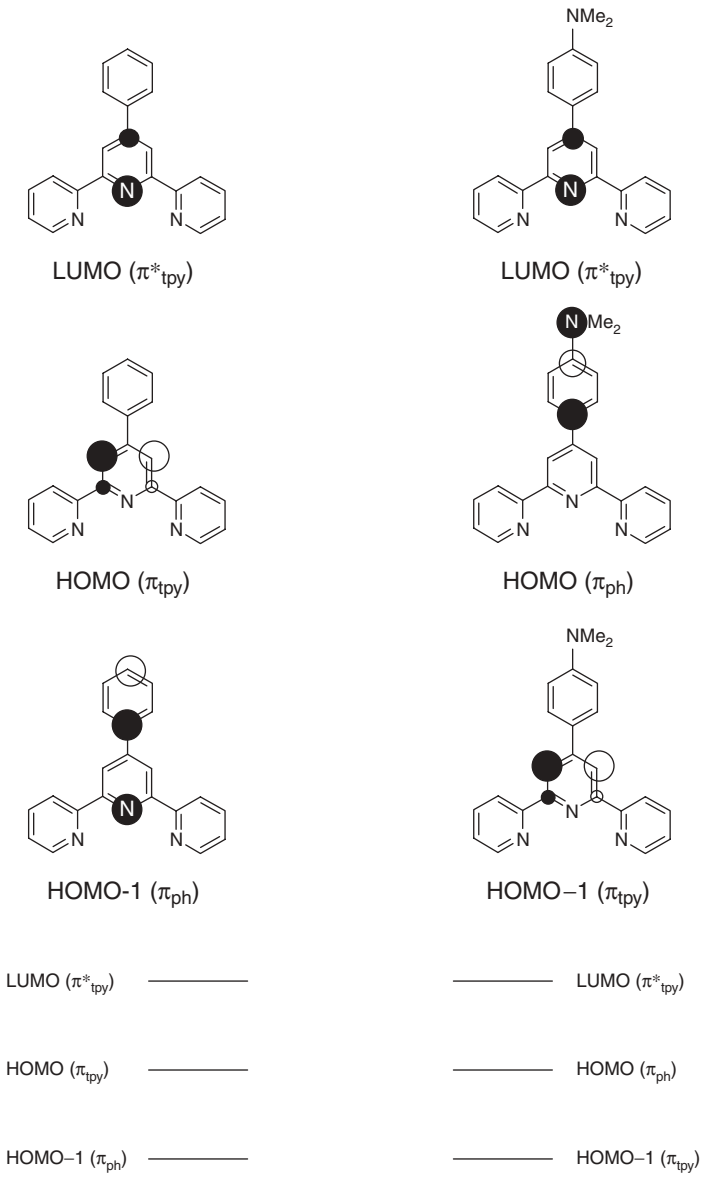

FIGURE 8. Calculated electronic state and energy level diagrams of HOMO, HOMO-1, and LUMO for the pyridines.

turn-on voltage of 6−6.5 V, current efficiencies of 0.85−1.1 cdA^{-1} (at 100 $mAcm^{-2}$), and maximum luminances of 1704−2819 cdm^{-2} were found (at 15 V) (Table 3).

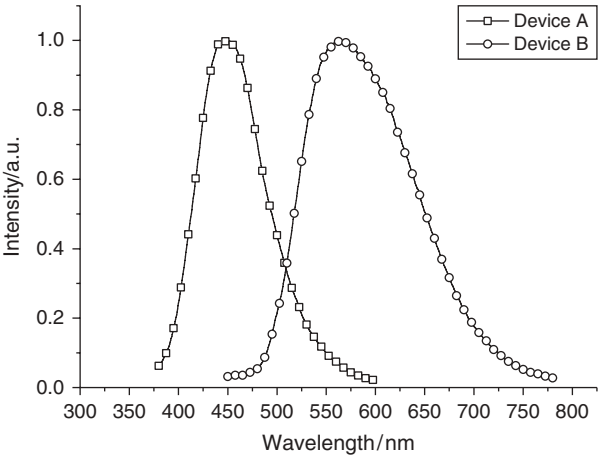

FIGURE 9. EL spectra of devices A and B.

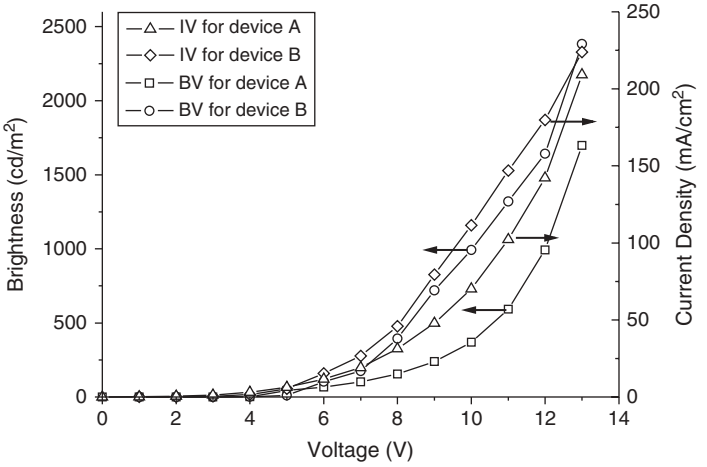

FIGURE 10. Current density-voltage-brightness (J-B-V) relationships for devices A and B.

III. ZINC(II) SCHIFF BASE POLYMER

Metal complexes with Schiff base ligands have useful applications in organic optoelectronics due to their outstanding photoluminescent (PL) and electroluminescent (EL) properties, and their ease of synthesis, which readily allows structural modification for optimization of material properties.[28] Hamada and co-workers pioneered the use of zinc(II) Schiff base complexes as blue to greenish white emitters for EL devices. We have demonstrated Pt(II) Schiff base triplet emitters as yellow dopants for organic light-emitting devices

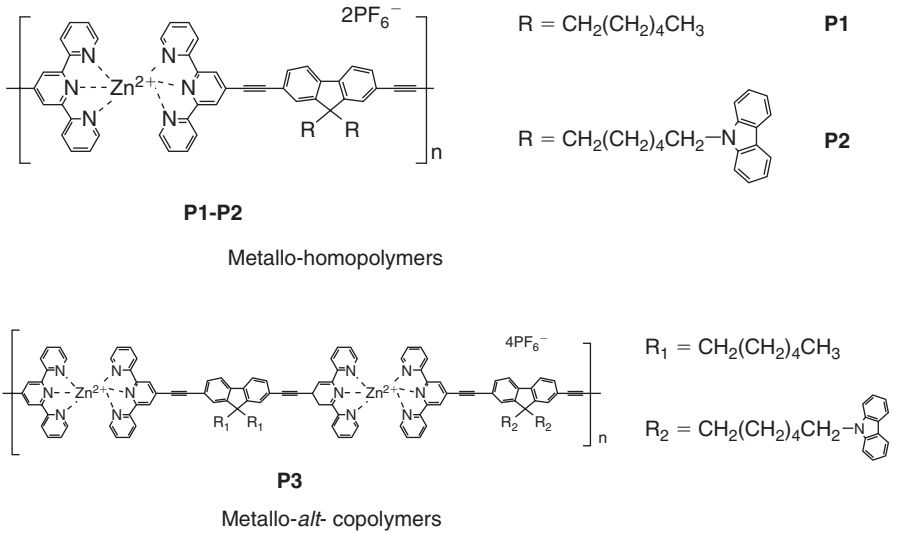

FIGURE 11. Zn(II) terpyridine polymers prepared by Lin.[27]

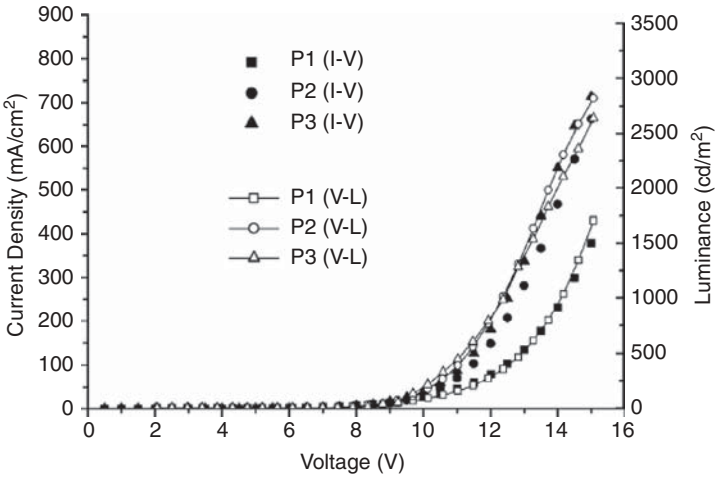

FIGURE 12. J-V-B relationship for PLEDs of Lin's devices.[27]

(OLEDs) and achieved white EL with Pt(II) Schiff base complexes in 2004.[29] Metal Schiff base complexes are potential candidates for the development of high performance PLEDs.

As early as 1968, self-assembled Schiff base polymers were developed by O'Connell and co-workers, by the reactions between divalent metal ions with monomers consisting of two Schiff base type cheating units separated by a

TABLE 3. Electroluminescence (EL) Properties of PLED Devices[a]

Polymer	$\lambda_{max,EL}$ (nm)	V_{on} (V)[b]	Maximum Lummescence (cd/m^2)(V)	Current Efficiency (cd/A)[c]	CIE Coordinates (x,y)
P1	551	6.0	1704 (14.5)	0.85	(0.41, 0.52)
P2	549	6.5	2819 (15)	1.11	(0.41, 0.53)
P3	550	6.0	2640 (15)	1.10	(0.41, 0.52)

[a]Device structure: ITO/PEDOT:PSS/polymer(**P1**–**P3**)/BCP/Alq_3/LiF/Al, where the polymer (**P1**–**P3**) is an emitting layer.
[b]V_{on} is the turn-on voltage.
[c]Current efficiencies were obtained at 100 mA/cm^2.

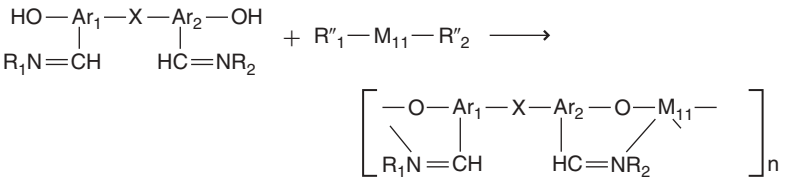

FIGURE 13. Schiff base coordination polymers prepared by O'connell.

spacer group X (Fig. 13). These reported Schiff base polymers show high thermal stability (no weight loss up to 400°C) but have a low solubility in organic solvents.

In 1980 Karampurala et al prepared VO^{2+}, Mn^{2+}, Zn^{2+}, Cr^{3+}, and Fe^{3+}-based Schiff base polymers from 5,5′-methylene bis-salicylaldehyde and aniline.[4] Similar to the polymers prepared by O'Connell, all of these polymers are insoluble in common organic solvents. It is not possible to characterize these insoluble polymers by conventional methods, such as osmometry and viscometry, and only elemental analyses and IR can be used for characterization. Instead of 5,5′-methylene bis-salicylaldehyde, hydrazinecarboxamide was subsequently used as monomer for the reactions (Fig. 14).[30] However, the solubility issue had not been resolved, all of the VO^{2+}, Mn^{2+}, Zn^{2+}, Cr^{3+}, and Fe^{3+} Schiff base polymers are insoluble in common solvents.

The first soluble Schiff base coordination polymer was reported by Archer et al. in 1985,[31] which was prepared by condensation of 1,2,4,5-tetraamino benzene (TAB) with tetrakis(salicyladehydato)zirconium(IV) ($Zr(sal)_4$) in dry dimethyl sulfoxide (Fig. 15). The polymer has a number-average molecular weight of up to 4.9×10^4 based on inherent viscosity, gel permeation chromatography, and elemental analyses and shows no decomposition at temperature <500°C.

Soluble Eu(III) and Y(III) Schiff base polymers were prepared by similar methods in 1996 (Fig. 16).[32] The Eu(III) polymers were found to be highly

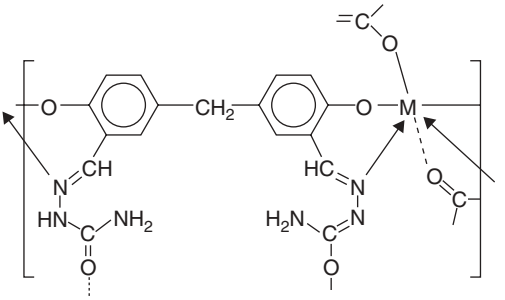

FIGURE 14. Hydrazinecarboxamide based coordination polymers prepared by Karampurala.

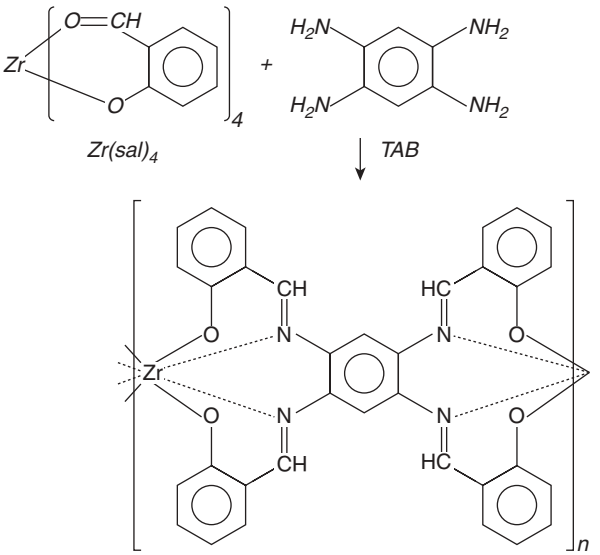

FIGURE 15. Synthetic scheme for soluble Zr (IV) Schiff base polymers.

emissive, with a maximum emission quantum yield of 0.74 in DMF-methanol-ether at 77 K.

As in the case of terpyridine-based polymers, we first reported the application of Zn(II) Schiff base polymers in PLEDs.[33] We prepared a family of soluble self-assembled Zn(II) Schiff base polymers, which are thermally stable, structurally diverse and easily modified (Fig. 17). The number-average molecular weight (M_n) of the polymers range from 13580 to 20440, as determined using gel permeation chromatography (GPC) with polystyrene as a standard in THF (tetrahydrofuran) at 35°C. The decomposition temperature (T_d) of the polymers range from 389° (**2g**) to 461°C (**2h**). No phase transition was observed in DSC up to 300°C for these polymers (Table 4).

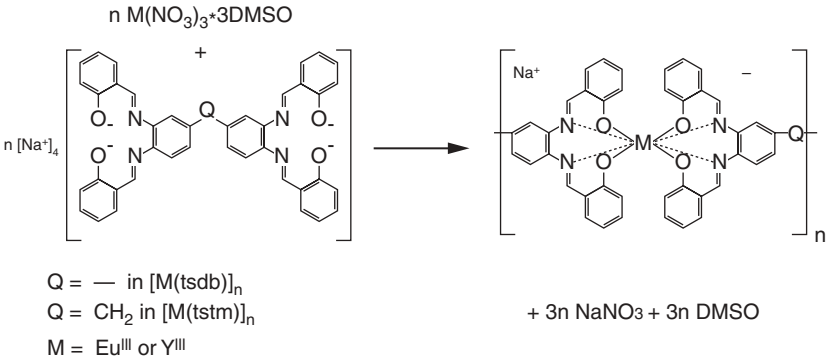

FIGURE 16. Eu(III) and Y(III) based soluable coordionation polymers.

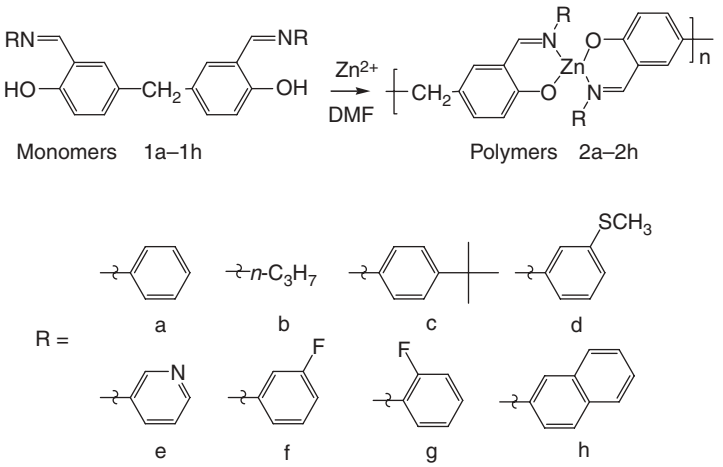

FIGURE 17. Synthetic scheme of Zn(II) Schiff base polymers.

Figure 18 shows the topographic image of **2c**. The thin film has a surface roughness of 0.8–1.5 nm (R. M. S) in the 5 × 5 μm^2 scan area. The morphological smoothness reveals that only a limited number of pin holes were introduced into the device layers with this polymer. The film has good optical quality and provides good contact with the next layer of deposited material.

Photophysical data of polymers **2a**–**2h** are summarized in Table 5. Polymers **2a**–**2h** exhibit similar absorption spectra in DMF solution. Three absorption bands, with λ_{max} at 280–309, 311–358, and 408–427 nm, respectively, are observed. For example, **2a** shows strong absorption bands at 315 and 351 nm (a = 34.6 and 23.1 $dm^3\,g^{-1}\,cm^{-1}$, accordingly) and one moderate band at 408 nm, which is absent in the free ligand (4,4′-methylene-*bis*-[2-(*N*-phenylformimidoyl) phenol]). The high-energy absorption bands are assigned to spin-allowed singlet

TABLE 4. Physical Properties of Polymers **2a**–**2h**

Polymer	M_n	M_w	Yield/%	T_d/°C
2a	13580	24170	79	450
2b	19500	29440	82	420
2c	16660	31150	75	453
2d	16570	27500	69	429
2e			73	441
2f	20440	30600	85	404
2g	19720	29180	83	389
2h			71	461

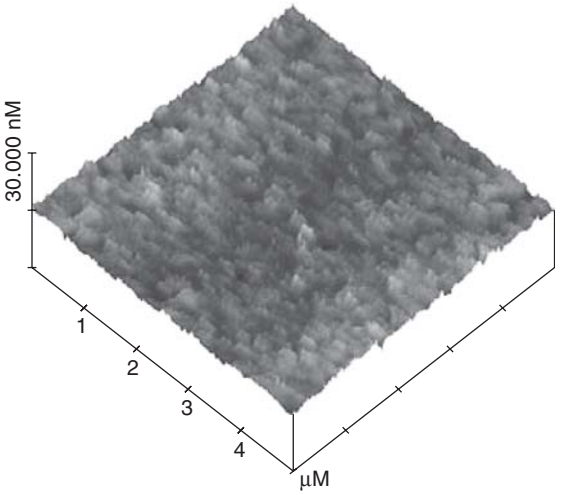

FIGURE 18. AFM (topographic) image of **2c** on ITO glass.

intraligand (^{1}IL) transition of the Schiff base ligand. Because zinc(II) does not participate in electronic transitions in the UV-VIS spectral region, the absorption at 408 nm is assigned to ligand-centered (LC) π-π* transition of the Schiff base ligand. It has been shown that the electronic absorption bands of metal 8-hydroxyquinolate chelates involve transitions from the filled π orbital (HOMO) of the phenoxide to the unfilled π* orbital (LUMO) of the pyridyl group.[34] A similar assignment can be made to our system in that the HOMOs of the Schiff base ligand systems are localized on the phenoxide units and the LUMOs are at the imine group.

The PL emissions of the polymers in DMF solutions, which span from blue to yellow color (blue for **2b**, green for **2a** and **2c**, and yellow for **2h** with λ_{max} at 458, 508, 501, and 562 nm, respectively, on excitation at 360 nm), are assigned to intraligand (π*-π) fluorescence. The quantum yields (Φ_{PL}) range

TABLE 5. Photophysical Properties of Polymers **2a**–**2h**

Polymer	$\lambda_{max,\ abs}$ (nm)/ a ($dm^3\ g^{-1}cm^{-1}$)[a]	$\lambda_{max,\ PL\ sol}$ (nm)/ $\Phi_{PL\ sol}$[b,c]	$\lambda_{max,\ PL\ film}$ (nm)/ $\Phi_{PL\ film}$[b,c]
2a	315(34.6), 351 (23.1), 408 (12.0)	508/0.06	538/0.13
2b	282 (20.7), 325 (28.7), 378 (11.0)	458/0.09	509/0.04
2c	291 (24.3), 311 (26.5), 413 (18.1)	501/0.15	536/0.13
2d	304 (27.2), 319 (26.0), 351 (30.1)	534[d]	–
2e	286 (57.7), 352 (24.1), 425 (11.4)	518/0.02	534/0.07
2f	305 (54.3), 322 (47.4), 345 (41.2)	516/0.34	538/0.15
2g	284 (34.6), 309 (32.3), 324 (30.1), 352 (26.0), 427 (3.5)	514/0.20	538/0.19
2h	280 (44.6), 358 (48.3)	562[d]	–

[a]Concentration at 10^{-5} g dm^{-3} in DMF.
[b]The thickness of the films was 30–50 nm.
[c]Excitation wavelength was at 350 nm.
[d]PL quantum yield was less than 0.01.

from 2% for **2e** to 34% for **2f**. The emission color could be tuned upon incorporation of different functional groups, R, along the polymer chain. A significant tuning can be achieved by changing the conjugation length of the R group; red shift in emission maximum for >2149 cm^{-1} was observed for **2a** as compared with **2b**, a red shift of a further 1891 cm^{-1} was achieved by incorporation of one additional phenyl ring as in the case of **2h.**

Thin film samples of these polymers give yellowish orange emission with λ_{max} at 534–538 nm, except for **2b** (λ_{max} at 509 nm) and **2c** (λ_{max} at 536 nm). The emission from a thin film sample of **2g** (λ_{max} at 538 nm) shows a Stokes shift of 792 cm^{-1} from that of PL recorded in DMF solution. The shift is attributed to excimer formation resulting from π-π stacking interactions in the solid state. Polymer **2c** exhibits a more greenish EL emission compared to the other polymers, probably due to the presence of the bulky *t*-butyl groups, which prohibits aggregation of the polymer chains and suppresses excimer formation.

Polymers **2c** and **2g** were fabricated into PLEDs C and D using standard spin-coating and vacuum deposition methods (Fig. 19). The configuration is indium-tin-oxide (ITO)/PEDOT:PSS (3,4-polyethylenedioxythiophene:polystyrene sulfonate, 30 nm)/polymer (30–50 nm)/BCP (2,9-dimethyl-4,7-diphenyl-1,10-phenanthroline, 20 nm)/Alq_3 (tris(8-quinolinonato)aluminium, 20 nm)/LiF (0.5 nm)/Al (200 nm). Device C (with **2c**) at a bias voltage of 8 V shows a green emission with λ_{max} at 536 nm and CIE_1931 coordinates of $x = 0.30$ and $y = 0.55$; the EL intensity is augmented with increasing bias voltage. The turn-on voltage is approximately 5 V, the maximum efficiency of the device is 2.0 cd A^{-1} at 8 V, and the maximum luminance is 3120 cd m^{-2} was obtained at 15 V. Device D (with **2g**) exhibits an orange EL (λ_{max} at 584 nm, CIE_1931 coordinates: $x = 0.54$, $y = 0.45$) and an onset voltage at 6 V. The maximum efficiency and luminance are

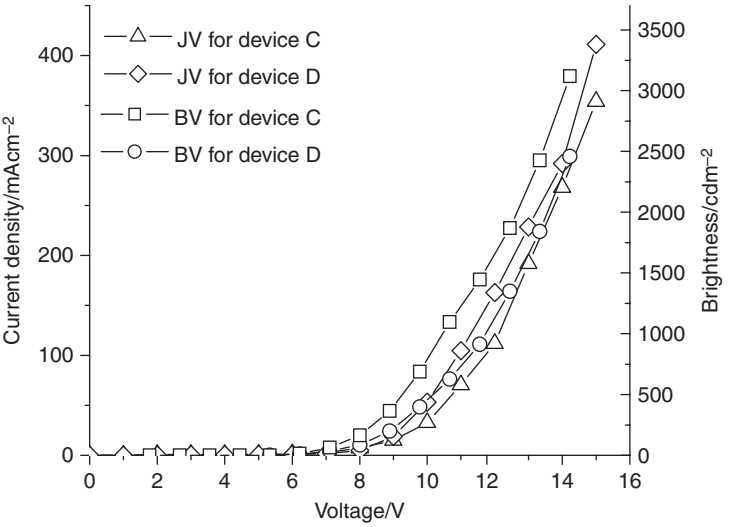

FIGURE 19. J-V-B relationships for device C and D.

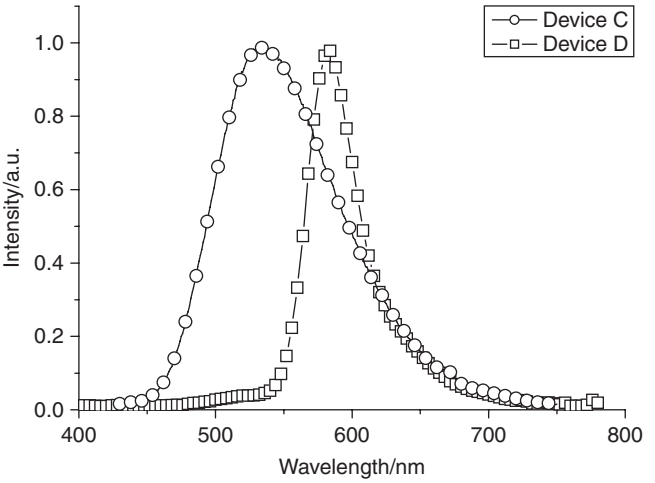

FIGURE 20. EL spectra for device C and D.

2.6 cd A^{-1} at 8 V and 2460 cd m^{-2} at 15 V, respectively. Neither of the EL from devices C and D exactly matches the corresponding PL from thin films (Fig. 20). The EL was observed at lower energy and could be attributed to recombination of excitons at the narrow interface of the films in PLEDs, while the broad PL spectra could originate from the bulk polymer film upon UV excitation.[15]

Subsequently, Cao et al. incorpated electron and hole transporting groups on to the zinc(II) Schiff base polymer chain for PLEDs application (Fig. 21).[35] Fluorene and carbazole-containing polymers were prepared by reacting the

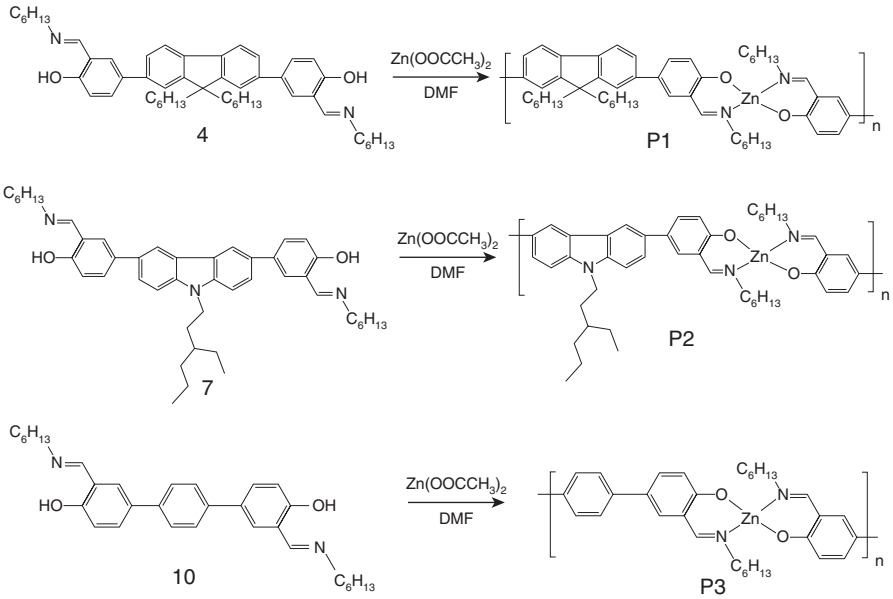

FIGURE 21. Zinc(II) Schiff base polymer prepared by Cao.

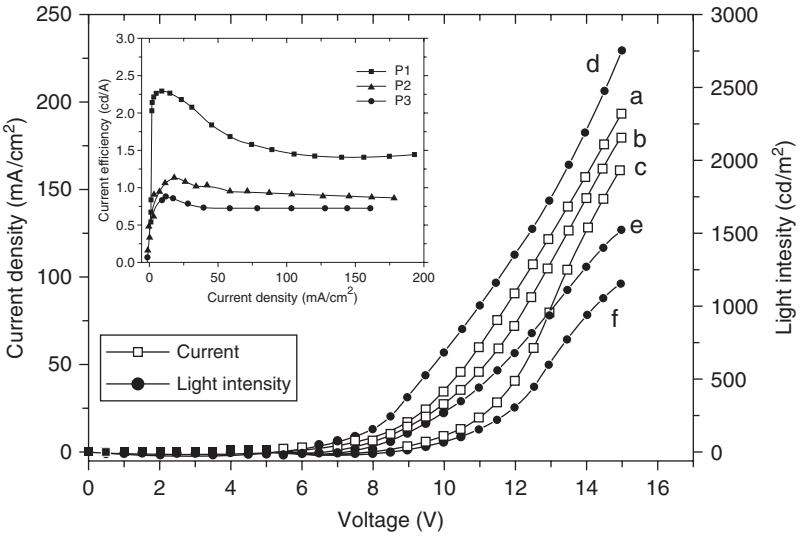

FIGURE 22. J-V-B relationship of Cao's devices.

monomers with $Zn(OAc)_2$ in DMF. These polymers show high emission quantum efficiencies (Φ: 0.42–0.51), good thermal stability (T_d: 311–386°C) and form good-quality thin films by spin coating method. Light-emitting diodes with the configuration ITO/PEDOT/polymer/BCP/Alq_3/LiF/Al were found to be efficient green emitters, with maximum current efficiencies of 0.9–2.3 cd A^{-1} (Fig. 22).

IV. SUMMARY

Investigation of self-assembled metal coordionation polymers has attracted and will continue to attract significant interest. Novel functional metal coordination polymers can be easily synthesized by self-assembly reactions involving minimal quantities of reagent and no catalyst. Soluble zinc(II) terpyridine and Schiff base coordination polymers have been prepared by self-assembly polymerization. These self-assembled zinc(II) polymers show good thermal stability and are highly emissive, and their applications in the development of high-performance light-emitting devices (PLEDs) have been demonstrated.

V. ACKNOWLEDGMENT

The work described in this chapter was partially supported by a grant from the University Grants Committee of the Hong Kong Special Administrative Region, China (Project No. [AoE/P-03/08])

VI. REFERENCES

1. W. Lin, Z. Wang, L. Ma, *J. Am. Chem. Soc.,* **121,** *11249* (1999).
2. (a) T. Yuen, C. L. Lin, T. W. Mihalisin, M. A. Lawandy, J. Li, *J. Appl. Phys.,* **87,** *6001* (2000); (b) A. K. Sra, M. Andruth, O. Kahn, S. Golhen, L. Ouahab, J. V. Yakhmi, *Angew. Chem. Int. Ed.,* **38,** *2606* (1999).
3. (a) M. Albrecht, M. Lutz, A. L. Spek, G. van Koten, *Nature,* **406,** *970* (2000); (b) J. A. Real, E. Andrés, M. C. Muñoz, M. Julve, T. Granier, A. Bousseksou, F. Varret, *Science,* **268,** *265* (1995).
4. M. Kimura, T. Horai, K. Hanabusa, H. Shirai, *Adv. Mater.,* **10,** *459* (1998).
5. R. F. Heck, *Org. React.,* **27,** *345* (1982).
6. J. J. O'Connell, U.S. Pat., 3,373,077, (1968).
7. A. M. Karampurwale, R. P. Patel, J. R. Shah, *Angewan. Makromolek. Chem.,* **89,** *57* (1980).
8. E. C. Constable, *Macromol. Symp.,* **98,** *503* (1995).
9. A. El-Ghayoury, A. P. H. J. Schenning, E. W. Meijer, *Polym. Sci. Part A Polym. Chem.,* **40,** *4020* (2002).
10. J. Hjelm, E. C. Constable, E. Figgemeier. A. Hagfeldt, R. Handel, C. E. Housecrotft, E. Mukhtar, Schofield. E *Chem. Commun., 284* (2002).
11. R. Dobrawa, F. Würthner, *Chem. Commun., 1878* (2002).
12. (a) L. Akcelrud, *Prog. Polym. Sci.,* **28,** *875* (2003); (b) U. Mitschke, P. Bauerle, *J. Mater. Chem.,* **10,** *1471* (2000); (c) A. Kraft, A. C. Grimsdale, A. B. Holmes, *Angew. Chem. Int. Ed.,* **37,** *402* (1998); (d) S. C. Yu, C. C. Kwok, W. K. Chan, C. M. Che, *Adv. Mat.,* **15,** *1643* (2003).
13. J. C. Scott, J. H. Kaufman, P. J. Brock, R. DiPietro, J. Salem, J. A. Goitia, *J. Appl. Phys.,* **79,** *2745* (1996).
14. U. Scherf, E. J. W. List, *Adv. Mater.,* **14,** *477* (2002).

15. (a) C. Xia, R. C. Advincula, *Marcomolecules,* **34,** *5854* (2001); (b) V. N. Bliznyyuk, S. A. Carter, J. C. Scott, G. Klarner, R. D. Miller, D. C. Miller, *Marcomolecules,* **32,** *361* (1999); (c) G. Klarner, J. I. Lee, V. Y. Lee, E. Chan, J. P. Chen, A. Nelson, D. Markiewicz, R. Siemens, J. C. Scott, R. D. Miller, *Chem. Mater.,* **11,** *1800* (1999).
16. (a) M. A. Baldo, D. F. O'Brien, M. E. Thompson, S. R. Forrest, *Physical Review B,* **60,** *14422* (1999); (b) S. Lamansky, P. Djurovich, D. Murphy, F. Ael-Razzaq, H. E. Lee, C. Adachi, P. E. Burrows, S. R. Forrest, M. E. Thompson, *J. Am. Chem. Soc.,* **123,** *4304* (2001); (c) Y. Y. Lin, S. C. Chan, M. C. W. Chan, Y. J. Hou, N. Y. Zhu, C. M. Che, Y. Liu, Y. Wang, *Chem. Eur. J.,* **9,** *1263* (2003); (d) W. Lu, B. X. Mi, M. C. Chan, W. Z. Hui, N. Y. Zhu, S. T. Lee, C. M. Che, *Chem. Commun., 206* (2002); (e) S. C. Chan, M. C. W. Chan, C. M. Che, Y. Wang, K. K. Cheung, N. Y. Zhu, *Chem. Eur. J.,* **7,** *4180* (2001).
17. (a) S. C. Yu, X. Gong, W. K. Chan, *Macromolecules,* **31,** *5639* (1998); (b) S. C. Yu, S. Hou, W. K. Chan, *Macromolecules,* **32,** *5251* (1999); (c) S. C. Yu, S. Hou, W. K. Chan, *Macromolecules,* **33,** *3259* (2000); (d) W. K. Chan, X. Gong, W. Y. Ng, *Appl. Phys. Lett.,* **71,** *2919* (1997).
18. (a) W. Y. Ng, X. Gong, W. K. Chan, *Chem. Mater.,* **11,** *1165* (1999); (b) K. D. Ley, C. E. Whittle, M. D. Bartberger, K. S. Schanze, *J. Am. Chem. Soc.,* **119,** *3423* (1997); (c) A. A. Farah, W. J. Pietro, *Polym. Bull.,* **43,** *135* (1999); (d) J. S. Wilson, A. S. Dhoot, A. J. A. B. Seeley, M. S. Khan, A. Khler, R. H. Friend, *Nature,* **413,** *828* (2001).
19. S.G. Morgan, F.H. Burstall, *J. Chem. Soc., 20* (1931).
20. M. Kimura, M. Sano, T. Muto, K. Hanabusa, H. Shirai, *Macromolecules,* **32,** *7951* (1999).
21. J. A. Barron, S. Glazier, S. Bernhard, K. Takada, P. L. Houston, H. D. Abruna, *Inorg. Chem.,* **42,** *1448* (2003).
22. S. C. Yu, C. C. Kwok, W. K. Chan, C. M. Che, *Adv. Mater., 1643* (2003).
23. H. Mattoussi, H. Murata, C. D. Merritt, Y. Lizumi, J. Kido, Z. H. Kafafi, *Appl. Phys. Lett.,* **86,** *2642* (1999).
24. (a) R. H. Holyer, C. D. Hubbard, S. F. A. Kettle, R. G. Wilkins, *Inorg. Chem.,* **5,** *622* (1966); (b) G. Albano, E. C. Vincenzo, Constable, M. Maestri, *Inorg. Chim. Acta.,* **277,** *225* (1998).
25. T. Mutai, J. D. Cheon, S. Arita, K. Araki, *J. Chem., Perkin Trans.* **2,** *1045* (2001).
26. N. W. Alcock, P. R. Barker, J. M. Haider, M. J. Hannon, C. L. Painting, Z. Pikramenou, E. A. Plummer, K. Rissanen, P. Saarenketo, *J. Chem. Soc. Dalton Tran., 1447* (2000).
27. (a) Y. Y. Chen, Y. T. Tao, H. C. Lin, *Macromolecules,* **39,** *8559* (2006); (b) Y. Y. Chen, C. H. Lin, *Polymer,* **48,** *5268* (2007).
28. (a) K.H. Chang, C. C. Huang, Y. H. Liu, Y. H. Hu, P. T. Chou, Y. C. Lin, *J. Chem. Soc., Dalton Trans., 1731* (2004); (b) P. F. Wang, Z. Hong, Z. Y. Xie, S. W. Tong, O. Y. Wong, C. S. Lee, N. B. Wong, L. S. Hung, S. T. Lee, *Chem. Commun., 1664* (2003); (c) Y. Hamada, T. Sano, M. Fujita, T. Fujii, Y. Nishio, K. Shibata, *Jpn. J. Appl. Phys.,* **32,** ***L511*** **(**1993); (d) T. Sano, Y. Nishio, Y. Hamada, H. Takahashi, T. Usuki, K. Shibata, *J. Mater. Chem.,* **10,** *157* (2000); (e) C. M. Che, S. C. Chan, H. F. Xiang, M. C. W. Chan, Y. Liu, Y. Wang, *Chem. Commun., 1484* (2004).
29. C. M. Che, S. C. Chan, H. F. Xiang, M. C. W. Chan, Y. Liu, Y. Wang, *Chem. Commun., 1484* (2004).
30. A. M. Karampurwale, A. Ray, R. P. Patel, *Synth. React. Inorg. Met.-Org. Chem,* **19,** *219* (1989).
31. R. D. Archer, M. L. Illingsworth, D. N. Rau, C. J. Hardiman, *Macromolecules, 1371* (1985).
32. H. Chen, R. D. Archer, *Macromolecules,* **29,** *1957* (1996).
33. C. C. Kwok, Y. C. Yu, I. H. T. Sham, C. M. Che, *Chem. Commun., 2758* (2004).
34. C. H. Chen, J. Shi, *Coord. Chem. Rev.,* **171,** *161* (1998).
35. Q. Peng, M. Xie, Y. Huang, Z. Lu, Y. Cao, *Macromol. Chem. Phys.,* **206,** *2373* (2005).

CHAPTER 11

Redox and Photo Functions of Metal Complex Oligomer and Polymer Wires on the Electrode

Mariko Miyachi and Hiroshi Nishihara

Department of Chemistry, School of Science, The University of Tokyo, 7-3-1 Hongo, Bunkyo-ku, Tokyo 113-0033, Japan

CONTENTS

Macromolecules Containing Metal and Metal-like Elements,
Volume 10: Photophysics and Photochemistry of Metal-Containing Polymers,
Edited by Alaa S. Abd-El Aziz, Charles E. Carraher Jr., Pierre D. Harvey, Charles U. Pittman Jr., Martel Zeldin.

I. INTRODUCTION

Molecular assembly has been attracting attention as a promising method in nanotechnology and is expected to provide a breakthrough in the miniaturization and functionalization of electronic devices. Up to now, the miniaturization and integration of devices have progressed via top-down technology, especially fine processing technology of semiconductors, which dominate today's electronics.[1] Fine processing technology, however, is faced with difficulties in miniaturization on the nanometer scale because of the wavelength limitation of optical lithography and/or its cost.

Another noteworthy approach for miniaturization and functionalization is a bottom-up technology using molecular assembly. Since bottom-up technology employs the principle of building up molecules from the surface of substrates, nano-scale fabrication is essentially possible employing this approach. In addition, various functional devices can be obtained, as functional molecules can be employed in the system. For example, photoelectric conversion devices can be obtained with photoreceptor molecules,[2,3] ion sensors can be obtained with ion-capturing molecules,[4] and biological functions can be obtained with biomolecules.[5,6] Many such devices take advantage of the redox properties of the molecules; consequently, they work in electrolyte solution—a *wet system*.

The operation of molecular devices in wet systems can yield performances unobtainable in dry systems. For example, molecular devices in wet systems can provide characteristic electron transfer control. While wet systems have a disadvantage in performance speed because of the slow mobility of ions, they have a notable advantage in fine and precise control of the direction and kinetics of electron transfer, even at room temperature. This characteristic can lead to a low noise level, because electron transfer is governed by the absolute electrochemical potentials of a series of molecules coexisting in the system.

Even a small potential difference, in the order of a millivolt can offer definitive control of electron transfer (the noise level in a dry system at room temperature is 5 mV).

In addition to the above, molecular devices in wet systems have the potential to acquire ultimate functions achieved in nature. Since the fine tuning of different molecular functionalities affords the ultimate functions in nature,[7–10] molecular devices with various combinations of molecules in wet systems have the possibility of providing the highest performance.

In this chapter, we describe three different systems with which to construct electro- and photo-functional molecular assemblies on electrode surfaces. The first is the bottom-up fabrication of redox-conducting metal complex oligomers on an electrode surface and their characteristic redox conduction behavior, distinct from conventional redox polymers.[11–13] The second is a photoelectric conversion system using a porphyrin and redox-conducting metal complex.[14] The third is the use of a cyanobacterial photosystem I with molecular wires for a biophotosensor and photoelectrode.[15,16] These systems will be the precursors of new types of molecular devices working in electrolyte solution.

II. BOTTOM-UP FABRICATION OF REDOX-CONDUCTING METAL COMPLEX OLIGOMERS ON AN ELECTRODE SURFACE AND THEIR REDOX CONDUCTION BEHAVIOR

The control of electron transfer is a critical issue in the fabrication of molecular electronic devices from the viewpoint of electronic circuit formation; however, electron transfer processes of redox polymer-coated electrodes fabricated using a conventional polymer-coating method usually shows a diffusion-like behavior because the redox sites are randomly distributed in the polymer film (Fig. 1a);[17–20] consequently, it is difficult to control the electron transfer direction in three dimensions.

In contrast, a new type of redox polymer-coated electrode has recently been fabricated using the bottom-up method, in which redox-active molecules are connected with molecular wires, and the wires act as the current collector.[11–13] In this case, electrons can be transported through the wires, and control of the electron transfer pathway is possible by changing the structure of the molecular wires. If the wire has a linear structure, redox active molecules with the wire connections exhibit a structure similar to that of a beaded curtain (Fig. 1b), in which the electron transfers in a straightforward manner along each line. Furthermore, when the wire is composed of redox active molecules, we observe the promising phenomenon that the electron transfers via the redox process in the wire, whose mechanism would

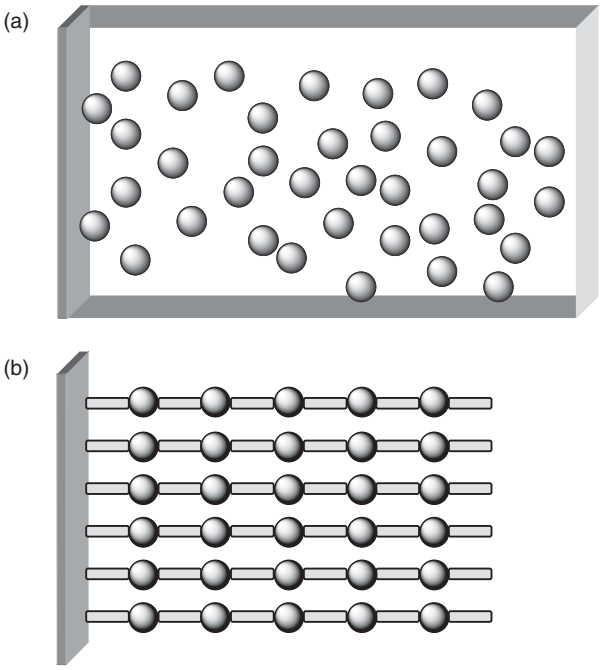

FIGURE 1. Two types of films with redox complexes on the electrode. (a) Conventional redox polymer film (redox sites (circles) are randomly located). (b) Highly ordered film prepared by the bottom-up method.

be different from the conventional diffusion process. An extension of the bottom-up method would enable the construction of molecular electronic circuits.

In this section, we describe the fabrication of metal complex oligomer and polymer wires composed of bis(terpyridine)metal complexes using the bottom-up method.[11–13] This method has an advantage in fabricating organized structures of rigid redox polymer wires with the desired numbers of redox metal complexes. We also present a new electron-transport mechanism applicable to the organized redox polymer wires-coated electrode.

A. Bottom-Up Fabrication of Metal Complex Oligomer and Polymer Wires

We selected two types of molecular wires to form desired structures for the electrode. The first has a linear structure with a bis-terpyridine moiety ($\mathbf{L_1}$: azobenzene-bridged bis-terpyridine ligand, $\mathbf{L_2}$: phenylene-bridged bis-terpyridine ligand), as illustrated in Figure 2. This type of wire can form a linear structure such as a bead curtain. The second has a triangular structure with three terpyridine

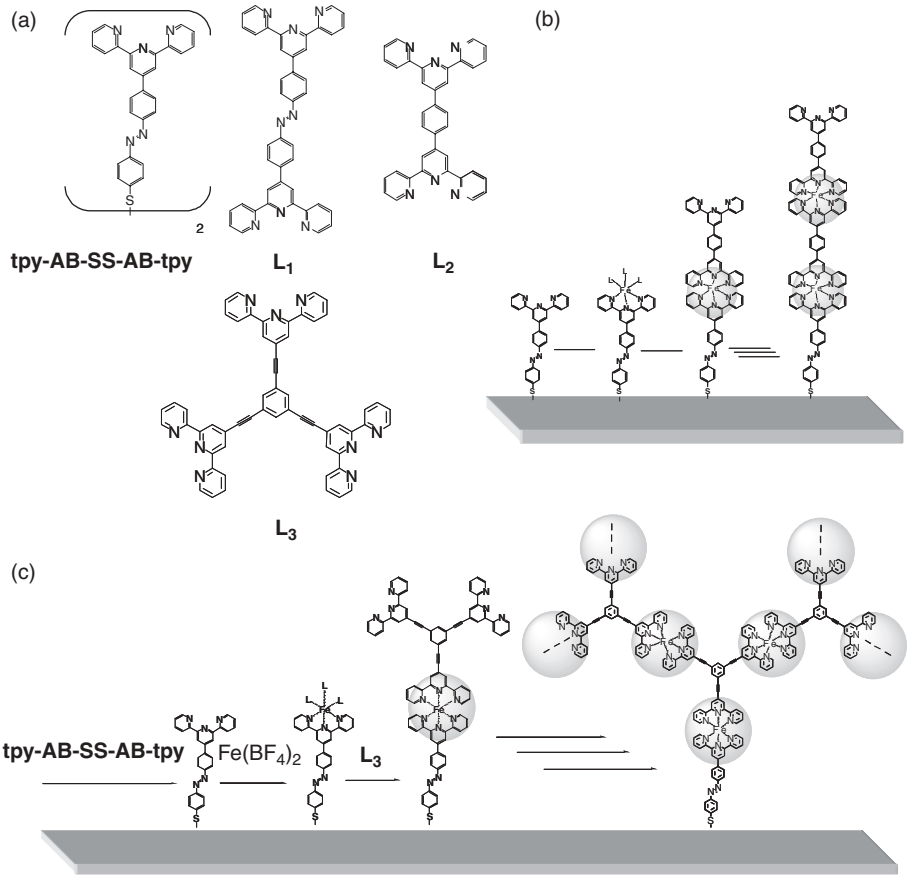

FIGURE 2. Chemical structures of the ligands and stepwise coordination methods to prepare linear and branched oligomer and polymer wires on an Au/mica or Au/ITO plate. (Reprinted with permission from Ref. 13.)

moieties (**L_3**: 1,3,5-C_6H_3(terpyridine)$_3$) (Fig. 2). This type of wire can form a branched structure such as that of a dendrite.

A typical method for fabricating multiple complex layers is illustrated in Figure 2.[11,12] First, an Au/mica or Au/ITO plate is immersed in a chloroform solution of **tpy-AB-SS-AB-tpy** (tpy=2,2′:6′,2″ -terpyridyl), providing Au-S-AB-tpy SAM on the plate. In the case of connecting the Fe(II) ion, the tpy-terminated plate is immersed in 0.1 M $Fe(BF_4)_2$ aq or $(NH_4)_2Fe(SO_4)_2$ aq to form a metal complex. Subsequently, the metal-terminated surface is immersed in a chloroform solution of the ligand **L_1** or **L_2** to form a bis(tpy)iron structure (Fig. 2b). The latter two processes are repeated for the preparation of multilayered bis(tpy)iron (II) complex films with linear structures. When **L_3** is used instead of **L_1** or **L_2**, the resulting molecular wires have a dendritic structure (Fig. 2c).

It is also possible to prepare the film with bis(tpy)cobalt complex oligomers and polymers. In addition to the process of bis(tpy)iron(II) complex films, a process of electrochemical oxidation from Co^{II} to Co^{III} is required after immersing the plate in a chloroform solution of $\mathbf{L_1}$, in which the plate is held at 0.3 V (vs. Ag/Ag^+) to obtain multilayered bis(tpy)cobalt complex films.[11] Hereafter, the film for the *n*th complexation cycles using metal ion and bridging ligand $\mathbf{L}_x$ is abbreviated as $[n\mathrm{ML}_x]$.

The films with linear oligomers can be quantitatively fabricated by stepwise coordination unless steric hindrance occurs. In $[n\mathrm{Fe}\mathbf{L_1}]$ and $[n\mathrm{Fe}\mathbf{L_2}]$ ($n = 1-10$), a quantitative increase in molecular surface coverage Γ with increasing n was confirmed by an increase in an absorption peak at 592 nm ascribed to the MLCT transition in the ultraviolet-visible (UV-VIS) spectra, and by the amount of charge for the reversible redox reaction of the Fe^{III}/Fe^{II} couple, which appeared at 0.67 V vs. ferrocenium/ferrocene (Fc^+/Fc) in the cyclic voltammograms (CV) in $Bu_4NClO_4-CH_2Cl_2$ (Figs. 3 and 4). In contrast,

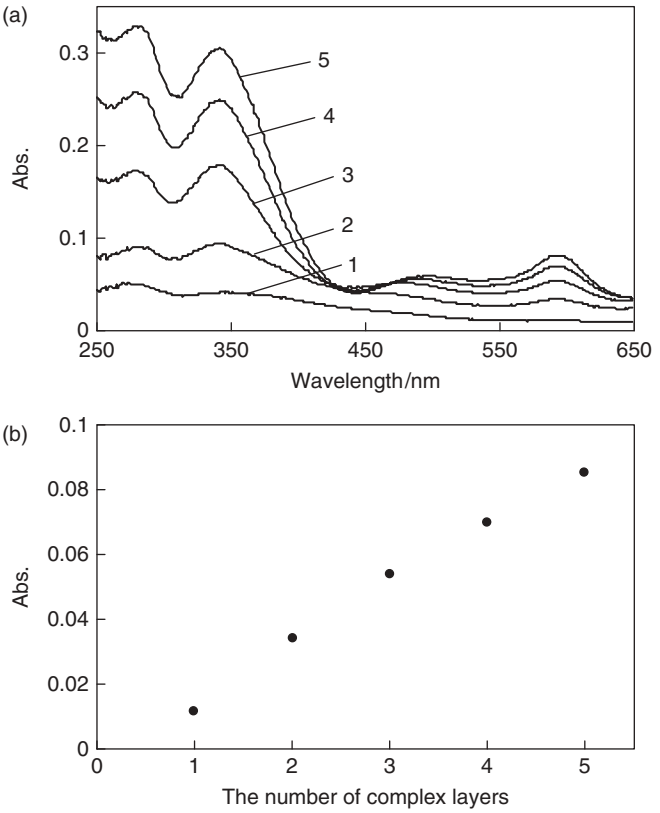

FIGURE 3. (a) UV-VIS absorption spectra of $[n\mathrm{Fe}\mathbf{L_1}]$ (n=1–5), and (b) plots of the absorption peak at 592 nm vs. the number of complex layers. (Reprinted with permission from Ref. 13.)

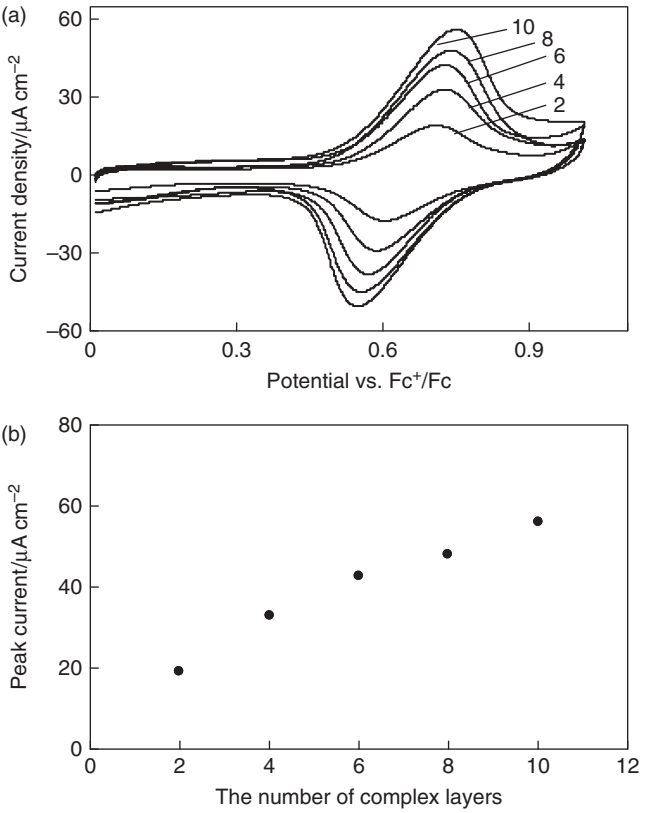

FIGURE 4. (a) Cyclic voltammograms of [nFe$\mathbf{L_1}$] (n = 2, 4, 6, 8, and 10) in 0.1 M Bu_4NClO_4–CH_2Cl_2 at a scan rate of 0.1 V s^{-1}, and (b) plots of the anodic peak current vs. the number of complex layers. (Reprinted with permission from Ref. 13.)

in the case of the film with a dendritic structure, the increase in molecular surface coverage Γ should ideally follow the 2^n-1 relationship with increasing n. The ideal increase in surface coverage, however, stopped beyond four complex layers (Fig. 5) because of collisions between the edge of the molecular wires and the Au electrode surface, as expected from the MM+ calculation (Fig. 6). Once the n value exceeded 4, the increase in Γ slowed and approached the relationship for that of linear polymers, [nFe$\mathbf{L_2}$] (Fig. 5), which is reasonable because for both linear and branched wires only vertical space is available for additional molecular growth.

The formations of these films were visually observed using secondary electron microscopy (SEM) and scanning tunneling microscopy (STM). Figure 7 shows top views and cross-sectional views of a 47 complex layers film with a linear structure, [47Co$\mathbf{L_1}$], on a Au electrode. The visualized thickness of [47Co$\mathbf{L_1}$] in the cross-sectional views was $\sim$100 nm, in good agreement with

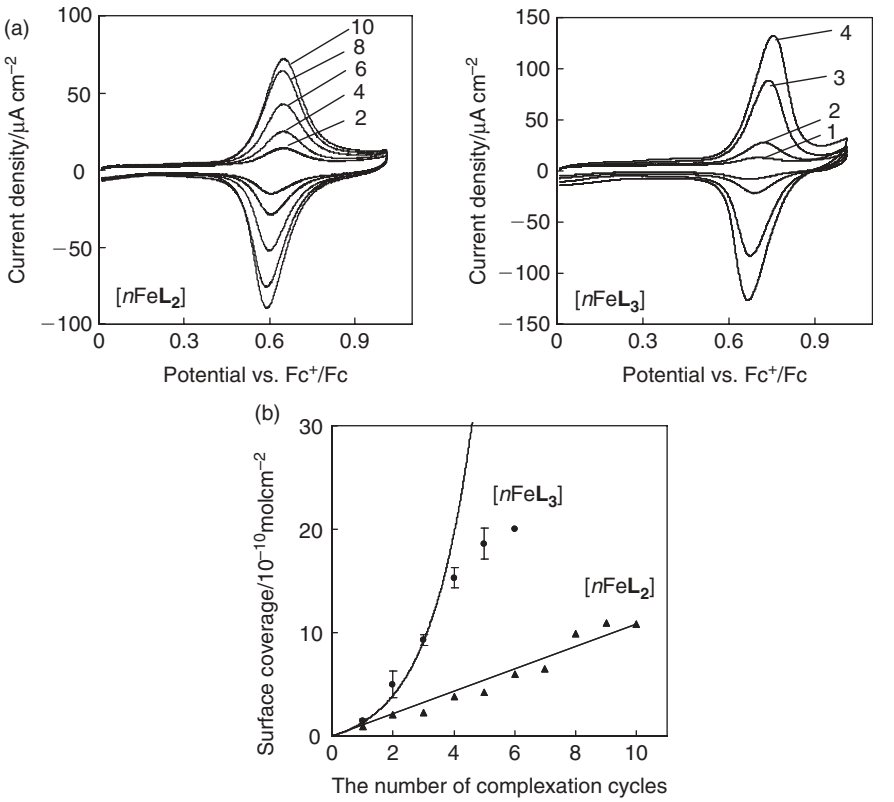

FIGURE 5. (a) Cyclic voltammograms of [nFe$\mathbf{L_2}$] (n = 2, 4, 6, 8, 10) and [nFe$\mathbf{L_3}$] (n = 1–4) in 1 M Bu_4NClO_4–CH_2Cl_2 at a scan rate of 0.1 V s^{-1}, and (b) plots of the coverage of redox-active sites, Γ (mol cm^{-2}) vs. n for [nFe$\mathbf{L_2}$] and [nFe$\mathbf{L_3}$]. The lines in the figure show the relationship of Γ=C × n for [nFe$\mathbf{L_2}$] and that of Γ=C (2^n − 1) for [nFe$\mathbf{L_3}$]. (Reprinted with permission from Ref. 13.)

the ideal thickness of 94 nm (1 molecular unit length, 2 nm).[11] STM observations distinguished the different structures of the films. In the film with a linear structure, uniform 6 nm-o.d. circular domains were confirmed, where distinct differences between each generation could not be obtained. This observation indicates the uniform structure of the film. In contrast, for the film with loosely distributed oligomer wires with dendritic structure composed of Fe complex, the increase in generations was clearly reflected in the STM image. In the case of [1Fe$\mathbf{L_2}$$nFe\mathbf{L_3}$], the complex with $\mathbf{L_3}$ stacked onto the sparse coverage of [1Fe$\mathbf{L_2}$] provided an image of circular dots whose diameters increased with the number of complexation cycles (Fig. 8). These results strongly support the formation of ideal structures by the stepwise coordination method on the surface.

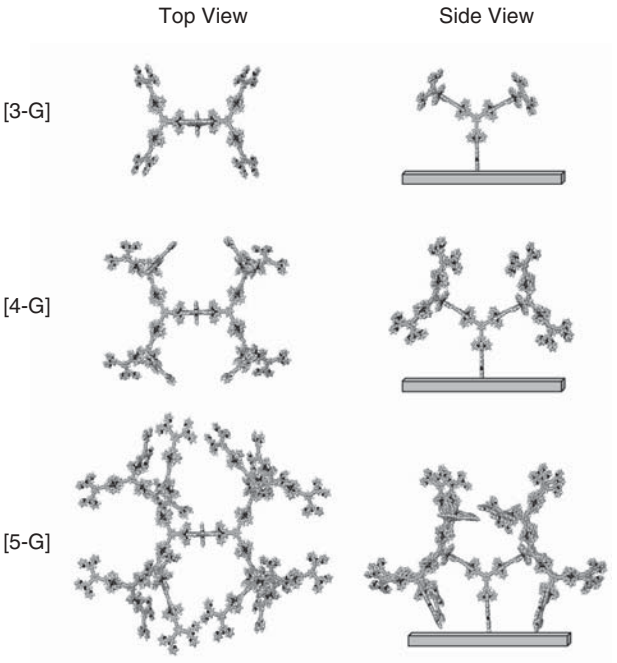

FIGURE 6. Molecular structures of [nFe$\mathbf{L_3}$] (n = 3, 4, 5) acquired by MM+ calculation. (Reprinted with permission from Ref. 13.)

B. Electron Transport Behavior of the Molecular Wires on the Electrode

We describe here that the redox oligomer wires fabricated with the stepwise coordination method show characteristic electron transport behavior distinct from conventional redox polymers. Redox polymers are representative electron-conducting substances in which redox species are connected to form a polymer wire.[21–25] The electron transport was treated according to the concept of redox conduction, based on the diffusional motion of collective electron transfer pathways, composed of electron hopping terms and/or physical diffusion.[17,18,26–30] In the characterization of redox conduction, the Cottrell equation can be applied to the initial current–time curve after the potential step in potential step chronoamperometry (PSCA), which causes the redox reaction of the redox polymer film:

$$i = -n_e FAC(D_{app}/\pi t)^{1/2} \tag{1}$$

where n_e, F, A, C, and D_{app} refer to the number of electrons, the Faraday constant, the electrode area, the concentration of redox sites in the film, and the

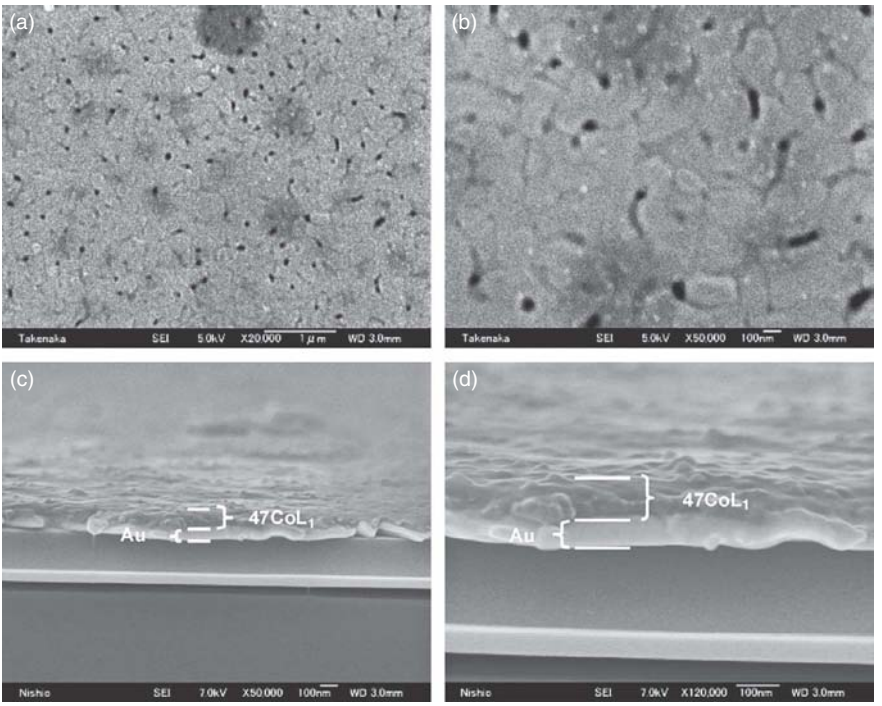

FIGURE 7. SEM images of [47Co$\mathbf{L_1}$]: (a,b) top view; (c,d) cross-sectional view. (Reprinted with permission from Ref. 13.)

apparent diffusion coefficient of collective electron transfer pathways in the film, respectively.[31–41]

We first attempted to evaluate D_{app} for the $Fe(tpy)_2$ oligomer wires prepared by stepwise formation on a gold electrode using PSCA, but in most cases, the plots of i vs. $t^{1/2}$ did not show any region of straight lines intersecting the origin, indicating that electron transport analysis based on the diffusion process is not applicable.[42] Figure 9 shows the $i-t$ plots after the potential step from 0.96 to 0.36 V vs. Fc^+/Fc for reduction of the Fe^{III} complex moieties in linear $Fe(tpy)_2$ oligomer wires, [n$\mathbf{FeL_2}$] (n = 2, 4, 6, and 8), and in branched oligomer wires [nFe$\mathbf{L_3}$] (n = 2, 3, and 4), in 1 M $Bu_4NClO_4-CH_2Cl_2$. In all cases, the curvatures for the Fe^{III}/Fe^{II} couple showed a similar behavior. In the initial period, a quasi-plateau region appeared, and a rapid decrease in current followed. It is obvious that the branched wires [nFe$\mathbf{L_3}$] showed much longer time-constant current flow behavior $\sim$0.12 s for [4Fe$\mathbf{L_3}$]; Fig. 9b) than that of the linear wires [nFe$\mathbf{L_2}$] ($\sim$0.05 s for [8Fe$\mathbf{L_2}$]; Fig. 9a).

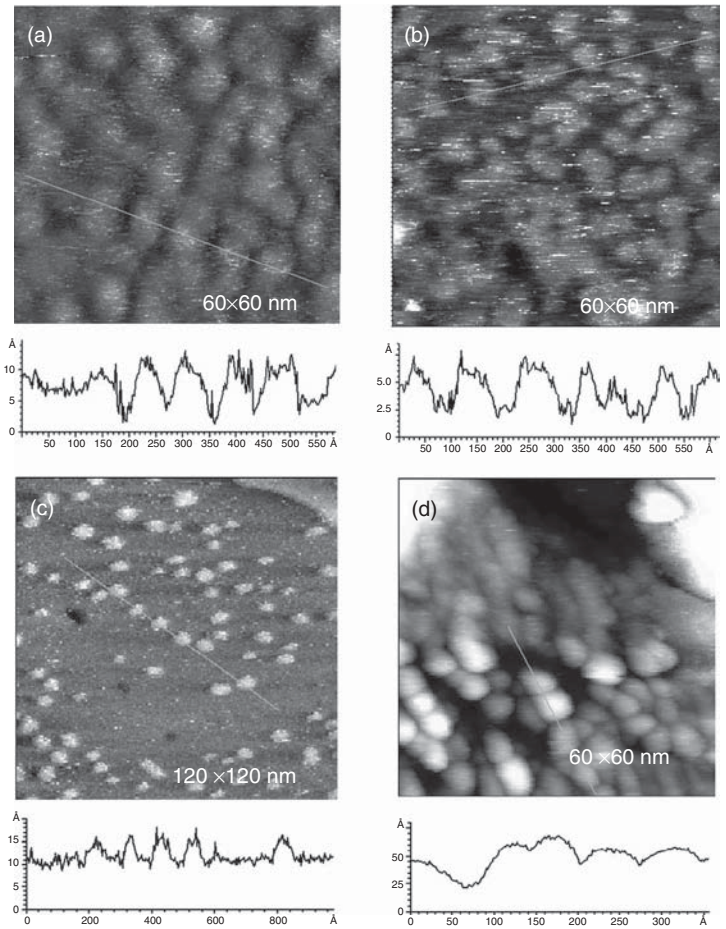

FIGURE 8. STM images of (a) [2Fe$\mathbf{L_1}$], (b) [2Fe$\mathbf{L_3}$], and (c,d) [1Fe$\mathbf{L_2}$*n*Fe$\mathbf{L_3}$] (n=3, 4, t_1=10 s). (Reprinted with permission from Ref. 13.)

This difference strongly supports the dominance of the through-bond electron transport pathway. This occurs because if the simple diffusion process containing through-space electron transfer is dominant, the electron transport kinetics of the branched oligomer film is similar to, or faster than, that of the linear oligomer films, as the density of redox sites in the branched oligomer film is similar to, or higher than, that in the linear oligomer films.

An explanation of the characteristic *i-t* behaviors requires the application of simple kinetic determination based on the molecular-level sequential redox

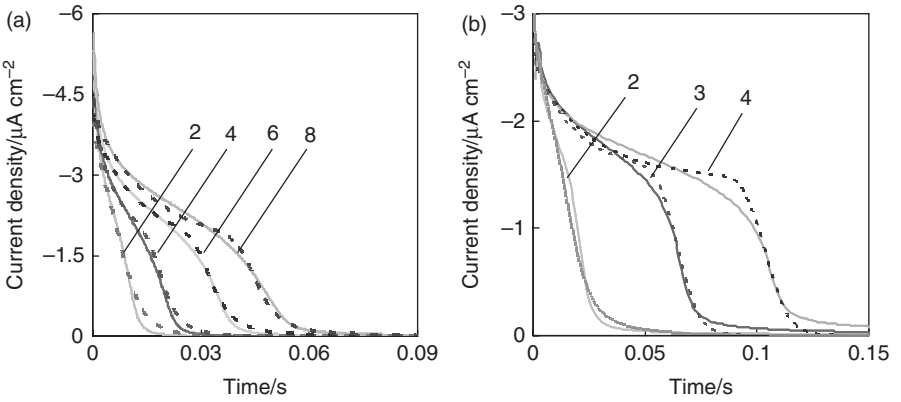

FIGURE 9. Current-time plots after the potential step from 0.96 to 0.36 V vs. Fc^+/Fc to reduce the Fe^{III} complex moieties in (a) [*n*Fe**L**$_2$] (*n*=2, 4, 6, and 8) and in (b) [*n*Fe**L**$_3$] (*n*=2, 3, and 4) in 1 M $Bu_4NClO_4-CH_2Cl_2$ (*solid lines*). The numbers in the figure refer to *n*. Simulated curves in dotted lines are obtained with k_1=240 s^{-1}, k_2 (**L**$_2$)=1.7 × 10^{13} cm^2 mol^{-1} s^{-1}, and C_{dl}=10 μC cm^{-2} for [2Fe**L**$_2$]; k_1=240 s^{-1}, k_2 (**L**$_2$)=1.7 × 10^{13} cm^2 mol^{-1} s^{-1}, and C_{dl}=12 μC cm^{-2} for [4Fe**L**$_2$]; k_1=210 s^{-1}, k_2 (**L**$_2$)=1.6 × 10^{13} cm^2 mol^{-1} s^{-1}, and C_{dl}=27 μC cm^{-2} for [6Fe**L**$_2$]; and k_1=210 s^{-1}, k_2 (**L**$_2$)=1.2 × 10^{13} cm^2 mol^{-1} s^{-1} and C_{dl}=40 μC cm^{-2} for [8Fe**L**$_2$] for A, and obtained with k_1=270 s^{-1}, k_2 (**L**$_2$)=4.9 × 10^{13} cm^2 mol^{-1} s^{-1} and C_{dl}=19 μC cm^{-2} for [2Fe**L**$_3$]; k_1=270 s^{-1}, k_2 (**L**$_3$)=5.0 × 10^{12} cm^2 mol^{-1} s^{-1}, and C_{dl}=19 μC cm^{-2} for [3Fe**L**$_3$]; and k_1=260 s^{-1}, k_2 (**L**$_3$)=4.4 × 10^{12} cm^2 mol^{-1} s^{-1}, and C_{dl}=27 μC cm^{-2} for [4Fe**L**$_3$]. (Reprinted with permission from Ref. 13.)

conduction along molecular wires, as displayed in Figure 10. The concept of this mechanism is as follows. When an oxidized complex, Ox, in molecular wires is reduced to form a reduced complex, Red, with application of a sufficient overpotential to prevent back electron transfer in PSCA, the electron transfer kinetics in the case of the *n*th complex sequence can be written as follows:

$$\begin{aligned}
&\mathrm{Ox}_1 + \mathrm{e}^- \rightarrow \mathrm{Red}_1, && \text{rate constant} : k_1 \quad \text{(a)}\\
&\mathrm{Red}_1 + \mathrm{Ox}_2 \rightarrow \mathrm{Ox}_1 + \mathrm{Red}_2, && \text{rate constant} : k_2 \quad \text{(b)}\\
&\mathrm{Red}_2 + \mathrm{Ox}_3 \rightarrow \mathrm{Ox}_2 + \mathrm{Red}_3, && \text{rate constant} : k_3 \quad \text{(c)}\\
&- - - - - && \\
&\mathrm{Red}_{n-1} + \mathrm{Ox}_n \rightarrow \mathrm{Ox}_{n-1} + \mathrm{Red}_n, && \text{rate constant} : k_n \quad \text{(d)}
\end{aligned} \tag{2}$$

where Red_i and Ox_i are reduced and oxidized forms, respectively, in the *i*th layer or generation in the film, and

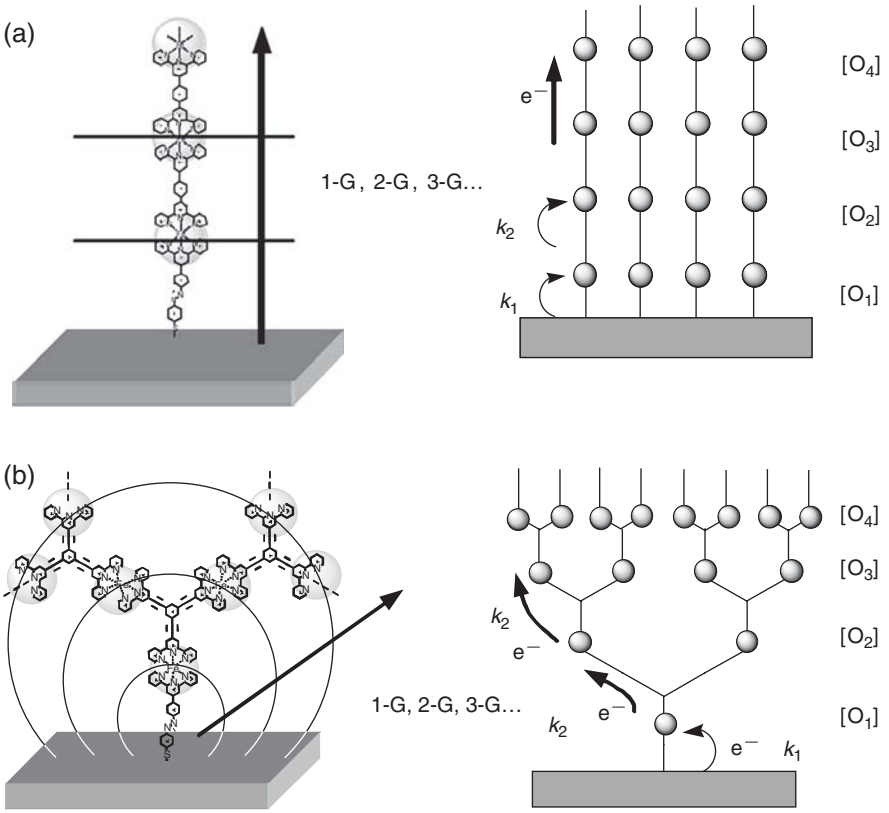

FIGURE 10. Images of the electron transfer mechanisms in (a) linear and (b) branched molecular wires. (Reprinted with permission from Ref. 13.)

$$
\begin{aligned}
\mathrm{d}[\mathrm{Ox}_1]/\mathrm{d}t &= -k_1[\mathrm{Ox}_1] + k_2([\mathrm{Ox}_1]_0 - [\mathrm{Ox}_1])[\mathrm{Ox}_2] && \text{(a)}\\
\mathrm{d}[\mathrm{Ox}_2]/\mathrm{d}t &= -k_2([\mathrm{Ox}_1]_0 - [\mathrm{Ox}_1])[\mathrm{Ox}_2] + ([\mathrm{Ox}_3]_0/[\mathrm{Ox}_2]_0)k_2([\mathrm{Ox}_2]_0 \\
&\quad -[\mathrm{Ox}_2])[\mathrm{Ox}_3] && \text{(b)}\\
\mathrm{d}[\mathrm{Ox}_3]/\mathrm{d}t &= -([\mathrm{Ox}_3]_0/[\mathrm{Ox}_2]_0)k_2([\mathrm{Ox}_2]_0 - [\mathrm{Ox}_2])[\mathrm{Ox}_3] \\
&\quad +([\mathrm{Ox}_4]_0/[\mathrm{Ox}_2]_0)k_2([\mathrm{Ox}_3]_0 - [\mathrm{Ox}_3])[\mathrm{Ox}_4] && \text{(c)} \qquad (3)\\
&- - - - - \\
\mathrm{d}[\mathrm{Ox}_{n-1}]/\mathrm{d}t &= -([\mathrm{Ox}_{n-1}]_0/[\mathrm{Ox}_{n-2}]_0)k_2([\mathrm{O}_{n-2}]_0 - [\mathrm{Ox}_{n-2}])[\mathrm{Ox}_{n-1}] \\
&\quad +([\mathrm{Ox}_n]_0/[\mathrm{Ox}_{n-2}]_0)k_2([\mathrm{Ox}_{n-1}]_0 - [\mathrm{Ox}_{n-1}])[\mathrm{Ox}_n] && \text{(d)}\\
\mathrm{d}[\mathrm{Ox}_n]/\mathrm{d}t &= -([\mathrm{Ox}_n]_0/[\mathrm{Ox}_{n-2}]_0)k_2([\mathrm{Ox}_{n-1}]_0 - [\mathrm{Ox}_{n-1}])[\mathrm{Ox}_n] && \text{(e)}
\end{aligned}
$$

where $[\mathrm{Ox}_i]_0$ and $[\mathrm{Ox}_i]$ are the initial and present two-dimensional concentrations, respectively, of the oxidized form of the redox moiety in the *i*th layer or generation in mol cm^{-2}.

The reaction kinetics is controlled by two factors: k_1 (s^{-1}) for the electron transfer between the nearest redox site and the electrode, and k_2 ($cm^2\ mol^{-1}\ s^{-1}$), for the electron transfer between the neighboring redox sites in a molecular wire. Here, the rate of electron transfer to the neighboring site in a polymer wire is assumed to be constant in a primary approximation. In the case of linear oligomer wires such as [*n*Fe**L$_1$**] and [*n*Fe**L$_2$**],

$$\begin{aligned}[\mathrm{Red}_1] + [\mathrm{Ox}_1] = [\mathrm{Red}_2] + [\mathrm{Ox}_2] = [\mathrm{Red}_3] + [\mathrm{Ox}_3] \\ = \cdots = [\mathrm{Red}_n] + [\mathrm{Ox}_n] = \text{constant}\end{aligned} \tag{4}$$

and in the case of branched oligomer wires, [*n*Fe**L$_3$**],

$$\begin{aligned}[\mathrm{Ox}_1] + [\mathrm{Red}_1] = ([\mathrm{Ox}_2] + [\mathrm{Red}_2])/3 = ([\mathrm{Ox}_3] + [\mathrm{Red}_3])/7 \\ = \cdots = ([\mathrm{Red}_n] + [\mathrm{Ox}_n])/(2^n - 1) = \text{constant}\end{aligned} \tag{5}$$

The practical current can be observed as $d[Ox_1]/dt$, which implies that the constant current flows in the initial period when the electron transfer between the neighboring redox sites is sufficiently fast compared to that between the electrode and the first redox site. The numerical calculation involving the double-layer capacitance, which decays exponentially with time, provided the simulated curves with parameters $k_1 = 220 \pm 10\ s^{-1}$ and k_2 (**L$_2$**) $= 1.4 \pm 0.1 \times 10^{13}\ cm^2\ mol^{-1}\ s^{-1}$ and C_{dl}=25 ± 15 μC cm^{-2}, satisfactorily reproducing all of the experimental results of [*n*Fe**L$_2$**] (n = 2, 4, 6, and 8), as shown in Figure 9a. The similar calculation of [*n*Fe**L$_3$**] (n = 2, 3, and 4) provided simulated curves with parameters k_1=260 ± 10 s^{-1} and k_2 (**L$_3$**) $= 4.8 \pm 0.2 \times 10^{12}\ cm^2\ mol^{-1}\ s^{-1}$ with the inclusion of C_{dl} of 22 ± 4 μC cm^{-2} (Fig. 9b). The similarity of the k_1 values between [*n*Fe**L$_2$**] and [*n*Fe**L$_3$**] is reasonable because the first Fe complex layer is the same in both cases. The k_2 value for the branched oligomer wire is lower than that for the linear wire, since the bridging ligand in the former is *m*-phenylene with a shorter π-conjugation than that in the latter with *p*-phenylene.

In this section, we described the quantitative formation of redox-conducting metal complex oligomer films achieved by selecting the conditions of stepwise coordination reactions at the electrode surface, and the characteristic through-bond electron transport of the molecular wires thus formed. These results indicate that by repeating the connection of metal ions and bridging ligands, we can synthesize polymer wires of various shapes with a desired number of metal complex units. One important advantage of this method is that we can easily prepare heterometal and heteroligand complex polymer wires by placing different kinds of metal ions and different kinds of bridging ligands at desired positions, after which we can accumulate multiple molecular functionalities, connected with the through-bond redox

conduction, which are important in the construction of molecular devices. The following section describes an example that displays photoelectric conversion.

III. PHOTOELECTRIC CONVERSION SYSTEM USING PORPHYRIN AND REDOX-CONDUCTING METAL COMPLEX WIRES

Here, we introduce the application of molecular wires described in the former section to a photoelectric conversion system. Construction of photoelectric conversion systems is a significant theme directly linked to environmental and energy issues. In nature, highly efficient photoelectric conversion ($\sim$100%) is achieved in photosynthesis. This ultimate function is realized by the appropriate arrangement of functional materials, which prevents back electron transfers and generates efficient electron transfers. Considering the photoelectric conversion system in nature, molecular assembly is potentially an effective tool in the construction of an efficient photoelectric conversion system. Using this method of molecular assembly, the arrangement of photoreceptors, donors, and acceptors has recently been used for a photoelectric conversion system. For example, Imahori et al. succeeded in the construction of a photoelectric conversion system with high quantum efficiency and long life, using donor–photosensitizer–acceptor molecules.[2,3] They selected a ferrocene-porphyrin-fullerene triad for the donor–photosensitizer–acceptor molecule, constructing integrated artificial photoelectric conversion assemblies on a gold electrode. This system established a cascade of photoinduced energy transfer and multistep electron transfer, achieving a high quantum yield of 50%.[2] They also reported an extremely long-lived, charge-separated state using a ferrocene-zinc-porphyrin—freebase-porphyrin—fullerene tetrad, for which the lifetime is 0.38 s, comparable to that for the bacterial photosynthetic reaction center.[3]

While molecular assembly has proven to be effective for a photoelectric conversion system, coordination reactions are possibly a simple approach for connecting such functional molecules, as presented in the previous section. We applied the stepwise coordination method to prepare a photoelectric conversion system. Since the molecular wire exhibits redox conduction through the wire,[11,13] efficient photo-electron transport through the redox sites in the wire is also expected. In this section, we demonstrate the fabrication of a photoelectric conversion system using ITO electrodes modified with $M(tpy)_2$ (M = Co, Fe, Zn) complex wires with a terminal porphyrin moiety as a photosensitizer. The behavior of photo-electron transfer from porphyrin to ITO through the molecular wire was investigated by changing the metal element in the $M(tpy)_2$ moieties.[14]

A. Bottom-Up Fabrication of the Porphyrin-Terminated Redox-Conducting Metal Complex Film on ITO

We fabricated the modified ITO electrodes[4] by a combination of SAM formation with a terpyridine derivative and stepwise metal-terpyridine coordination reactions in a similar manner as that described in the previous section (Fig. 11).[11,13] A cleaned ITO was immersed in a 0.1 M solution of 4-[2,2′:6′,2″-terpyridin]-4′-yl-benzoic acid (**tpy-BzA**) in chloroform for 12 h to anchor the carboxyl group to ITO. Subsequently, the modified ITO was immersed in an aqueous solution of 0.1 M $CoCl_2$, $Fe(BF_4)_2$ or $Zn(BF_4)_2$ for 2−3 h to form metal-terpyridine coordination reactions. Finally, the metal-coordinated ITO was immersed in a 0.1 M acetonitrile solution of a terpyridine-functionalized porphyrin, **tpy-ZnTPP**, providing the target molecular wires, **[M-ZnTPP]**, on electrodes (Fig. 11). In addition, a cleaned ITO was immersed in a 0.1 M ethanol solution of carboxylate-functionalized porphyrin, $\mathbf{C_{10}ZnTPP}$, to afford a modified ITO as a reference.

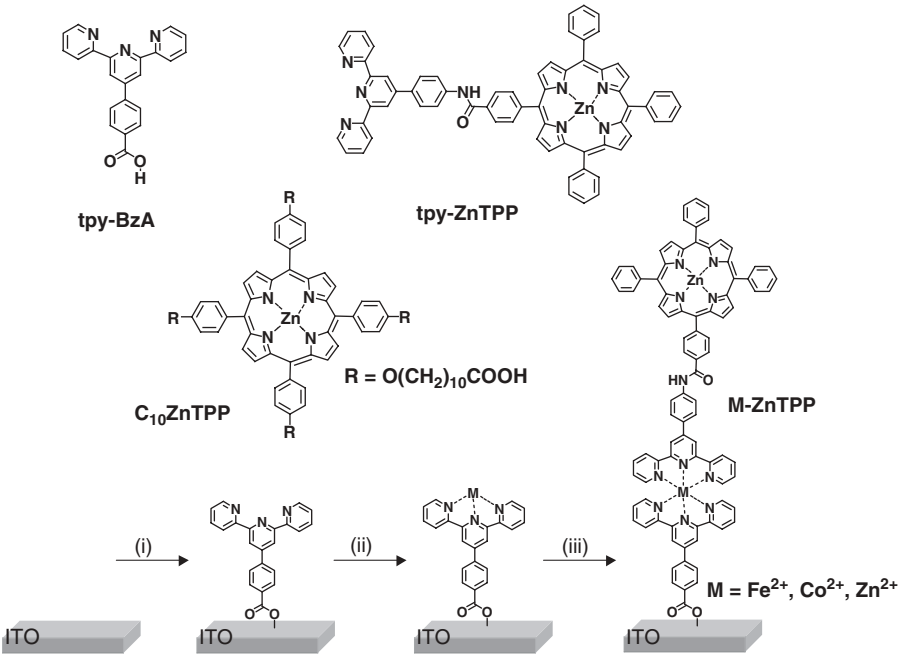

FIGURE 11. Chemical structure of the ligands used in this chapter, and stepwise coordination methods for the preparation of modified ITO electrodes: (i) immobilization of **tpy-BzA**, (ii) complexation with a metal ion, and (iii) complexation with **tpy-ZnTPP**. (Reprinted with permission from Ref. 14.)

B. Photoelectrochemical Properties of the Porphyrin-Terminated Redox-Conducting Metal Complex Film on ITO

The ITO modification having a Co-complex with **tpy-ZnTPP** (**[Co-ZnTPP]**), or an Fe-complex with **tpy-ZnTPP** (**[Fe-ZnTPP]**), or a Zn-complex with **tpy-ZnTPP** (**[Zn-ZnTPP]**), or the reference porphyrin **C_{10}ZnTPP** was confirmed by CV in $Bu_4NClO_4-CH_2Cl_2$ and by UV-VIS spectroscopy in a manner similar to that described earlier.

Photoelectrochemical properties of the modified ITO as working electrodes were measured in an argon-saturated 0.1 M Na_2SO_4 aqueous solution containing 50 mM triethanolamine (TEA) as an electron sacrificer. Upon irradiation of monochromatic light between 400 and 600 nm for **[M-ZnTPP]**/ITO and **C_{10}ZnTPP/**ITO, an anodic photocurrent appeared immediately, whose magnitude depended on the applied potential and the excitation wavelength (Fig. 12). A difference was observed at the potential at which the photocurrent for each electrode intersected at zero (E_F) (Fig. 12). The potential was more positive as follows: **[Co-ZnTPP]** $<$ **[Zn-ZnTPP]** $\approx$ **[Fe-ZnTPP]**$<$ **C_{10}ZnTPP**. These results indicate an association between photoelectron transfer and the molecular orbital levels of the molecular wires. Because only **[Co-ZnTPP]** has the level of the *d* orbital between the level of the S_1 state of the porphyrin and the ground state (Fig. 13), the *d*-orbital possibly transfers photoelectrons effectively. In addition, the π-conjugated chain of terpyridine possibly transfers photoelectrons more effectively than the alkyl chain of

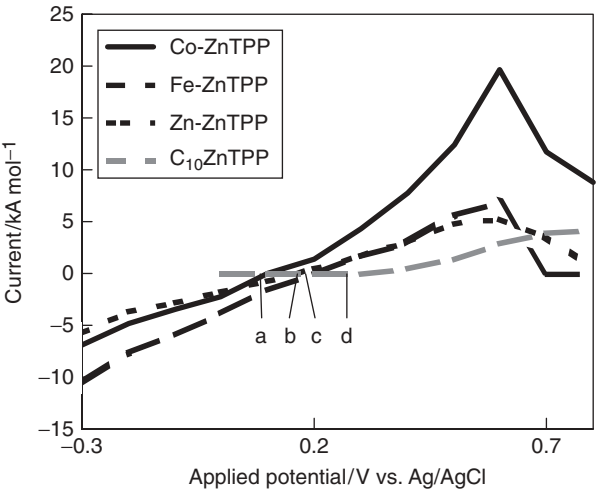

FIGURE 12. Potential dependence of the anodic photocurrent of modified ITO electrodes excited at 410 nm: (a) E_F (**[Co-ZnTPP]**), (b) E_F (**[Zn-ZnTPP]**), (c) E_F (**[Fe-ZnTPP]**), and (d) E_F (**C_{10}ZnTPP**). (Reprinted with permission from Ref. 14.)

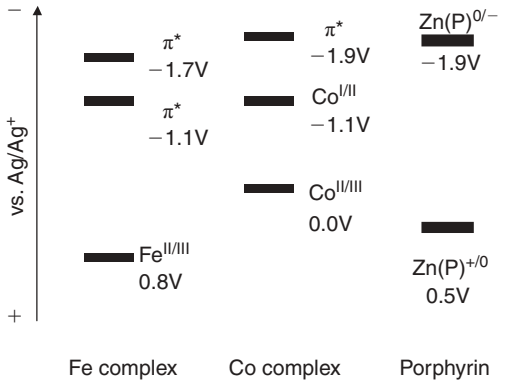

FIGURE 13. Energy diagram for modified ITO electrodes. (Reprinted with permission from Ref. 14.)

C_{10}ZnTPP, based on a comparison of data for **[Zn-ZnTPP]**, **[Fe-ZnTPP]**, and **C_{10}ZnTPP**. The results of quantum efficiency also support these assertions.

This section described the fabrication of ITO electrodes modified with porphyrin-terminated $M(tpy)_2$ complex wires by the stepwise coordination method, and it is demonstrated that the electronic nature of the molecular wire is critical to the photoelectron transfer from the porphyrin to ITO. These results suggest that the new facile fabrication method of molecular assemblies is effective in the construction of photoelectron transfer systems. The system could be upgraded by extending the wire length, embedding the redox potential step in the wire, increasing the photoreceptors in the wire, and/or incorporating donors and acceptors.

IV. BIOPHOTOSENSOR AND BIOPHOTOELECTRODE COMPOSED OF CYANOBACTERIAL PHOTOSYSTEM I AND MOLECULAR WIRES

In the previous section, we described a photoelectric conversion system made of porphyrin-terminated molecular wires. In this section, we introduce a biomolecule as a terminal photon-absorbing unit to connect to molecular wires, for the purpose of developing bioconjugated photonic devices. A combination of biotechnology and nanotechnology has been increasingly employed in recent studies, as biological systems operate on the nanoscale.[43–46] Forming electronic communication between biomaterials and electronic transducers is a fundamental challenge in the rapidly developing field of bioelectronics.

For example, Willner and co-workers accomplished electrical communication between glucose oxidase (GOx) and a gold electrode using molecular-level assembly.[5,6] Unprecedentedly effective electron transfer was observed from the FAD moiety to the electrode through the Au-nano particles (electron transfer turnover rate, 4500 s^{-1}), derived from molecular conjugation and bioconjugation.

Photosynthesis, another potential target of bioconjugation, is one of the most important processes in nature. In photosynthesis, photoelectric conversion with nearly 100% efficiency is involved in the primary process.[47–48] Such a high performance of photosystem I (PSI) is due to its well-designed spatial configuration. A large number of trials have applied such biological systems to electronic devices. For example, chloroplasts coated on an SnO_2 electrode have been examined as photoelectrochemical cells.[49–53]

Some reports have dealt with the immobilization of intact PSI onto electrodes, intended for photoelectrochemical devices. Cliffel and co-workers reported the adsorption of intact PSI onto an Au electrode surface using SAM modification of the electrode preliminary to PSI adsorption.[54–57] In these reports, PSI and SAM were connected by hydrogen bonding, and the orientation of PSI on the electrode varied. The orientation of PSI on the electrode is important, as the junction between PSI and electrodes favorably locates near the electron transfer chain. Therefore, direct modification of the electron transfer chain in PSI, based on molecular-level assembly, is a powerful tool for PSI use as a photonic device; however, few investigations have employed PSI as a photonic device based on molecular-level assembly.

We recently succeeded in using the functional bionic component, PSI, for photonic devices using molecular-level assembly. Two topics are introduced in this section. The first concerns a biophotosensor in which PSI is directly coupled with an artificial electronic device (a field-effect transistor; FET) via a molecular wire designed at the molecular level (Fig. 14). The second is a biophotoelectrode composed of PSI, ITO, and a molecular wire.

A. Biophotosensor Composed of Cyanobacterial Photosystem I, Molecular Wire, Gold Nanoparticle, and Transistor

Thermosynechococcus elongatus (*T. elongatus*) *BP-1*, employed as an origin of PSI, was used for a photoreceptor. The advantages of the PSI from *T. elongates* are its high thermal stability at temperatures $> 55°C$[58] and the efficient electron transfer activity of the isolated PSI.[59–61] While intensive research has been devoted to the molecular structure of PSI, its electron transfer mechanism and kinetics, and the treatment of living materials for the extraction of PSI,[62–66] the only high-resolution X-ray structure (2.5 Å) is now available for PSI from *T. elongatus*.[67] According to the literature, the PSI is composed of 12 protein subunits with a well-ordered electron transfer chain, located in the center of the protein (Fig. 15). PSI catalyzes the light-driven

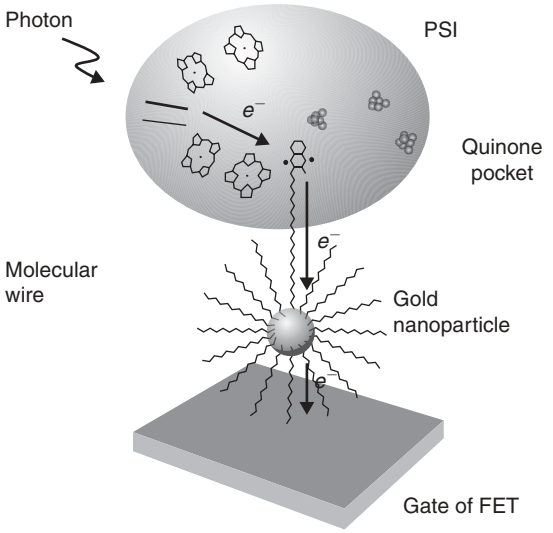

FIGURE 14. The concept of the biophotosensor composed of PSI and a transistor via molecular wire. (Reprinted with permission from Ref. 15.)

electron transfer. When PSI is irradiated, the special pair of chlorophylls (P700) is excited, followed by a stepwise electron transfer from P700 to F_B via A_0, A_1 (vitamin K_1; VK_1) (Fig. 16), F_x, and F_A without any backward transfer. Such events induce a through-membrane charge separation, with the resulting efficiency of electron transfer being $\sim$100%.[47,48]

The reconstitution process of PSI with a molecular wire is illustrated in Figure 16. After the extraction of VK_1 from the isolated intact PSI (Fig. 16a and b) using 50% water-saturated diethyl ether, the VK_1-free PSI was reconstituted with a specifically designed molecular wire of 1-[15-(3-methyl-1,4-naphthoquinon-2-yl)]pentadecyl thiolate-protected gold nanoparticle, **NQC15S-AuNP** (Fig. 17). After the removal of VK_1 from intact PSI, the naphthoquinone-sulfur-linked molecular wire equipped with a gold nanoparticle (**NQC15S-AuNP**, particle size: $\sim$1.6 nm)[68] was treated with VK_1-free PSI in an MES buffer solution to give a reconstituted PSI (**NQC15S-AuNP@PSI**) (Fig. 16c). The **NQC15S-AuNP** possesses three advantageous characteristics:

(1) A naphthoquinone unit is located at the end of a molecular wire to fit into the pocket (so-called quinone pocket) from which VK_1 has been extracted.
(2) The redox potential of naphthoquinone is suitable for the output of electrons from the A_0 site to a molecular wire.
(3) A sufficient molecular length of the wire is provided for the output of electrons from the pocket lacking VK_1 to the surface external to PSI, since the molecular wire has the same length of C15 alkyl-chain as that of VK_1 itself (Fig. 17).

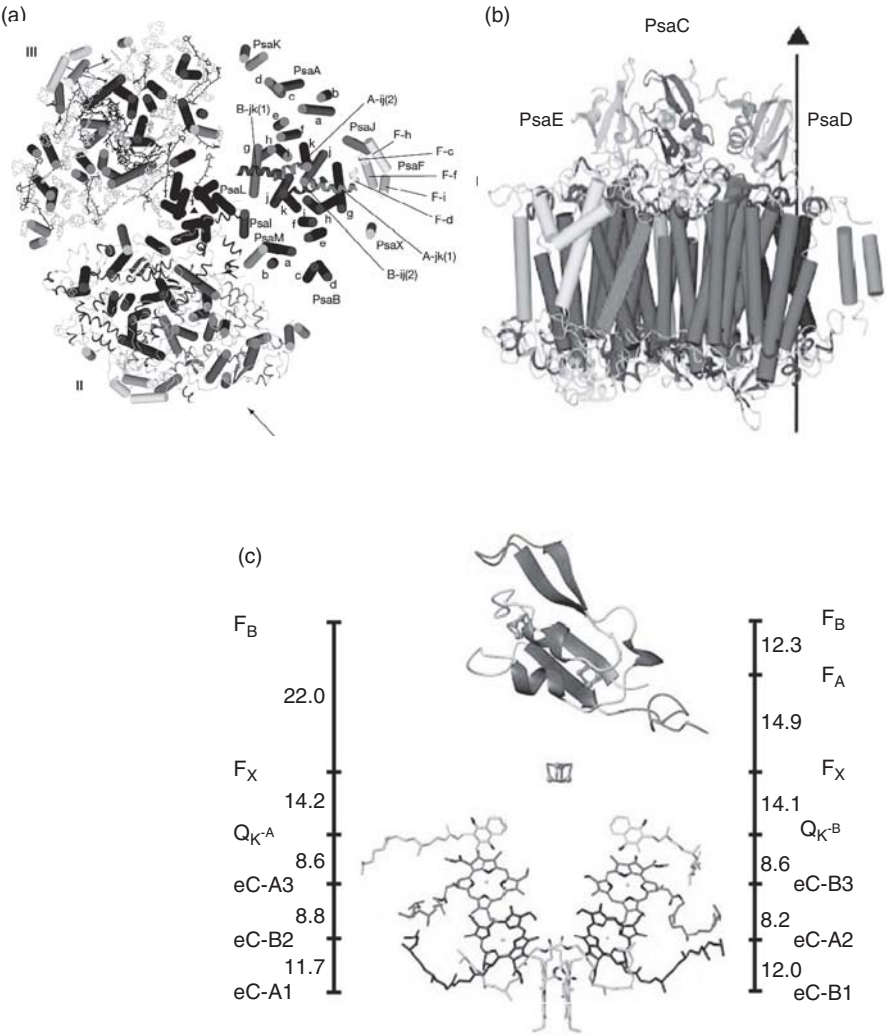

FIGURE 15. X-ray structure of cyanobacterial PSI: (a) top view of PSI trimer, (b) side view (view direction indicated by the arrow at monomer II in (a)), (c) view of the cofactors of the electron transfer chain in PSI monomer. (Reprinted with permission from Ref. 67.)

Reconstitution of PSI with **NQC15S-AuNP** was identified by TEM observation. Figure 18 shows the image of **NQC15S-AuNP@PSI**, in which can be seen both a large gray circle (10 nm-o.d.), attributed to PSI, and a small, clear and black dot (2 nm-o.d.), attributed to **NQC15S-AuNP**. Every gray circle (PSI) has one or two black dots (**NQC15S-AuNP**). Considering that one PSI has two VK_1 pockets, this stoichiometry indicates no random aggregations

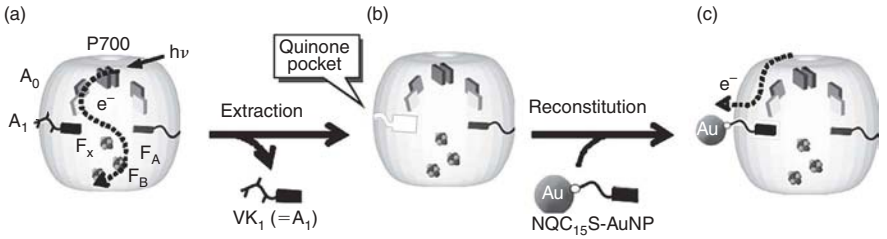

FIGURE 16. The process of the reconstitution of PSI with a molecular wire: (a) intact PSI, (b) VK_1-free PSI, and (c) **NQC15S-AuNP@PSI**. (Reprinted with permission from Ref. 15.)

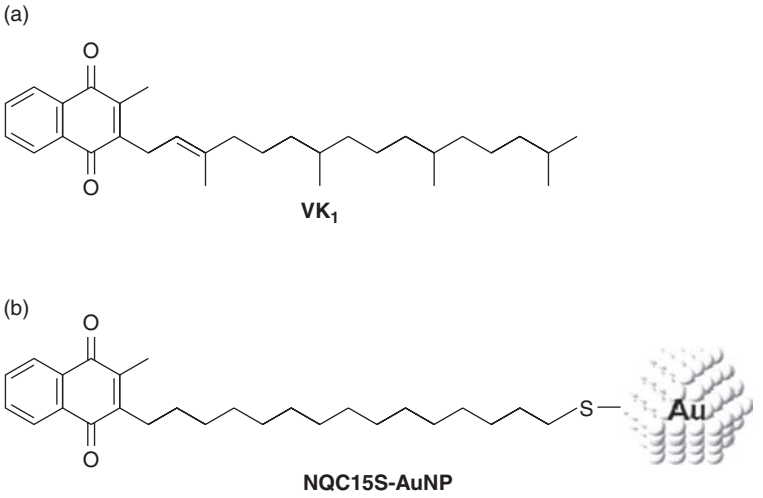

FIGURE 17. Molecular structure of (a) VK_1 and (b) **NQC15S-AuNP**.

and only connections via reconstitution at the VK_1 sites. A common photoactivity test of reconstituted PSI with **NQC15S-AuNP** was also useful in confirming that the 2-methyl-1,4-naphthoquinone moiety of **NQC15S-AuNP** was fitted to the quinone pocket of PSI and worked as a mediator of the electron transport system in PSI.[15]

A photocurrent measurement of **NQC15S-AuNP@PSI** chemically connected to a 1,4-benzenedimethanethiol SAM-modified gold electrode was carried out in the presence of sodium L-ascorbate (NaAs) as a sacrificial reagent and 2,6-dichloroindophenol sodium hydrate (DCIP) as a mediator in a MES-NaOH (pH 6.4) buffer solution containing $NaClO_4$ as an electrolyte at 0 V vs. Ag/AgCl. A clear peak at 680 nm was observed, consistent with the absorption spectrum of PSI and indicating that these photocurrent responses were due to the photoexcitation of PSI. Finally, this system was applied to the gate of an FET, demonstrating the potential of the system as an electronic imaging device.[15]

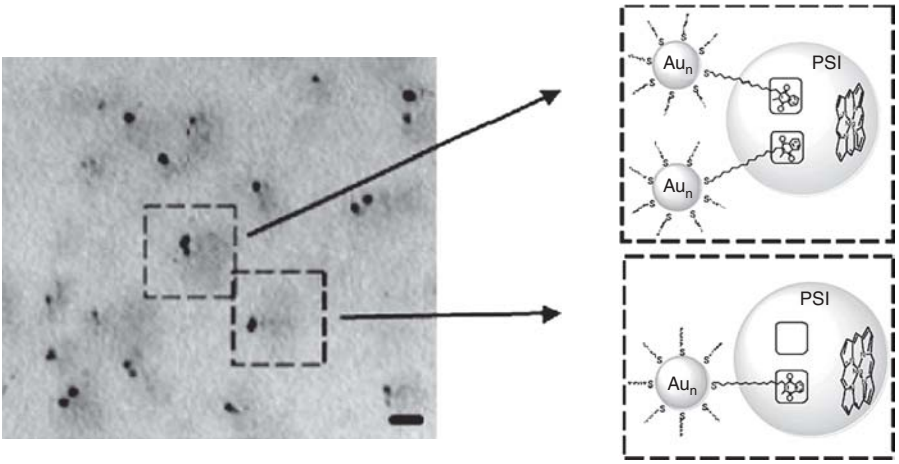

FIGURE 18. TEM images of **NQC15S-AuNP@PSI**. The scale bar is 10 nm. (Reprinted with permission from Ref. 15.)

B. Biophotoelectrode Composed of Cyanobacterial Photosystem I and Molecular Wires

The previous section described the connection of a biocomponent PSI to a gold nanoparticle-attached molecular wire with a methylnaphthoquinone moiety to construct a photosensor. In this section, we present a combination of this technique, to connect PSI to an artificial molecular wire, with the technique used for ITO modification with molecular wires described earlier for the development of a biophotoelectrode.

The new molecular wire (**tpy-C_{15}NQ**) designed for the biophotoelectrode is a compound with a chemical structure similar to VK_1, possessing a naphthoquinone moiety for insertion into the quinone pocket of PSI and a terpyridine moiety for connecting to a Co(II) ion at the surface of a modified ITO.[16] Reconstitution of PSI with **tpy-C_{15}NQ** in a similar manner to that shown earlier afforded **tpy-C_{15}NQ@PSI**, for which photoactivity was confirmed by the absorption change of P700,[15] thus indicating that the 2-methyl-1,4-naphthoquinone moiety of **tpy-C_{15}NQ** fitted into the quinone pocket of PSI and worked as a mediator of the electron transport system in PSI.

We fabricated a PSI-immobilized ITO electrode, **PSI_tpy-C_{15}NQ_ITO**, by a combination of SAM formation with a terpyridine derivative and stepwise metal-terpyridine coordination reactions in a similar manner as given earlier (Fig. 19). First, a cleaned ITO electrode was immersed in a chloroform solution of 0.1 mM *p*-terpyridylbenzoic acid for 12 h at 25°C. Next, the modified ITO electrode was immersed in 0.1 M $CoCl_2$*aq* for 0.5 h at 25°C, which formed

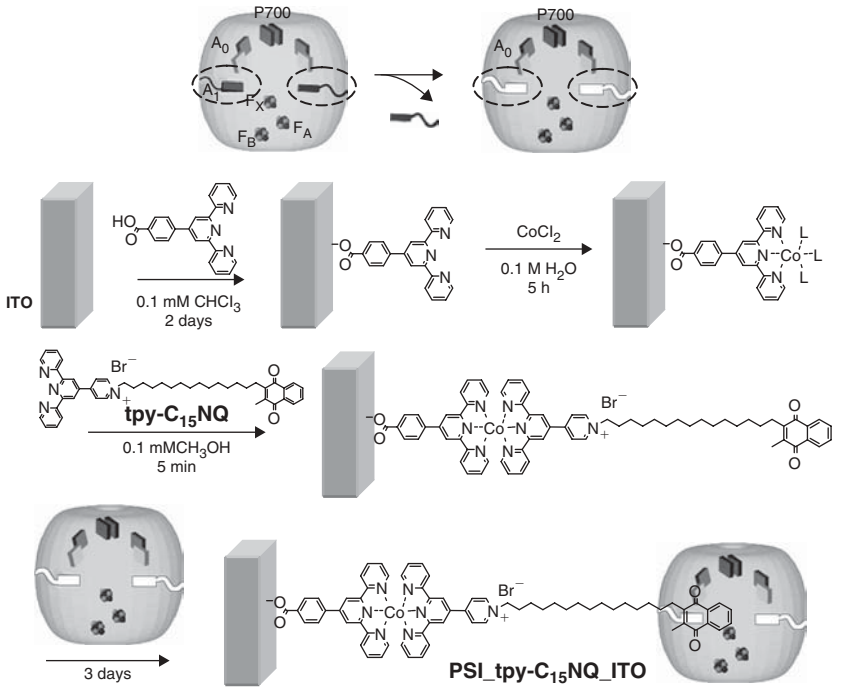

FIGURE 19. The procedure for the immobilization of VK_1-free PSI onto **tpy-C_{15}NQ**-modified ITO electrode.

metal complexation. The modified ITO electrode was then immersed in a 0.1 mM methanol solution of **tpy-C_{15}NQ** for 5 min. Finally, the modified ITO electrode was immersed in an aqueous solution of 1 μg/mL VK_1-free PSI containing an MES buffer, thereby yielding the reconstituted ITO electrode (**PSI_tpy-C_{15}NQ_ITO**).

The absorption spectrum of **PSI_tpy-C_{15}NQ_ITO** was nearly identical to that of the native PSI solution (Fig. 20); however, the λ_{max} value of the *Q* band of chlorophylls (~690 nm) was ~11 nm red shifted due to the oriented aggregation of PSI onto the ITO electrode.

Figure 21 displays photocurrent responses and a photocurrent action spectrum of **PSI_tpy-C_{15}NQ_ITO** at −0.05 V vs. Ag/AgCl in the presence of NaAs as a sacrificial reagent and DCIP as a mediator in a MES-NaOH (pH 6.4) buffer solution containing $NaClO_4$ as an electrolyte. The action spectrum shows a maximum around 660−680 nm, approximately corresponding with the absorption spectrum of PSI and indicating that photocurrent responses were due to the photoexcitation of PSI.

In this section, we have shown two types of biophotonic systems using PSI and molecular wires. The first type uses a combination of PSI, molecular

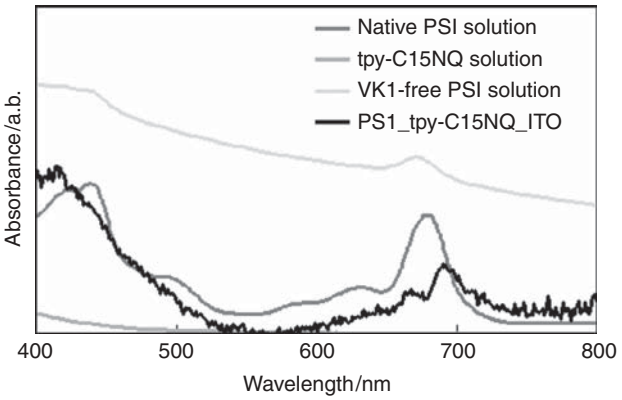

FIGURE 20. Visible light absorption spectra of PSI solutions and **PSI_tpy-C_{15}NQ_ITO**.

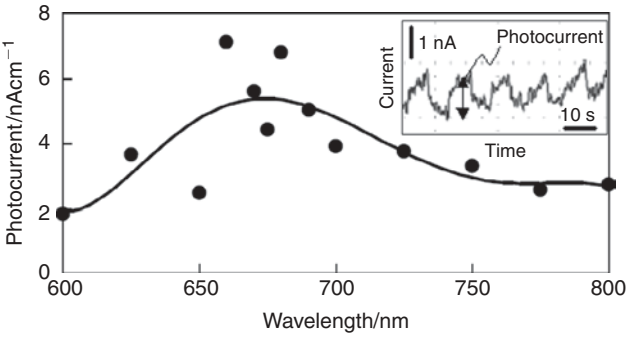

FIGURE 21. Current response under 660 nm light irradiation (*inset*) and a photocurrent action spectrum upon **PSI_tpy-C_{15}NQ_ITO** in a MES-NaOH (pH 6.4) buffer solution containing 50 mM NaAs, 2.5 mM DCIP, and 100 mM $NaClO_4$ at $E=-0.05$ V vs. Ag/AgCl.

wire, gold nanoparticle, and transistor gate to fabricate a photosensor. Molecular recognition of PSI enabled its connection with a molecular wire, leading to the stable photoresponse of the biophotosensor. The final goal of this system is to sense a small number of photons by using the single-electron transferability of a gold nanoparticle. The second type demonstrates a new method for the immobilization of PSI on ITO, which would be useful in the construction of a photovoltaic cell because the simple solution immersion method can use any electrodes with different shapes and areas. Both topics demonstrate that bioconjugation and the surface bottom-up fabrication of molecular wires are useful approaches in the development of biomolecular devices.

V. CONCLUSION

In this chapter, we presented three different systems of molecular assemblies using molecular wires. The first involved the fabrication of the molecular wire system with metal complex oligomer or polymer wires composed of bis(terpyridine)metal complexes using the bottom-up method. This system showed characteristic electron transfer distinct from conventional redox polymers. The second involved the fabrication of a photoelectric conversion system using ITO electrodes modified with porphyrin-terminated bis(terpyridine)metal complex wires by the stepwise coordination method, which demonstrated that the electronic nature of the molecular wire is critical to the photoelectron transfer from the porphyrin to ITO. This system proposed a new, facile fabrication method of molecular assemblies effective for photoelectron transfer. The third involved the fabrication of a bioconjugated photonic system composed of molecular wires and photosystem I. The feasibility of the biophotosensor and the biophotoelectrode has been demonstrated. This system proposed that the bioconjugation and the surface bottom-up fabrication of molecular wires are useful approaches in the development of biomolecular devices. These three systems of molecular assemblies will provide unprecedented functional molecular devices with desired structures and electron transfer control.

VI. REFERENCES

1. ITRS, *Lithography*, available at www.itrs.net/Links/2007ITRS/2007_Chapters/2007_Lithography.pdf (2007).
2. H. Imahori, H. Norieda, H. Yamada, Y. Nishimura, I. Yamada, Y. Sakata, S. Fukuzumi, *J. Am. Chem. Soc.,* **123,** *100* (2001).
3. H. Imahori, D. M. Guldi, K. Tamaki, Y. Yoshida, C. Luo, Y. Sakata, S. Fukuzumi, *J. Am. Chem. Soc.,* **123,** *6617* (2001).
4. S. Zhang, C. M. Cardona, L. Echegoyen, *Chem. Commun.,* **43,** *4461* (2006).
5. Y. Xiao, F. Patolsky, E. Katz, J. F. Hainfeld, I. Willner, *Science,* **299,** *1877* (2003).
6. O. Lioubashevski, V. I. Chegel, F. Patolsky, E. Katz, I. Willner, *J. Am. Chem. Soc.,* **126,** *7133* (2004).
7. G. C. Dismukes, *Science,* **292,** *447* (2001).
8. A. W. Rutherford, A. Boussac, *Science,* **303,** *1782* (2004).
9. H. Fukuzawa, E. Suzuki, Y. Komukai, S. Miyachi, *Proc. Natl. Acad. Sci. U. S. A.,* **89,** *4437* (1992).
10. I. B. Frank, P. Lundgren, Y. B. Chen, H. Küpper, Z. Kolber, B. Bergman, P. Falkowski, *Science,* **294,** *1534* (2001).
11. K. Kanaizuka, M. Murata, Y. Nishimori, I. Mori, K. Nishio, H. Masuda, H. Nishihara, *Chem. Lett.,* **34,** *534* (2005).
12. Y. Nishimori, K. Kanaizuka, M. Murata, H. Nishihara, *Chem. Asian J.,* **2,** *367* (2007).

13. H. Nishihara, K. Kanaizuka, Y. Nishimori, Y. Yamanoi, *Coord. Chem. Rev.,* **251,** *2674* (2007).
14. M. Miyachi, M. Ohta, M. Nakai, Y. Kubota, Y. Yamanoi, T. Yonezawa, H. Nishihara, *Chem. Lett.,* **37,** *404* (2008).
15. N. Terasaki, N. Yamamoto, K. Tamada, M. Hattori, T. Hiraga, A. Tohri, I. Sato, M. Iwai, M. Iwai, S. Taguchi, I. Enami, Y. Inoue, Y. Yamanoi, T. Yonezawa, K. Mizuno, M. Murata, H. Nishihara, S. Yoneyama, M. Minakata, T. Ohmori, M. Sakai, M. Fujii, *Biochim. Biophys. Acta,* **1767,** *653* (2007).
16. M. Miyachi, Y. Yamanoi, T. Yonezawa, H. Nishihara, M. Iwai, M. Konno, M. Iwai, Y. Inoue, *J. Nanosci. Nanotech*, **9,** *1722* (2009).
17. P. G. Pickup, R.W. Murray, *J. Electrochem. Soc.,* **131,** *833* (1984).
18. H. C. Hurrell, H.D. Abruña, *Inorg. Chem.,* **29,** *736* (1990).
19. J. Ochmanska, P.G. Pickup, *J. Electroanal. Chem.,* **297,** *197* (1991).
20. S. S. Zhu, T.M. Swager, *J. Am. Chem. Soc.* **119,** *12568* (1997).
21. P. G. Pickup, R.W. Murray, *J. Am. Chem. Soc.,* **105,** *4510* (1983).
22. P. G. Pickup, W. Kutner, C. R. Leidner, R. W. Murray, *J. Am. Chem. Soc.,* **106,** *1991* (1984).
23. E. D. Chidsey, R. W. Murray, *J. Phys. Chem.,* **90,** *1479* (1986).
24. J. Hjelm, R. W. Handel, A. Hagfeldt, E. C. Constable, C. E. Housecraft, R. J. Forster, *Inorg. Chem.,* **44,** *1073* (2005).
25. G. Zotti, G. Schiavon, S. Zecchin, A. Berlin, G. Pagani, A. Canavesi, *Synth. Met.,* **76,** *255* (1996).
26. J. Ochmanska, P. G. Pickup, *J. Electroanal. Chem.,* **297,** *197* (1991).
27. S. S. Zhu, T. M. Swager, *J. Am. Chem. Soc.,* **119,** *12568* (1997).
28. H. J. Dahms, *Phys. Chem.,* **72,** *362* (1968).
29. I. Ruff, V. J. Friedrich, *J. Phys. Chem.,* **76,** *162* (1972).
30. D. N. Blauch, J.-M. Savéant, *J. Am. Chem. Soc.,* **114,** *3323* (1992).
31. P. Daum, J. R. Lenhard, D. Rolison, R. W. Murray, *J. Am. Chem. Soc.,* **102,** *4649* (1980).
32. K.-N. Kuo, R. W. Murray, *J. Electroanal. Chem.,* **131,** *37* (1982).
33. P. Burgmayer, R. W. Murray, *J. Electroanal. Chem.,* **135,** *335* (1982).
34. S. Nakahama, R. W. Murray, *J. Electroanal. Chem.,* **158,** *303* (1983).
35. K. Sigehara, N. Oyama, F. C. Anson, *J. Am. Chem. Soc.,* **103,** *2552* (1981).
36. C. R. Martin, I. Rubinstein, A. J. Bard, *J. Am. Chem. Soc.,* **104,** *4817* (1982).
37. H. S. White, J. Leddy, A. J. Bard, *J. Am. Chem. Soc.,* **104,** *4811* (1982).
38. L. Roullier, E. Waldner, E. Laviron, *J. Electroanal. Chem.,* **139,** *199* (1982).
39. L. Roullier, E. Waldner, *J. Electroanal. Chem.,* **187,** *97* (1985).
40. J. G. Eaves, H. S. Munro, D. Parker, *Inorg. Chem.,* **26,** *644* (1987).
41. R. A. Saraceno, G. H. Riding, H. R. Allcock, A. G. Ewing, *J. Am. Chem. Soc.,* **110,** *7254* (1988).
42. A. J. Bard, L. R. Faulkner, *Electrochemical Methods: Fundamentals and Applications,* 2nd ed., Wiley, New York, 2001.
43. D. Chen, G. Wang, J. Li, *J. Phys. Chem. C,* **111,** *2351* (2007).
44. K. Kinbara, T. Aida, *Chem. Rev.,* **105,** *1377* (2005).
45. E. Katz, I. Willner, *Angew. Chem. Int. Ed.,* **43,** *6042* (2004).
46. C. M. Niemeyer, *Angew. Chem. Int. Ed.,* **40,** *4128* (2001).
47. R. Emerson, R. V. Chalmers, C. Cederstand, *Proc. Natl. Acad. Sci. U.S.A.,* **43,** *133* (1957).

48. R. Emerson, R. V. Chalmers, C. Cederstand, M. Brody, *Science,* **123,** *673* (1956).
49. A. F. Janzen, M. Seibert, *Nature,* **286,** *584* (1980).
50. R. Bhardwaj, R. L. Pan, E. L. Gross, *Nature,* **289,** *396* (1981).
51. I. Lee, J. W. Lee, E. Greenbaum, *Phys. Rev. Lett.,* **79,** *3294* (1997).
52. E. Katz, *J. Electroanal. Chem.,* **365,** *157* (1994).
53. B. S. Ko, B. Babcock, G. K. Jennings, S. G. Tilden, R. R. Peterson, D. Cliffel, E. Greenbaum, *Langmuir,* **20,** *4033* (2004).
54. B. S. Ko, B. Babcock, G. K. Jennings, S. G. Tilden, R. R. Peterson, D. Cliffel, *Langmuir,* **20,** *4033* (2004).
55. M. Ciobanu, H. A. Kincaid, G. K. Jennings, D. E. Cliffel, *Langmuir,* **21,** *692* (2005).
56. H. A. Kincaid, T. Niedringhaus, M. Ciobanu, D. E. Cliffel, G. K. Jennings, *Langmuir,* **22,** *8114* (2006).
57. M. Ciobanu, H. A. Kincaid, V. Lo, A. D. Dukes, G. K. Jennings, D. E. Cliffel, *J. Electroanal. Chem.,* **599,** *72* (2007).
58. T. Yamaoka, K. Satoh, S. Satoh, *Plant Cell Physiol.,* **19,** *943* (1978).
59. H. Koike, K. Satoh, S. Katoh, *Plant Cell Physiol.,* **23,** *293* (1982).
60. B. L. Epel, J. Neumann, *Biochim. Biophys. Acta,* **325,** *520* (1973).
61. M. Iwaki, S. Ito, *FEBS Lett.,* **256,** *11* (1989).
62. P. Fromme, P. Jordan, N. Krauβ, *Biochim. Biophys. Acta,* **1507,** *5* (2001).
63. K. Brettel, *Biochim. Biophys. Acta,* **1318,** *322* (1997).
64. S. Bahatyrova, R. N. Frese, C. A. Siebert, J. D. Olsen, K.O. van der Werf, R. van Grondelle, R. A. Niederman, P. A. Bullough, C. Otto, C.N. Hunter, *Nature,* **430,** *1058* (2004).
65. A. Ben-Shem, F. Frolow, N. Nelson, *Nature,* **426,** *630* (2003).
66. C. W. Mullineaux, M. J. Tobin, G. R. Jones, *Nature,* **390,** *421* (1997).
67. P. Jordan, P. Fromme, H. T. Witt, O. Klukas, W. Saenger, N. Krauβ, *Nature,* **411,** *909* (2001).
68. S. Chen, R. S. Ingram, M. J. Hostetler, J. J. Pietron, R. W. Murray, T. G. Schaaff, J. T. Khoury, M. M. Alvarez, R. L. Whetten, *Science,* **280,** *2098* (1998).

Index

Macromolecules Containing Metal and Metal-like Elements,
Volume 10: Photophysics and Photochemistry of Metal-Containing Polymers,
Edited by Alaa S. Abd-El Aziz, Charles E. Carraher Jr., Pierre D. Harvey, Charles U. Pittman Jr., Martel Zeldin.